Copy No. _____

Defence Research and Development Canada
Recherche et développement pour la défense Canada

DEFENCE R&D DÉFENSE

Experimental investigation of the strength of damaged pressure hulls – Phases 5 & 6

The influence of out-of-circularity on collapse

John R. MacKay

Defence R&D Canada – Atlantic

Technical Memorandum
DRDC Atlantic TM 2010-239
March 2011

Canada

This page intentionally left blank.

Experimental investigation of the strength of damaged pressure hulls - Phases 5 & 6

The influence of out-of-circularity on collapse

John R. MacKay

Defence R&D Canada – Atlantic

Technical Memorandum
DRDC Atlantic TM 2010-239
March 2011

Principal Author

Original signed by John R. MacKay

John R. MacKay

Defence Scientist, Warship Performance Section

Approved by

Original signed by Neil G. Pegg

Neil G. Pegg

Head, Warship Performance Section

Approved for release by

Original signed by Ron Kuwahara for

Calvin V. Hyatt

Chair, Document Review Panel

Abstract

Collapse tests were performed on twelve small-scale ring-stiffened cylinders. The test specimens were machined from aluminium tubing, and then mechanically deformed in order to introduce more realistic levels of out-of-circularity (OOC) in the critical collapse mode. Six of the test specimens had additional damage in the form of artificial corrosion thinning, which was introduced by machining away some of the shell plating. Corrosion damage was found to affect the strength of cylinders in different ways, depending on its orientation with respect to the OOC shape. When the corrosion damage was aligned with an inward lobe of the applied OOC shape, the effects of thinning and imperfections were additive and led to significant decreases in collapse pressure. When the hull thinning was collocated with outward OOC lobes, the corrosion damage tended to reduce the overall OOC, and only a small reduction in collapse pressure was noted, primarily due to the high stresses in the thinned shell itself. Finite element models were used to simulate the mechanical procedure used to apply OOC to the cylinders. The predicted residual stress field was in the elastic range of the material, and subsequent collapse analysis indicated that those residual stresses resulted in a 3% reduction in collapse pressure compared to a stress-relieved model. It is not thought that residual stresses have significantly affected the collapse behaviour of the actual test specimens. Finite element models based on the measured shape and material properties of forty specimens tested in the current and previous testing phases were able to predict the experimental collapse pressures with an accuracy of 9.5%, with 95% confidence.

Résumé

Douze cylindres à petite échelle, renforcés d'anneaux ont été soumis à des essais d'affaissement. Les éprouvettes étaient des tubes d'aluminium usinés puis mécaniquement déformés afin de leur donner un niveau plus réaliste d'ovalisation en mode d'affaissement critique. Des dommages supplémentaires ont été infligés à six des cylindres d'essai, sous forme d'amincissement par corrosion artificielle, réalisée par un usinage d'érosion du bordé extérieur. Les dommages associés à la corrosion ont eu des effets différents sur la résistance des cylindres, selon l'orientation de la corrosion par rapport à l'ovalisation. Lorsque la corrosion suivait la ligne du bossage intérieur de l'ovalisation, les effets de l'amincissement et des imperfections étaient cumulatifs et ont conduit à d'importantes réductions de la pression d'affaissement. Lorsque l'amincissement de la coque était au même endroit que les lignes de bossage extérieures de l'ovalisation, les dommages attribuables à la corrosion avaient tendance à amener une réduction généralisée de l'ovalisation. On n'a remarqué qu'une faible réduction de la pression d'affaissement, due essentiellement au niveau élevé de contraintes sur le bordé aminci. On a utilisé un nombre défini de modèles d'éléments pour simuler la procédure mécanique d'ovalisation des cylindres. Le champ de contrainte résiduelle s'inscrivait dans la zone d'élasticité du matériau et les analyses subséquentes de l'affaissement indiquaient que ces contraintes résiduelles causaient une réduction de 3 % de la pression d'affaissement par rapport au modèle stabilisé (sans contrainte). On ne pense pas que les contraintes résiduelles ont eu une incidence marquée sur le comportement à l'affaissement des éprouvettes. Le nombre défini de modèles d'éléments basés sur la forme mesurée et les propriétés du métal de quarante spécimens soumis à l'essai, à l'étape actuelle et aux étapes précédentes, ont permis de prédire les pressions d'affaissement expérimentales avec une précision de 9,5 % et un degré de confiance de 95 %.

This page intentionally left blank.

Executive summary

Experimental investigation of the strength of damaged pressure hulls - Phases 5 & 6: The influence of out-of-circularity on collapse

J.R. MacKay; DRDC Atlantic TM 2010-239; Defence R&D Canada – Atlantic; March 2011.

Introduction: The governments of Canada and the Netherlands have jointly sponsored an experimental program to investigate the impact of corrosion damage on the structural capacity of submarine pressure hulls. The end goal of the program is to generate corrosion tolerance guidelines that can be used by engineers to make informed maintenance decisions for the Victoria and Walrus class submarines. Earlier stages of the test program studied the effect of corrosion thinning on pressure hulls using small-scale ring-stiffened cylinders. Those test specimens were machined from aluminium tubing in order to isolate the effect of corrosion from other factors, such as residual stresses and large-amplitude out-of-circularity (OOC). The current technical memorandum summarizes collapse tests on six intact and six corroded cylinder specimens that were intentionally deformed after machining in order to introduce more realistic levels of OOC.

Results: Corrosion damage was found to affect the strength of cylinders in different ways, depending on its orientation with respect to the OOC shape. When the corrosion damage was aligned with an inward lobe of the applied OOC shape, the effects of thinning and imperfections were additive and led to significant decreases in collapse pressure. When the hull thinning was collocated with outward OOC lobes, the corrosion damage effectively reduced the overall OOC, and only a small reduction in collapse pressure was noted, primarily due to the high stresses in the thinned shell itself. Numerical models of forty specimens tested in the current and previous testing phases were able to predict the experimental collapse pressures with an accuracy of 9.5%, with 95% confidence.

Significance: The current work highlights the importance of the interaction of corrosion damage with the actual shape of the pressure hull. When assessing corrosion damage to real submarines, it is necessary to model the true shape of the hull, and the correct orientation of the thinning with respect to that shape. The out-of-circularity that was applied to the test specimens can be viewed as a form of severe denting damage, and thus the cylinders with corrosion thinning had multiple damage cases. While there was found to be significant interaction between the two types of damage, it appears that in the worst case, the total impact of the damage is approximately equal to the sum of the denting and hull thinning acting independently.

Future plans: Collapse testing for the final stage of this experimental program has already been completed. Phase 7 included the testing of as-machined cylinders with multiple corrosion patches. In some cases the corrosion patches were randomly arranged, while in others the patches were intentionally distributed to align with the critical n=3 collapse mode. Analysis of the experimental data is still required, as are numerical simulations of the collapse tests. Following those tasks, DRDC`s effort will be directed at using numerical models to develop corrosion tolerance guidelines for pressure hulls.

Sommaire

Experimental investigation of the strength of damaged pressure hulls - Phases 5 & 6: The influence of out-of-circularity on collapse

J.R. MacKay; DRDC Atlantic TM 2010-239; R & D pour la défense Canada – Atlantique; Mars 2011.

Introduction : Les gouvernements du Canada et des Pays-Bas ont conjointement commandité un programme d'expérimentation visant à déterminer l'incidence des dommages attribuables à la corrosion sur la capacité structurelle des coques épaisses de sous-marin. L'objectif ultime du programme est d'élaborer des lignes directrices concernant la tolérance à la corrosion qui permettraient aux ingénieurs de prendre des décisions éclairées quant à la maintenance des sous-marins des classes VICTORIA et WALRUS. Les premières étapes du programme d'essai portaient sur l'étude des effets de l'amincissement dû à la corrosion sur les coques épaisses. Cette étude a été faite sur des cylindres en aluminium de petite échelle et renforcés par des anneaux. Ces éprouvettes sont des tubes d'aluminium usinés de manière à isoler les facteurs attribuables à la corrosion des autres facteurs tels que les contraintes résiduelles et l'ovalisation de grande amplitude. Le document technique résume les essais d'affaissement effectués sur six éprouvettes intactes et sur six éprouvettes corrodées, déformées intentionnellement après avoir été usinées de manière à présenter un niveau plus réaliste d'ovalisation.

Résultats : L'incidence de la corrosion sur la résistance des cylindres varie selon son orientation par rapport à l'ovalisation. Lorsque les dommages attribuables à la corrosion sont en ligne avec le bossage intérieur de la déformation, les effets de l'amincissement et des imperfections sont cumulatifs et conduisent à des diminutions considérables de la pression d'affaissement. Par contre, lorsque l'amincissement de la coque se situe au niveau des bosses extérieures de la déformation, les dommages dus à la corrosion ont pour effet d'atténuer l'ensemble de l'ovalisation. On n'a relevé qu'une petite réduction de la pression d'affaissement due essentiellement aux fortes contraintes s'exerçant sur le bordé aminci même. Une modélisation numérique des quarante éprouvettes soumises à l'essai au cours de la phase actuelle et des phases précédentes a permis de prédire les pressions d'affaissement expérimentales avec une précision de 9,5 % et un degré de confiance de 95 %.

Importance : Les travaux en cours soulignent l'importance de la corrélation entre les dommages attribuables à la corrosion et la forme réelle de la coque épaisse. L'évaluation des dommages dus à la corrosion sur les véritables coques de sous-marins nécessite une modélisation de la forme réelle de la coque et l'orientation correcte de l'amincissement en fonction de cette forme. L'ovalisation appliquée aux éprouvettes peut être considérée comme un bosselage sévère, ainsi les cylindres corrodés présentaient plusieurs cas de dommages. Bien qu'une corrélation importante ait été relevée entre les deux types de dommages, il semble que dans le pire des cas, l'incidence totale des dommages soit à peu près égale à la somme des effets distincts du bosselage et de l'amincissement de la coque.

Perspectives : L'essai d'affaissement de l'étape finale de ce programme expérimental est déjà terminé. La phase 7 comprenait l'essai de cylindres usinés tels quels avec plusieurs plaques de corrosion. Dans certains cas, les plaques de corrosion avaient été arrangées de façon aléatoire, alors que dans d'autres elles avaient été placées de manière à être en ligne avec le mode d'affaissement critique n=3. L'analyse des données expérimentales reste à faire, ainsi que les simulations numériques des essais d'affaissement. Ceci fait, RDDC concentrera ses efforts sur l'utilisation de modèles numériques pour élaborer des lignes directrices concernant la tolérance à la corrosion des coques épaisses.

This page intentionally left blank.

Table of contents

List of figures

List of tables

This page intentionally left blank.

Acknowledgements

The experimental program described herein and in previous technical memorandums [1]-[4] is a collaborative effort of DRDC Atlantic and the Netherlands Ministry of Defence. This work falls under a Memorandum of Understanding between Canada and the Netherlands that allows the exchange of information pertaining to the design of surface ships and submarines [5].

The author would like to thank DRDC's partners in the Netherlands, especially Mr. Adrian van der Made of the Ministry of Defence, and Mr. Wim Trouwborst and Mr. André Glas of TNO for their many contributions to this collaborative project. Furthermore, the author thanks the Submarine Scientific Support Service Level Agreement for providing financial support; DRDC Atlantic technologists Mr. Alex Ritchie and Mr. Dave Wright for their efforts in preparing, trouble-shooting and undertaking the experimental pressure testing program; the DRDC Atlantic Mechanical Services group for their technical support and use of their pressure testing facility; the DRDC Atlantic Prototype Development and Corrosion and Metallurgy groups for preparing and testing tensile coupon samples; also, Dr. Neil Pegg and Dr. Malcolm Smith of DRDC Atlantic, and Dr. Fred van Keulen and Mr. Theo Bosman of the Delft University of Technology, for meaningful discussions regarding this work.

This page intentionally left blank.

1 Introduction

The effect of corrosion-induced pressure hull thinning on the structural capacity, and the related operational capability, i.e. deep diving depth (DDD), of in-service Canadian submarines is typically addressed using numerical models, especially nonlinear finite element (FE) modeling [6]. The FE results are interpreted with a large degree of conservatism; for example, by calculating the percent reduction in collapse pressure due to hull thinning using numerical models and applying that reduction to the design formulae collapse pressures that are used to determine DDD. That conservatism is required since, until recently [7],[8] the numerical models had not been validated against experimental results and there was no certainty that they correctly captured the structural response of the corroded hull.

The challenge of assessing the strength of the damaged hull can be avoided by repairing the corrosion damage. Weld overlay is currently used to repair corrosion pits on submarine hulls, and in the future it may prove to be a cost effective way to restore hull thickness that has been lost due to larger patches of general corrosion damage; however, the secondary effects of weld repair over large areas, especially residual stresses and distortions, are not well understood, and the limitations of the method are not yet known [9]. Until those issues are addressed, it will be necessary to operate submarines with unrepaired general corrosion damage, which requires reliable assessments of the damaged hull capacity. Furthermore, weld repairs affect hull maintenance budgets and scheduling, so that corrosion tolerance guidelines are required to facilitate repair decisions. Those guidelines must consider a range of corrosion depths, areas and locations, and can only be generated in a practical way by performing a series of numerical analyses.

The test results presented in the current technical memorandum are part of a larger experimental program that was initiated to address the lack of experimental data available in the literature for the collapse of pressure hulls with corrosion damage [10]. The overall goals of the testing program are to study the structural behaviour of damaged hulls, including a qualitative understanding of the collapse mechanisms involved and a quantitative description of the reductions in collapse pressure that can be expected for a given magnitude of thinning. Furthermore, the test program was designed to facilitate comparisons between experimental and numerical models, with the goal of validating the numerical methodology for future assessments of damaged submarines and for generating corrosion tolerance guidelines.

The test specimens are small-scale submarine pressure hulls, consisting of ring-stiffened cylinders machined from aluminium tubing and tested to collapse under external hydrostatic pressure. Corrosion damage is artificially introduced in selected models by machining away material from the shell or ring-stiffeners. Some of the test models from previous phases of testing are shown in Figure 1.

Phases 1-3 of the testing program [1]-[3] were aimed at studying the influence of corrosion depth and area on the most important failure modes for pressure hulls: interframe collapse of the hull plating between ring-stiffeners and overall collapse of an entire compartment. Those experiments indicated that hull thinning reduces collapse pressures by hastening the onset of yielding in the damaged shell. Early yielding is caused by high stresses in the corroded shell that arise due to the reduced hull cross-section, which must resist the same loading as the intact regions of the hull.

Furthermore, one-sided thinning of the hull results in a load-path eccentricity since the mid-planes of the corroded and intact regions of the shell are offset. The shell eccentricity leads to local bending moments and stresses at the corroded shell, further hastening the onset of local shell yielding, and leading to a more general destabilizing bending moment acting on the overall shell-stiffener section.

Figure 1: Some typical experimental models from previous phases of testing [10], before and after collapse testing. Clockwise from top-left: L510-No12, an internally-stiffened cylinder with a large patch of corrosion thinning, after volume-control testing; L510-No6, an intact internally-stiffened cylinder after volume-control testing, showing interframe dimples superimposed on an overall collapse mode; L510-No2, before testing, showing dog-bone stiffener corrosion at inset; L300-No4, a short cylinder with heavy stiffeners and a small patch of shell corrosion, showing the specimen after testing with a conventional apparatus; L300-No1, a short intact cylinder failing by interframe collapse, and showing the specimen after testing with a volume-control apparatus.

In [1]-[3], overall collapse was found to be more greatly affected by corrosion thinning than interframe collapse. This is due to the reserve strength of the heavy ring-stiffeners found in interframe models, which were able to carry the load shed by the corroded shell when it failed locally, and because the models failing by overall collapse were more sensitive to the shell eccentricity due to one sided thinning. That eccentricity has a similar effect on overall collapse as an out-of-circularity imperfection. The ratio of the percent reduction in overall collapse pressure to the percent hull thinning was found to be approximately one-to-one.

Phase 4 of the testing program [4] examined the influence of material properties, especially yield strength, on overall collapse of damaged and intact models, as well as the effect of cyclic pressure loading past the yield limit. The relationship between yield stress and overall collapse pressure was found to be approximately linear in the range of yield stresses considered, so that a 10% increase in yield stress results in an 8-9% increase in collapse pressure. That relationship holds for both intact and corroded models. Constant amplitude cyclic loading of a corroded cylinder past the yield limit did not apparently affect the collapse strength of that model, despite the growth in permanent deformation with each load cycle.

In Phases 1-4 of the overall experimental program, the effects of corrosion thinning were studied in isolation from other strength-reducing factors arising from fabrication of real pressure hulls; these include large-amplitude out-of-circularity (OOC) and residual stresses caused by welding and cold bending of hull plating and stiffeners. This was accomplished by machining the test specimens from aluminium tubing, resulting in ring-stiffened cylinders with very small magnitudes of OOC. Residual stresses arising from the manufacture of the extruded aluminium tubing from which the cylinders were machined, and from the machining process itself, were considered to be negligible relative to residual stresses in real pressure hulls.

It is important to further develop understanding of the effect of corrosion damage on pressure hull collapse, and to provide additional test data for the validation of numerical models, which has already begun with the FE simulation of models from Phases 1 to 3 [7],[8]. The current technical memorandum presents test results from Phases 5 and 6 of the overall experimental program, whereby the corrosion study has been extended to cylinders with more realistic levels of out-of-circularity, based on standard design and fabrication tolerances. Phase 5 and 6 specimens were tested in the timeframe extending from January to June of 2009. Phase 5 saw the testing of six “intact” cylinders with large-amplitude out-of-circularity imperfections, which were introduced by mechanically deforming the models. Otherwise, the Phase 5 specimens were nominally identical to some of the models tested in Phases 2 and 3. In Phase 6, the OOC study was extended to six “damaged” models with artificial corrosion.

Numerical studies of the interaction between corrosion thinning and OOC [11] indicate that, in general, overall collapse pressure decreases with increasing depths of thinning; however, the effect of corrosion thinning was found to be dependent on its circumferential extent and its orientation with respect to out-of-circularity. The numerical models predicted that overall collapse strength does not monotonically decrease with the circumferential extent of thinning. The load-path eccentricity resulting from one-sided thinning effectively increases or decreases the imperfection magnitude depending on whether the corrosion is in-phase or out-of-phase with the OOC. This leads to cases whereby, as the thinning is extended around the cylinder, the collapse pressure actually increases relative to cases with smaller extents of thinning. In a similar manner, shell thinning that is out-of-phase with OOC (i.e. collocated with an outward bulge) can increase

the collapse pressure, while out-of-phase shell thickening can decrease the collapse pressure with respect to a similar intact model. Furthermore, shell thinning was found to have a greater effect on collapse strength for models having small magnitudes of OOC, due to its relatively greater influence on OOC. Phase 5 and 6 test specimens were designed to test the conclusions reached in [11], especially the interaction of corrosion damage with the shape and magnitude of out-of-circularity.

This technical memorandum begins with a description of the test models and experimental procedures in Sections 2 and 3, respectively. The experimental results for each of the twelve test models are presented in Section 4. Section 5 presents the results of finite element analyses aimed at simulating the collapse experiments. A general discussion is presented in Section 6, including trends observed in the experiments and the numerical modeling. Conclusions of the current study and the entire testing program to date are given in Section 7.

2 Test specimens

The twelve specimens tested during Phases 5 and 6 are listed in Table 1, along with the corresponding nominal out-of-circularity and corrosion damage, and the testing phase. The nominal specimen geometry is described in greater detail in Section 2.1. This includes the axisymmetric configuration, which is common to all Phase 5 and 6 specimens, the artificial corrosion damage, and the target out-of-circularity magnitudes and modes. The specimen fabrication methods, including the introduction of corrosion damage and out-of-circularity in the models, are also described in Section 2.1. The actual out-of-circularity shape and shell thickness of each specimen was characterized by taking measurements on each specimen. The results of those surveys are given in Section 2.2. Tensile testing was performed on coupons machined from each specimen after collapse testing; the material properties derived from those tests are reported in Section 2.2.3. The instrumentation plans, describing the location of strain gauges fixed to each cylinder, are presented in Section 2.4.

Table 1: Overview of Phase 5 and Phase 6 experimental specimens

Specimen Name	**Nominal Out-of-Circularity**[a]	**Artificial Corrosion Damage**[b]	**Status**
L510-No13	*n*=3, *m*=1, 0.5%	42x42x0.6 mm, out-of-phase	Tested in Phase 6
L510-No14	*n*=3, *m*=1, 0.5%	42x42x0.6 mm, in-phase	Tested in Phase 6
L510-No17	*n*=3, *m*=1, 0.3%	None	Tested in Phase 5
L510-No18	*n*=3, *m*=1, 0.3%	None	Tested in Phase 5
L510-No19	*n*=3, *m*=1, 0.5%	100x100x0.4 mm, in-phase	Tested in Phase 6
L510-No20	*n*=3, *m*=1, 0.5%	100x100x0.4 mm, in-phase	Tested in Phase 6
L510-No25	*n*=3, *m*=1, 0.5%	None	Tested in Phase 5
L510-No26	*n*=3, *m*=1, 0.5%	None	Tested in Phase 5
L510-No33	*n*=3, *m*=1, 0.5%	None	Tested in Phase 5
L510-No34	*n*=3, *m*=2, 0.3%	None	Tested in Phase 5
L510-No35	*n*=3, *m*=1, 0.5%	42x42x0.6 mm, in-phase	Tested in Phase 6
L510-No36	*n*=3, *m*=1, 0.5%	42x42x0.6 mm, out-of-phase	Tested in Phase 6

a. Out-of-circularity is defined by *n*, the number of complete waves about the circumference, *m*, the number of half waves over the cylinder length, and the maximum eccentricity relative to the shell radius.

b. Corrosion was applied to the outside of the shell in a rectangular area, orthogonal to ring-stiffeners and centred at mid-length of the cylinder. Corrosion is specified by the axial times the circumferential extents, times the depth of thinning. “In-phase” refers to corrosion patches that align with an inward lobe of the dominant OOC mode, while the corrosion is collocated with an outward lobe of the OOC for “out-of-phase” cases.

2.1 Specimen design and fabrication

2.1.1 Axisymmetric geometry and fabrication

Each of the Phase 5 and 6 specimens were machined on a CNC lathe from 6082-T6 aluminium alloy tubing. The CNC machining was performed by Gizom B.V. of the Netherlands. Figure 2 shows photographs of a typical intact specimen, L510-No25, before testing and before the strain gauges have been attached to the cylinder. Photographs of selected specimens after the strain gauges have been applied are shown in the description of the instrumentation in Section 2.4.

The nominal axisymmetric geometry, which is common to all Phase 5 and 6 specimens, is shown in Figure 3. Each of the cylinders has eight internal T-section ring-stiffeners uniformly distributed over the central region of the cylinder. The ring-stiffeners and shell were proportioned so that the cylinders would fail by overall elasto-plastic collapse of the shell and stiffeners. This required the bending stiffness of the stiffeners to be small, relative to the shell stiffness. The thick end rings and tapered end bays were designed to prevent undesired end bay failures and to provide enough material to secure the end caps with bolts.

Figure 2: Photographs of a typical intact specimen, L510-No25, before testing.

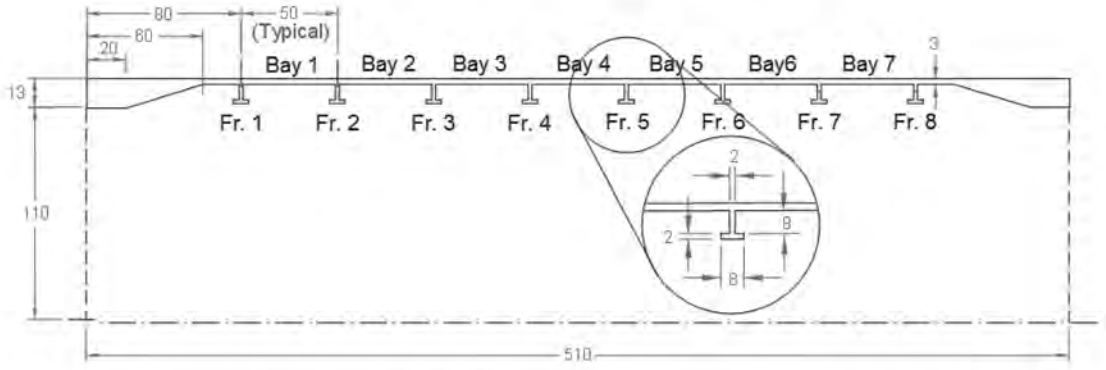

Figure 3: Nominal axisymmetric geometry (mm) of all Phase 5 and 6 specimens

2.1.2 Artificial corrosion damage

Artificial corrosion damage was introduced into Phase 6 specimens after the axisymmetric structures were machined. Corrosion damage was simulated by machining away material on the outside of the cylinder shell, in square patches of uniform depth, centred at the mid-length of the cylinders. The corrosion machining was performed by the Electronic and Mechanical Support Division (DEMO) of the Delft University of Technology in the Netherlands. The nominal, or target, corrosion damage for each Phase 6 specimen is given in Table 1. For specimens L510-No13, L510-No14, L510-No35 and L510-No36, the corrosion spans approximately 85% of the central bay, with approximately 20% thinning. The corrosion patch for specimens L510-No19 and L510-No20 is shallower but larger in area, with approximately 13% thinning of the shell over one complete bay in the centre of the cylinder and two half-bays on either side. Photographs of typical damaged specimens before testing are shown in Figure 4. Each corrosion patch was aligned so that it was collocated with either an inward lobe ("in-phase") or an outward lobe ("out-of-phase") of the applied out-of-circularity mode. The orientation of the corrosion patch for each Phase 6 cylinder, with respect to the OOC shape, is given in Table 1.

2.1.3 Mechanical application of out-of-circularity

The design collapse pressure of a pressure hull is determined by assuming that the maximum out-of-circularity is equal to 0.005 times the hull radius [12], or in the common terminology, 0.5%. For overall collapse predictions, it is also assumed that the OOC is in the worst possible mode. Construction tolerances generally require the OOC of the as-built hull to be less than one-third of the design value, or approximately 0.17%. This allows for the growth of OOC in service, and also compensates for the OOC-like effect of internal decks and other secondary structure [12].

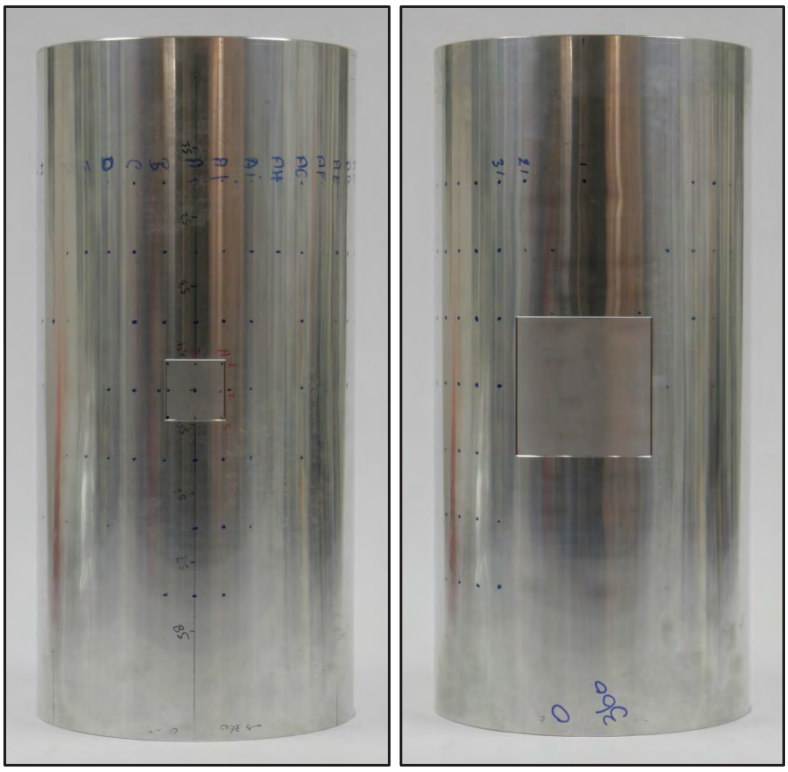

Figure 4: Photographs of typical damaged specimens before testing. Specimen L510-No13, with a small corrosion patch, is shown on the left, and specimen L510-No19, with a large corrosion patch, is shown on the right.

Measurements of test cylinders from previous phases, which were nominally identical to the Phase 5 and 6 specimens and were manufactured in the same way, show that the maximum OOC after machining was less than or equal to 0.12% [10]. That value is approximately 0.7 times the standard build tolerance and less than 0.25 times the design OOC magnitude. Thus, the OOC magnitude in the as-machined cylinders is somewhat less than for as-built hulls and significantly less than the design and through-life assumptions. Furthermore, the measured OOC was found to be dominated by the n=2 mode, where n is the number of complete imperfection waves about the circumference, while the critical shape for overall collapse predictions for the cylinders was n=3 [10].

The goal of Phase 5 and 6 testing was to study the collapse of intact and corroded cylinders with OOC in the critical n=3 mode, with magnitudes at either the design value of 0.5% or at an "in-service" value of 0.3%, approximately mid-way between the design and construction tolerances. Since the machining process results in a small OOC magnitude in the wrong mode, the cylinders were mechanically deformed to achieve the desired shapes.

The application of OOC to a cylinder involved placing it inside the triangular steel frame shown in Figure 5. The three bolts connecting the frame members were then tightened, resulting in applied forces and corresponding displacements at three points equally spaced around the

circumference. A trial and error process was used to determine the amount of bolt torque required to plastically deform the cylinders, as indicated by residual displacements after releasing the frame bolts. The process started at the central stiffeners and the desired shape of the entire cylinder was arrived at by incrementally increasing the permanent deformations at stations along the length of the cylinder. The OOC shape was characterized after each increment by mounting the cylinder on a lathe and using a dial gauge fixed to the machine to measure the radial eccentricity.

The targeted OOC mode shapes and magnitudes are given in Table 1. The desired longitudinal OOC shape was a half sine wave over the length of the cylinder, or m=1, for all of the cylinders except L510-No34. For that intact specimen, a full sine wave was applied over the length, i.e. m=2, so that the n=3 circumferential mode was offset by 60° at opposite ends of the cylinders.

Out-of-circularity was applied to damaged cylinders after the corrosion patches had been machined. For cylinders with in-phase corrosion damage, the corrosion patch was aligned with the triangular frame so that one of the reaction forces, and therefore one of the inward lobes of the OOC, was collocated with the centre of the patch. The cylinder position in the frame was offset by 60° for cylinders with out-of-phase corrosion. The corrosion patch in all damaged specimens, except L510-No13 and L510-No36, was in-phase with the out-of-circularity.

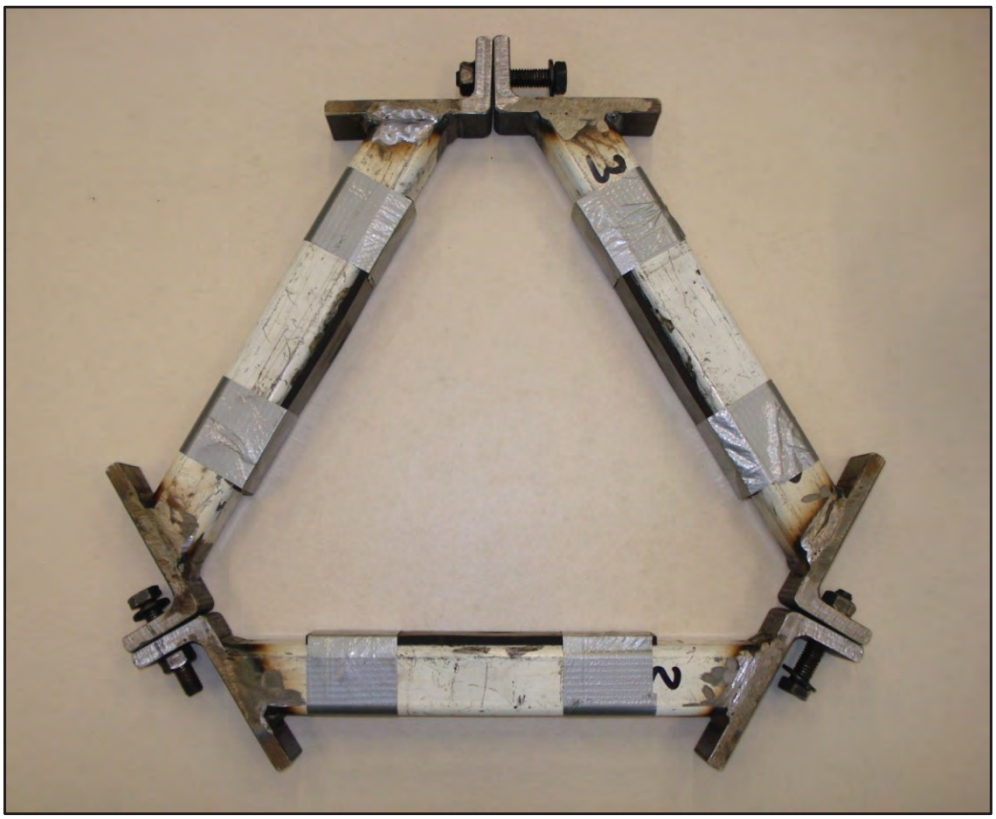

Figure 5: Frame apparatus used to mechanically apply out-of-circularity in the cylinder specimens.

The mechanical application of OOC necessarily results in residual stresses that are locked into the material after the frame load is released. Since those stresses could affect the strength of the cylinders in unknown ways, it was desired to have the specimens stress relieved. An additional cylinder, not listed in Table 1, was fabricated and subjected to the mechanical application of out-of-circularity in an n=3, m=1 mode. The specimen was subsequently heat treated in an attempt to relieve the residual stresses. The OOC of the cylinder was re-measured, and the post heat treatment shape was found to be in an n=2 mode with the amplitude gradually diminishing from one end of the cylinder to the other. The magnitude of OOC was also increased, especially at one end of the cylinder. It is not known what caused the distortions during heat treatment, but they may be related to non-uniform cooling of the cylinder. Since the original target OOC shape was lost, the cylinder was discarded, and the heat treatment was not applied to any of the other cylinders. Therefore, all Phase 5 and 6 cylinders had an unknown residual stress field before pressure testing.

2.2 Measured specimen geometry

The as-built geometries of the Phase 5 and the Phase 6 specimens were determined using different methods. Those methodologies are outlined below in Section 2.2.1, followed by a summary of the measurement results in Section 2.2.2. A comparison of different techniques for measuring out-of-circularity is presented in Section 2.2.3.

2.2.1 Methodology

2.2.1.1 Phase 5 specimens

Stork Intermes B.V. of the Netherlands used a coordinate-measuring machine (CMM) to measure the radius of the Phase 5 specimens at stiffener and mid-bay locations after the mechanical application of out-of-circularity. Measurements were taken at 36 circumferential locations (10° intervals) on both the inside and outside surfaces. This procedure allowed the out-of-circularity imperfections, the shell thickness at mid-bay and the combined stiffener-shell height to be derived. The rated accuracy of the CMM is ±0.0025 mm when using standard measurement probes; however, it has been estimated that the accuracy drops to ±0.02 mm when using the longer probes that were required to measure these cylinders.

The final out-of-circularity of Phase 5 specimens was also characterized using two other methods: by mounting the cylinders on a lathe and using a displacement gauge to measure the eccentricities on the outside of the shell at each stiffener location, and by using a chord gauge.

A chord gauge is an instrument used to measure the out-of-circularity in cylindrical structures. The gauge length is based on the nominal circumference of the cylinder and the desired number of measurements. For example, the chord gauge shown in Figure 6 was fabricated specifically for the cylinder specimens discussed herein, so that 18 measurements could be taken around the circumference. Displacement gauge readings, taken at equal intervals, are subtracted from the zero gauge reading, taken on a flat surface, giving the chord height at each location. The chord heights are then converted to radial eccentricities in the following manner. First, a Fourier decomposition of the chord heights is performed, yielding a set of Fourier coefficients describing

those data. Those coefficients are then multiplied by factors, based on the measurement angle and Fourier mode, giving a new set of coefficients that describes the radial eccentricities. The radial eccentricity at each chord gauge measurement location can then be calculated by expanding the Fourier series. A complete description of chord gauge theory and its accuracy is given in [13].

Chord gauge measurements were taken on Phase 5 cylinders after the application of OOC using the chord gauge shown in Figure 6. The dial gauge shown in that photograph was replaced by a digital displacement gauge having an accuracy of 0.0025 mm. Radial eccentricities were derived using a computer program called ChordGauge, written by Malcolm Smith of DRDC Atlantic and based on the theory in [13].

Figure 6: Chord gauge device used to measure the out-of-circularity of Phase 5 cylinder specimens.

2.2.1.2 Phase 6 specimens

The geometries of Phase 6 specimens were measured by TNO Built Environment and Geosciences, with support from Bosman Naval Engineering, both of the Netherlands. The measurement of Phase 6 cylinders, which is described in detail in [14], included characterization of the shell thickness using an ultrasonic thickness (UT) probe and of out-of-circularity using laser displacement gauges.

UT measurements were taken on each Phase 6 cylinder midway between the ring-stiffeners at seven axial and 36 circumferential locations. Additional UT readings were taken at the corrosion patches. A three-by-three measurement grid was used for the small patches on cylinders L510-No13, L510-No14, L510-No35and L510-No36, while the larger patches on specimens L510-No19 and L510-No20 were measured on a five-by-five grid. The rated accuracy of the UT probe is 0.001 mm; however, the curved surface of the cylinders resulted in some fluctuation of the third decimal place of the probe readout, so that the effective accuracy of the thickness measurements is 0.01 mm [14].

The out-of-circularity of Phase 6 specimens was measured using seven laser displacement gauges mounted in series on an aluminium frame. The cylinder specimens were rotated on a turntable, which was attached to the frame holding the gauges in such a way as to allow the distance between the gauges and the outside of the cylinders to be measured. The seven gauges were spaced 50 mm apart, so that all of the mid-bay locations could be measured at one time, or seven of the eight ring-stiffener locations. Three sets of measurements were taken on each specimen: all mid-bay locations, stiffeners one through seven, and stiffeners two through eight. The measurements were repeated at least once at each location for verification.

A typical set of OOC measurements was taken by rotating the cylinder on the turntable while recording the laser displacement gauge data and the turntable angle, which was measured with potentiometers, at a sampling rate of 250 Hz. The gauge readings were later modified by subtracting the mean value for each circumferential location and multiplying by negative one to give the radial eccentricity. The data for each set was initially reduced by averaging the eccentricity value over one degree. Repeated or overlapping sets of measurements were then averaged giving a set of 360 measured eccentricities for each stiffener and mid-bay location. Eccentricity readings taken at corrosion patches were corrected by adjusting for the depth of corrosion based on UT readings of the shell.

The averaged and corrected OOC data showed some high-frequency noise due to the interaction of the lasers and the reflective aluminium surface [14]. Fourier decompositions were performed on each set of circumferential data, and the final out-of-circularity data sets reported in this document were produced by expanding the Fourier series using only modes $n \leq 18$, thus eliminating the noise, and further reducing the number of circumferential points to 36. These data are referred to as the smoothed and reduced, or filtered, out-of-circularity measurements.

The laser displacement gauge measurements are accurate to 0.001 mm. The entire system described above was verified by comparison with the mechanical dial gauge readings that were taken during and after the mechanical application of OOC to confirm that the desired shape was produced.

2.2.2 Summary of measurement results

In this section, the out-of-circularity and thickness measurements taken on each specimen are summarized. The results are based on the CMM measurements for Phase 5 specimens, and on the laser displacement gauge and UT gauge data for Phase 6 specimens.

The geometric measurements for each specimen are tabulated in Annex B. The presented data includes complete CMM radial measurements on the inside and outside of Phase 5 specimens, shell thicknesses derived from those data, as well as radial eccentricities derived from mechanical displacement gauge and chord gauge measurements. For Phase 6 specimens, the filtered laser displacement gauge out-of-circularity readings and complete UT gauge readings are given, along with the mechanical displacement gauge results.

Out-of-circularity plots for each specimen are presented in Annex C, including three-dimensional graphical representations of the OOC in each model, typical circumferential and axial OOC measurements, and the orientation of corrosion patches with respect to out-of-circularity. Plots showing the circumferential distribution of shell thickness at representative axial locations are also given in Annex C. Similar plots presented for some of the specimens in the current section are not duplicated in the annex.

2.2.2.1 Out-of-circularity measurements

Figure 7 shows a graphical representation of the out-of-circularity for a typical specimen, L510-No18, with an n=3 circumferential wave number distributed over the length in a half sine wave. The contour map was generated by fitting the radial eccentricity measurements taken outside the shell to a double Fourier series that characterizes the entire two-dimensional shell surface. The double Fourier series was then applied to the coordinates of the nodes in a finite element (FE) model of the cylinder, resulting in the three-dimensional map shown in Figure 7. The double Fourier series technique, which is described in Annex A, results in some discrepancies between the measured data and the nonlinear map, but the error is typically less than 2%.

Figure 8 and Figure 9 show the circumferential and axial imperfection modes, respectively, for specimen L510-No18 based on the CMM measurements. The dominant n=3 circumferential mode is clearly shown in Figure 8, and both figures show the OOC amplitude increasing from the cylinder ends to the mid-length. All other specimens, except L510-No34 and L510-No17, show a similar pattern, even though the imperfection magnitudes vary.

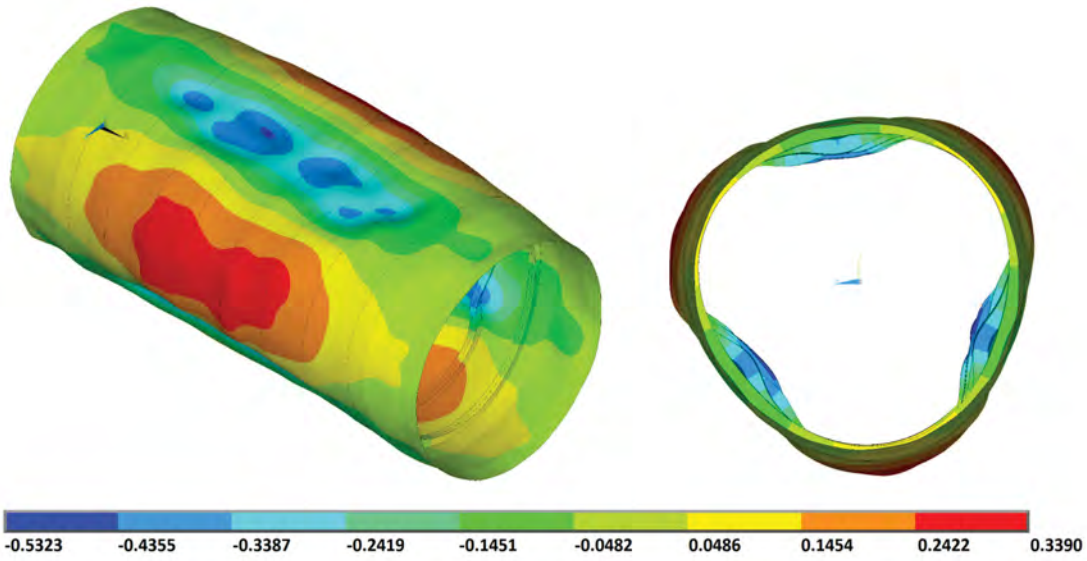

Figure 7: Graphical representation of out-of-circularity of specimen L510-No18. The colour contour maps describe the radial eccentricity (mm) based on a double Fourier analysis of the measurements of the outer shell taken by the CMM. The out-of-circularity is also indicated by the deformed shape of the model, whereby the imperfections are magnified by a factor of 50.

L510-No34 was intentionally deformed to have the n=3 circumferential mode distributed over the length of the cylinder in a complete sine wave. A graphical representation of the final OOC in that cylinder is shown in Figure 10, and the circumferential and axial imperfection modes are shown in Figure 11 and Figure 12, respectively. The m=2 axial mode, with a complete sine wave over the cylinder length, is clearly shown in those figures.

Specimen L510-No17 is atypical in that the imperfections can be seen to be highly influenced by the n=2 mode at the cylinder ends. This is most clearly shown by the circumferential OOC mode for Frame 1 in Figure 13. The post-machining shapes of the cylinders, although they were not measured for this study, are likely characterized by a dominant n=2 mode. That is suggested by the post-machining shapes of similar cylinders tested during previous phases of the experimental program [10]. Since L510-No17 has the second smallest applied OOC magnitude, the post-machining shape may be more noticeable than in other specimens with larger OOC amplitudes applied in the n=3 mode.

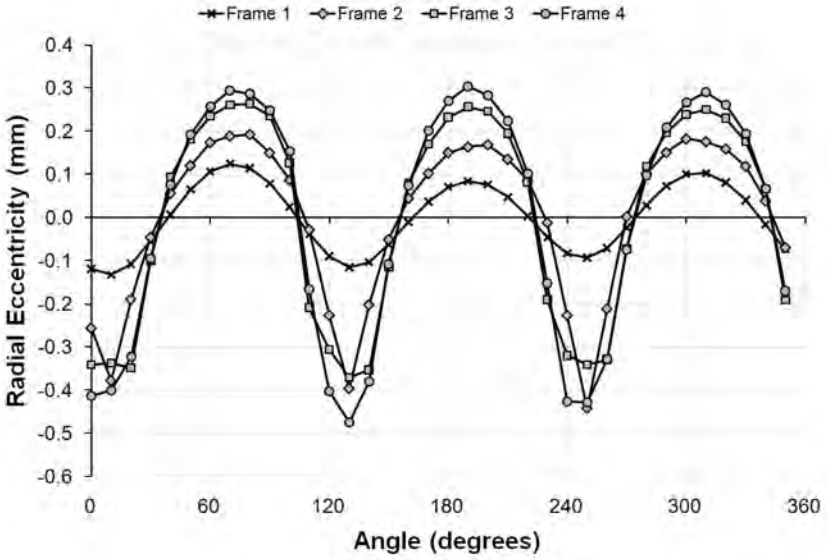

Figure 8: Showing the circumferential out-of-circularity mode of specimen L510-No18 based on measurements at the outside of the shell surface. All measurements taken about the circumference using a CMM are shown for axial locations nearby the indicated ring-stiffeners.

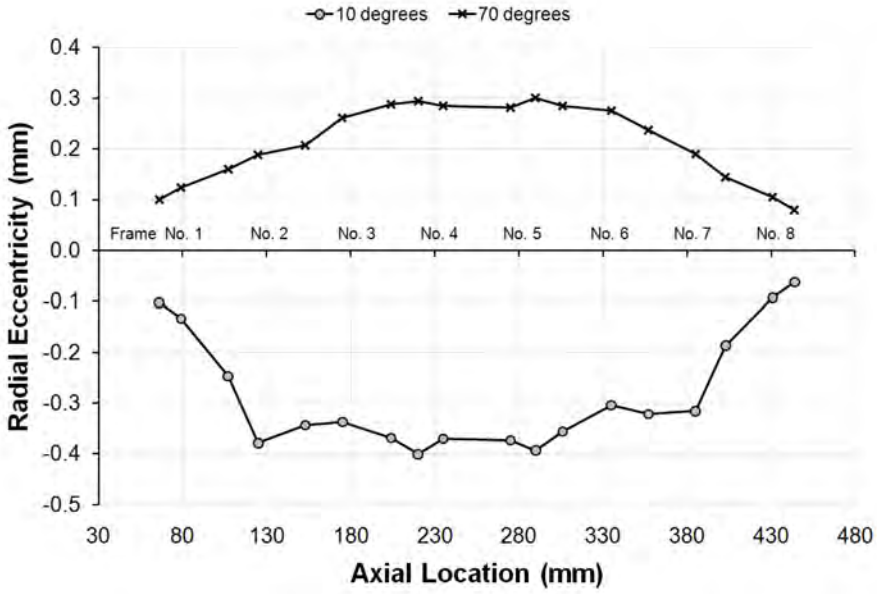

Figure 9: Showing the axial out-of-circularity mode of specimen L510-No18 based on measurements at the outside of the shell surface. All measurements taken over the cylinder length using a CMM are shown for circumferential locations associated with the maximum inward and outward radial eccentricities (10° and 70°, respectively).

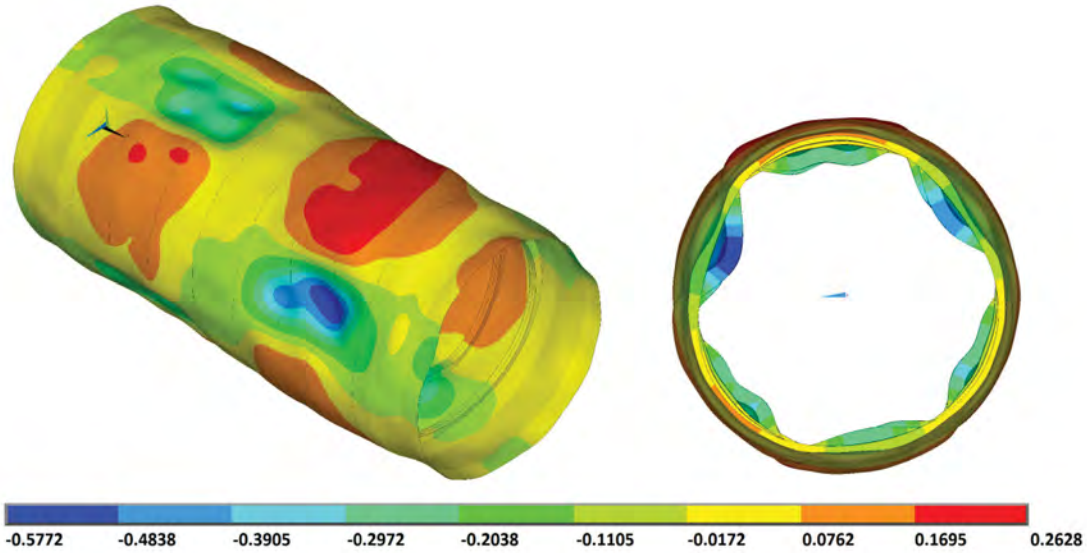

Figure 10: Graphical representation of out-of-circularity of specimen L510-No34. The colour contour maps describe the radial eccentricity (mm) based on a double Fourier analysis of the measurements of the outer shell taken by the CMM. The out-of-circularity is also indicated by the deformed shape of the model, whereby the imperfections are magnified by a factor of 50.

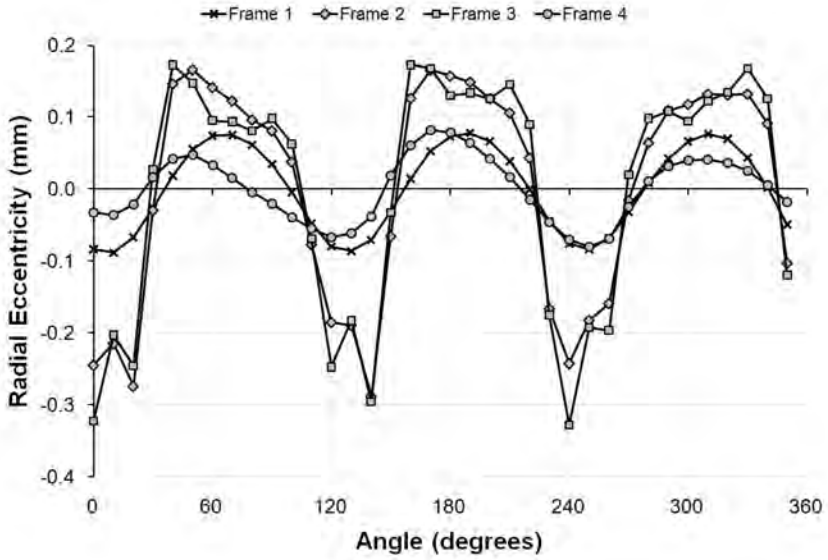

Figure 11: Showing the circumferential out-of-circularity mode of specimen L510-No34 based on measurements at the outside of the shell surface. All measurements taken about the circumference using a CMM are shown for axial locations nearby the indicated ring-stiffeners.

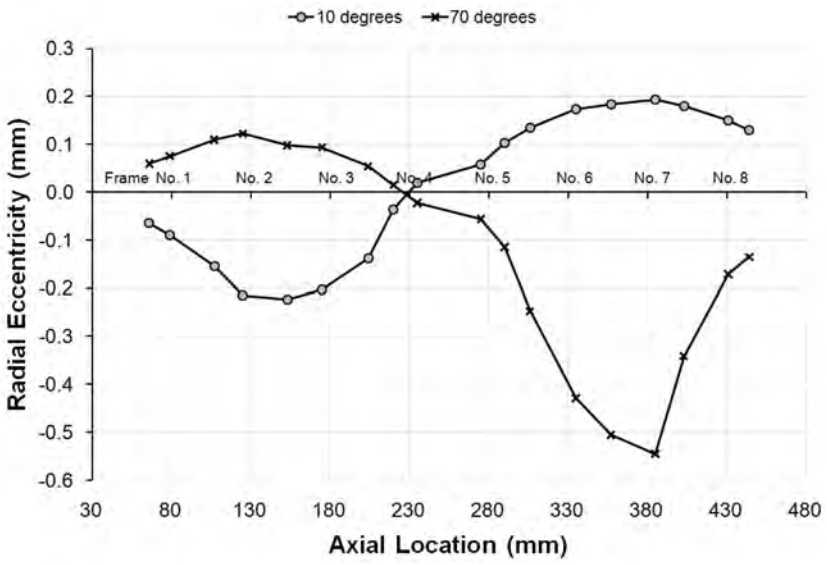

Figure 12: Showing the axial out-of-circularity mode of specimen L510-No34 based on measurements at the outside of the shell surface. All measurements taken over the cylinder length using a CMM are shown for circumferential locations associated with the maximum inward and outward radial eccentricities (10° and 70°, respectively).

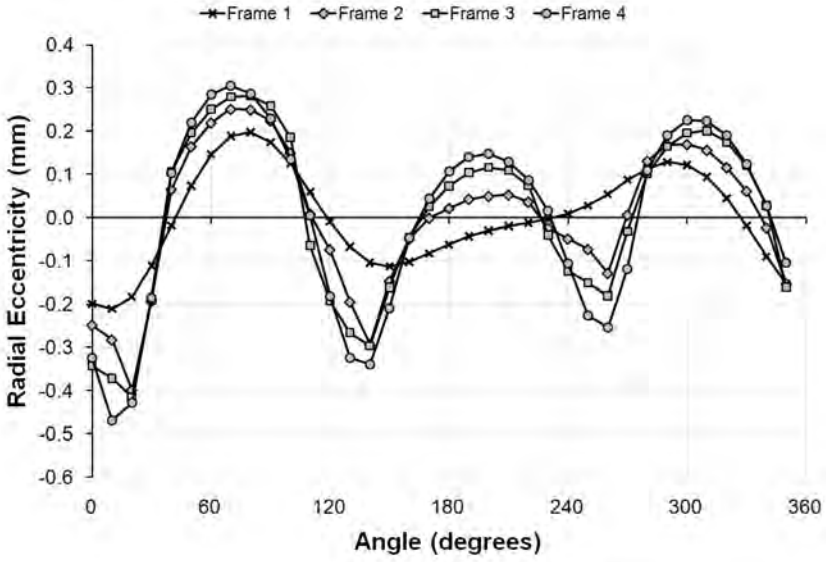

Figure 13: Showing the circumferential out-of-circularity mode of specimen L510-No17 based on measurements at the outside of the shell surface. All measurements taken about the circumference using a CMM are shown for axial locations nearby the indicated ring-stiffeners.

The measured out-of-circularities of all Phase 5 and 6 specimens are summarized in Table 2. That table lists the maximum inward and outward radial eccentricities for each specimen, as well as the maximum average eccentricity, which is taken as half the difference between the maximum inward and outward values at each axial measurement location. Table 2 also lists the maximum imperfection amplitudes for individual circumferential mode numbers derived from Fourier decompositions at each axial location.

The data in Table 2 indicate that the mechanical procedure for introducing out-of-circularity into the cylinders resulted in large inward deformations, when compared to the outward lobes. This probably results from large plastic strains near the contact points with the frame apparatus used to deform the cylinders.

Table 2: Summary of measured eccentricities and Fourier decompositions for outer shell radii.

Specimen Name	**Maximum Radial Eccentricity[a] (mm)**			**Maximum Fourier Amplitude[b], A_n (mm)**				
	Outward	**Inward**	**Average**	***n*=2**	***n*=3**	***n*=4**	***n*=5**	***n*=6**
L510-No13	0.353	0.866	0.610	0.069	0.476	0.076	0.023	0.201
L510-No14	0.476	0.814	0.615	0.091	0.554	0.046	0.036	0.163
L510-No17	0.305	0.479	0.391	0.136	0.285	0.027	0.019	0.085
L510-No18	0.337	0.503	0.399	0.023	0.366	0.022	0.023	0.090
L510-No19	0.585	0.935	0.746	0.078	0.680	0.095	0.082	0.193
L510-No20	0.396	0.814	0.558	0.069	0.369	0.064	0.054	0.172
L510-No25	0.533	0.908	0.712	0.039	0.647	0.024	0.021	0.222
L510-No26	0.589	1.144	0.866	0.068	0.709	0.069	0.035	0.222
L510-No33	0.565	1.117	0.841	0.039	0.760	0.028	0.065	0.295
L510-No34	0.225	0.545	0.385	0.060	0.249	0.042	0.037	0.140
L510-No35	0.563	0.960	0.753	0.076	0.679	0.083	0.061	0.202
L510-No36	0.627	1.174	0.842	0.125	0.639	0.055	0.115	0.258

a. Outward and inward eccentricities are based on the absolute maximum values of the positive and negative deviation, respectively, from the mean outer shell radius for all axial measurement locations. The average eccentricities are computed at each axial measurement location, and taken as half the difference between the maximum outward and inward eccentricities. The reported average eccentricity is the maximum value for all of the axial measurement locations. Eccentricities for Phase 5 specimens are based on the CMM measurements. Eccentricities for Phase 6 specimens are based on the smoothed measured data.

b. Maximum Fourier amplitudes, based on decomposition of outer shell radii at all axial measurement locations, are reported. Fourier amplitudes for n>6 are negligible. Fourier decompositions for Phase 5 specimens are based on the CMM measurements. Fourier decompositions for Phase 6 specimens are based on the raw measured eccentricities.

It is also clear from the data in Table 2 that the mechanical procedure was successful at producing final configurations dominated by the n=3 mode. Except for L510-No17, the n=3 amplitude for each specimen was at least five times as great as the amplitudes for n=2, n=4 and n=5. The significant n=2 component of the L510-No17 shape has already been discussed. The n=6 amplitudes are the second largest for all cylinders except L510-No17, and are equal to, on average, approximately one-third of the corresponding n=3 amplitude. The relatively large n=6 amplitudes are likely associated with the sharp inward lobes of the applied OOC.

Three different eccentricity criteria are used herein to quantify the OOC magnitude in the test specimens: (1) the absolute maximum eccentricity, e_{max}, which is the value used for assessing hulls during construction and in service [12]; (2) the maximum average eccentricity, e_{avg}, which was the value used to assess the cylinder shape during the application of OOC; and (3) the maximum n=3 Fourier amplitude, e_3, which gives an indication of the OOC in the target mode, as well as the critical collapse mode. Figure 14 shows an example of each of the various eccentricities for specimen L510-No18.

The measured out-of-circularities are compared with the target values in Table 3. The percentage OOC is defined by dividing measured eccentricity values by the mean shell radius. The resulting percentage OOCs indicate that, based on e_{avg}, the applied imperfections are reasonably close to the target values, especially considering the trial-and-error nature of the procedure; furthermore, the OOCs, as defined by e_3, are also close to the nominal values. However, a strict application of the design rules and tolerances in [12], i.e. using e_{max}, indicates that the actual imperfections are significantly larger (on average, greater than 50% larger) than the target values.

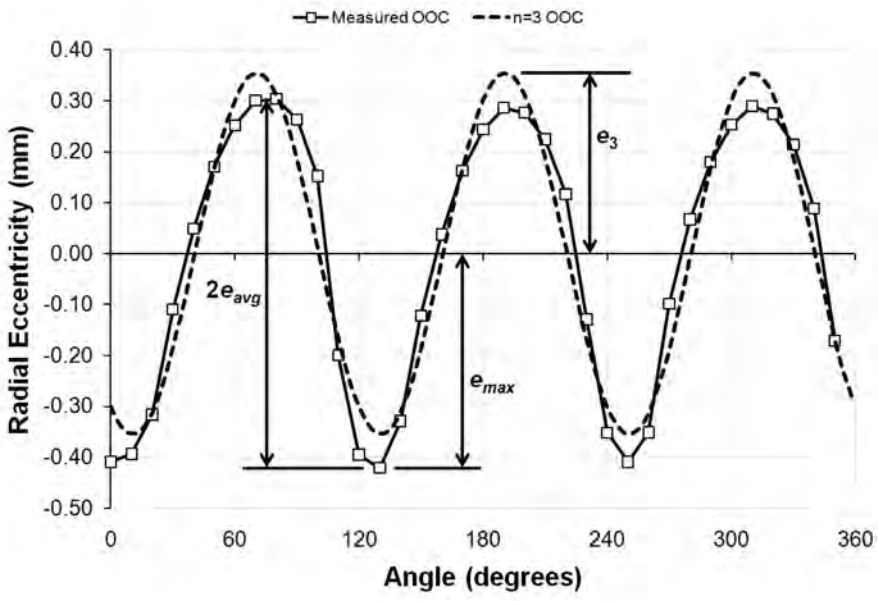

Figure 14: Definitions for various out-of-circularity magnitude criteria; showing CMM measurements taken on the outside of the shell surface at Frame 5 of specimen L510-No18, as well as the n=*3 component of the Fourier decomposition.*

Table 3: Comparison of final specimen out-of-circularity magnitudes with target values, based on various eccentricity parameters.

Specimen Name	Out-of-Circularity[a] based on the Indicated Eccentricity			
	e_{nom} [b]	e_{max} [c]	e_{avg} [d]	e_3 [e]
L510-No13	0.5%	0.71%	0.50%	0.39%
L510-No14	0.5%	0.67%	0.51%	0.46%
L510-No17	0.3%	0.39%	0.32%	0.23%
L510-No18	0.3%	0.41%	0.33%	0.30%
L510-No19	0.5%	0.77%	0.61%	0.56%
L510-No20	0.5%	0.67%	0.46%	0.30%
L510-No25	0.5%	0.75%	0.59%	0.53%
L510-No26	0.5%	0.94%	0.71%	0.58%
L510-No33	0.5%	0.92%	0.69%	0.63%
L510-No34	0.3%	0.45%	0.32%	0.20%
L510-No35	0.5%	0.79%	0.62%	0.56%
L510-No36	0.5%	0.97%	0.69%	0.53%

a. Out-of-circularity is taken as the quotient of the radial eccentricity and the nominal mid-plane radius of the shell (121.5 mm).

b. e_{nom} is the eccentricity associated with the nominal or target out-of-circularity, as specified in Table 1. e_{nom} is equal to 0.3645 mm and 0.6075 mm for 0.3% and 0.5% OOC, respectively.

c. e_{max} is the greater of the inward and outward maximum eccentricities given in Table 2.

d. e_{avg} is the average maximum eccentricity given in Table 2.

e. e_3 is the n=3 Fourier amplitude given in Table 2.

Table 4 lists the circumferential locations of the inward OOC lobes, in order to confirm that the OOC was applied in such a way as to produce the desired orientation with respect to the corrosion damage. Since not all of the corrosion patches are located at 0°, the corrosion angles are also listed in Table 4. The data in that table indicate that all of the in-phase corrosion patches are centred within a few degrees of one of the inward n=3 OOC lobes, and furthermore, that the out-of-phase patches are exactly mid-way between inward lobes. The correctness of the corrosion patch locations is further corroborated by plotting the out-of-circularity in the central bay with the circumferential extents of corrosion. Figure 15 and Figure 16 show such plots for specimens with out-of-phase (L510-No13) and in-phase (L510-No14) corrosion, respectively. Graphical representations of the out-of-circularity generated using FE models as described above, which show the location of the corrosion patches on the deformed models, are presented in Figure 17 and Figure 18 for L510-No13 and L510-No14, respectively.

Table 4: Circumferential location of maximum out-of-circularity amplitudes and corrosion patches, where applicable.

Specimen Name	**Circumferential Location of Maximum Inward Out-of-Circularity at the Central Bay**[a]			**Corrosion Patch**	
				Location of Centre	**Phase with respect to OOC**
L510-No13	60°	170°	300°	0°	Out-of-phase
L510-No14	60°	160°	300°	165°	In-phase
L510-No17	10°	130°	250°	N/A	N/A
L510-No18	10°	130°	250°	N/A	N/A
L510-No19	10°	120°	230°	0°	In-phase
L510-No20	60°	180°	300°	183.5°	In-phase
L510-No25	10°	130°	250°	N/A	N/A
L510-No26	0°	120°	240°	N/A	N/A
L510-No33	10°	130°	250°	N/A	N/A
L510-No34	0/70°	140/190°	240/310°	N/A	N/A
L510-No35	0°	110°	230°	0°	In-phase
L510-No36	60°	180°	300°	0°	Out-of-Phase

a. For L510-No34, which has an m=2 axial OOC mode, the maximum inward OOC is given for Bay 2/Bay 6 representing the phase shift in the n=3 circumferential mode at opposite ends of the cylinder.

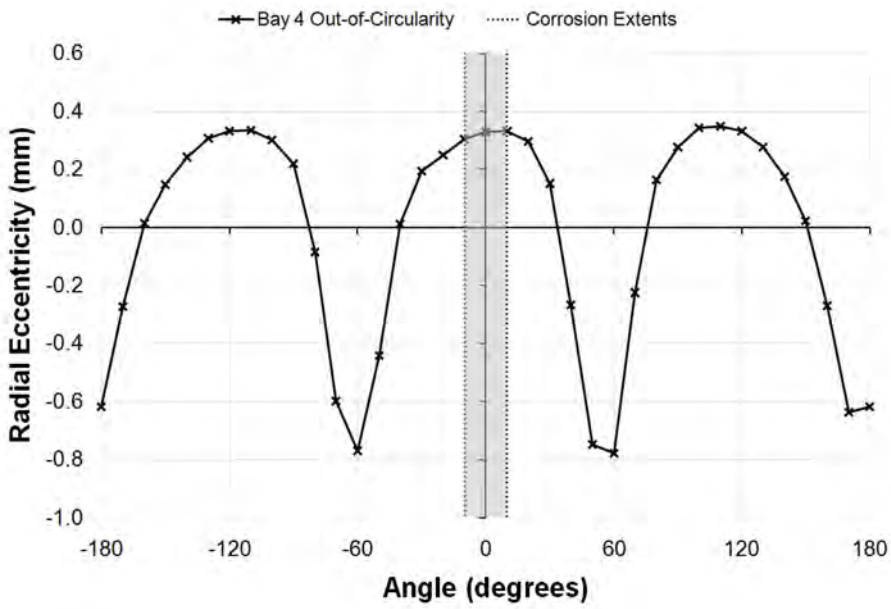

Figure 15: Showing the circumferential out-of-circularity mode of specimen L510-No13 based on the filtered laser displacement gauge measurements at the outside of the shell surface at the central bay. The circumferential extents of the small, out-of-phase corrosion patch are indicated by the dashed lines and shaded area.

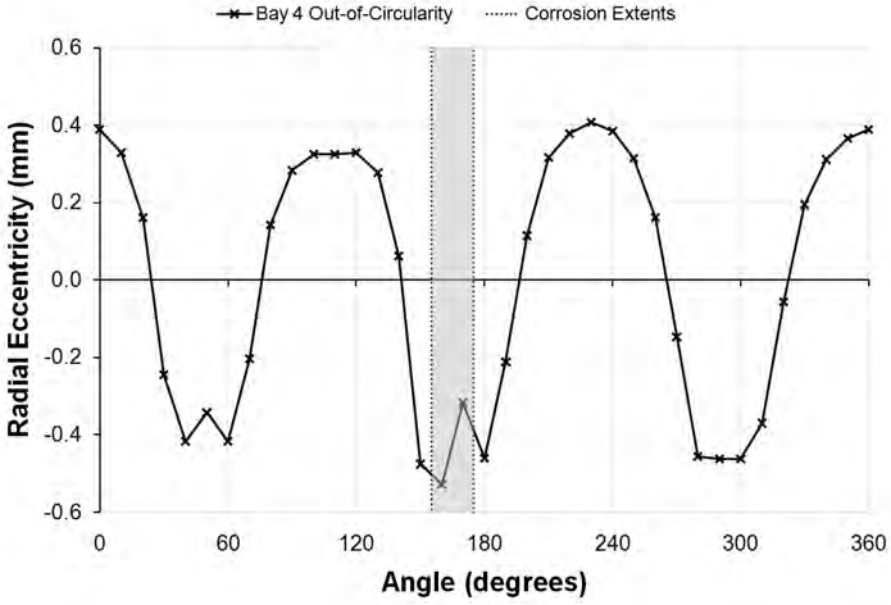

Figure 16: Showing the circumferential out-of-circularity mode of specimen L510-No14 based on the filtered laser displacement gauge measurements at the outside of the shell surface at the central bay. The circumferential extents of the small, in-phase corrosion patch are indicated by the dashed lines and shaded area.

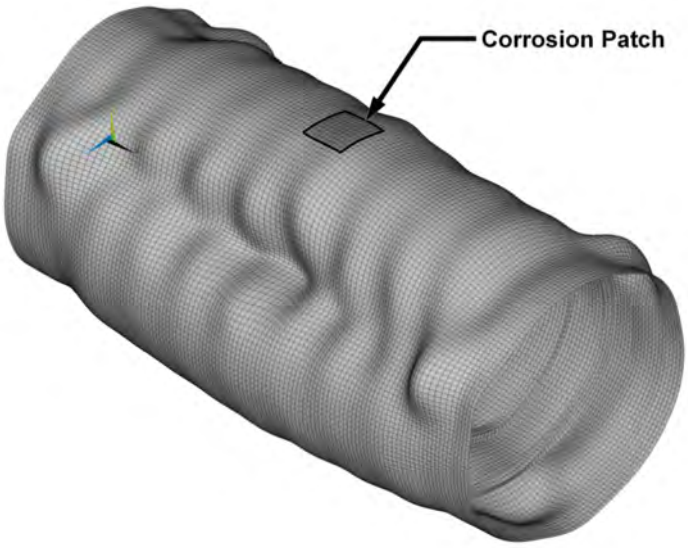

Figure 17: Graphical representation of out-of-circularity of specimen L510-No13, showing the location of the out-of-phase corrosion patch with respect to the out-of-circularity shape. The out-of-circularity is indicated by the deformed shape of the model, whereby the imperfections are magnified by a factor of 50.

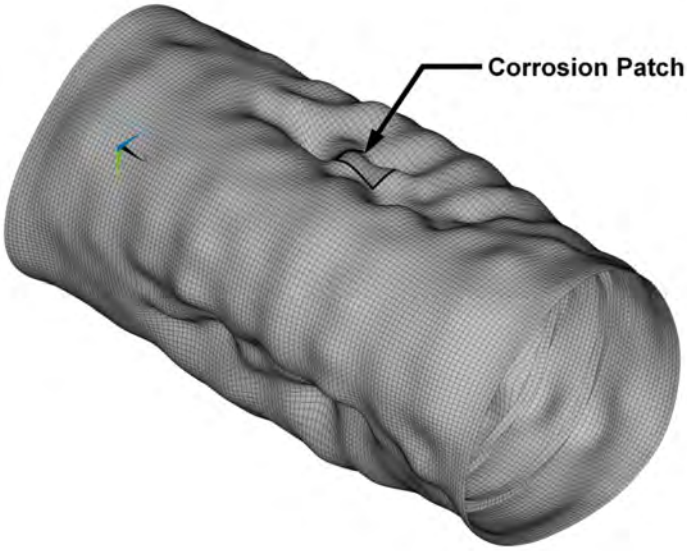

Figure 18: Graphical representation of out-of-circularity of specimen L510-No14, showing the location of the in-phase corrosion patch with respect to the out-of-circularity shape. The out-of-circularity is indicated by the deformed shape of the model, whereby the imperfections are magnified by a factor of 50.

2.2.2.2 Shell thickness measurements

A summary of the measured shell thicknesses is presented in Table 5. The fabrication tolerance on the shell thickness for machining the axisymmetric, i.e. intact, geometry was ±0.05 mm [14]. From the data in Table 5, it can be seen that, while the mean measured shell thicknesses in the intact regions of the cylinders met the fabrication tolerance, there was significant variation in the shell thickness in each cylinder. The minimum and maximum measured shell thicknesses indicate that the maximum deviations from the nominal shell thickness were between 0.13 and 0.37 mm, significantly exceeding the allowable tolerance. The data in Table 5 also show that the mean shell thicknesses in the corrosion patches were within ±0.09 mm of nominal values, and that the maximum measured discrepancies with the nominal value were between 0.09 and 0.17 mm.

The nominal, or target, percentage corrosion thinning values are compared with the as-measured values in Table 6. That table shows that, while the thickness of the corrosion patches were out-of-tolerance, the as-measured thinning percentages were within ±3.5% of the targeted values. Table 6 also shows a comparison of the as-measured corrosion depth with the maximum variation in the intact shell thickness, taken as the difference between the maximum and minimum measured shell thickness for a given cylinder. The thickness variation in intact regions is of the same order of magnitude as the corrosion depth, and ranges between 0.48 and 0.92 times the corrosion depth.

Table 5: Summary of measured shell thicknesses of experimental specimens

Specimen Name	**Shell Thickness in Undamaged Region[a] (mm)**					**Shell Thickness in Corroded Region[b] (mm)**				
	Nom.	**Mean**	**Min.**	**Max.**	**COV**	**Nom.**	**Mean**	**Min.**	**Max.**	**COV**
L510-No13	3.0	2.988	2.816	3.115	1.91%	2.4	2.417	2.356	2.495	1.89%
L510-No14	3.0	3.035	2.882	3.207	2.60%	2.4	2.359	2.309	2.402	1.26%
L510-No17	3.0	2.946	2.694	3.203	3.46%	-	-	-	-	-
L510-No18	3.0	2.983	2.872	3.117	1.69%	-	-	-	-	-
L510-No19	3.0	3.044	2.896	3.168	1.89%	2.6	2.622	2.515	2.767	2.65%
L510-No20	3.0	3.012	2.817	3.238	3.11%	2.6	2.554	2.453	2.616	1.86%
L510-No25	3.0	2.985	2.812	3.315	2.07%	-	-	-	-	-
L510-No26	3.0	2.977	2.811	3.293	2.08%	-	-	-	-	-
L510-No33	3.0	2.989	2.868	3.374	2.30%	-	-	-	-	-
L510-No34	3.0	2.968	2.813	3.111	1.76%	-	-	-	-	-
L510-No35	3.0	3.009	2.875	3.231	2.32	2.4	2.469	2.437	2.502	0.85%
L510-No36	3.0	3.023	2.809	3.169	2.63%	2.4	2.312	2.278	2.368	1.43%

a. For Phase 5 specimens, shell thicknesses are calculated by subtracting outer and inner shell radii, using the raw measured radii less n=1 Fourier components to account for the offset of the measurement apparatus from the axis of revolution. For Phase 6, thicknesses are based on UT measurements.

b. Shell thicknesses in corroded regions of Phase 6 specimens are based on UT readings. Thickness data in the corroded regions for specimens L510-No13, L510-No14, L510-No35 and L510-No36 are based on 9-11 UT readings, while 25 readings were taken on specimens L510-No19 and L510-No20.

Table 6: Corrosion thinning and variation in shell thickness

Specimen Name	Corrosion Thinning		Measured Corrosion Depth[a] (mm)	Maximum Variation in Intact Shell Thickness[b] (mm)
	Nominal	Measured[a]		
L510-No13	20.0%	19.1%	0.571	0.299
L510-No14	20.0%	22.3%	0.676	0.325
L510-No17	-	-	-	0.509
L510-No18	-	-	-	0.245
L510-No19	13.3%	13.9%	0.422	0.272
L510-No20	13.3%	15.2%	0.458	0.421
L510-No25	-	-	-	0.503
L510-No26	-	-	-	0.482
L510-No33	-	-	-	0.506
L510-No34	-	-	-	0.298
L510-No35	20.0%	17.9%	0.540	0.356
L510-No36	20.0%	23.5%	0.711	0.360

a. Measured corrosion thinning is based on the mean measured intact and corroded shell thicknesses.

b. Maximum variation in intact shell thickness is taken as the difference between the maximum and minimum measured shell thicknesses in intact regions.

The circumferential distribution of shell thickness at representative axial locations is shown in Figure 19 and Figure 20 for the intact specimen L510-No17 and the corroded specimen L510-No20, respectively. The n=2 variation of the shell thickness about the circumference of these specimens is typical. The similarity of the magnitude of the corrosion depth and the circumferential variation in shell thickness is clearly shown in the figure for L510-No20. That specimen represents the extreme case, but it demonstrates that the variation in shell thickness due to sources both intentional, i.e. corrosion application, and unintentional, i.e. machining, must be considered when interpreting the experimental results. It has been suggested the cause of the shell thickness variation was clamping forces applied to the models when they were mounted in the CNC lathe, which deformed the models during the machining process [14].

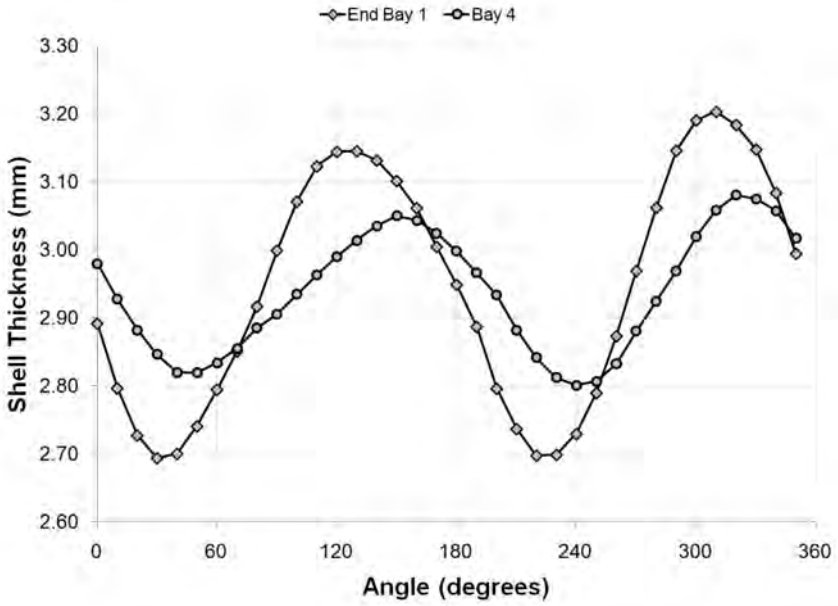

Figure 19: Showing the circumferential distribution of shell thickness at representative axial locations for specimen L510-No17, based on CMM measurements of the inner and outer shell radii.

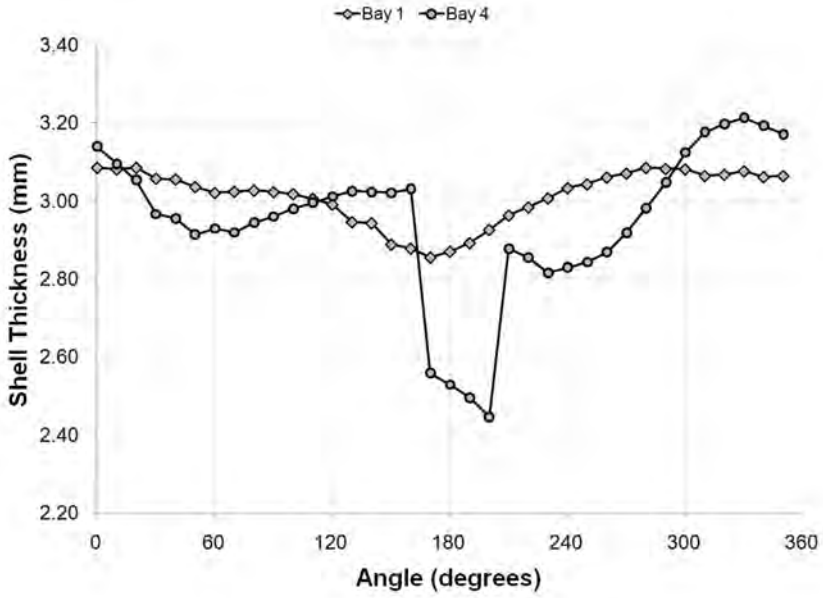

Figure 20: Showing the circumferential distribution of shell thickness at representative axial locations for specimen L510-No20, based on ultrasonic thickness gauge readings.

2.2.3 Comparison of measurement techniques

As discussed in Section 2.2.1, out-of-circularity measurements were taken on each specimen using two or three different methods. Phase 5 specimens were measured with a CMM, as well as with a mechanical displacement gauge and a chord gauge. Phase 6 specimens were measured with laser and mechanical displacement gauges.

Figure 21 shows measured out-of-circularity shapes for a typical Phase 5 specimen, L510-No18, at a central ring-stiffener. CMM and mechanical displacement gauge measurements were taken at 10° increments, while chord gauge readings were taken every 20°. The figure shows good agreement between the various measurement techniques, with respect to both imperfection mode and amplitude.

A comparison of the raw, smoothed, and filtered laser displacement gauge data for a typical Phase 6 specimen, L510-No13, is shown in Figure 22. The measured data are shown for a frame location near the end of the cylinder, where the OOC is smallest and the high-frequency noise in the raw measurements is most obvious. The figure shows that the smoothing procedure, whereby Fourier modes n>18 have been removed, has preserved the overall OOC shape while eliminating the noise. Figure 22 also shows the filtered data, which is the smoothed data reduced to 36 circumferential points. Displacement gauge readings were not taken at the frames near the ends of Phase 6 cylinders.

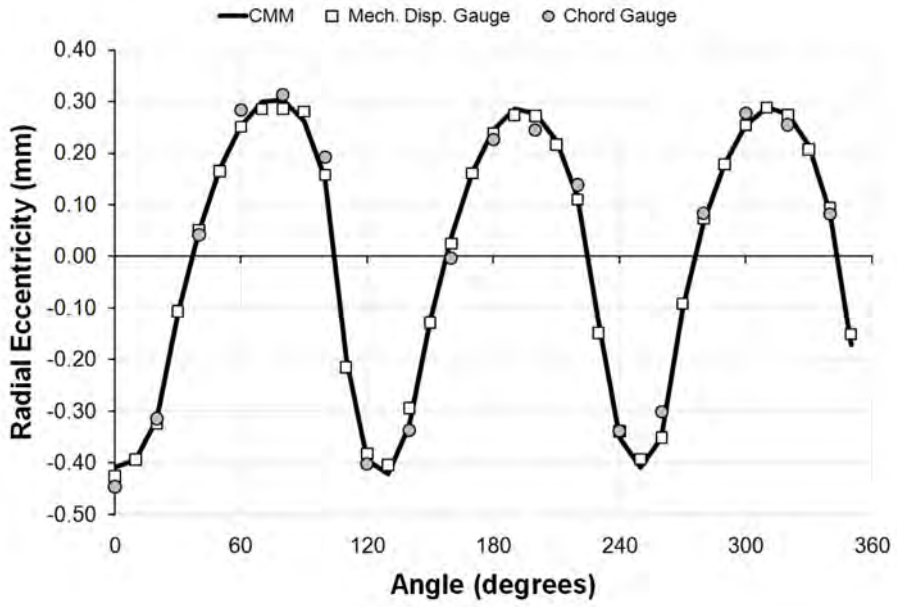

Figure 21: Out-of-circularity of specimen L510-No18 at Frame 5, based on CMM, mechanical displacement gauge, and chord gauge measurements.

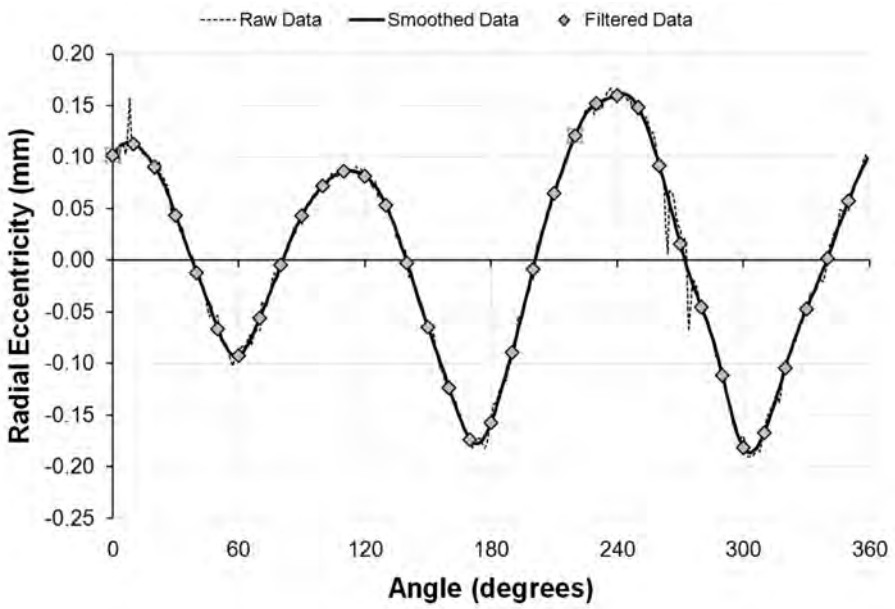

Figure 22: Out-of-circularity of specimen L510-No13 at Frame 1, showing the raw average laser displacement gauge measurements, the smoothed data whereby only Fourier modes n≤18 are included, and the filtered data whereby the smoothed data spacing is reduced to 10 degree increments.

Figure 23 shows raw and filtered laser displacement gauge data taken at Frame 5 of specimen L510-No13, along with the corresponding mechanical displacement gauge measurements. The overall shape and magnitude of OOC, as measured by the laser and mechanical gauges, is similar; however, there is a small offset in the phase angles of the measured shapes, which may be attributed to using slightly different zero angle locations. Other Phase 6 specimens show a similar trend.

Similar plots for all Phase 5 and 6 specimens indicate that the measurement procedures are in good qualitative agreement with each other; however, it is also desirable to quantify the agreement. This was done by calculating the error in the mechanical displacement gauge and chord gauge measurements, using the CMM and laser displacement gauge measurements as the benchmark. The error was calculated for each specimen in two ways: by comparing the maximum OOC amplitude predicted by each method, and by comparing all of the measurements on a point-by-point basis. The latter comparison gives the "total" error in describing the OOC shape. It is defined by the following equation:

$$Total\_Error = \sqrt{\frac{\sum_{i=1}^{N}\left(e_i - e_{ref,i}\right)^2}{\sum_{i=1}^{N}\left(e_{ref,i}\right)^2}} \quad (1)$$

where N is the total number of measurement comparisons, e_i is the radial eccentricity at a given location for the measurement method in question, and $e_{ref,i}$ is the eccentricity for the reference measurement method, i.e. CMM and laser gauge readings for Phase 5 and 6 specimens, respectively.

Table 7 lists the maximum measured eccentricities, along with the associated error, for each specimen and measurement technique. The total error is also tabulated. For Phase 5 specimens, the mechanical displacement gauge measurements were, on average, more accurate, relative to the CMM data, than the chord gauge measurements for both error criteria. On average with either method, the maximum amplitude is predicted to within 6%, while the total error in characterizing the OOC shape is predicted within 12%. For Phase 6 specimens, the mechanical displacement gauge measurements showed a similar average error, compared to laser measurements, in predicting the maximum eccentricity, at approximately 6%, while the average total error is significantly higher, at approximately 24%. That is likely due to the slight shift in phase angles between the laser and mechanical gauge measurements, which tends to magnify the error at locations between inward and outward OOC lobes where the imperfection gradients are largest.

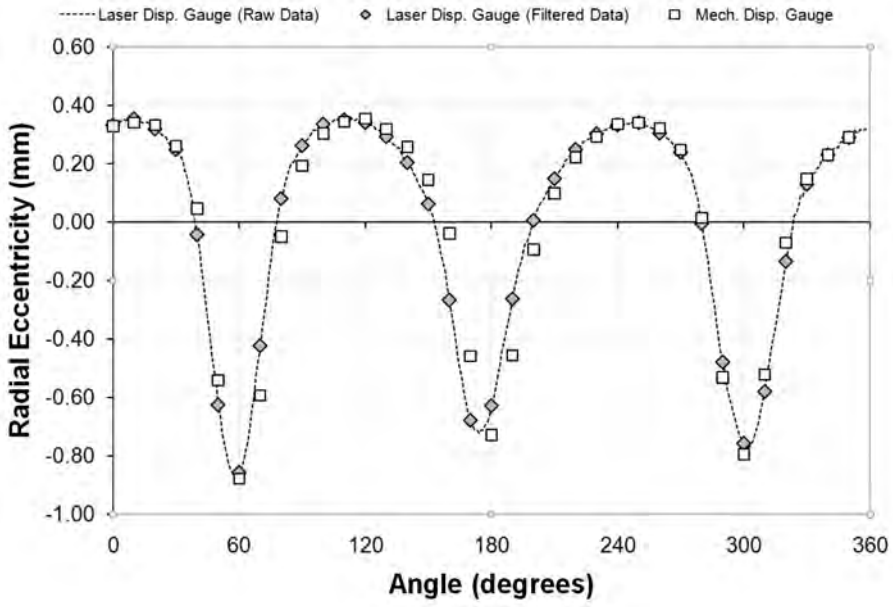

Figure 23: Out-of-circularity of specimen L510-No13 at Frame 5, showing the raw average laser displacement gauge measurements, the associated filtered data, and the mechanical displacement gauge data.

Table 7: Comparison of various techniques for measuring out-of-circularity

Specimen Name	Maximum Inward Eccentricity (mm) as Measured by the Indicated Method[a]				Error[b] in Maximum Inward Eccentricity		Total Error[c]	
	CMM	Laser Disp. Gauge	Mech. Disp. Gauge	Chord Gauge	Mech. Disp. Gauge	Chord Gauge	Mech. Disp. Gauge	Chord Gauge
L510-No13	-	0.856	0.879	-	2.7%	-	20.4%	-
L510-No14	-	0.610	0.610	-	-0.1%	-	23.5%	-
L510-No17	0.429	-	0.440	0.485	2.5%	13.1%	5.2%	16.1%
L510-No18	0.427	-	0.426	0.446	-0.3%	4.4%	7.5%	11.8%
L510-No19	-	0.894	0.917	-	2.6%	-	20.0%	-
L510-No20	-	0.803	0.622	-	-22.6%	-	43.6%	-
L510-No25	0.839	-	0.857	0.820	2.2%	-2.2%	5.5%	9.4%
L510-No26	0.782	-	0.862	0.806	10.1%	3.0%	7.6%	11.8%
L510-No33	1.104	-	1.037	1.178	-6.0%	6.7%	11.5%	10.9%
L510-No34	0.396	-	0.421	0.419	6.5%	5.9%	13.1%	11.5%
L510-No35	-	0.892	0.885	-	-0.8%	-	19.4%	-
L510-No36	-	1.174	1.211	-	3.1%	-	19.7%	-
Average absolute value of error for Phase 5 specimens					*4.6%*	*5.9%*	*8.4%*	*11.9%*
Average absolute value of error for Phase 6 specimens					*6.1%*	-	*24.4%*	-
Average absolute value of error for all specimens					*5.4%*	*5.9%*	*16.4%*	*11.9%*

a. Maximum eccentricities are based on measurement locations for which data is available for all methods. For Phase 5 specimens, CMM, mechanical displacement gauge and chord gauge measurements are compared at frame locations at 20 degree increments. For Phase 6 specimens, laser and mechanical displacement gauge measurements are compared at Frames 3 through 6, and at 10 degree increments.

b. Reported error is relative to the CMM and laser displacement gauge measurements for Phase 5 and 6 specimens, respectively.

c. Total error is based on Eq. (1).

2.3 Measured material properties

All Phase 5 and 6 specimens were machined from aluminium alloy AA-6082-T6, which has a minimum yield strength in tension of 250-260 MPa, a minimum tensile strength of 290-310 MPa, and an elongation at break of 10% [15]. A summary of the measured material properties for specimens tested in previous phases of the experimental program, and which were constructed of the same aluminium alloy, is presented in Table 8. The tensile testing indicated that the cylinder material was anisotropic, with the circumferential yield strength approximately 10% less than the axial value [10]. There was also found to be some variation, approximately 10%, in the material properties between different batches of extruded tubing.

Table 8: Measured engineering material properties in the axial and circumferential direction for Phase 1, 2 and 3 specimens, which were constructed of AA-6082-T6. The mean properties are reported for each batch of material [10].

Material Batch	Coupon Direction	Young's Modulus (GPa)	Yield Strength, 0.2% Offset (MPa)	Tensile Strength (MPa)
Batch No. 1	Circumferential	72.7	272	333
Batch No. 1	Axial	73.2	304	373
Batch No. 2	Circumferential	67.9	297	349
Batch No. 2	Axial	70.7	327	385
Batch No. 3	Circumferential	80.6	303	330
Batch No. 3	Axial	74.3	317	348

Collapse testing of cylinders from Phases 1-3 showed that the collapse behaviour is dominated by circumferential stresses and strains [10], and numerical simulations showed that it is sufficient to use the circumferential material properties in an isotropic material model in order to correctly predict the collapse pressure [7],[8]. The anisotropy is likely related to the extrusion process for the aluminium tubing, which could preferentially align the grain structure in the axial direction.

For those reasons, only the circumferential material properties have been characterized for Phase 5 and 6 specimens. Three tensile coupons were machined from one of the thick end rings of each cylinder after collapse testing in order to characterize the properties for individual cylinders. Furthermore, the Phase 5 and 6 specimens were fabricated from two different batches of aluminium tubing, so that characterizing the material for each specimen would allow the variation within and between batches to be determined.

The thickness and curvature of the cylinder end rings necessitated the use of under-sized coupons with threaded grips to offset the short grip length. The shape and dimensions of the under-sized coupons are shown in Figure 24. Photographs of similar tensile coupons machined from Phase 2 cylinders, taken after tensile testing was completed, are shown in Figure 25.

The mean measured circumferential material properties for each specimen are listed in Table 9. Those data indicate that, in all cases, the circumferential properties exceed the minimum specified values for yield stress, tensile strength and elongation at break. In general, the yield stresses and tensile strengths for Phase 5 and 6 cylinders are higher than those measured in the previous phases listed in Table 8.

The material properties for specimens within the Phase 5 and 6 batches were quite uniform. For Phase 5, the maximum variation between cylinders for Young's modulus, yield stress and tensile strength was 6.9%, 2.9% and 2.4%, respectively. The material properties of Phase 6 cylinders showed a similar consistency. However, there is some variability in properties between those material batches. The average yield stress for Phase 6 specimens is 8.2% greater than the average value for Phase 5 specimens, and the Phase 6 tensile strength is 6.4% greater than for Phase 5. Young's modulus and elongation at break were similar for the two batches, agreeing within 1%.

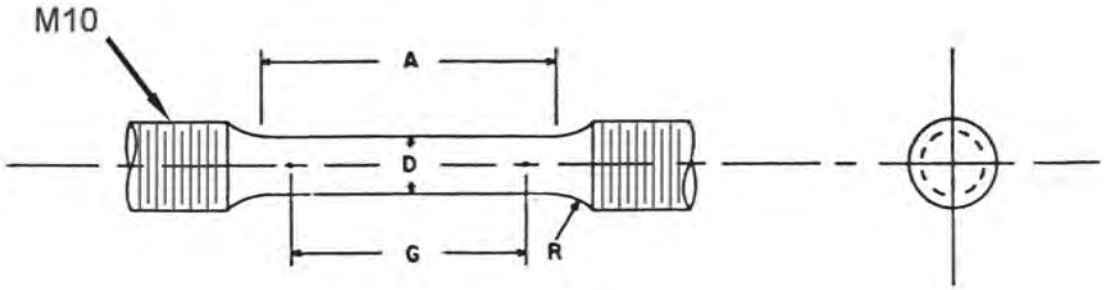

Figure 24: Dimensions for under-sized tensile testing coupons with threaded grips, where D=4 mm, G=20 mm, A=24 mm, and R=4 mm.

Figure 25: Typical post-testing configuration of under-sized tensile coupons, showing coupons taken from Phase 2 cylinders [2] constructed from AA-6082-T6 tubing.

The measured values of Young's modulus for Phase 5 and 6 specimens are significantly lower than the typical handbook value of approximately 70 GPa [16], as well as the measured values for previous testing phases listed in Table 8. Young's modulus is typically measured using two extensometers on the coupon so that any unintentional bending stresses can be factored out. In the current coupon tests, only one extensometer was used, so that it is not known if the low values for Young's modulus represent the true material behaviour or if they are a result of bending stresses in the specimens.

Table 9: Measured engineering material properties in the circumferential direction for Phase 5 and 6 specimens, reporting the mean properties determined from three coupons machined from each cylinder model after collapse testing.

Specimen Name	Young's Modulus (GPa)	Yield Strength, 0.2% Offset (MPa)	Tensile Strength (MPa)	Elongation at Break
L510-No13	55.6	327.5	347.3	12.6%
L510-No14	55.2	334.2	349.9	11.0%
L510-No17	58.2	306.0	327.8	12.8%
L510-No18	57.2	305.1	328.0	11.7%
L510-No19	58.0	328.9	349.6	10.6%
L510-No20	56.4	325.1	346.2	14.1%
L510-No25	56.8	305.4	329.4	12.0%
L510-No26	58.9	309.6	332.5	11.7%
L510-No33	57.6	300.9	324.8	14.1%
L510-No34	55.1	301.0	325.0	10.7%
L510-No35	56.6	331.6	352.4	13.9%
L510-No36	58.6	330.8	347.3	10.2%
Average for Phase 5	*57.3*	*304.7*	*327.9*	*12.1%*
Average for Phase 6	*56.7*	*329.7*	*348.8*	*12.0%*

Typical engineering stress-strain curves for Phase 5 and 6 specimens are plotted in Figure 26. The stress-strain curves were derived from load cell and extensometer data, and calliper measurements of coupon diameter. Figure 26 shows that the general material behaviour for both groups of specimens is similar, with a sharp "knee" near the yield stress, a small strain hardening modulus and significant ductility before the occurrence of both the ultimate load and rupture. The difference in yield stress and ultimate strength between the material batches is clearly shown in the figure.

The measured material properties for individual tensile coupons are listed in Table 103 in Annex D. Measured engineering stress-strain curves derived for each coupon sample are also tabulated in that annex. The load cell and extensometer data used to generate the stress-strain data was acquired at a rate of 10 Hz during coupon testing. The stress-strain data reported in Annex D has been reduced to an equivalent sampling rate of 0.1 Hz by discarding 99 data points out of 100. The difference between stress-strain curves derived from the full and reduced data is shown in Figure 26.

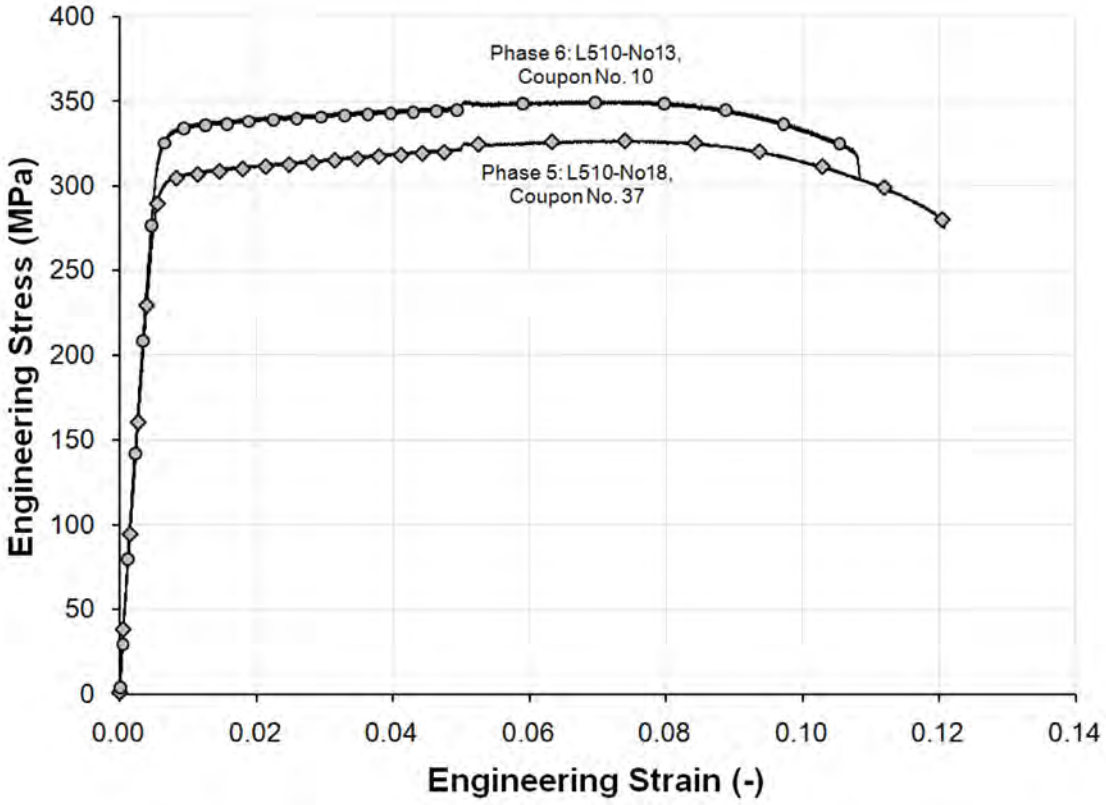

Figure 26: Typical engineering stress-strain curves derived from tensile testing of coupons machined from the circumferential direction of Phase 5 and 6 cylinders. The solid lines represent the full data sets acquired at 10 Hz, while the markers indicate the data remaining after reduction to 0.1 Hz.

2.4 Instrumentation

This section presents strain gauge instrumentation plans for Phase 5 and 6 cylinders, including schematic drawings, and strain gauge identification, type and location. Strain gauges were fixed to Phase 5 and 6 cylinders by the Naval Engineering Test Establishment (NETE) of LaSalle, Quebec. The strain gauge locations for each specimen are tabulated in Annex E.

In the following instrumentation plans, a “uni-axial gauge” refers to a general purpose, linear pattern, strain gauge (Vishay Micro-Measurements gauge designated CEA-13-250UW-350). A “bi-axial gauge” refers to a two-element 90° tee stacked rosette (Vishay Micro- Measurements gauge designated CEA-13-125WT-350). All uni-axial gauges on ring-stiffeners were aligned in the circumferential direction, and all bi-axial strain gauges were aligned with the axial and circumferential axes of the cylinders. Strain gauge locations are defined with respect to the centre of the strain gauge grid. Strain gauge readings are accurate to 0.5% of the reported value.

2.4.1 Phase 5 specimens

Each Phase 5 cylinder, except for L510-No34, which is discussed separately below, was instrumented with twenty-four bi-axial and twenty-four uni-axial gauges in the following manner. Twelve uni-axial gauges were fixed to each of the two central ring-stiffeners (Frames 4 and 5) at 30° increments about the circumference. Twelve bi-axial gauges were fixed to the outside of the shell mid-way between the two central ring-stiffeners in Bay 4 at 30° increments about the circumference. Lastly, a row of thirteen bi-axial gauges were attached to the outside of the shell along the length of the cylinder at each mid-bay and ring-stiffener location, starting at Bay 1 (see Table 10). The latter group of gauges includes one of the twelve gauges running about the circumference in Bay 4. A photograph of the instrumented specimen L510-No18, showing a typical strain gauge arrangement on the outside of the cylinder, is presented in Figure 27(a).

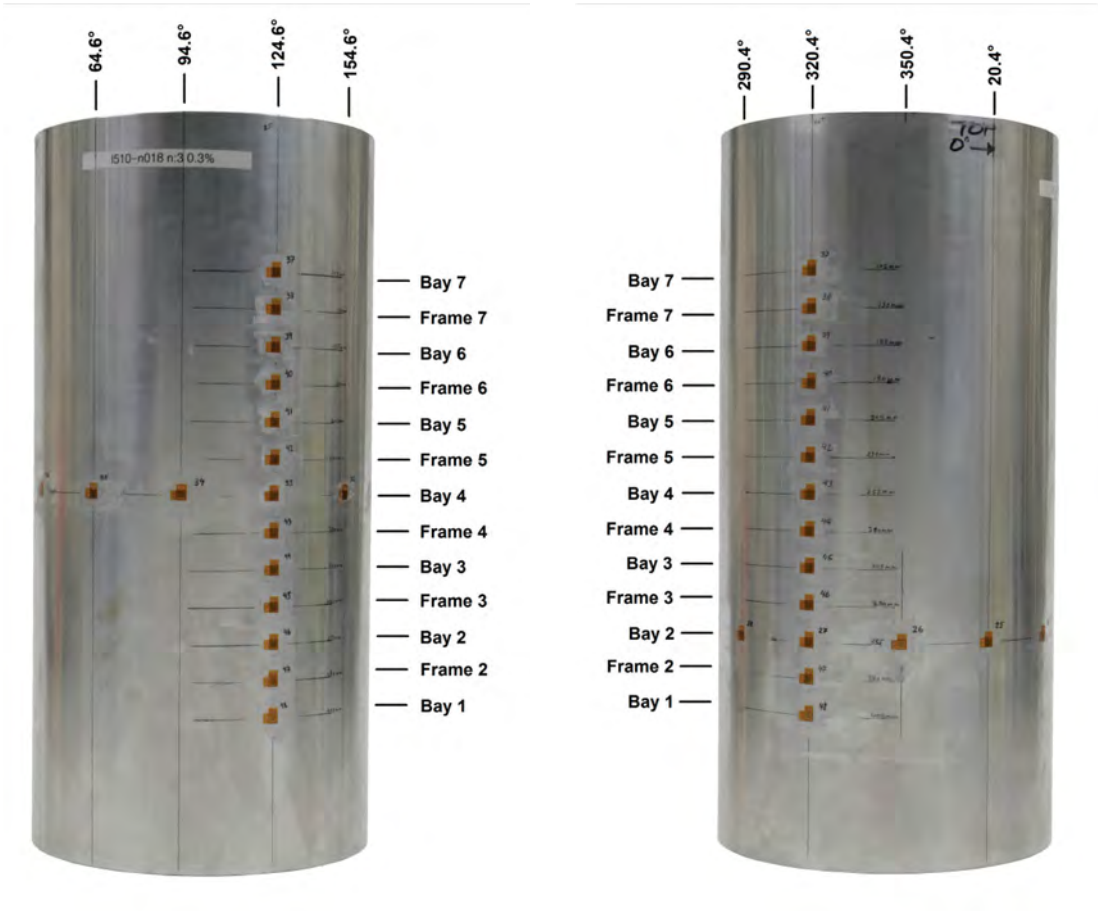

(a) L510-No18 **(b) L510-No34**

Figure 27: Instrumented Phase 5 specimens, showing bi-axial strain gauges on the outside of specimens L510-No18 (a) and L510-No34 (b). All other Phase 5 specimens are similar to L510-No18, except that the angular location of the row of gauges along the cylinder length varies from specimen to specimen (see Table 10).

Table 10: Summary of strain gauge locations for Phase 5 specimens.

Specimen Name	Frames with Strain Gauges	Bay with Strain Gauges about the Circumference	Angular Location of the Row of Gauges over the Cylinder Length
L510-No17	Frame Nos. 4 & 5	Bay No. 4	140.0°
L510-No18	Frame Nos. 4 & 5	Bay No. 4	124.6°
L510-No25	Frame Nos. 4 & 5	Bay No. 4	260.0°
L510-No26	Frame Nos. 4 & 5	Bay No. 4	260.0°
L510-No33	Frame Nos. 4 & 5	Bay No. 4	6.4°
L510-No34	Frame Nos. 3 & 6	Bay No. 2	320.4°

The instrumentation plan for specimen L510-No34 was the same as for other Phase 5 specimens, except that the uni-axial gauges were fixed to Frames 3 and 6, rather than Frames 4 and 5, and the ring of bi-axial gauges was located in Bay 2 rather than Bay 4. Those changes were intended to capture the highest stresses and failure location in the specimen, which is fundamentally different than the other Phase 5 cylinders due to the m=2 axial OOC shape. A photograph of the instrumented specimen is presented in Figure 27(b).

When developing the instrumentation plans for individual specimens, an attempt was made to locate the row of gauges along the length of the cylinder at the circumferential angle corresponding with the maximum OOC. The gauges running about the circumference on the ring-stiffeners and the shell were located so that the starting angle coincided with the row of gauges along the cylinder length. Unfortunately, the cylindrical coordinate system used to measure the cylinder OOC, including the zero angle location, the positive angle direction and the positive axial direction, was not preserved for the application of strain gauges. As a result, some of the gauges were not fixed at the intended angular or axial location. All tables and figures in this document refer to the as-fixed strain gauge locations, with respect to the OOC coordinate system, not the locations specified in the original instrumentation plans.

The strain gauge locations for all Phase 5 specimens are summarized in Table 10. By comparing the locations of the rows of gauges along the cylinder length in Table 10 to the angular locations of maximum OOC in Table 4, it can be seen that, despite the confusion with the coordinate system, each of the rows of gauges is located at or near one of the inward lobes of the n=3 OOC shape, if not the most severe lobe. However, it can be seen from Figure 12 that the maximum OOC for specimen L510-No34 is located near Bay 6, while the ring of strain gauges were fixed to the shell at Bay 2.

2.4.2 Phase 6 specimens

Phase 6 specimens were instrumented with strain gauges based on either of two plans, depending on whether the cylinder had a small or a large corrosion patch. It was assumed that the corrosion patches were located at 0° during the application of strain gauges; however, as noted in Table 4,

two of the Phase 6 cylinders had corrosion patches that were offset from the 0° mark. The strain gauge locations reported herein have been adjusted for the offset from 0°, as necessary.

Specimens L510-No13, L510-No14, L510-No35 and L510-No36 had a small 42x42 mm corrosion patch. The strain gauge layout in the region of the small corrosion patch is shown schematically in Figure 28, and the overall cylinder instrumentation was as follows. Twelve uni-axial gauges were fixed to the flanges of each of the two central ring-stiffeners, Frames 4 and 5, at 30° increments. Twelve bi-axial gauges were fixed to the outside of the shell in Bay 4, mid-way between Frames 4 and 5, at 30° increments. One of those gauges was located at the centre of the corrosion patch. Four additional bi-axial gauges were fixed to the shell at that axial location. Two of those gauges were located inside the corrosion patch at ±7.5° from the centre of the patch, and the other two gauges were located outside of the patch at ±15° from its centre. Two bi-axial gauges were also fixed to the outside of the shell opposite Frames 4 and 5. Those gauges were just outside the corrosion patch, and circumferentially aligned with its centre. On the inside of the shell in Bay 4, one bi-axial gauge was fixed at the centre of the corrosion patch, as well as four others offset ±9.8° and ±15° from the centre of the patch.

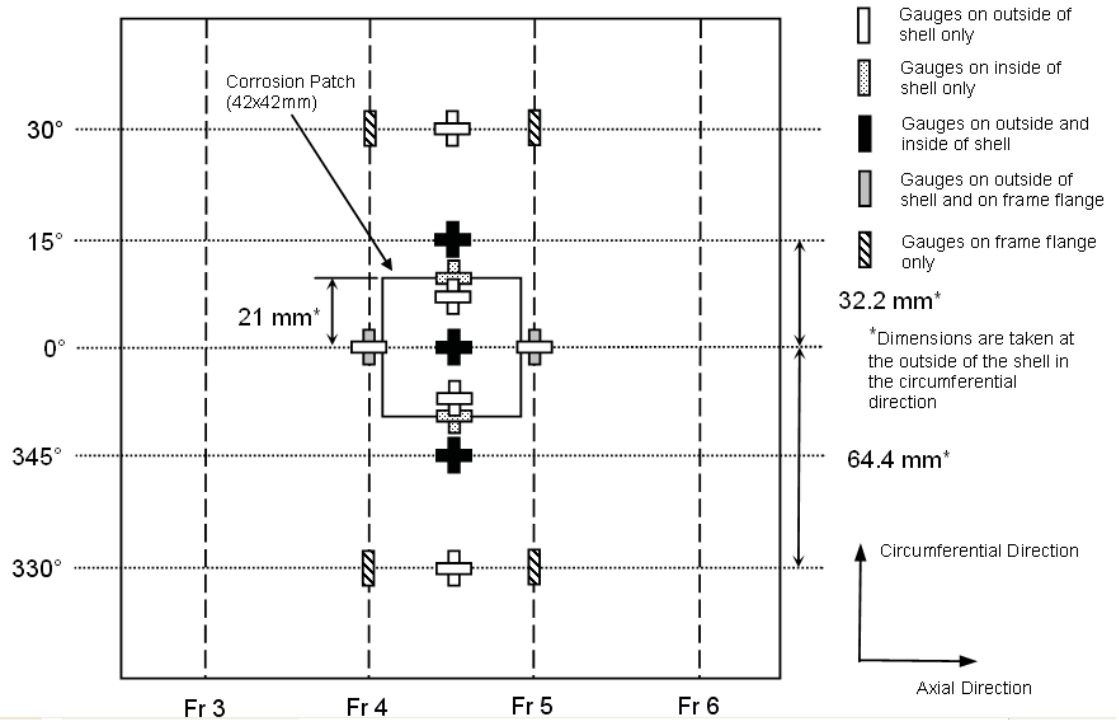

Figure 28: Strain gauge layout near the small corrosion patch for specimens L510-No13, L510-No14, L510-No35 and L510-No36. The indicated angles are shifted by -165° for L510-No14.

The strain gauge layout in the region of the large 100x100 mm corrosion patch for specimens L510-No19 and L510-No20 is shown schematically in Figure 29. Those cylinders were instrumented in the following manner. Twelve uni-axial gauges were fixed to the flanges of both central ring-stiffeners at 30° increments, as well as two extra gauges at ±15° from the centre of the corrosion patch. Bi-axial gauges were attached to the outside of the shell, inside the corrosion patch, in a 3x3 grid. Axial grid locations corresponded to Frames 4 and 5 and the centre of Bay 4, while circumferential locations corresponded to the centre of the patch and ±15° from the centre. Bi-axial gauges were also attached to the outside of Bay 4 at ±30° from the patch centre. On the inside of the shell in Bay 4, bi-axial gauges were attached at the centre of the patch and at ±15°, ±23.3°, and ±30° from the patch centre.

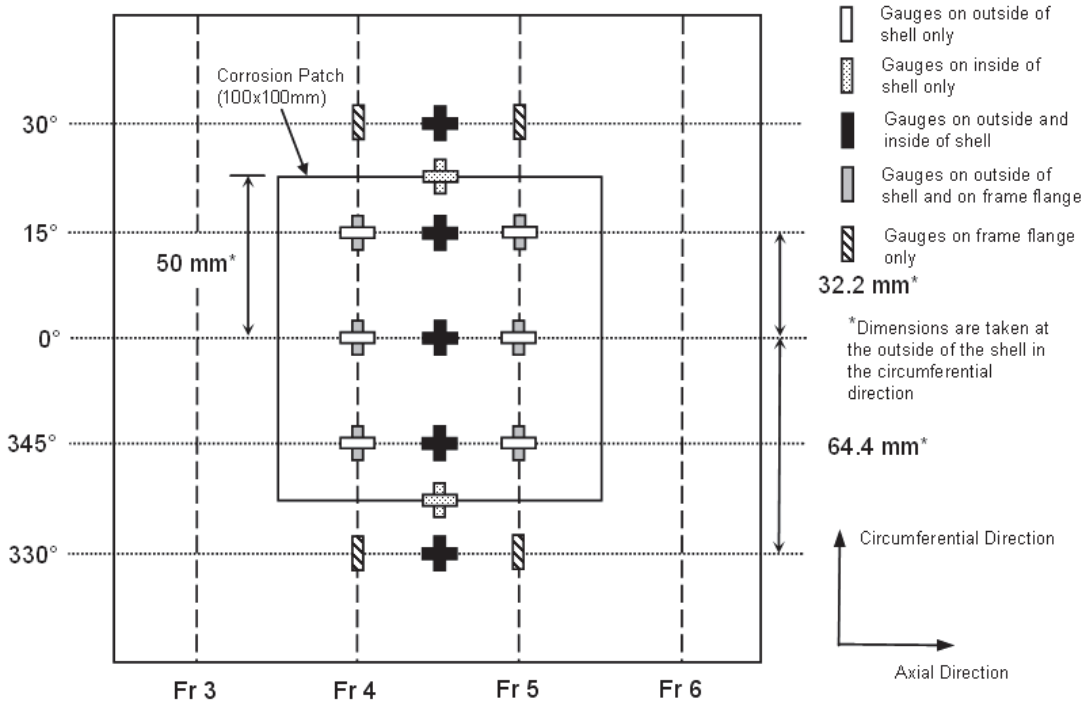

Figure 29: Strain gauge layout near the large corrosion patch for specimens L510-No19 and L510-No20. The indicated angles are shifted by -183.5° for L510-No20.

3 Experimental apparatus and procedures

The test specimens were loaded to collapse under external pressure in the DRDC Atlantic high pressure testing facility, using the so-called “volume-control” method. In this method, shown schematically in Figure 30, a fluid-filled specimen is uniformly pressurized inside and outside to a level greater than the specimen collapse pressure. The fluid inside the specimen is then isolated from the tank by closing a “cross-over” valve. The loading stage begins by releasing the pressurized fluid from inside the specimen using a second “fluid-release” valve, resulting in a net external pressure load on the shell.

The volume-control apparatus is realized by connecting a network of high-pressure hoses, pipes, and needle valves to a standard pressure testing apparatus, as shown in Figure 30. The volume-control method is described in greater detail in [3] and [17]. The use of this method has eliminated the excessive post-collapse deformations and rupture that occurred while using a conventional test apparatus with air-backed specimens in Phase 1 [1], e.g. see specimen L300-No4 in Figure 1. A non-conductive mineral oil was used as the testing fluid in the volume-control apparatus, rather than water. This prevented shorting of the electronic equipment without the requirement to seal strain gauges and lead wires against water infiltration.

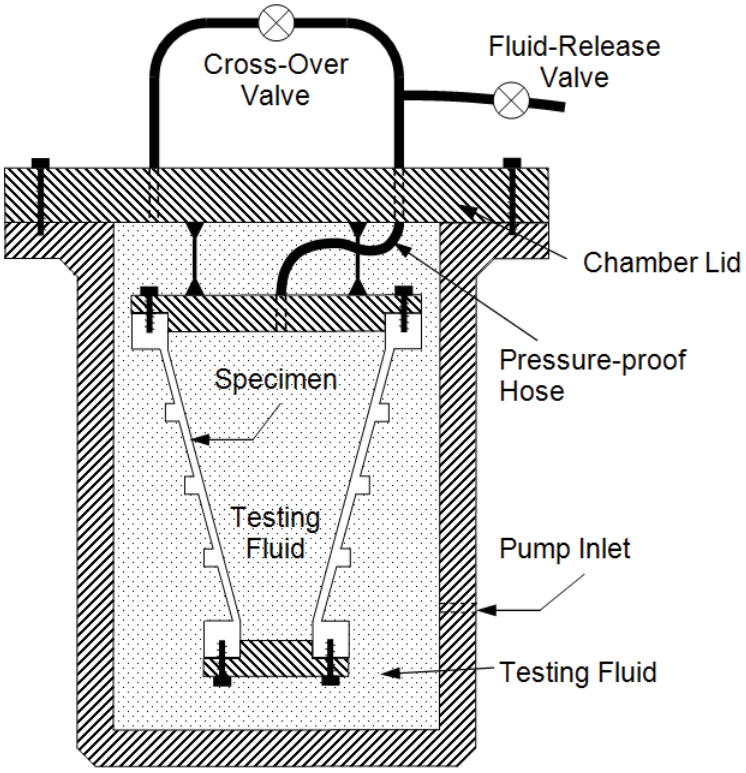

Figure 30: Schematic diagram of volume-control pressure testing apparatus.

Before testing a cylinder, heavy steel end caps were attached to either end of the specimen with bolts. The “bottom” end cap had threaded holes for the watertight electronic connectors that connected the strain gauges with the data acquisition system, via additional connectors at the base of the pressure chamber. The “top” end cap was fitted with threaded holes for filling the specimen with the testing fluid and completing the pressure testing loop. The end caps were machined from mild steel, and the design geometry for the top end cap is shown in Figure 31. The end cap joints were made watertight using an adhesive polymer sealant (PR-1422, manufactured by PRC-Desoto International).

The transducers used to measure the chamber and specimen pressures had ranges of 17.2 and 34.5 MPa, respectively. The transducers were accurate to within 0.25% of their range (0.043 and 0.086 MPa, respectively) for all errors. The net pressure on the specimen (i.e. tank pressure less the specimen pressure) is reported in this document to three significant figures and is associated with the accuracy of the tank transducer (±0.09 MPa).

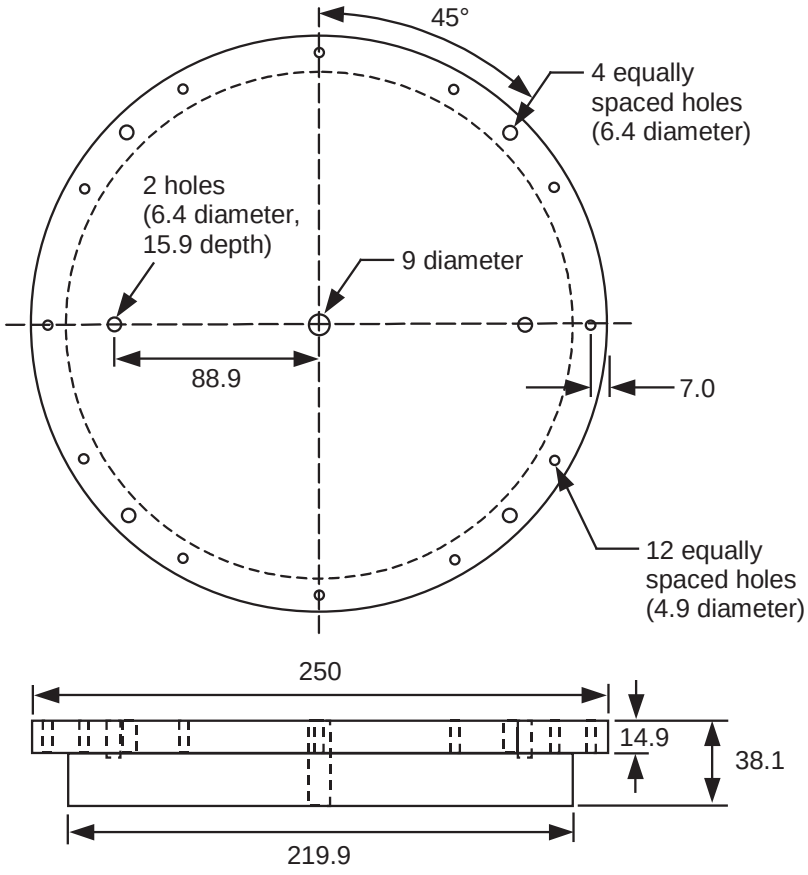

Figure 31: Schematic drawing of “top” specimen end cap.

Each specimen underwent two types of tests: 1) one or more loading cycles in the elastic range to check the instrumentation and pressure testing equipment, and 2) loading up to the ultimate or collapse pressure, after which the specimen was unloaded and removed from the pressure tank for inspection of the collapse shape. Except where noted, the pre-pressure load on the system for elastic and collapse tests was approximately 3 MPa and 13.5 MPa, respectively. Pre-pressurization for collapse tests that were performed immediately after an elastic cycle was typically undertaken by increasing the pre-pressure load directly, rather than de-pressurizing the system and starting from zero.

The testing history for each Phase 5 and 6 specimen, including testing date, type of test, pre- and maximum pressure and any testing irregularities, are reported in the experimental results in Section 4. Strain gauge and pressure transducer readings were taken at a sampling rate of 100 Hz for all tests. Reported collapse pressures are based on the maximum recorded pressure load, while yield pressures are based on the first occurrence of the von Mises equivalent stress reaching the 0.2% yield stress of the material in the circumferential direction. The procedure for calculating stresses from measured strain values is described in [3].

4 Experimental results

Experimental results for individual specimens, including a description of the failure mode and selected pressure-strain histories are described in Sections 4.1 and 4.2 for Phase 5 and 6 specimens, respectively. Complete pressure-strain data for all specimens, and additional information derived from those data, are found in the annexes (see Table 11).

Reported yield and collapse pressures were determined using the full set of experimental data recorded at a sampling rate of 100 Hz. Unless otherwise noted, pressure-strain plots shown in Annex H and elsewhere were constructed using experimental data reduced to an equivalent sampling rate of 20 Hz (i.e. four out of five data points were discarded) to facilitate manipulation of the data.

The reported yield pressures were derived from strain gauge data by assuming that the as-tested cylinders were in a stress-relieved condition; that is, the effect of the residual stresses that necessarily arose during application of OOC were neglected. As such, the reported yield pressures may be greater or less than the actual yield pressures, depending on the interaction of the residual stresses with the applied loads. Nonetheless, the reported yield pressures are still useful for comparing the relative magnitudes of applied stresses in different locations of the cylinders and also provide estimates of the actual yield pressure.

Table 11: Experimental results found in the annexes

Annex	**Description**	**Page**
Annex F	Tank, specimen and net pressures measured during volume-control collapse testing plotted against the time	261
Annex G	Tables summarizing the pressures causing first yield at each strain gauge location for all specimens	267
Annex H	Pressure-strain plots for each strain gauge location for all specimens	291
Annex I	Figures showing the circumferential distribution of strain for each cylinder specimen through-out the loading regime	369
Annex J	Plots of circumferential bending strains derived by Fourier decomposition over the course of loading, for intact regions of specimens only	399
Annex K	Figures showing the distribution of strain over the length of Phase 5 cylinders	413

4.1 Phase 5: specimens without corrosion damage

This section presents collapse testing results for specimens tested in Phase 5, none of which had artificial corrosion damage. The final deformed shapes of the Phase 5 specimens after collapse testing are shown in the photographs in Figure 32. Collapse pressures and pressures causing first yield in the shell and stiffeners at strain gauge locations are summarized in Table 12.

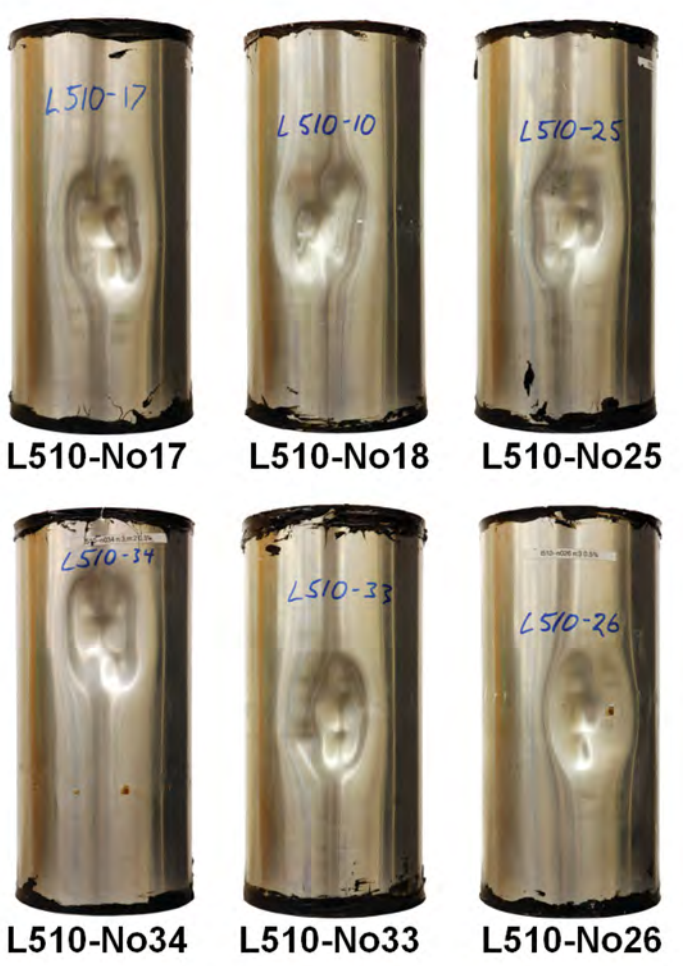

Figure 32: Phase 5 specimens, without artificial corrosion damage, after collapse testing. Clockwise from top-left: L510-No17 and L510-No18, both with 0.3% OOC in n=*3 and* m=*1 circumferential and axial modes, respectively; L510-No25, L510-No26 and L510-No33, all with 0.5% OOC in* n=*3 and* m=*1 circumferential and axial modes, respectively; and L510-No34, with 0.3% OOC in* n=*3 and* m=*2 circumferential and axial modes, respectively.*

Table 12: Summary of yield and collapse pressures for Phase 5 specimens, without artificial corrosion damage.

Specimen	First Yielding of the Shell [a]		First Yielding of the Stiffener [b]		Collapse Pressure, P_c [c] (MPa)
	Location	P_y [c] (MPa)	Location	P_y [c] (MPa)	
L510-No17	Outside mid-bay no. 4 at 20°	7.35	Stiffener no. 4 at 50°	7.72	7.84
L510-No18	Outside mid-bay no. 6 at 124.6°	7.57	Stiffener no. 4 at 184.6°	7.50	7.71
L510-No25	Outside mid-bay no. 4 at 20°	6.76	Stiffener no. 4 at 80°	6.57	7.13
L510-No26	Outside mid-bay no. 3 at 260°	6.55	Stiffener no. 5 at 80°	6.31	7.05
L510-No33	Did not yield before collapse		Stiffener no. 5 at 186.4°	6.69	7.03
L510-No34	Outside mid-bay no. 2 at 20.4°	7.52	Did not yield before collapse		8.02

a. Based on the first occurrence of the von Mises stress reaching the circumferential yield stress, for measurements taken at bi-axial strain gauge locations. Residual stresses due to applying out-of-circularity are neglected.

b. Based on the first occurrence of the uni-axial circumferential flange stress reaching the circumferential yield stress, for measurements taken at strain gauge locations. Residual stresses due to applying out-of-circularity are neglected.

c. Yield pressures, P_y, and collapse pressures, P_c, are accurate to within ±0.09 MPa.

4.1.1 L510-No17

The nominal out-of-circularity of specimen L510-No17 was 0.3% in an n=3, m=1 mode. The as-measured shape of the cylinder was found to be in the target mode, with amplitude somewhat greater than the nominal value, depending on the definition of OOC chosen (see Table 3). L510-No17 underwent a single elastic loading cycle (see Table 13) before it was loaded to collapse, failing at a pressure of 7.84 MPa. The applied pressure dropped suddenly to approximately 2.9 MPa shortly after the peak load was reached (see Figure 166 in Annex F). The specimen was then completely unloaded by allowing the specimen and tank pressures to equalize.

After collapse testing, the specimen showed a permanent buckle at approximately 20° spanning the three central bays, with significant deformation of shell and stiffeners (see Figure 32), which is consistent with overall collapse. Figure 33 shows the strain distribution about the circumference at Frame 4 at various loading increments up to the collapse pressure. An overall n=3 mode is apparent throughout the loading history, with the amplitude increasing with the pressure load.

Table 13: Testing procedures for specimen L510-No17

Test Name	Date	Test Type	Pre-Pressure (MPa)	Maximum Pressure (MPa)	Notes
Trial 1	12 Jan 2009	Elastic	3.22	1.04	Circumferentially oriented gauge outside mid-bay no. 7 at 140° showed some drift during pre-pressurization, i.e. at zero net pressure load. The gauge seemed to function normally during specimen loading.
Trial 2	12 Jan 2009	Collapse	13.66	7.84	Same as above.

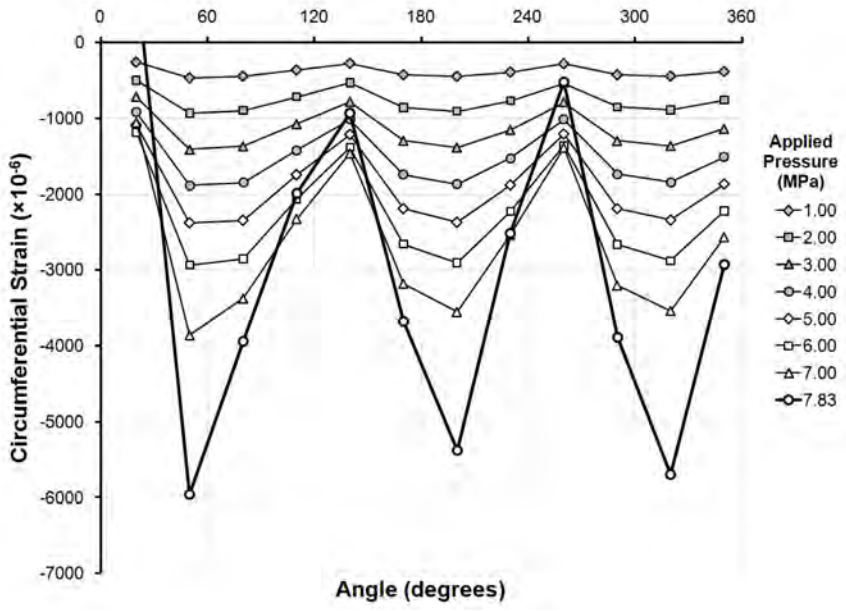

Figure 33: Circumferential strain distribution at the flange of Frame 4 of specimen L510-No17, at pressures up to and including the collapse pressure.

The strain distribution at the collapse load is plotted with the initial out-of-circularity at Frame 4 in Figure 34. The n=3 phase angles of the strain and OOC plots are offset by approximately 60°, which is as expected since inward and outward OOC lobes lead to, respectively, tensile and compressive bending strains at the stiffener flange. Figure 35 and Figure 36 show similar circumferential strain distribution plots based on measurements taken outside the shell in the central bay. Those figures show similar n=3 bending strains in the shell, except that they are, as expected, in-phase with the initial out-of-circularity.

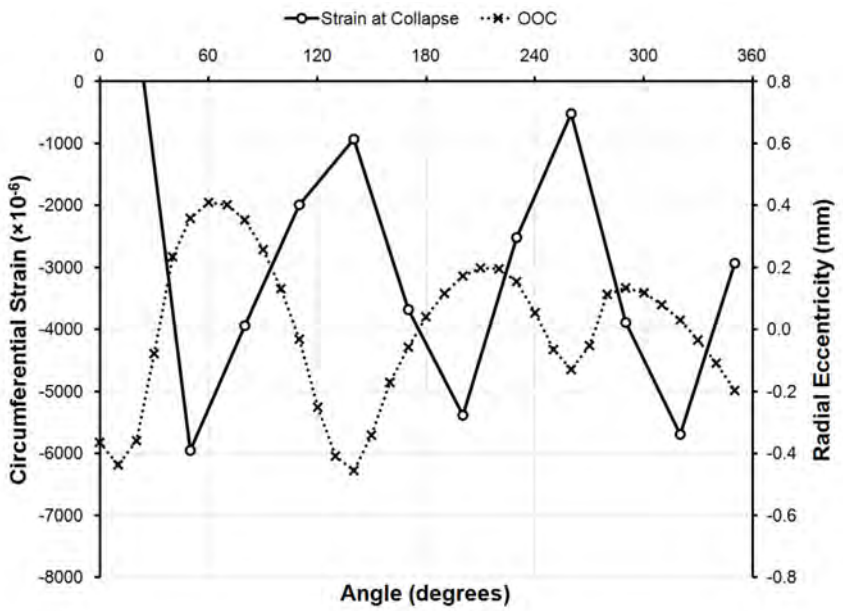

Figure 34: Circumferential strain distribution at the flange of Frame 4 of specimen L510-No17 at the collapse pressure, plotted with the initial out-of-circularity at that location.

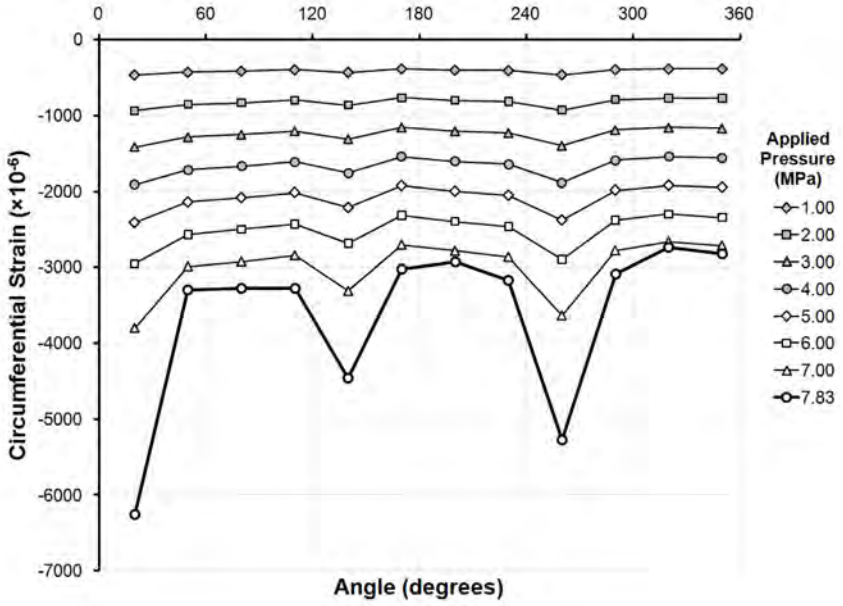

Figure 35: Circumferential strain distribution outside the shell in the centre of Bay 4 of specimen L510-No17, at pressures up to and including the collapse pressure.

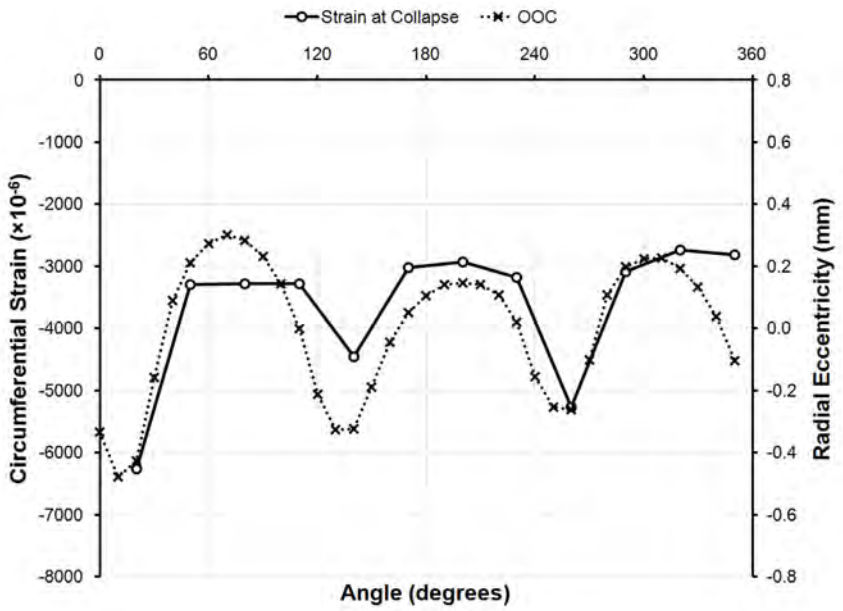

Figure 36: Circumferential strain distribution outside the shell at Bay 4 of specimen L510-No17 at the collapse pressure, plotted with the initial out-of-circularity at that location.

The strain distribution plots in Figure 33 to Figure 36 show that the maximum compressive and tensile strains at the collapse pressure in the shell and frame, respectively, occurred at the location of the post-testing buckle at 20°. The post-collapse deformations were therefore concentrated at the dominant buckling lobe of the overall n=3 mode. Due to the dynamic nature of the collapse event and the resulting large velocities and strain rates, the instrumentation was unable to capture the transition from the n=3 mode to a single-lobed deformation pattern.

Fourier decompositions were performed on the circumferential strain data in order to qualitatively understand the cylinder deformation. In Figure 37 and Figure 38, the results of the Fourier analyses of the shell and frame strains, respectively, are plotted against the applied pressure. The bending strains in the frame (Figure 37) were clearly dominated by an n=3 mode over the entire loading history and especially as the collapse load was approached; however, the n=6 mode also contributed to the overall strain distribution throughout loading. The shell bending strain distribution (Figure 38) was influenced approximately equally by the n=3 and n=6 modes. The large n=6 contribution resulted from deep and narrow troughs in the compressive strain response that arose due to similar troughs in the initial shape of the cylinder (see Figure 36).

The circumferential strain distribution plots and Fourier decompositions indicate that the cylinder failed in the targeted n=3 collapse mode. Figure 39 shows the strain distribution outside the shell at the collapse pressure over of the length of the cylinder at one of the inward lobes of the initial OOC shape (140°). The compressive shell strain at mid-bay can be seen to be greater than the shell strain outside frames over the length of the cylinder. Furthermore, the axial strain distribution clearly conforms to the expectations for the m=1, half sine wave initial shape.

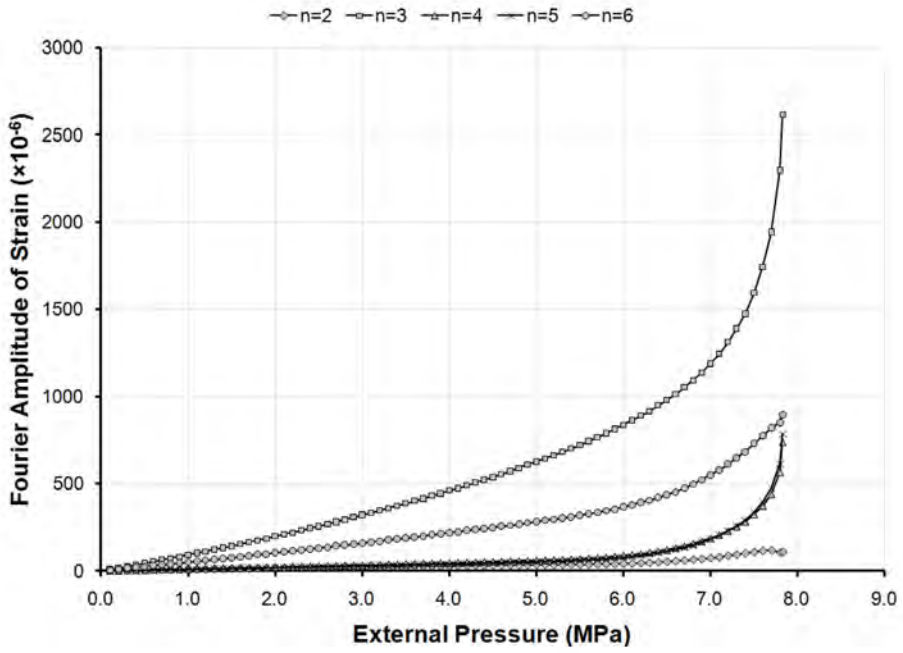

Figure 37: Bending strain amplitudes at the flange of Frame 4 of specimen L510-No17, derived from Fourier decomposition, and plotted against the applied pressure.

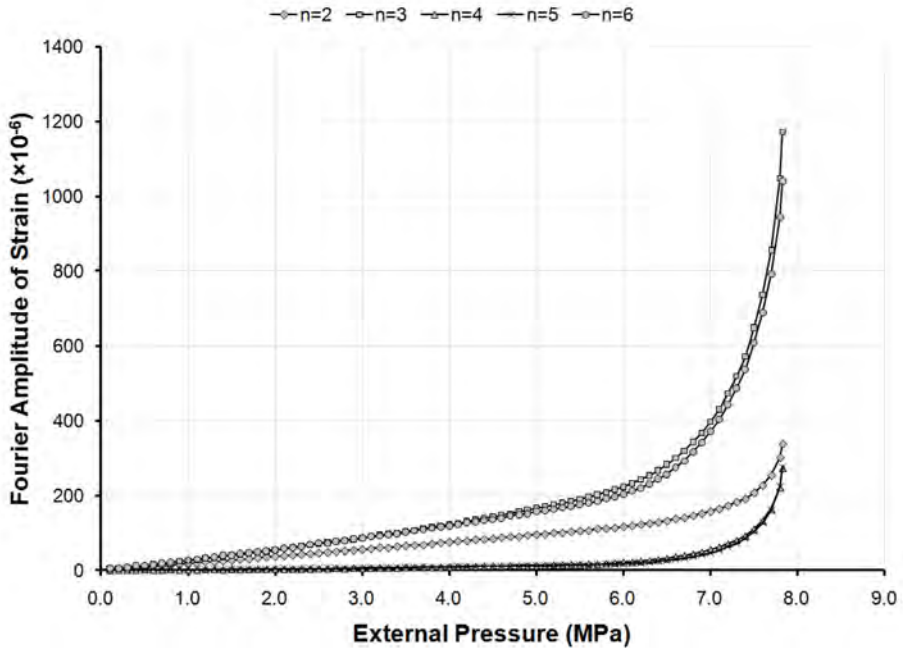

Figure 38: Bending strain amplitudes outside the shell in Bay 4 of specimen L510-No17, derived from Fourier decomposition, and plotted against the applied pressure.

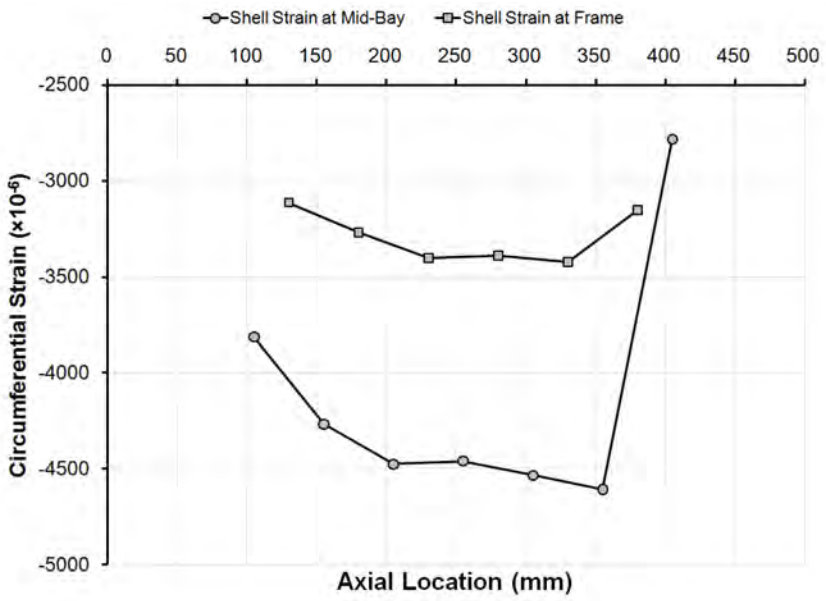

Figure 39: Axial distribution of circumferential strains at 140° measured at the collapse pressure for specimen L510-No17.

Figure 40 shows pressure-strain curves for L510-No17 derived from strain gauges near the location of collapse at 20°. That figure shows the large compressive strain due to inward bending of the shell at the centre of the buckling lobe. Bending of the frame flange led to large compressive stains at the frame at the edge of the buckling lobe and smaller compressive strains at the centre of the lobe, which became tensile as the collapse load was approached. The onset of yielding in the cylinder occurred at the shell in the central bay, where collapse deformations were eventually concentrated. The stiffeners initially yielded in compression at the outside edge of the buckling lobe, and collapse followed soon thereafter.

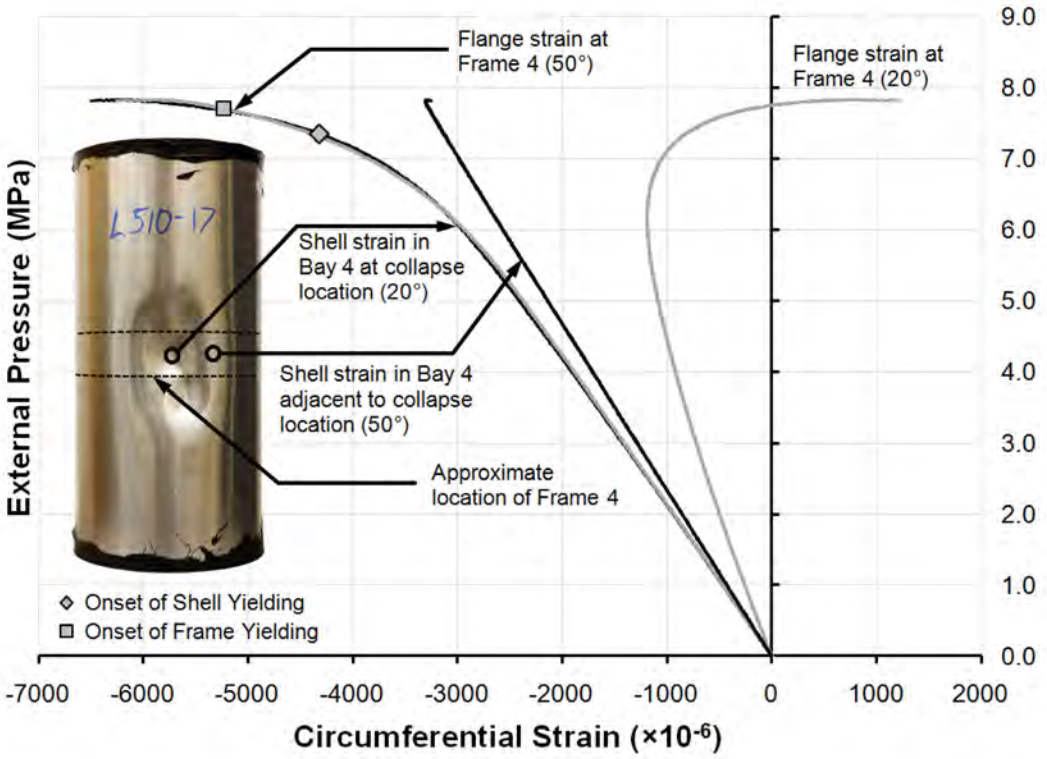

Figure 40: Selected pressure-strain curves near the collapse site for specimen L510-No17.

4.1.2 L510-No18

The nominal out-of-circularity of specimen L510-No18 was the same as for L510-No17 (0.3% OOC in an n=3, m=1 mode), and the as-measured shapes of those cylinders were found to be similar (see Table 3). L510-No18 underwent a single elastic loading cycle (see Table 14) before it was loaded to collapse, failing at a pressure of 7.71 MPa. The applied pressure dropped suddenly to approximately 3.0 MPa shortly after the peak load was reached, and stabilized at pressure of 3.4 MPa (see Figure 167 in Annex F), after which the specimen was unloaded.

Table 14: Testing procedures for specimen L510-No18

Test Name	Date	Test Type	Pre-Pressure (MPa)	Maximum Pressure (MPa)	Notes
Trial 1	16 Jan 2009	Elastic	3.54	1.03	Circumferentially oriented gauge outside mid-bay no. 7 at 124.6° showed some drift during pre-pressurization, i.e. at zero net pressure load. The gauge seemed to function normally during specimen loading.
Trial 2	16 Jan 2009	Collapse	13.77	7.71	Same as above.

The final deformed shape of the specimen after collapse testing was characterized by a permanent buckle centred near 245° and spanning the three central bays (see Figure 32). In general, the response of L510-No18 was similar to L510-No17, with an overall *n*=3 collapse mode, and post-collapse deformations concentrated at one of the inward OOC lobes. The circumferential strain distribution and Fourier decomposition plots for this cylinder can be found in Annex I and Annex J, respectively.

The pressure-strain plots for L510-No18 in Figure 41 are, in general, similar to those shown in Figure 40 for L510-No17. Both specimens showed divergent shell and stiffener strains at the centre and edge of the buckling lobe, and collapse that followed soon after yielding of the frame flange. Figure 41 shows a sudden reversal in the shell strain at the collapse site in the post-collapse region. It is possible that the gauge was not located at the exact centre of the buckling lobe, so that tensile bending strains that grew with the developing buckle led to the strain reversal.

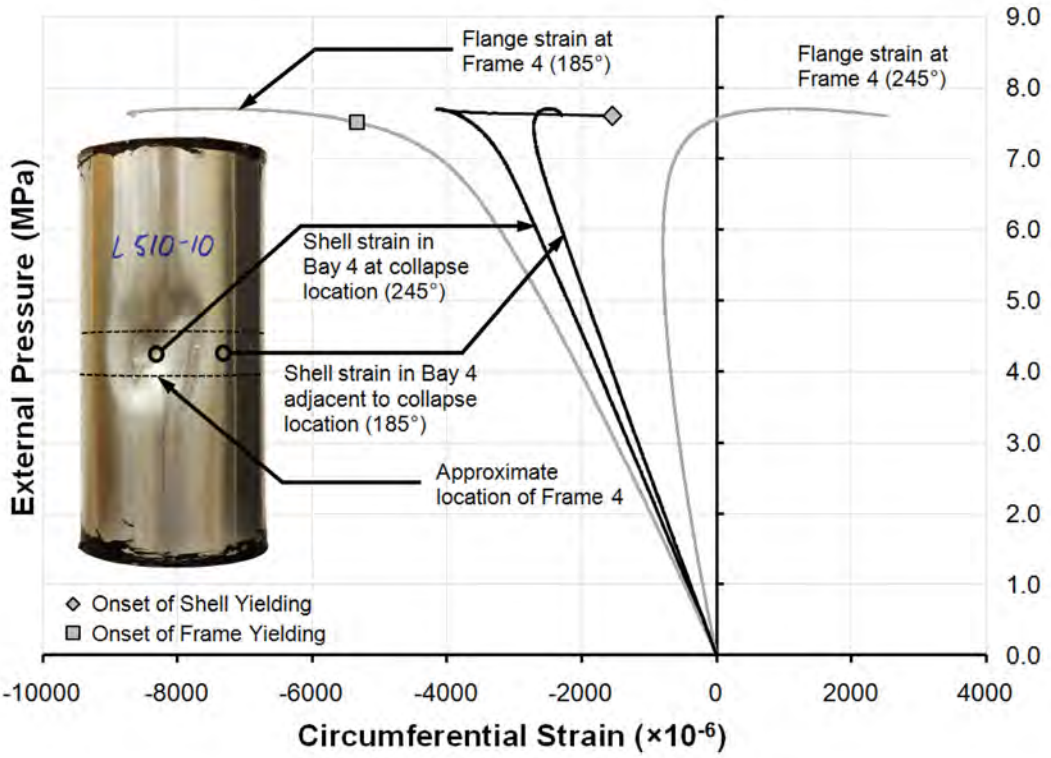

Figure 41: Selected pressure-strain curves near the collapse site for specimen L510-No18.

4.1.3 L510-No25

It was intended that specimen L510-No25 would have 0.5% OOC in an *n*=3, *m*=1 mode. The geometric measurements of that specimen indicate that, while the target OOC mode was achieved, the actual OOC amplitude was significantly larger than the nominal value (see Table 3). L510-No25 was loaded elastically two times: once during the standard elastic cycle before collapse testing, and a second time, unintentionally, during the pre-pressurization stage of the

collapse test (see Table 15). The maximum pressure sustained by the cylinder during the collapse test was 7.13 MPa, and the post-testing shape of the specimen was characterized by a large, overall collapse lobe at 20° (see Figure 32).

Collapse of specimen L510-No25 developed in much the same way as for specimens L510-No17 and L510-No18; that is, with large n=3 bending strains aligned with the initial OOC shape and increasing nonlinearly as the collapse load was approached, and concentration of the post-collapse deformation at one of the dominant n=3 lobes. Plots showing the strain distribution about the circumference, Fourier decomposition of those strains, and the length-wise distribution of strains are given in Annex I, Annex J and Annex K, respectively.

Selected pressure-strain curves for sites near the collapse location on L510-No25 are shown in Figure 42. The overall response of the cylinder is similar to that of L510-No17 and L510-No18, with one important distinction: the frame flanges have yielded before the shell. This is related to the OOC amplitude, which was greater in L510-No25 than in the other cylinders. The relative magnitude of bending stress, compared to the axisymmetric or direct stress, increases with the OOC amplitude. Furthermore, bending stresses are higher in the frame flanges than in the shell plating due to the lesser amount of material in the frames and the relatively large distance between the flange and the neutral axis of the combined stiffener-shell section. So, large OOC amplitudes lead to stresses in the frame flanges which are large relative to the shell stresses. The difference in OOC magnitude between, say, L510-No17 and L510-No25 was great enough that the frame flanges of the former specimen yielded after the shell, and those of the latter yielded before the shell.

It must be kept in mind that the preceding discussion is based on calculated yield pressures that neglect the effect of residual stresses. It is possible that, if the residual stresses are considered, the flanges of L510-No25 may actually yield after the shell. Those considerations have been studied using numerical models, and will be discussed in Section 5. Nonetheless, the general trend of higher flange stresses with larger OOC amplitudes is still valid.

Table 15: Testing procedures for specimen L510-No25

Test Name	**Date**	**Test Type**	**Pre-Pressure (MPa)**	**Maximum Pressure (MPa)**	**Notes**
Trial 1	20 Jan 2009	Elastic	3.20	1.02	Circumferentially oriented gauge outside mid-bay no. 7 at 260° showed some drift during pre-pressurization, i.e. at zero net pressure load. The gauge seemed to function normally during specimen loading.
Trial 2	20 Jan 2009	Collapse	13.76	7.13	Same as above. Also, a pressure load of approximately 1.5 MPa was applied during the initial stages of pre-pressurization due to a closed cross-over value. The valve was subsequently opened, reducing the net pressure to zero for the remainder of the pre-pressurization phase.

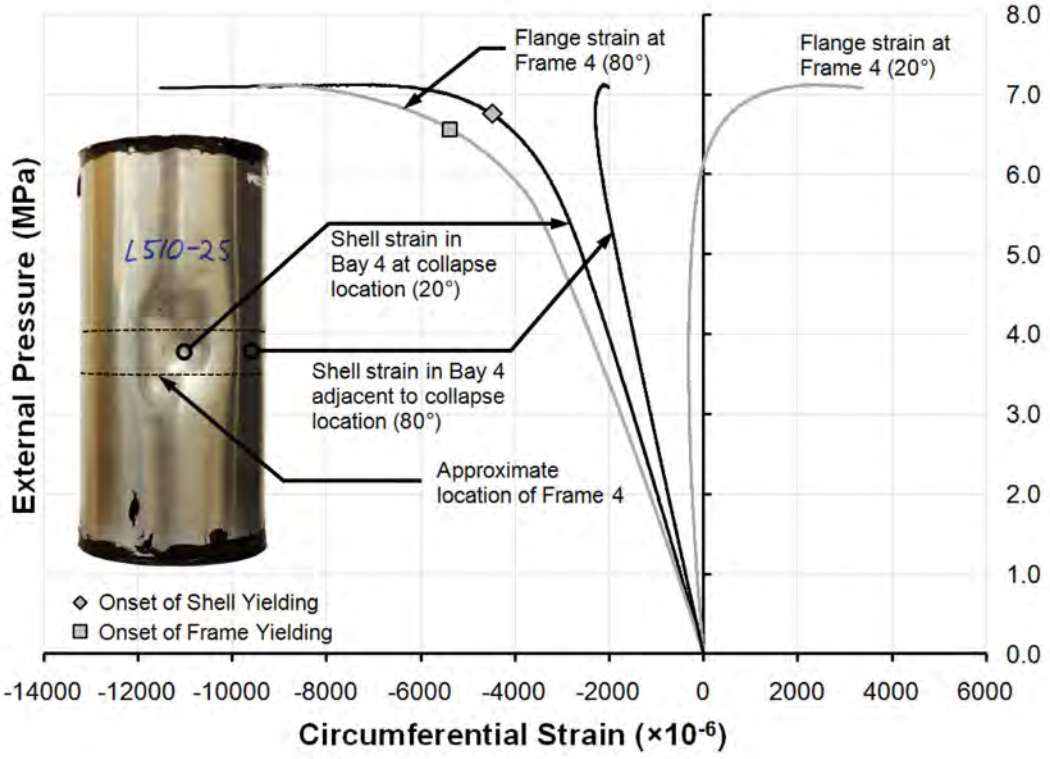

Figure 42: Selected pressure-strain curves near the collapse site for specimen L510-No25.

4.1.4 L510-No26

The nominal applied out-of-circularity of specimen L510-No26 was 0.5% in an *n*=3, *m*=1 mode, i.e. the same target OOC as L510-No25. However, the as-measured OOC of L510-No26 was even greater than L510-No25, and the OOC of both cylinders exceeded the nominal value. L510-No26 was loaded elastically once, as shown in Table 16, and then tested to collapse, resisting a maximum pressure of 7.05 MPa. After collapse testing, the cylinder showed a permanent buckle spanning the central bays at approximately 125-130°, as shown in Figure 32.

The response and collapse of L510-No26 was very similar to the previously discussed specimens, especially L510-No25. The large OOC amplitude for L510-No26 led to large *n*=3 bending strains, especially in the frame flanges. The pressure-strain curves in Figure 43 show that, in this case, the shell did not yield near the collapse site before collapse, although there were no strain gauges located at the centre of the buckling lobe. Furthermore, the yield pressure data in Table 154 in Annex G indicate that the shell yielded at other inward OOC lobes before the collapse pressure was reached.

Table 16: Testing procedures for specimen L510-No26

Test Name	Date	Test Type	Pre-Pressure (MPa)	Maximum Pressure (MPa)	Notes
Trial 1	26 Jan 2009	Elastic	3.05	1.03	Circumferentially oriented gauge outside mid-bay no. 7 at 260° showed some drift during pre-pressurization, i.e. at zero net pressure load. The gauge seemed to function normally during specimen loading. Some noise in the pressure readings was noted.
Trial 2	26 Jan 2009	Collapse	13.55	7.05	Same as above, except noise in pressure readings was eliminated.

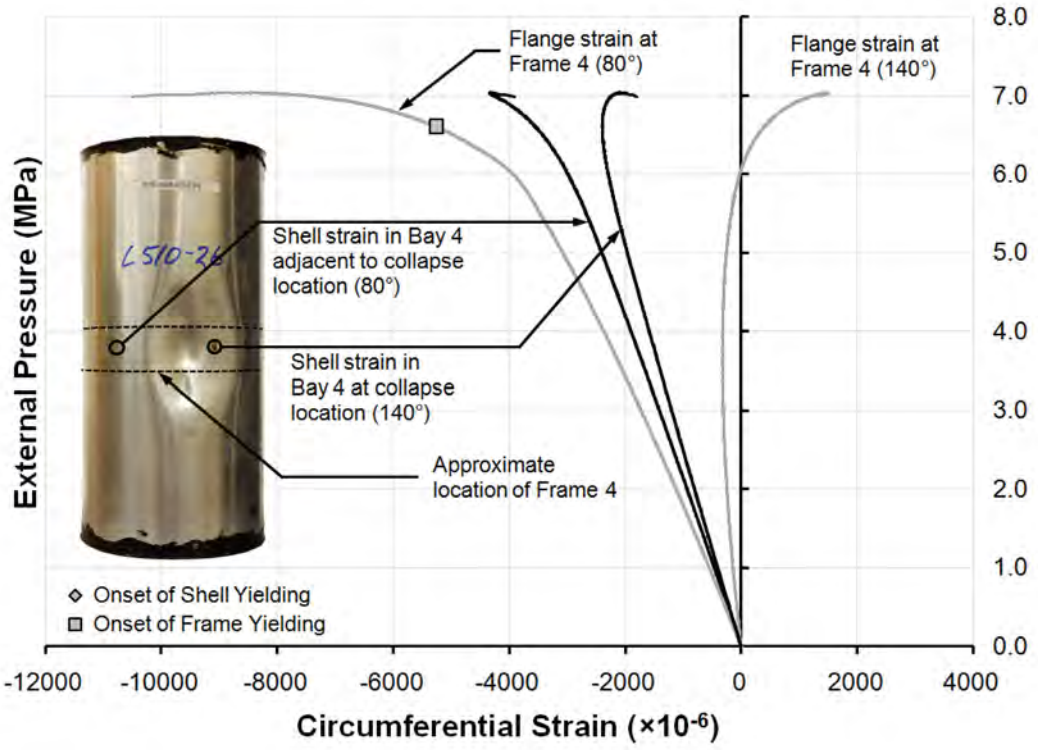

Figure 43: Selected pressure-strain curves near the collapse site for specimen L510-No26.

4.1.5 L510-No33

L510-No33 was the third cylinder without corrosion that was intended to have 0.5% OOC in an n=3, m=1 mode. The actual out-of-circularity amplitude was found to be greater than the target value and nearly identical to that of L510-No26 (see Table 3). L510-No33 was loaded elastically three times. The extra elastic cycles were required to resolve a problem with the polymer sealant for the end-caps, which failed, causing a loss of applied pressure during loading (see Table 17). The failure of the end-cap sealant was attributed to greater than normal gaps between the end-cap

and the cylinder end-ring caused by warping of the cylinders during OOC application. The watertight integrity problems were resolved, however, and the cylinder was loaded to collapse, failing at a pressure of 7.03 MPa.

The post-testing shape of L510-No33, with a single large buckling lobe centred at approximately 140°, is shown in Figure 32. Selected pressure-strain curves near the final post-testing dent are shown in Figure 44. The strain gauge configuration was such that there were no gauges at the circumferential location where the final collapse lobe was located. Nonetheless, the general trends of the curves are similar to the previously discussed specimens; that is, large tensile and compressive bending strains in the frame flange near the centre and edge of the buckling lobe, respectively, and the opposite trend for the shell strains.

The overall collapse mode of L510-No33 was somewhat different than the previously discussed specimens. As expected, the circumferential distribution of strain in the frame flanges was characterized by an n=3 mode up to and including the collapse pressure (see Figure 45), and the n=3 strain distribution was offset by 60° from applied OOC (see Figure 46). Furthermore, Fourier decomposition of the flange strains over the entire loading history, plotted in Figure 47, confirms that the flange deformation was dominated by the n=3 mode throughout loading.

Table 17: Testing procedures for specimen L510-No33

Test Name	Date	Test Type	Pre-Pressure (MPa)	Maximum Pressure (MPa)	Notes
Trial 1	28 Jan 2009	Elastic	3.60	1.04	Gauge on Frame 5 at 96.4° showed some drift after pre-pressurization, but before net loading. After loading the cylinder to 1.0 MPa, the net pressure dropped steadily to 0.6 MPa over approximately 3 minutes, after which the specimen was unloaded. The cross-over was not opened in the initial stages of de-pressurization, so that an internal pressure of 0.9 MPa was mistakenly applied to the specimen. Inspection of the specimen after unloading revealed that the polymer sealant at the end-cap joint had failed, causing the loss of net pressure.
Trial 2	4 Feb 2010	Elastic	3.57	1.00	The leaking end-cap was removed, re-sealed and re-loaded. Again, the net pressure was found to drop steadily, although at a slower rate, to 0.8 MPa over a 3 minute duration.
Trial 3	5 Feb 2009	Elastic	3.56	1.04	Additional sealant was applied to the leaking end-cap and the specimen was able to hold the pressure load. The gauge on Frame 5 (see Trial 1 notes) continued to be a problem.
Trial 4	5 Feb 2009	Collapse	13.96	7.03	N/A

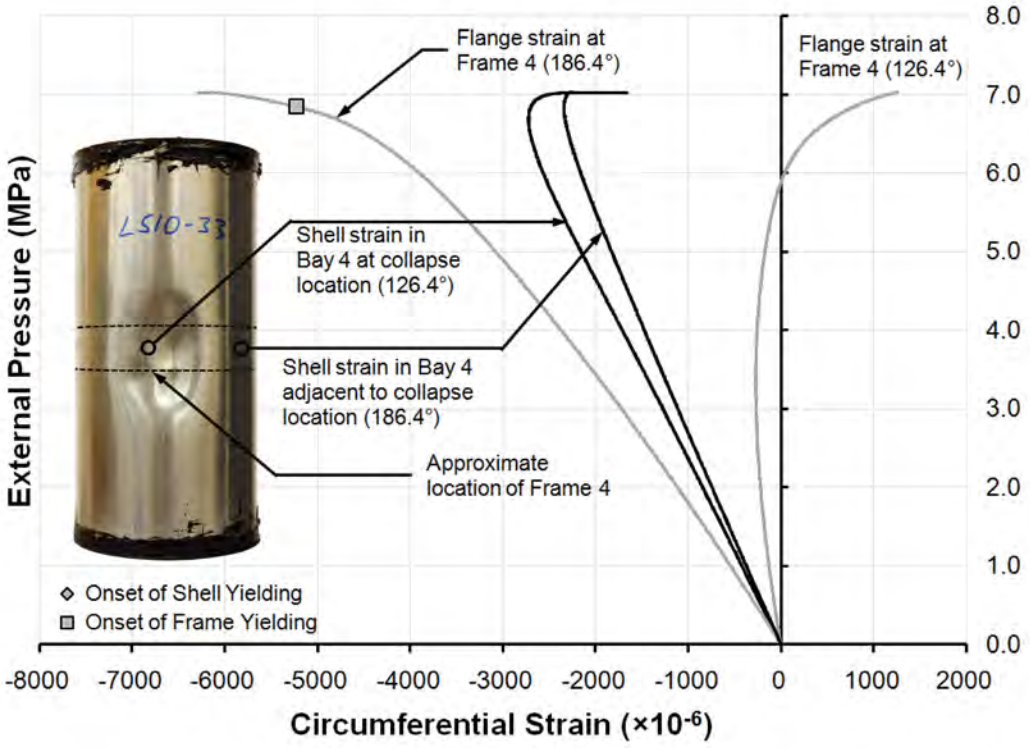

Figure 44: Selected pressure-strain curves near the collapse site for specimen L510-No33.

While the flange strain distribution followed the expected trend, the circumferential distribution of shell strains did not. In Figure 48, a n=3 mode can be discerned in the shell strain distribution in the earlier stages of loading; however, as the collapse pressure was approached, the distribution appeared to be dominated by an n=2 mode. From Figure 49 it can be seen that two of the three compressive strain maxima at collapse are aligned with inward lobes of the initial OOC shape, as expected, but that the third OOC lobe is roughly aligned with a maxima in the compressive strain.

Fourier decomposition of the shell strains, shown in Figure 50, indicate that the initial response was actually dominated by the n=6 mode, and to a lesser extent, the n=3 mode. However, the n=2 strains became increasingly important as the collapse load was approached, until, at the collapse pressure, the n=2 and n=3 stains were of approximately the same magnitude, and somewhat greater than the n=6 component. The final deformed configuration of the cylinder shows an inward dent at 140°, and a large compressive shell strain would be expected to arise near that location. It is unclear if the n=2 mode observed in the shell strains is a real phenomena caused by, for example, shakedown of residual stresses related to the application of OOC during the additional elastic load cycles, or if it arises due to the absence of strain data at the centre of the buckling lobe.

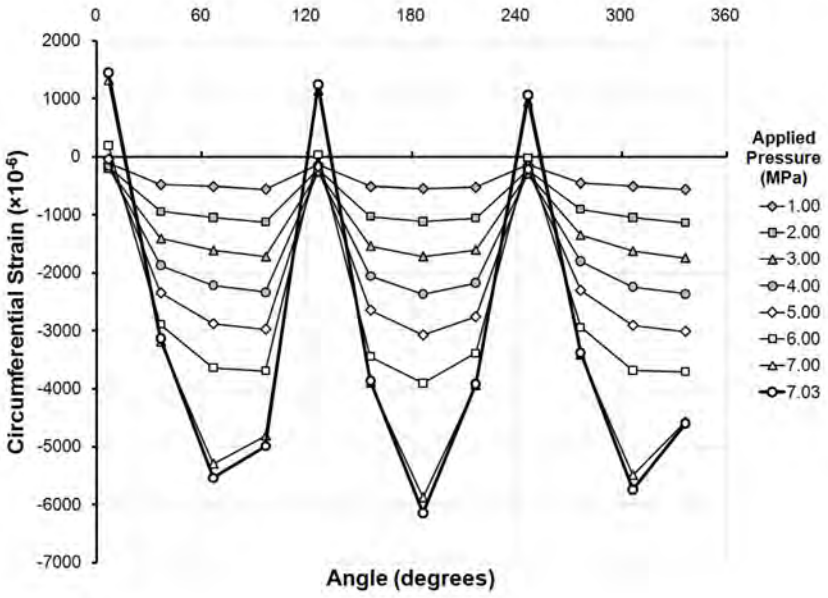

Figure 45: Circumferential strain distribution at the flange of Frame 4 of specimen L510-No33, at pressures up to and including the collapse pressure.

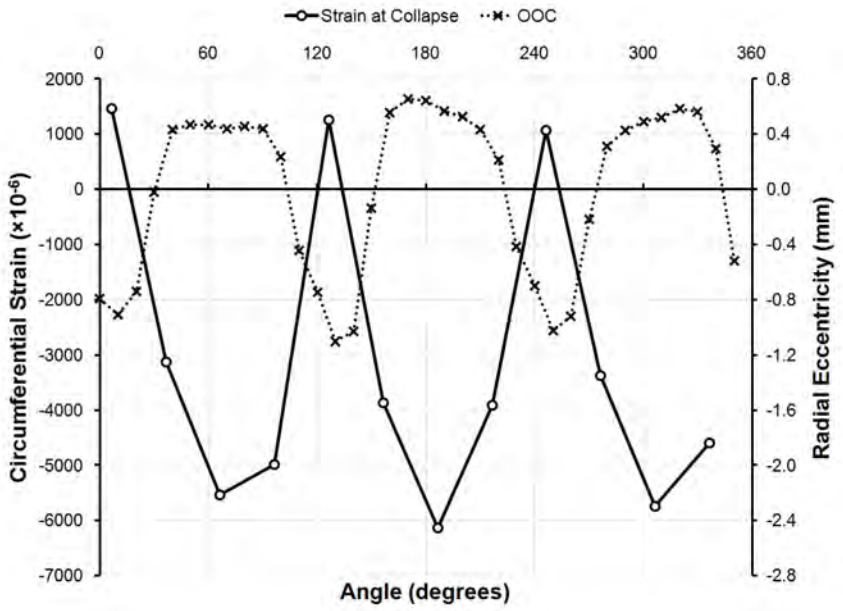

Figure 46: Circumferential strain distribution at the flange of Frame 4 of specimen L510-No33 at the collapse pressure, plotted with the initial out-of-circularity at that location.

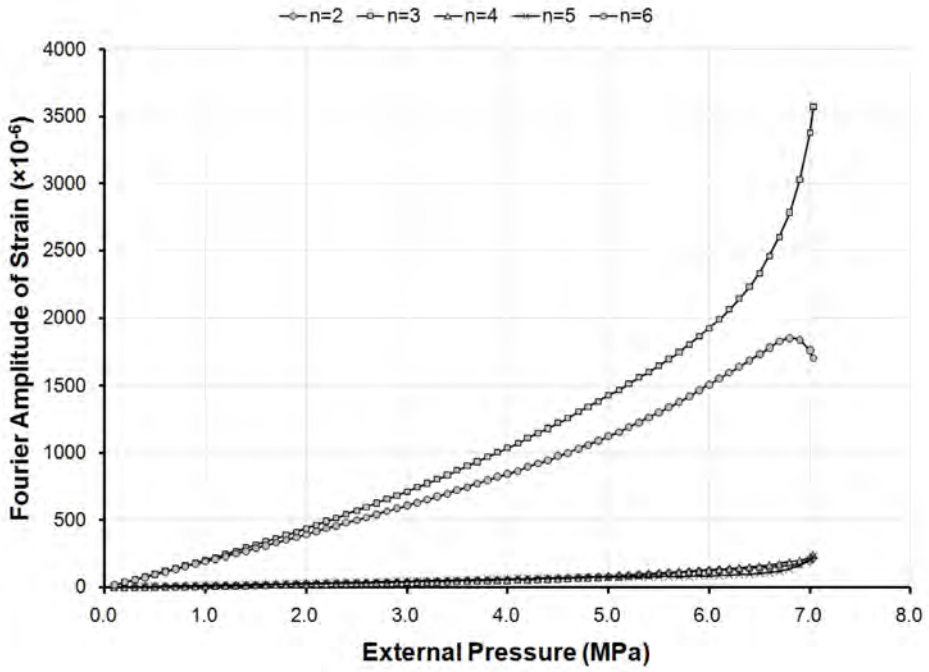

Figure 47: Bending strain amplitudes at the flange of Frame 4 of specimen L510-No33, derived from Fourier decomposition, and plotted against the applied pressure.

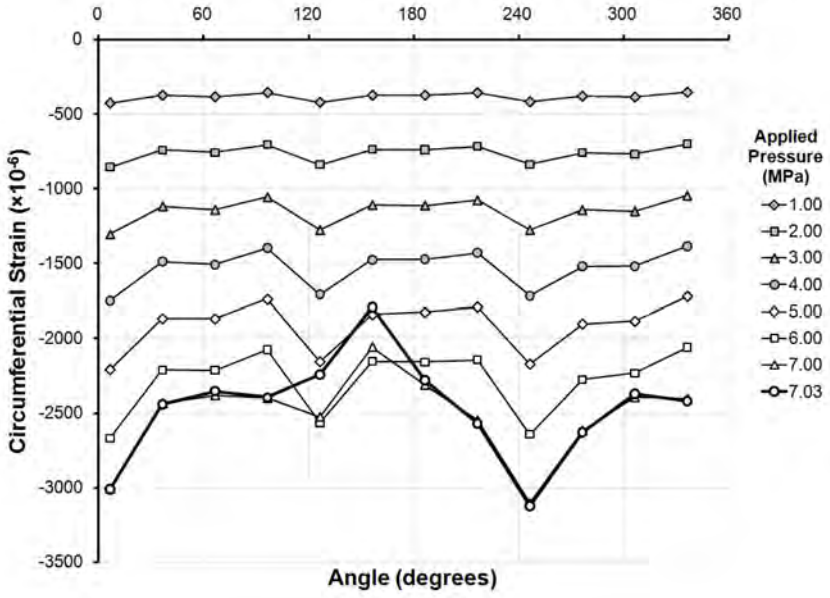

Figure 48: Circumferential strain distribution outside the shell in the centre of Bay 4 of specimen L510-No33, at pressures up to and including the collapse pressure.

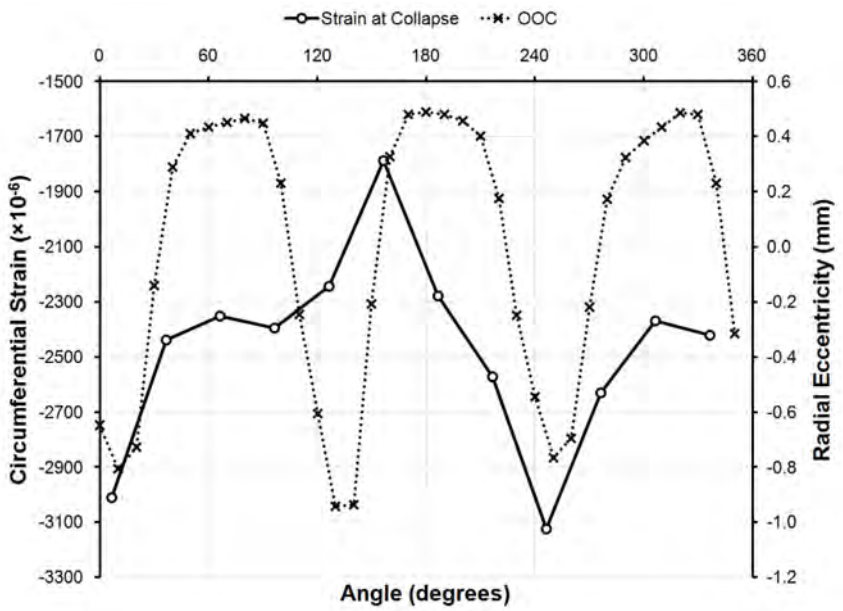

Figure 49: Circumferential strain distribution outside the shell at Bay 4 of specimen L510-No33 at the collapse pressure, plotted with the initial out-of-circularity at that location.

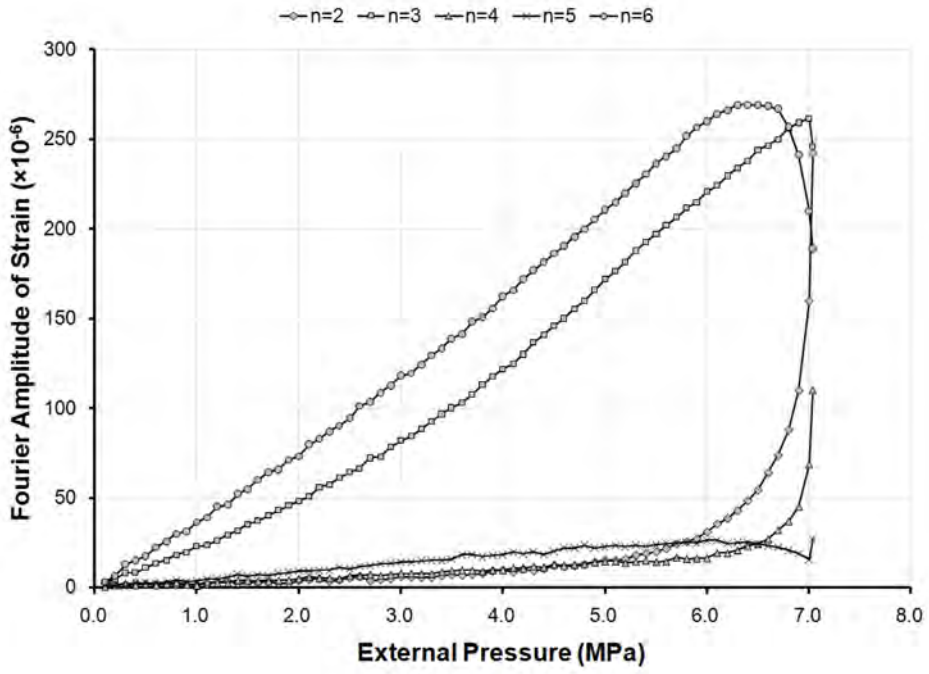

Figure 50: Bending strain amplitudes outside the shell in Bay 4 of specimen L510-No33, derived from Fourier decomposition, and plotted against the applied pressure.

4.1.6 L510-No34

The target out-of-circularity for specimen L510-No34 was unique in that the goal was to produce an imperfection with n=3 waves about the circumference, distributed over the cylinder length in a complete sine wave (m=2). The geometric measurements indicated that the desired shape was achieved, and that the OOC amplitude was reasonably close to the target value of 0.3%. L510-No34 underwent a single elastic loading cycle before it was pressurized to collapse, failing at an external pressure of 8.02 MPa (see Table 18). The final post-testing configuration of the cylinder was a large overall buckle at approximately 65° and spanning bays 5 to 7, as shown in Figure 32.

Figure 51 shows the distribution of circumferential strains over the length of the cylinder at an angle corresponding to an outward OOC lobe in first half of the specimen (bays 1 to 3) and an inward lobe in the latter half (bays 5-7). The shell strains at collapse follow the expected pattern, with smaller compressive strains at the outward OOC lobe and large strains at the inward lobe.

Table 18: Testing procedures for specimen L510-No34

Test Name	Date	Test Type	Pre-Pressure (MPa)	Maximum Pressure (MPa)	Notes
Trial 1	16 Feb 2009	Elastic	3.53	1.02	N/A
Trial 2	16 Feb 2009	Collapse	13.63	8.02	N/A

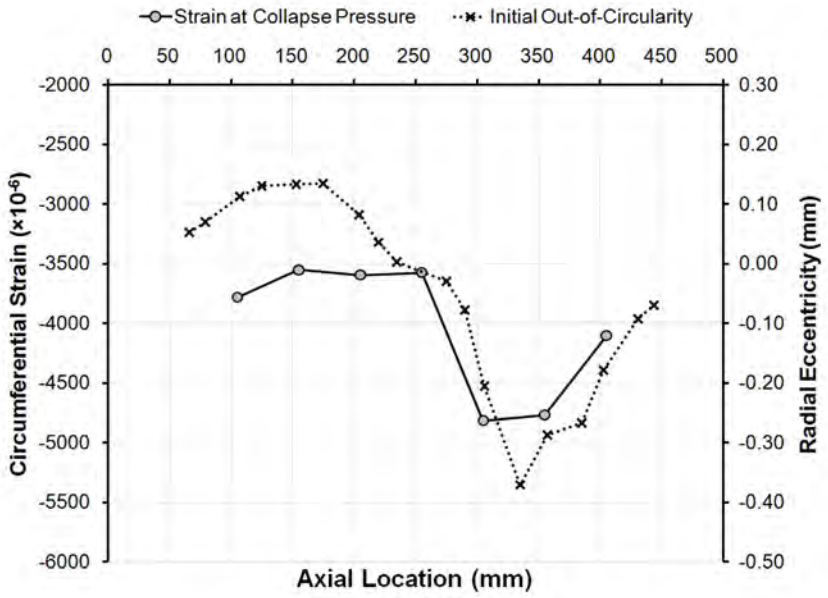

Figure 51: Distribution of circumferential shell strains at mid-bay locations over the length of specimen L510-No34 at 320.4°, based on strain measurements taken at the collapse pressure and plotted with the initial out-of-circularity at that location.

Figure 52 and Figure 53 show the circumferential distribution of strain at collapse at Frame 6, near the site of collapse, and Bay 2, respectively, along with the initial out-of-circularity at those locations. The strain distribution is consistent with the *n*=3 OOC, being out-of-phase at the frame and in-phase outside the shell at mid-bay. Fourier decompositions of those strains show that the *n*=6 strains were somewhat greater than the *n*=3 strains at Frame 6 (Figure 54), while the *n*=3 mode dominated the response at Bay 2, especially as the collapse load was approached (Figure 55).

Unfortunately, neither the row of gauges over the cylinder length, nor the ring of gauges around the shell circumference, coincided with the collapse site. However, pressure-strain plots for strain gauges on Frame 6, near the collapse site, are plotted in Figure 56. None of those gauges were located at the exact centre of the buckling lobe, so that the plotted strains are relatively small. Nonetheless, the response is as expected, with compressive bending strains in the flange away from the buckling lobe and tensile bending strains nearer the centre.

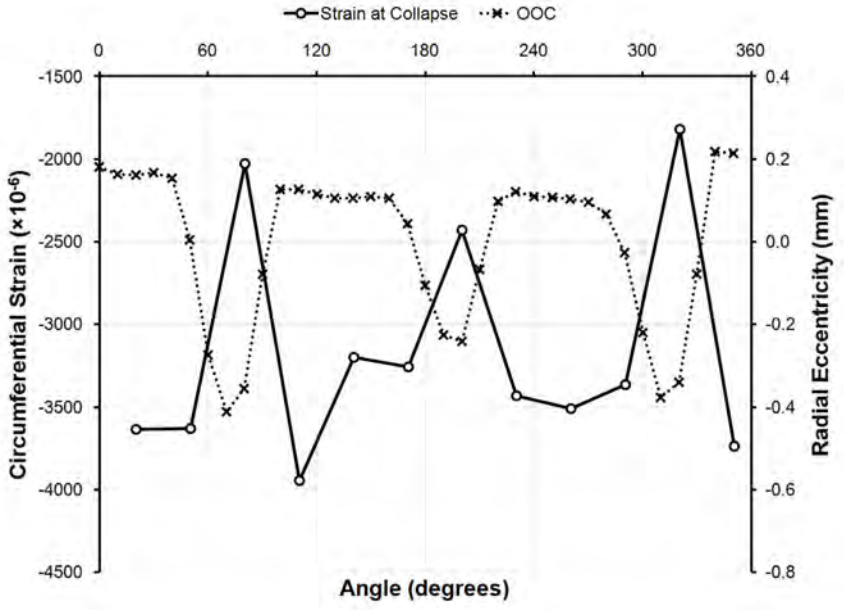

Figure 52: Circumferential strain distribution at the flange of Frame 6 of specimen L510-No34 at the collapse pressure, plotted with the initial out-of-circularity at that location.

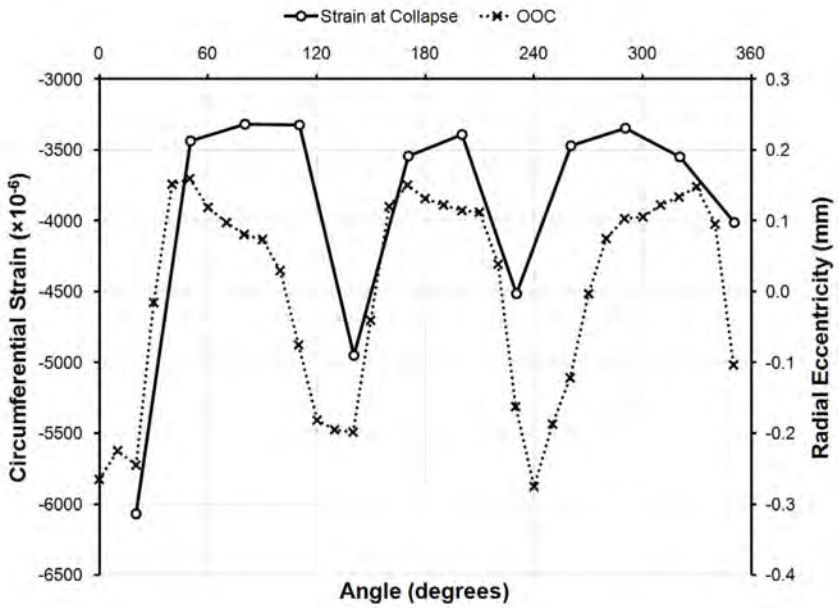

Figure 53: Circumferential strain distribution outside the shell at Bay 2 of specimen L510-No34 at the collapse pressure, plotted with the initial out-of-circularity at that location.

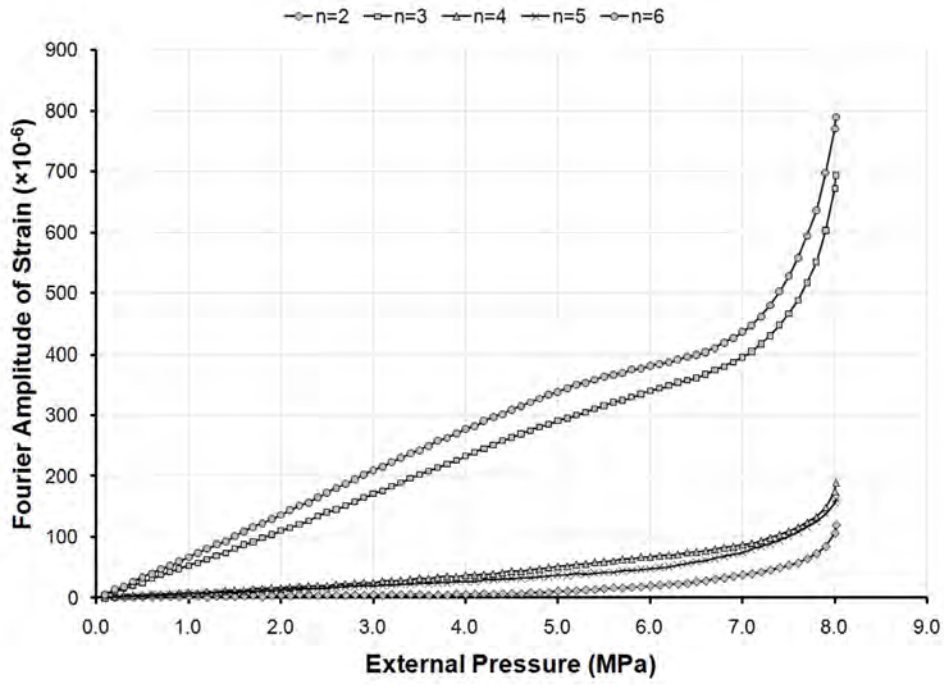

Figure 54: Bending strain amplitudes at the flange of Frame 6 of specimen L510-No34, derived from Fourier decomposition, and plotted against the applied pressure.

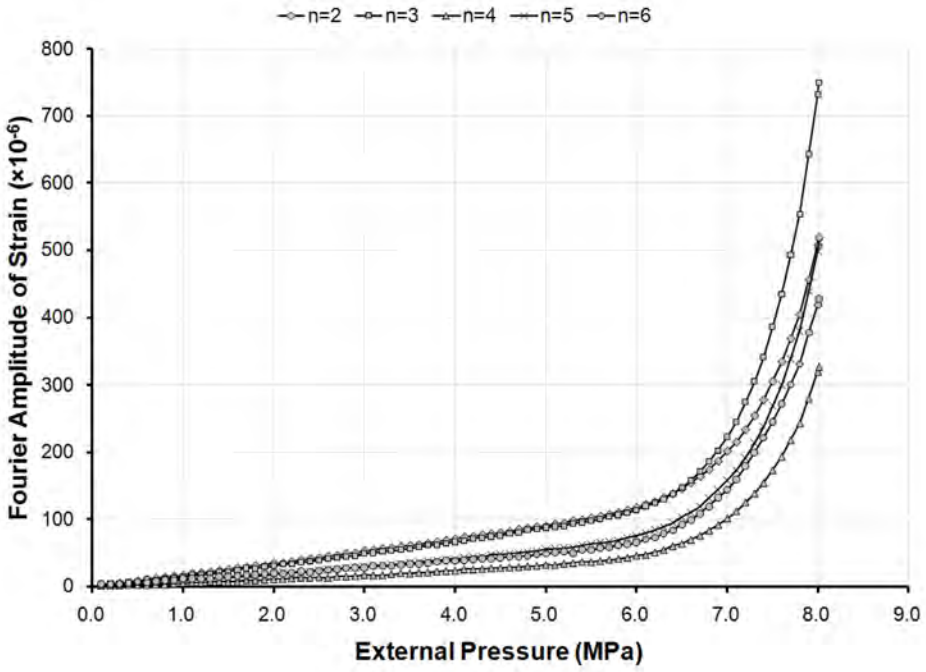

Figure 55: Bending strain amplitudes outside the shell in Bay 2 of specimen L510-No34, derived from Fourier decomposition, and plotted against the applied pressure.

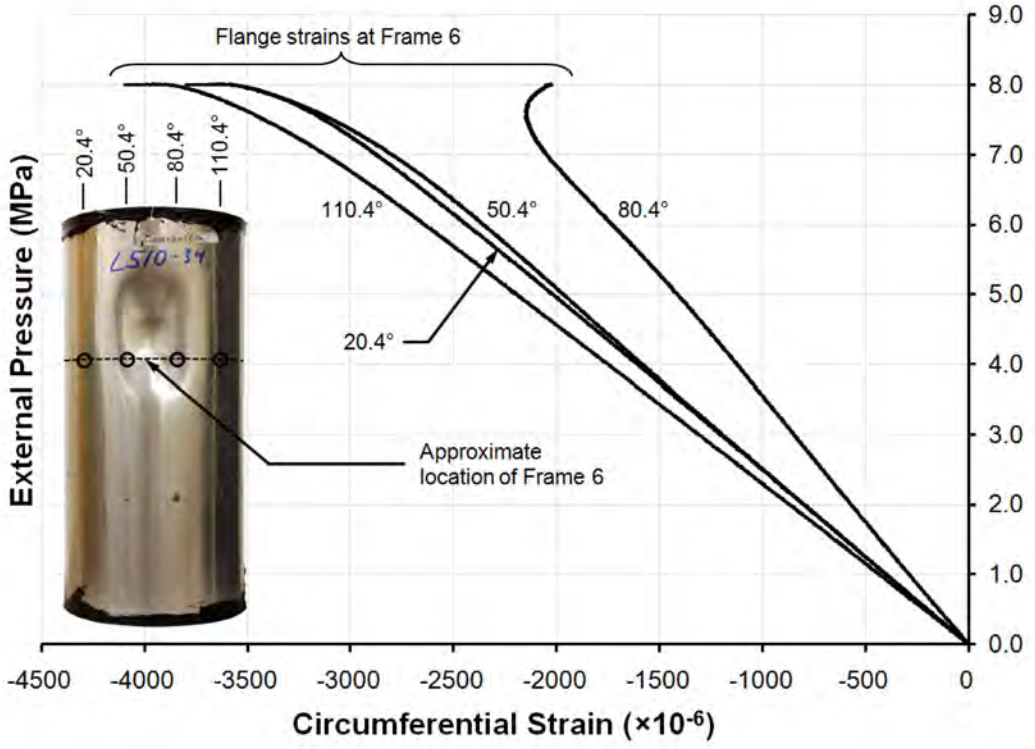

Figure 56: Selected pressure-strain curves near the collapse site for specimen L510-No34.

4.2 Phase 6: specimens with corrosion damage

This section presents collapse testing results for specimens tested in Phase 6, which had artificial corrosion damage. The nominal out-of-circularity of all Phase 6 specimens was 0.5% in an *n*=3, *m*=1 mode. The specimens differed in the corrosion patch depth, area and orientation with respect to the OOC mode. The final deformed shapes of the Phase 6 specimens after collapse testing are shown in the photographs in Figure 57. Collapse pressures and pressures causing first yield in the shell and stiffeners at strain gauge locations are summarized in Table 19.

Figure 57: Phase 6 specimens, with artificial corrosion damage and 0.5% OOC in n=*3*, m=*1 mode, after collapse testing. Clockwise from top-left: L510-No13, with a 42x42x0.6 mm, out-of-phase corrosion patch, showing photographs of the collapse location and the corrosion patch location relative to the collapse site; L510-No14, with a 42x42x0.6 mm, in-phase corrosion patch; L510-No19 and L510-No20, with 100x100x0.4 mm, in-phase corrosion patches; L510-No35, with a 42x42x0.6 mm, in-phase corrosion patch; and L510-No36, with a 42x42x0.6 mm, out-of-phase corrosion patch, showing photographs of the corrosion patch location relative to the collapse site and the collapse location itself.*

Table 19: Summary of yield and collapse pressures for Phase 6 specimens, with artificial corrosion damage.

Specimen	First Yielding of the Shell [a]		First Yielding of the Stiffener [b]		Collapse Pressure, P_c [c] (MPa)
	Location	P_y [c] (MPa)	Location	P_y [c] (MPa)	
L510-No13	Outside mid-bay no. 4 at 60°	6.56	Did not yield before collapse		7.55
L510-No14	Outside mid-bay no. 4 at 157.5°	5.43	Did not yield before collapse		6.93
L510-No19	Outside mid-bay no. 4 at 15°	6.61	Stiffener no. 4 at 300°	6.67	6.67
L510-No20	Outside mid-bay no. 4 at 183.5°	6.21	Did not yield before collapse		6.93
L510-No35	Outside mid-bay no. 4 at 352.5°	5.18	Did not yield before collapse		6.58
L510-No36	Outside mid-bay no. 4 at 300°	6.85	Stiffener no. 4 at 240°	6.89	7.22

a. Based on the first occurrence of the von Mises stress reaching the circumferential yield stress, for measurements taken at bi-axial strain gauge locations. Residual stresses due to applying out-of-circularity are neglected.

b. Based on the first occurrence of the uni-axial circumferential flange stress reaching the circumferential yield stress, for measurements taken at strain gauge locations. Residual stresses due to applying out-of-circularity are neglected.

c. Yield pressures, P_y, and collapse pressures, P_c, are accurate to within ±0.09 MPa.

4.2.1 L510-No13

Specimen L510-No13 had a square corrosion patch, spanning approximately 87.5% of the unsupported shell in the central frame bay. Shell thickness measurements revealed that the as-built corrosion thinning was approximately 19%, compared to a target value of 20% (see Table 6). The as-measured shape of the cylinder was found to be in the target OOC mode, with amplitude somewhat greater than the nominal value, depending on the criterion (see Table 3). Furthermore, shape measurements placed the corrosion patch at an outward lobe of the OOC imperfection, resulting in the intended out-of-phase configuration (see Table 4). The testing history for L510-No13 is given in Table 20.

Table 20: Testing procedures for specimen L510-No13

Test Name	Date	Test Type	Pre-Pressure (MPa)	Maximum Pressure (MPa)	Notes
Trial 1	1 Jun 2009	Elastic	3.19	1.06	N/A
Trial 2	1 Jun 2009	Collapse	13.77	7.55	N/A

L510-No13 collapsed at a pressure of 7.55 MPa, after which the applied pressure dropped suddenly to approximately 3.2 MPa (see Figure 164 in Annex F). The specimen was then completely unloaded. After collapse testing, the specimen showed a permanent buckle at approximately 60° spanning the three central bays. It can be seen from the photograph in Figure 57 that overall collapse occurred away from the corrosion patch. The collapse location at 60° coincides with the largest inward OOC lobe at the mid-length of the cylinder (see Figure 118 in Annex C), and is near the thinnest shell region outside the corrosion patch (see Figure 120 in Annex C).

The evolution of the n=3 circumferential bending strains at the flange of Frame 4 is shown in Figure 58, and the expected 60° phase shift between the bending strains at collapse and the initial OOC mode is shown in Figure 59. Fourier amplitudes for Frame 4, shown in Figure 60, confirm that the n=3 mode was dominant from the onset of loading up to the collapse pressure.

The circumferential bending strains outside the shell are shown at various loading increments in Figure 61. They are plotted for the collapse pressure, along with the initial OOC, in Figure 62. If the large compressive strains in the corrosion patch near 0° are ignored, the bending strains can be seen to follow the expected n=3 mode until just before collapse; thereafter, the compressive strain at the collapse location (60°) became smaller, contrary to expectations for the centre of an inward buckling lobe. The largest compressive strain outside the corrosion patch was at 300° at the collapse pressure. While it is possible that the strain gauge at 60° was damaged or de-bonded near the collapse load, it seems likely that the collapse mode actually was dominated by an inward buckling lobe at 300° at the collapse load. The final post-testing configuration, with a large dent at 60°, therefore resulted from the dynamic post-collapse response of the cylinder. That is supported by the strain distribution in the shell after the cylinder was unloaded, shown in Figure 63, with steep strain gradients around 60°, as would be expected at the collapse site.

The reversal of the circumferential shell strain at 60° is also shown in the pressure-strain curves in Figure 64. That figure shows the strain response until shortly after the peak load was reached; the remainder of the post-peak response is not plotted, since the data acquisition rate was not sufficient to capture the dynamic response. The pressure-strain curves show that the compressive shell strain in the corrosion patch (at an outward OOC lobe) was approximately the same magnitude as the intact shell strain at an inward OOC lobe for most of the loading history; however, the intact shell yielded first, ultimately leading to collapse of the cylinder at a location distant from the corrosion. The frame flanges did not yield before collapse at any of the measured locations, so that overall collapse was due to failure of the shell rather than the frames, or some combination thereof.

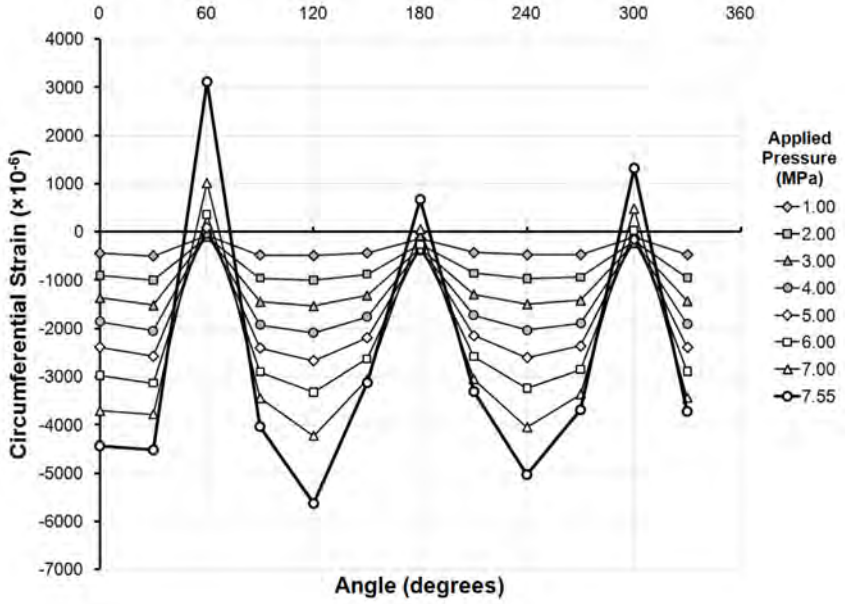

Figure 58: Circumferential strain distribution at the flange of Frame 4 of specimen L510-No13, at pressures up to and including the collapse pressure.

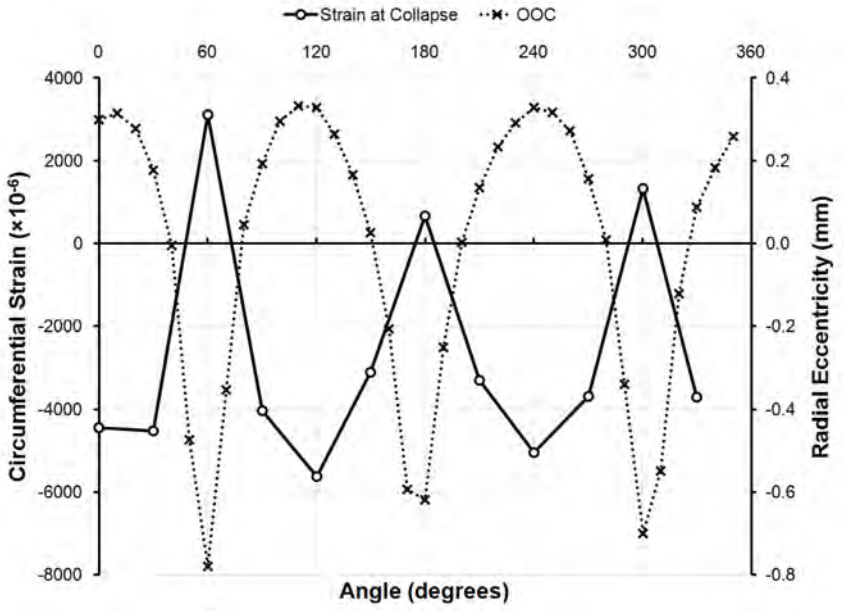

Figure 59: Circumferential strain distribution at the flange of Frame 4 of specimen L510-No13 at the collapse pressure, plotted with the initial out-of-circularity at that location.

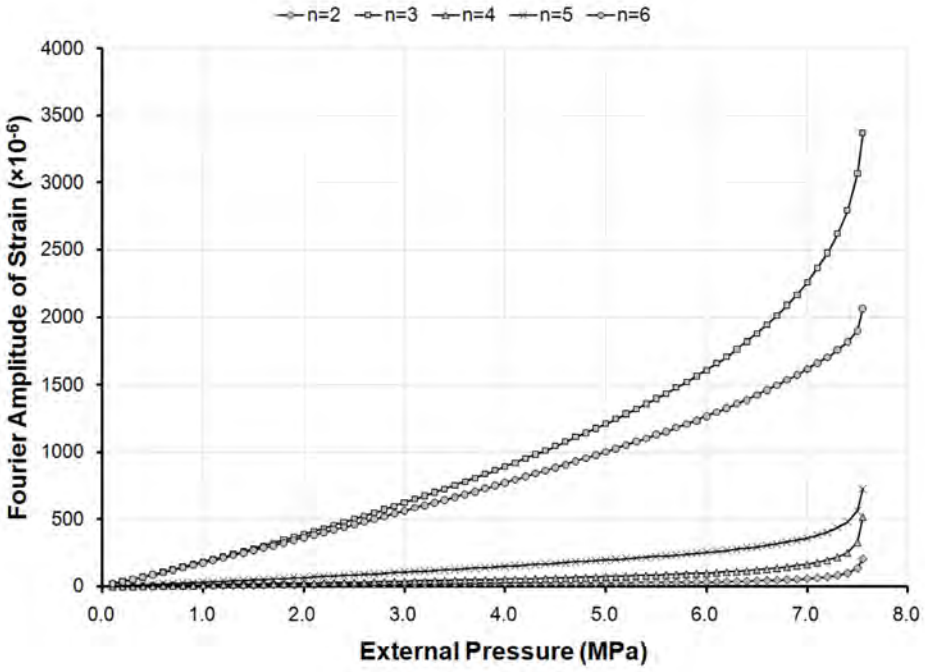

Figure 60: Bending strain amplitudes at the flange of Frame 4 of specimen L510-No13, derived from Fourier decomposition, and plotted against the applied pressure.

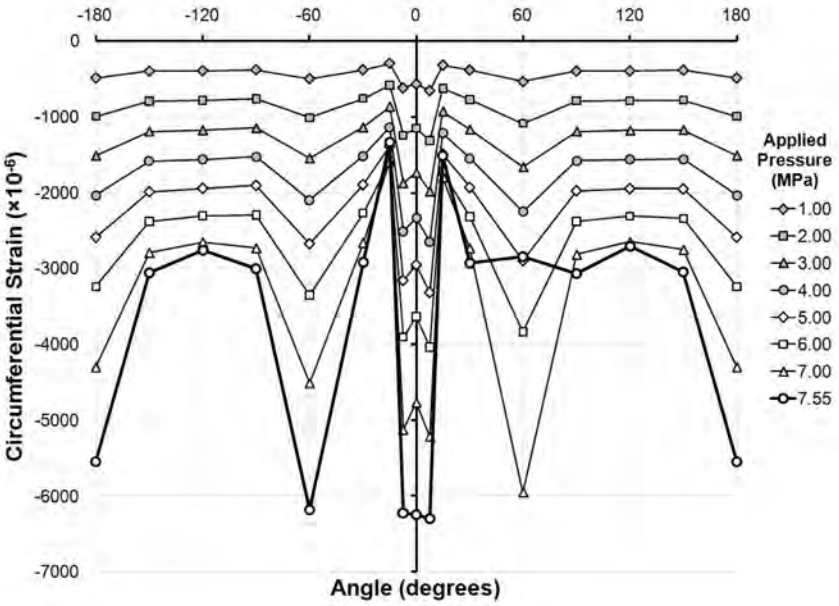

Figure 61: Circumferential strain distribution outside the shell in the centre of Bay 4 of specimen L510-No13, at pressures up to and including the collapse pressure.

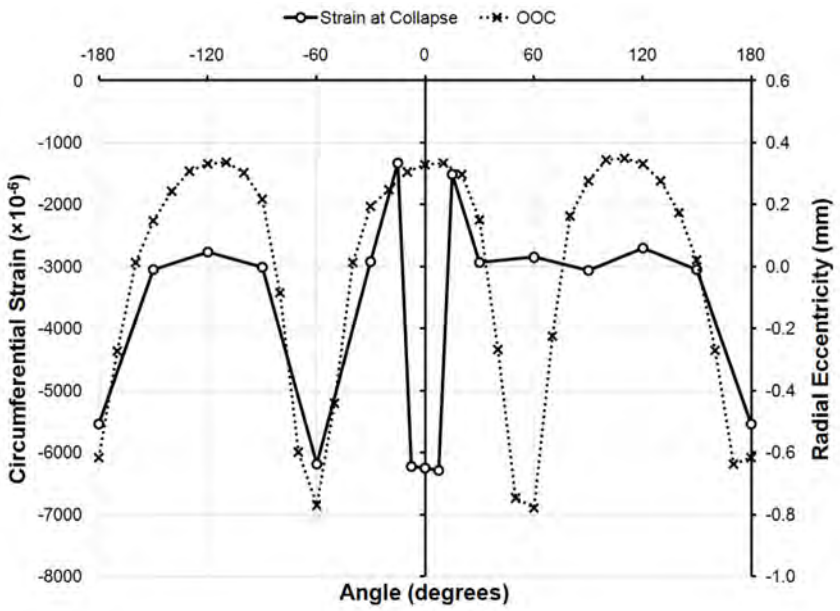

Figure 62: Circumferential strain distribution outside the shell at Bay 4 of specimen L510-No13 at the collapse pressure, plotted with the initial out-of-circularity at that location.

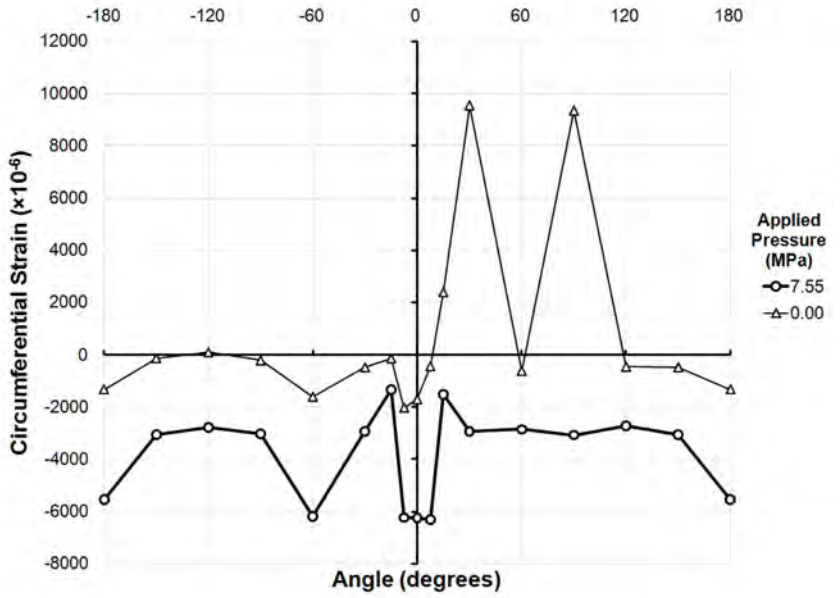

Figure 63: Circumferential strain distribution outside the shell in the centre of Bay 4 of specimen L510-No13, at the collapse pressure and after the specimen has been unloaded.

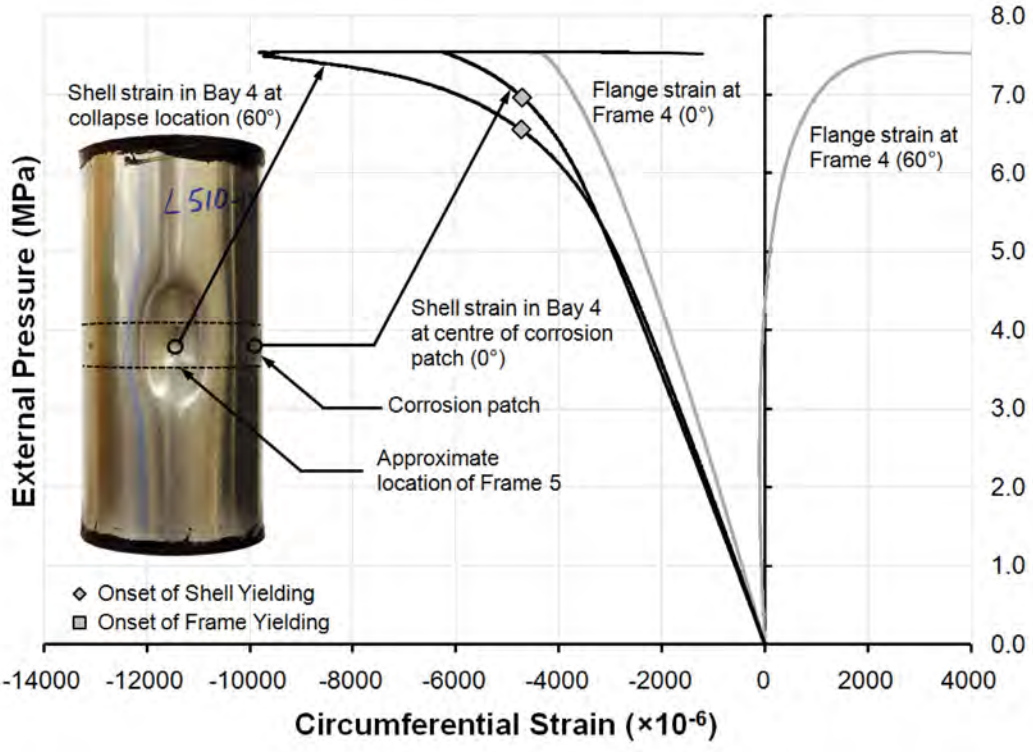

Figure 64: Selected pressure-strain curves near the collapse site for specimen L510-No13.

4.2.2 L510-No14

Specimen L510-No14 had the same small but deep corrosion patch as L510-No13, except the corrosion damage was intended to be in-phase with the applied OOC. Shape measurements of the cylinder showed that the OOC was in the correct mode and the amplitude was close to, but somewhat greater than, the target value of 0.5% (see Table 3). The artificial corrosion damage was slightly more severe than intended, with a depth equal to approximately 22% of the intact shell thickness (see Table 6). Finally, the OOC and shell thickness measurements confirmed that the corrosion patch was in-phase with the initial imperfection mode (see Table 4).

The testing history of L510-No14 is shown in Table 21. After an initial elastic loading cycle, the cylinder was loaded to collapse, giving a collapse pressure of 6.93 MPa. After collapse, the applied pressure dropped sharply to under 3 MPa, and after some fluctuations, stabilized at approximately 3.8 MPa until the cylinder was unloaded (see Figure 165 in Annex F). The final post-testing configuration of the specimen is shown in the photograph in Figure 57. In this case, the large multi-bay overall collapse lobe is centred around the corrosion patch, which was located at 165° at one of the inward OOC lobes.

The circumferential distribution of flange strain at Frame 4 at the collapse pressure, shown in Figure 65 along with the initial OOC, point to an overall n=3 collapse mode. The tensile bending strain was largest at 165°, where the corrosion patch was located. Fourier decompositions of the

flange strains, shown in Figure 66, confirm that the *n*=3 bending strains dominated the cylinder response up to the collapse pressure. At the outside of the shell, the *n*=3 mode is less pronounced due to the large compressive strains at the in-phase corrosion patch (see Figure 67). Nonetheless, small local troughs in the circumferential strain were collocated with inward OOC lobes. Figure 67 also shows that the compressive strains were greatest at the corrosion patch edges due to the bending moments arising from the shell eccentricity between the intact and corroded shell.

Table 21: Testing procedures for specimen L510-No14

Test Name	Date	Test Type	Pre-Pressure (MPa)	Maximum Pressure (MPa)	Notes
Trial 1	4 Jun 2009	Elastic	3.42	1.04	Tank pressure dropped by a small amount (approximately 0.05 MPa) while the specimen was loaded and all valves were closed. That may have been caused by a small leak in the sealant at the cylinder end-caps. The pressure drop did not hinder subsequent collapse testing of the cylinder.
Trial 2	4 Jun 2009	Collapse	13.75	6.93	N/A

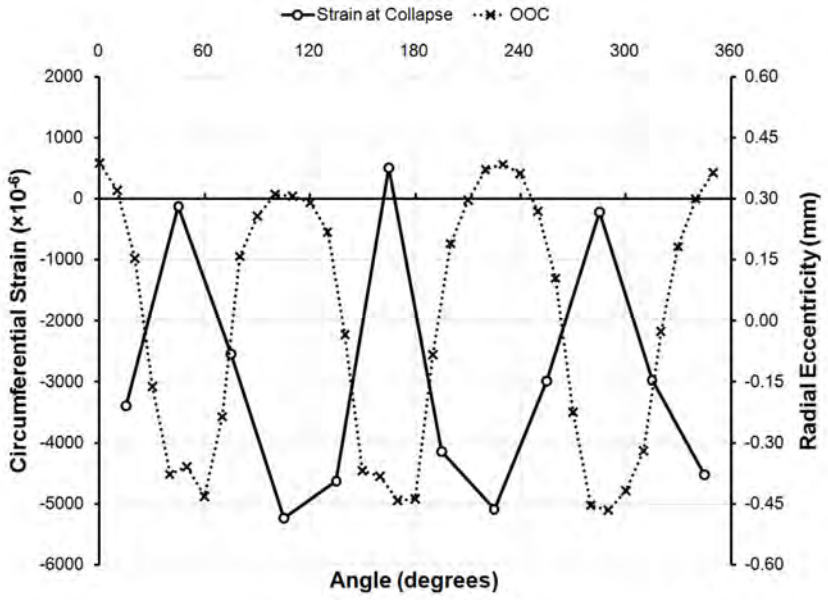

Figure 65: Circumferential strain distribution at the flange of Frame 4 of specimen L510-No14 at the collapse pressure, plotted with the initial out-of-circularity at that location.

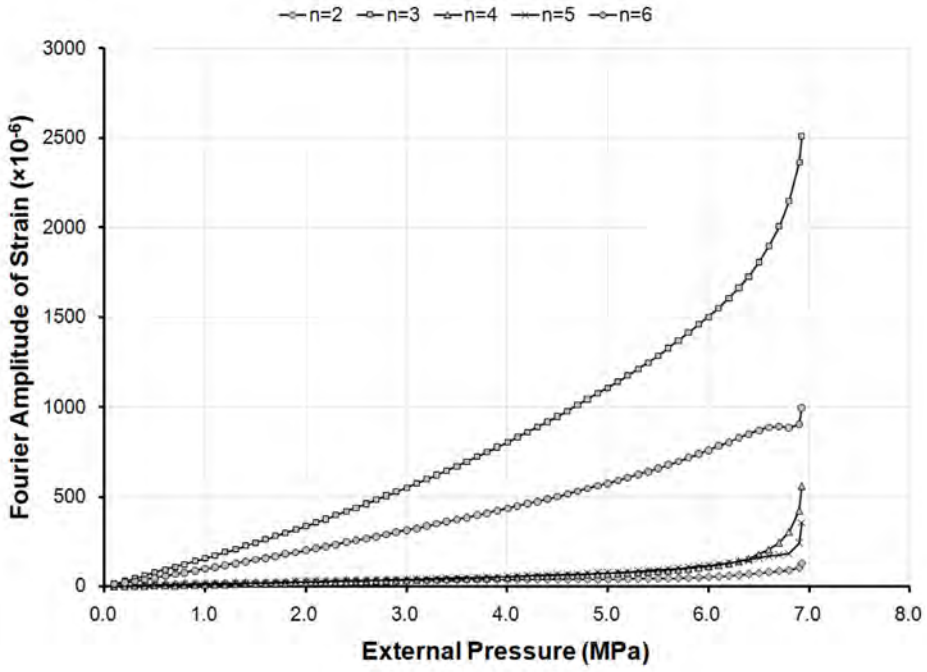

Figure 66: Bending strain amplitudes at the flange of Frame 4 of specimen L510-No14, derived from Fourier decomposition, and plotted against the applied pressure.

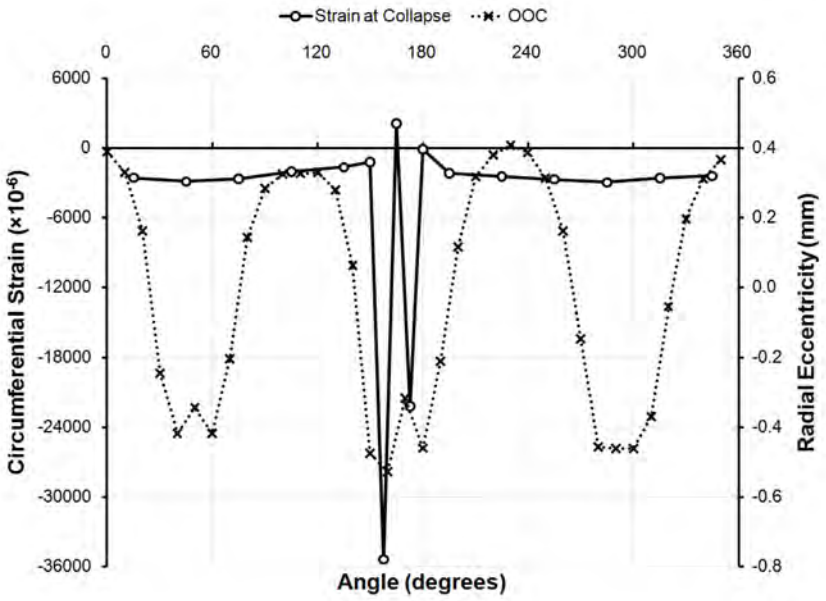

Figure 67: Circumferential strain distribution outside the shell at Bay 4 of specimen L510-No14 at the collapse pressure, plotted with the initial out-of-circularity at that location.

Figure 68 shows selected pressure-strain curves for circumferentially oriented gauges near the collapse location at the corrosion patch. The largest compressive strains throughout the loading regime were found to be outside the shell at the inside edge of the corrosion patch, and yielding occurred first at that location. At the centre of the patch, the compressive strains were greater on the inside of the shell than on the outside, with the outer shell strain reversing direction as the collapse load was approached, resulting in tensile strain at the collapse pressure. The tensile and compressive bending strains at the outside and inside of the corrosion patch, respectively, suggest outward bending at the centre of the patch. The outward bending may be due to the small local outward lobe in the initial OOC at the centre of the corrosion patch, as shown in Figure 16 and Figure 18. The pressure-strain curves also show that the bending strains in the frame flanges were, as expected, tensile near the corrosion patch (and maximum inward OOC) and compressive at a location 60° offset from the corrosion patch. Furthermore, the flanges did not yield before collapse, which was immediately preceded by yielding at the outside of the shell at the centre of the corrosion patch.

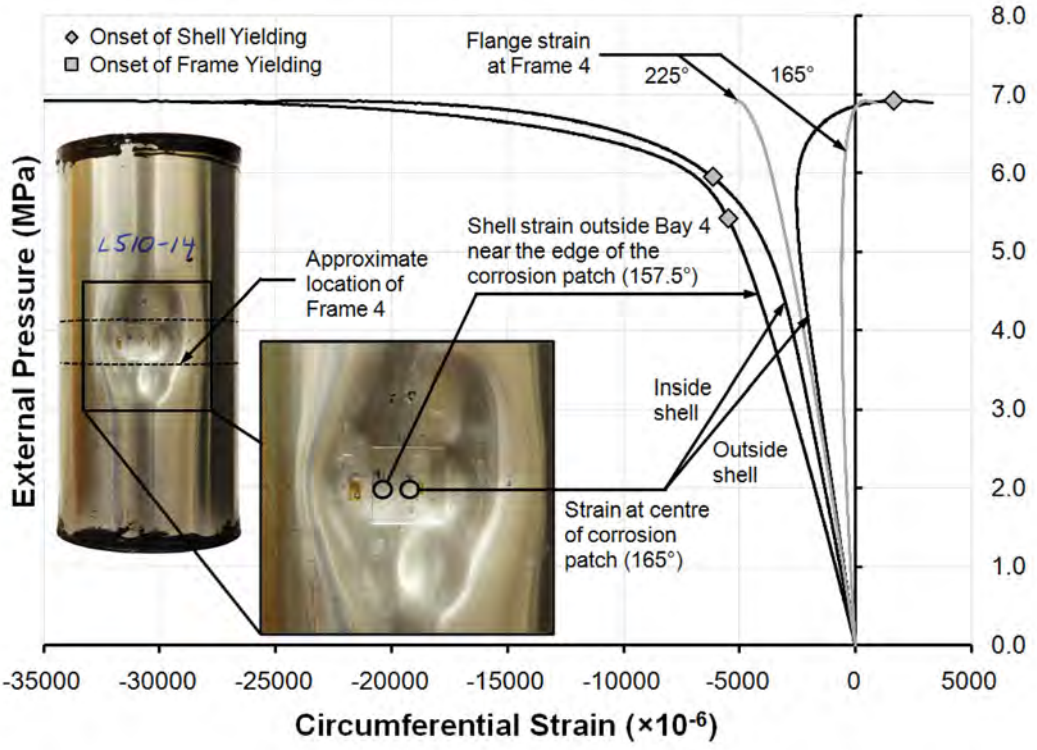

Figure 68: Selected pressure-strain curves near the collapse site for specimen L510-No14.

4.2.3 L510-No19

Specimen L510-No19 had a large, shallow corrosion patch that was in-phase with the *n*=3 OOC mode. The initial OOC was found to be in good agreement with the targeted shape, while the OOC magnitude was somewhat greater than the nominal value of 0.5% (see Table 3). Shape and thickness measurements indicated that the corrosion patch was centred about the inward lobe of

the applied OOC near 0°, as shown in Figure 129 and Figure 132 in Annex C. The as-measured corrosion thinning was found to be 13.9%, compared to the target value of 13.3%.

The testing history of L510-No19 is summarized in Table 22. After the cylinder underwent an elastic load cycle, it was tested to collapse, failing at a pressure of 6.67 MPa. The applied pressure dropped off rapidly soon after the peak load was reached, to a pressure of approximately 4.5 MPa. The final deformed shape of the cylinder after collapse testing is shown in the photograph in Figure 57. It can be seen that collapse occurred at the corrosion patch, with large deformation of both the shell and stiffeners suggesting an overall collapse mode.

The circumferential strain distribution in the ring-stiffeners was very similar to L510-No14, with large tensile bending strains near the corrosion patch (see Figure 348 to Figure 351 in Annex I). The evolution of the circumferential strains outside the shell, near the corrosion patch, is shown below in Figure 69. As with L510-No14, the compressive strains were greatest at the edges of the corrosion patch due to the eccentricity effect. As the collapse load was approached, the strains near one of the edges of the patch and, especially, at the centre of the corrosion patch, began to reverse direction. That can also be seen in the pressure-strain plots shown in Figure 70. The large buckling lobe covering the entire corrosion patch was superimposed on several smaller interframe buckling lobes. The strain gauges at 0° and 15° were located near the edges of one of those smaller buckling lobes, so that the strain reversals are associated with tensile bending strains. That buckling lobe was collocated with a local inward dent in the applied OOC, which can be seen in Figure 129 and Figure 132 in Annex C.

Figure 70 also shows the circumferential strain on the inside of the shell at the edge of the corrosion patch (23.3°). Compressive strains due to inward bending of the shell arose at that location as the collapse load was approached and the overall buckling lobe began to form. Large compressive strains were also found to occur at the stiffener flange at 300°, due to inward bending forces generated by the corrosion patch and OOC. Yielding occurred almost simultaneously at the stiffener flange and the corroded shell, and collapse followed immediately thereafter.

Table 22: Testing procedures for specimen L510-No19

Test Name	**Date**	**Test Type**	**Pre-Pressure (MPa)**	**Maximum Pressure (MPa)**	**Notes**
Trial 1	26 Jun 2009	Elastic	3.79	1.04	N/A
Trial 2	26 Jun 2009	Collapse	13.70	6.67	N/A

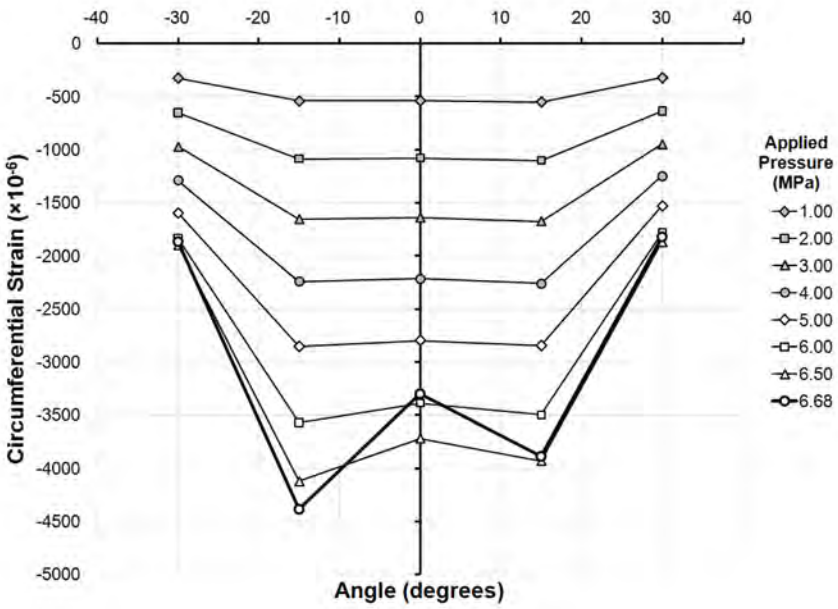

Figure 69: Circumferential strain distribution outside the shell in the centre of Bay 4 of specimen L510-No19, at pressures up to and including the collapse pressure.

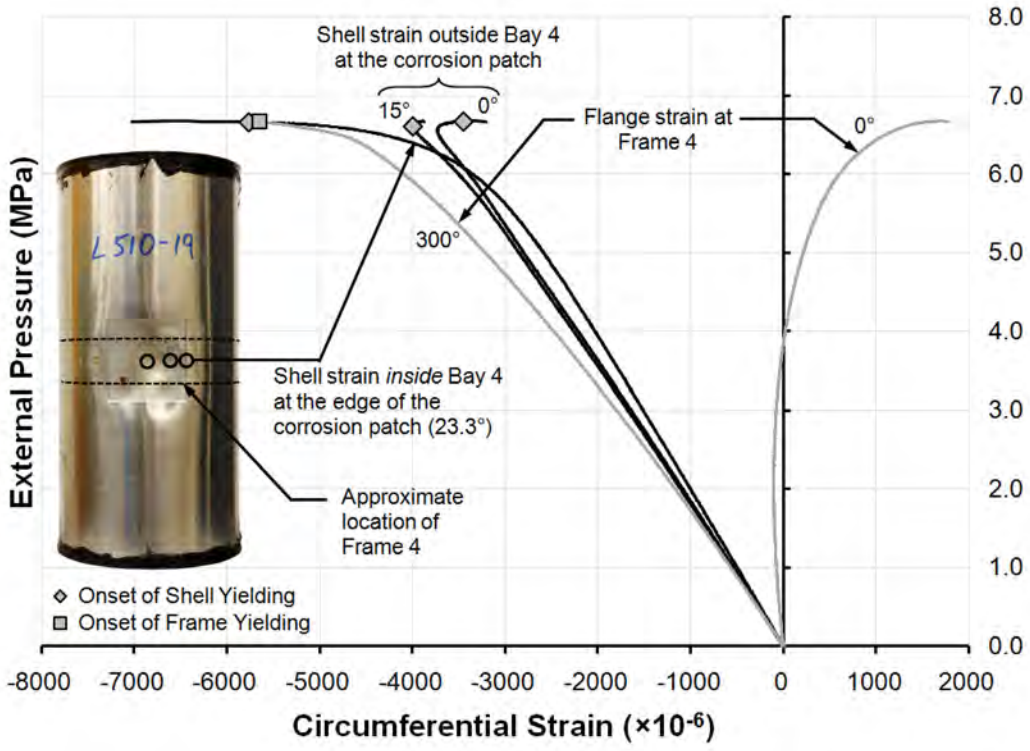

Figure 70: Selected pressure-strain curves near the collapse site for specimen L510-No19.

4.2.4 L510-No20

L510-No20 was nominally identical to L510-No19, and had the same large, in-phase corrosion patch and target OOC shape; however, Table 3 shows that the as-measured OOC magnitude of L510-No20 was considerably smaller than that of L510-No19, while Table 6 indicates that the corrosion thinning was greater in L510-No20, at 15.2%, compared to 13.9% in L510-No19. The corrosion patch in L510-No20 was centred at 183.5°, so that it was in-phase with the maximum inward OOC at 180° (see Table 4). Figure 135 and Figure 138 in Annex C show small local dents in the OOC shape at the centre of the corrosion patch in L510-No20, whereas the local dents were located near the circumferential edges of the patch in L510-No19.

L510-No20 was subjected to a single load cycle in the elastic range before it was loaded to collapse (see Table 23). The collapse pressure was found to be 6.93 MPa. In general, the response of L510-No20 was similar to L510-No19; however, the strain distribution in the region of corrosion damage showed opposite trends in the two cylinders. Figure 69, above, shows that, in L510-No19, the largest compressive strains outside the shell occurred at the edges of the corrosion patch, while Figure 71 shows that, for L510-No20, the largest compressive strains occurred in the centre of the patch for most of the loading history. The corresponding strain distribution on the inside shell of L510-No20 is shown in Figure 72. The large compressive strains at the edges of the patch are consistent with inward bending at the centre of the patch. The different responses in the corrosion patches of L510-No19 and L510-No20 are likely related to the relative locations of the local dents in the patches, as discussed above.

Figure 73 shows pressure-strain curves for strain gauges near the corrosion patch and collapse location on L510-No20. The shell strain reversal at the centre of the corrosion patch occurred after the outside of the shell had yielded. Since the final configuration of the cylinder after testing shows a permanent dent at the centre of the patch, it is likely that the strain reversal was due to the transition from bending to membrane behaviour at that location. That hypothesis is corroborated by the fact that the strain changed directions on both the inside and outside of the shell, at approximately the same pressure. The strain gauges at the corroded shell were the only ones that indicated that yielding had occurred before the onset of collapse, so that failure of the cylinder was ultimately due to overall collapse precipitated by shell damage.

Table 23: Testing procedures for specimen L510-No20

Test Name	Date	Test Type	Pre-Pressure (MPa)	Maximum Pressure (MPa)	Notes
Trial 1	30 Jun 2009	Elastic	3.70	1.06	N/A
Trial 2	30 Jun 2009	Collapse	13.62	6.93	N/A

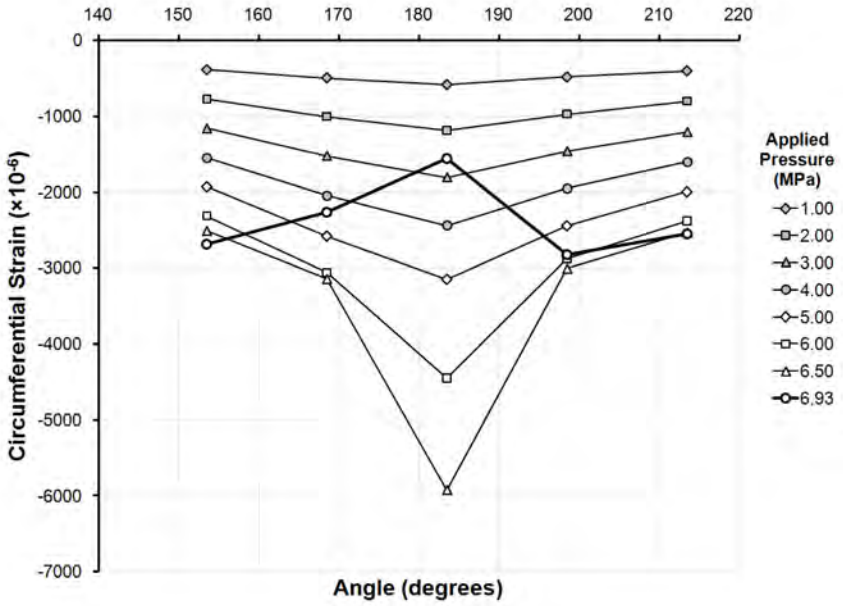

Figure 71: Circumferential strain distribution outside the shell in the centre of Bay 4 of specimen L510-No20, at pressures up to and including the collapse pressure.

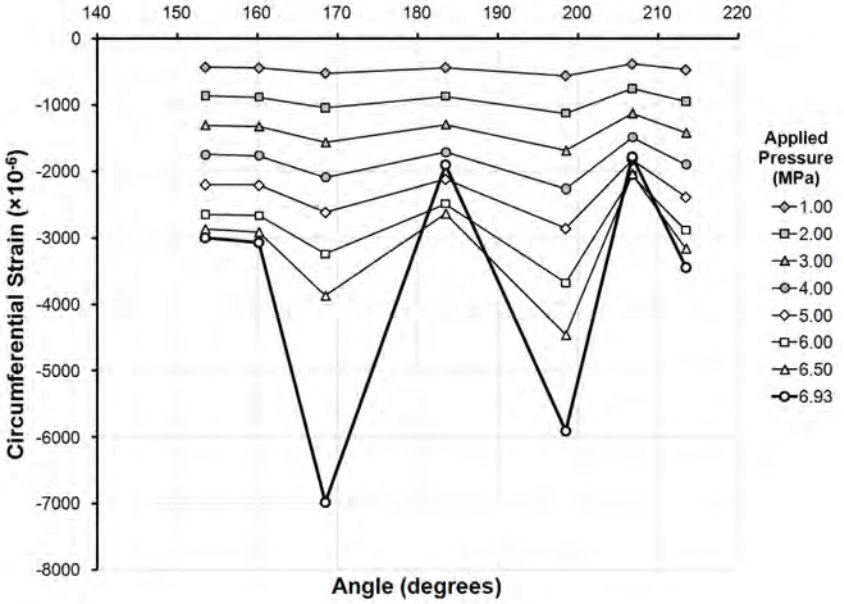

Figure 72: Circumferential strain distribution inside the shell in the centre of Bay 4 of specimen L510-No20, at pressures up to and including the collapse pressure.

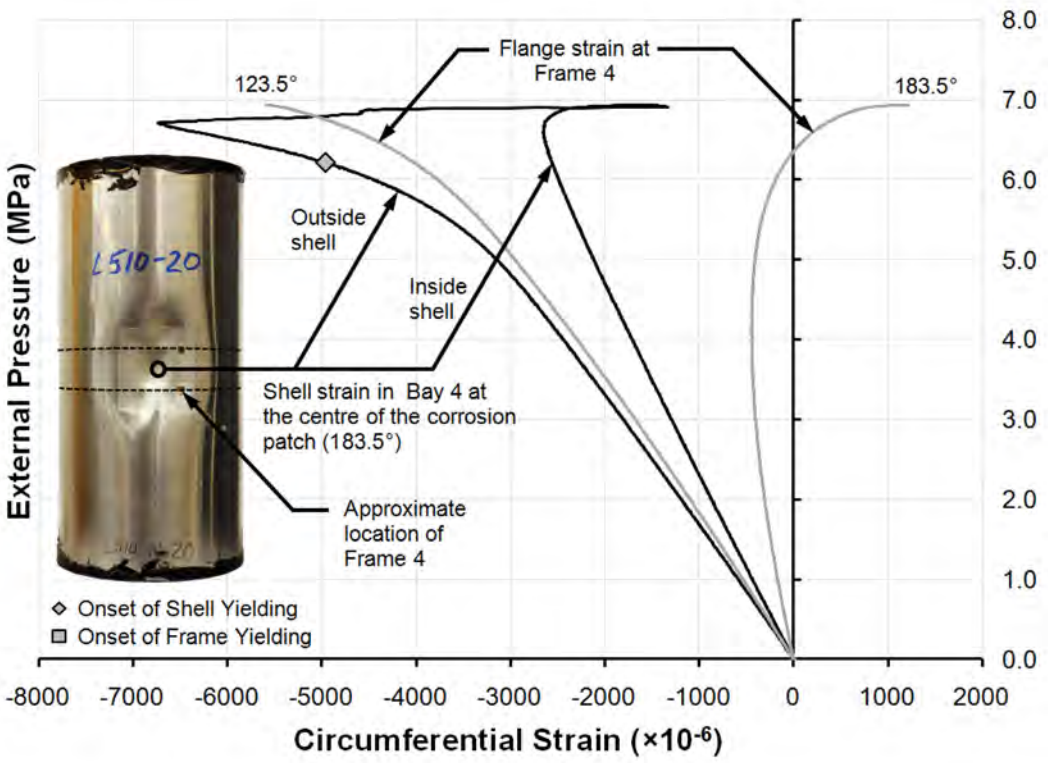

Figure 73: Selected pressure-strain curves near the collapse site for specimen L510-No20.

4.2.5 L510-No35

Specimen L510-No35 was nominally identical to L510-No14, having a small, deep corrosion patch oriented in-phase with the *n*=3 out-of-circularity shape. When comparing the as-measured cylinders, L510-No35 had a significantly greater OOC magnitude (Table 3), but a shallower depth of corrosion thinning (Table 6), than L510-No14. The corrosion patch on L510-No35 was located at 0°, and coincided with the maximum inward OOC at the mid-length of the cylinder (see Table 4, above, and Figure 153 and Figure 156 in Annex C). The testing history of the specimen is given in Table 24, which indicates that it collapsed at a pressure of 6.58 MPa. The post-testing photograph in Figure 57 shows that overall collapse of the specimen was concentrated around the in-phase corrosion patch.

The distribution of strain on the outside of the shell at the collapse pressure is shown in Figure 74. The largest compressive strains were at the corrosion patch, especially near the edges. Local troughs in the strain distribution were also apparent at the inward OOC lobes away from the corrosion patch, although those strain magnitudes were much smaller than at the corrosion patch.

The pressure-strain curves in Figure 75 show that the cylinder initially yielded at the outside of the shell, at the edge of the corrosion patch. The strains at the inside and outside of the shell, in

the centre of the corrosion patch, were nearly identical until the onset of yielding at the edge of the patch. Thereafter, the compressive strains on opposite sides of the shell diverged, becoming greater on the inside and smaller on the outside of the shell. A similar, but more pronounced, trend was observed in L510-No14, and was attributed to bending forces resulting from a local outward dent at the centre of the corrosion patch. The OOC measurements for L510-No35 do not indicate a similar dent in that specimen, suggesting that the behaviour must be at least partially related to other causes, such as the eccentricity due to one-sided thinning. Nonetheless, the shell strain outside the centre of the corrosion patch reversed direction a second time, just before the onset of collapse, and both the inner and outer compressive strains increased monotonically thereafter. The strain gauge data indicate that yielding of the cylinder was confined to the shell region in and around the corrosion patch, with yielding of the stiffeners delayed until after collapse.

Table 24: Testing procedures for specimen L510-No35

Test Name	Date	Test Type	Pre-Pressure (MPa)	Maximum Pressure (MPa)	Notes
Trial 1	9 Jun 2009	Elastic	3.60	0.97	N/A
Trial 2	9 Jun 2009	Collapse	13.71	6.58	N/A

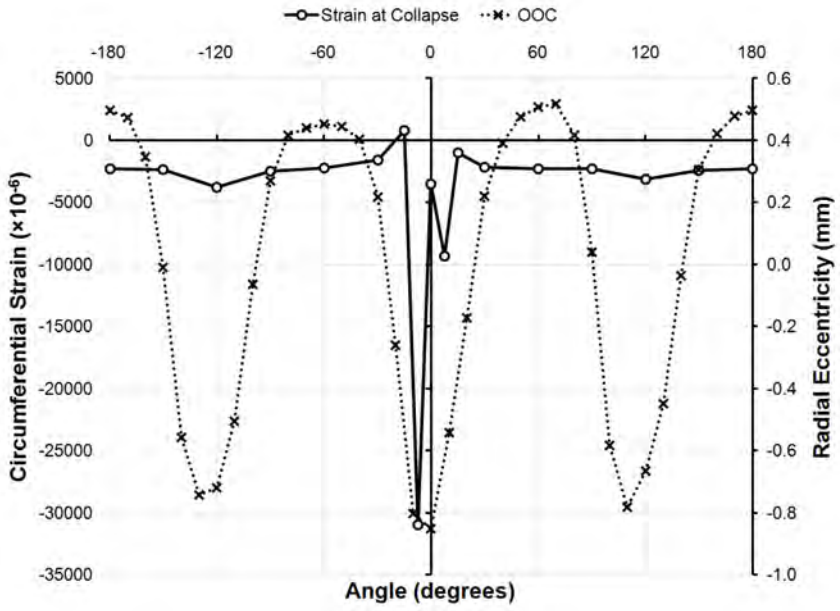

Figure 74: Circumferential strain distribution outside the shell at Bay 4 of specimen L510-No35 at the collapse pressure, plotted with the initial out-of-circularity at that location.

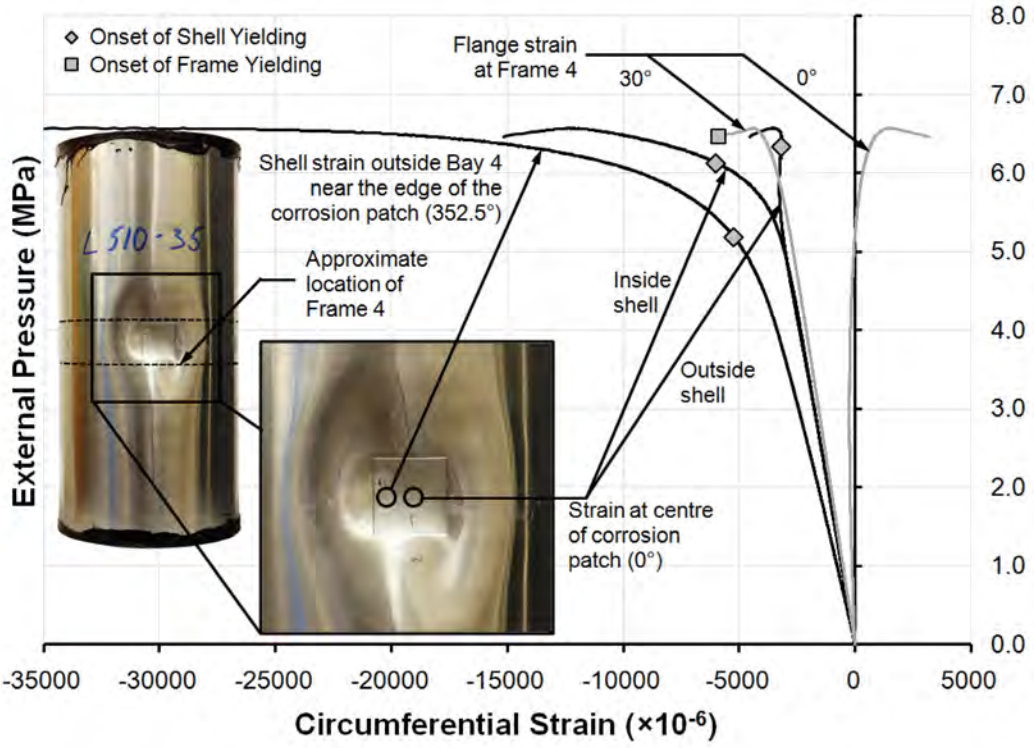

Figure 75: Selected pressure-strain curves near the collapse site for specimen L510-No35.

4.2.6 L510-No36

Specimen L510-No36 had a small, deep corrosion patch that was out-of-phase with the applied OOC mode. L510-No36 was nominally identical to L510-No13, but the former specimen had a larger OOC amplitude (Table 3) and greater depth of corrosion thinning (Table 6). Figure 159 and Figure 162 in Annex C show that the corrosion was collocated with the maximum outward OOC lobe, although the patch was offset slightly to one side of the peak OOC. The testing history in Table 25 indicates that the cylinder was tested once in the elastic range and then pressurized to collapse, failing at 7.22 MPa.

Photographs of L510-No36 after collapse testing, shown in Figure 57, show that the cylinder failed by overall collapse at a location away from the corrosion patch. The large buckling lobe at 300° spanned approximately three bays, from Frame 4 to Frame 7, and was offset from the corrosion patch by 60°. It can be seen from the axial distribution of out-of-circularity at 300°, shown in Figure 161 in Annex C, that the OOC for L510-No36 was greatest in the same half of the cylinder in which the collapse lobe occurred.

In general, L510-No36 showed a similar response as its companion specimen, L510-No13. Figure 76 shows the circumferential distribution of shell strain at the collapse pressure. The behaviour of the corrosion patch, with large compressive strains at the edges, was typical. Furthermore, the overall shell response can be seen to follow the n=3 pattern of the initial OOC shape. Since the

overall buckling lobe was not centred at the mid-length of the cylinder, strain gauge data were not available at the location of failure. Nonetheless, Figure 76 shows that the compressive strains in the central bay were greatest in the intact shell at 300°, near the collapse site, despite the presence of the corrosion patch. The pressure-strain curves in Figure 77 show a similar trend. That figure also shows that the shell yielded first at 300°, at the edge of the buckling lobe, although strain measurements were not available at the centre of the collapse site. Furthermore, yielding occurred almost simultaneously at the stiffener flange, 60° away from the buckling lobe, due to inward bending at that location.

Table 25: Testing procedures for specimen L510-No36

Test Name	Date	Test Type	Pre-Pressure (MPa)	Maximum Pressure (MPa)	Notes
Trial 1	19 Jun 2009	Elastic	3.66	1.04	N/A
Trial 2	19 Jun 2009	Collapse	13.64	7.22	N/A

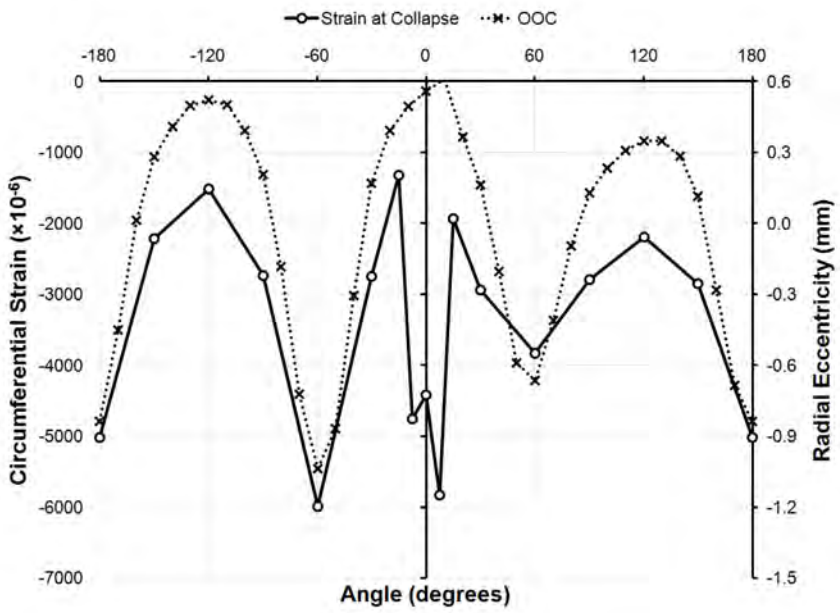

Figure 76: Circumferential strain distribution outside the shell at Bay 4 of specimen L510-No36 at the collapse pressure, plotted with the initial out-of-circularity at that location.

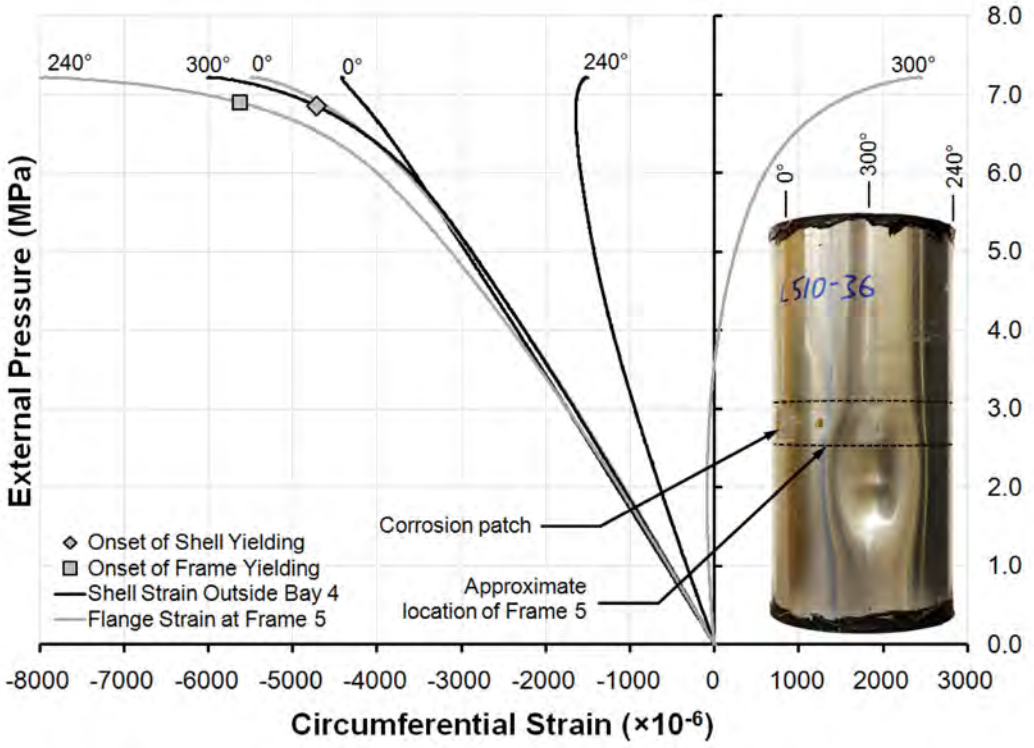

Figure 77: Selected pressure-strain curves near the collapse site for specimen L510-No36.

5 Numerical modeling

Numerical modeling of test specimens was performed in two stages. In the first stage, nonlinear finite element (FE) models were used to simulate the mechanical application of out-of-circularity in order to predict the residual stress field and its effect on collapse. Those analyses considered a generic cylinder model and out-of-circularity and are described in Section 5.1. In the second stage, standard FE modeling and analysis procedures, which were developed based on simulations of cylinders tested in Phases 1-3 [8], were used to predict collapse pressures for specific test specimens. In those analyses, described in Section 5.2, residual stresses arising from application of the OOC were neglected.

5.1 Simulation of mechanical application of out-of-circularity

Finite element analyses were performed in order to estimate the location and magnitude of residual stresses in a cylinder specimen arising from the mechanical application of out-of-circularity, as well as the effect of the residual stresses on the collapse behaviour of the cylinder. The target OOC for the FE simulation was an n=3, m=1 mode, with a maximum amplitude of approximately 0.5%. Furthermore, the simulation attempted to duplicate the actual procedure for applying OOC to the test specimens, which is described in Section 2.1.3. The commercial FE program ANSYS [18] was used to perform the nonlinear FE analyses.

5.1.1 Finite element modeling procedures

The OOC simulations used a generic finite element model having the nominal axisymmetric dimensions of the test specimens (see Figure 3). Since the simulations were concerned with the application of n=3 OOC, only one-third of the cylinder circumference (120°) was modeled, with symmetry boundary conditions applied to the circumferential edges of the model. The generic FE model, shown in Figure 78, was constructed of 4-node shell elements (SHELL181 in ANSYS), with 16 elements between stiffeners, 80 elements along the 120° circumferential arc, 3 elements through the web depth and 4 elements across the flange breadth. A bi-linear elastic-plastic material model was used with an isotropic von Mises yield surface and kinematic hardening. The material properties were based on the measured circumferential properties for L510-No17, with E=58,200 MPa, ν=0.32, σ_y=306 MPa and E_t=350 MPa, where E is Young's modulus, ν is Poisson's ratio, σ_y is the 0.2% yield stress and E_t is the tangent, or strain hardening, modulus.

Out-of-circularity was applied to the real test specimens by plastically deforming the cylinders using the triangular frame shown in Figure 5. OOC was built up gradually over the length of the cylinder by applying deformations in a step-by-step manner. In the FE simulation, the deformations were produced by applying pressure loads over the estimated contact area of the triangular frame with the cylinder shell. The assumed FE contact areas, which are shown in Figure 78, were 50 mm wide in the axial direction, extended 25.4 mm around the circumference, and were centred at ring-stiffeners.

Since the actual sequence of iteratively building up the OOC was unknown for any specific test specimen, one had to be assumed. The assumed loading history is summarized in Table 26,

whereby pressure loads were applied at Frame 5, Frame 4, Frame 3 and Frame 6, in that order. Loading was applied to one frame at time, and the cylinder was completely unloaded before the next load cycle began. Each load was applied incrementally using load control, taking into account nonlinear geometry and material behaviour. The pressure loads required to give the desired OOC magnitude and axial distribution were arrived at by trial and error.

A collapse analysis of the model under external pressure was performed after the OOC simulation. A uniform external pressure load was applied to the shell, with equivalent edge pressures at the cylinder ends to represent the axial load transferred from the end caps. During the collapse analysis, the symmetry boundary conditions used in the OOC simulation were retained, and the model was simply supported at the cylinder ends and at the intersection of the thick end rings with the tapered shell section. Those boundary conditions resulted in a "quasi-clamped" constraint whereby out-of-plane bending was prevented at the cylinder ends, while end-warping was allowed. The pressure load was applied incrementally using an arc length method, which allowed the analysis to be carried into the post-collapse region. Two collapse analyses were performed: one in which the permanent deformation, residual stresses and material history from the OOC simulation were included in the model; and a second, stress-relieved, case whereby only the final deformation shape was retained from the OOC simulation.

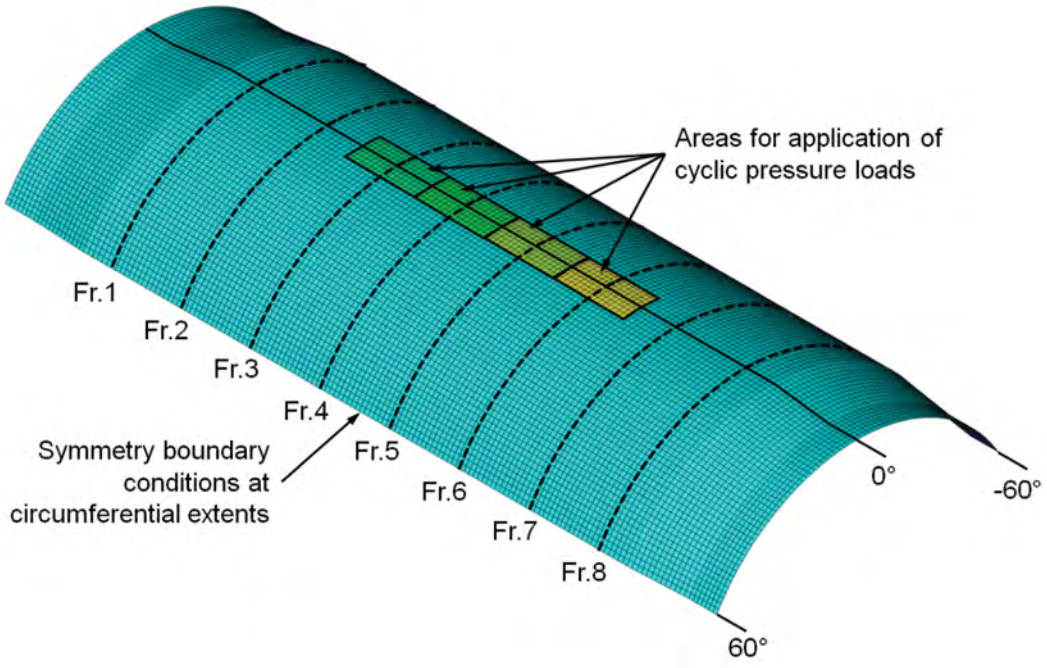

Figure 78: Generic finite element model used to simulate the mechanical application of out-of-circularity to cylinder specimens; showing location frames, areas for application of cyclic pressure loads, and symmetry boundary conditions for the 120° cylindrical arc.

Table 26: Loading history for out-of-circularity application simulation of the generic finite element model.

Load Cycle	Maximum Load		
	Local Pressure (MPa)	**Equivalent Radial Force (kN)**	**Location**
No. 1	14.0	17.8	Frame 5
No. 2	13.0	16.5	Frame 4
No. 3	13.0	16.5	Frame 3
No. 4	13.0	16.5	Frame 6

5.1.2 Predicted out-of-circularity

The radial displacement at Frame 5, throughout the out-of-circularity simulation, is shown in Figure 79. The applied displacement and net residual deformation was largest during the first load cycle, whereby the load was applied directly to Frame 5. Thereafter, the load was applied at other frames, resulting in smaller increases in permanent deformation at Frame 5. Figure 80 shows the circumferential distribution of displacements at Frame 5 for each load cycle. That figure shows the same trend noted above, with large permanent deformation after load cycle no. 1, followed by more modest increases during later load cycles. Furthermore, the displacement distribution about the 120° arc is indicative of an n=3 OOC mode, and the sharp OOC trough after the first load cycle was attenuated to a certain extent as the cylinder was loaded at other frames.

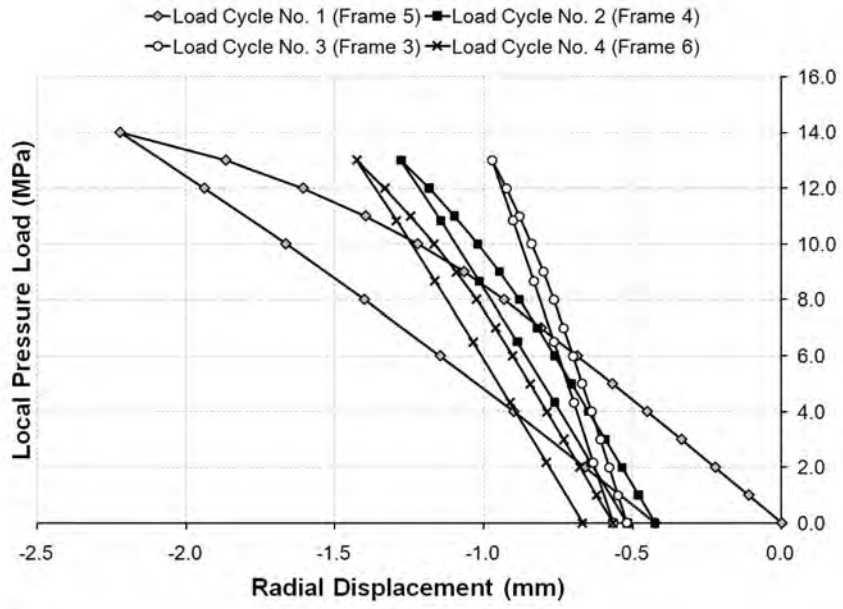

Figure 79: Radial displacement of Frame 5 of the generic FE model at 0° during the out-of-circularity application simulation.

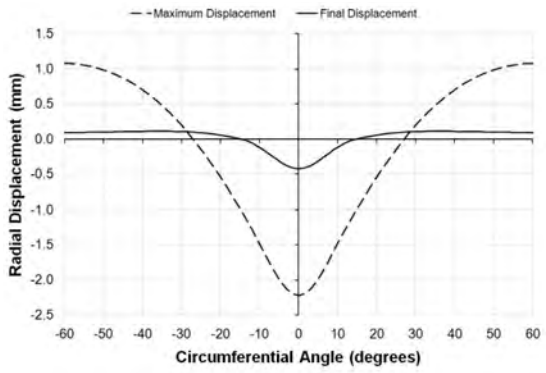

(a) Cycle No. 1, with load at Frame 5

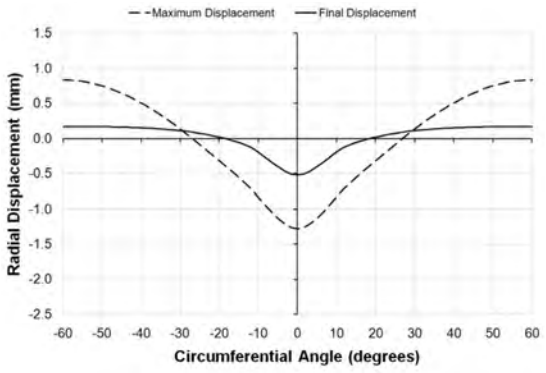

(b) Cycle No. 2, with load at Frame 4

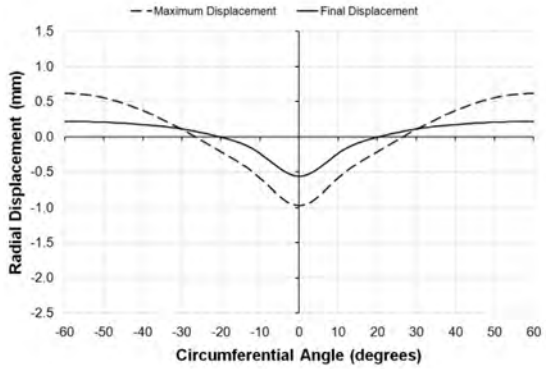

(c) Cycle No. 3, with load at Frame 3

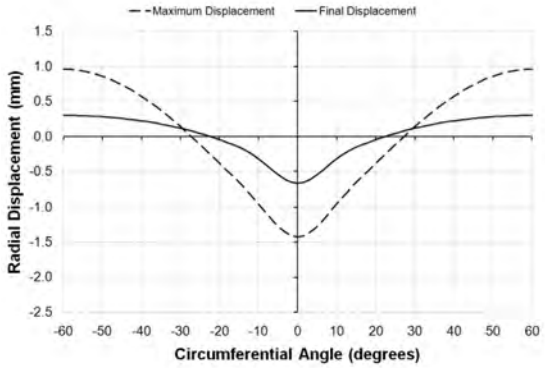

(d) Cycle No. 4, with load at Frame 6

Figure 80: Circumferential distribution of radial displacements at Frame 5 at various stages of out-of-circularity application, as predicted by the generic finite element model; showing the maximum displacement after the load was applied and the final displacement after the load was removed for each load cycle.

Figure 81 shows the axial distribution of permanent displacements at 0° at the end of each load cycle. It can be seen that the target m=1 axial mode was approached more closely with each successive load cycle, and that the maximum radial displacement occurred mid-way between stiffeners. The evolution of the overall OOC shape is shown through contour plots of the radial displacement, which are superimposed on the deformed FE model in Figure 82.

The final configuration of the FE model was sufficiently close to the target OOC mode for the purposes of the current study, and the maximum OOC was found to be 0.714 mm, or approximately 0.59%. Furthermore, the predicted OOC shape is reasonably similar to the final shape of the test specimens; see, for example, the OOC shape of L510-No25 in Figure 139 in Annex C. More direct comparisons of the OOC modes for the FE model and L510-No25 are shown in Figure 83 and Figure 84, which show the circumferential and axial modes, respectively. In Figure 83, the circumferential OOC mode in L510-No25 is offset by approximately 10° with respect to the FE model, but otherwise the shapes and magnitudes of the models are similar. The

final shape of the FE model, especially in the axial direction, is quite complex, especially considering the relatively simple loading history of the model. It is unlikely that an accurate simulation of the process of applying OOC to a real test specimen could be performed without detailed knowledge of the sequence and magnitude of loading.

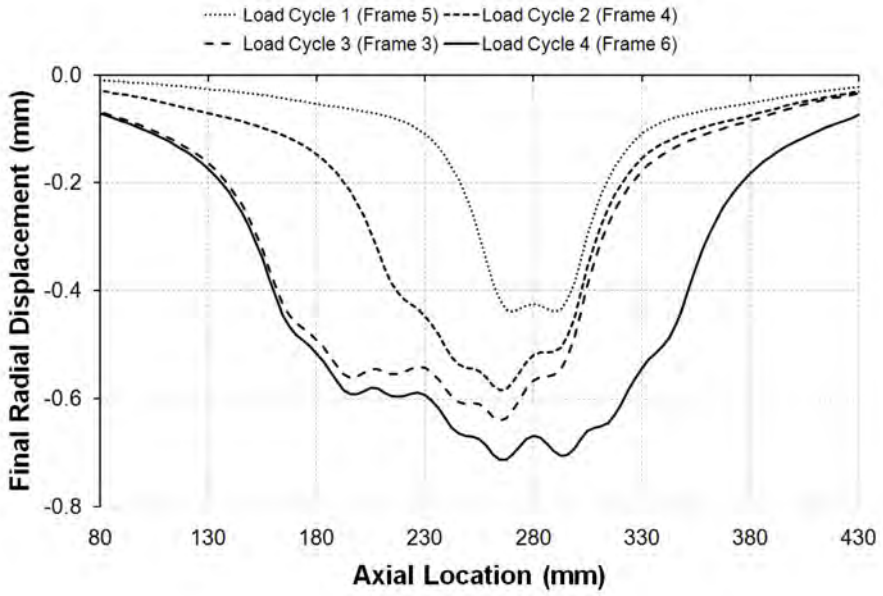

Figure 81: Axial distribution of radial displacements at 0° at various stages of out-of-circularity application, as predicted by the generic finite element model; showing the final displacement at the end of each load cycle. Tick-marks on the horizontal axis correspond with the frame locations on the cylinder.

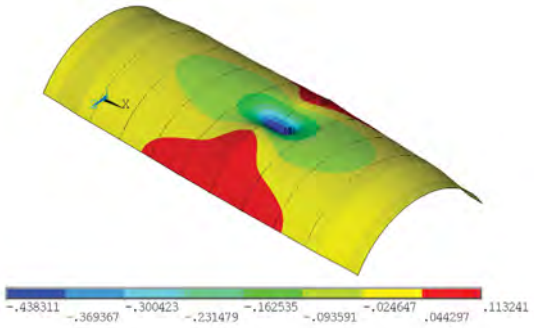

(a) Cycle No. 1, with load at Frame 5

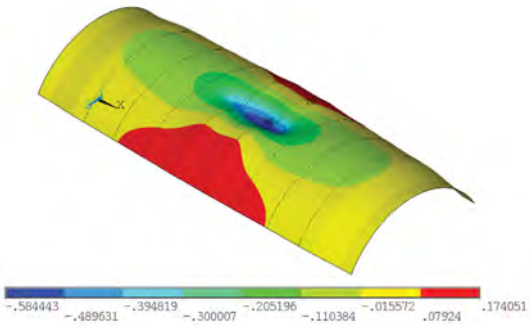

(b) Cycle No. 2, with load at Frame 4

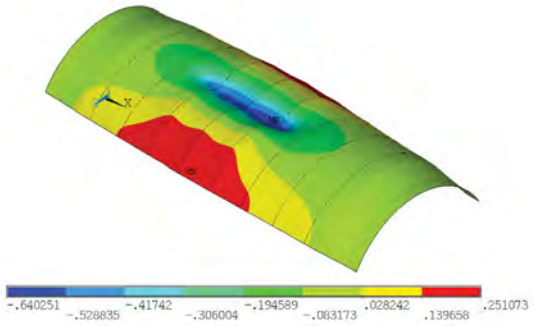

(c) Cycle No. 3, with load at Frame 3

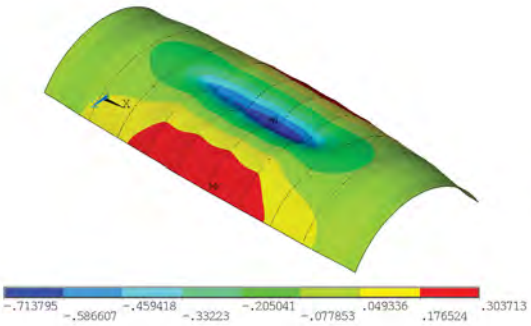

(d) Cycle No. 4, with load at Frame 6

Figure 82: Radial displacement (mm) contour plots for the generic finite element model simulations of out-of-circularity application; showing contour plots after each load cycle has been completed. The out-of-circularity is also indicated by the deformed shape of the model, whereby the displacements are exaggerated for clarity.

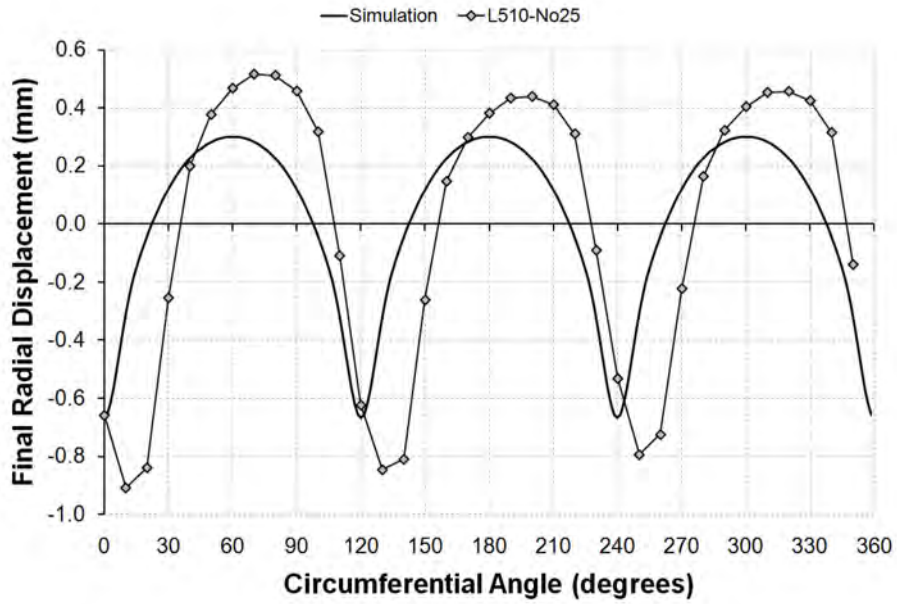

Figure 83: Comparison of the final out-of-circularity at Frame 5 for the generic finite element model and specimen L510-No25.

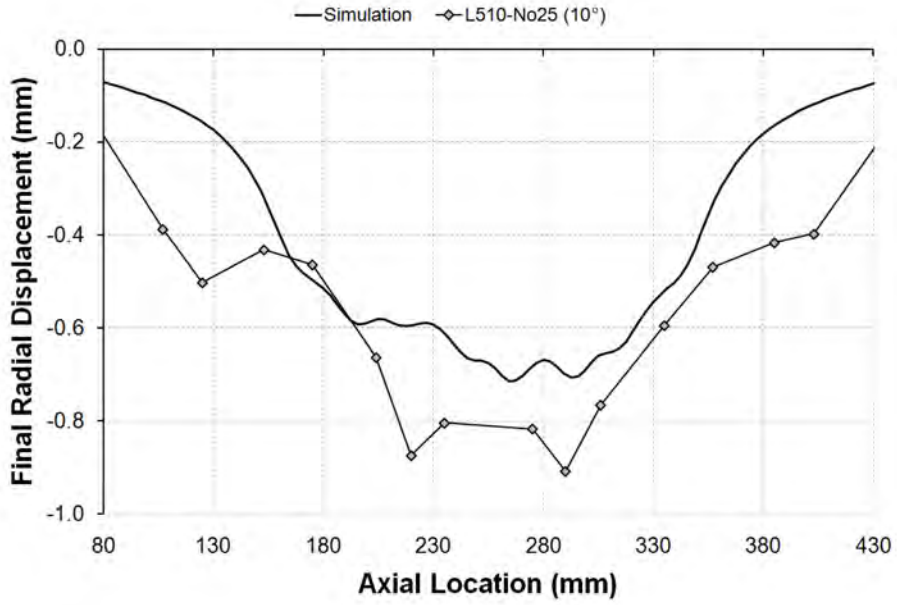

Figure 84: Comparison of the final deformation along the length of the cylinder at the maximum inward out-of-circularity for the generic finite element model (0°) and specimen L510-No25 (10°). Tick-marks on the horizontal axis correspond with the frame locations on the cylinders.

5.1.3 Predicted residual stresses

Figure 85 and Figure 86 show contour plots of the von Mises stress during load cycles no. 1 and 4. Stresses in areas shown in red exceed the yield stress of the model. Figure 85(a) shows that, halfway through the first load cycle, yielding was concentrated in the shell and stiffeners near the area of loading. The residual stresses after unloading, shown in Figure 85(b), were significant, especially in the stiffener flange of Frame 5, but not yield-level. Further yielding occurred during the loading portion of each subsequent load cycle. The final stress state of the model, as shown in Figure 86(b), was characterized by near-yield-level stresses in the stiffener flanges at the maximum inward OOC and smaller stresses in the shell at the same location.

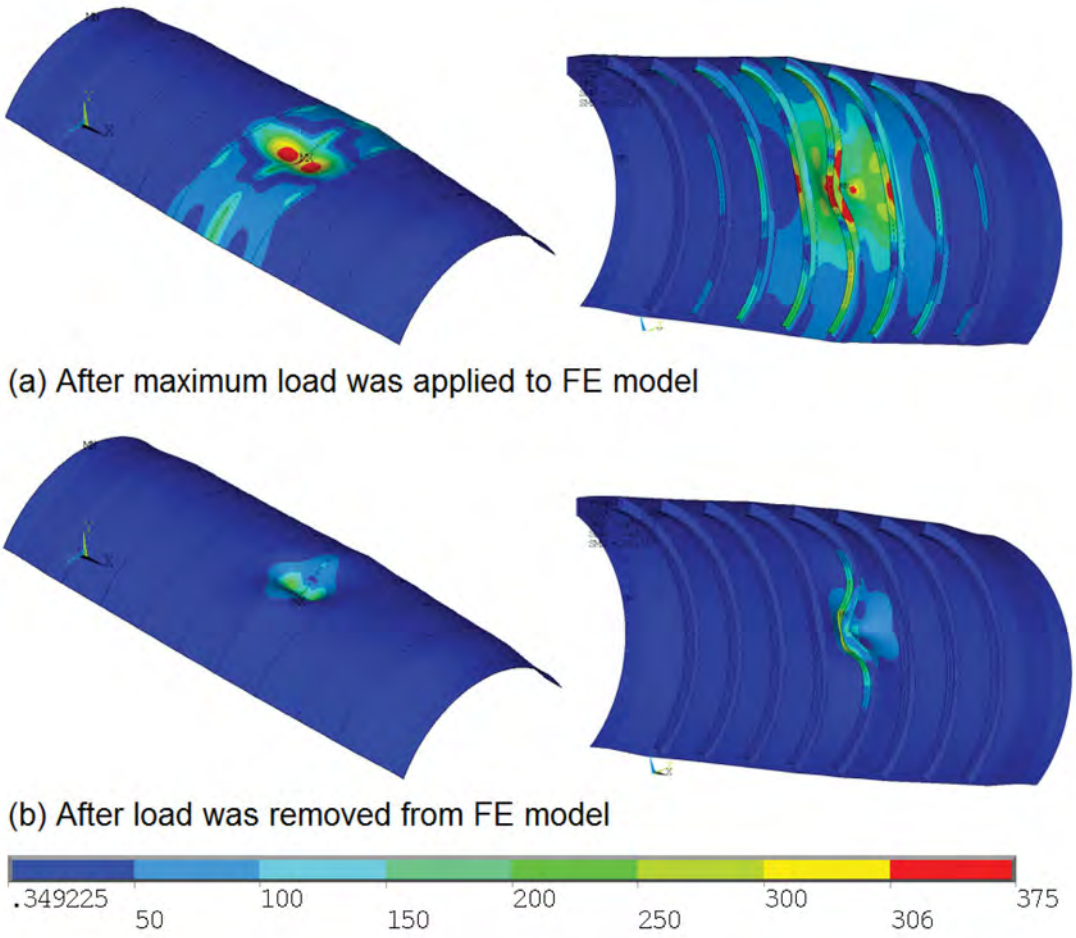

Figure 85: von Mises stress (MPa) contour plots for the generic finite element model simulations of out-of-circularity application; showing contour plots (a) after loading and (b) after unloading during load cycle no. 1. Areas with a von Mises stress greater than the yield stress are shown in red. The radial displacements are indicated by the deformed shape of the model, whereby the deformations are exaggerated for clarity.

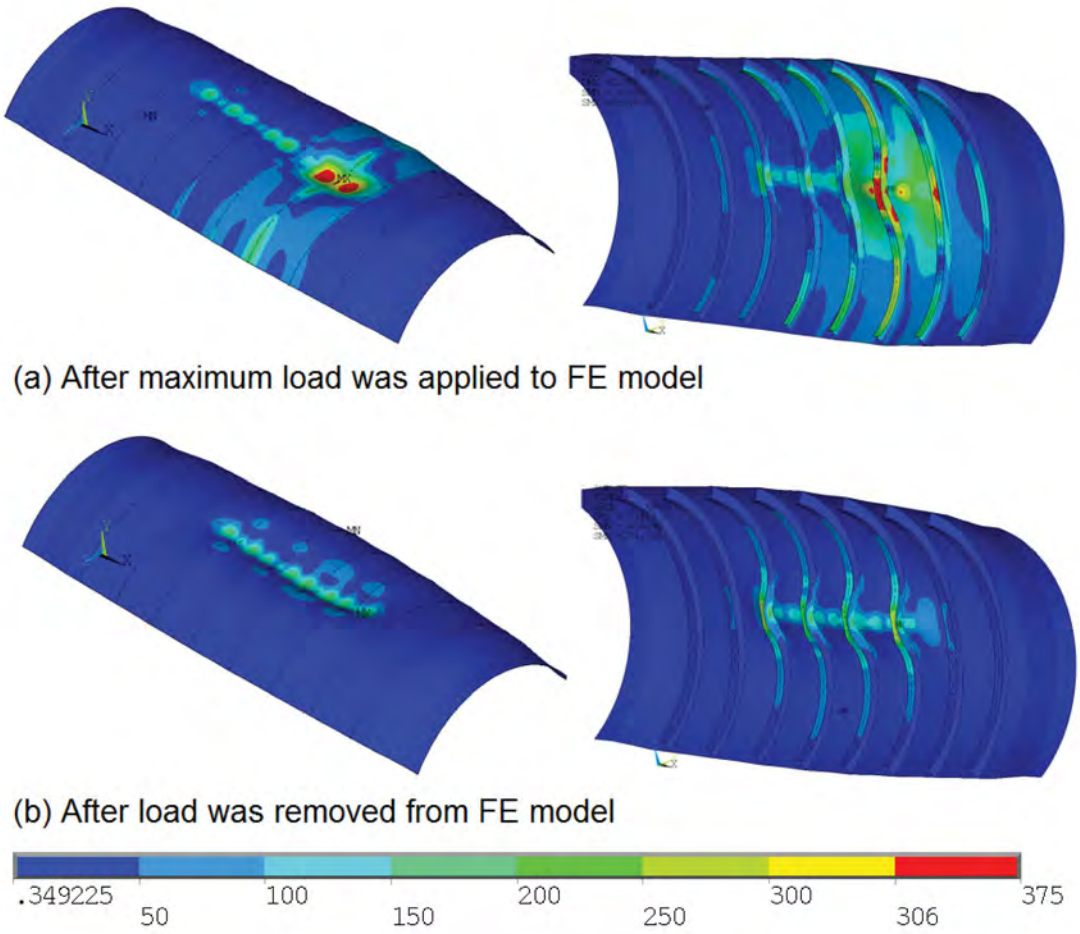

Figure 86: von Mises stress (MPa) contour plots for the generic finite element model simulations of out-of-circularity application; showing contour plots (a) after loading and (b) after unloading during load cycle no. 4. Areas with a von Mises stress greater than the yield stress are shown in red. The radial displacements are indicated by the deformed shape of the model, whereby the deformations are exaggerated for clarity. The stress contours in (b) represent the residual stress distribution in the model before collapse analysis.

The circumferential stresses at the end of the OOC simulation are shown in Figure 87. Large tensile and compressive stresses were predicted at the outside of the shell and at the stiffener flange, respectively. Those stresses were concentrated near the areas of load application and maximum inward displacements at 0°.

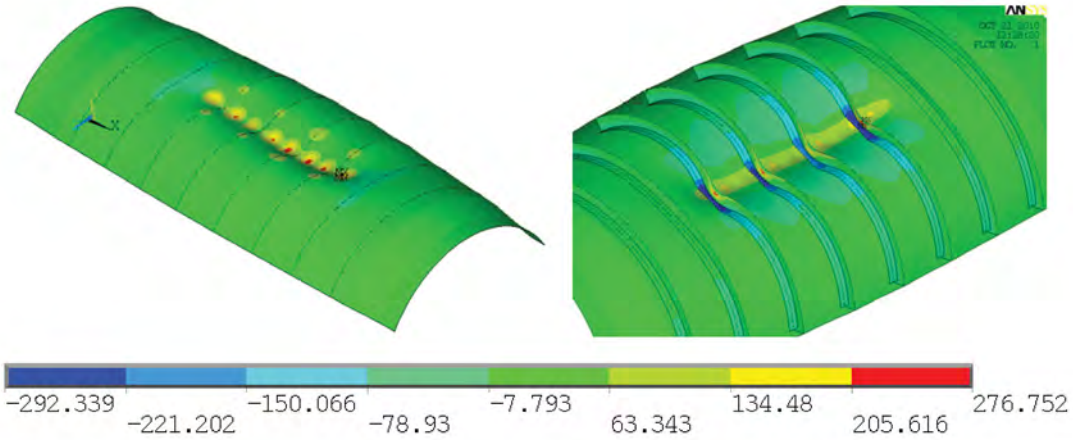

Figure 87: Circumferential stress (MPa) contour plots for the generic finite element model simulations of out-of-circularity application; showing contour plots after unloading during load cycle no. 4. The stress contours in represent the residual stress distribution in the model before collapse analysis.

5.1.4 Collapse predictions

The collapse modes for of the "full simulation" and stress-relieved models are shown in Figure 88 and Figure 89, respectively. Those figures show that both models failed in an overall n=3 mode, and that the radial displacements at collapse were greatest in the full simulation model. The displacements in the full simulation model included the final deformation from the OOC simulation. When the OOC displacements were subtracted from the collapse displacements, the full simulation model actually had smaller displacements at collapse than the stress-relieved models.

Load-displacement curves for the full simulation and stress-relieved models are given in Figure 90. The displacements are plotted for a node at 0° at the shell in Bay no. 4, mid-way between stiffeners. The behaviour of the models was similar for most of the pressure loading history, but the model with residual stresses collapsed at a lower pressure, 7.48 MPa, compared to the stress-relieved model, which reached a peak pressure of 7.72 MPa. It was expected that bending moments resulting from out-of-circularity would produce tensile and compressive stresses at the stiffener and shell, respectively. Since the applied stresses would be opposite in sign from the circumferential residual stresses, as discussed above in Section 5.1.3, the net result was anticipated to be an increase in collapse pressure compared to the stress-relieved case. When the opposite trend was observed in the collapse predictions, the residual stress distributions were revisited.

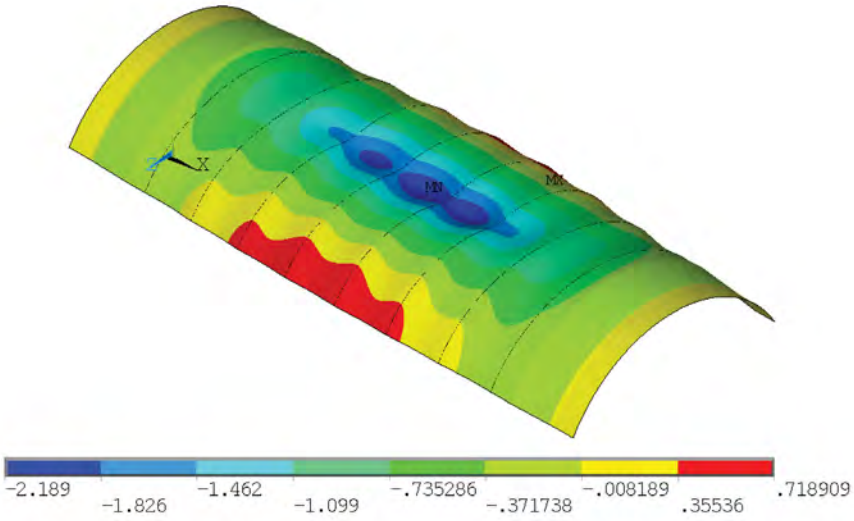

Figure 88: Deformed shape of the generic FE model at the peak load during the collapse analysis; showing a radial displacement (mm) contour plot for the FE model whereby the out-of-circularity application was simulated. The collapse mode is also indicated by the deformed shape of the model, whereby the displacements are exaggerated for clarity. The displacement contour values include the final displacements from the out-of-circularity simulation.

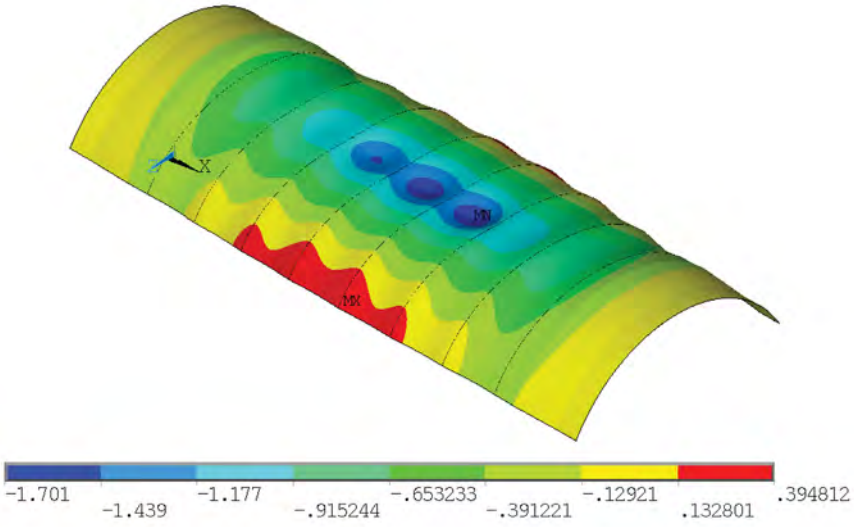

Figure 89: Deformed shape of the generic FE model at the peak load during the collapse analysis; showing a radial displacement (mm) contour plot for the stress-relieved FE model. The collapse mode is also indicated by the deformed shape of the model, whereby the displacements are exaggerated for clarity.

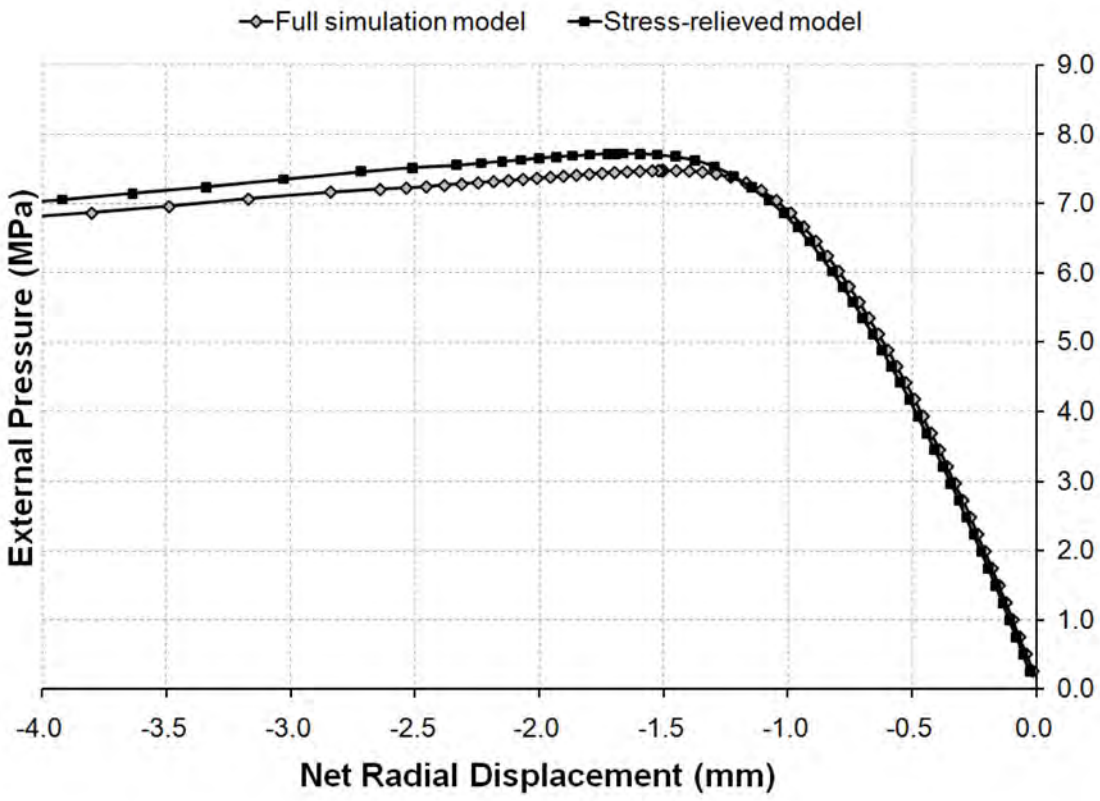

Figure 90: Load-displacement curves at the maximum out-of-circularity in Bay no. 4 for the collapse analysis of the generic FE models with and without residual stresses.

The von Mises stress distributions at the collapse load for the full simulation and stress-relieved models are shown in Figure 91 and Figure 92, respectively. Both models failed by overall collapse precipitated by yielding at the outside of the shell plating at the maximum inward OOC, and yielding of the frame flanges at the maximum outward OOC. Those locations are consistent with the expected locations of large compressive bending stresses due to out-of-circularity. Figure 87 shows that the residual stresses are in tension at the shell at the maximum inward OOC, which would tend to increase the strength of that model compared to the stress-relieved model.

Figure 93 shows the circumferential residual stresses in a section of the full simulation model near the maximum outward OOC. It can be seen that the residual stresses in the frame flanges were quite small compared to the yield stress, but were in compression, and were thus collocated with applied compressive bending stresses during pressure loading. Therefore, the smaller collapse strength of the full simulation model was due to small, elastic residual stresses away from the maximum inward OOC, rather than the significant yielding that occurred at the contact region during OOC application.

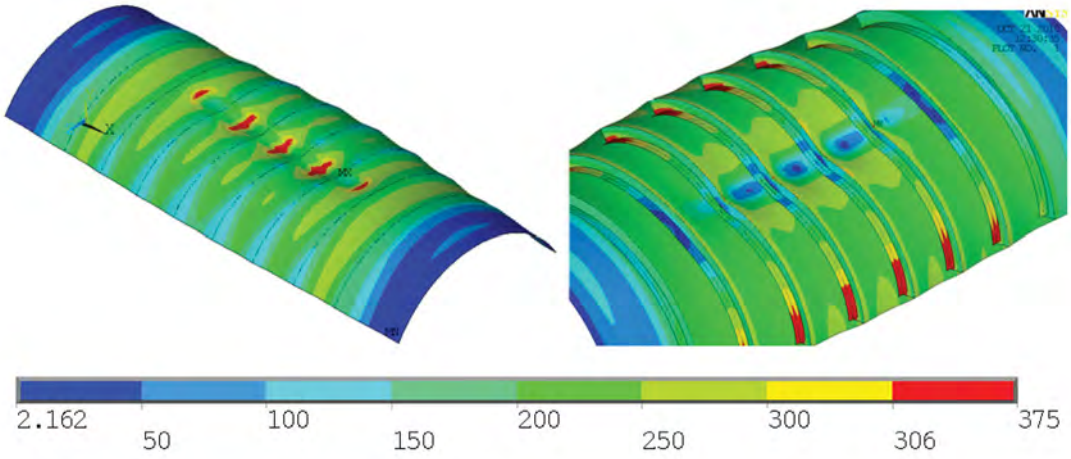

Figure 91: von Mises stress (MPa) contours at the peak load during the collapse analysis for the FE model whereby the out-of-circularity application was simulated. Areas with a von Mises stress greater than the yield stress are shown in red.

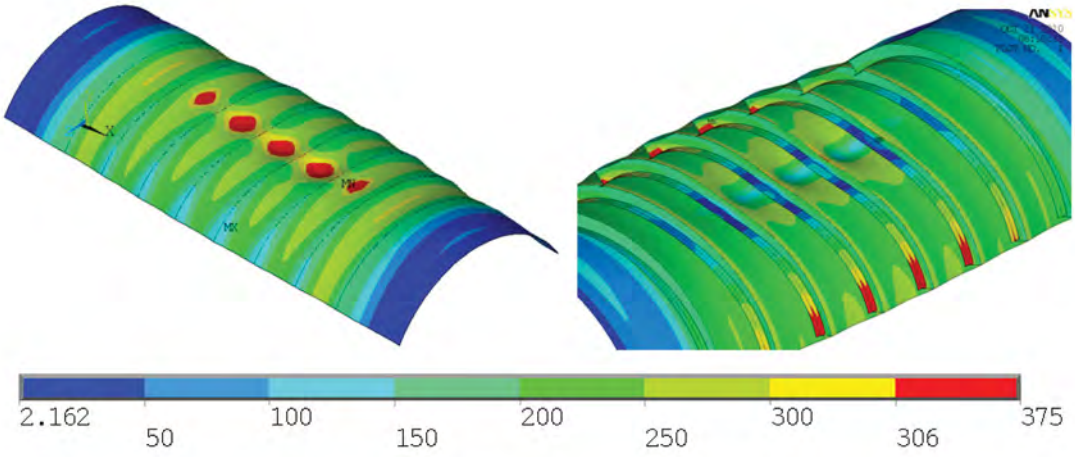

Figure 92: von Mises stress (MPa) contours at the peak load during the collapse analysis for the stress-relieved FE model. Areas with a von Mises stress greater than the yield stress are shown in red.

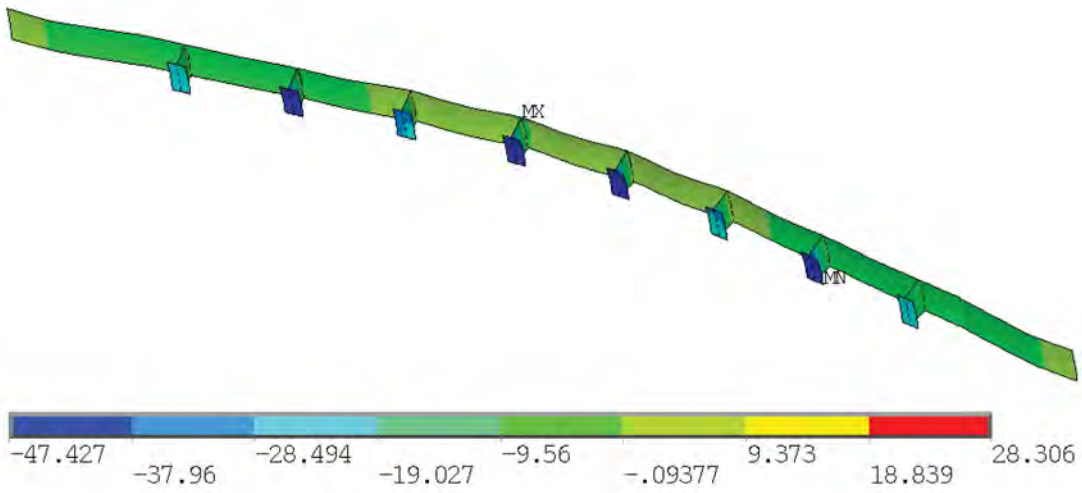

Figure 93: Circumferential stress (MPa) contour plot for the generic finite element model simulation of out-of-circularity application; showing a section of the model at the maximum outward out-of-circularity (-60°) after load cycle no. 4. The stress contours represent the circumferential residual stress distribution in the model before collapse analysis.

5.2 Nonlinear collapse predictions neglecting residual stresses

Finite element collapse predictions were generated for each of the Phase 5 and 6 test specimens. The effect of residual stresses due to the mechanical application of out-of-circularity was neglected in the analyses for several reasons. First, the OOC simulation described in Section 5.1, which requires several load steps, is computationally expensive compared to a single collapse analysis. Second, it has been shown that detailed information regarding the loading sequence and magnitude is required in order to predict the actual OOC shape; that data is not available for any of the test specimens. Finally, in the simulation described above, residual stresses arising from the OOC procedure were found to have a small (approximately 3%) affect on the collapse pressure compared to the stress-relieved model. Therefore, neglecting residual stresses in the collapse simulations was not expected to introduce significant errors with respect to the predicted collapse pressures.

5.2.1 Finite element modeling procedures

The finite element modeling procedures used for Phase 5 and 6 cylinders were based on the methodology developed for numerical simulations of Phase 1-3 test specimens, as reported in [8]. The DRDC program CylMesh was used to generate FE models that were subsequently analyzed using ANSYS [18]. The FE meshes modeled the full extent of each cylinder and consisted of shell elements. Mid-plane offsets were used for shell elements at the corrosion patches.

The mesh densities of the models were based on previous FE modeling of similar cylinders [8]. Nonetheless, mesh convergence studies were performed on representative cylinder configurations. The results of those studies, which are presented in Annex L, validated the previous work. A typical converged mesh had 288 elements about the circumference, 19 elements between frames, and 4 elements on both the stiffener web and flange. A typical mesh for an intact, Phase 5, specimen is shown in Figure 94, and meshes for corroded, Phase 6, cylinders with small and large corrosion patches are shown in Figure 95 and Figure 96, respectively.

Nonlinear maps of the measured out-of-circularity imperfections and shell thicknesses were derived through double Fourier series decompositions (see Annex A) and applied to the nodal positions and shell elements in the FE model. Stress-strain curves for FE analysis were generated by averaging the measured circumferential curves for each model. The potentially artificially low Young's moduli were corrected by replacing the elastic portions of the measured curves with elastic strains based on a Young's modulus of 70 GPa. The resulting engineering material curves were used to generate true stress-strain curves, which were implemented via multi-linear material models with isotropic yield surfaces and kinematic hardening.

The pressure loading was applied in the same way as for the collapse analyses of the generic model, and quasi-clamped boundary conditions were used (see Section 5.1.1). Collapse pressures were predicted via nonlinear analysis, including large displacements and material plasticity. An arc length method was used, and an initial load increment of 0.25 MPa was used to start each analysis. The modeling and analysis procedures for CylMesh/ANSYS analyses are given in greater detail in [8], along with some of the modeling studies that helped define those procedures.

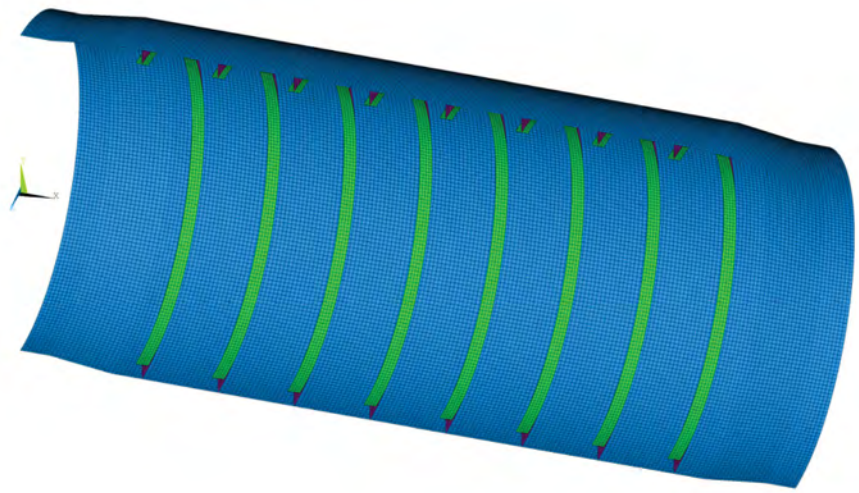

Figure 94: Typical finite element model for an intact (Phase 5) test specimen; showing one-half of the FE model of L510-No18.

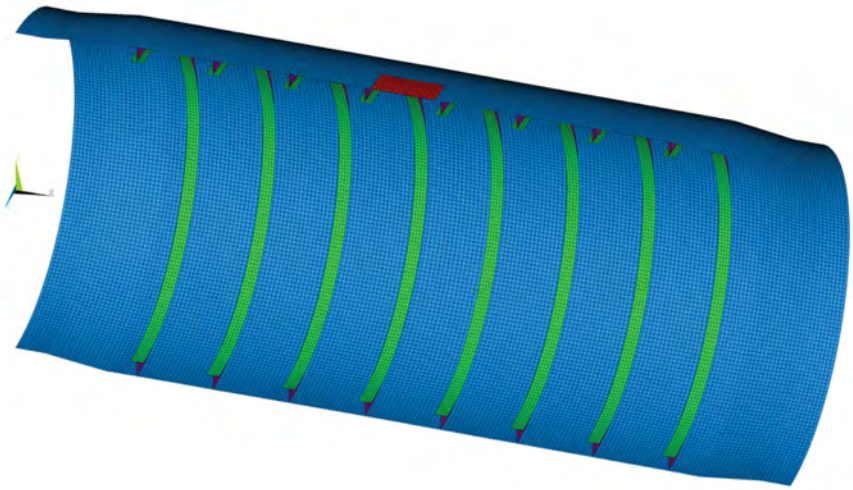

Figure 95: Typical finite element model for a Phase 6 test specimen with a small corrosion patch; showing one-half of the FE model of L510-No13, with the corrosion patch in red.

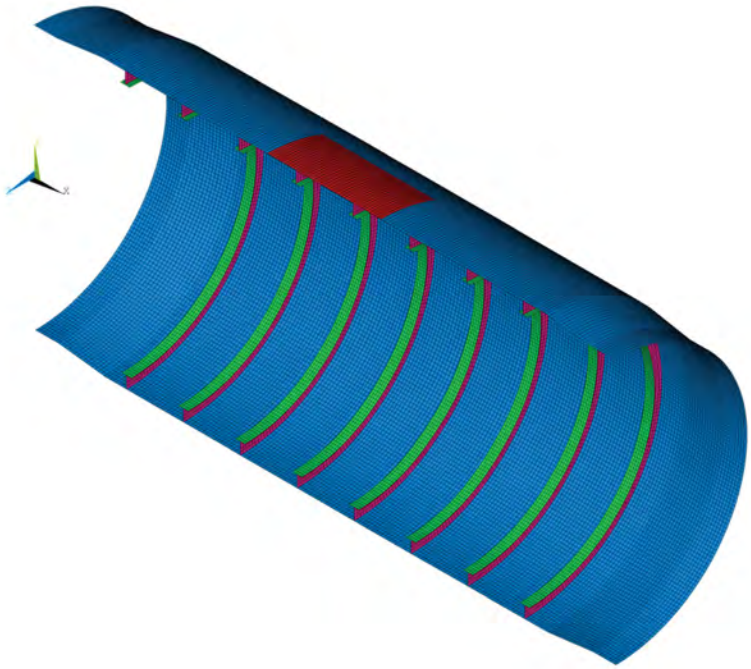

Figure 96: Typical finite element model for a Phase 6 test specimen with a large corrosion patch; showing one-half of the FE model of L510-No19, with the corrosion patch in red.

5.2.2 Collapse predictions for Phase 5 specimens

Collapse modes predicted by the FE models of Phase 5 specimens are shown in Figure 97. Numerical predictions of collapse pressure and location for Phase 5 specimens are given in Table 27. That table also lists the modeling uncertainty factor, X_m, for each experimental-numerical comparison, taken as the experimental collapse pressure divided by the predicted collapse pressure. X_m is indicative of the accuracy of given numerical model.

The Phase 5 FE models over-predicted the experimental collapse pressures by between 3 and 5%, which is consistent with the expected error due to neglecting the residual stresses due to OOC application. In all but two cases, collapse occurred at a different OOC lobe in the FE models compared to the test specimens. In some cases, the maximum out-of-circularity was nearly identical at two inward OOC lobes, so that small perturbations in the test specimen may have influenced which lobe dominated the post-collapse behaviour. Those perturbations, which could possibly be related to the residual stress field, were not captured by the FE models.

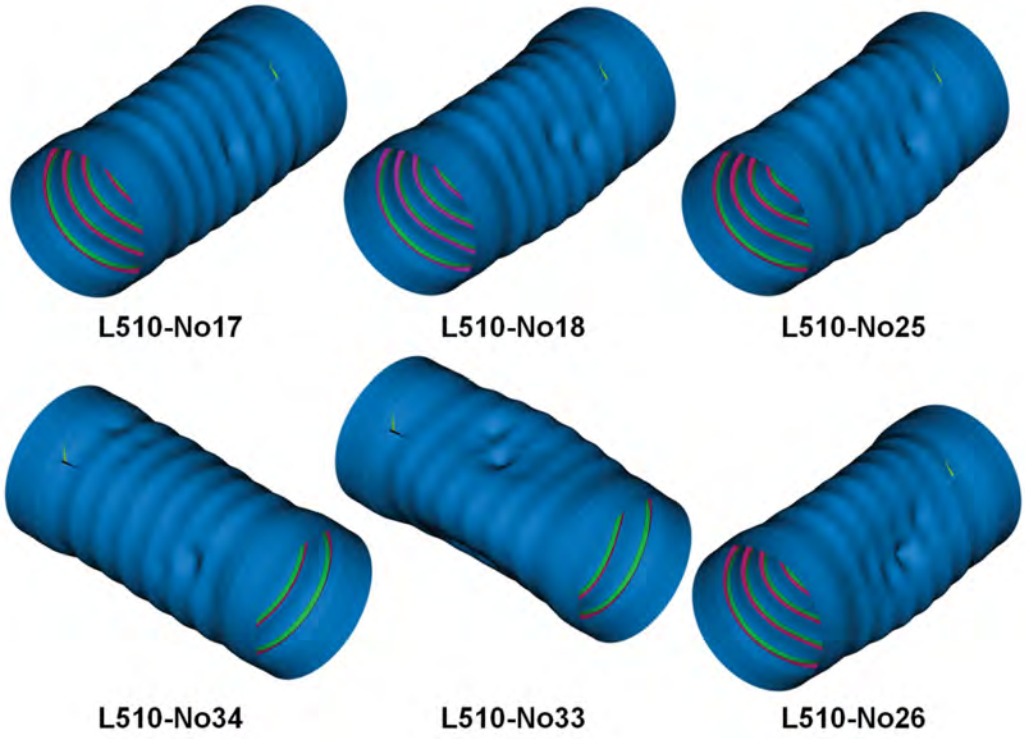

Figure 97: Collapse modes predicted by finite element models for Phase 5 specimens, without artificial corrosion damage; showing deformed shape of the FE model at the predicted collapse pressure. The FE displacements are scaled by a factor of 20 for clarity. Clockwise from top-left: L510-No17 and L510-No18, both with 0.3% OOC in n=*3 and* m=*1 circumferential and axial modes, respectively; L510-No25, L510-No26 and L510-No33, all with 0.5% OOC in* n=*3 and* m=*1 circumferential and axial modes, respectively; and L510-No34, with 0.3% OOC in* n=*3 and* m=*2 circumferential and axial modes, respectively.*

Figure 98 and Figure 99 show typical experimental and numerical pressure-strain plots for L510-No18 and L510-No34, respectively. The agreement between the experimental and numerical curves is very good, especially in the linear-elastic portions. Yielding was delayed in the numerical models as a result of neglecting residual stresses, so that, as the collapse pressure was approached, the numerical models tended to under-predict the compressive and tensile strains.

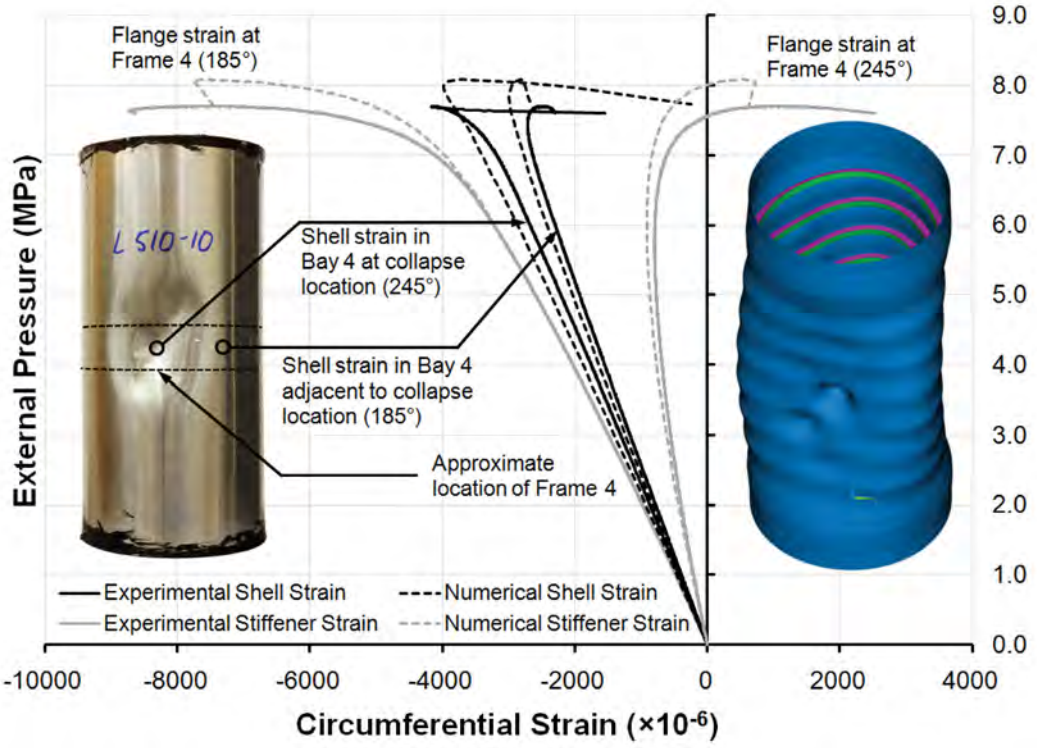

Figure 98: Comparison of experimental and numerical pressure-strain curves for locations near the experimental collapse site of L510-No18; also shown is a post-testing photograph of the specimen and the deformed shape of the numerical model after the final load step in the analysis. The displacements in the numerical model are scaled by a factor of 20 for clarity.

Table 27: Finite element collapse predictions for Phase 5 test specimens, based on models whereby the residual stresses due to out-of-circularity application are neglected.

Specimen	Collapse Location		Collapse Pressure (MPa)		
	Experiment	Prediction	Experiment	Prediction	Modeling Uncertainty Factor, X_m
L510-No17	Bays 3-5, 20°	Bay 4, 246.3°	7.84	8.24	0.952
L510-No18	Bays 3-5, 245°	Bay 4, 256.3°	7.71	8.08	0.954
L510-No25	Bays 3-5, 20°	Bay 3, 245.0°	7.13	7.46	0.955
L510-No26	Bays 3-5, 125-130°	Bay 4, 240.0°	7.05	7.27	0.970
L510-No33	Bays 3-5, 140°	Bay 4, 16.3°	7.03	7.37	0.953
L510-No34	Bays 5-7, 65°	Bay 6, 65.0°	8.02	8.37	0.959

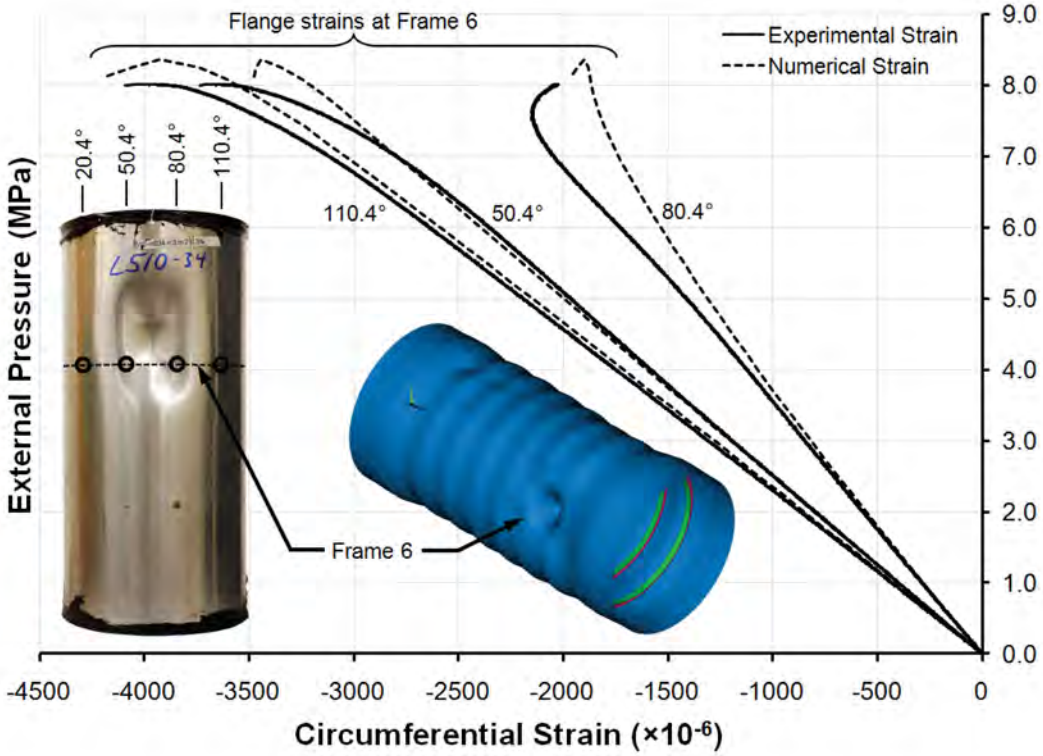

Figure 99: Comparison of experimental and numerical pressure-strain curves for locations near the experimental collapse site of L510-No34; also shown is a post-testing photograph of the specimen and the deformed shape of the numerical model after the final load step in the analysis. The displacements in the numerical model are scaled by a factor of 20 for clarity.

5.2.3 Collapse predictions for Phase 6 specimens

Finite element collapse predictions for Phase 6 specimens are given in Table 28, and the predicted collapse modes are shown in Figure 100. The FE models over-predicted the collapse pressures of the corroded test specimens by, at most, 5.3%. The predicted collapse locations agreed with the experimental results for all cylinders with corrosion, even with respect to the local buckling lobes at the corrosion patches.

Typical pressure-strain curves derived from the Phase 6 experiments and the corresponding numerical models are shown in Figure 101 and Figure 102. The curves for L510-No14 in Figure 101 show that the numerical curves under-predicted the bending strains at the centre of the corrosion patch; otherwise, the numerical curves show good agreement with the experimental results. For L510-No19, shown in Figure 102, there is good agreement between all experimental and numerical pressure-strain curves, except the strain near the edge of the corrosion patch. The numerical model predicted large compressive strains at that location as the collapse load was approached, while the experimental strains reversed direction due to bending effects. Both the test specimen and the numerical model showed a local buckling lobe near the same edge of the corrosion patch, so the strain discrepancy is likely associated with the combined effects of a small difference in the location of the buckle and high bending strain gradients.

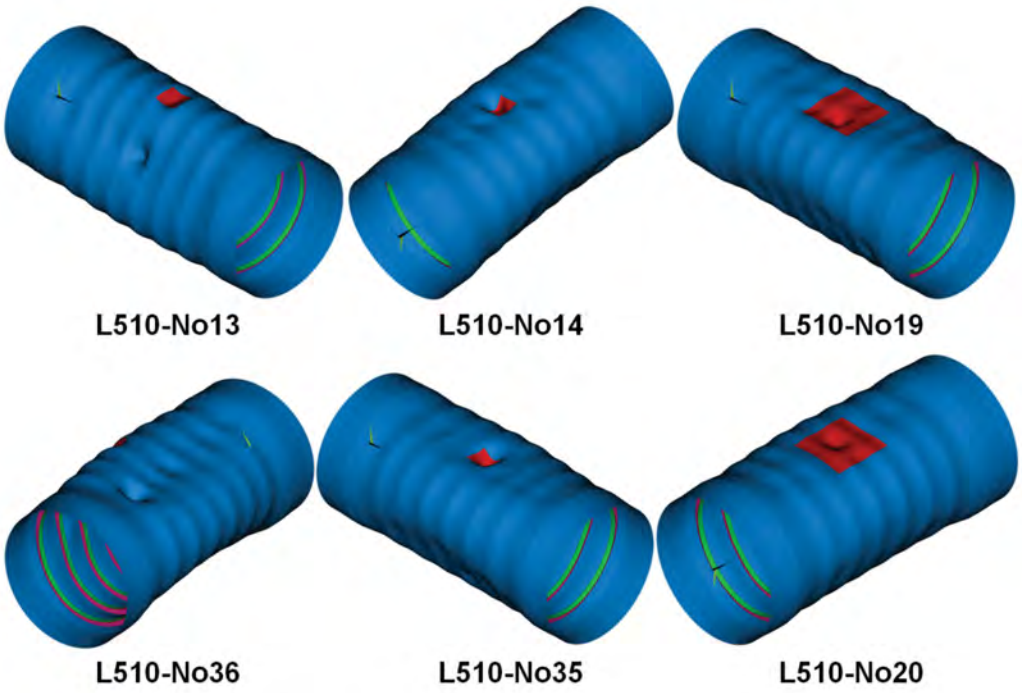

Figure 100: Finite element collapse modes for Phase 6 specimens. Corrosion patches are shown in red, and the FE displacements are scaled by a factor of 20 for clarity. Clockwise from top-left: L510-No13, with a 42x42x0.6 mm, out-of-phase corrosion patch; L510-No14, with a 42x42x0.6 mm, in-phase corrosion patch; L510-No19 and L510-No20, with 100x100x0.4 mm, in-phase corrosion patches; L510-No35, with a 42x42x0.6 mm, in-phase corrosion patch; and L510-No36, with a 42x42x0.6 mm, out-of-phase corrosion patch.

Table 28: Finite element collapse predictions for Phase 6 test specimens, based on models whereby the residual stresses due to out-of-circularity application are neglected.

Specimen	Collapse Location		Collapse Pressure (MPa)		
	Experiment	Prediction	Experiment	Prediction	Modeling Uncertainty Factor, X_m
L510-No13	Bays 3-5, 60°	Bay 4, 56.1°	7.55	7.97	0.947
L510-No14	Bays 3-5, 165°	Bay 4, 159.1°	6.93	7.21	0.962
L510-No19	Bays 3-5, 10°	Bay 4, 8.4°	6.67	6.86	0.973
L510-No20	Bays 3-5, 183.5°	Bay 4, 179.0°	6.93	7.20	0.963
L510-No35	Bays 3-5, 0°	Bay 4, 357.8°	6.58	6.93	0.949
L510-No36	Bays 4-6, 300°	Bay 6, 301.4°	7.22	7.59	0.951

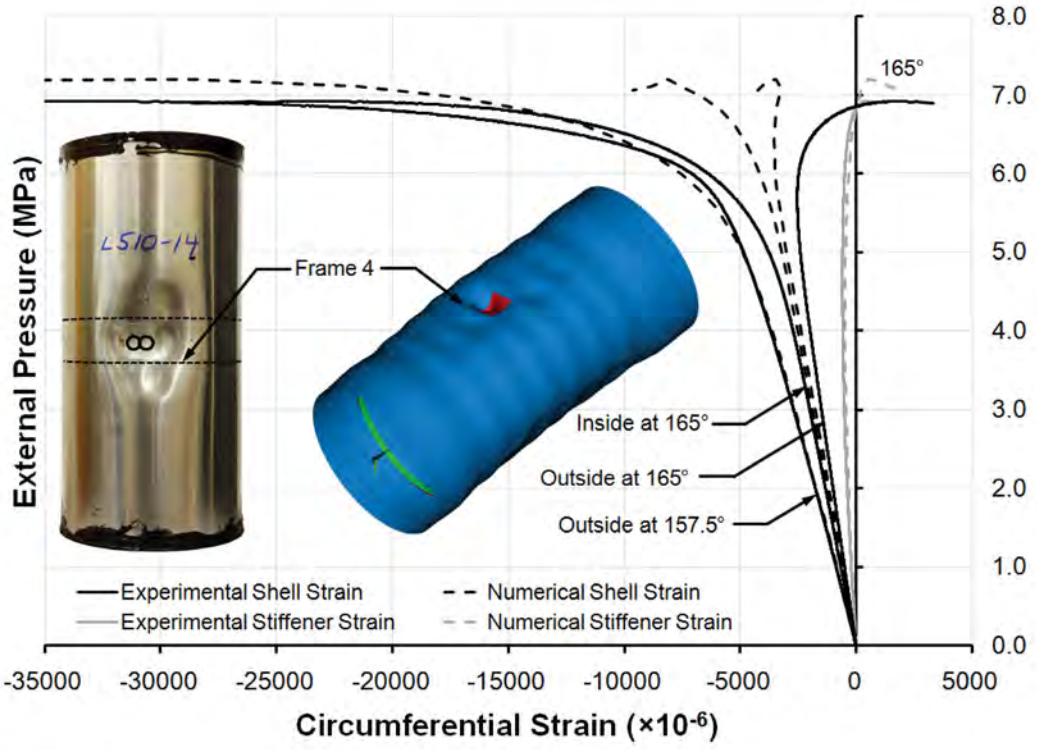

Figure 101: Comparison of experimental and numerical pressure-strain curves for locations near the experimental collapse site of specimen L510-No14; also shown is a post-testing photograph of the specimen and the deformed shape of the numerical model at the predicted collapse pressure. The displacements in the numerical model are scaled by a factor of 20.

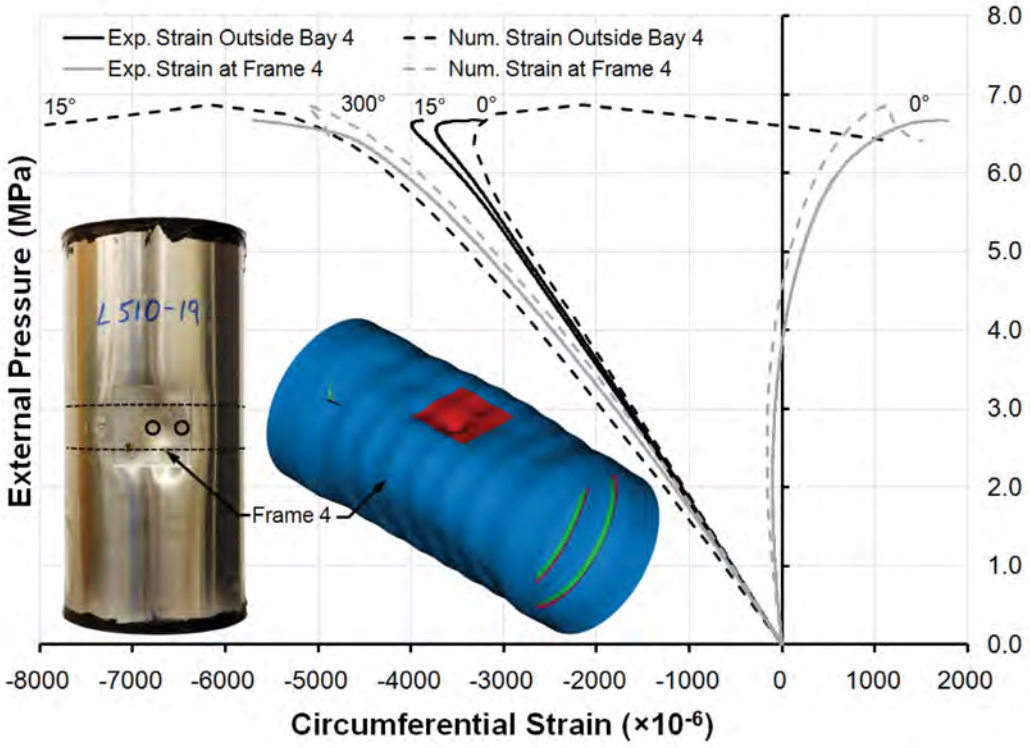

Figure 102: Comparison of experimental and numerical pressure-strain curves for locations near the experimental collapse site of specimen L510-No19; also shown is a post-testing photograph of the specimen and the deformed shape of the numerical model at the predicted collapse pressure. The displacements in the numerical model are scaled by a factor of 20.

6 General discussion

6.1 Effect of out-of-circularity on the collapse of intact specimens

The various out-of-circularity criteria for individual test specimens, as summarized in Table 3, are plotted against the corresponding experimental collapse pressures in Figure 103. That figure validates the expected trend of decreasing collapse pressures with increasing OOC, which is valid for all OOC criteria. The results for L510-No34 deviate somewhat from the general trend due to the m=2 axial OOC mode, which results in relatively smaller bending stresses, due to the shorter effective length of the cylinder, and greater collapse pressures than for similar models with OOC in the critical m=1 axial mode.

The collapse results for Phase 5 specimens (except L510-No34), along with results for similar as-machined intact models from previous testing phases, are plotted against OOC in Figure 104. The collapse pressures were normalized by dividing the actual collapse pressure, P_c, by the boiler pressure, P_b, for each specimen. The boiler pressure, $P_b=\sigma_y h/a$, predicts the onset of yielding in infinitely long cylindrical shells, so that the effect of the variation in yield stress between test specimens is factored out of the normalized collapse pressure, $P_c^*=P_c/P_b$. The boiler pressure was determined for each specimen by taking σ_y as the measured circumferential yield stress, h as the mean measured shell thickness in intact regions of the specimen, and a as the nominal mid-plane shell radius.

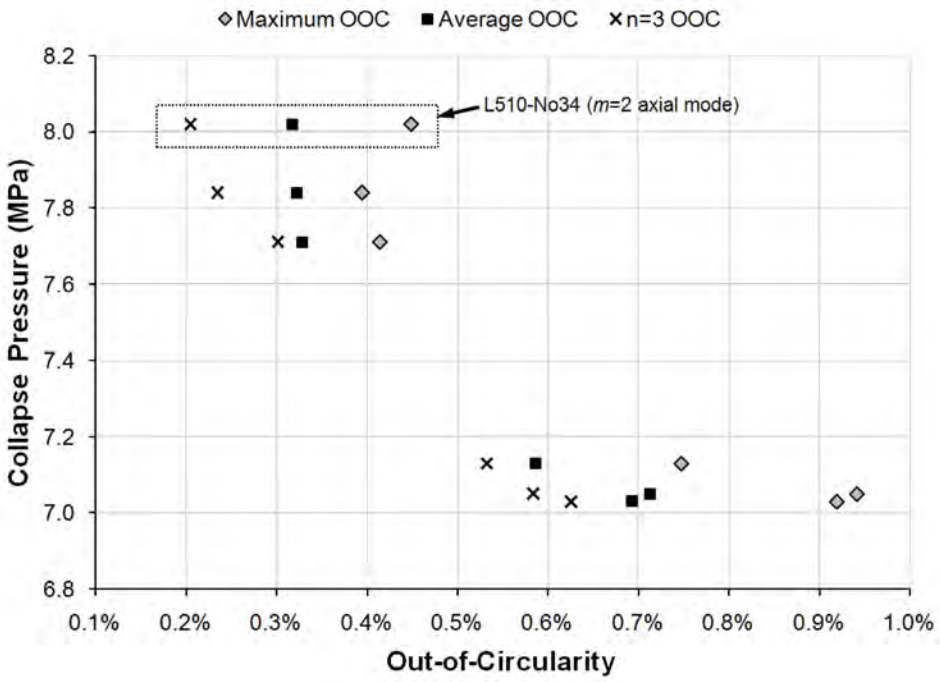

Figure 103: Collapse pressure versus out-of-circularity for intact specimens tested in Phase 5.

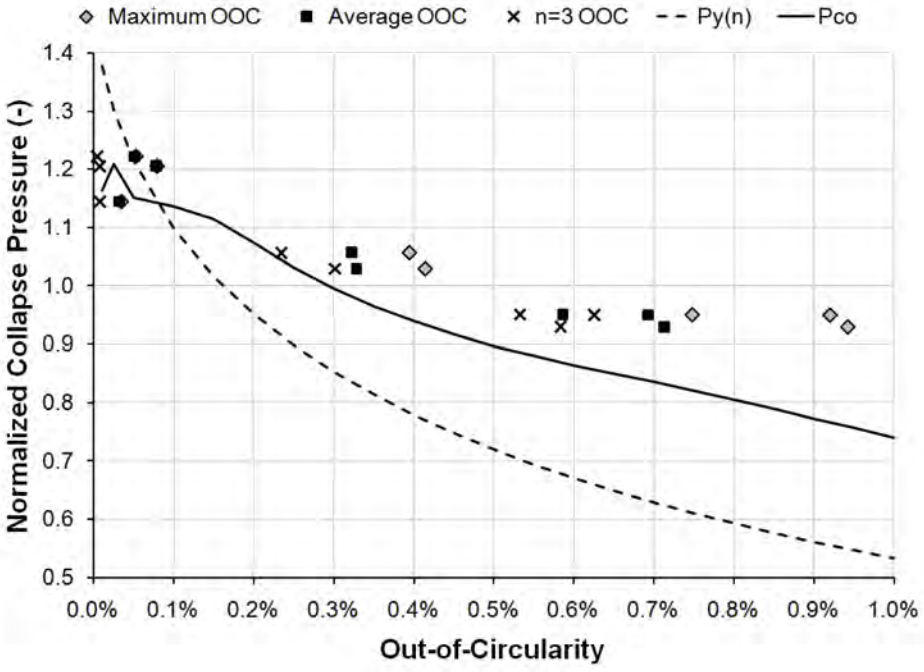

Figure 104: Normalized collapse pressure versus out-of-circularity for intact specimens tested in Phases 2-5; also shown are curves based on the pressure causing yield of the stiffener flange, $P_{y(n)}$*, and the elasto-plastic overall collapse pressure based on Kendrick's finite difference method,* P_{co}*.*

Also shown in Figure 104 are curves based on overall collapse predictions using: (1) an analytical formula for the pressure causing yielding of the stiffener flange, $P_{y(n)}$; and (2) Kendrick's finite difference method that predicts the elasto-plastic collapse pressure of a ring-frame, P_{co}, adjusted for the finite length of a cylinder. The methods for calculating $P_{y(n)}$ and P_{co} are described in [12]. The current predictions are based on the average measured material properties and nominal geometry of the Phase 5 cylinders (see Figure 3), and assume n=3 out-of-circularity.

The experimental data in Figure 104 show that previously tested cylinders with small OOC magnitudes follow the same general trend as the Phase 5 specimens. Furthermore, the experimental results follow the trend predicted by the P_{co} calculations, even though Kendrick's method underpredicts the experimental collapse pressure by more than 10% for larger values of OOC. Those underpredictions may be due to a conservative correction factor that accounts for the finite length of the cylinders. The frame yield pressure, $P_{y(n)}$, is shown to be an even more conservative method of predicting overall collapse, largely because it does not allow for any reserve strength in the frames after the onset of yielding.

Previous nonlinear finite element modeling has shown that 0.5% OOC in the critical mode can reduce the collapse pressure of a pressure hull by up to 25% compared to a shape-perfect hull [19]. Kendrick's elasto-plastic method predicts a 26% reduction in collapse pressure for 0.5% OOC with the Phase 5 geometry and material, which is in good agreement with [19]. The $P_{y(n)}$

curve in Figure 104 predicts a 51% reduction for the same level of OOC, largely because the analytical equation does not consider the post-yielding strength of the cylinder.

Quadratic curves were fit to the experimental data in Figure 104 and used to estimate the collapse pressure reduction for the test specimens. The experimental curves for maximum, average and n=3 OOC gave collapse pressure reductions of 16.6%, 19.5% and 19.8%, respectively, for 0.5% OOC, compared to the shape-perfect case (i.e. the intercept of the fitted curves with the vertical axis in Figure 104). Those values are somewhat less than the predicted reductions, possibly due to the effect of strain-hardening which was not considered in the numerical models.

6.2 Effect of out-of-circularity on the collapse of corroded specimens

Corrosion damage interacts with out-of-circularity by effectively increasing or decreasing the imperfection amplitude depending on whether the corrosion is in-phase or out-of-phase with OOC. Previous numerical modeling [11] has predicted that out-of-phase corrosion damage will have a much smaller effect on collapse pressure than in-phase corrosion. Some of the numerical models have even predicted a small increase in collapse pressure compared to the intact case for out-of-phase corrosion.

The experimental collapse pressures for Phase 5 and 6 specimens are plotted against the corresponding maximum out-of-circularity in Figure 105. The collapse pressures of cylinders with out-of-phase and in-phase corrosion fall above and below a line fit to the intact collapse pressures, respectively. While that trend is consistent with expectations based on the numerical modeling, the greater strength of cylinders with out-of-phase corrosion, compared to intact specimens, may be misleading since the average yield stress of the corroded cylinders was 8% greater than for the intact group (see Table 9). The effect of yield stress was factored out by normalizing the collapse pressures, as described in Section 6.1. Figure 106 shows that, with the normalized collapse pressures, the overall trend was the same, but the strength of cylinders with out-of-phase corrosion was somewhat less than the intact specimens.

When looking at the corroded specimens in isolation, it is difficult to discern any clear trend in the effect of the various OOC criteria on collapse pressure (Figure 107) since the effect is integrally connected with both the amplitude and phase of OOC. The effect of OOC phase can be factored out of the comparison by using an effective out-of-circularity that approximately accounts for the increase or decrease in OOC due the corrosion damage. Effective OOC is defined as the measured out-of-circularity plus and minus half the measured depth of corrosion for in-phase and out-of-phase corrosion patches, respectively. Figure 108 shows that when the measured OOC is replaced by the effective OOC, the trend of decreasing collapse pressure with increasing OOC becomes apparent for the corroded specimens.

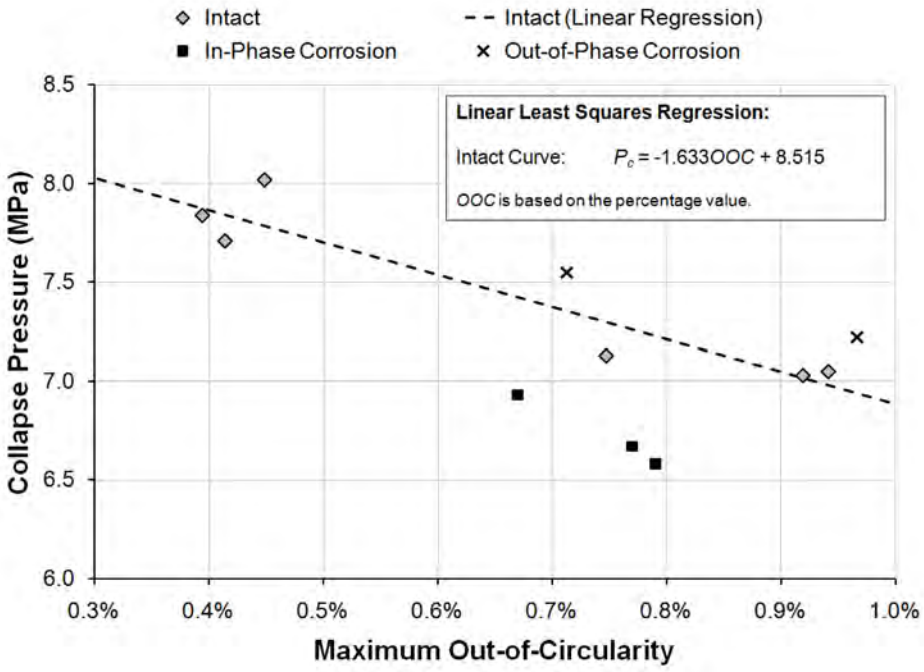

Figure 105: Collapse pressure versus maximum OOC for all Phase 5 and 6 specimens.

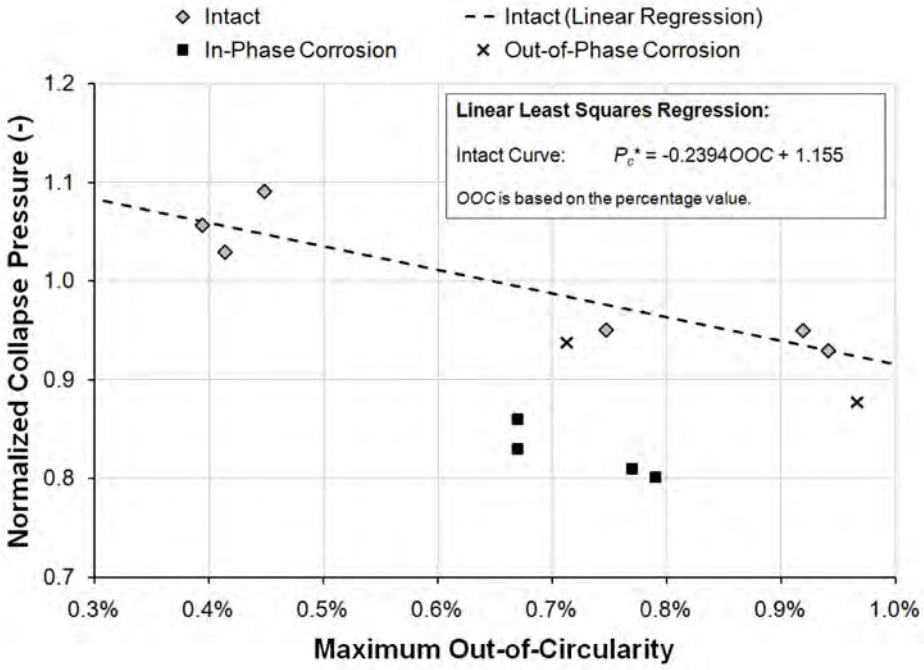

Figure 106: Normalized collapse pressure versus OOC for all Phase 5 and 6 specimens.

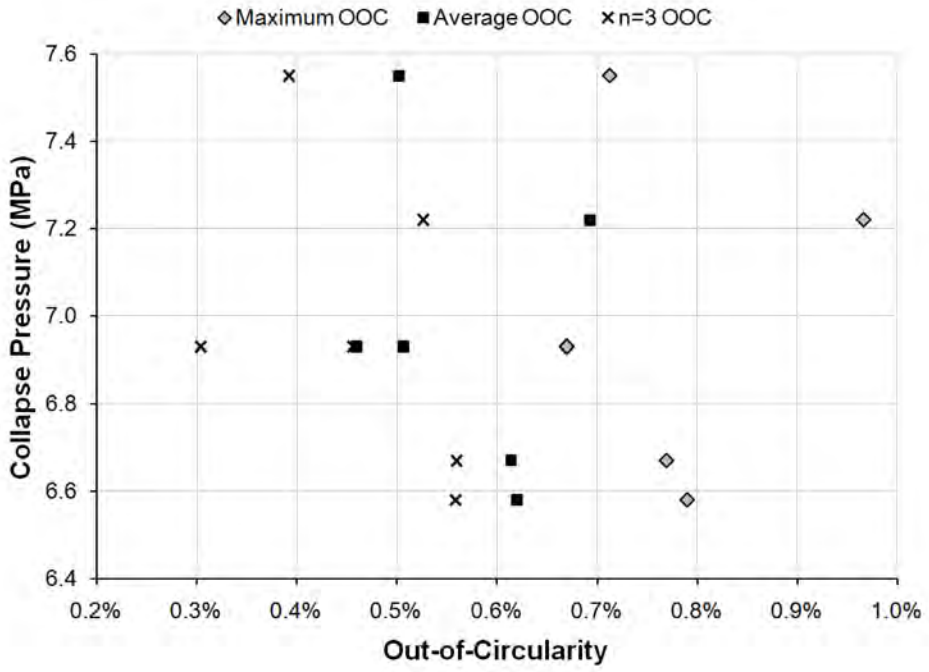

Figure 107: Collapse pressure versus OOC for corroded specimens tested in Phase 6.

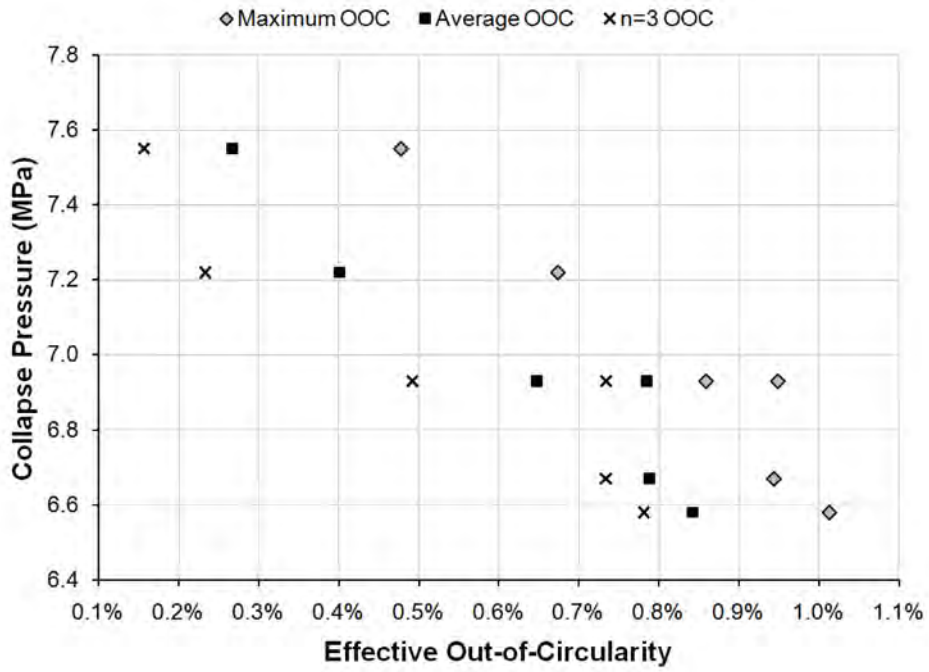

Figure 108: Collapse pressure versus effective OOC for corroded specimens tested in Phase 6.

The effective OOC methodology was extended to previously tested specimens that had corrosion damage and small-amplitude, as-machined OOC. The corrosion damage was assumed to be in-phase with the out-of-circularity for those cylinders. Figure 109 shows the normalized collapse pressures for all corroded cylinders tested to date versus the corresponding effective OOC, based on the maximum measured value. Overall, there is a very clear trend linking increased OOC with decreased collapse pressures. Furthermore, there does not appear to be a significant difference between cylinders with 13.3% and 20% nominal thinning. That may be misleading, however, since measurements of the specimens indicated that there were significant deviations from the nominal values of thinning. The actual corrosion thinning for cylinders with 13.3% and 20% nominal thinning ranged from 11.7-15.9% and 17.9-23.5%, respectively.

The entire experimental program, with respect to the effect of out-of-circularity, is summarized in Figure 110, whereby the normalized collapse pressures are plotted against the effective OOC. That figure shows that, on average, the experimental collapse pressures for corroded specimens fall between 10 and 15% below intact collapse pressures, and that both intact and corroded specimens showed similar sensitivity to out-of-circularity. Linear least squares regression of the intact and corroded data gave lines with slopes equal to -0.294 and -0.254, respectively. That indicates that intact specimens were slightly more sensitive to OOC, since collapse of the corroded specimens was influenced by the corrosion thinning itself, not just its effect on out-of-circularity.

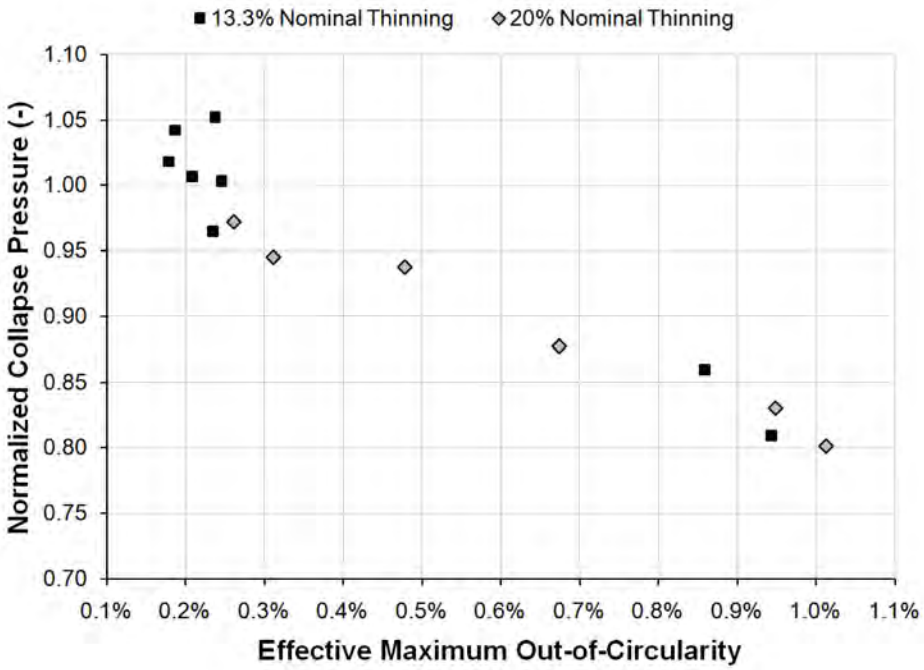

Figure 109: Normalized collapse pressure versus effective maximum OOC for corroded specimens tested in Phases 2-6.

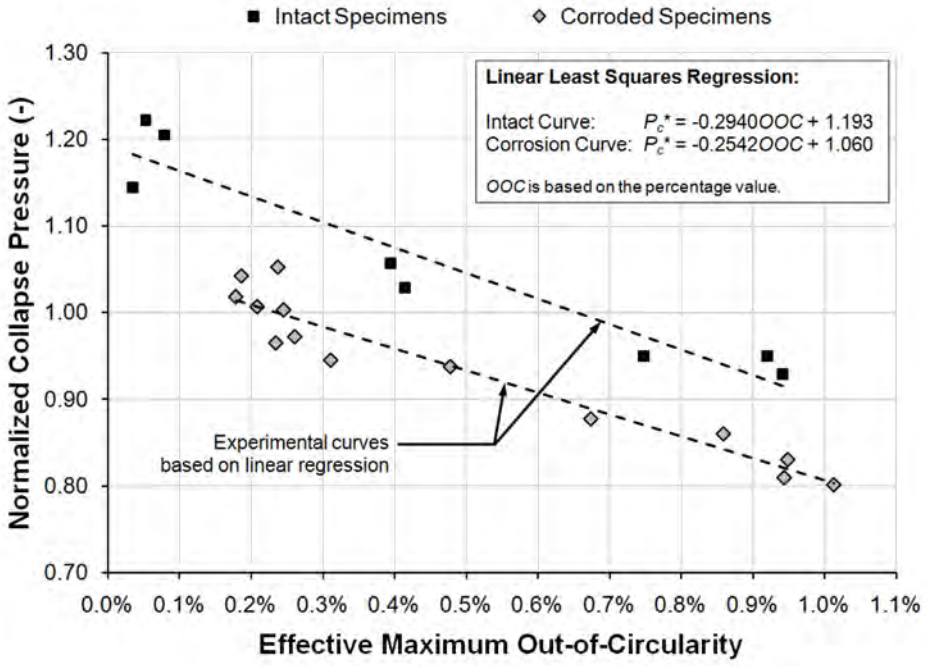

Figure 110: Normalized collapse pressure versus effective maximum OOC for intact and corroded specimens tested in Phases 2-6.

Figure 111 shows the reduction in collapse pressure due to the maximum measured corrosion thinning for all specimens tested in Phases 2-6 that failed by overall collapse. The data for the as-machined specimens has been reproduced from [4]. The collapse strength reductions for those data were derived by comparing the normalized collapse pressures for intact and corroded models that were machined from the same batch of aluminium material. The reductions based on the large-amplitude OOC specimens from Phases 5 and 6 were not arrived at by directly comparing intact and corroded models, since, due to the variation in OOC amplitude between specimens, it was not possible to compare cylinders with the same level of OOC. Instead, the linear regression curve for the intact models, shown in Figure 106, was used as the baseline against which individual corroded specimens from Phase 6 were compared. The comparisons between Phase 5 and 6 cylinders were also based on the normalized collapse pressures in order to factor out the effect of yield strength variability between specimens.

The two main expectations before Phase 5 and 6 testing were that in-phase corrosion would have a greater impact on collapse pressure than out-of-phase corrosion, and that cylinders with large-amplitude OOC would be less sensitive to in-phase corrosion damage than their small-amplitude OOC, as-machined counterparts. The first expectation has already been confirmed (see Figure 106) and is corroborated by the data in Figure 111, which shows that the out-of-phase data falls well below the general trend.

The experimental data does not confirm the second assumption that corrosion sensitivity decreases with OOC amplitude. In Figure 111, it can be seen that the collapse strength reductions for the cylinders with in-phase corrosion fall within the general scatter of the as-machined data, and furthermore, lie on both sides of the linear regression curve that was fit to the as-machined data.

Corrosion patches that cover different areas are lumped together in Figure 111. Since corrosion area may also have an impact on the collapse strength, the data from Figure 111 has been sorted by corrosion patch size and re-plotted in Figure 112. Unfortunately, there is insufficient data for a given corrosion patch size to derive any conclusions. In general, the large amount of experimental scatter that is built up by comparing specimens from separate material batches, and with different levels of OOC, makes it difficult to draw any strong conclusions regarding the sensitivity of the cylinders to corrosion damage relative to the level of initial imperfections.

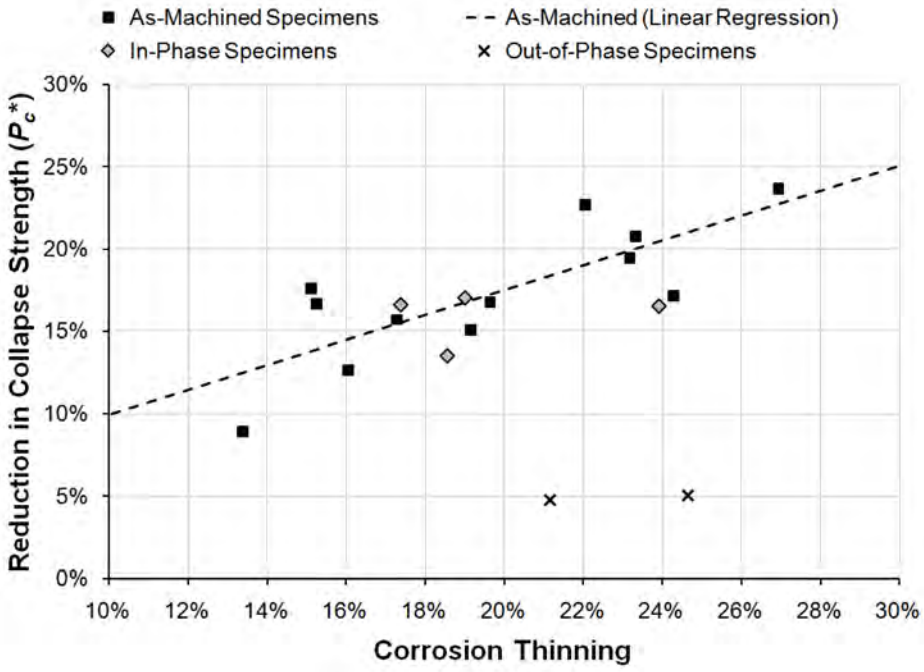

Figure 111: Reduction in collapse pressure versus the maximum corrosion thinning for all specimens tested in Phases 2-6 that failed by overall collapse.

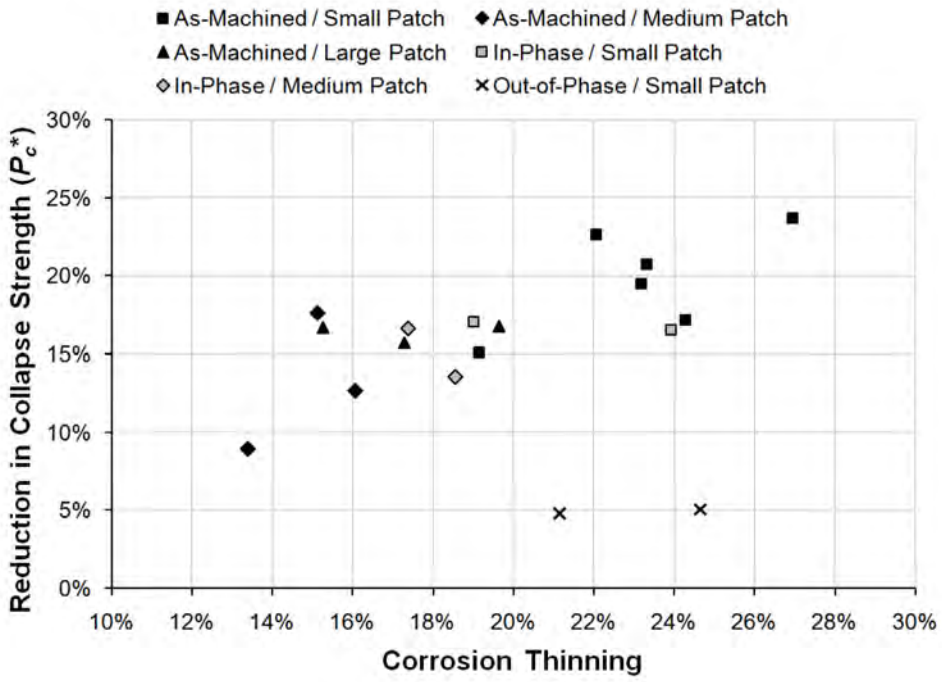

Figure 112: Reduction in collapse pressure versus the maximum corrosion thinning for all specimens tested in Phases 2-6 that failed by overall collapse; sorted by corrosion patch size.

6.3 Effect of residual stresses on collapse

The effect of residual stresses that arose during the mechanical application of out-of-circularity was not considered in the preceding discussion of OOC. As mentioned in Section 2.1.3, an attempt to stress-relieve a deformed cylinder was unsuccessful, so that an experimental comparison of specimens with and without residual stresses was not possible. Furthermore, the residual stresses in the cylinders were not measured before collapse testing, so that the only way to estimate the pre-testing stress state of the specimens was through numerical simulation of the OOC application.

Despite the necessity of making assumptions regarding the sequence of mechanical deformations, and the introduction of modeling simplifications with respect to the actual loading process, the simulation described in Section 5.1 predicted a final OOC shape that was reasonably close to some of the actual specimens. Yielding was found to be concentrated around the regions of contact of the mechanical frame with the cylinder shell, and the residual stresses were predicted to be in the elastic range. Furthermore, despite the plastic deformations around the contact area, the critical residual stresses were found to be located at the frames, at the outward OOC lobes. The sign of those stresses were the same as the applied bending stresses due to OOC, while the stresses at the contact area counteracted the applied stresses at that location.

The numerical simulations predicted that the residual stresses reduced the collapse pressure by approximately 3% with respect to an identical, but stress-relieved model. The OOC magnitude of

the simulation model was approximately 0.6%, based on the maximum eccentricity. Although no further simulations were performed, it is expected that smaller OOC magnitudes would result in lower residual stresses, with a corresponding lesser effect on collapse pressure. Therefore, residual stresses are not thought to have significantly affected the results of the current study with respect to the effects of out-of-circularity and corrosion damage.

6.4 Effect of residual stresses and multiple damage cases on collapse

Denting damage can occur in real hulls through collisions or weapon loads. The mechanical application of OOC to the test specimens can be considered a severe damage case with two components that could affect collapse strength: geometric imperfections and residual stresses. If we take, for example, a damage case that increases the overall OOC magnitude from 0.1% to 0.6%, the experimental curve fit to the intact cylinder data in Figure 110 predicts a reduction in collapse pressure of 12.6%. Since it is based on the experiments, that strength reduction includes both OOC and residual stress effects. The numerical simulations predict that, at the same OOC magnitude, residual stresses reduce the collapse pressure by an additional 3% over and above the OOC effects. So, the geometric imperfections resulting from the denting damage would have approximately 3 times as much influence on the collapse pressure as the residual stresses.

The combined effect of denting and corrosion damage can also be estimated based on the experimental data. The experimental curve for the corroded specimens in Figure 110 is not useful for this exercise since effective OOC data were used instead of the actual values. A similar plot is shown in Figure 113, but with the actual maximum OOC rather than the effective value. Furthermore, this example case will look at 13.3% corrosion thinning that is in-phase with the dent, so only those types of models are included in Figure 113. The experimental curves predict that the corrosion damage will reduce the collapse pressure of a hull with 0.1% OOC by 14.2%. If the hull then sustains denting damage resulting in 0.6% OOC that is in-phase with the corrosion, the hull strength is reduced by a total of 25.6% with respect to original intact hull.

The previous calculations showed that the same dent reduces the collapse pressure of an intact hull by 12.6%. So, taking the effects of the corrosion and denting damage in isolation, the reduced collapse pressure would be cumulative, $P_c(1\text{-}0.142)(1\text{-}0.126)=0.75\ P_c$, or a 25% strength reduction. That value is only marginally smaller than the 25.6% strength reduction that takes account of interaction between the damage cases. This is not surprising, since the slopes of the intact and corroded experimental curves in Figure 113 are nearly equal.

The damage cases studied here represent the extreme limit, in that the denting damage coincided with the critical failure mode of the hull, and the corrosion damage was preferentially aligned with one of the dents. Nonetheless, the examples serve to demonstrate that, even in the extreme cases, the effects of corrosion and denting are additive, and interaction between the two types of damage is not a concern as long as the most pessimistic case of in-phase corrosion is assumed. It has been shown in Section 6.2 that the consequences of out-of-phase corrosion are significantly less severe.

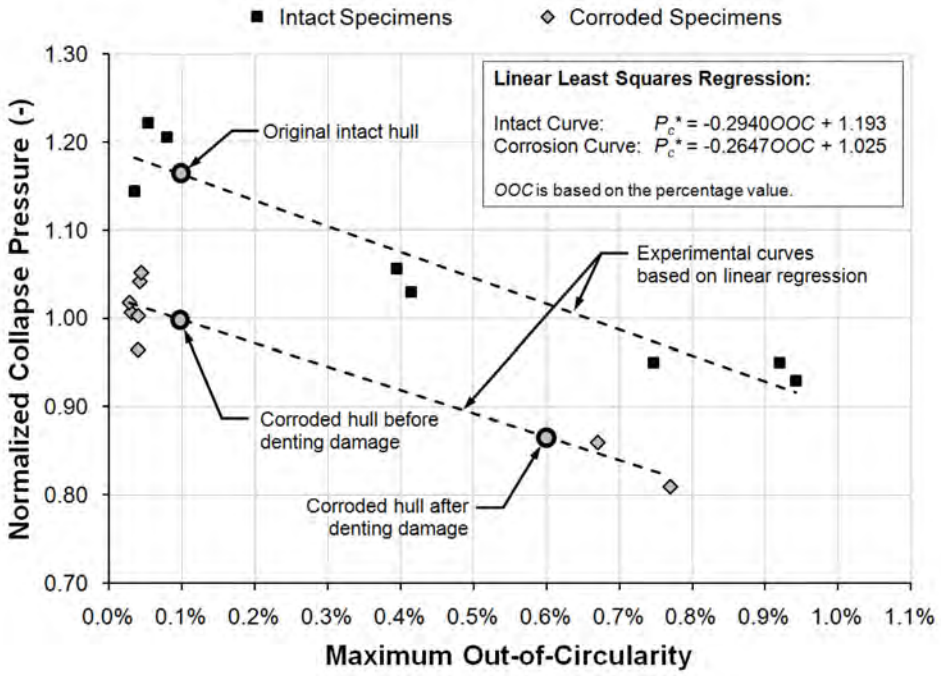

Figure 113: Normalized collapse pressure versus maximum out-of-circularity for intact and corroded specimens, with 13.3% nominal thinning in-phase with OOC, tested in Phases 2-6.

6.5 Accuracy of finite element models

The experimental and numerical collapse pressures for Phase 5 and 6 specimens are compared in Figure 114. The numerical collapse predictions are based on the standard finite element models described in Section 5.2, whereby the residual stresses were neglected. The experimental-numerical comparisons in Figure 114 show that the numerical models have overpredicted the collapse pressures by less than approximately 5%, and that there is a very small amount of scatter in the predictions.

The mean and standard deviation of the modeling uncertainty factor, X_m, for a group of similar experimental-numerical comparisons can be used to derive the accuracy of the overall numerical methodology for solving a given problem. The mean of X_m is referred to as the bias, and the scatter in predictions is typically quantified by the coefficient of variation, COV, taken as the standard deviation of X_m divided by the bias. The bias and COV were used to predict the expected range of X_m for a given level of confidence. The uncertainty introduced by using a bias and COV based on a finite sample was accounted for by using a *t*-distribution, which is similar to a normal distribution but with heavier tails. The accuracy of the predictions, for the same level of confidence, was taken as the absolute maximum difference between the extreme values of the prediction interval and unity. The statistical analyses presented here are based on a standard confidence level of 95%. The methodology for quantifying model accuracy is described in greater detail in [20].

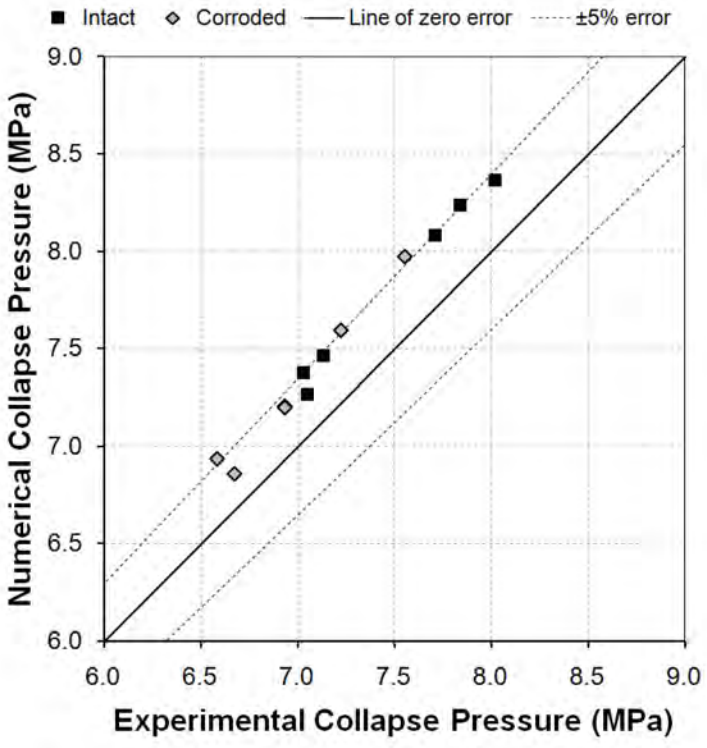

Figure 114: Comparison of experimental collapse pressures for Phase 5 and 6 specimens with those predicted by CylMesh/ANSYS finite element models.

The statistical properties, including bias, COV, 95% prediction interval and accuracy, for the experimental-numerical comparisons for Phase 5 and 6 specimens are listed in Table 29. The bias, which is the same for the intact and corroded sub-sets of data, and for the entire group of models, indicates that the FE models, on average, overpredicted the collapse pressures by 4.3%. Furthermore, the COVs, which are all less than or equal 1%, validate the small amount of scatter shown in Figure 114.

Numerical models based on the same methodology used in the current study predicted the collapse pressures of intact and corroded specimens tested in Phases 1-3 within 16.9 and 8.7%, respectively, with 95% confidence [8]. The accuracy was 11.4% with the same level of confidence for the entire set of Phase 1-3 numerical models. By comparison, the 6-7% accuracies determined for the Phase 5 and 6 FE models (see Table 29) are significantly better, especially when comparing the accuracies for intact specimens from the two groups of models. The improved numerical accuracy for intact specimens with large-amplitude out-of-circularities was expected, since the geometric imperfections have a similar influence as one-sided shell thinning in corroded test specimens for which the FE models showed good accuracy even with small OOC amplitudes.

Table 29: Accuracy of CylMesh/ANSYS finite element collapse pressure predictions for Phase 5 and 6 test specimens.

Sample	**Sample Size**	**Bias**	**COV**	**95% Prediction Interval for X_m**	**Accuracy with 95% Confidence**
Intact specimens	6	0.957	0.7%	$0.938 \leq X_{m,n+1} \leq 0.976$	6.2%
Corroded specimens	6	0.957	1.0%	$0.930 \leq X_{m,n+1} \leq 0.985$	7.0%
All specimens	12	0.957	0.9%	$0.939 \leq X_{m,n+1} \leq 0.976$	6.1%

The experimental collapse pressures for all specimens tested in Phases 1-6 are plotted against the corresponding CylMesh/ANSYS FE predictions in Figure 115. The numerical results for Phase 1-3 specimens were taken from [8]. Phase 4 numerical data are based on unpublished FE results [21] that followed the standard modeling and analysis methodology established in [8]. It is clear from the data in Figure 115 that the numerical models tended to overpredict the actual collapse pressures, and that the numerical modeling error was no greater than approximately 10%. Furthermore, it can be seen that the scatter in numerical predictions is much less for the Phase 5 and 6 specimens than for specimens tested in earlier phases. That improvement is likely due to specimen-specific material properties, which were not available for specimens tested in Phases 1-3, and to the previously mentioned effect of large-amplitude OOC on the collapse predictions. Figure 116 shows the same Phase 1-6 data, but sorted by corrosion damage rather than by testing phase. The scatter is clearly greater in the FE predictions for intact specimens compared to corroded cylinders.

The results of the statistical analysis of the numerical predictions for all Phase 1-6 specimens are summarized in Table 30. That data confirms that the numerical predictions for the last three phases of testing, whereby specimen-specific material properties were available, were more accurate than the predictions for the initial phases, whereby material models relied on properties determined for an entire batch of aluminium tubing. With the addition of the Phase 4-6 data, the overall accuracy of the standard numerical methodology improved from 11.4%, as reported in [8], to 9.5% with 95% confidence. That improvement is largely due to the increased accuracy of intact specimen predictions (16.9% for Phases 1-3 versus 11.5% for Phases 1-6). The numerical accuracy for corroded specimens also improved with the inclusion of the Phase 4 and 6 data, but to a lesser extent than for intact cylinders (8.7% for Phases 1-3 versus 8.1% for Phases 1-6).

A method to extend the statistical analysis to derive a partial safety factor (PSF) to be used with numerical collapse predictions was presented in [20]. The general strategy was to predict a lower bound for a future value of X_m, rather than a prediction interval, such as those given in Table 29 and Table 30. The partial safety factor is simply taken as the inverse of the lower bound value, $(X_m)_{\min}$. In [20], the level of confidence was increased from 95% to 99.5% in order to ensure the high degree of safety required for submarine design. Based on the methodology presented in [20], and the experimental-numerical comparisons for Phases 1-3 [8], the PSF for CylMesh/ANSYS FE models would be 1.17 for 99.5% confidence. Considering all of the Phase 1-6 FE models, the PSF is reduced to 1.13 for the same level of confidence. That value is comparable with currently used partial safety factors for interframe and overall collapse.

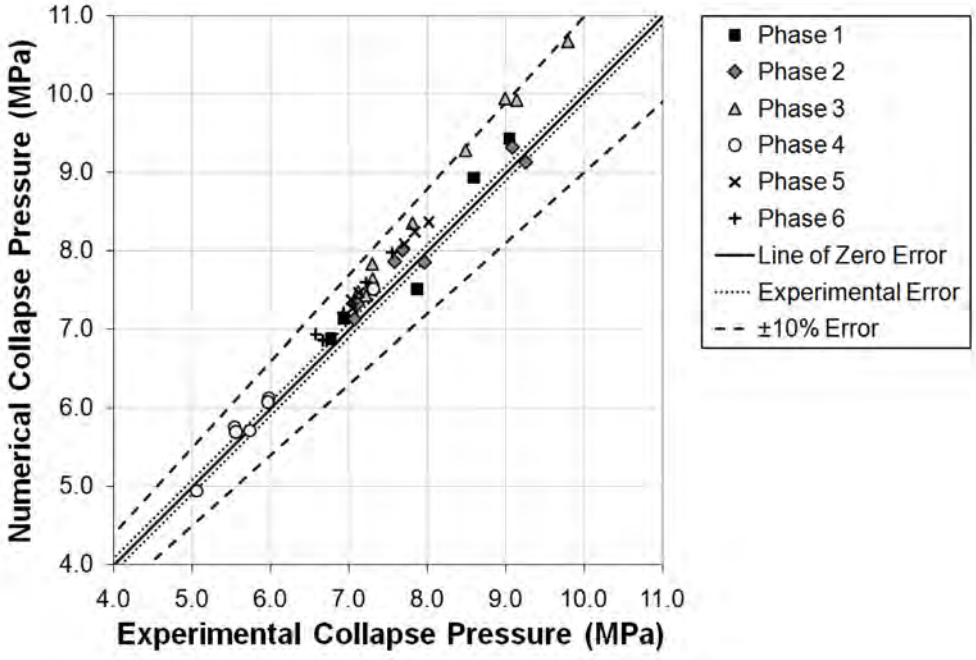

Figure 115: Comparison of experimental and numerical collapse pressures for all Phase 1-6 test specimens, sorted by testing phase.

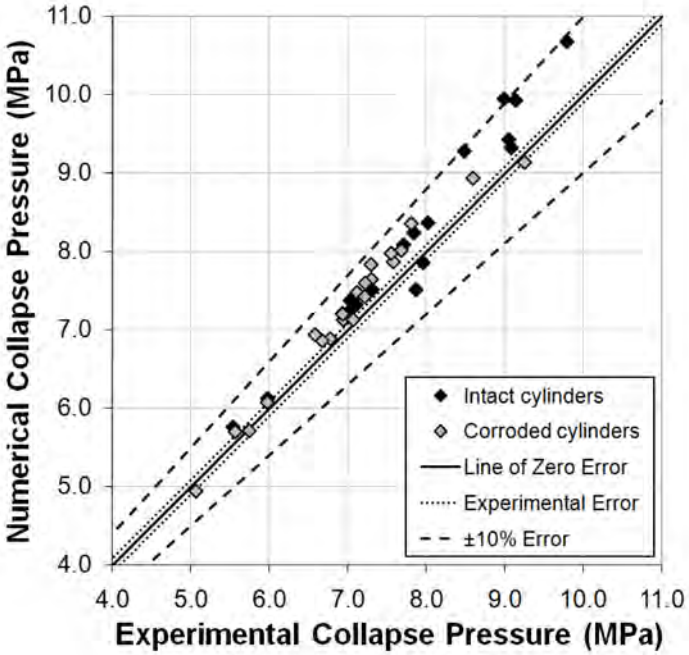

Figure 116: Comparison of experimental and numerical collapse pressures for all Phase 1-6 test specimens, sorted by corrosion damage.

Table 30: Accuracy of CylMesh/ANSYS finite element collapse pressure predictions for test specimens from all testing phases.

Sample	**Sample Size**	**Bias**	**COV**	**95% Prediction Interval for X_m**	**Accuracy with 95% Confidence**
Phase 1	5	0.986	3.7%	$0.876 \leq X_{m,n+1} \leq 1.095$	12.4%
Phase 2	7	0.984	2.3%	$0.924 \leq X_{m,n+1} \leq 1.043$	7.6%
Phase 3	9	0.933	2.4%	$0.879 \leq X_{m,n+1} \leq 0.988$	12.1%
Phase 4	7	0.986	2.2%	$0.930 \leq X_{m,n+1} \leq 1.042$	7.0%
Phase 5	6	0.957	0.7%	$0.938 \leq X_{m,n+1} \leq 0.976$	6.2%
Phase 6	6	0.957	1.0%	$0.930 \leq X_{m,n+1} \leq 0.985$	7.0%
Intact specimens	17	0.957	3.4%	$0.885 \leq X_{m,n+1} \leq 1.028$	11.5%
Corroded specimens	22	0.969	2.5%	$0.919 \leq X_{m,n+1} \leq 1.020$	8.1%
All specimens	40	0.965	3.0%	$0.905 \leq X_{m,n+1} \leq 1.025$	9.5%

7 Conclusions

Destabilizing bending moments introduced by large-amplitude out-of-circularities that were applied to the cylinder specimens were found to significantly decrease the collapse strength of the cylinders compared to as-machined specimens with small initial imperfections. For an intact cylinder with 0.5% OOC in the critical mode, the overall collapse pressure was reduced by approximately 20% compared to shape-perfect cylinders. Those results are similar to the results of numerical modeling studies, which predicted collapse pressure reductions of approximately 25% for the same level of OOC.

It was confirmed that corrosion thinning impacts collapse strength in two ways: through higher stresses in the damaged shell, and by changing the effective magnitude of out-of-circularity. Corrosion patches that were preferentially aligned with the dominant out-of-circularity mode were found to be more detrimental to collapse strength than damage that was out-of-phase with OOC. Four cylinders with in-phase corrosion damage, and an average shell thinning of 20%, were found have collapse pressures there were approximately 16% less than similar intact cylinders. On the other hand, two specimens with out-of-phase corrosion and a larger value of average thinning at 23%, yielded collapse pressures that were only 5% less than their intact counterparts. In the first case, the in-phase corrosion effectively increased the out-of-circularity amplitude, while out-of-phase corrosion had the opposite effect, resulting in less severe reductions to cylinder strength. The scatter in experimental results was found to be too great to confirm or reject the hypothesis that cylinders with large-amplitude out-of-circularity are less sensitive to corrosion thinning due to its relatively smaller impact on OOC compared to as-machined specimens.

The current work highlights the importance of the interaction of corrosion damage with the actual shape of the pressure hull. When assessing corrosion damage to real submarines, it is necessary to model the true shape of the hull, and the correct orientation of the thinning with respect to that shape. The out-of-circularity that was applied to the test specimens can be viewed as a form of severe denting damage, and thus the cylinders with corrosion thinning had multiple damage cases. While there was found to be significant interaction between the two types of damage, it appears that in the worst case of in-phase corrosion, the total impact of the damage is approximately equal to the sum of the denting and hull thinning acting independently.

Numerical simulations suggest that the mechanical procedure used to apply OOC to the cylinders resulted in significant plastic deformation of the specimens, especially where the forces were applied; however, the final predicted residual stress field was in the elastic range of the material. Subsequent collapse analysis indicated that those residual stresses resulted in a 3% reduction in collapse pressure compared to a stress-relieved model, so that residual stresses are not thought to have significantly affected the collapse behaviour of the test specimens.

Nonlinear finite element analyses of individual Phase 5 and 6 specimens, based on the measured shape and material properties, were found to overpredict the experimental collapse pressures by approximately 5%. Most of the error in the numerical models can be attributed to the neglect of residual stresses due to OOC application. A compilation of experimental-numerical comparisons for the forty specimens that have been tested and analyzed to date indicates that DRDC`s standard numerical methodology is accurate to within 9.5%, with 95% confidence. Based on the same

data, the working value for a partial safety factor for numerical pressure hull predictions is 1.13, with 99.5% confidence.

Collapse testing for the final stage of this experimental program has already been completed. Phase 7 included the testing of as-machined cylinders with multiple corrosion patches. In some cases the corrosion patches were randomly arranged, while in others the patches were intentionally distributed to align with the critical n=3 collapse mode. Analysis of the experimental data is still required, as are numerical simulations of the collapse tests. Following those tasks, DRDC`s effort will be directed at using numerical models to develop corrosion tolerance guidelines for pressure hulls.

References

[1] MacKay, J.R. (2007). Experimental investigation of the strength of damaged pressure hulls – Phase 1. (DRDC Atlantic TM 2006-304). Defence Research and Development Canada – Atlantic.

[2] MacKay, J.R. (2007). Experimental investigation of the strength of damaged pressure hulls – Phase 2, Summary of experimental results. (DRDC Atlantic TM 2007-013). Defence Research and Development Canada – Atlantic.

[3] MacKay, J.R. (2008). Experimental investigation of the strength of damaged pressure hulls – Phase 3. (DRDC Atlantic TM 2008-093). Defence Research and Development Canada – Atlantic.

[4] MacKay, J.R. (2010). Experimental investigation of the strength of damaged pressure hulls – Phase 4: The influence of material properties on pressure hull collapse. (DRDC Atlantic TM 2009-299). Defence Research and Development Canada – Atlantic.

[5] Department of National Defence (1980). Canada – Netherlands Information Exchange Project between the Department of National Defence of Canada and the Netherlands Ministry of Defence Pertaining to the Design of Surface Ships and Submarines. 10984, Department of National Defence, Canada.

[6] MacKay, J.R., Smith, M.J., and Pegg, N.G. (2006). Design of pressure hulls using nonlinear finite element analysis. (OMAE2006-92591). In *Proceedings of the 25th International Conference on Offshore Mechanics and Arctic Engineering*. Hamburg, Germany: ASME.

[7] Jiang, L., MacKay, J.R., Wallace, J., Smith, M.J., Norwood, M., Bosman, T. (2008). Finite element modeling of collapse experiments of ring stiffened cylinders with simulated corrosion damage. In *Warship 2008: Naval Submarines 9*. Glasgow: Royal Institution of Naval Architects.

[8] MacKay, J.R., Jiang, L., and Glas, A.H. (2010). Accuracy of nonlinear finite element collapse predictions for submarine pressure hulls with and without artificial corrosion damage. DRDC Atlantic SL-2010-314. Submitted to *Marine Structures*, January 2010.

[9] Bayley, C. and Mackay, J. (2009). Strategic Research Agenda: Verification and Validation of Numerical Welding Approaches. (DRDC Atlantic TM 2009-170). Defence Research and Development Canada – Atlantic.

[10] MacKay, J.R., Smith, M.J., van Keulen, F., Bosman, T.N. and Pegg, N.G. (2010). Experimental Investigation of the Strength and Stability of Submarine Pressure Hulls with and without Artificial Corrosion Damage. *Marine Structures*, 23, 339-359.

[11] Smith, M.J. and MacKay, J.R. (2005). Overall elasto-plastic collapse of ring stiffened cylinders with corrosion damage. *Transactions of the Royal Institution of Naval Architects Part 1A – International Journal of Maritime Engineering*.

[12] DPA (2001). SSP74: Design of Submarine Structures. (Sea Systems Publication 74). Defence Procurement Agency, United Kingdom Ministry of Defence.

[13] Kendrick, S.B. (1977). Shape imperfections in cylinders and spheres: Their importance in design and methods of measurement. *Journal of Strain Analysis*, 12(2), 117-122.

[14] Bosman, T.N. (2008). Measurements cylinders 2008. Bosman Naval Engineering, The Netherlands.

[15] Online Materials Information Source – MatWeb (online), Automation Creations, Inc., http://www.matweb.com (Access date: 3 November 2010).

[16] Hibbeler, R.C. (1997). Mechanics of Materials, Third Edition. Toronto: Prentice Hall Canada, Inc.

[17] MacKay, J.R. and van Keulen, F. (2010). A review of external pressure testing techniques for shells including a novel volume-control method. *Experimental Mechanics*, 50, 753-772.

[18] SAS IP, Inc. (2007). Release 11.0 Documentation for ANSYS. ANSYS Inc.

[19] Creswell, D.J. and Dow, R.S. (1986). The application of nonlinear analysis to ship and submarine structures. In C.S. Smith and J.D. Clarke, (Eds.), *Advances in Marine Structures: Proceedings of an International Conference*, pp. 174-200. Dunfermline, Scotland: Admiralty Research Establishment.

[20] MacKay, J.R., van Keulen, F., and Smith, M.J. (2011). Quantifying the accuracy of numerical collapse predictions for the design of submarine pressure hulls. *Thin-Walled Structures*, 49, 145-156.

[21] MacKay, J.R. (2010). Unpublished finite element modeling results for Phase 4 test specimens.

[22] Lin, X. and Teng, J.G. (2003). Iterative Fourier decomposition of imperfection measurements at non-uniformly distributed sampling points. *Thin-Walled Structures*, 31, 901-924.

This page intentionally left blank.

Annex A Double Fourier series methodology

A two-dimensional, or double, Fourier series is the product of two single Fourier series, and the decomposition is carried out using a similar numerical integration technique. The numerical integration scheme, and thus the entire decomposition, is only accurate for evenly spaced data; however, the test model imperfections were measured on a grid that was irregular in the axial direction. This was overcome by extending the iterated single Fourier decomposition method presented in [22], which was developed for unevenly spaced data, to a double Fourier series.

In the iterated method, an initial Fourier decomposition is performed using a standard trapezoidal rule for the numerical integration. The function described by the resulting Fourier series is then compared to the original data, giving a set of errors or residuals associated with each data point. Fourier decomposition is then performed on the residuals, and the coefficients describing the series are added to the original set of coefficients. This process is repeated until the desired accuracy is achieved, or until the decomposition cannot be improved through additional iterations.

Fourier series are cyclical functions, and are therefore well-suited to describe closed-loop systems, such as the radial imperfections about the circumference of the cylinders described herein. A double Fourier series would ideally describe the surface of a toroid, since that shape is a closed loop in the two principal directions. Unfortunately, the length of a cylinder is finite and does not form a closed loop. This presents a problem when a double Fourier series is used to describe the cylinder surface, since using that method implies that the imperfections are identical at the ends of the cylinder. This can be overcome by mirroring the imperfection data about one of the cylinder ends, and performing the double Fourier decomposition on the artificially cyclical data. That was the method chosen for Phase 5 cylinders. For Phase 6 specimens, it was found that the mirroring process resulted in greater errors between the measured imperfections and the double Fourier series than decompositions that were performed on the original, non-mirrored data; and so the original imperfection data was used in all double Fourier series decompositions for Phase 6 specimens.

This page intentionally left blank.

Annex B Measured geometry

B.1 L510-No13

Table 31: Out-of-circularity of specimen L510-No13 based on laser displacement gauge measurements – Part 1

Angle (degrees)	Radial Eccentricity[a] (mm) at Indicated Axial Location (mm)							
	Frame 1	**Bay 1**	**Frame 2**	**Bay 2**	**Frame 3**	**Bay 3**	**Frame 4**	**Bay 4**
	80	105	130	155	180	205	230	255
0	0.102	0.141	0.180	0.188	0.248	0.266	0.298	**0.329**
10	0.113	0.148	0.188	0.201	0.246	0.262	0.315	0.333
20	0.091	0.120	0.163	0.170	0.216	0.211	0.278	0.297
30	0.044	0.045	0.111	0.059	0.147	0.102	0.177	0.151
40	-0.012	-0.093	-0.052	-0.177	-0.014	-0.193	-0.004	-0.268
50	-0.066	-0.308	-0.326	-0.378	-0.395	-0.562	-0.473	-0.747
60	-0.092	-0.228	-0.303	-0.340	-0.544	-0.551	-0.779	-0.779
70	-0.056	-0.019	-0.112	-0.140	-0.298	-0.188	-0.353	-0.224
80	-0.004	0.050	0.012	0.053	0.004	0.093	0.046	0.163
90	0.043	0.108	0.098	0.157	0.173	0.215	0.192	0.278
100	0.072	0.139	0.157	0.220	0.243	0.283	0.295	0.344
110	0.087	0.165	0.183	0.238	0.276	0.312	0.333	0.350
120	0.082	0.154	0.189	0.231	0.264	0.288	0.327	0.331
130	0.054	0.120	0.154	0.176	0.215	0.229	0.264	0.278
140	-0.002	0.042	0.084	0.099	0.132	0.127	0.166	0.174
150	-0.064	-0.050	-0.021	-0.039	0.005	-0.007	0.025	0.022
160	-0.123	-0.181	-0.233	-0.241	-0.216	-0.249	-0.206	-0.270
170	-0.173	-0.337	-0.404	-0.436	-0.505	-0.537	-0.593	-0.636
180	-0.157	-0.291	-0.287	-0.394	-0.491	-0.532	-0.618	-0.617
190	-0.089	-0.097	-0.123	-0.192	-0.224	-0.246	-0.251	-0.273
200	-0.008	-0.006	-0.008	-0.001	-0.001	0.002	0.002	0.014
210	0.065	0.087	0.089	0.113	0.136	0.138	0.134	0.147
220	0.121	0.147	0.160	0.193	0.219	0.231	0.233	0.242
230	0.152	0.194	0.207	0.241	0.270	0.290	0.291	0.308
240	0.160	0.211	0.238	0.265	0.289	0.303	0.329	0.331
250	0.148	0.193	0.232	0.262	0.276	0.299	0.316	0.335
260	0.092	0.163	0.194	0.209	0.224	0.242	0.271	0.301
270	0.016	0.075	0.114	0.099	0.138	0.123	0.156	0.218
280	-0.045	-0.066	-0.053	-0.106	-0.013	-0.089	0.009	-0.086
290	-0.111	-0.282	-0.349	-0.359	-0.320	-0.429	-0.340	-0.599
300	-0.181	-0.374	-0.405	-0.431	-0.591	-0.593	-0.699	-0.770
310	-0.167	-0.157	-0.235	-0.265	-0.460	-0.352	-0.549	-0.441
320	-0.104	-0.042	-0.088	-0.062	-0.134	-0.042	-0.121	0.013
330	-0.047	0.026	0.014	0.074	0.083	0.113	0.089	0.193
340	0.002	0.085	0.089	0.136	0.179	0.201	0.183	0.248
350	0.058	0.115	0.142	0.180	0.222	0.239	0.258	0.305

a. Radial eccentricities are based on the filtered measurements taken at the outside of the cylinder shell. Eccentricities at corrosion patches (shaded cells with bold face font) have been corrected for the corroded shell thickness.

Table 32: Out-of-circularity of specimen L510-No13 based on laser displacement gauge measurements – Part 2

Angle (degrees)	Radial Eccentricity[a] (mm) at Indicated Axial Location (mm)							
	Bay 4	**Frame 5**	**Bay 5**	**Frame 6**	**Bay 6**	**Frame 7**	**Bay 7**	**Frame 8**
	255	280	305	330	355	380	405	430
0	**0.329**	0.331	0.266	0.256	0.196	0.153	0.086	0.035
10	0.333	0.353	0.261	0.261	0.196	0.164	0.089	0.036
20	0.297	0.318	0.182	0.205	0.136	0.146	0.048	0.018
30	0.151	0.248	0.030	0.077	0.006	0.082	-0.029	-0.025
40	-0.268	-0.043	-0.231	-0.095	-0.193	-0.082	-0.139	-0.070
50	-0.747	-0.625	-0.486	-0.328	-0.377	-0.299	-0.211	-0.108
60	-0.779	-0.856	-0.502	-0.508	-0.384	-0.362	-0.195	-0.108
70	-0.224	-0.423	-0.230	-0.341	-0.171	-0.239	-0.092	-0.063
80	0.163	0.080	0.064	-0.017	0.070	0.032	0.057	0.007
90	0.278	0.261	0.226	0.161	0.185	0.150	0.131	0.077
100	0.344	0.335	0.301	0.262	0.240	0.199	0.170	0.128
110	0.350	0.350	0.315	0.314	0.262	0.224	0.192	0.160
120	0.331	0.340	0.301	0.307	0.248	0.231	0.186	0.166
130	0.278	0.292	0.237	0.244	0.202	0.201	0.147	0.127
140	0.174	0.203	0.143	0.132	0.115	0.130	0.074	0.050
150	0.022	0.062	-0.017	-0.013	-0.016	0.024	-0.022	-0.035
160	-0.270	-0.267	-0.240	-0.194	-0.197	-0.182	-0.153	-0.119
170	-0.636	-0.678	-0.448	-0.397	-0.375	-0.370	-0.256	-0.173
180	-0.617	-0.627	-0.485	-0.478	-0.404	-0.381	-0.266	-0.185
190	-0.273	-0.263	-0.297	-0.306	-0.257	-0.237	-0.179	-0.151
200	0.014	0.005	-0.065	-0.064	-0.052	-0.021	-0.065	-0.095
210	0.147	0.148	0.097	0.088	0.079	0.070	0.010	-0.024
220	0.242	0.248	0.206	0.191	0.163	0.133	0.076	0.042
230	0.308	0.302	0.270	0.261	0.207	0.167	0.129	0.088
240	0.331	0.332	0.292	0.281	0.230	0.190	0.151	0.122
250	0.335	0.340	0.278	0.261	0.215	0.194	0.163	0.133
260	0.301	0.304	0.222	0.202	0.182	0.178	0.146	0.106
270	0.218	0.238	0.115	0.089	0.102	0.134	0.079	0.074
280	-0.086	-0.005	-0.090	-0.038	-0.061	-0.005	-0.018	0.020
290	-0.599	-0.479	-0.341	-0.222	-0.251	-0.210	-0.116	-0.026
300	-0.770	-0.757	-0.461	-0.381	-0.310	-0.286	-0.158	-0.065
310	-0.441	-0.579	-0.324	-0.374	-0.236	-0.250	-0.122	-0.080
320	0.013	-0.135	-0.079	-0.175	-0.079	-0.093	-0.042	-0.052
330	0.193	0.129	0.083	0.009	0.036	0.017	0.009	-0.031
340	0.248	0.230	0.176	0.122	0.122	0.080	0.050	0.001
350	0.305	0.288	0.230	0.207	0.169	0.117	0.075	0.023

a. Radial eccentricities are based on the filtered measurements taken at the outside of the cylinder shell. Eccentricities at corrosion patches (shaded cells with bold face font) have been corrected for the corroded shell thickness.

Table 33: Out-of-circularity of specimen L510-No13 based on mechanical displacement gauge measurements

Angle (degrees)	Radial Eccentricity[a] (mm) at Indicated Axial Location (mm)							
	Frame 1	**Frame 2**	**Frame 3**	**Frame 4**	**Frame 5**	**Frame 6**	**Frame 7**	**Frame 8**
	80	130	180	230	280	330	380	430
0	-	-	0.248	0.292	0.328	0.272	-	-
10	-	-	0.238	0.297	0.341	0.254	-	-
20	-	-	0.209	0.261	0.333	0.199	-	-
30	-	-	0.148	0.179	0.260	0.080	-	-
40	-	-	0.002	0.027	0.047	-0.086	-	-
50	-	-	-0.362	-0.391	-0.541	-0.314	-	-
60	-	-	-0.555	-0.763	-0.879	-0.513	-	-
70	-	-	-0.357	-0.488	-0.594	-0.420	-	-
80	-	-	-0.059	-0.055	-0.050	-0.085	-	-
90	-	-	0.065	0.149	0.192	0.128	-	-
100	-	-	0.232	0.262	0.304	0.243	-	-
110	-	-	0.271	0.317	0.343	0.299	-	-
120	-	-	0.278	0.330	0.354	0.312	-	-
130	-	-	0.246	0.296	0.319	0.272	-	-
140	-	-	0.181	0.223	0.257	0.185	-	-
150	-	-	0.067	0.101	0.145	0.056	-	-
160	-	-	-0.083	-0.066	-0.039	-0.103	-	-
170	-	-	-0.373	-0.406	-0.459	-0.296	-	-
180	-	-	-0.545	-0.669	-0.730	-0.458	-	-
190	-	-	-0.325	-0.417	-0.456	-0.416	-	-
200	-	-	-0.070	-0.074	-0.093	-0.144	-	-
210	-	-	0.100	0.090	0.098	0.044	-	-
220	-	-	0.199	0.210	0.222	0.170	-	-
230	-	-	0.260	0.285	0.292	0.249	-	-
240	-	-	0.288	0.326	0.335	0.279	-	-
250	-	-	0.280	0.325	0.341	0.266	-	-
260	-	-	0.230	0.276	0.322	0.198	-	-
270	-	-	0.133	0.159	0.247	0.089	-	-
280	-	-	-0.036	-0.019	0.014	-0.053	-	-
290	-	-	-0.391	-0.412	-0.533	-0.220	-	-
300	-	-	-0.611	-0.712	-0.796	-0.400	-	-
310	-	-	-0.376	-0.437	-0.522	-0.359	-	-
320	-	-	-0.057	-0.044	-0.070	-0.121	-	-
330	-	-	0.110	0.098	0.148	0.033	-	-
340	-	-	0.189	0.193	0.230	0.144	-	-
350	-	-	0.231	0.257	0.290	0.219	-	-

a. Radial eccentricity is taken as the raw gauge reading less the n=0 and n=1 Fourier components at that axial location.

Table 34: Measured shell thicknesses for specimen L510-No13 – global measurements

Angle (degrees)	Shell Thickness[a] (mm) at Indicated Axial Location (mm)						
	Bay 1	**Bay 2**	**Bay 3**	**Bay 4**	**Bay 5**	**Bay 6**	**Bay 7**
	105	155	205	255	305	355	405
0	2.940	2.959	3.005	**2.358**	2.935	2.929	2.972
10	2.923	2.957	2.971	2.962	2.939	2.951	3.005
20	2.894	2.948	2.973	2.949	2.955	2.989	3.037
30	2.887	2.922	2.948	2.924	2.948	3.003	3.048
40	2.885	2.915	2.816	2.904	2.945	2.994	3.058
50	2.903	2.895	2.879	2.901	2.955	2.998	3.057
60	2.933	2.906	2.867	2.908	2.947	2.987	3.054
70	2.965	2.907	2.886	2.920	2.942	2.974	3.029
80	2.984	2.912	2.870	2.876	2.894	2.957	2.997
90	3.030	2.845	2.933	2.923	2.931	2.942	2.967
100	3.060	2.961	2.956	2.948	2.933	2.937	2.940
110	3.082	3.001	2.978	2.959	2.924	2.890	2.918
120	3.085	3.015	2.997	2.975	2.952	2.916	2.900
130	3.093	3.029	3.021	2.984	2.960	2.905	2.894
140	3.107	3.057	3.028	2.998	2.967	2.913	2.898
150	3.101	3.049	3.011	3.028	2.973	2.930	2.905
160	3.101	3.066	3.036	3.047	2.974	2.927	2.913
170	3.089	3.062	3.056	3.059	2.985	2.951	2.947
180	3.059	3.043	3.056	3.026	2.990	2.974	2.980
190	3.043	3.025	3.050	3.022	2.994	2.992	3.012
200	3.018	3.002	3.034	3.010	2.994	3.006	3.041
210	3.017	3.000	3.018	2.996	2.994	3.017	3.066
220	3.008	3.002	2.964	2.964	2.988	3.011	3.095
230	3.009	2.980	2.986	2.970	2.958	3.006	3.115
240	3.036	2.995	2.984	2.975	2.972	3.025	3.098
250	3.046	2.999	2.984	2.983	2.987	3.015	3.098
260	3.067	3.004	2.989	2.988	2.991	3.048	3.097
270	3.081	2.992	2.993	2.988	3.008	3.055	3.065
280	3.102	2.979	2.963	2.997	3.025	3.055	3.030
290	3.106	3.028	3.009	3.011	3.022	3.036	2.975
300	3.078	3.024	3.009	3.025	3.037	3.017	2.934
310	3.084	3.016	3.015	3.021	3.033	2.988	2.926
320	3.067	3.012	3.013	3.037	3.031	2.956	2.915
330	3.041	3.000	3.024	3.041	3.006	2.926	2.913
340	3.020	2.988	3.028	3.040	2.975	2.917	2.926
350	2.970	2.970	3.025	3.013	2.950	2.924	2.953

a. Shell thickness determined by ultrasonic thickness gauge measurements of the shell. Corroded locations are indicated by shaded cells with bold faced font.

Table 35: Measured shell thicknesses for specimen L510-No13 – corrosion patch measurements

Angle (degrees)	**Shell Thickness[a] (mm) at Indicated Axial Location (mm)**		
	235	255	275
-9	2.421	2.426	2.495
0	2.393	2.386	2.461
9	2.356	2.367	2.446

a. Shell thickness determined by ultrasonic thickness gauge measurements of the shell.

B.2 L510-No14

Table 36: Out-of-circularity of specimen L510-No14 based on laser displacement gauge measurements – Part 1

Angle (degrees)	Radial Eccentricity[a] (mm) at Indicated Axial Location (mm)							
	Frame 1	**Bay 1**	**Frame 2**	**Bay 2**	**Frame 3**	**Bay 3**	**Frame 4**	**Bay 4**
	80	105	130	155	180	205	230	255
0	0.132	0.134	0.223	0.306	0.299	0.387	0.387	0.389
10	0.082	0.092	0.150	0.247	0.225	0.328	0.321	0.329
20	0.030	0.040	0.034	0.001	0.108	0.157	0.153	0.161
30	-0.031	-0.039	-0.105	-0.291	-0.052	-0.291	-0.163	-0.245
40	-0.082	-0.092	-0.156	-0.153	-0.204	-0.493	-0.378	-0.417
50	-0.100	-0.114	-0.211	-0.455	-0.465	-0.623	-0.358	-0.343
60	-0.090	-0.074	-0.170	-0.329	-0.438	-0.328	-0.432	-0.418
70	-0.060	-0.067	-0.064	-0.013	-0.044	-0.055	-0.236	-0.203
80	-0.020	-0.021	0.030	0.135	0.154	0.202	0.158	0.143
90	0.018	0.023	0.099	0.193	0.213	0.278	0.257	0.283
100	0.044	0.071	0.133	0.213	0.227	0.333	0.311	0.324
110	0.059	0.079	0.137	0.197	0.217	0.310	0.306	0.325
120	0.052	0.065	0.105	0.182	0.180	0.325	0.291	0.330
130	0.030	0.034	0.037	0.126	0.129	0.261	0.217	0.278
140	-0.011	-0.006	-0.040	0.012	-0.009	0.143	-0.035	0.062
150	-0.043	-0.055	-0.121	-0.173	-0.160	-0.302	-0.370	-0.476
160	-0.057	-0.079	-0.160	-0.159	-0.355	-0.558	-0.383	**-0.528**
170	-0.056	-0.074	-0.173	-0.396	-0.522	-0.814	-0.442	**-0.317**
180	-0.037	-0.049	-0.111	-0.341	-0.296	-0.423	-0.438	-0.460
190	0.000	-0.034	-0.022	-0.043	0.039	-0.013	-0.083	-0.211
200	0.044	0.018	0.075	0.109	0.179	0.214	0.189	0.115
210	0.075	0.064	0.139	0.193	0.255	0.310	0.296	0.316
220	0.092	0.097	0.187	0.248	0.298	0.391	0.372	0.379
230	0.088	0.108	0.195	0.254	0.298	0.391	0.384	0.407
240	0.058	0.090	0.156	0.253	0.269	0.416	0.362	0.386
250	0.012	0.055	0.081	0.180	0.195	0.333	0.269	0.314
260	-0.031	0.001	-0.020	0.063	0.079	0.246	0.105	0.161
270	-0.091	-0.073	-0.137	-0.217	-0.121	-0.256	-0.224	-0.147
280	-0.115	-0.125	-0.196	-0.208	-0.272	-0.542	-0.454	-0.457
290	-0.122	-0.132	-0.247	-0.361	-0.504	-0.696	-0.466	-0.462
300	-0.100	-0.121	-0.226	-0.471	-0.554	-0.541	-0.419	-0.462
310	-0.056	-0.068	-0.121	-0.165	-0.229	-0.167	-0.319	-0.370
320	0.007	-0.022	0.000	0.064	0.080	0.086	-0.026	-0.056
330	0.056	0.037	0.101	0.205	0.206	0.261	0.182	0.195
340	0.099	0.102	0.180	0.280	0.271	0.344	0.300	0.311
350	0.127	0.134	0.220	0.309	0.304	0.386	0.364	0.366

a. Radial eccentricities are based on the filtered measurements taken at the outside of the cylinder shell. Eccentricities at corrosion patches (shaded cells with bold face font) have been corrected for the corroded shell thickness.

Table 37: Out-of-circularity of specimen L510-No14 based on laser displacement gauge measurements – Part 2

Angle (degrees)	Radial Eccentricity[a] (mm) at Indicated Axial Location (mm)							
	Bay 4	**Frame 5**	**Bay 5**	**Frame 6**	**Bay 6**	**Frame 7**	**Bay 7**	**Frame 8**
	255	280	305	330	355	380	405	430
0	0.389	0.395	0.433	0.341	0.355	0.235	0.185	0.116
10	0.329	0.348	0.407	0.310	0.346	0.201	0.158	0.120
20	0.161	0.242	0.261	0.212	0.239	0.120	0.088	0.098
30	-0.245	-0.185	-0.049	-0.007	0.019	-0.006	0.010	0.055
40	-0.417	-0.373	-0.476	-0.338	-0.608	-0.142	-0.051	0.005
50	-0.343	-0.385	-0.571	-0.550	-0.599	-0.204	-0.094	-0.028
60	-0.418	-0.533	-0.590	-0.419	-0.354	-0.179	-0.098	-0.032
70	-0.203	-0.197	-0.236	-0.059	-0.026	-0.080	-0.072	-0.025
80	0.143	0.223	0.243	0.174	0.182	0.031	-0.020	-0.008
90	0.283	0.287	0.315	0.219	0.219	0.101	0.040	0.015
100	0.324	0.293	0.325	0.236	0.238	0.140	0.077	0.027
110	0.325	0.289	0.307	0.217	0.236	0.145	0.084	0.018
120	0.330	0.271	0.315	0.202	0.222	0.120	0.074	0.002
130	0.278	0.247	0.286	0.144	0.180	0.058	0.024	-0.036
140	0.062	-0.045	0.160	0.039	0.100	-0.044	-0.046	-0.076
150	-0.476	-0.419	-0.195	-0.160	-0.100	-0.187	-0.123	-0.106
160	**-0.528**	-0.352	-0.572	-0.401	-0.486	-0.278	-0.158	-0.118
170	**-0.317**	-0.536	-0.593	-0.557	-0.482	-0.264	-0.157	-0.095
180	-0.460	-0.505	-0.703	-0.396	-0.434	-0.174	-0.115	-0.049
190	-0.211	-0.058	-0.297	-0.011	-0.079	-0.027	-0.048	0.007
200	0.115	0.249	0.223	0.184	0.136	0.099	0.051	0.075
210	0.316	0.346	0.384	0.291	0.262	0.201	0.133	0.133
220	0.379	0.407	0.454	0.340	0.311	0.254	0.191	0.169
230	0.407	0.396	0.465	0.356	0.365	0.276	0.215	0.171
240	0.386	0.371	0.444	0.328	0.324	0.253	0.208	0.143
250	0.314	0.291	0.389	0.266	0.304	0.191	0.150	0.087
260	0.161	0.155	0.273	0.135	0.173	0.069	0.045	0.012
270	-0.147	-0.205	-0.002	-0.072	0.030	-0.097	-0.079	-0.077
280	-0.457	-0.440	-0.495	-0.392	-0.517	-0.306	-0.194	-0.139
290	-0.462	-0.475	-0.679	-0.610	-0.730	-0.390	-0.255	-0.178
300	-0.462	-0.576	-0.686	-0.555	-0.467	-0.305	-0.240	-0.182
310	-0.370	-0.468	-0.642	-0.295	-0.231	-0.187	-0.172	-0.136
320	-0.056	-0.018	-0.011	0.023	0.057	-0.053	-0.085	-0.081
330	0.195	0.242	0.300	0.186	0.188	0.064	0.012	-0.015
340	0.311	0.343	0.396	0.287	0.280	0.157	0.096	0.044
350	0.366	0.376	0.417	0.332	0.345	0.208	0.160	0.084

a. Radial eccentricities are based on the filtered measurements taken at the outside of the cylinder shell. Eccentricities at corrosion patches (shaded cells with bold face font) have been corrected for the corroded shell thickness.

Table 38: Out-of-circularity of specimen L510-No14 based on mechanical displacement gauge measurements

Angle (degrees)	Radial Eccentricity[a] (mm) at Indicated Axial Location (mm)							
	Frame 1	**Frame 2**	**Frame 3**	**Frame 4**	**Frame 5**	**Frame 6**	**Frame 7**	**Frame 8**
	80	130	180	230	280	330	380	430
0	-	-	0.278	0.354	0.409	0.358	-	-
10	-	-	0.210	0.303	0.364	0.330	-	-
20	-	-	0.093	0.199	0.261	0.255	-	-
30	-	-	-0.072	-0.176	-0.144	0.046	-	-
40	-	-	-0.192	-0.352	-0.386	-0.282	-	-
50	-	-	-0.470	-0.353	-0.372	-0.506	-	-
60	-	-	-0.519	-0.394	-0.536	-0.496	-	-
70	-	-	-0.150	-0.360	-0.372	-0.191	-	-
80	-	-	0.140	0.070	0.102	0.076	-	-
90	-	-	0.209	0.214	0.262	0.166	-	-
100	-	-	0.233	0.268	0.289	0.190	-	-
110	-	-	0.231	0.293	0.289	0.201	-	-
120	-	-	0.202	0.286	0.288	0.192	-	-
130	-	-	0.158	0.249	0.274	0.172	-	-
140	-	-	0.071	0.155	0.194	0.105	-	-
150	-	-	-0.075	-0.190	-0.260	0.003	-	-
160	-	-	-0.195	-0.363	-0.400	-0.166	-	-
170	-	-	-0.441	-0.379	-0.372	-0.403	-	-
180	-	-	-0.439	-0.476	-0.589	-0.522	-	-
190	-	-	-0.091	-0.277	-0.295	-0.182	-	-
200	-	-	0.132	0.117	0.152	0.098	-	-
210	-	-	0.222	0.265	0.324	0.226	-	-
220	-	-	0.268	0.343	0.401	0.292	-	-
230	-	-	0.284	0.375	0.412	0.312	-	-
240	-	-	0.267	0.358	0.387	0.294	-	-
250	-	-	0.205	0.318	0.323	0.288	-	-
260	-	-	0.074	0.131	0.172	0.214	-	-
270	-	-	-0.124	-0.241	-0.204	-0.034	-	-
280	-	-	-0.289	-0.473	-0.465	-0.403	-	-
290	-	-	-0.567	-0.462	-0.502	-0.597	-	-
300	-	-	-0.505	-0.415	-0.610	-0.531	-	-
310	-	-	-0.119	-0.282	-0.413	-0.261	-	-
320	-	-	0.132	0.029	0.041	-0.003	-	-
330	-	-	0.238	0.190	0.257	0.146	-	-
340	-	-	0.294	0.297	0.341	0.255	-	-
350	-	-	0.306	0.379	0.379	0.359	-	-

a. Radial eccentricity is taken as the raw gauge reading less the n=0 and n=1 Fourier components at that axial location.

Table 39: Measured shell thicknesses for specimen L510-No14 – global measurements

Angle (degrees)	Shell Thickness[a] (mm) at Indicated Axial Location (mm)						
	Bay 1	**Bay 2**	**Bay 3**	**Bay 4**	**Bay 5**	**Bay 6**	**Bay 7**
	105	155	205	255	305	355	405
0	3.207	3.159	3.073	3.016	2.998	2.930	2.906
10	3.184	3.160	3.063	2.985	2.970	2.919	2.884
20	3.149	3.145	3.057	2.968	2.945	2.910	2.895
30	3.095	3.111	3.052	2.962	2.932	2.913	2.928
40	3.046	3.085	3.050	2.971	2.952	2.935	2.967
50	2.989	3.054	3.038	2.993	2.979	2.964	3.000
60	2.949	3.032	3.045	3.030	3.027	3.012	3.047
70	2.931	3.020	3.058	3.061	3.082	3.062	3.079
80	2.930	3.015	3.075	3.100	3.142	3.108	3.120
90	2.936	3.021	3.092	3.127	3.179	3.146	3.142
100	2.958	3.028	3.102	3.144	3.195	3.171	3.143
110	2.976	3.042	3.099	3.139	3.189	3.169	3.121
120	3.003	3.053	3.092	3.134	3.171	3.146	3.100
130	3.032	3.061	3.077	3.101	3.136	3.105	3.074
140	3.049	3.058	3.054	3.063	3.095	3.061	3.039
150	3.045	3.052	3.040	3.022	3.048	3.020	3.006
160	3.036	3.046	3.011	**2.373**	3.017	2.989	2.970
170	3.021	3.021	2.983	**2.342**	2.982	2.969	2.949
180	3.014	2.991	2.954	2.930	2.955	2.945	2.940
190	3.000	2.962	2.933	2.907	2.935	2.935	2.933
200	2.981	2.943	2.906	2.896	2.930	2.935	2.942
210	2.957	2.929	2.885	2.885	2.940	2.949	2.964
220	2.937	2.926	2.882	2.903	2.940	2.967	3.001
230	2.932	2.944	2.910	2.918	2.942	2.982	3.037
240	2.945	2.962	2.941	2.945	2.958	3.004	3.082
250	2.964	2.992	2.972	2.970	2.972	3.019	3.104
260	2.986	3.017	3.005	2.992	2.991	3.028	3.113
270	3.010	3.062	3.045	3.026	3.023	3.038	3.107
280	3.047	3.097	3.084	3.053	3.065	3.061	3.107
290	3.071	3.125	3.112	3.077	3.099	3.085	3.102
300	3.088	3.140	3.142	3.110	3.119	3.086	3.091
310	3.109	3.152	3.154	3.129	3.127	3.085	3.078
320	3.128	3.142	3.151	3.131	3.120	3.067	3.056
330	3.153	3.145	3.136	3.116	3.103	3.064	3.020
340	3.183	3.144	3.117	3.090	3.072	3.001	2.982
350	3.206	3.152	3.088	3.056	3.036	2.962	2.942

a. Shell thickness determined by ultrasonic thickness gauge measurements of the shell. Corroded locations are indicated by shaded cells with bold faced font.

Table 40: Measured shell thicknesses for specimen L510-No14 – corrosion patch measurements

Angle (degrees)	**Shell Thickness[a] (mm) at Indicated Axial Location (mm)**		
	235	255	275
156	2.400	2.402	2.386
165	2.357	2.351	2.350
174	2.361	2.321	2.309

a. Shell thickness determined by ultrasonic thickness gauge measurements of the shell.

B.3 L510-No17

Table 41: Outer radii of specimen L510-No17 based on CMM measurements – Part 1

Angle (°)	Outer radii [a] (mm) at indicated axial location (mm)								
	End Bay 1	**Frame 1**	**Bay 1**	**Frame 2**	**Bay 2**	**Frame 3**	**Bay 3**	**Frame 4**	**Bay 4**
	66	79	107	125	153	175	204	220	235
0	122.843	122.836	122.863	122.829	122.784	122.773	122.642	122.825	122.819
10	122.830	122.815	122.799	122.776	122.748	122.721	122.673	122.653	122.642
20	122.852	122.832	122.738	122.646	122.706	122.652	122.683	122.660	122.661
30	122.903	122.890	122.857	122.829	122.855	122.849	122.870	122.869	122.888
40	122.974	122.971	123.017	123.069	123.069	123.116	123.096	123.119	123.098
50	123.044	123.051	123.099	123.144	123.154	123.176	123.185	123.197	123.177
60	123.102	123.111	123.147	123.182	123.182	123.201	123.206	123.224	123.201
70	123.135	123.141	123.166	123.189	123.188	123.200	123.194	123.208	123.186
80	123.139	123.139	123.155	123.172	123.171	123.177	123.158	123.155	123.134
90	123.115	123.105	123.110	123.127	123.129	123.128	123.096	123.066	123.049
100	123.065	123.048	123.037	123.042	123.023	123.035	122.981	122.943	122.934
110	123.004	122.975	122.943	122.885	122.783	122.767	122.748	122.792	122.766
120	122.940	122.901	122.855	122.797	122.665	122.628	122.543	122.591	122.541
130	122.885	122.840	122.754	122.669	122.611	122.548	122.486	122.441	122.414
140	122.848	122.802	122.700	122.572	122.561	122.516	122.475	122.423	122.418
150	122.830	122.795	122.751	122.716	122.676	122.653	122.603	122.557	122.556
160	122.830	122.810	122.818	122.824	122.797	122.779	122.745	122.729	122.714
170	122.843	122.835	122.862	122.878	122.869	122.863	122.848	122.840	122.826
180	122.860	122.863	122.897	122.917	122.921	122.929	122.925	122.925	122.910
190	122.881	122.892	122.930	122.950	122.964	122.982	122.982	122.987	122.972
200	122.907	122.916	122.954	122.977	122.998	123.020	123.021	123.026	123.016
210	122.932	122.939	122.972	122.996	123.019	123.040	123.040	123.044	123.045
220	122.958	122.959	122.982	123.004	123.013	123.034	123.031	123.037	123.054
230	122.989	122.980	122.987	122.962	122.934	122.950	122.937	123.007	123.005
240	123.023	123.006	122.999	122.961	122.906	122.897	122.795	122.922	122.872
250	123.060	123.036	122.999	122.953	122.915	122.899	122.865	122.840	122.811
260	123.099	123.074	123.018	122.920	122.870	122.897	122.911	122.847	122.842
270	123.134	123.117	123.098	123.069	123.051	123.069	123.061	123.013	123.034
280	123.157	123.152	123.179	123.212	123.211	123.224	123.227	123.266	123.272
290	123.166	123.174	123.219	123.258	123.278	123.303	123.328	123.371	123.382
300	123.156	123.172	123.227	123.270	123.302	123.347	123.377	123.420	123.427
310	123.126	123.147	123.209	123.259	123.299	123.358	123.389	123.428	123.435
320	123.076	123.099	123.169	123.223	123.269	123.334	123.362	123.396	123.405
330	123.013	123.033	123.105	123.163	123.211	123.275	123.301	123.327	123.340
340	122.946	122.958	123.021	123.075	123.113	123.175	123.196	123.217	123.235
350	122.885	122.888	122.930	122.932	122.943	122.972	122.975	123.069	123.070

a. Raw radial measurements, i.e. not corrected for the offset of the measurement apparatus from the axis of revolution.

Table 42: Outer radii of specimen L510-No17 based on CMM measurements – Part 2

Angle (°)	Outer radii [a] (mm) at indicated axial location (mm)								
	Bay 4	**Frame 5**	**Bay 5**	**Frame 6**	**Bay 6**	**Frame 7**	**Bay 7**	**Frame 8**	**End Bay 2**
	275	290	306	335	357	385	403	431	444
0	122.788	122.771	122.847	122.817	122.816	122.767	122.783	122.887	122.905
10	122.708	122.709	122.766	122.791	122.782	122.777	122.811	122.876	122.896
20	122.780	122.811	122.770	122.733	122.800	122.774	122.853	122.894	122.906
30	122.971	122.999	122.934	122.901	122.947	122.981	122.959	122.931	122.931
40	123.131	123.122	123.100	123.110	123.084	123.075	123.032	122.975	122.963
50	123.210	123.195	123.177	123.173	123.133	123.098	123.063	123.015	122.996
60	123.241	123.232	123.208	123.198	123.148	123.116	123.084	123.042	123.020
70	123.234	123.232	123.205	123.194	123.152	123.126	123.096	123.054	123.033
80	123.188	123.195	123.173	123.164	123.139	123.125	123.093	123.047	123.031
90	123.109	123.124	123.112	123.112	123.106	123.100	123.069	123.020	123.013
100	122.999	123.019	123.007	123.025	123.011	123.032	122.999	122.978	122.984
110	122.805	122.827	122.822	122.788	122.808	122.790	122.832	122.929	122.954
120	122.486	122.548	122.643	122.645	122.665	122.664	122.737	122.888	122.927
130	122.409	122.431	122.531	122.583	122.638	122.693	122.783	122.872	122.913
140	122.444	122.480	122.541	122.551	122.654	122.736	122.819	122.877	122.912
150	122.604	122.649	122.670	122.714	122.774	122.843	122.866	122.895	122.921
160	122.740	122.774	122.801	122.848	122.873	122.899	122.908	122.924	122.941
170	122.835	122.861	122.890	122.928	122.933	122.941	122.948	122.955	122.964
180	122.906	122.926	122.950	122.981	122.978	122.980	122.983	122.983	122.985
190	122.960	122.977	122.994	123.015	123.013	123.012	123.008	123.000	123.001
200	122.996	123.014	123.023	123.030	123.031	123.032	123.022	123.007	123.004
210	123.022	123.040	123.035	123.028	123.030	123.035	123.020	123.000	122.998
220	123.035	123.054	123.022	123.005	122.996	123.012	122.996	122.984	122.986
230	122.952	122.966	122.935	122.914	122.913	122.887	122.927	122.967	122.978
240	122.702	122.731	122.826	122.857	122.867	122.821	122.887	122.958	122.974
250	122.691	122.696	122.800	122.854	122.880	122.912	122.937	122.965	122.986
260	122.820	122.853	122.868	122.847	122.905	122.955	122.985	122.985	122.994
270	123.031	123.067	123.027	123.000	123.015	123.039	123.029	123.014	123.014
280	123.221	123.218	123.172	123.149	123.116	123.091	123.068	123.043	123.037
290	123.322	123.301	123.259	123.231	123.176	123.133	123.100	123.065	123.051
300	123.371	123.352	123.309	123.278	123.215	123.167	123.126	123.080	123.057
310	123.388	123.369	123.325	123.292	123.233	123.189	123.139	123.080	123.054
320	123.371	123.354	123.308	123.274	123.227	123.192	123.135	123.062	123.037
330	123.320	123.302	123.256	123.222	123.190	123.167	123.109	123.028	123.007
340	123.227	123.211	123.160	123.133	123.107	123.104	123.051	122.979	122.969
350	123.052	123.028	123.005	122.981	122.961	122.935	122.922	122.926	122.929

a. Raw radial measurements, i.e. not corrected for the offset of the measurement apparatus from the axis of revolution.

Table 43: Inner radii of specimen L510-No17 based on CMM measurements – Part 1

Angle (°)	Inner radii [a] (mm) at indicated axial location (mm)								
	End Bay 1	**Frame 1**	**Bay 1**	**Frame 2**	**Bay 2**	**Frame 3**	**Bay 3**	**Frame 4**	**Bay 4**
	66	79	107	125	153	175	204	220	235
0	119.932	109.896	119.959	109.861	119.834	109.792	119.658	109.800	119.861
10	120.014	109.967	119.966	109.874	119.850	109.789	119.746	109.700	119.737
20	120.103	110.050	119.960	109.807	119.862	109.782	119.817	109.746	119.804
30	120.188	110.150	120.118	110.014	120.051	110.011	120.048	109.993	120.068
40	120.251	110.234	120.284	110.273	120.288	110.309	120.305	110.267	120.304
50	120.282	110.292	120.352	110.341	120.375	110.371	120.403	110.352	120.382
60	120.286	110.303	120.371	110.349	120.388	110.366	120.397	110.362	120.390
70	120.266	110.269	120.326	110.313	120.348	110.329	120.337	110.315	120.352
80	120.206	110.185	120.247	110.243	120.280	110.261	120.257	110.228	120.267
90	120.103	110.070	120.135	110.135	120.185	110.170	120.157	110.099	120.158
100	119.984	109.946	120.006	109.990	120.021	110.030	120.010	109.943	120.011
110	119.876	109.816	119.860	109.783	119.732	109.716	119.738	109.756	119.809
120	119.793	109.721	119.734	109.665	119.577	109.555	119.505	109.517	119.553
130	119.742	109.662	119.629	109.521	119.506	109.439	119.424	109.346	119.398
140	119.721	109.644	119.589	109.438	119.452	109.404	119.394	109.295	119.377
150	119.738	109.671	119.672	109.592	119.579	109.532	119.521	109.410	119.495
160	119.781	109.730	119.776	109.734	119.739	109.672	119.681	109.587	119.657
170	119.855	109.813	119.886	109.835	119.860	109.796	119.821	109.716	119.784
180	119.929	109.909	119.989	109.930	119.970	109.905	119.937	109.834	119.891
190	120.015	110.010	120.074	110.017	120.059	110.010	120.031	109.936	119.982
200	120.132	110.111	120.148	110.097	120.140	110.100	120.104	110.023	120.058
210	120.217	110.193	120.203	110.139	120.202	110.153	120.157	110.086	120.137
220	120.282	110.247	120.247	110.199	120.217	110.190	120.183	110.120	120.187
230	120.312	110.276	120.254	110.168	120.148	110.125	120.108	110.120	120.168
240	120.313	110.263	120.249	110.162	120.105	110.086	119.975	110.057	120.048
250	120.289	110.242	120.213	110.119	120.093	110.071	120.044	109.978	119.982
260	120.241	110.191	120.131	110.040	119.992	110.042	120.062	109.950	119.991
270	120.178	110.133	120.164	110.110	120.111	110.139	120.155	110.065	120.138
280	120.104	110.071	120.165	110.178	120.207	110.217	120.261	110.259	120.337
290	120.026	110.012	120.137	110.152	120.206	110.234	120.306	110.305	120.406
300	119.966	109.959	120.091	110.106	120.171	110.224	120.313	110.308	120.405
310	119.921	109.918	120.045	110.057	120.148	110.209	120.302	110.283	120.379
320	119.886	109.886	120.014	110.032	120.119	110.180	120.270	110.240	120.331
330	119.856	109.858	119.987	109.993	120.091	110.137	120.218	110.173	120.275
340	119.849	109.850	119.960	109.968	120.040	110.072	120.139	110.091	120.193
350	119.875	109.860	119.948	109.886	119.935	109.916	119.955	109.988	120.071

a. Raw radial measurements, i.e. not corrected for the offset of the measurement apparatus from the axis of revolution.

Table 44: Inner radii of specimen L510-No17 based on CMM measurements – Part 2

Angle (°)	Inner radii [a] (mm) at indicated axial location (mm)								
	Bay 4	**Frame 5**	**Bay 5**	**Frame 6**	**Bay 6**	**Frame 7**	**Bay 7**	**Frame 8**	**End Bay 2**
	275	290	306	335	357	385	403	431	444
0	119.847	109.797	119.917	109.859	119.907	109.801	119.867	109.945	120.003
10	119.820	109.775	119.870	109.856	119.884	109.822	119.884	109.922	119.975
20	119.935	109.910	119.904	109.820	119.910	109.829	119.921	109.925	119.963
30	120.155	110.128	120.090	109.990	120.060	110.024	120.021	109.948	119.970
40	120.336	110.263	120.267	110.206	120.202	110.120	120.088	109.980	119.987
50	120.412	110.335	120.349	110.260	120.238	110.129	120.109	110.004	120.005
60	120.430	110.356	120.368	110.275	120.236	110.135	120.122	110.019	120.025
70	120.393	110.336	120.351	110.260	120.217	110.136	120.121	110.026	120.036
80	120.322	110.278	120.308	110.229	120.202	110.128	120.122	110.021	120.043
90	120.221	110.186	120.234	110.174	120.179	110.112	120.113	110.011	120.036
100	120.092	110.065	120.116	110.084	120.087	110.054	120.063	109.993	120.032
110	119.870	109.847	119.907	109.842	119.887	109.828	119.921	109.977	120.037
120	119.520	109.558	119.706	109.698	119.737	109.717	119.843	109.965	120.041
130	119.431	109.406	119.568	109.605	119.701	109.745	119.895	109.960	120.042
140	119.430	109.426	119.537	109.551	119.697	109.765	119.911	109.954	120.035
150	119.567	109.558	119.639	109.668	119.796	109.835	119.925	109.942	120.020
160	119.702	109.664	119.755	109.774	119.872	109.858	119.932	109.938	120.007
170	119.803	109.750	119.843	109.832	119.907	109.872	119.941	109.940	120.004
180	119.893	109.827	119.911	109.879	119.935	109.889	119.953	109.940	120.001
190	119.962	109.906	119.968	109.919	119.950	109.906	119.944	109.930	119.980
200	120.028	109.981	120.023	109.955	119.968	109.916	119.939	109.900	119.941
210	120.097	110.052	120.068	109.984	119.990	109.923	119.938	109.861	119.884
220	120.152	110.114	120.096	109.997	119.991	109.918	119.924	109.830	119.840
230	120.101	110.055	120.036	109.953	119.943	109.828	119.870	109.819	119.827
240	119.853	109.856	119.951	109.946	119.935	109.810	119.858	109.838	119.847
250	119.848	109.831	119.942	109.973	119.987	109.939	119.950	109.883	119.893
260	119.962	109.983	120.008	109.980	120.030	110.011	120.029	109.946	119.952
270	120.143	110.167	120.150	110.105	120.132	110.097	120.091	110.008	120.021
280	120.304	110.274	120.259	110.221	120.206	110.138	120.132	110.065	120.082
290	120.366	110.305	120.306	110.255	120.238	110.159	120.166	110.109	120.136
300	120.378	110.298	120.314	110.259	120.249	110.175	120.190	110.139	120.180
310	120.356	110.277	120.298	110.244	120.248	110.189	120.205	110.165	120.212
320	120.321	110.243	120.267	110.214	120.240	110.191	120.214	110.163	120.223
330	120.273	110.197	120.218	110.166	120.213	110.177	120.199	110.133	120.194
340	120.205	110.133	120.153	110.099	120.156	110.125	120.146	110.073	120.133
350	120.070	109.987	120.036	109.978	120.036	109.963	120.019	110.002	120.057

a. Raw radial measurements, i.e. not corrected for the offset of the measurement apparatus from the axis of revolution.

Table 45: Out-of-circularity of specimen L510-No17 based on mechanical displacement gauge measurements

Angle (degrees)	Radial Eccentricity[a] (mm) at Indicated Axial Location (mm)							
	Frame 1	**Frame 2**	**Frame 3**	**Frame 4**	**Frame 5**	**Frame 6**	**Frame 7**	**Frame 8**
	80	130	180	230	280	330	380	430
0	-0.195	-0.277	-0.343	-0.318	-0.379	-0.283	-0.290	-0.110
10	-0.202	-0.276	-0.378	-0.476	-0.438	-0.298	-0.265	-0.116
20	-0.185	-0.408	-0.428	-0.440	-0.324	-0.347	-0.251	-0.096
30	-0.124	-0.223	-0.234	-0.196	-0.116	-0.173	-0.039	-0.045
40	-0.024	0.053	0.088	0.091	0.063	0.073	0.087	0.006
50	0.074	0.157	0.193	0.221	0.172	0.175	0.125	0.063
60	0.148	0.217	0.254	0.291	0.248	0.229	0.159	0.092
70	0.192	0.240	0.281	0.312	0.282	0.246	0.178	0.106
80	0.202	0.264	0.286	0.296	0.283	0.248	0.192	0.105
90	0.185	0.246	0.272	0.244	0.257	0.217	0.187	0.080
100	0.125	0.175	0.206	0.139	0.176	0.151	0.119	0.040
110	0.055	0.006	-0.051	0.001	0.004	-0.074	-0.111	-0.012
120	-0.016	-0.093	-0.194	-0.189	-0.277	-0.205	-0.233	-0.056
130	-0.083	-0.200	-0.259	-0.324	-0.366	-0.266	-0.202	-0.073
140	-0.111	-0.297	-0.298	-0.328	-0.325	-0.296	-0.153	-0.073
150	-0.112	-0.152	-0.160	-0.193	-0.144	-0.130	-0.036	-0.045
160	-0.104	-0.036	-0.050	-0.057	-0.025	-0.005	0.001	-0.036
170	-0.086	0.000	0.013	0.035	0.046	0.060	0.030	-0.013
180	-0.060	0.020	0.065	0.093	0.103	0.102	0.061	0.005
190	-0.036	0.042	0.098	0.132	0.140	0.115	0.083	0.021
200	-0.021	0.056	0.111	0.140	0.152	0.123	0.098	0.031
210	-0.004	0.062	0.106	0.125	0.161	0.106	0.081	0.019
220	-0.007	0.049	0.074	0.084	0.146	0.066	0.053	0.005
230	0.001	-0.036	-0.042	0.016	0.026	-0.050	-0.100	-0.018
240	0.008	-0.061	-0.113	-0.109	-0.247	-0.127	-0.166	-0.027
250	0.017	-0.072	-0.148	-0.218	-0.319	-0.150	-0.092	-0.026
260	0.039	-0.146	-0.188	-0.243	-0.204	-0.186	-0.058	-0.010
270	0.072	-0.025	-0.045	-0.109	-0.018	-0.060	0.018	0.014
280	0.107	0.124	0.099	0.111	0.114	0.078	0.056	0.038
290	0.126	0.169	0.167	0.196	0.177	0.141	0.087	0.059
300	0.126	0.176	0.204	0.225	0.204	0.178	0.112	0.068
310	0.101	0.178	0.207	0.227	0.205	0.184	0.124	0.063
320	0.051	0.133	0.181	0.189	0.176	0.156	0.124	0.046
330	-0.015	0.079	0.130	0.120	0.125	0.105	0.100	0.011
340	-0.084	-0.017	0.038	0.023	0.034	0.018	0.037	-0.032
350	-0.159	-0.125	-0.140	-0.112	-0.114	-0.120	-0.118	-0.083

a. Radial eccentricity is taken as the raw gauge reading less the n=0 and n=1 Fourier components at that axial location.

Table 46: Out-of-circularity of specimen L510-No17 based on chord gauge measurements

Angle (degrees)	Radial Eccentricity[a] (mm) at Indicated Axial Location (mm)							
	Frame 1	**Frame 2**	**Frame 3**	**Frame 4**	**Frame 5**	**Frame 6**	**Frame 7**	**Frame 8**
	80	130	180	230	280	330	380	430
0	-0.193	-0.225	-0.312	-0.362	-0.399	-0.253	-0.227	-0.102
20	-0.185	-0.398	-0.411	-0.485	-0.291	-0.346	-0.190	-0.098
40	-0.028	0.108	0.106	0.109	0.056	0.085	0.092	-0.005
60	0.141	0.210	0.225	0.290	0.260	0.204	0.135	0.074
80	0.200	0.274	0.279	0.345	0.276	0.240	0.072	0.096
100	0.136	0.120	0.183	0.169	0.185	0.132	0.101	0.043
120	-0.001	-0.065	-0.173	-0.114	-0.254	-0.199	-0.204	-0.043
140	-0.098	-0.326	-0.312	-0.339	-0.306	-0.301	-0.132	-0.062
160	-0.109	-0.032	-0.051	-0.072	-0.044	0.015	0.029	-0.030
180	-0.072	0.014	0.058	0.021	0.111	0.110	0.115	0.016
200	-0.045	0.078	0.124	0.084	0.136	0.141	0.102	0.026
220	-0.015	0.024	0.069	0.026	0.150	0.051	0.051	0.003
240	0.016	-0.011	-0.092	-0.071	-0.232	-0.131	-0.186	-0.040
260	0.068	-0.140	-0.179	-0.139	-0.174	-0.197	-0.096	-0.023
280	0.120	0.151	0.106	0.188	0.107	0.081	0.013	0.032
300	0.124	0.135	0.176	0.221	0.218	0.164	0.107	0.070
320	0.037	0.128	0.176	0.170	0.166	0.176	0.129	0.056
340	-0.095	-0.047	0.025	-0.041	0.035	0.028	0.088	-0.011

a. Radial eccentricities are determined by performing Fourier decompositions of the chord height measurements, followed by expansion of the Fourier series with modified coefficients, yielding the eccentricities. The eccentricities presented here do not include the n=0 and n=1 Fourier components.

Table 47: Shell thicknesses for specimen L510-No17 based on CMM measurements

Angle (degrees)	Shell Thickness[a] (mm) at Indicated Axial Location (mm)									
	End 1	**Bay 1**	**Bay 2**	**Bay 3**	**Bay 4**	**Bay 4**	**Bay 5**	**Bay 6**	**Bay 7**	**End 2**
	66	107	153	204	235	275	306	357	403	444
0	2.892	2.900	2.947	2.992	2.980	2.968	2.963	2.953	2.962	2.963
10	2.797	2.827	2.895	2.936	2.928	2.918	2.932	2.944	2.977	2.986
20	2.727	2.774	2.843	2.875	2.882	2.877	2.905	2.935	2.984	3.009
30	2.694	2.733	2.804	2.831	2.846	2.848	2.885	2.931	2.989	3.026
40	2.700	2.730	2.782	2.800	2.820	2.829	2.873	2.923	2.994	3.040
50	2.741	2.741	2.782	2.791	2.819	2.829	2.868	2.933	3.000	3.050
60	2.795	2.773	2.799	2.817	2.834	2.841	2.877	2.945	3.005	3.048
70	2.851	2.835	2.846	2.864	2.855	2.869	2.889	2.962	3.011	3.043
80	2.917	2.906	2.898	2.906	2.885	2.890	2.895	2.957	3.001	3.024
90	2.999	2.971	2.952	2.944	2.905	2.907	2.902	2.940	2.977	3.004
100	3.071	3.031	3.011	2.973	2.934	2.922	2.909	2.929	2.949	2.967
110	3.123	3.082	3.060	3.010	2.963	2.944	2.926	2.919	2.915	2.922
120	3.144	3.122	3.097	3.037	2.990	2.970	2.941	2.916	2.890	2.879
130	3.145	3.125	3.114	3.059	3.014	2.976	2.960	2.919	2.874	2.853
140	3.132	3.115	3.118	3.077	3.035	3.006	2.994	2.932	2.886	2.847
150	3.102	3.081	3.105	3.076	3.050	3.023	3.014	2.947	2.911	2.862
160	3.062	3.047	3.065	3.056	3.043	3.019	3.023	2.964	2.939	2.885
170	3.005	2.979	3.015	3.019	3.024	3.009	3.018	2.985	2.965	2.905
180	2.949	2.914	2.956	2.979	2.998	2.987	3.006	2.999	2.983	2.923
190	2.887	2.859	2.908	2.942	2.966	2.968	2.990	3.017	3.015	2.957
200	2.796	2.812	2.860	2.907	2.933	2.936	2.960	3.017	3.031	2.997
210	2.737	2.773	2.817	2.874	2.882	2.892	2.926	2.996	3.031	3.048
220	2.698	2.741	2.795	2.839	2.841	2.850	2.885	2.963	3.022	3.082
230	2.699	2.737	2.783	2.820	2.812	2.819	2.860	2.931	3.010	3.092
240	2.729	2.754	2.797	2.813	2.801	2.819	2.838	2.899	2.986	3.073
250	2.790	2.788	2.816	2.815	2.807	2.815	2.824	2.866	2.951	3.048
260	2.873	2.890	2.872	2.844	2.832	2.834	2.831	2.855	2.926	3.005
270	2.969	2.935	2.932	2.902	2.881	2.869	2.853	2.871	2.916	2.966
280	3.062	3.017	2.996	2.964	2.924	2.903	2.895	2.905	2.923	2.939
290	3.146	3.082	3.064	3.021	2.969	2.947	2.942	2.942	2.930	2.911
300	3.191	3.136	3.122	3.065	3.020	2.990	2.991	2.976	2.941	2.885
310	3.203	3.162	3.143	3.090	3.058	3.034	3.030	3.004	2.948	2.861
320	3.184	3.154	3.142	3.096	3.081	3.058	3.051	3.012	2.943	2.843
330	3.148	3.113	3.113	3.090	3.075	3.060	3.055	3.009	2.940	2.853
340	3.084	3.059	3.066	3.064	3.057	3.041	3.030	2.988	2.941	2.884
350	2.995	2.977	3.002	3.028	3.017	3.005	2.998	2.966	2.945	2.928

a. Shell thicknesses were derived by subtracting the measured inner radii from the corresponding outer radii, after correcting the radius data for the n=1 offset.

B.4 L510-No18

Table 48: Outer radii of specimen L510-No18 based on CMM measurements – Part 1

Angle (°)	Outer radii [a] (mm) at indicated axial location (mm)								
	End Bay 1	**Frame 1**	**Bay 1**	**Frame 2**	**Bay 2**	**Frame 3**	**Bay 3**	**Frame 4**	**Bay 4**
	66	79	107	125	153	175	204	220	235
0	123.000	122.990	122.966	122.937	122.959	122.926	122.845	122.930	123.030
10	122.976	122.958	122.888	122.797	122.865	122.899	122.879	122.901	122.961
20	122.974	122.961	122.954	122.949	122.923	122.848	122.869	122.935	123.000
30	122.991	122.990	123.031	123.064	123.051	123.050	123.058	123.103	123.118
40	123.017	123.026	123.077	123.121	123.144	123.193	123.199	123.215	123.215
50	123.042	123.057	123.107	123.152	123.180	123.229	123.240	123.261	123.260
60	123.052	123.072	123.115	123.158	123.182	123.226	123.236	123.262	123.260
70	123.046	123.063	123.100	123.138	123.159	123.198	123.203	123.224	123.220
80	123.020	123.028	123.061	123.096	123.113	123.146	123.146	123.152	123.144
90	122.971	122.970	122.993	123.022	123.036	123.068	123.064	123.045	123.033
100	122.911	122.896	122.906	122.918	122.900	122.912	122.884	122.896	122.853
110	122.850	122.817	122.794	122.782	122.701	122.539	122.504	122.521	122.512
120	122.803	122.753	122.649	122.554	122.501	122.410	122.288	122.247	122.245
130	122.776	122.720	122.562	122.374	122.373	122.321	122.236	122.138	122.133
140	122.780	122.728	122.633	122.552	122.462	122.324	122.248	122.217	122.195
150	122.810	122.771	122.735	122.707	122.630	122.556	122.497	122.474	122.435
160	122.857	122.829	122.813	122.800	122.766	122.754	122.697	122.665	122.623
170	122.904	122.887	122.880	122.876	122.864	122.861	122.840	122.805	122.763
180	122.941	122.936	122.934	122.937	122.935	122.946	122.918	122.905	122.867
190	122.968	122.968	123.001	122.982	122.983	123.003	122.980	122.972	122.974
200	122.980	122.981	122.994	123.010	123.010	123.031	123.014	123.002	122.972
210	122.980	122.976	122.996	123.018	123.011	123.026	123.015	122.994	122.967
220	122.969	122.958	122.977	123.000	122.977	122.962	122.937	122.940	122.912
230	122.960	122.936	122.937	122.949	122.889	122.746	122.655	122.747	122.762
240	122.961	122.925	122.860	122.769	122.721	122.671	122.463	122.547	122.630
250	122.979	122.941	122.832	122.602	122.540	122.706	122.671	122.610	122.595
260	123.017	122.989	122.941	122.866	122.799	122.770	122.824	122.785	122.685
270	123.068	123.059	123.088	123.123	123.097	123.077	123.079	123.096	123.088
280	123.124	123.131	123.191	123.249	123.277	123.313	123.307	123.332	123.341
290	123.169	123.192	123.267	123.334	123.376	123.432	123.452	123.491	123.499
300	123.197	123.231	123.312	123.382	123.432	123.506	123.541	123.596	123.609
310	123.204	123.242	123.328	123.399	123.457	123.541	123.584	123.647	123.667
320	123.186	123.224	123.310	123.385	123.483	123.535	123.579	123.642	123.666
330	123.150	123.181	123.276	123.354	123.397	123.485	123.530	123.579	123.603
340	123.100	123.118	123.199	123.262	123.297	123.371	123.400	123.452	123.466
350	123.047	123.050	123.103	123.148	123.136	123.101	123.118	123.196	123.236

a. Raw radial measurements, i.e. not corrected for the offset of the measurement apparatus from the axis of revolution.

Table 49: Outer radii of specimen L510-No18 based on CMM measurements – Part 2

Angle (°)	Outer radii [a] (mm) at indicated axial location (mm)								
	Bay 4	**Frame 5**	**Bay 5**	**Frame 6**	**Bay 6**	**Frame 7**	**Bay 7**	**Frame 8**	**End Bay 2**
	275	290	306	335	357	385	403	431	444
0	123.020	122.911	122.907	122.934	122.935	122.919	122.963	122.979	122.985
10	122.937	122.880	122.872	122.898	122.816	122.811	122.904	122.946	122.960
20	122.961	122.906	122.870	122.823	122.770	122.923	122.939	122.943	122.956
30	123.062	123.051	122.997	122.892	122.868	123.002	122.989	122.961	122.965
40	123.152	123.147	123.123	123.126	123.085	123.066	123.027	122.989	122.984
50	123.200	123.197	123.188	123.205	123.159	123.108	123.059	123.017	123.002
60	123.207	123.211	123.202	123.234	123.160	123.120	123.077	123.032	123.013
70	123.173	123.189	123.176	123.181	123.132	123.107	123.067	123.026	123.008
80	123.105	123.128	123.115	123.113	123.078	123.066	123.032	122.997	122.985
90	123.003	123.025	123.018	123.014	123.000	122.999	122.972	122.948	122.942
100	122.830	122.862	122.847	122.880	122.886	122.900	122.888	122.878	122.889
110	122.504	122.463	122.546	122.611	122.676	122.757	122.777	122.810	122.838
120	122.245	122.234	122.332	122.372	122.396	122.490	122.652	122.759	122.803
130	122.147	122.181	122.297	122.391	122.381	122.460	122.618	122.740	122.791
140	122.210	122.263	122.334	122.335	122.458	122.605	122.677	122.759	122.810
150	122.415	122.467	122.491	122.505	122.605	122.712	122.756	122.809	122.852
160	122.607	122.640	122.676	122.738	122.773	122.814	122.837	122.875	122.905
170	122.755	122.786	122.825	122.882	122.889	122.904	122.916	122.943	122.961
180	122.874	122.904	122.932	122.976	122.970	122.977	122.986	123.000	123.010
190	122.959	122.988	123.007	123.039	123.028	123.034	123.036	123.040	123.041
200	123.006	123.034	123.045	123.068	123.062	123.070	123.065	123.058	123.057
210	123.014	123.040	123.045	123.064	123.070	123.083	123.064	123.051	123.055
220	122.972	122.999	122.993	123.020	123.045	123.064	123.041	123.022	123.033
230	122.829	122.820	122.859	122.898	122.939	122.994	122.981	122.984	123.002
240	122.697	122.669	122.740	122.734	122.711	122.760	122.884	122.950	122.975
250	122.684	122.678	122.743	122.783	122.686	122.721	122.862	122.938	122.965
260	122.801	122.804	122.842	122.804	122.722	122.914	122.941	122.957	122.975
270	123.113	123.115	123.060	122.972	122.909	123.059	123.039	123.003	123.006
280	123.362	123.337	123.278	123.247	123.211	123.186	123.124	123.060	123.048
290	123.521	123.493	123.434	123.407	123.345	123.277	123.198	123.117	123.090
300	123.629	123.604	123.538	123.501	123.411	123.337	123.253	123.160	123.122
310	123.687	123.662	123.591	123.539	123.439	123.365	123.283	123.182	123.137
320	123.686	123.663	123.587	123.533	123.433	123.363	123.281	123.178	123.136
330	123.623	123.601	123.531	123.478	123.392	123.330	123.247	123.149	123.115
340	123.483	123.465	123.404	123.372	123.305	123.256	123.183	123.097	123.076
350	123.244	123.181	123.160	123.186	123.153	123.136	123.084	123.037	123.028

a. Raw radial measurements, i.e. not corrected for the offset of the measurement apparatus from the axis of revolution.

Table 50: Inter radii of specimen L510-No18 based on CMM measurements – Part 1

Angle (°)	Inner radii [a] (mm) at indicated axial location (mm)								
	End Bay 1	**Frame 1**	**Bay 1**	**Frame 2**	**Bay 2**	**Frame 3**	**Bay 3**	**Frame 4**	**Bay 4**
	66	79	107	125	153	175	204	220	235
0	120.010	109.989	120.003	109.916	119.942	109.897	119.819	109.888	120.026
10	119.986	109.963	119.931	109.815	119.860	109.868	119.860	109.853	119.953
20	120.000	109.977	120.004	109.968	119.932	109.849	119.856	109.905	119.990
30	120.034	110.023	120.101	110.107	120.082	110.060	120.069	110.090	120.124
40	120.069	110.074	120.168	110.183	120.200	110.232	120.232	110.238	120.247
50	120.090	110.108	120.208	110.224	120.249	110.290	120.294	110.316	120.322
60	120.082	110.110	120.208	110.230	120.254	110.297	120.315	110.342	120.351
70	120.045	110.076	120.171	110.199	120.223	110.268	120.299	110.322	120.331
80	119.986	110.012	120.102	110.136	120.122	110.206	120.242	110.251	120.272
90	119.914	109.927	120.017	110.040	120.055	110.105	120.159	110.131	120.157
100	119.858	109.847	119.917	109.918	119.896	109.915	119.951	109.954	119.966
110	119.827	109.786	119.798	109.774	119.687	109.522	119.536	109.534	119.595
120	119.814	109.750	119.666	109.547	119.496	109.384	119.312	109.253	119.294
130	119.810	109.745	119.611	109.403	119.384	109.284	119.241	109.107	119.171
140	119.831	109.780	119.708	109.576	119.482	109.301	119.235	109.173	119.209
150	119.882	109.837	119.820	109.754	119.659	109.534	119.484	109.428	119.440
160	119.936	109.899	119.895	109.856	119.800	109.744	119.692	109.632	119.624
170	119.971	109.949	119.968	109.937	119.906	109.881	119.835	109.789	119.775
180	119.992	109.988	120.028	109.998	119.988	109.976	119.943	109.904	119.898
190	120.017	110.017	120.065	110.042	120.042	110.041	120.016	109.986	119.986
200	120.037	110.028	120.073	110.068	120.060	110.068	120.050	110.025	120.030
210	120.009	110.012	120.056	110.066	120.049	110.055	120.044	110.016	120.024
220	119.981	109.966	120.023	110.029	120.001	109.972	119.957	109.954	119.967
230	119.922	109.906	119.960	109.948	119.894	109.734	119.656	109.740	119.815
240	119.885	109.857	119.842	109.733	119.702	109.650	119.454	109.550	119.675
250	119.875	109.840	119.789	109.562	119.488	109.657	119.655	109.592	119.633
260	119.894	109.866	119.882	109.781	119.742	109.714	119.809	109.759	119.713
270	119.942	109.929	120.025	110.036	120.042	110.002	120.062	110.066	120.132
280	120.006	110.011	120.129	110.163	120.230	110.248	120.297	110.312	120.389
290	120.066	110.086	120.216	110.260	120.336	110.378	120.451	110.475	120.552
300	120.105	110.138	120.282	110.327	120.412	110.462	120.543	110.578	120.666
310	120.126	110.168	120.317	110.362	120.453	110.504	120.586	110.626	120.725
320	120.131	110.173	120.313	110.364	120.443	110.500	120.565	110.615	120.715
330	120.120	110.151	120.278	110.326	120.385	110.446	120.500	110.538	120.633
340	120.094	110.108	120.223	110.251	120.280	110.325	120.365	110.407	120.484
350	120.052	110.047	120.135	110.138	120.119	110.052	120.080	110.137	120.243

a. Raw radial measurements, i.e. not corrected for the offset of the measurement apparatus from the axis of revolution.

Table 51: Inner radii of specimen L510-No18 based on CMM measurements – Part 2

Angle (°)	Inner radii [a] (mm) at indicated axial location (mm)								
	Bay 4	**Frame 5**	**Bay 5**	**Frame 6**	**Bay 6**	**Frame 7**	**Bay 7**	**Frame 8**	**End Bay 2**
	275	290	306	335	357	385	403	431	444
0	120.005	109.882	119.889	109.885	119.854	109.818	119.913	109.879	119.884
10	119.910	109.826	119.844	109.817	119.717	109.707	119.848	109.842	119.858
20	119.931	109.857	119.833	109.738	119.658	109.815	119.890	109.853	119.867
30	120.044	110.007	119.967	109.814	119.774	109.912	119.964	109.895	119.908
40	120.163	110.135	120.118	110.079	120.034	110.009	120.036	109.956	119.963
50	120.246	110.225	120.220	110.205	120.151	110.094	120.105	110.024	120.018
60	120.289	110.284	120.276	110.261	120.196	110.150	120.157	110.081	120.075
70	120.280	110.297	120.291	110.269	120.198	110.174	120.172	110.119	120.111
80	120.231	110.257	120.256	110.227	120.167	110.160	120.159	110.114	120.106
90	120.140	110.154	120.161	110.130	120.097	110.096	120.109	110.070	120.063
100	119.946	109.967	119.971	109.980	119.978	109.994	120.027	109.994	119.992
110	119.590	109.533	119.640	109.679	119.750	109.825	119.902	109.902	119.917
120	119.305	109.290	119.402	109.432	119.443	109.530	119.753	109.819	119.845
130	119.179	109.191	119.339	109.398	119.401	109.467	119.689	109.768	119.798
140	119.219	109.245	119.350	109.318	119.437	109.571	119.709	109.754	119.786
150	119.404	109.427	119.485	109.453	119.551	109.649	119.753	109.769	119.799
160	119.586	109.596	119.653	109.671	119.696	109.726	119.808	109.798	119.830
170	119.741	109.747	119.804	109.808	119.803	109.803	119.872	109.840	119.863
180	119.878	109.880	119.920	109.917	119.889	109.875	119.935	109.883	119.905
190	119.982	109.980	120.014	109.993	119.963	109.939	119.991	109.926	119.938
200	120.042	110.041	120.069	110.042	120.011	109.993	120.029	109.964	119.976
210	120.054	110.058	120.078	110.054	120.025	110.025	120.038	109.985	120.005
220	120.009	110.019	120.031	110.020	120.017	110.026	120.037	109.986	120.008
230	119.866	109.835	119.898	109.898	119.927	109.968	119.997	109.969	120.001
240	119.730	109.700	119.778	109.753	119.707	109.750	119.919	109.960	119.993
250	119.711	109.695	119.781	109.794	119.693	109.725	119.913	109.968	120.002
260	119.828	109.820	119.886	109.821	119.735	109.925	120.013	110.008	120.028
270	120.143	110.125	120.115	109.984	119.926	110.081	120.126	110.069	120.068
280	120.396	110.354	120.330	110.263	120.240	110.215	120.215	110.132	120.115
290	120.557	110.512	120.487	110.427	120.377	110.311	120.289	110.187	120.155
300	120.671	110.625	120.592	110.522	120.444	110.365	120.341	110.213	120.170
310	120.731	110.679	120.649	110.558	120.466	110.382	120.360	110.212	120.166
320	120.720	110.672	120.631	110.543	120.443	110.360	120.329	110.181	120.141
330	120.640	110.597	120.551	110.476	120.376	110.298	120.256	110.118	120.093
340	120.486	110.446	120.409	110.355	120.272	110.201	120.162	110.039	120.025
350	120.236	110.145	120.152	110.143	120.097	110.052	120.045	109.951	119.950

a. Raw radial measurements, i.e. not corrected for the offset of the measurement apparatus from the axis of revolution.

Table 52: Out-of-circularity of specimen L510-No18 based on mechanical displacement gauge measurements

Angle (degrees)	Radial Eccentricity[a] (mm) at Indicated Axial Location (mm)							
	Frame 1	**Frame 2**	**Frame 3**	**Frame 4**	**Frame 5**	**Frame 6**	**Frame 7**	**Frame 8**
	80	130	180	230	280	330	380	430
0	-0.109	-0.232	-0.350	-0.344	-0.426	-0.292	-0.246	-0.084
10	-0.127	-0.379	-0.336	-0.403	-0.393	-0.315	-0.327	-0.098
20	-0.105	-0.196	-0.366	-0.330	-0.324	-0.341	-0.181	-0.083
30	-0.067	-0.049	-0.133	-0.122	-0.106	-0.202	-0.062	-0.044
40	-0.005	0.038	0.085	0.061	0.051	0.067	0.045	0.005
50	0.049	0.124	0.178	0.180	0.166	0.191	0.123	0.060
60	0.091	0.167	0.233	0.249	0.251	0.253	0.181	0.102
70	0.105	0.181	0.250	0.268	0.285	0.268	0.193	0.109
80	0.101	0.199	0.252	0.276	0.286	0.246	0.184	0.095
90	0.100	0.176	0.261	0.269	0.281	0.205	0.153	0.060
100	0.043	0.100	0.152	0.178	0.158	0.106	0.070	0.000
110	-0.023	-0.013	-0.196	-0.136	-0.215	-0.153	-0.079	-0.060
120	-0.084	-0.235	-0.301	-0.389	-0.382	-0.323	-0.335	-0.112
130	-0.113	-0.398	-0.364	-0.468	-0.404	-0.298	-0.318	-0.123
140	-0.100	-0.238	-0.338	-0.395	-0.294	-0.343	-0.150	-0.098
150	-0.060	-0.069	-0.144	-0.140	-0.128	-0.160	-0.046	-0.049
160	-0.017	0.046	0.037	0.040	0.025	0.046	0.033	-0.013
170	0.028	0.105	0.169	0.196	0.161	0.158	0.100	0.034
180	0.059	0.146	0.230	0.272	0.239	0.222	0.149	0.075
190	0.075	0.171	0.256	0.304	0.274	0.247	0.174	0.102
200	0.068	0.169	0.249	0.283	0.272	0.244	0.181	0.098
210	0.047	0.147	0.206	0.230	0.217	0.191	0.164	0.084
220	0.005	0.093	0.087	0.121	0.110	0.083	0.106	0.037
230	-0.037	-0.001	-0.179	-0.125	-0.148	-0.104	-0.020	-0.019
240	-0.070	-0.229	-0.310	-0.382	-0.339	-0.292	-0.313	-0.077
250	-0.077	-0.437	-0.313	-0.412	-0.392	-0.286	-0.346	-0.106
260	-0.065	-0.235	-0.349	-0.368	-0.352	-0.309	-0.178	-0.098
270	-0.047	-0.001	-0.096	-0.107	-0.092	-0.175	-0.054	-0.061
280	0.010	0.100	0.105	0.089	0.073	0.055	0.053	-0.012
290	0.057	0.150	0.191	0.192	0.178	0.170	0.122	0.032
300	0.093	0.188	0.237	0.257	0.255	0.229	0.160	0.070
310	0.115	0.183	0.246	0.278	0.289	0.244	0.171	0.085
320	0.083	0.154	0.233	0.255	0.275	0.227	0.164	0.079
330	0.043	0.110	0.177	0.183	0.207	0.167	0.124	0.049
340	-0.001	0.032	0.075	0.057	0.095	0.063	0.057	0.004
350	-0.065	-0.071	-0.132	-0.117	-0.150	-0.087	-0.053	-0.044

a. Radial eccentricity is taken as the raw gauge reading less the n=0 and n=1 Fourier components at that axial location.

Table 53: Out-of-circularity of specimen L510-No18 based on chord gauge measurements

Angle (degrees)	Radial Eccentricity[a] (mm) at Indicated Axial Location (mm)							
	Frame 1	**Frame 2**	**Frame 3**	**Frame 4**	**Frame 5**	**Frame 6**	**Frame 7**	**Frame 8**
	80	130	180	230	280	330	380	430
0	-0.121	-0.274	-0.338	-0.419	-0.446	-0.319	-0.290	-0.079
20	-0.125	-0.253	-0.377	-0.333	-0.314	-0.327	-0.193	-0.081
40	-0.017	0.040	0.056	0.047	0.042	0.046	0.002	0.006
60	0.088	0.176	0.211	0.269	0.284	0.254	0.189	0.089
80	0.118	0.220	0.273	0.294	0.314	0.258	0.180	0.096
100	0.042	0.120	0.190	0.202	0.192	0.130	0.129	0.004
120	-0.070	-0.176	-0.291	-0.385	-0.402	-0.320	-0.291	-0.107
140	-0.095	-0.271	-0.372	-0.405	-0.336	-0.329	-0.140	-0.115
160	-0.014	0.006	0.039	0.036	-0.004	0.028	-0.009	-0.013
180	0.066	0.113	0.205	0.269	0.227	0.221	0.147	0.088
200	0.068	0.147	0.237	0.274	0.245	0.230	0.134	0.117
220	-0.003	0.076	0.107	0.140	0.139	0.105	0.112	0.042
240	-0.104	-0.177	-0.315	-0.399	-0.338	-0.282	-0.298	-0.079
260	-0.081	-0.239	-0.336	-0.325	-0.301	-0.285	-0.130	-0.107
280	0.038	0.117	0.114	0.085	0.084	0.040	0.038	-0.026
300	0.118	0.186	0.247	0.287	0.278	0.233	0.191	0.062
320	0.096	0.166	0.252	0.267	0.255	0.229	0.150	0.082
340	-0.004	0.025	0.097	0.096	0.082	0.089	0.080	0.020

a. Radial eccentricities are determined by performing Fourier decompositions of the chord height measurements, followed by expansion of the Fourier series with modified coefficients, yielding the eccentricities. The eccentricities presented here do not include the n=0 and n=1 Fourier components.

Table 54: Shell thicknesses for specimen L510-No18 based on CMM measurements

Angle (degrees)	Shell Thickness[a] (mm) at Indicated Axial Location (mm)									
	End 1	**Bay 1**	**Bay 2**	**Bay 3**	**Bay 4**	**Bay 4**	**Bay 5**	**Bay 6**	**Bay 7**	**End 2**
	66	107	153	204	235	275	306	357	403	444
0	2.968	2.950	3.005	3.018	3.000	3.010	3.014	3.080	3.054	3.110
10	2.979	2.953	2.995	3.017	3.007	3.025	3.027	3.102	3.062	3.113
20	2.970	2.953	2.990	3.016	3.012	3.032	3.038	3.117	3.058	3.101
30	2.965	2.942	2.972	2.999	2.998	3.023	3.034	3.101	3.036	3.071
40	2.963	2.927	2.955	2.981	2.975	2.998	3.012	3.059	3.005	3.035
50	2.977	2.925	2.944	2.966	2.947	2.966	2.977	3.019	2.969	2.999
60	3.002	2.938	2.950	2.945	2.920	2.933	2.937	2.975	2.936	2.953
70	3.041	2.967	2.959	2.932	2.902	2.910	2.897	2.947	2.912	2.911
80	3.079	2.999	3.020	2.933	2.885	2.892	2.873	2.923	2.890	2.893
90	3.108	3.021	3.010	2.937	2.890	2.882	2.872	2.916	2.878	2.891
100	3.105	3.034	3.038	2.965	2.901	2.904	2.892	2.920	2.875	2.907
110	3.078	3.043	3.045	3.001	2.932	2.934	2.921	2.939	2.888	2.929
120	3.042	3.027	3.040	3.007	2.965	2.959	2.944	2.963	2.911	2.964
130	3.018	2.995	3.019	3.024	2.975	2.986	2.972	2.990	2.939	2.996
140	2.996	2.963	3.011	3.038	2.997	3.007	2.997	3.029	2.975	3.025
150	2.972	2.949	2.996	3.035	3.005	3.026	3.016	3.060	3.007	3.051
160	2.957	2.944	2.991	3.023	3.006	3.032	3.032	3.081	3.032	3.071
170	2.963	2.933	2.974	3.018	2.994	3.023	3.028	3.088	3.043	3.091
180	2.969	2.918	2.961	2.982	2.972	3.000	3.017	3.080	3.047	3.096
190	2.964	2.942	2.947	2.966	2.989	2.978	2.994	3.063	3.039	3.091
200	2.945	2.917	2.954	2.960	2.940	2.962	2.974	3.047	3.028	3.069
210	2.966	2.930	2.957	2.963	2.938	2.956	2.963	3.038	3.014	3.036
220	2.972	2.935	2.968	2.965	2.938	2.953	2.956	3.019	2.991	3.010
230	3.014	2.952	2.978	2.980	2.938	2.951	2.951	3.002	2.969	2.986
240	3.042	2.986	3.001	2.985	2.943	2.953	2.952	2.992	2.949	2.967
250	3.065	3.007	3.026	2.989	2.950	2.956	2.949	2.981	2.933	2.948
260	3.076	3.018	3.030	2.985	2.958	2.955	2.942	2.974	2.913	2.934
270	3.077	3.019	3.023	2.985	2.942	2.951	2.931	2.970	2.897	2.925
280	3.064	3.016	3.017	2.978	2.937	2.947	2.933	2.958	2.893	2.923
290	3.050	3.005	3.006	2.969	2.933	2.945	2.932	2.956	2.895	2.927
300	3.038	2.985	2.989	2.967	2.928	2.939	2.932	2.956	2.901	2.946
310	3.026	2.969	2.971	2.969	2.929	2.938	2.929	2.964	2.914	2.967
320	3.006	2.958	3.012	2.987	2.939	2.950	2.944	2.982	2.946	2.994
330	2.987	2.965	2.984	3.008	2.961	2.969	2.969	3.010	2.987	3.023
340	2.969	2.949	2.996	3.016	2.975	2.986	2.987	3.029	3.019	3.056
350	2.966	2.949	2.998	3.026	2.988	3.001	3.001	3.055	3.040	3.085

a. Shell thicknesses were derived by subtracting the measured inner radii from the corresponding outer radii, after correcting the radius data for the n=1 offset.

B.5 L510-No19

Table 55: Out-of-circularity of specimen L510-No19 based on laser displacement gauge measurements – Part 1

Angle (degrees)	Radial Eccentricity[a] (mm) at Indicated Axial Location (mm)							
	Frame 1	**Bay 1**	**Frame 2**	**Bay 2**	**Frame 3**	**Bay 3**	**Frame 4**	**Bay 4**
	80	105	130	155	180	205	230	255
0	-0.220	-0.496	-0.602	-0.688	-0.853	-0.623	-0.720	**-0.769**
10	-0.144	-0.297	-0.470	-0.479	-0.589	-0.727	-0.773	**-0.793**
20	-0.002	-0.048	-0.157	-0.033	-0.028	-0.452	-0.358	**-0.148**
30	0.133	0.226	0.293	0.282	0.293	0.379	0.404	0.352
40	0.191	0.282	0.340	0.379	0.408	0.473	0.486	0.501
50	0.222	0.287	0.347	0.410	0.459	0.516	0.556	0.564
60	0.191	0.249	0.296	0.385	0.455	0.490	0.525	0.559
70	0.125	0.191	0.242	0.348	0.403	0.452	0.465	0.499
80	0.037	0.107	0.150	0.277	0.303	0.317	0.298	0.331
90	-0.071	0.010	0.043	0.086	0.008	0.024	-0.073	-0.052
100	-0.179	-0.146	-0.223	-0.330	-0.459	-0.431	-0.609	-0.522
110	-0.249	-0.337	-0.478	-0.686	-0.829	-0.663	-0.670	-0.644
120	-0.257	-0.389	-0.503	-0.781	-0.798	-0.659	-0.611	-0.696
130	-0.176	-0.368	-0.439	-0.433	-0.251	-0.482	-0.460	-0.554
140	-0.061	-0.180	-0.072	-0.042	0.104	-0.096	0.040	-0.097
150	0.065	0.110	0.250	0.226	0.289	0.239	0.329	0.242
160	0.162	0.223	0.309	0.351	0.405	0.379	0.441	0.419
170	0.206	0.278	0.354	0.413	0.469	0.477	0.515	0.506
180	0.212	0.287	0.331	0.417	0.473	0.490	0.518	0.533
190	0.168	0.258	0.296	0.408	0.417	0.487	0.444	0.502
200	0.087	0.184	0.213	0.334	0.304	0.371	0.289	0.364
210	-0.014	0.089	0.083	0.164	-0.031	0.119	-0.141	-0.017
220	-0.096	-0.058	-0.177	-0.255	-0.480	-0.456	-0.655	-0.574
230	-0.159	-0.270	-0.517	-0.598	-0.776	-0.833	-0.739	-0.728
240	-0.193	-0.387	-0.554	-0.715	-0.846	-0.725	-0.594	-0.633
250	-0.153	-0.358	-0.419	-0.509	-0.397	-0.616	-0.537	-0.542
260	-0.070	-0.190	-0.165	-0.124	0.061	-0.220	-0.112	-0.141
270	0.036	0.069	0.213	0.185	0.287	0.295	0.361	0.267
280	0.102	0.206	0.300	0.343	0.395	0.469	0.467	0.443
290	0.135	0.241	0.327	0.386	0.454	0.525	0.493	0.506
300	0.137	0.237	0.309	0.377	0.436	0.514	0.483	0.513
310	0.106	0.203	0.265	0.326	0.388	0.484	0.446	0.491
320	0.052	0.142	0.184	0.245	0.294	0.383	0.371	0.400
330	-0.027	0.041	0.080	0.093	0.132	0.199	0.150	0.126
340	-0.116	-0.057	-0.068	-0.200	-0.258	-0.373	-0.314	**-0.460**
350	-0.180	-0.341	-0.383	-0.563	-0.641	-0.725	-0.716	**-0.751**

a. Radial eccentricities are based on the filtered measurements taken at the outside of the cylinder shell. Eccentricities at corrosion patches (shaded cells with bold face font) have been corrected for the corroded shell thickness.

Table 56: Out-of-circularity of specimen L510-No19 based on laser displacement gauge measurements – Part 2

Angle (degrees)	Radial Eccentricity[a] (mm) at Indicated Axial Location (mm)							
	Bay 4	**Frame 5**	**Bay 5**	**Frame 6**	**Bay 6**	**Frame 7**	**Bay 7**	**Frame 8**
	255	280	305	330	355	380	405	430
0	**-0.769**	-0.717	-0.719	-0.785	-0.608	-0.551	-0.501	-0.292
10	**-0.793**	-0.843	-0.548	-0.526	-0.452	-0.419	-0.319	-0.247
20	**-0.148**	-0.213	-0.133	-0.173	-0.185	-0.314	-0.255	-0.135
30	0.352	0.318	0.225	0.230	0.134	0.086	0.073	0.041
40	0.501	0.481	0.383	0.392	0.327	0.360	0.291	0.156
50	0.564	0.573	0.510	0.524	0.441	0.442	0.372	0.245
60	0.559	0.581	0.534	0.557	0.456	0.446	0.380	0.260
70	0.499	0.497	0.500	0.520	0.406	0.366	0.336	0.228
80	0.331	0.326	0.341	0.365	0.273	0.228	0.245	0.146
90	-0.052	-0.165	-0.043	-0.058	0.019	0.034	0.137	0.040
100	-0.522	-0.587	-0.571	-0.700	-0.319	-0.282	-0.130	-0.098
110	-0.644	-0.630	-0.709	-0.766	-0.553	-0.551	-0.543	-0.178
120	-0.696	-0.735	-0.564	-0.494	-0.473	-0.404	-0.369	-0.181
130	-0.554	-0.403	-0.372	-0.299	-0.323	-0.274	-0.225	-0.149
140	-0.097	0.089	-0.061	0.075	-0.100	-0.153	-0.281	-0.085
150	0.242	0.323	0.212	0.279	0.130	0.183	0.043	0.004
160	0.419	0.457	0.355	0.385	0.273	0.302	0.205	0.064
170	0.506	0.522	0.440	0.448	0.336	0.316	0.252	0.094
180	0.533	0.523	0.473	0.469	0.341	0.264	0.219	0.086
190	0.502	0.454	0.459	0.419	0.289	0.184	0.177	0.054
200	0.364	0.254	0.345	0.282	0.193	0.063	0.095	0.005
210	-0.017	-0.327	-0.013	-0.197	-0.013	-0.052	0.021	-0.049
220	-0.574	-0.737	-0.573	-0.814	-0.325	-0.235	-0.101	-0.092
230	-0.728	-0.628	-0.780	-0.837	-0.538	-0.365	-0.223	-0.101
240	-0.633	-0.591	-0.572	-0.429	-0.427	-0.286	-0.224	-0.088
250	-0.542	-0.417	-0.329	-0.214	-0.233	-0.175	-0.141	-0.042
260	-0.141	0.044	-0.017	0.124	-0.030	-0.143	-0.141	0.022
270	0.267	0.325	0.238	0.293	0.159	0.114	0.029	0.088
280	0.443	0.423	0.347	0.358	0.307	0.315	0.225	0.148
290	0.506	0.480	0.399	0.395	0.339	0.333	0.273	0.177
300	0.513	0.482	0.431	0.423	0.345	0.306	0.250	0.158
310	0.491	0.461	0.427	0.411	0.306	0.243	0.187	0.120
320	0.400	0.370	0.362	0.371	0.245	0.146	0.105	0.042
330	0.126	0.091	0.111	0.187	0.077	0.019	0.004	-0.051
340	**-0.460**	-0.479	-0.359	-0.323	-0.229	-0.136	-0.103	-0.146
350	**-0.751**	-0.602	-0.727	-0.894	-0.588	-0.411	-0.366	-0.244

a. Radial eccentricities are based on the filtered measurements taken at the outside of the cylinder shell. Eccentricities at corrosion patches (shaded cells with bold face font) have been corrected for the corroded shell thickness.

Table 57: Out-of-circularity of specimen L510-No19 based on mechanical displacement gauge measurements

Angle (degrees)	Radial Eccentricity[a] (mm) at Indicated Axial Location (mm)							
	Frame 1	**Frame 2**	**Frame 3**	**Frame 4**	**Frame 5**	**Frame 6**	**Frame 7**	**Frame 8**
	80	130	180	230	280	330	380	430
0	-	-	-0.841	-0.704	-0.871	-0.642	-	-
10	-	-	-0.425	-0.771	-0.807	-0.472	-	-
20	-	-	0.063	-0.256	-0.086	-0.108	-	-
30	-	-	0.277	0.427	0.318	0.190	-	-
40	-	-	0.416	0.538	0.494	0.357	-	-
50	-	-	0.470	0.579	0.570	0.464	-	-
60	-	-	0.473	0.576	0.634	0.517	-	-
70	-	-	0.430	0.512	0.574	0.561	-	-
80	-	-	0.338	0.368	0.408	0.480	-	-
90	-	-	0.124	0.049	-0.037	0.102	-	-
100	-	-	-0.352	-0.500	-0.522	-0.515	-	-
110	-	-	-0.722	-0.707	-0.594	-0.788	-	-
120	-	-	-0.917	-0.626	-0.710	-0.609	-	-
130	-	-	-0.487	-0.593	-0.624	-0.412	-	-
140	-	-	0.000	-0.182	-0.069	-0.084	-	-
150	-	-	0.211	0.240	0.224	0.184	-	-
160	-	-	0.362	0.391	0.379	0.310	-	-
170	-	-	0.445	0.483	0.461	0.407	-	-
180	-	-	0.472	0.517	0.494	0.437	-	-
190	-	-	0.442	0.490	0.497	0.413	-	-
200	-	-	0.356	0.354	0.376	0.383	-	-
210	-	-	0.106	0.020	-0.125	0.054	-	-
220	-	-	-0.391	-0.571	-0.681	-0.644	-	-
230	-	-	-0.730	-0.801	-0.680	-0.897	-	-
240	-	-	-0.881	-0.627	-0.649	-0.491	-	-
250	-	-	-0.443	-0.573	-0.454	-0.235	-	-
260	-	-	0.073	-0.093	0.082	0.108	-	-
270	-	-	0.305	0.387	0.340	0.282	-	-
280	-	-	0.428	0.521	0.458	0.354	-	-
290	-	-	0.472	0.556	0.510	0.394	-	-
300	-	-	0.458	0.545	0.554	0.420	-	-
310	-	-	0.395	0.495	0.535	0.424	-	-
320	-	-	0.276	0.378	0.398	0.428	-	-
330	-	-	0.006	0.042	-0.138	0.059	-	-
340	-	-	-0.448	-0.637	-0.633	-0.587	-	-
350	-	-	-0.761	-0.826	-0.626	-0.846	-	-

a. Radial eccentricity is taken as the raw gauge reading less the n=0 and n=1 Fourier components at that axial location.

Table 58: Measured shell thicknesses for specimen L510-No19 – global measurements

Angle (degrees)	Shell Thickness[a] (mm) at Indicated Axial Location (mm)						
	Bay 1	**Bay 2**	**Bay 3**	**Bay 4**	**Bay 5**	**Bay 6**	**Bay 7**
	105	155	205	255	305	355	405
0	2.973	3.073	3.115	**2.631**	3.017	2.982	3.033
10	3.016	3.079	3.101	**2.582**	2.997	3.012	3.031
20	3.042	3.064	3.078	**2.531**	2.993	3.023	3.033
30	3.068	3.056	3.041	2.961	2.991	3.024	3.001
40	3.082	3.040	3.027	2.966	2.997	3.021	3.013
50	3.100	3.033	3.006	2.963	2.998	3.006	2.992
60	3.114	3.031	3.016	2.972	3.003	2.995	2.963
70	3.142	3.037	3.020	2.993	3.007	2.988	2.945
80	3.158	3.051	3.013	3.007	3.010	2.976	2.924
90	3.168	3.062	3.041	3.023	3.013	2.973	2.906
100	3.164	3.059	3.045	3.033	3.012	2.967	2.896
110	3.158	3.061	3.061	3.037	3.010	2.967	2.901
120	3.133	3.068	3.069	3.049	3.011	2.962	2.899
130	3.088	3.059	3.075	3.037	3.010	2.958	2.905
140	3.091	3.071	3.087	3.052	3.016	2.975	2.964
150	3.065	3.064	3.086	3.046	2.998	2.976	2.977
160	3.066	3.063	3.079	3.019	2.988	2.995	3.054
170	3.063	3.042	3.059	2.999	2.963	3.003	3.100
180	3.059	3.030	3.024	2.984	2.977	3.003	3.124
190	3.065	3.043	3.041	2.994	2.980	3.046	3.139
200	3.066	3.041	3.032	2.981	2.968	3.090	3.161
210	3.083	3.037	3.020	2.980	2.995	3.114	3.144
220	3.107	3.042	3.020	2.977	2.995	3.114	3.110
230	3.128	3.052	3.026	2.971	3.044	3.117	3.092
240	3.140	3.062	3.023	2.962	3.060	3.120	3.080
250	3.145	3.071	3.033	2.996	3.101	3.113	3.068
260	3.136	3.070	3.015	3.015	3.110	3.100	3.056
270	3.139	3.061	3.028	3.061	3.126	3.093	3.017
280	3.119	3.058	3.050	3.106	3.127	3.098	3.019
290	3.091	3.044	3.060	3.140	3.134	3.090	3.000
300	3.069	3.031	3.085	3.145	3.134	3.092	2.948
310	3.043	3.008	3.096	3.162	3.142	3.095	2.984
320	3.014	3.006	3.139	3.153	3.126	3.078	2.998
330	2.994	3.011	3.141	3.132	3.091	3.040	2.990
340	2.974	3.015	3.142	**2.723**	3.068	3.013	3.004
350	2.978	3.061	3.121	**2.662**	3.030	2.985	3.013

a. Shell thickness determined by ultrasonic thickness gauge measurements of the shell. Corroded locations are indicated by shaded cells with bold faced font.

Table 59: Measured shell thicknesses for specimen L510-No19 – corrosion patch measurements

Angle (degrees)	**Shell Thickness[a] (mm) at Indicated Axial Location (mm)**				
	208	231.5	255	278.5	302
-21.8	2.767	2.672	2.731	2.633	2.714
-10.9	2.729	2.596	2.688	2.609	2.671
0.0	2.681	2.591	2.633	2.606	2.599
10.9	2.635	2.608	2.580	2.578	2.542
21.8	2.583	2.554	2.529	2.516	2.515

a. Shell thickness determined by ultrasonic thickness gauge measurements of the shell.

B.6 L510-No20

Table 60: Out-of-circularity of specimen L510-No20 based on laser displacement gauge measurements – Part 1

Angle (degrees)	Radial Eccentricity[a] (mm) at Indicated Axial Location (mm)							
	Frame 1	**Bay 1**	**Frame 2**	**Bay 2**	**Frame 3**	**Bay 3**	**Frame 4**	**Bay 4**
	80	105	130	155	180	205	230	255
0	0.114	0.159	0.209	0.216	0.263	0.260	0.293	0.276
10	0.108	0.155	0.183	0.215	0.248	0.253	0.271	0.274
20	0.087	0.118	0.151	0.166	0.219	0.143	0.204	0.136
30	0.037	0.021	0.106	0.004	0.121	-0.054	-0.006	-0.066
40	-0.023	-0.181	-0.136	-0.250	-0.185	-0.223	-0.124	-0.181
50	-0.093	-0.168	-0.225	-0.233	-0.347	-0.281	-0.264	-0.299
60	-0.098	-0.147	-0.171	-0.208	-0.217	-0.233	-0.346	-0.306
70	-0.086	-0.167	-0.287	-0.269	-0.244	-0.160	-0.175	-0.155
80	-0.028	0.016	-0.124	-0.058	-0.187	-0.107	-0.132	-0.117
90	0.038	0.107	0.119	0.144	0.073	0.031	-0.082	0.010
100	0.079	0.147	0.170	0.214	0.197	0.218	0.193	0.240
110	0.103	0.157	0.198	0.242	0.274	0.318	0.348	0.367
120	0.105	0.161	0.209	0.263	0.312	0.344	0.393	0.393
130	0.075	0.131	0.201	0.249	0.296	0.291	0.345	0.337
140	0.018	0.086	0.162	0.178	0.207	0.143	0.165	0.148
150	-0.053	-0.030	0.017	-0.046	-0.008	-0.083	-0.055	-0.110
160	-0.118	-0.190	-0.316	-0.376	-0.386	-0.284	-0.121	-0.235
170	-0.151	-0.220	-0.308	-0.400	-0.440	-0.408	-0.435	**-0.435**
180	-0.145	-0.223	-0.240	-0.255	-0.259	-0.373	-0.550	**-0.532**
190	-0.114	-0.312	-0.285	-0.301	-0.296	-0.249	-0.243	**-0.253**
200	-0.034	-0.104	-0.109	-0.149	-0.194	-0.139	-0.149	**-0.069**
210	0.047	0.098	0.112	0.113	0.093	0.021	-0.098	-0.029
220	0.106	0.180	0.193	0.229	0.215	0.201	0.208	0.181
230	0.139	0.211	0.229	0.281	0.291	0.310	0.336	0.347
240	0.146	0.222	0.238	0.300	0.318	0.342	0.392	0.380
250	0.133	0.222	0.241	0.306	0.324	0.321	0.334	0.333
260	0.110	0.186	0.219	0.277	0.268	0.227	0.233	0.220
270	0.048	0.093	0.170	0.126	0.157	0.033	0.021	-0.013
280	-0.041	-0.126	-0.121	-0.244	-0.138	-0.176	-0.132	-0.166
290	-0.124	-0.268	-0.389	-0.456	-0.438	-0.314	-0.229	-0.240
300	-0.163	-0.208	-0.280	-0.287	-0.378	-0.320	-0.311	-0.314
310	-0.168	-0.267	-0.264	-0.249	-0.216	-0.232	-0.274	-0.238
320	-0.134	-0.156	-0.235	-0.186	-0.280	-0.145	-0.132	-0.119
330	-0.048	0.040	0.002	0.047	-0.073	-0.022	-0.088	-0.050
340	0.031	0.114	0.159	0.190	0.172	0.127	0.011	0.078
350	0.099	0.139	0.204	0.215	0.239	0.221	0.198	0.208

a. Radial eccentricities are based on the filtered measurements taken at the outside of the cylinder shell. Eccentricities at corrosion patches (shaded cells with bold face font) have been corrected for the corroded shell thickness.

Table 61: Out-of-circularity of specimen L510-No20 based on laser displacement gauge measurements – Part 2

Angle (degrees)	Radial Eccentricity[a] (mm) at Indicated Axial Location (mm)							
	Bay 4	**Frame 5**	**Bay 5**	**Frame 6**	**Bay 6**	**Frame 7**	**Bay 7**	**Frame 8**
	255	280	305	330	355	380	405	430
0	0.276	0.252	0.220	0.192	0.163	0.128	0.089	0.048
10	0.274	0.277	0.250	0.214	0.196	0.143	0.130	0.068
20	0.136	0.260	0.180	0.207	0.188	0.153	0.104	0.048
30	-0.066	0.031	0.037	0.172	0.136	0.124	0.041	0.007
40	-0.181	-0.152	-0.117	0.071	-0.055	0.053	-0.059	-0.047
50	-0.299	-0.242	-0.348	-0.233	-0.393	-0.212	-0.219	-0.096
60	-0.306	-0.398	-0.440	-0.616	-0.546	-0.469	-0.307	-0.119
70	-0.155	-0.259	-0.252	-0.477	-0.301	-0.339	-0.165	-0.102
80	-0.117	-0.114	-0.037	-0.072	0.037	-0.019	0.008	-0.042
90	0.010	-0.033	0.123	0.188	0.200	0.145	0.095	0.033
100	0.240	0.214	0.247	0.255	0.248	0.193	0.166	0.098
110	0.367	0.361	0.311	0.288	0.267	0.220	0.188	0.145
120	0.393	0.395	0.325	0.301	0.267	0.233	0.208	0.170
130	0.337	0.368	0.278	0.282	0.247	0.224	0.189	0.148
140	0.148	0.214	0.173	0.231	0.206	0.197	0.140	0.094
150	-0.110	-0.079	-0.001	0.139	0.141	0.145	0.069	0.013
160	-0.235	-0.149	-0.151	-0.013	-0.041	-0.007	-0.056	-0.079
170	**-0.435**	-0.379	-0.383	-0.401	-0.434	-0.410	-0.278	-0.155
180	**-0.532**	-0.601	-0.571	-0.803	-0.713	-0.643	-0.403	-0.195
190	**-0.253**	-0.339	-0.400	-0.590	-0.497	-0.388	-0.292	-0.174
200	**-0.069**	-0.164	-0.079	-0.103	-0.064	-0.017	-0.092	-0.119
210	-0.029	-0.073	0.083	0.225	0.191	0.143	0.042	-0.045
220	0.181	0.222	0.216	0.290	0.254	0.176	0.113	0.027
230	0.347	0.344	0.288	0.289	0.232	0.182	0.130	0.082
240	0.380	0.388	0.291	0.256	0.218	0.171	0.145	0.113
250	0.333	0.339	0.261	0.231	0.194	0.166	0.147	0.133
260	0.220	0.265	0.188	0.186	0.177	0.158	0.143	0.122
270	-0.013	0.054	0.065	0.141	0.156	0.139	0.118	0.084
280	-0.166	-0.135	-0.059	0.073	0.081	0.109	0.061	0.038
290	-0.240	-0.211	-0.199	-0.078	-0.160	-0.048	-0.074	-0.024
300	-0.314	-0.294	-0.322	-0.393	-0.409	-0.320	-0.194	-0.069
310	-0.238	-0.318	-0.296	-0.489	-0.361	-0.359	-0.184	-0.092
320	-0.119	-0.170	-0.138	-0.251	-0.122	-0.149	-0.075	-0.077
330	-0.050	-0.066	-0.005	0.003	0.047	0.005	-0.007	-0.049
340	0.078	0.037	0.101	0.123	0.115	0.071	0.021	-0.013
350	0.208	0.157	0.159	0.161	0.130	0.101	0.058	0.025

a. Radial eccentricities are based on the filtered measurements taken at the outside of the cylinder shell. Eccentricities at corrosion patches (shaded cells with bold face font) have been corrected for the corroded shell thickness.

Table 62: Out-of-circularity of specimen L510-No20 based on mechanical displacement gauge measurements

Angle (degrees)	Radial Eccentricity[a] (mm) at Indicated Axial Location (mm)							
	Frame 1	**Frame 2**	**Frame 3**	**Frame 4**	**Frame 5**	**Frame 6**	**Frame 7**	**Frame 8**
	80	130	180	230	280	330	380	430
0	-	-	0.258	0.346	0.063	0.113	-	-
10	-	-	0.248	0.336	0.089	0.139	-	-
20	-	-	0.224	0.247	0.115	0.165	-	-
30	-	-	0.126	0.007	0.051	0.189	-	-
40	-	-	-0.195	-0.094	-0.049	0.157	-	-
50	-	-	-0.387	-0.229	-0.031	-0.100	-	-
60	-	-	-0.235	-0.279	-0.129	-0.495	-	-
70	-	-	-0.272	-0.248	-0.113	-0.533	-	-
80	-	-	-0.269	-0.180	-0.075	-0.208	-	-
90	-	-	0.025	-0.169	-0.061	0.056	-	-
100	-	-	0.188	0.112	-0.017	0.171	-	-
110	-	-	0.266	0.294	0.094	0.226	-	-
120	-	-	0.318	0.348	0.139	0.244	-	-
130	-	-	0.330	0.354	0.156	0.242	-	-
140	-	-	0.283	0.267	0.148	0.229	-	-
150	-	-	0.116	0.018	0.083	0.207	-	-
160	-	-	-0.261	-0.135	-0.027	0.183	-	-
170	-	-	-0.507	-0.356	-0.071	-0.063	-	-
180	-	-	-0.309	-0.547	-0.248	-0.516	-	-
190	-	-	-0.281	-0.322	-0.257	-0.622	-	-
200	-	-	-0.312	-0.094	0.020	-0.325	-	-
210	-	-	0.056	-0.067	-0.015	0.093	-	-
220	-	-	0.225	0.164	-0.008	0.163	-	-
230	-	-	0.296	0.348	0.115	0.159	-	-
240	-	-	0.332	0.377	0.114	0.152	-	-
250	-	-	0.338	0.363	0.096	0.145	-	-
260	-	-	0.305	0.252	0.080	0.140	-	-
270	-	-	0.167	-0.001	0.052	0.139	-	-
280	-	-	-0.252	-0.141	-0.051	0.142	-	-
290	-	-	-0.537	-0.269	-0.056	-0.009	-	-
300	-	-	-0.316	-0.365	-0.068	-0.271	-	-
310	-	-	-0.251	-0.287	-0.067	-0.281	-	-
320	-	-	-0.257	-0.164	-0.045	-0.188	-	-
330	-	-	0.074	-0.124	-0.030	0.013	-	-
340	-	-	0.214	0.052	-0.012	0.059	-	-
350	-	-	0.250	0.187	0.014	0.086	-	-

a. Radial eccentricity is taken as the raw gauge reading less the n=0 and n=1 Fourier components at that axial location.

Table 63: Measured shell thicknesses for specimen L510-No20 – global measurements

Angle (degrees)	Shell Thickness[a] (mm) at Indicated Axial Location (mm)						
	Bay 1	**Bay 2**	**Bay 3**	**Bay 4**	**Bay 5**	**Bay 6**	**Bay 7**
	105	155	205	255	305	355	405
0	3.086	3.060	3.109	3.140	3.135	3.147	2.989
10	3.082	3.052	3.074	3.096	3.107	3.076	2.971
20	3.086	3.043	3.040	3.054	3.094	3.004	2.945
30	3.058	3.024	2.998	2.967	3.041	3.232	2.927
40	3.056	3.016	2.996	2.956	3.017	3.207	2.941
50	3.037	3.009	2.994	2.914	2.978	2.941	2.950
60	3.022	3.016	3.001	2.930	2.959	2.952	2.969
70	3.025	3.008	2.961	2.920	2.920	2.936	2.978
80	3.028	3.009	2.989	2.945	2.910	3.147	3.006
90	3.024	3.004	3.014	2.961	2.936	2.912	3.014
100	3.019	3.036	3.033	2.981	2.959	2.922	3.037
110	3.007	3.037	3.028	2.996	2.972	2.916	3.056
120	2.992	3.028	3.038	3.012	3.000	3.156	3.067
130	2.947	3.009	3.065	3.026	3.020	2.961	3.090
140	2.944	2.997	3.068	3.024	3.006	2.975	3.048
150	2.889	2.949	3.039	3.022	3.038	2.989	3.093
160	2.879	2.931	3.021	3.031	3.031	2.972	3.045
170	2.856	2.903	3.038	**2.559**	2.996	2.964	3.009
180	2.871	2.869	2.995	**2.530**	2.983	3.238	3.035
190	2.893	2.845	2.954	**2.497**	2.960	2.934	3.003
200	2.927	2.819	2.913	**2.447**	2.914	3.176	3.000
210	2.964	2.843	2.827	2.878	2.873	3.114	2.984
220	2.985	2.866	2.823	2.855	2.841	3.093	2.955
230	3.008	2.931	2.840	2.817	2.841	2.871	2.960
240	3.034	2.988	2.869	2.830	2.841	3.118	2.959
250	3.044	3.040	2.924	2.844	2.842	3.091	2.968
260	3.061	3.076	2.984	2.869	2.866	3.091	2.974
270	3.071	3.107	3.066	2.919	2.891	2.886	2.998
280	3.086	3.135	3.125	2.983	2.934	2.921	3.025
290	3.083	3.155	3.178	3.048	2.959	2.922	3.039
300	3.082	3.160	3.212	3.125	2.993	2.947	3.027
310	3.065	3.160	3.224	3.177	3.034	3.178	3.049
320	3.068	3.151	3.233	3.198	3.077	2.972	3.047
330	3.077	3.133	3.222	3.214	3.102	2.964	2.971
340	3.062	3.114	3.192	3.193	3.130	2.955	3.021
350	3.065	3.085	3.149	3.172	3.146	3.219	3.009

a. Shell thickness determined by ultrasonic thickness gauge measurements of the shell. Corroded locations are indicated by shaded cells with bold faced font.

Table 64: Measured shell thicknesses for specimen L510-No20 – corrosion patch measurements

Angle (degrees)	**Shell Thickness[a] (mm) at Indicated Axial Location (mm)**				
	208	231.5	255	278.5	302
163.0	2.616	2.574	2.575	2.584	2.571
173.2	2.594	2.573	2.580	2.583	2.535
183.5	2.562	2.576	2.543	2.599	2.503
193.7	2.536	2.575	2.494	2.593	2.469
204.0	2.507	2.579	2.458	2.615	2.453

a. Shell thickness determined by ultrasonic thickness gauge measurements of the shell.

B.7 L510-No25

Table 65: Outer radii of specimen L510-No25 based on CMM measurements – Part 1

Angle (°)	Outer radii [a] (mm) at indicated axial location (mm)								
	End Bay 1	**Frame 1**	**Bay 1**	**Frame 2**	**Bay 2**	**Frame 3**	**Bay 3**	**Frame 4**	**Bay 4**
	66	79	107	125	153	175	204	220	235
0	122.947	122.942	122.840	122.812	122.934	122.876	122.671	122.772	122.996
10	122.908	122.888	122.744	122.692	122.802	122.849	122.666	122.523	122.669
20	122.903	122.888	122.881	122.870	122.674	122.716	122.739	122.610	122.689
30	122.922	122.923	122.971	122.979	122.794	122.842	122.985	123.051	123.056
40	122.955	122.972	123.037	123.089	123.103	123.167	123.217	123.306	123.337
50	122.997	123.024	123.095	123.168	123.241	123.318	123.339	123.397	123.430
60	123.033	123.062	123.135	123.210	123.284	123.373	123.382	123.428	123.438
70	123.045	123.076	123.145	123.214	123.275	123.363	123.368	123.403	123.398
80	123.029	123.056	123.117	123.175	123.219	123.292	123.303	123.324	123.306
90	122.989	123.001	123.049	123.093	123.112	123.163	123.181	123.182	123.153
100	122.926	122.915	122.941	122.962	122.935	122.957	122.946	122.952	122.904
110	122.854	122.816	122.767	122.747	122.637	122.517	122.423	122.398	122.447
120	122.791	122.725	122.518	122.332	122.317	122.109	121.776	121.792	121.967
130	122.758	122.678	122.434	122.226	122.210	122.111	121.790	121.595	121.700
140	122.760	122.685	122.545	122.431	122.198	122.120	121.892	121.716	121.765
150	122.792	122.734	122.651	122.566	122.326	122.293	122.264	122.188	122.123
160	122.844	122.804	122.752	122.713	122.631	122.579	122.546	122.509	122.454
170	122.903	122.883	122.855	122.842	122.812	122.775	122.721	122.681	122.639
180	122.962	122.956	122.948	122.946	122.930	122.917	122.861	122.821	122.777
190	123.009	123.010	123.016	123.024	123.016	123.019	122.973	122.936	122.892
200	123.029	123.034	123.050	123.068	123.068	123.086	123.052	123.019	122.978
210	123.028	123.026	123.044	123.070	123.079	123.105	123.096	123.064	123.032
220	123.002	122.990	123.005	123.025	123.024	123.061	123.045	123.048	123.008
230	122.969	122.941	122.920	122.920	122.850	122.783	122.716	122.703	122.776
240	122.944	122.901	122.783	122.677	122.641	122.475	122.297	122.329	122.494
250	122.940	122.894	122.738	122.595	122.625	122.586	122.375	122.164	122.309
260	122.960	122.929	122.881	122.836	122.593	122.648	122.577	122.397	122.477
270	123.006	122.997	123.022	123.002	122.651	122.837	122.967	122.988	122.991
280	123.067	123.078	123.136	123.185	123.188	123.273	123.330	123.410	123.431
290	123.125	123.162	123.248	123.340	123.450	123.546	123.579	123.653	123.687
300	123.174	123.228	123.345	123.455	123.569	123.695	123.739	123.820	123.850
310	123.201	123.267	123.404	123.523	123.632	123.772	123.835	123.924	123.957
320	123.198	123.265	123.413	123.539	123.642	123.781	123.867	123.967	124.006
330	123.161	123.221	123.374	123.499	123.590	123.722	123.832	123.935	123.986
340	123.096	123.141	123.288	123.397	123.460	123.580	123.674	123.800	123.840
350	123.016	123.040	123.123	123.205	123.210	123.226	123.222	123.315	123.452

a. Raw radial measurements, i.e. not corrected for the offset of the measurement apparatus from the axis of revolution.

Table 66: Outer radii of specimen L510-No25 based on CMM measurements – Part 2

Angle (°)	Outer radii [a] (mm) at indicated axial location (mm)								
	Bay 4	**Frame 5**	**Bay 5**	**Frame 6**	**Bay 6**	**Frame 7**	**Bay 7**	**Frame 8**	**End Bay 2**
	275	290	306	335	357	385	403	431	444
0	122.986	122.798	122.711	122.922	122.968	122.847	122.795	122.917	122.932
10	122.674	122.505	122.571	122.727	122.763	122.765	122.727	122.862	122.888
20	122.711	122.524	122.584	122.631	122.520	122.632	122.772	122.863	122.884
30	123.101	123.038	122.955	122.801	122.586	122.714	122.848	122.906	122.915
40	123.413	123.419	123.303	123.212	123.125	123.143	123.055	122.981	122.967
50	123.504	123.509	123.458	123.418	123.359	123.297	123.182	123.058	123.027
60	123.504	123.513	123.483	123.467	123.387	123.312	123.215	123.110	123.071
70	123.459	123.465	123.451	123.442	123.348	123.279	123.206	123.129	123.087
80	123.363	123.373	123.356	123.354	123.271	123.217	123.164	123.107	123.074
90	123.210	123.226	123.222	123.209	123.163	123.137	123.098	123.048	123.036
100	122.951	123.007	123.003	122.999	123.014	123.042	123.003	122.958	122.956
110	122.505	122.501	122.522	122.692	122.741	122.821	122.825	122.841	122.869
120	122.049	121.926	121.813	122.205	122.323	122.358	122.565	122.730	122.790
130	121.746	121.648	121.759	122.009	122.098	122.295	122.453	122.658	122.739
140	121.781	121.650	121.823	122.042	122.074	122.200	122.376	122.642	122.730
150	122.154	122.171	122.227	122.246	122.195	122.328	122.460	122.693	122.770
160	122.501	122.577	122.579	122.591	122.630	122.731	122.739	122.800	122.844
170	122.670	122.734	122.773	122.819	122.876	122.927	122.911	122.901	122.926
180	122.787	122.846	122.895	122.957	122.989	123.016	123.000	122.989	122.997
190	122.882	122.934	122.982	123.045	123.050	123.063	123.051	123.047	123.046
200	122.954	122.998	123.039	123.088	123.075	123.080	123.070	123.066	123.062
210	122.995	123.032	123.063	123.083	123.072	123.074	123.063	123.052	123.050
220	122.957	123.012	123.014	123.024	123.030	123.048	123.028	123.008	123.016
230	122.715	122.692	122.739	122.863	122.879	122.925	122.929	122.950	122.976
240	122.437	122.344	122.319	122.505	122.617	122.674	122.788	122.899	122.943
250	122.267	122.171	122.284	122.447	122.524	122.688	122.761	122.880	122.933
260	122.442	122.336	122.414	122.539	122.475	122.606	122.749	122.905	122.957
270	122.948	122.923	122.897	122.839	122.685	122.802	122.885	122.978	123.010
280	123.402	123.397	123.316	123.260	123.193	123.204	123.130	123.080	123.081
290	123.642	123.626	123.570	123.538	123.473	123.413	123.298	123.178	123.146
300	123.800	123.777	123.714	123.674	123.584	123.503	123.387	123.250	123.194
310	123.909	123.873	123.794	123.739	123.622	123.533	123.420	123.280	123.214
320	123.963	123.919	123.822	123.743	123.612	123.520	123.406	123.272	123.200
330	123.953	123.906	123.799	123.685	123.557	123.470	123.358	123.221	123.158
340	123.818	123.807	123.681	123.560	123.451	123.382	123.277	123.136	123.090
350	123.431	123.339	123.331	123.338	123.251	123.198	123.109	123.029	123.007

a. Raw radial measurements, i.e. not corrected for the offset of the measurement apparatus from the axis of revolution.

Table 67: Inner radii of specimen L510-No25 based on CMM measurements – Part 1

Angle (°)	Inner radii [a] (mm) at indicated axial location (mm)								
	End Bay 1	**Frame 1**	**Bay 1**	**Frame 2**	**Bay 2**	**Frame 3**	**Bay 3**	**Frame 4**	**Bay 4**
	66	79	107	125	153	175	204	220	235
0	119.928	109.870	119.828	109.754	119.913	109.829	119.652	109.714	119.952
10	119.930	109.855	119.754	109.677	119.806	109.825	119.684	109.496	119.666
20	119.963	109.898	119.915	109.886	119.701	109.732	119.774	109.620	119.721
30	119.996	109.947	120.034	110.023	119.831	109.869	120.049	110.080	120.112
40	120.043	110.023	120.129	110.145	120.179	110.208	120.306	110.368	120.428
50	120.089	110.082	120.191	110.229	120.328	110.362	120.434	110.465	120.521
60	120.139	110.126	120.220	110.268	120.365	110.411	120.468	110.488	120.517
70	120.151	110.136	120.225	110.266	120.354	110.393	120.452	110.447	120.458
80	120.115	110.103	120.200	110.221	120.290	110.314	120.379	110.347	120.343
90	120.062	110.032	120.128	110.134	120.171	110.176	120.246	110.186	120.172
100	119.980	109.931	120.004	109.996	119.982	109.957	119.992	109.938	119.906
110	119.897	109.815	119.818	109.767	119.673	109.497	119.445	109.354	119.450
120	119.815	109.708	119.556	109.350	119.346	109.121	118.803	108.795	118.992
130	119.764	109.641	119.453	109.240	119.230	109.109	118.824	108.602	118.739
140	119.755	109.635	119.546	109.424	119.197	109.122	118.909	108.732	118.805
150	119.768	109.663	119.632	109.538	119.302	109.272	119.284	109.184	119.148
160	119.809	109.721	119.727	109.663	119.605	109.535	119.559	109.504	119.472
170	119.865	109.792	119.827	109.771	119.774	109.711	119.720	109.647	119.639
180	119.937	109.871	119.920	109.877	119.878	109.834	119.835	109.763	119.750
190	120.006	109.943	119.992	109.960	119.956	109.930	119.933	109.863	119.841
200	120.049	109.993	120.045	110.017	120.026	110.004	120.018	109.946	119.927
210	120.072	110.023	120.070	110.045	120.067	110.049	120.083	110.006	119.998
220	120.064	110.017	120.059	110.032	120.042	110.035	120.062	110.014	119.997
230	120.056	110.001	120.005	109.959	119.905	109.785	119.759	109.688	119.798
240	120.046	109.982	119.890	109.754	119.732	109.537	119.372	109.369	119.550
250	120.046	109.978	119.856	109.709	119.746	109.620	119.479	109.225	119.391
260	120.062	110.003	119.997	109.955	119.723	109.746	119.683	109.468	119.571
270	120.082	110.045	120.116	110.113	119.746	109.926	120.074	110.052	120.082
280	120.122	110.098	120.203	110.259	120.287	110.334	120.360	110.488	120.214
290	120.146	110.152	120.282	110.371	120.519	110.578	120.436	110.703	120.312
300	120.170	110.191	120.338	110.437	120.586	110.682	120.529	110.830	120.431
310	120.183	110.207	120.363	110.469	120.601	110.710	120.638	110.889	120.569
320	120.168	110.184	120.348	110.457	120.572	110.680	120.757	110.893	120.716
330	120.124	110.122	120.301	110.400	120.503	110.598	120.766	110.837	120.868
340	120.044	110.034	120.230	110.300	120.384	110.455	120.615	110.690	120.763
350	119.973	109.937	120.087	110.114	120.155	110.109	120.170	110.191	120.378

a. Raw radial measurements, i.e. not corrected for the offset of the measurement apparatus from the axis of revolution.

Table 68: Inner radii of specimen L510-No25 based on CMM measurements – Part 2

Angle (°)	Inner radii [a] (mm) at indicated axial location (mm)								
	Bay 4	**Frame 5**	**Bay 5**	**Frame 6**	**Bay 6**	**Frame 7**	**Bay 7**	**Frame 8**	**End Bay 2**
	275	290	306	335	357	385	403	431	444
0	119.959	109.746	119.705	109.891	119.944	109.850	119.821	109.954	119.990
10	119.688	109.470	119.601	109.722	119.767	109.790	119.764	109.904	119.950
20	119.753	109.523	119.629	109.643	119.538	109.671	119.816	109.901	119.940
30	120.171	110.037	120.023	109.811	119.605	109.747	119.895	109.925	119.940
40	120.513	110.467	120.405	110.222	120.161	110.157	120.093	109.969	119.954
50	120.603	110.562	120.567	110.433	120.387	110.301	120.199	110.016	119.988
60	120.588	110.562	120.586	110.473	120.397	110.291	120.204	110.047	120.018
70	120.526	110.494	120.525	110.435	120.352	110.242	120.182	110.051	120.026
80	120.407	110.379	120.419	110.337	120.278	110.174	120.139	110.022	120.005
90	120.233	110.220	120.274	110.186	120.171	110.097	120.074	109.970	119.967
100	119.973	109.991	120.047	109.974	120.021	110.011	119.990	109.890	119.907
110	119.529	109.469	119.549	109.668	119.750	109.792	119.822	109.793	119.835
120	119.087	108.943	118.836	109.208	119.332	109.353	119.573	109.698	119.772
130	118.808	108.654	118.820	109.019	119.109	109.302	119.469	109.640	119.734
140	118.838	108.659	118.875	109.045	119.080	109.207	119.390	109.630	119.732
150	119.196	109.143	119.276	109.233	119.180	109.325	119.465	109.681	119.773
160	119.533	109.562	119.630	109.561	119.623	109.715	119.747	109.770	119.845
170	119.684	109.699	119.817	109.778	119.877	109.912	119.924	109.873	119.916
180	119.774	109.792	119.922	109.909	119.990	109.995	120.010	109.962	119.983
190	119.841	109.869	119.996	109.991	120.042	110.039	120.054	110.021	120.040
200	119.921	109.931	120.045	110.031	120.066	110.050	120.073	110.046	120.065
210	119.978	109.977	120.072	110.030	120.057	110.043	120.064	110.034	120.055
220	119.961	109.970	120.029	109.973	120.009	110.014	120.028	109.983	120.016
230	119.743	109.661	119.760	109.813	119.858	109.883	119.919	109.913	119.956
240	119.498	109.369	119.361	109.487	119.602	109.650	119.773	109.843	119.898
250	119.352	109.210	119.353	109.448	119.528	109.671	119.745	109.813	119.870
260	119.538	109.396	119.495	109.569	119.502	109.604	119.736	109.841	119.893
270	120.046	109.981	119.997	109.891	119.726	109.810	119.886	109.927	119.954
280	120.491	110.487	120.433	110.333	120.267	110.229	120.154	110.048	120.036
290	120.721	110.699	120.683	110.622	120.559	110.466	120.353	110.167	120.121
300	120.845	110.817	120.802	110.735	120.660	110.561	120.458	110.259	120.193
310	120.914	110.866	120.844	110.760	120.673	110.581	120.496	110.304	120.245
320	120.931	110.867	120.825	110.716	120.631	110.541	120.472	110.299	120.257
330	120.894	110.826	120.774	110.625	120.541	110.465	120.401	110.250	120.229
340	120.754	110.710	120.631	110.486	120.412	110.365	120.306	110.160	120.155
350	120.369	110.227	120.266	110.273	120.213	110.176	120.133	110.054	120.064

a. Raw radial measurements, i.e. not corrected for the offset of the measurement apparatus from the axis of revolution.

Table 69: Out-of-circularity of specimen L510-No25 based on mechanical displacement gauge measurements

Angle (degrees)	Radial Eccentricity[a] (mm) at Indicated Axial Location (mm)							
	Frame 1	**Frame 2**	**Frame 3**	**Frame 4**	**Frame 5**	**Frame 6**	**Frame 7**	**Frame 8**
	80	130	180	230	280	330	380	430
0	-0.155	-0.382	-0.456	-0.753	-0.661	-0.400	-0.347	-0.155
10	-0.181	-0.518	-0.477	-0.883	-0.903	-0.593	-0.462	-0.198
20	-0.155	-0.302	-0.550	-0.743	-0.857	-0.674	-0.507	-0.184
30	-0.091	-0.141	-0.399	-0.212	-0.271	-0.477	-0.405	-0.128
40	-0.019	0.015	-0.012	0.132	0.196	-0.006	0.046	-0.040
50	0.059	0.138	0.226	0.326	0.371	0.293	0.254	0.058
60	0.121	0.236	0.369	0.458	0.473	0.424	0.312	0.137
70	0.155	0.285	0.429	0.528	0.519	0.469	0.351	0.174
80	0.149	0.290	0.428	0.545	0.526	0.472	0.335	0.194
90	0.137	0.281	0.412	0.509	0.466	0.398	0.309	0.163
100	0.058	0.180	0.249	0.345	0.322	0.241	0.260	0.098
110	-0.037	-0.011	-0.145	-0.180	-0.132	-0.012	0.065	0.000
120	-0.126	-0.417	-0.544	-0.786	-0.620	-0.471	-0.376	-0.107
130	-0.162	-0.483	-0.494	-0.867	-0.849	-0.626	-0.412	-0.178
140	-0.148	-0.296	-0.450	-0.713	-0.796	-0.570	-0.520	-0.203
150	-0.092	-0.152	-0.296	-0.162	-0.243	-0.374	-0.426	-0.150
160	-0.031	0.004	-0.023	0.133	0.147	-0.026	-0.018	-0.072
170	0.034	0.130	0.150	0.292	0.299	0.191	0.171	0.007
180	0.089	0.210	0.301	0.395	0.383	0.326	0.266	0.087
190	0.124	0.254	0.367	0.459	0.435	0.388	0.286	0.130
200	0.120	0.262	0.389	0.477	0.440	0.385	0.271	0.136
210	0.091	0.229	0.355	0.448	0.406	0.341	0.236	0.111
220	0.029	0.137	0.266	0.330	0.305	0.225	0.174	0.055
230	-0.042	-0.030	-0.109	-0.185	-0.144	0.006	0.004	-0.017
240	-0.105	-0.321	-0.488	-0.656	-0.529	-0.423	-0.277	-0.085
250	-0.130	-0.435	-0.479	-0.844	-0.796	-0.546	-0.297	-0.123
260	-0.119	-0.268	-0.457	-0.685	-0.710	-0.551	-0.419	-0.120
270	-0.081	-0.144	-0.348	-0.172	-0.211	-0.333	-0.317	-0.101
280	-0.011	0.007	0.010	0.158	0.175	0.042	0.040	-0.028
290	0.060	0.131	0.239	0.325	0.329	0.272	0.216	0.061
300	0.120	0.221	0.352	0.425	0.415	0.360	0.282	0.120
310	0.147	0.271	0.398	0.485	0.454	0.397	0.292	0.152
320	0.143	0.275	0.386	0.492	0.461	0.374	0.265	0.145
330	0.096	0.231	0.321	0.439	0.419	0.303	0.216	0.102
340	0.021	0.134	0.184	0.309	0.318	0.175	0.131	0.025
350	-0.068	-0.021	-0.105	-0.168	-0.137	-0.004	0.001	-0.064

a. Radial eccentricity is taken as the raw gauge reading less the n=0 and n=1 Fourier components at that axial location.

Table 70: Out-of-circularity of specimen L510-No25 based on chord gauge measurements

Angle (degrees)	Radial Eccentricity[a] (mm) at Indicated Axial Location (mm)							
	Frame 1	**Frame 2**	**Frame 3**	**Frame 4**	**Frame 5**	**Frame 6**	**Frame 7**	**Frame 8**
	80	130	180	230	280	330	380	430
0	-0.152	-0.416	-0.514	-0.660	-0.588	-0.387	-0.340	-0.156
20	-0.161	-0.229	-0.467	-0.635	-0.820	-0.635	-0.473	-0.178
40	-0.030	-0.005	0.006	0.170	0.231	-0.030	0.037	-0.039
60	0.119	0.247	0.406	0.474	0.452	0.389	0.317	0.137
80	0.159	0.253	0.399	0.511	0.516	0.439	0.310	0.186
100	0.062	0.195	0.253	0.323	0.289	0.255	0.232	0.086
120	-0.117	-0.394	-0.600	-0.779	-0.585	-0.403	-0.353	-0.105
140	-0.146	-0.245	-0.414	-0.720	-0.814	-0.541	-0.475	-0.192
160	-0.035	-0.036	-0.028	0.106	0.156	-0.030	-0.006	-0.072
180	0.093	0.204	0.334	0.411	0.350	0.307	0.267	0.094
200	0.126	0.213	0.360	0.489	0.455	0.360	0.271	0.138
220	0.031	0.159	0.285	0.400	0.312	0.211	0.179	0.050
240	-0.114	-0.298	-0.506	-0.557	-0.446	-0.404	-0.270	-0.095
260	-0.124	-0.218	-0.405	-0.694	-0.745	-0.507	-0.427	-0.135
280	-0.010	-0.029	-0.029	0.085	0.156	0.045	0.032	-0.011
300	0.118	0.223	0.353	0.361	0.352	0.371	0.292	0.126
320	0.144	0.223	0.341	0.408	0.438	0.371	0.269	0.141
340	0.038	0.153	0.225	0.305	0.291	0.188	0.138	0.024

a. Radial eccentricities are determined by performing Fourier decompositions of the chord height measurements, followed by expansion of the Fourier series with modified coefficients, yielding the eccentricities. The eccentricities presented here do not include the n=0 and n=1 Fourier components.

Table 71: Shell thicknesses for specimen L510-No25 based on CMM measurements

Angle (degrees)	Shell Thickness[a] (mm) at Indicated Axial Location (mm)									
	End 1	**Bay 1**	**Bay 2**	**Bay 3**	**Bay 4**	**Bay 4**	**Bay 5**	**Bay 6**	**Bay 7**	**End 2**
	66	107	153	204	235	275	306	357	403	444
0	3.020	3.007	3.022	3.000	2.996	3.025	3.005	3.032	2.995	2.966
10	2.981	2.987	3.000	2.972	2.967	2.987	2.970	3.004	2.981	2.961
20	2.944	2.964	2.974	2.961	2.956	2.959	2.956	2.987	2.971	2.964
30	2.931	2.938	2.967	2.943	2.945	2.934	2.934	2.985	2.966	2.992
40	2.918	2.910	2.927	2.924	2.934	2.905	2.900	2.965	2.970	3.026
50	2.914	2.908	2.918	2.927	2.946	2.906	2.894	2.973	2.987	3.047
60	2.901	2.920	2.921	2.942	2.980	2.922	2.901	2.987	3.011	3.057
70	2.901	2.926	2.925	2.951	3.008	2.941	2.930	2.992	3.020	3.061
80	2.921	2.925	2.931	2.964	3.049	2.962	2.942	2.985	3.017	3.064
90	2.934	2.930	2.944	2.980	3.072	2.985	2.952	2.985	3.013	3.060
100	2.953	2.945	2.954	2.999	3.101	2.986	2.960	2.983	2.998	3.035
110	2.963	2.958	2.967	3.026	3.099	2.984	2.978	2.981	2.985	3.018
120	2.982	2.971	2.971	3.019	3.084	2.969	2.981	2.980	2.972	2.997
130	2.999	2.990	2.981	3.013	3.061	2.945	2.942	2.978	2.962	2.983
140	3.008	3.007	2.999	3.024	3.061	2.948	2.952	2.981	2.962	2.973
150	3.026	3.027	3.024	3.019	3.062	2.964	2.955	3.004	2.972	2.972
160	3.036	3.032	3.023	3.019	3.064	2.972	2.952	2.995	2.969	2.973
170	3.038	3.034	3.037	3.027	3.063	2.989	2.958	2.989	2.965	2.985
180	3.024	3.032	3.048	3.044	3.079	3.014	2.973	2.989	2.969	2.989
190	3.000	3.027	3.058	3.052	3.082	3.041	2.986	3.001	2.979	2.983
200	2.976	3.005	3.038	3.036	3.069	3.031	2.993	3.002	2.981	2.977
210	2.951	2.974	3.010	3.008	3.028	3.014	2.989	3.012	2.987	2.978
220	2.932	2.944	2.977	2.969	2.992	2.991	2.983	3.019	2.991	2.987
230	2.907	2.912	2.942	2.937	2.936	2.967	2.977	3.022	3.006	3.011
240	2.891	2.887	2.905	2.896	2.891	2.932	2.954	3.017	3.014	3.040
250	2.887	2.876	2.878	2.862	2.845	2.908	2.927	3.001	3.019	3.063
260	2.891	2.877	2.866	2.853	2.825	2.896	2.915	2.978	3.021	3.069
270	2.917	2.898	2.904	2.850	2.812	2.895	2.895	2.968	3.010	3.066
280	2.938	2.925	2.898	2.923	3.120	2.903	2.878	2.936	2.991	3.058
290	2.973	2.958	2.931	3.096	3.267	2.913	2.882	2.925	2.963	3.042
300	2.998	2.998	2.981	3.162	3.315	2.946	2.907	2.935	2.948	3.021
310	3.014	3.032	3.032	3.152	3.282	2.988	2.946	2.962	2.946	2.993
320	3.027	3.056	3.069	3.067	3.195	3.026	2.993	2.993	2.957	2.967
330	3.035	3.065	3.089	3.028	3.025	3.054	3.022	3.028	2.981	2.955
340	3.051	3.051	3.077	3.026	3.001	3.060	3.047	3.050	2.993	2.961
350	3.043	3.030	3.058	3.026	3.005	3.060	3.063	3.049	2.999	2.969

a. Shell thicknesses were derived by subtracting the measured inner radii from the corresponding outer radii, after correcting the radius data for the n=1 offset.

B.8 L510-No26

Table 72: Outer radii of specimen L510-No26 based on CMM measurements – Part 1

Angle (°)	Outer radii [a] (mm) at indicated axial location (mm)								
	End Bay 1	**Frame 1**	**Bay 1**	**Frame 2**	**Bay 2**	**Frame 3**	**Bay 3**	**Frame 4**	**Bay 4**
	66	79	107	125	153	175	204	220	235
0	122.930	122.928	122.948	122.911	122.902	122.836	122.627	122.850	122.900
10	122.859	122.852	122.836	122.800	122.746	122.669	122.562	122.589	122.730
20	122.827	122.819	122.783	122.696	122.674	122.534	122.451	122.585	122.741
30	122.827	122.829	122.843	122.834	122.866	122.886	122.938	123.071	123.136
40	122.848	122.870	122.959	123.057	123.122	123.266	123.316	123.402	123.425
50	122.880	122.919	123.037	123.144	123.235	123.361	123.416	123.470	123.492
60	122.909	122.956	123.071	123.175	123.252	123.361	123.400	123.458	123.471
70	122.924	122.969	123.066	123.157	123.216	123.302	123.332	123.389	123.397
80	122.918	122.952	123.027	123.097	123.140	123.208	123.232	123.275	123.278
90	122.893	122.906	122.951	122.999	123.028	123.078	123.099	123.114	123.110
100	122.854	122.843	122.849	122.870	122.872	122.904	122.888	122.892	122.847
110	122.817	122.779	122.723	122.680	122.605	122.513	122.453	122.389	122.233
120	122.794	122.732	122.600	122.421	122.280	122.072	121.914	121.829	121.492
130	122.797	122.720	122.556	122.382	122.210	122.046	121.833	121.670	121.599
140	122.826	122.750	122.589	122.409	122.241	122.057	121.855	121.685	121.748
150	122.881	122.817	122.693	122.568	122.453	122.352	122.246	122.173	122.154
160	122.953	122.905	122.844	122.790	122.727	122.705	122.640	122.614	122.543
170	123.028	122.996	122.955	122.936	122.902	122.882	122.838	122.794	122.733
180	123.093	123.069	123.047	123.038	123.012	123.001	122.952	122.912	122.853
190	123.117	123.110	123.100	123.097	123.074	123.065	123.015	122.984	122.933
200	123.120	123.116	123.111	123.113	123.097	123.096	123.051	123.020	122.978
210	123.099	123.090	123.084	123.088	123.080	123.088	123.058	123.020	122.983
220	123.062	123.043	123.026	123.026	123.015	123.031	122.996	122.963	122.895
230	123.022	122.988	122.942	122.908	122.846	122.792	122.696	122.594	122.441
240	122.990	122.944	122.855	122.701	122.591	122.439	122.159	122.227	122.010
250	122.978	122.930	122.832	122.701	122.581	122.447	122.214	122.188	122.185
260	122.992	122.953	122.874	122.765	122.694	122.478	122.244	122.374	122.451
270	123.030	123.014	122.990	122.952	122.943	122.848	122.824	123.034	123.077
280	123.088	123.097	123.148	123.210	123.262	123.382	123.434	123.511	123.539
290	123.148	123.184	123.289	123.387	123.478	123.618	123.693	123.755	123.782
300	123.195	123.251	123.386	123.503	123.600	123.739	123.813	123.902	123.930
310	123.216	123.285	123.435	123.558	123.662	123.792	123.868	123.973	124.008
320	123.204	123.274	123.425	123.556	123.656	123.791	123.873	123.977	124.016
330	123.163	123.222	123.365	123.496	123.605	123.746	123.835	123.914	123.952
340	123.095	123.137	123.262	123.384	123.484	123.637	123.703	123.770	123.781
350	123.010	123.032	123.109	123.180	123.225	123.258	123.250	123.319	123.367

a. Raw radial measurements, i.e. not corrected for the offset of the measurement apparatus from the axis of revolution.

Table 73: Outer radii of specimen L510-No26 based on CMM measurements – Part 2

Angle (°)	Outer radii [a] (mm) at indicated axial location (mm)								
	Bay 4	**Frame 5**	**Bay 5**	**Frame 6**	**Bay 6**	**Frame 7**	**Bay 7**	**Frame 8**	**End Bay 2**
	275	290	306	335	357	385	403	431	444
0	122.727	122.866	122.794	122.808	122.841	122.867	122.920	122.926	122.934
10	122.684	122.698	122.712	122.623	122.704	122.749	122.848	122.904	122.925
20	122.660	122.661	122.781	122.711	122.817	122.851	122.904	122.934	122.951
30	123.103	123.109	123.109	123.145	123.098	123.099	123.045	123.001	123.005
40	123.392	123.383	123.344	123.336	123.271	123.229	123.159	123.080	123.067
50	123.465	123.454	123.416	123.399	123.335	123.292	123.224	123.147	123.123
60	123.455	123.465	123.420	123.402	123.342	123.308	123.249	123.182	123.156
70	123.395	123.420	123.376	123.360	123.305	123.279	123.231	123.178	123.158
80	123.282	123.314	123.279	123.271	123.221	123.201	123.164	123.135	123.129
90	123.112	123.130	123.124	123.132	123.089	123.078	123.054	123.055	123.067
100	122.842	122.849	122.860	122.913	122.898	122.911	122.916	122.951	122.986
110	122.202	122.395	122.362	122.488	122.631	122.706	122.764	122.842	122.898
120	121.298	121.949	121.889	122.164	122.314	122.465	122.613	122.749	122.821
130	121.584	121.774	121.842	121.955	122.154	122.313	122.512	122.692	122.771
140	121.703	121.753	121.857	121.943	122.240	122.362	122.525	122.685	122.754
150	122.164	122.223	122.320	122.443	122.511	122.593	122.642	122.722	122.772
160	122.563	122.626	122.678	122.746	122.738	122.752	122.761	122.784	122.814
170	122.755	122.799	122.838	122.873	122.862	122.865	122.856	122.852	122.864
180	122.880	122.930	122.938	122.963	122.945	122.948	122.930	122.910	122.908
190	122.970	123.022	123.014	123.022	122.996	122.998	122.973	122.945	122.941
200	123.017	123.067	123.055	123.048	123.014	123.012	122.982	122.955	122.954
210	123.013	123.038	123.046	123.029	122.992	122.989	122.959	122.940	122.948
220	122.901	122.902	122.877	122.918	122.921	122.930	122.910	122.907	122.933
230	122.389	122.567	122.163	122.579	122.750	122.807	122.835	122.874	122.915
240	121.806	122.285	121.939	122.405	122.443	122.608	122.758	122.859	122.911
250	122.147	122.228	122.306	122.251	122.418	122.573	122.753	122.879	122.931
260	122.395	122.388	122.581	122.520	122.694	122.788	122.871	122.941	122.978
270	123.082	123.106	123.116	123.165	123.109	123.109	123.062	123.034	123.046
280	123.546	123.542	123.504	123.484	123.383	123.309	123.220	123.134	123.118
290	123.779	123.758	123.691	123.643	123.522	123.438	123.330	123.214	123.176
300	123.918	123.889	123.792	123.719	123.595	123.509	123.394	123.261	123.207
310	123.991	123.954	123.838	123.746	123.617	123.525	123.407	123.265	123.203
320	123.995	123.952	123.830	123.728	123.591	123.495	123.372	123.229	123.170
330	123.921	123.864	123.753	123.658	123.518	123.416	123.297	123.161	123.111
340	123.733	123.671	123.553	123.496	123.376	123.294	123.192	123.075	123.043
350	123.300	123.281	123.138	123.077	123.135	123.114	123.058	122.989	122.977

a. Raw radial measurements, i.e. not corrected for the offset of the measurement apparatus from the axis of revolution.

Table 74: Inner radii of specimen L510-No26 based on CMM measurements – Part 1

Angle (°)	Inner radii [a] (mm) at indicated axial location (mm)								
	End Bay 1	**Frame 1**	**Bay 1**	**Frame 2**	**Bay 2**	**Frame 3**	**Bay 3**	**Frame 4**	**Bay 4**
	66	79	107	125	153	175	204	220	235
0	119.934	109.979	119.983	109.961	119.951	109.890	119.646	109.829	119.911
10	119.871	109.907	119.875	109.850	119.798	109.697	119.588	109.619	119.761
20	119.849	109.883	119.825	109.761	119.732	109.582	119.479	109.633	119.783
30	119.863	109.909	119.894	109.905	119.934	109.929	119.971	110.110	120.187
40	119.893	109.962	120.031	110.148	120.214	110.343	120.389	110.485	120.507
50	119.929	110.020	120.131	110.260	120.344	110.466	120.515	110.577	120.599
60	119.969	110.067	120.177	110.307	120.376	110.487	120.522	110.588	120.605
70	119.995	110.088	120.184	110.296	120.354	110.445	120.479	110.535	120.549
80	120.000	110.081	120.155	110.236	120.291	110.353	120.394	110.431	120.435
90	119.975	110.034	120.081	110.133	120.180	110.221	120.263	110.263	120.265
100	119.930	109.965	119.974	109.993	120.012	110.033	120.032	110.020	119.990
110	119.881	109.884	119.827	109.782	119.722	109.603	119.555	109.464	119.320
120	119.841	109.816	119.681	109.505	119.363	109.172	118.992	108.914	118.555
130	119.822	109.784	119.613	109.437	119.269	109.104	118.889	108.715	118.651
140	119.817	109.781	119.612	109.436	119.261	109.086	118.870	108.704	118.761
150	119.836	109.813	119.694	109.565	119.446	109.329	119.223	109.126	119.135
160	119.884	109.874	119.801	109.762	119.698	109.660	119.601	109.570	119.514
170	119.941	109.943	119.893	109.887	119.846	109.823	119.779	109.744	119.630
180	119.977	109.995	119.966	109.976	119.946	109.933	119.883	109.859	119.807
190	119.991	110.022	120.019	110.031	120.013	110.010	119.970	109.944	119.899
200	119.989	110.030	120.042	110.056	120.059	110.061	120.029	109.999	119.968
210	119.980	110.018	120.034	110.049	120.066	110.081	120.062	110.023	119.996
220	119.965	109.997	120.001	110.012	120.016	110.045	120.017	109.988	119.925
230	119.952	109.969	119.935	109.913	119.857	109.811	119.719	109.617	119.468
240	119.937	109.938	119.858	109.727	119.605	109.492	119.180	109.293	119.065
250	119.935	109.933	119.839	109.727	119.604	109.489	119.249	109.244	119.262
260	119.950	109.956	119.878	109.791	119.718	109.520	119.272	109.421	119.519
270	119.997	110.022	120.000	109.975	119.962	109.865	119.820	110.049	120.149
280	120.079	110.123	120.166	110.236	120.282	110.406	120.413	110.552	120.283
290	120.163	110.232	120.324	110.427	120.502	110.651	120.500	110.794	120.395
300	120.232	110.322	120.439	110.558	120.649	110.778	120.607	110.934	120.530
310	120.256	110.364	120.493	110.625	120.726	110.839	120.738	110.998	120.692
320	120.240	110.351	120.488	110.625	120.747	110.840	120.876	110.992	120.860
330	120.192	110.290	120.415	110.559	120.690	110.792	120.850	110.922	120.946
340	120.117	110.197	120.301	110.440	120.554	110.676	120.713	110.778	120.759
350	120.025	110.083	120.146	110.223	120.282	110.277	120.252	110.306	120.350

a. Raw radial measurements, i.e. not corrected for the offset of the measurement apparatus from the axis of revolution.

Table 75: Inner radii of specimen L510-No26 based on CMM measurements – Part 2

Angle (°)	Inner radii [a] (mm) at indicated axial location (mm)								
	Bay 4	**Frame 5**	**Bay 5**	**Frame 6**	**Bay 6**	**Frame 7**	**Bay 7**	**Frame 8**	**End Bay 2**
	275	290	306	335	357	385	403	431	444
0	119.696	109.853	119.766	109.780	119.811	109.839	119.860	109.872	119.859
10	119.685	109.707	119.713	109.610	119.707	109.744	119.794	109.857	119.847
20	119.676	109.704	119.802	109.724	119.838	109.870	119.870	109.903	119.883
30	120.132	110.142	120.146	110.177	120.134	110.139	120.037	109.996	119.957
40	120.455	110.455	120.404	110.400	120.328	110.296	120.178	110.104	120.047
50	120.551	110.550	120.491	110.483	120.405	110.378	120.266	110.196	120.126
60	120.568	110.584	120.511	110.505	120.429	110.407	120.304	110.252	120.193
70	120.526	110.556	120.487	110.478	120.401	110.383	120.294	110.265	120.216
80	120.417	110.459	120.402	110.401	120.327	110.310	120.232	110.233	120.195
90	120.246	110.270	120.252	110.263	120.208	110.191	120.132	110.169	120.145
100	119.957	109.965	119.971	110.025	120.023	110.028	120.006	110.079	120.070
110	119.250	109.471	119.430	109.574	119.750	109.826	119.861	109.976	119.995
120	118.323	109.008	118.945	109.249	119.419	109.586	119.713	109.879	119.916
130	118.606	108.807	118.895	109.004	119.244	109.428	119.605	109.806	119.853
140	118.690	108.778	118.900	108.980	119.316	109.461	119.597	109.771	119.811
150	119.119	109.186	119.344	109.436	119.563	109.656	119.686	109.772	119.794
160	119.513	109.589	119.695	109.739	119.773	109.789	119.769	109.805	119.813
170	119.692	109.756	119.832	109.848	119.862	109.870	119.835	109.851	119.833
180	119.819	109.882	119.914	109.916	119.918	109.933	119.890	109.889	119.864
190	119.916	109.978	119.975	109.968	119.951	109.969	119.925	109.916	119.886
200	119.979	110.034	120.011	109.996	119.964	109.984	119.933	109.930	119.906
210	119.999	110.026	120.024	109.998	119.953	109.977	119.927	109.934	119.916
220	119.902	109.914	119.872	109.915	119.899	109.936	119.901	109.927	119.912
230	119.378	109.600	119.134	109.611	119.757	109.841	119.851	109.919	119.925
240	118.829	109.354	118.978	109.479	119.482	109.689	119.803	109.934	119.954
250	119.200	109.308	119.405	109.349	119.497	109.678	119.819	109.978	120.003
260	119.436	109.472	119.695	109.616	119.790	109.905	119.965	110.060	120.073
270	120.129	110.155	120.230	110.263	120.220	110.238	120.167	110.164	120.154
280	120.606	110.609	120.613	110.589	120.489	110.438	120.331	110.265	120.227
290	120.829	110.807	120.776	110.722	120.608	110.550	120.442	110.331	120.268
300	120.951	110.913	120.844	110.762	120.656	110.598	120.490	110.352	120.270
310	121.003	110.957	120.854	110.749	120.641	110.583	120.485	110.328	120.237
320	120.977	110.925	120.807	110.681	120.575	110.498	120.407	110.247	120.175
330	120.883	110.826	120.703	110.592	120.470	110.398	120.292	110.161	120.105
340	120.680	110.625	120.486	110.415	120.311	110.248	120.150	110.049	120.014
350	120.246	110.231	120.074	110.008	120.087	110.064	119.998	109.944	119.924

a. Raw radial measurements, i.e. not corrected for the offset of the measurement apparatus from the axis of revolution.

Table 76: Out-of-circularity of specimen L510-No26 based on mechanical displacement gauge measurements

Angle (degrees)	Radial Eccentricity[a] (mm) at Indicated Axial Location (mm)							
	Frame 1	**Frame 2**	**Frame 3**	**Frame 4**	**Frame 5**	**Frame 6**	**Frame 7**	**Frame 8**
	80	130	180	230	280	330	380	430
0	-0.098	-0.195	-0.431	-0.630	-0.589	-0.554	-0.356	-0.208
10	-0.145	-0.335	-0.599	-0.833	-0.743	-0.681	-0.496	-0.223
20	-0.161	-0.413	-0.720	-0.862	-0.759	-0.617	-0.368	-0.180
30	-0.118	-0.293	-0.373	-0.353	-0.266	-0.130	-0.082	-0.088
40	-0.053	-0.031	0.100	0.157	0.140	0.156	0.084	0.014
50	0.019	0.112	0.336	0.342	0.309	0.297	0.206	0.105
60	0.079	0.208	0.373	0.449	0.425	0.375	0.273	0.171
70	0.103	0.243	0.377	0.514	0.492	0.432	0.303	0.184
80	0.119	0.236	0.364	0.487	0.495	0.426	0.287	0.195
90	0.099	0.230	0.344	0.446	0.423	0.359	0.218	0.162
100	0.031	0.133	0.217	0.292	0.215	0.197	0.093	0.066
110	-0.046	-0.032	-0.148	-0.101	-0.179	-0.193	-0.082	-0.028
120	-0.104	-0.281	-0.554	-0.618	-0.624	-0.492	-0.298	-0.114
130	-0.130	-0.334	-0.544	-0.767	-0.721	-0.654	-0.413	-0.158
140	-0.110	-0.305	-0.504	-0.767	-0.696	-0.678	-0.338	-0.155
150	-0.054	-0.170	-0.251	-0.314	-0.243	-0.161	-0.102	-0.109
160	0.011	-0.003	0.085	0.156	0.162	0.152	0.042	-0.039
170	0.080	0.162	0.259	0.333	0.342	0.317	0.149	-0.003
180	0.125	0.239	0.375	0.462	0.447	0.383	0.215	0.067
190	0.142	0.271	0.401	0.491	0.511	0.413	0.238	0.093
200	0.121	0.254	0.389	0.465	0.484	0.394	0.201	0.085
210	0.074	0.197	0.330	0.400	0.392	0.327	0.162	0.057
220	0.002	0.098	0.209	0.263	0.172	0.156	0.059	0.003
230	-0.071	-0.063	-0.108	-0.167	-0.264	-0.299	-0.110	-0.063
240	-0.132	-0.289	-0.524	-0.656	-0.665	-0.544	-0.346	-0.115
250	-0.162	-0.355	-0.564	-0.802	-0.779	-0.737	-0.440	-0.118
260	-0.160	-0.338	-0.609	-0.791	-0.769	-0.595	-0.273	-0.076
270	-0.136	-0.286	-0.392	-0.278	-0.160	-0.041	-0.001	0.000
280	-0.041	-0.038	0.109	0.199	0.251	0.274	0.160	0.085
290	0.052	0.131	0.307	0.390	0.389	0.382	0.250	0.145
300	0.127	0.242	0.395	0.485	0.462	0.415	0.292	0.173
310	0.168	0.295	0.328	0.488	0.495	0.402	0.278	0.171
320	0.174	0.300	0.416	0.511	0.466	0.361	0.210	0.104
330	0.140	0.247	0.362	0.402	0.365	0.272	0.118	0.023
340	0.073	0.160	0.266	0.274	0.186	0.145	0.014	-0.073
350	-0.017	0.006	-0.023	-0.068	-0.166	-0.257	-0.147	-0.152

a. Radial eccentricity is taken as the raw gauge reading less the n=0 and n=1 Fourier components at that axial location.

Table 77: Out-of-circularity of specimen L510-No26 based on chord gauge measurements

Angle (degrees)	Radial Eccentricity[a] (mm) at Indicated Axial Location (mm)							
	Frame 1	**Frame 2**	**Frame 3**	**Frame 4**	**Frame 5**	**Frame 6**	**Frame 7**	**Frame 8**
	80	130	180	230	280	330	380	430
0	-0.076	-0.230	-0.431	-0.641	-0.542	-0.468	-0.342	-0.201
20	-0.144	-0.398	-0.679	-0.806	-0.745	-0.628	-0.384	-0.189
40	-0.059	0.012	0.117	0.206	0.206	0.174	0.088	0.000
60	0.063	0.217	0.367	0.442	0.448	0.331	0.251	0.168
80	0.098	0.220	0.367	0.486	0.567	0.401	0.282	0.189
100	0.020	0.084	0.196	0.284	0.251	0.151	0.093	0.064
120	-0.081	-0.288	-0.498	-0.586	-0.532	-0.405	-0.224	-0.109
140	-0.085	-0.282	-0.504	-0.761	-0.806	-0.631	-0.349	-0.153
160	0.016	0.070	0.126	0.182	0.034	0.206	0.036	-0.049
180	0.118	0.260	0.349	0.415	0.354	0.329	0.185	0.067
200	0.108	0.246	0.370	0.458	0.546	0.385	0.214	0.094
220	-0.008	0.079	0.184	0.260	0.270	0.110	0.055	0.010
240	-0.136	-0.327	-0.494	-0.600	-0.476	-0.463	-0.290	-0.107
260	-0.149	-0.354	-0.602	-0.769	-0.738	-0.650	-0.293	-0.089
280	-0.030	-0.003	0.124	0.212	0.252	0.263	0.146	0.057
300	0.116	0.242	0.374	0.465	0.379	0.375	0.267	0.163
320	0.160	0.290	0.387	0.487	0.414	0.393	0.241	0.122
340	0.069	0.164	0.247	0.265	0.119	0.127	0.022	-0.038

a. Radial eccentricities are determined by performing Fourier decompositions of the chord height measurements, followed by expansion of the Fourier series with modified coefficients, yielding the eccentricities. The eccentricities presented here do not include the n=0 and n=1 Fourier components.

Table 78: Shell thicknesses for specimen L510-No26 based on CMM measurements

Angle (degrees)	Shell Thickness[a] (mm) at Indicated Axial Location (mm)									
	End 1	**Bay 1**	**Bay 2**	**Bay 3**	**Bay 4**	**Bay 4**	**Bay 5**	**Bay 6**	**Bay 7**	**End 2**
	66	107	153	204	235	275	306	357	403	444
0	3.057	3.014	3.001	2.988	2.971	3.050	3.029	3.026	3.054	3.060
10	3.055	3.016	3.005	3.000	2.967	3.025	3.005	2.997	3.047	3.064
20	3.050	3.018	3.004	3.004	2.980	3.013	2.987	2.986	3.030	3.055
30	3.038	3.012	2.998	3.017	2.987	3.005	2.976	2.975	3.004	3.035
40	3.030	2.994	2.974	2.982	2.978	2.971	2.953	2.960	2.978	3.009
50	3.024	2.970	2.957	2.970	2.966	2.951	2.943	2.950	2.957	2.988
60	3.009	2.956	2.938	2.948	2.957	2.924	2.928	2.937	2.945	2.957
70	2.991	2.940	2.921	2.933	2.948	2.905	2.910	2.930	2.937	2.938
80	2.972	2.923	2.900	2.914	2.954	2.898	2.898	2.923	2.935	2.931
90	2.962	2.913	2.891	2.918	2.958	2.897	2.895	2.911	2.924	2.922
100	2.957	2.910	2.894	2.929	2.975	2.911	2.909	2.905	2.915	2.919
110	2.956	2.920	2.907	2.972	3.026	2.974	2.954	2.910	2.908	2.908
120	2.961	2.932	2.929	2.983	3.046	2.991	2.961	2.923	2.906	2.913
130	2.969	2.945	2.942	3.002	3.047	2.989	2.964	2.935	2.913	2.927
140	2.991	2.968	2.968	3.026	3.077	3.017	2.969	2.946	2.936	2.955
150	3.014	2.979	2.985	3.057	3.091	3.043	2.987	2.966	2.963	2.990
160	3.027	3.013	2.996	3.054	3.088	3.041	2.988	2.980	2.999	3.014
170	3.035	3.022	3.015	3.067	3.141	3.048	3.009	3.009	3.028	3.045
180	3.055	3.033	3.015	3.056	3.068	3.041	3.022	3.030	3.047	3.058
190	3.058	3.026	3.005	3.025	3.032	3.029	3.035	3.043	3.053	3.069
200	3.059	3.009	2.975	2.982	2.991	3.008	3.034	3.044	3.053	3.062
210	3.044	2.986	2.949	2.951	2.945	2.982	3.011	3.028	3.036	3.045
220	3.022	2.960	2.932	2.919	2.913	2.963	2.988	3.006	3.012	3.032
230	2.997	2.942	2.924	2.913	2.896	2.975	3.012	2.972	2.985	2.999
240	2.985	2.935	2.924	2.903	2.857	2.940	2.941	2.937	2.956	2.964
250	2.981	2.936	2.920	2.891	2.821	2.912	2.881	2.894	2.933	2.933
260	2.988	2.945	2.924	2.890	2.824	2.925	2.863	2.876	2.904	2.908
270	2.989	2.946	2.937	2.929	2.811	2.924	2.865	2.860	2.891	2.891
280	2.976	2.948	2.946	2.942	3.142	2.913	2.868	2.865	2.885	2.888
290	2.965	2.940	2.953	3.125	3.272	2.929	2.896	2.885	2.883	2.903
300	2.955	2.933	2.939	3.140	3.293	2.950	2.928	2.912	2.898	2.930
310	2.966	2.939	2.936	3.079	3.214	2.979	2.969	2.950	2.916	2.956
320	2.983	2.946	2.920	2.951	3.069	3.013	3.009	2.995	2.958	2.984
330	3.002	2.970	2.938	2.957	2.931	3.041	3.042	3.029	2.998	2.993
340	3.020	2.992	2.962	2.968	2.967	3.061	3.059	3.051	3.035	3.016
350	3.036	3.003	2.985	2.997	2.976	3.069	3.062	3.039	3.053	3.039

a. Shell thicknesses were derived by subtracting the measured inner radii from the corresponding outer radii, after correcting the radius data for the n=1 offset.

B.9 L510-No33

Table 79: Outer radii of specimen L510-No33 based on CMM measurements – Part 1

Angle (°)	Outer radii [a] (mm) at indicated axial location (mm)								
	End Bay 1	**Frame 1**	**Bay 1**	**Frame 2**	**Bay 2**	**Frame 3**	**Bay 3**	**Frame 4**	**Bay 4**
	66	79	107	125	153	175	204	220	235
0	122.999	123.015	123.057	123.064	123.050	123.007	122.802	122.797	123.070
10	122.983	122.991	123.010	122.993	122.949	122.905	122.793	122.639	122.867
20	122.984	122.993	123.014	123.005	122.983	122.993	122.902	122.706	122.883
30	123.000	123.016	123.062	123.096	123.156	123.263	123.312	123.381	123.384
40	123.020	123.046	123.124	123.191	123.289	123.430	123.552	123.700	123.712
50	123.033	123.073	123.175	123.259	123.356	123.484	123.570	123.670	123.718
60	123.033	123.078	123.189	123.282	123.368	123.476	123.514	123.571	123.617
70	123.013	123.056	123.159	123.247	123.322	123.418	123.436	123.466	123.498
80	122.976	123.005	123.080	123.147	123.215	123.310	123.341	123.365	123.379
90	122.926	122.932	122.963	122.997	123.051	123.140	123.205	123.244	123.224
100	122.871	122.851	122.828	122.814	122.835	122.897	122.912	122.928	122.877
110	122.820	122.777	122.698	122.624	122.569	122.506	122.326	122.147	122.280
120	122.786	122.725	122.597	122.464	122.320	122.145	121.819	121.648	121.814
130	122.783	122.710	122.553	122.390	122.189	121.969	121.663	121.200	121.386
140	122.809	122.731	122.572	122.414	122.216	122.016	121.697	121.137	121.321
150	122.854	122.785	122.647	122.533	122.435	122.352	122.222	122.048	121.997
160	122.905	122.853	122.752	122.677	122.632	122.613	122.612	122.622	122.506
170	122.957	122.924	122.857	122.813	122.775	122.758	122.747	122.735	122.652
180	122.999	122.977	122.940	122.914	122.881	122.856	122.800	122.748	122.684
190	123.020	123.004	122.980	122.966	122.939	122.919	122.840	122.767	122.717
200	123.020	122.999	122.972	122.959	122.943	122.944	122.880	122.809	122.759
210	122.995	122.965	122.924	122.899	122.890	122.908	122.893	122.843	122.786
220	122.955	122.916	122.853	122.807	122.790	122.804	122.767	122.739	122.663
230	122.914	122.869	122.781	122.703	122.640	122.574	122.328	122.243	122.353
240	122.890	122.842	122.739	122.627	122.496	122.362	122.038	122.040	122.184
250	122.893	122.848	122.754	122.645	122.496	122.363	122.068	121.844	122.097
260	122.922	122.889	122.829	122.752	122.616	122.556	122.257	122.050	122.305
270	122.971	122.961	122.949	122.933	122.926	122.957	122.917	122.904	122.913
280	123.033	123.046	123.088	123.128	123.192	123.292	123.380	123.461	123.437
290	123.093	123.130	123.225	123.307	123.396	123.515	123.603	123.688	123.708
300	123.136	123.192	123.328	123.439	123.545	123.679	123.746	123.830	123.875
310	123.157	123.223	123.378	123.509	123.634	123.789	123.868	123.960	124.017
320	123.151	123.217	123.374	123.509	123.651	123.838	123.960	124.082	124.140
330	123.122	123.178	123.319	123.443	123.591	123.795	123.977	124.134	124.185
340	123.079	123.122	123.233	123.328	123.461	123.653	123.768	124.014	123.963
350	123.033	123.062	123.138	123.190	123.253	123.314	123.188	123.153	123.421

a. Raw radial measurements, i.e. not corrected for the offset of the measurement apparatus from the axis of revolution.

Table 80: Outer radii of specimen L510-No33 based on CMM measurements – Part 2

Angle (°)	Outer radii [a] (mm) at indicated axial location (mm)								
	Bay 4	**Frame 5**	**Bay 5**	**Frame 6**	**Bay 6**	**Frame 7**	**Bay 7**	**Frame 8**	**End Bay 2**
	275	290	306	335	357	385	403	431	444
0	122.990	122.889	122.979	122.997	122.933	123.010	123.017	122.994	122.985
10	122.821	122.787	122.837	122.846	122.926	122.982	122.994	122.980	122.980
20	122.760	122.638	122.812	122.922	122.981	123.006	123.011	122.991	122.989
30	123.202	123.099	123.124	123.179	123.114	123.075	123.054	123.022	123.013
40	123.571	123.533	123.404	123.331	123.226	123.158	123.112	123.061	123.040
50	123.616	123.590	123.493	123.408	123.300	123.232	123.168	123.097	123.065
60	123.541	123.550	123.482	123.427	123.333	123.271	123.196	123.115	123.081
70	123.434	123.459	123.420	123.391	123.312	123.256	123.187	123.109	123.080
80	123.314	123.331	123.313	123.298	123.230	123.180	123.125	123.072	123.059
90	123.155	123.152	123.145	123.143	123.086	123.044	123.021	123.011	123.021
100	122.820	122.820	122.819	122.881	122.851	122.859	122.888	122.937	122.973
110	122.261	122.136	122.302	122.392	122.497	122.651	122.752	122.865	122.923
120	121.860	121.820	121.985	122.109	122.253	122.501	122.659	122.812	122.885
130	121.590	121.703	121.921	122.070	122.272	122.482	122.634	122.791	122.869
140	121.524	121.601	121.947	122.192	122.371	122.530	122.658	122.801	122.874
150	122.038	122.084	122.270	122.466	122.543	122.623	122.719	122.835	122.896
160	122.529	122.566	122.585	122.649	122.687	122.733	122.796	122.881	122.926
170	122.715	122.738	122.750	122.782	122.802	122.839	122.874	122.928	122.957
180	122.785	122.837	122.850	122.880	122.893	122.918	122.933	122.961	122.979
190	122.835	122.898	122.916	122.945	122.946	122.958	122.959	122.970	122.981
200	122.882	122.933	122.952	122.970	122.951	122.949	122.946	122.954	122.968
210	122.894	122.925	122.939	122.949	122.915	122.896	122.902	122.923	122.942
220	122.757	122.777	122.785	122.853	122.812	122.808	122.837	122.880	122.909
230	122.426	122.287	122.431	122.510	122.606	122.705	122.773	122.843	122.880
240	122.277	122.182	122.277	122.339	122.477	122.643	122.742	122.827	122.866
250	122.262	122.281	122.379	122.470	122.584	122.688	122.767	122.838	122.874
260	122.400	122.358	122.551	122.685	122.761	122.798	122.839	122.877	122.903
270	122.932	122.893	122.952	123.025	122.982	122.949	122.944	122.940	122.944
280	123.438	123.402	123.319	123.278	123.185	123.113	123.066	123.013	122.995
290	123.710	123.658	123.552	123.468	123.350	123.263	123.178	123.081	123.040
300	123.873	123.831	123.710	123.612	123.477	123.378	123.265	123.131	123.073
310	123.996	123.948	123.817	123.703	123.553	123.442	123.309	123.154	123.087
320	124.086	124.015	123.866	123.736	123.574	123.444	123.309	123.149	123.085
330	124.101	124.000	123.841	123.701	123.529	123.385	123.261	123.119	123.065
340	123.878	123.805	123.660	123.566	123.395	123.272	123.177	123.074	123.037
350	123.341	123.183	123.276	123.233	123.130	123.125	123.085	123.027	123.007

a. Raw radial measurements, i.e. not corrected for the offset of the measurement apparatus from the axis of revolution.

Table 81: Inner radii of specimen L510-No33 based on CMM measurements – Part 1

Angle (°)	Inner radii [a] (mm) at indicated axial location (mm)								
	End Bay 1	**Frame 1**	**Bay 1**	**Frame 2**	**Bay 2**	**Frame 3**	**Bay 3**	**Frame 4**	**Bay 4**
	66	79	107	125	153	175	204	220	235
0	120.043	109.996	120.072	110.063	120.071	110.022	119.831	109.792	120.080
10	120.032	109.986	120.033	110.005	119.982	109.932	119.847	109.655	119.903
20	120.034	109.993	120.038	110.030	120.025	110.042	119.968	109.754	119.931
30	120.055	110.015	120.085	110.121	120.206	110.311	120.384	110.411	120.438
40	120.072	110.039	120.148	110.217	120.341	110.479	120.631	110.756	120.779
50	120.087	110.057	120.196	110.278	120.403	110.517	120.636	110.705	120.765
60	120.086	110.060	120.208	110.284	120.398	110.484	120.551	110.573	120.637
70	120.074	110.037	120.165	110.231	120.326	110.398	120.445	110.437	120.487
80	120.047	109.997	120.091	110.115	120.206	110.263	120.330	110.318	120.350
90	119.999	109.933	119.971	109.964	120.031	110.085	120.182	110.189	120.187
100	119.955	109.859	119.846	109.793	119.822	109.851	119.891	109.855	119.842
110	119.904	109.798	119.734	109.629	119.591	109.484	119.322	109.083	119.279
120	119.875	109.757	119.663	109.503	119.380	109.191	118.871	108.664	118.851
130	119.884	109.761	119.625	109.454	119.279	109.046	118.745	108.239	118.445
140	119.933	109.797	119.647	109.503	119.316	109.133	118.793	108.231	118.395
150	119.990	109.862	119.730	109.628	119.543	109.463	119.341	109.091	119.083
160	120.028	109.929	119.841	109.772	119.740	109.727	119.754	109.741	119.626
170	120.062	109.981	119.950	109.896	119.869	109.850	119.876	109.848	119.765
180	120.078	110.017	120.010	109.973	119.946	109.920	119.895	109.837	119.773
190	120.079	110.009	120.019	109.992	119.968	109.949	119.902	109.817	119.768
200	120.046	109.980	119.966	109.944	119.935	109.938	119.905	109.817	119.771
210	119.981	109.911	119.876	109.850	119.848	109.871	119.885	109.813	119.757
220	119.907	109.825	119.785	109.725	119.732	109.741	119.734	109.673	119.615
230	119.839	109.756	119.694	109.607	119.578	109.492	119.264	109.165	119.312
240	119.826	109.720	119.653	109.537	119.430	109.302	118.987	108.978	119.155
250	119.854	109.740	119.677	109.568	119.441	109.301	119.034	108.789	119.073
260	119.914	109.813	119.780	109.703	119.574	109.522	119.224	109.005	119.279
270	120.004	109.922	119.940	109.912	119.916	109.938	119.920	109.845	119.899
280	120.100	110.042	120.118	110.137	120.214	110.309	120.201	110.474	120.039
290	120.190	110.156	120.277	110.332	120.434	110.547	120.307	110.716	120.173
300	120.245	110.230	120.391	110.473	120.540	110.714	120.435	110.866	120.334
310	120.262	110.259	120.439	110.540	120.648	110.818	120.582	110.996	120.516
320	120.246	110.252	120.425	110.527	120.695	110.852	120.745	111.109	120.716
330	120.199	110.197	120.352	110.450	120.630	110.799	120.905	111.150	120.919
340	120.143	110.124	120.249	110.329	120.488	110.646	120.780	110.894	120.957
350	120.083	110.054	120.156	110.193	120.278	110.300	120.188	110.100	120.413

a. Raw radial measurements, i.e. not corrected for the offset of the measurement apparatus from the axis of revolution.

Table 82: Inner radii of specimen L510-No33 based on CMM measurements – Part 2

Angle (°)	Inner radii [a] (mm) at indicated axial location (mm)								
	Bay 4	**Frame 5**	**Bay 5**	**Frame 6**	**Bay 6**	**Frame 7**	**Bay 7**	**Frame 8**	**End Bay 2**
	275	290	306	335	357	385	403	431	444
0	120.017	109.874	120.001	109.986	119.916	109.971	119.990	109.924	119.917
10	119.871	109.787	119.873	109.860	119.937	109.984	120.006	109.940	119.918
20	119.822	109.674	119.852	109.968	120.010	110.050	120.054	109.981	119.950
30	120.264	110.108	120.171	110.237	120.159	110.143	120.124	110.037	119.993
40	120.648	110.573	120.459	110.393	120.278	110.231	120.189	110.092	120.039
50	120.684	110.612	120.537	110.449	120.341	110.290	120.226	110.122	120.066
60	120.581	110.542	120.506	110.434	120.348	110.295	120.234	110.123	120.073
70	120.446	110.416	120.416	110.355	120.295	110.243	120.191	110.092	120.064
80	120.310	110.256	120.287	110.224	120.186	110.133	120.104	110.044	120.044
90	120.139	110.064	120.099	110.050	120.025	109.977	119.989	109.979	120.018
100	119.812	109.717	119.771	109.783	119.795	109.798	119.864	109.910	119.976
110	119.278	109.051	119.281	109.321	119.470	109.615	119.762	109.853	119.927
120	118.922	108.809	119.011	109.105	119.267	109.506	119.700	109.818	119.894
130	118.672	108.722	118.977	109.094	119.315	109.521	119.696	109.817	119.892
140	118.624	108.670	119.024	109.257	119.433	109.594	119.731	109.837	119.903
150	119.142	109.136	119.372	109.549	119.628	109.702	119.796	109.868	119.907
160	119.660	109.658	119.707	109.744	119.782	109.808	119.873	109.898	119.912
170	119.843	109.822	119.860	109.865	119.891	109.899	119.933	109.921	119.918
180	119.886	109.895	119.928	109.936	119.957	109.952	119.966	109.933	119.927
190	119.908	109.925	119.966	109.962	119.983	109.958	119.973	109.926	119.924
200	119.914	109.923	119.972	109.951	119.959	109.922	119.945	109.909	119.915
210	119.888	109.884	119.928	109.904	119.893	109.850	119.888	109.877	119.908
220	119.734	109.701	119.753	109.789	119.785	109.760	119.820	109.840	119.884
230	119.399	109.194	119.394	109.444	119.584	109.666	119.769	109.814	119.864
240	119.274	109.114	119.251	109.302	119.462	109.625	119.746	109.813	119.863
250	119.265	109.222	119.365	109.420	119.577	109.687	119.788	109.846	119.885
260	119.401	109.316	119.545	109.663	119.766	109.820	119.886	109.905	119.921
270	119.943	109.839	119.957	110.025	120.005	109.995	120.007	109.981	119.968
280	120.474	110.388	120.335	110.302	120.224	110.172	120.131	110.058	120.023
290	120.762	110.658	120.582	110.496	120.396	110.322	120.241	110.120	120.069
300	120.877	110.836	120.749	110.628	120.521	110.420	120.324	110.157	120.090
310	120.935	110.947	120.846	110.696	120.583	110.456	120.351	110.165	120.095
320	120.996	111.001	120.880	110.703	120.575	110.429	120.316	110.145	120.091
330	121.068	110.976	120.844	110.650	120.508	110.343	120.238	110.096	120.065
340	120.880	110.756	120.657	110.506	120.359	110.213	120.136	110.028	120.016
350	120.336	110.122	120.275	110.186	120.095	110.067	120.047	109.967	119.959

a. Raw radial measurements, i.e. not corrected for the offset of the measurement apparatus from the axis of revolution.

Table 83: Out-of-circularity of specimen L510-No33 based on mechanical displacement gauge measurements

Angle (degrees)	Radial Eccentricity[a] (mm) at Indicated Axial Location (mm)							
	Frame 1	**Frame 2**	**Frame 3**	**Frame 4**	**Frame 5**	**Frame 6**	**Frame 7**	**Frame 8**
	80	130	180	230	280	330	380	430
0	-	-	-	-0.776	-0.582	-0.373	-	-
10	-	-	-	-0.838	-0.574	-0.526	-	-
20	-	-	-	-0.787	-0.747	-0.481	-	-
30	-	-	-	-0.086	-0.370	-0.174	-	-
40	-	-	-	0.375	0.202	0.064	-	-
50	-	-	-	0.427	0.353	0.215	-	-
60	-	-	-	0.414	0.409	0.319	-	-
70	-	-	-	0.416	0.421	0.361	-	-
80	-	-	-	0.454	0.414	0.363	-	-
90	-	-	-	0.487	0.379	0.349	-	-
100	-	-	-	0.351	0.253	0.163	-	-
110	-	-	-	-0.299	-0.290	-0.282	-	-
120	-	-	-	-0.684	-0.545	-0.519	-	-
130	-	-	-	-1.038	-0.563	-0.515	-	-
140	-	-	-	-1.037	-0.676	-0.392	-	-
150	-	-	-	-0.075	-0.250	-0.148	-	-
160	-	-	-	0.471	0.223	0.049	-	-
170	-	-	-	0.526	0.355	0.213	-	-
180	-	-	-	0.476	0.393	0.342	-	-
190	-	-	-	0.450	0.402	0.387	-	-
200	-	-	-	0.437	0.388	0.376	-	-
210	-	-	-	0.424	0.340	0.310	-	-
220	-	-	-	0.230	0.165	0.160	-	-
230	-	-	-	-0.348	-0.364	-0.248	-	-
240	-	-	-	-0.604	-0.538	-0.502	-	-
250	-	-	-	-0.921	-0.509	-0.486	-	-
260	-	-	-	-0.806	-0.586	-0.400	-	-
270	-	-	-	-0.073	-0.221	-0.134	-	-
280	-	-	-	0.322	0.162	0.058	-	-
290	-	-	-	0.395	0.298	0.202	-	-
300	-	-	-	0.400	0.362	0.284	-	-
310	-	-	-	0.421	0.400	0.330	-	-
320	-	-	-	0.473	0.420	0.327	-	-
330	-	-	-	0.499	0.402	0.270	-	-
340	-	-	-	0.327	0.291	0.143	-	-
350	-	-	-	-0.402	-0.216	-0.104	-	-

a. Radial eccentricity is taken as the raw gauge reading less the n=0 and n=1 Fourier components at that axial location.

Table 84: Out-of-circularity of specimen L510-No33 based on chord gauge measurements

Angle (degrees)	Radial Eccentricity[a] (mm) at Indicated Axial Location (mm)							
	Frame 1	**Frame 2**	**Frame 3**	**Frame 4**	**Frame 5**	**Frame 6**	**Frame 7**	**Frame 8**
	80	130	180	230	280	330	380	430
0	-0.076	-0.205	-0.452	-0.694	-0.567	-0.452	-0.212	-0.090
20	-0.080	-0.235	-0.477	-0.905	-0.771	-0.447	-0.180	-0.079
40	0.009	0.021	0.089	0.353	0.252	0.024	0.008	0.014
60	0.091	0.220	0.315	0.374	0.438	0.333	0.203	0.103
80	0.076	0.219	0.356	0.514	0.448	0.353	0.208	0.106
100	-0.028	0.012	0.155	0.348	0.185	0.210	0.013	0.007
120	-0.121	-0.242	-0.431	-0.583	-0.657	-0.529	-0.260	-0.096
140	-0.097	-0.260	-0.527	-1.178	-0.758	-0.360	-0.196	-0.107
160	0.023	0.009	0.110	0.435	0.261	0.059	0.009	-0.018
180	0.128	0.229	0.341	0.489	0.492	0.319	0.202	0.068
200	0.125	0.244	0.375	0.544	0.502	0.299	0.206	0.080
220	0.004	0.033	0.143	0.264	0.222	0.170	0.029	0.014
240	-0.117	-0.225	-0.438	-0.557	-0.626	-0.548	-0.217	-0.042
260	-0.128	-0.243	-0.491	-0.986	-0.705	-0.311	-0.184	-0.067
280	-0.019	-0.004	0.067	0.266	0.118	0.068	-0.005	0.002
300	0.086	0.193	0.310	0.359	0.373	0.319	0.171	0.064
320	0.103	0.212	0.380	0.580	0.486	0.311	0.184	0.062
340	0.018	0.022	0.175	0.378	0.308	0.181	0.021	-0.022

a. Radial eccentricities are determined by performing Fourier decompositions of the chord height measurements, followed by expansion of the Fourier series with modified coefficients, yielding the eccentricities. The eccentricities presented here do not include the n=0 and n=1 Fourier components.

Table 85: Shell thicknesses for specimen L510-No33 based on CMM measurements

Angle (degrees)	Shell Thickness[a] (mm) at Indicated Axial Location (mm)									
	End 1	**Bay 1**	**Bay 2**	**Bay 3**	**Bay 4**	**Bay 4**	**Bay 5**	**Bay 6**	**Bay 7**	**End 2**
	66	107	153	204	235	275	306	357	403	444
0	2.963	2.988	2.980	2.920	2.900	2.947	2.967	3.003	3.019	3.068
10	2.963	2.984	2.971	2.911	2.899	2.931	2.956	2.974	2.980	3.060
20	2.969	2.988	2.969	2.919	2.916	2.922	2.953	2.958	2.950	3.037
30	2.967	2.992	2.965	2.930	2.937	2.931	2.949	2.943	2.923	3.016
40	2.974	2.995	2.968	2.944	2.956	2.922	2.943	2.938	2.918	2.997
50	2.975	3.002	2.976	2.973	3.003	2.939	2.957	2.950	2.937	2.995
60	2.978	3.006	2.997	3.021	3.059	2.972	2.979	2.978	2.959	3.004
70	2.972	3.021	3.024	3.062	3.113	3.008	3.011	3.012	2.994	3.012
80	2.962	3.016	3.040	3.098	3.155	3.027	3.034	3.042	3.021	3.011
90	2.959	3.020	3.049	3.118	3.179	3.046	3.056	3.060	3.033	2.999
100	2.946	3.008	3.044	3.125	3.192	3.041	3.059	3.058	3.027	2.994
110	2.944	2.989	3.006	3.110	3.165	3.021	3.034	3.031	2.994	2.992
120	2.935	2.956	2.968	3.058	3.133	2.976	2.988	2.994	2.964	2.988
130	2.919	2.948	2.933	3.024	3.108	2.959	2.960	2.966	2.944	2.975
140	2.891	2.941	2.920	3.006	3.088	2.938	2.937	2.949	2.935	2.969
150	2.874	2.929	2.906	2.973	3.063	2.934	2.913	2.928	2.931	2.988
160	2.881	2.918	2.903	2.940	3.015	2.903	2.892	2.918	2.931	3.014
170	2.893	2.910	2.911	2.938	3.000	2.903	2.904	2.925	2.950	3.039
180	2.913	2.927	2.935	2.958	3.002	2.924	2.933	2.951	2.975	3.053
190	2.929	2.954	2.966	2.971	3.013	2.949	2.960	2.977	2.993	3.059
200	2.955	2.994	2.998	2.992	3.025	2.981	2.987	3.005	3.008	3.055
210	2.991	3.033	3.026	3.004	3.035	3.014	3.016	3.035	3.020	3.037
220	3.021	3.048	3.039	3.012	3.027	3.023	3.034	3.038	3.022	3.028
230	3.046	3.065	3.038	3.023	2.989	3.022	3.036	3.032	3.009	3.019
240	3.033	3.061	3.040	2.995	2.952	2.989	3.022	3.022	2.999	3.007
250	3.007	3.050	3.025	2.962	2.919	2.979	3.009	3.013	2.980	2.993
260	2.974	3.022	3.013	2.948	2.902	2.973	2.997	2.997	2.953	2.986
270	2.934	2.982	2.978	2.900	2.870	2.961	2.985	2.977	2.935	2.979
280	2.902	2.944	2.949	3.076	3.242	2.930	2.971	2.959	2.932	2.975
290	2.876	2.924	2.932	3.187	3.369	2.912	2.957	2.949	2.933	2.974
300	2.868	2.914	2.979	3.203	3.374	2.957	2.946	2.949	2.936	2.986
310	2.875	2.919	2.961	3.178	3.332	3.022	2.956	2.960	2.950	2.994
320	2.890	2.934	2.937	3.115	3.263	3.050	2.970	2.988	2.985	2.995
330	2.914	2.955	2.945	2.979	3.115	2.997	2.983	3.008	3.015	3.002
340	2.931	2.977	2.963	2.907	2.873	2.963	2.989	3.023	3.033	3.022
350	2.952	2.981	2.969	2.932	2.893	2.975	2.989	3.020	3.030	3.048

a. Shell thicknesses were derived by subtracting the measured inner radii from the corresponding outer radii, after correcting the radius data for the n=1 offset.

B.10 L510-No34

Table 86: Outer radii of specimen L510-No34 based on CMM measurements – Part 1

Angle (°)	Outer radii [a] (mm) at indicated axial location (mm)								
	End Bay 1	**Frame 1**	**Bay 1**	**Frame 2**	**Bay 2**	**Frame 3**	**Bay 3**	**Frame 4**	**Bay 4**
	66	79	107	125	153	175	204	220	235
0	122.990	122.963	122.772	122.799	122.776	122.719	122.916	123.011	123.058
10	122.977	122.950	122.871	122.815	122.806	122.819	122.902	123.004	123.062
20	122.979	122.961	122.902	122.753	122.783	122.783	122.901	123.014	123.062
30	122.994	122.988	122.994	122.980	122.999	123.032	123.034	123.044	123.059
40	123.016	123.020	123.083	123.150	123.161	123.182	123.121	123.061	123.049
50	123.031	123.043	123.100	123.150	123.152	123.130	123.102	123.056	123.030
60	123.030	123.047	123.088	123.118	123.104	123.080	123.062	123.032	123.000
70	123.018	123.034	123.062	123.079	123.066	123.051	123.029	123.001	122.969
80	122.994	123.006	123.030	123.045	123.042	123.040	123.010	122.971	122.945
90	122.959	122.966	122.995	123.011	123.019	123.031	122.991	122.942	122.924
100	122.918	122.915	122.943	122.962	122.969	122.997	122.952	122.912	122.912
110	122.875	122.862	122.833	122.830	122.850	122.841	122.868	122.886	122.908
120	122.840	122.821	122.703	122.721	122.741	122.668	122.789	122.865	122.906
130	122.826	122.809	122.743	122.703	122.717	122.711	122.759	122.862	122.910
140	122.839	122.821	122.700	122.607	122.714	122.606	122.719	122.879	122.926
150	122.867	122.860	122.833	122.821	122.864	122.852	122.888	122.930	122.949
160	122.903	122.908	122.966	123.020	123.029	123.071	123.023	122.971	122.961
170	122.936	122.951	123.013	123.056	123.058	123.052	123.030	122.990	122.965
180	122.961	122.978	123.027	123.059	123.047	123.032	123.013	122.989	122.961
190	122.973	122.992	123.028	123.052	123.039	123.027	123.002	122.977	122.945
200	122.975	122.991	123.027	123.045	123.044	123.041	123.001	122.961	122.929
210	122.970	122.976	123.016	123.029	123.046	123.055	123.000	122.942	122.922
220	122.955	122.950	122.967	122.985	122.987	123.025	122.963	122.920	122.931
230	122.942	122.920	122.785	122.783	122.792	122.758	122.865	122.898	122.919
240	122.934	122.903	122.698	122.726	122.696	122.631	122.807	122.885	122.923
250	122.937	122.910	122.827	122.794	122.791	122.766	122.815	122.886	122.927
260	122.962	122.940	122.843	122.838	122.874	122.789	122.853	122.910	122.943
270	123.001	122.989	122.982	122.987	122.999	123.003	122.981	122.966	122.973
280	123.042	123.041	123.069	123.085	123.091	123.107	123.064	123.013	122.998
290	123.078	123.085	123.115	123.134	123.125	123.113	123.085	123.044	123.015
300	123.105	123.118	123.142	123.158	123.140	123.123	123.097	123.063	123.027
310	123.121	123.133	123.158	123.172	123.158	123.144	123.113	123.071	123.035
320	123.117	123.130	123.161	123.181	123.178	123.176	123.130	123.073	123.039
330	123.093	123.104	123.151	123.178	123.190	123.198	123.135	123.066	123.041
340	123.057	123.061	123.106	123.143	123.142	123.171	123.101	123.050	123.046
350	123.018	123.005	122.946	122.939	122.937	122.910	122.995	123.027	123.054

a. Raw radial measurements, i.e. not corrected for the offset of the measurement apparatus from the axis of revolution.

Table 87: Outer radii of specimen L510-No34 based on CMM measurements – Part 2

Angle (°)	Outer radii [a] (mm) at indicated axial location (mm)								
	Bay 4	**Frame 5**	**Bay 5**	**Frame 6**	**Bay 6**	**Frame 7**	**Bay 7**	**Frame 8**	**End Bay 2**
	275	290	306	335	357	385	403	431	444
0	122.999	123.039	123.080	123.113	123.106	123.104	123.088	123.064	123.048
10	123.014	123.053	123.084	123.108	123.103	123.104	123.097	123.077	123.059
20	123.021	123.052	123.085	123.119	123.119	123.119	123.104	123.067	123.046
30	123.018	123.034	123.076	123.158	123.152	123.145	123.106	123.033	123.014
40	123.003	123.002	123.046	123.116	123.144	123.151	123.067	122.973	122.962
50	122.984	122.958	122.973	122.974	122.924	122.853	122.873	122.894	122.905
60	122.960	122.913	122.859	122.691	122.497	122.551	122.635	122.822	122.856
70	122.947	122.882	122.743	122.550	122.456	122.408	122.619	122.797	122.834
80	122.941	122.878	122.699	122.595	122.677	122.606	122.729	122.825	122.854
90	122.951	122.924	122.897	122.911	122.957	122.980	122.931	122.891	122.904
100	122.973	122.980	123.052	123.123	123.115	123.111	123.046	122.968	122.963
110	123.001	123.025	123.094	123.143	123.144	123.140	123.092	123.032	123.022
120	123.025	123.056	123.102	123.138	123.138	123.142	123.114	123.080	123.068
130	123.042	123.076	123.111	123.133	123.135	123.143	123.128	123.106	123.093
140	123.053	123.084	123.113	123.136	123.140	123.149	123.138	123.113	123.101
150	123.061	123.081	123.110	123.141	123.152	123.158	123.139	123.100	123.092
160	123.062	123.064	123.093	123.130	123.139	123.153	123.116	123.070	123.069
170	123.050	123.036	123.049	123.065	123.034	123.002	123.015	123.027	123.041
180	123.028	122.999	122.975	122.910	122.864	122.828	122.888	122.990	123.017
190	123.004	122.963	122.874	122.784	122.791	122.757	122.866	122.973	123.008
200	122.980	122.955	122.800	122.759	122.849	122.844	122.913	122.981	123.011
210	122.964	122.952	122.922	122.921	122.982	123.018	123.004	123.006	123.025
220	122.957	122.970	123.023	123.071	123.068	123.078	123.056	123.032	123.040
230	122.956	122.984	123.041	123.084	123.085	123.090	123.076	123.052	123.050
240	122.953	122.988	123.038	123.075	123.079	123.088	123.080	123.059	123.051
250	122.946	122.983	123.029	123.066	123.073	123.084	123.075	123.050	123.038
260	122.940	122.971	123.018	123.062	123.072	123.082	123.061	123.026	123.013
270	122.936	122.954	123.002	123.057	123.071	123.079	123.042	122.985	122.976
280	122.929	122.927	122.974	123.031	123.042	123.052	123.000	122.928	122.927
290	122.915	122.894	122.911	122.939	122.899	122.865	122.857	122.863	122.879
300	122.904	122.862	122.817	122.732	122.650	122.559	122.632	122.812	122.846
310	122.898	122.843	122.732	122.557	122.533	122.494	122.636	122.804	122.843
320	122.902	122.852	122.732	122.559	122.640	122.650	122.748	122.841	122.868
330	122.920	122.899	122.878	122.840	122.911	122.962	122.931	122.903	122.915
340	122.947	122.958	123.034	123.123	123.101	123.088	123.037	122.972	122.969
350	122.975	123.006	123.075	123.126	123.123	123.104	123.071	123.027	123.018

a. Raw radial measurements, i.e. not corrected for the offset of the measurement apparatus from the axis of revolution.

Table 88: Inner radii of specimen L510-No34 based on CMM measurements – Part 1

Angle (°)	Inner radii [a] (mm) at indicated axial location (mm)								
	End Bay 1	**Frame 1**	**Bay 1**	**Frame 2**	**Bay 2**	**Frame 3**	**Bay 3**	**Frame 4**	**Bay 4**
	66	79	107	125	153	175	204	220	235
0	120.095	110.098	119.881	109.950	119.886	109.811	120.008	110.111	120.115
10	120.066	110.063	119.961	109.927	119.890	109.888	119.968	110.088	120.101
20	120.037	110.040	119.975	109.851	119.855	109.844	119.954	110.079	120.089
30	120.015	110.036	120.052	110.043	120.056	110.060	120.076	110.095	120.086
40	120.007	110.034	120.114	110.206	120.198	110.205	120.146	110.099	120.065
50	119.997	110.026	120.111	110.182	120.171	110.142	120.113	110.086	120.036
60	119.974	110.006	120.079	110.123	120.105	110.079	120.065	110.053	120.011
70	119.947	109.978	120.041	110.072	120.048	110.037	120.030	110.016	119.983
80	119.928	109.954	120.002	110.025	119.996	110.016	119.995	109.982	119.951
90	119.914	109.919	119.959	109.991	119.960	110.004	119.969	109.950	119.922
100	119.894	109.889	119.917	109.949	119.918	109.973	119.935	109.929	119.907
110	119.875	109.860	119.825	109.838	119.836	109.825	119.867	109.912	119.915
120	119.851	109.845	119.731	109.779	119.777	109.685	119.815	109.910	119.928
130	119.864	109.866	119.813	109.784	119.782	109.751	119.800	109.924	119.948
140	119.917	109.917	119.792	109.736	119.802	109.690	119.771	109.964	119.968
150	119.973	109.987	119.942	109.960	119.968	109.937	119.958	110.032	120.003
160	120.017	110.046	120.087	110.177	120.145	110.179	120.112	110.086	120.032
170	120.037	110.084	120.130	110.204	120.174	110.162	120.129	110.109	120.050
180	120.046	110.092	120.127	110.185	120.150	110.131	120.110	110.106	120.048
190	120.036	110.082	120.114	110.160	120.127	110.112	120.096	110.084	120.028
200	120.030	110.063	120.099	110.130	120.106	110.106	120.075	110.054	120.005
210	120.020	110.031	120.064	110.099	120.081	110.104	120.042	110.018	119.968
220	119.991	109.985	119.993	110.033	119.994	110.050	119.975	109.980	119.939
230	119.955	109.928	119.776	109.810	119.779	109.754	119.853	109.936	119.922
240	119.905	109.878	119.667	109.737	119.674	109.613	119.785	109.894	119.905
250	119.872	109.857	119.794	109.777	119.766	109.727	119.790	109.886	119.908
260	119.873	109.868	119.794	109.817	119.843	109.748	119.822	109.896	119.912
270	119.924	109.920	119.935	109.957	119.958	109.946	119.943	109.943	119.932
280	119.992	109.993	120.035	110.073	120.065	110.065	120.036	109.992	119.961
290	120.072	110.078	120.122	110.152	120.123	110.095	120.077	110.038	119.993
300	120.154	110.164	120.194	110.215	120.167	110.136	120.109	110.082	120.025
310	120.219	110.233	120.250	110.272	120.211	110.198	120.149	110.123	120.051
320	120.247	110.272	120.287	110.314	120.256	110.260	120.191	110.153	120.083
330	120.228	110.266	120.299	110.334	120.296	110.305	120.223	110.168	120.107
340	120.185	110.229	120.263	110.306	120.266	110.285	120.201	110.164	120.126
350	120.136	110.162	120.084	110.089	120.058	110.009	120.095	110.139	120.130

a. Raw radial measurements, i.e. not corrected for the offset of the measurement apparatus from the axis of revolution.

Table 89: Inner radii of specimen L510-No34 based on CMM measurements – Part 2

Angle (°)	Inner radii [a] (mm) at indicated axial location (mm)								
	Bay 4	**Frame 5**	**Bay 5**	**Frame 6**	**Bay 6**	**Frame 7**	**Bay 7**	**Frame 8**	**End Bay 2**
	275	290	306	335	357	385	403	431	444
0	120.061	110.097	120.130	110.129	120.079	110.062	119.998	110.027	119.909
10	120.055	110.096	120.117	110.116	120.064	110.060	119.999	110.046	119.942
20	120.056	110.085	120.110	110.123	120.090	110.081	120.028	110.052	119.941
30	120.049	110.056	120.100	110.138	120.143	110.132	120.064	110.044	119.929
40	120.031	110.016	120.071	110.134	120.157	110.170	120.062	110.029	119.922
50	120.009	109.974	119.998	109.998	119.949	109.894	119.896	110.007	119.935
60	119.995	109.930	119.892	109.731	119.539	109.644	119.698	109.994	119.945
70	119.990	109.904	119.782	109.606	119.525	109.517	119.724	110.016	119.970
80	119.982	109.904	119.734	109.675	119.746	109.724	119.838	110.072	120.033
90	119.985	109.942	119.927	109.965	120.021	110.095	120.031	110.140	120.097
100	119.998	109.997	120.088	110.181	120.173	110.220	120.136	110.183	120.114
110	120.026	110.036	120.132	110.191	120.200	110.227	120.167	110.195	120.099
120	120.061	110.091	120.155	110.188	120.194	110.214	120.177	110.207	120.100
130	120.086	110.123	120.167	110.185	120.180	110.199	120.164	110.210	120.097
140	120.104	110.147	120.158	110.191	120.171	110.192	120.145	110.206	120.104
150	120.122	110.154	120.155	110.198	120.172	110.194	120.127	110.184	120.094
160	120.137	110.145	120.147	110.194	120.165	110.184	120.101	110.140	120.050
170	120.141	110.123	120.118	110.130	120.070	110.027	120.005	110.078	119.990
180	120.125	110.084	120.049	109.977	119.906	109.873	119.885	110.029	119.943
190	120.099	110.044	119.943	109.852	119.841	109.802	119.880	110.018	119.935
200	120.063	110.018	119.852	109.828	119.904	109.906	119.945	110.056	119.973
210	120.027	110.019	119.977	109.993	120.036	110.099	120.055	110.126	120.045
220	119.991	110.030	120.069	110.148	120.126	110.180	120.126	110.201	120.119
230	119.973	110.030	120.081	110.160	120.144	110.201	120.159	110.254	120.168
240	119.954	110.020	120.073	110.135	120.139	110.199	120.168	110.268	120.183
250	119.943	109.997	120.066	110.122	120.136	110.188	120.162	110.246	120.153
260	119.928	109.968	120.044	110.104	120.131	110.169	120.135	110.198	120.108
270	119.914	109.935	120.013	110.084	120.113	110.149	120.095	110.136	120.058
280	119.913	109.902	119.972	110.044	120.062	110.105	120.044	110.071	119.996
290	119.915	109.877	119.913	109.941	119.907	109.900	119.899	110.002	119.941
300	119.920	109.863	119.819	109.738	119.647	109.614	119.657	109.949	119.906
310	119.929	109.867	119.737	109.574	119.529	109.533	119.650	109.922	119.879
320	119.951	109.895	119.742	109.606	119.638	109.681	119.742	109.919	119.853
330	119.990	109.957	119.914	109.865	119.913	109.972	119.910	109.938	119.838
340	120.025	110.025	120.088	110.160	120.105	110.089	119.993	109.963	119.845
350	120.053	110.071	120.133	110.159	120.112	110.085	120.002	109.996	119.873

a. Raw radial measurements, i.e. not corrected for the offset of the measurement apparatus from the axis of revolution.

Table 90: Out-of-circularity of specimen L510-No34 based on mechanical displacement gauge measurements

Angle (degrees)	Radial Eccentricity[a] (mm) at Indicated Axial Location (mm)							
	Frame 1	**Frame 2**	**Frame 3**	**Frame 4**	**Frame 5**	**Frame 6**	**Frame 7**	**Frame 8**
	80	130	180	230	280	330	380	430
0	-0.093	-0.265	-0.301	-0.039	0.092	0.168	0.191	0.163
10	-0.091	-0.223	-0.226	-0.031	0.116	0.167	0.194	0.147
20	-0.068	-0.275	-0.263	-0.015	0.105	0.176	0.206	0.136
30	-0.028	-0.036	-0.007	0.017	0.078	0.186	0.221	0.096
40	0.021	0.143	0.182	0.037	0.033	0.156	0.212	0.023
50	0.062	0.167	0.142	0.040	-0.018	0.042	-0.071	-0.057
60	0.081	0.146	0.098	0.022	-0.077	-0.264	-0.382	-0.117
70	0.077	0.124	0.076	-0.002	-0.118	-0.425	-0.537	-0.157
80	0.064	0.101	0.075	-0.024	-0.138	-0.421	-0.383	-0.173
90	0.035	0.096	0.106	-0.022	-0.104	-0.102	-0.007	-0.123
100	-0.006	0.049	0.090	-0.014	-0.049	0.107	0.133	-0.055
110	-0.051	-0.088	-0.068	-0.038	0.004	0.158	0.167	0.041
120	-0.087	-0.182	-0.239	-0.050	0.069	0.153	0.175	0.112
130	-0.087	-0.206	-0.178	-0.048	0.085	0.136	0.168	0.132
140	-0.056	-0.271	-0.278	-0.022	0.097	0.158	0.171	0.137
150	-0.024	-0.080	-0.058	0.028	0.078	0.148	0.147	0.087
160	0.016	0.130	0.178	0.054	0.042	0.112	0.114	0.024
170	0.047	0.158	0.154	0.064	0.006	0.019	-0.062	-0.033
180	0.067	0.155	0.124	0.057	-0.034	-0.139	-0.224	-0.086
190	0.069	0.141	0.120	0.043	-0.069	-0.251	-0.292	-0.098
200	0.054	0.129	0.134	0.025	-0.079	-0.281	-0.200	-0.077
210	0.033	0.109	0.145	0.010	-0.038	-0.115	-0.020	-0.031
220	-0.006	0.048	0.104	-0.018	-0.005	0.051	0.064	0.005
230	-0.046	-0.176	-0.172	-0.039	0.023	0.119	0.111	0.044
240	-0.074	-0.230	-0.305	-0.055	0.043	0.122	0.124	0.066
250	-0.078	-0.184	-0.217	-0.056	0.052	0.127	0.138	0.077
260	-0.062	-0.163	-0.205	-0.043	0.054	0.133	0.149	0.073
270	-0.023	-0.019	0.007	-0.041	0.041	0.124	0.141	0.051
280	0.018	0.077	0.105	0.000	0.013	0.100	0.109	0.007
290	0.050	0.108	0.107	0.029	-0.039	0.034	-0.042	-0.049
300	0.071	0.124	0.102	0.039	-0.090	-0.184	-0.340	-0.124
310	0.078	0.129	0.115	0.038	-0.103	-0.371	-0.458	-0.173
320	0.066	0.136	0.137	0.036	-0.101	-0.396	-0.298	-0.129
330	0.035	0.126	0.156	0.024	-0.050	-0.113	0.033	-0.057
340	-0.006	0.086	0.136	0.010	0.015	0.182	0.161	0.030
350	-0.060	-0.085	-0.075	-0.015	0.066	0.183	0.187	0.088

a. Radial eccentricity is taken as the raw gauge reading less the n=0 and n=1 Fourier components at that axial location.

Table 91: Out-of-circularity of specimen L510-No34 based on chord gauge measurements

Angle (degrees)	Radial Eccentricity[a] (mm) at Indicated Axial Location (mm)							
	Frame 1	**Frame 2**	**Frame 3**	**Frame 4**	**Frame 5**	**Frame 6**	**Frame 7**	**Frame 8**
	80	130	180	230	280	330	380	430
0	-0.079	-0.229	-0.267	-0.030	0.099	0.159	0.180	0.135
20	-0.065	-0.250	-0.229	-0.022	0.099	0.205	0.171	0.129
40	0.012	0.162	0.185	0.042	0.025	0.132	0.203	0.038
60	0.065	0.140	0.101	0.030	-0.081	-0.287	-0.384	-0.138
80	0.054	0.104	0.085	0.004	-0.147	-0.419	-0.347	-0.151
100	-0.005	0.037	0.067	-0.034	-0.030	0.147	0.143	-0.030
120	-0.082	-0.171	-0.218	-0.053	0.039	0.120	0.155	0.070
140	-0.060	-0.287	-0.276	-0.040	0.077	0.161	0.125	0.087
160	0.019	0.133	0.188	0.050	0.057	0.105	0.126	0.044
180	0.074	0.158	0.141	0.063	0.003	-0.058	-0.174	-0.044
200	0.067	0.144	0.134	0.039	-0.057	-0.283	-0.191	-0.053
220	0.003	0.067	0.108	-0.008	-0.005	0.088	0.057	0.011
240	-0.079	-0.254	-0.298	-0.053	0.021	0.062	0.095	0.061
260	-0.079	-0.176	-0.202	-0.064	0.021	0.111	0.112	0.047
280	-0.002	0.071	0.097	0.014	-0.014	0.054	0.120	-0.024
300	0.064	0.114	0.094	0.032	-0.066	-0.159	-0.294	-0.138
320	0.075	0.141	0.144	0.032	-0.077	-0.369	-0.270	-0.093
340	0.016	0.095	0.145	0.000	0.038	0.231	0.173	0.047

a. Radial eccentricities are determined by performing Fourier decompositions of the chord height measurements, followed by expansion of the Fourier series with modified coefficients, yielding the eccentricities. The eccentricities presented here do not include the n=0 and n=1 Fourier components.

Table 92: Shell thicknesses for specimen L510-No34 based on CMM measurements

Angle (degrees)	Shell Thickness[a] (mm) at Indicated Axial Location (mm)									
	End 1	**Bay 1**	**Bay 2**	**Bay 3**	**Bay 4**	**Bay 4**	**Bay 5**	**Bay 6**	**Bay 7**	**End 2**
	66	107	153	204	235	275	306	357	403	444
0	2.900	2.903	2.894	2.909	2.936	2.929	2.936	2.997	3.056	3.102
10	2.915	2.921	2.921	2.935	2.955	2.952	2.954	3.011	3.064	3.082
20	2.945	2.937	2.933	2.950	2.971	2.962	2.965	3.003	3.044	3.072
30	2.979	2.951	2.948	2.961	2.972	2.967	2.968	2.985	3.013	3.055
40	3.008	2.978	2.967	2.980	2.986	2.974	2.970	2.968	2.980	3.015
50	3.030	2.995	2.986	2.993	2.997	2.979	2.971	2.960	2.956	2.951
60	3.052	3.014	3.004	3.003	2.996	2.972	2.968	2.949	2.922	2.897
70	3.064	3.024	3.022	3.005	2.993	2.965	2.964	2.927	2.885	2.857
80	3.058	3.030	3.049	3.022	3.004	2.970	2.971	2.931	2.887	2.820
90	3.036	3.034	3.061	3.028	3.012	2.978	2.979	2.942	2.902	2.813
100	3.015	3.024	3.052	3.023	3.018	2.990	2.976	2.952	2.918	2.861
110	2.990	3.003	3.014	3.006	3.005	2.990	2.974	2.959	2.939	2.940
120	2.980	2.966	2.963	2.979	2.991	2.980	2.963	2.964	2.957	2.991
130	2.953	2.922	2.933	2.963	2.975	2.971	2.959	2.978	2.988	3.024
140	2.913	2.900	2.909	2.951	2.971	2.964	2.972	2.996	3.021	3.029
150	2.885	2.880	2.893	2.932	2.956	2.953	2.971	3.009	3.044	3.033
160	2.878	2.868	2.881	2.912	2.940	2.937	2.963	3.005	3.049	3.056
170	2.892	2.871	2.880	2.901	2.923	2.919	2.946	2.995	3.045	3.088
180	2.910	2.889	2.892	2.902	2.921	2.911	2.941	2.988	3.039	3.111
190	2.933	2.903	2.906	2.904	2.921	2.911	2.943	2.979	3.020	3.109
200	2.943	2.918	2.932	2.923	2.928	2.921	2.959	2.972	3.000	3.071
210	2.949	2.943	2.959	2.954	2.954	2.939	2.953	2.969	2.978	3.009
220	2.966	2.967	2.988	2.984	2.991	2.965	2.959	2.962	2.956	2.946
230	2.990	3.002	3.009	3.007	2.994	2.979	2.963	2.955	2.937	2.902
240	3.034	3.027	3.018	3.017	3.012	2.993	2.965	2.950	2.929	2.881
250	3.071	3.029	3.022	3.019	3.011	2.994	2.959	2.941	2.922	2.893
260	3.096	3.048	3.028	3.025	3.023	3.001	2.969	2.940	2.930	2.907
270	3.086	3.047	3.039	3.032	3.029	3.008	2.980	2.952	2.945	2.912
280	3.059	3.037	3.026	3.022	3.026	3.002	2.992	2.968	2.948	2.918
290	3.016	2.998	3.002	3.003	3.008	2.985	2.984	2.976	2.944	2.920
300	2.961	2.955	2.973	2.984	2.990	2.969	2.984	2.983	2.956	2.917
310	2.911	2.916	2.949	2.960	2.970	2.954	2.979	2.979	2.961	2.936
320	2.879	2.883	2.925	2.936	2.945	2.936	2.973	2.975	2.978	2.983
330	2.873	2.862	2.898	2.910	2.922	2.916	2.946	2.968	2.989	3.043
340	2.880	2.854	2.880	2.899	2.911	2.909	2.930	2.965	3.011	3.087
350	2.888	2.873	2.883	2.900	2.914	2.911	2.926	2.980	3.033	3.108

a. Shell thicknesses were derived by subtracting the measured inner radii from the corresponding outer radii, after correcting the radius data for the n=1 offset.

B.11 L510-No35

Table 93: Out-of-circularity of specimen L510-No35 based on laser displacement gauge measurements – Part 1

Angle (degrees)	Radial Eccentricity[a] (mm) at Indicated Axial Location (mm)							
	Frame 1	**Bay 1**	**Frame 2**	**Bay 2**	**Frame 3**	**Bay 3**	**Frame 4**	**Bay 4**
	80	105	130	155	180	205	230	255
0	-0.249	-0.415	-0.631	-0.688	-0.805	-0.737	-0.879	**-0.851**
10	-0.195	-0.293	-0.559	-0.498	-0.705	-0.647	-0.775	-0.542
20	-0.050	-0.004	-0.001	-0.063	-0.250	-0.176	-0.172	-0.171
30	0.080	0.124	0.198	0.218	0.291	0.229	0.280	0.219
40	0.180	0.205	0.283	0.330	0.387	0.386	0.415	0.390
50	0.230	0.246	0.316	0.359	0.444	0.438	0.530	0.477
60	0.236	0.262	0.331	0.362	0.433	0.466	0.553	0.508
70	0.206	0.222	0.278	0.321	0.426	0.446	0.532	0.516
80	0.135	0.153	0.212	0.254	0.334	0.357	0.438	0.417
90	0.028	0.042	0.091	0.104	0.196	0.080	0.113	0.039
100	-0.092	-0.090	-0.067	-0.235	-0.286	-0.401	-0.567	-0.584
110	-0.188	-0.334	-0.492	-0.651	-0.802	-0.721	-0.781	-0.781
120	-0.228	-0.395	-0.634	-0.619	-0.705	-0.742	-0.837	-0.666
130	-0.190	-0.209	-0.258	-0.316	-0.437	-0.472	-0.533	-0.449
140	-0.118	-0.051	-0.014	-0.012	-0.016	0.012	0.064	-0.035
150	-0.028	0.050	0.112	0.202	0.265	0.292	0.320	0.306
160	0.046	0.131	0.208	0.277	0.329	0.393	0.432	0.423
170	0.097	0.180	0.250	0.328	0.386	0.417	0.475	0.479
180	0.117	0.186	0.264	0.324	0.384	0.415	0.471	0.496
190	0.107	0.169	0.221	0.286	0.354	0.365	0.419	0.473
200	0.065	0.097	0.154	0.225	0.266	0.273	0.322	0.346
210	0.003	0.011	0.045	0.089	0.121	0.048	0.044	-0.010
220	-0.057	-0.101	-0.091	-0.214	-0.279	-0.309	-0.420	-0.556
230	-0.083	-0.227	-0.417	-0.544	-0.673	-0.603	-0.675	-0.742
240	-0.087	-0.258	-0.527	-0.596	-0.646	-0.696	-0.860	-0.719
250	-0.046	-0.141	-0.214	-0.338	-0.522	-0.530	-0.658	-0.505
260	0.011	-0.006	0.022	-0.031	-0.129	-0.104	-0.030	-0.063
270	0.070	0.092	0.150	0.203	0.288	0.254	0.344	0.270
280	0.105	0.157	0.234	0.298	0.395	0.390	0.455	0.417
290	0.126	0.195	0.275	0.333	0.433	0.434	0.500	0.439
300	0.117	0.191	0.266	0.315	0.412	0.402	0.478	0.453
310	0.080	0.153	0.232	0.279	0.345	0.364	0.442	0.445
320	0.012	0.071	0.138	0.183	0.256	0.257	0.344	0.402
330	-0.064	-0.027	0.034	0.062	0.113	0.121	0.187	0.218
340	-0.153	-0.133	-0.117	-0.137	-0.088	-0.172	-0.217	-0.259
350	-0.223	-0.252	-0.292	-0.410	-0.516	-0.530	-0.755	-0.801

a. Radial eccentricities are based on the filtered measurements taken at the outside of the cylinder shell. Eccentricities at corrosion patches (shaded cells with bold face font) have been corrected for the corroded shell thickness.

Table 94: Out-of-circularity of specimen L510-No35 based on laser displacement gauge measurements – Part 2

Angle (degrees)	Radial Eccentricity[a] (mm) at Indicated Axial Location (mm)							
	Bay 4	**Frame 5**	**Bay 5**	**Frame 6**	**Bay 6**	**Frame 7**	**Bay 7**	**Frame 8**
	255	280	305	330	355	380	405	430
0	**-0.851**	-0.815	-0.706	-0.745	-0.546	-0.371	-0.309	-0.218
10	-0.542	-0.575	-0.662	-0.745	-0.609	-0.739	-0.417	-0.227
20	-0.171	-0.337	-0.275	-0.241	-0.206	-0.271	-0.175	-0.131
30	0.219	0.244	0.172	0.170	0.115	0.139	0.039	-0.007
40	0.390	0.412	0.369	0.316	0.269	0.240	0.160	0.088
50	0.477	0.498	0.449	0.424	0.333	0.319	0.229	0.160
60	0.508	0.535	0.473	0.436	0.357	0.307	0.235	0.191
70	0.516	0.539	0.457	0.398	0.297	0.273	0.197	0.168
80	0.417	0.471	0.364	0.291	0.220	0.190	0.130	0.124
90	0.039	0.136	0.103	0.141	0.110	0.090	0.038	0.049
100	-0.584	-0.601	-0.270	-0.141	-0.101	-0.026	-0.043	-0.039
110	-0.781	-0.750	-0.509	-0.544	-0.514	-0.195	-0.149	-0.108
120	-0.666	-0.597	-0.753	-0.811	-0.670	-0.596	-0.286	-0.148
130	-0.449	-0.636	-0.808	-0.609	-0.430	-0.507	-0.257	-0.136
140	-0.035	-0.148	-0.125	-0.029	-0.018	-0.035	-0.070	-0.068
150	0.306	0.345	0.325	0.271	0.231	0.160	0.061	-0.003
160	0.423	0.443	0.448	0.391	0.335	0.253	0.138	0.048
170	0.479	0.512	0.477	0.445	0.372	0.270	0.173	0.089
180	0.496	0.524	0.482	0.422	0.337	0.253	0.164	0.088
190	0.473	0.492	0.409	0.338	0.269	0.184	0.114	0.063
200	0.346	0.394	0.269	0.207	0.175	0.100	0.047	0.020
210	-0.010	-0.057	-0.038	0.029	0.072	0.007	-0.013	-0.027
220	-0.556	-0.777	-0.420	-0.239	-0.169	-0.064	-0.084	-0.069
230	-0.742	-0.820	-0.593	-0.584	-0.538	-0.203	-0.165	-0.103
240	-0.719	-0.486	-0.579	-0.725	-0.634	-0.489	-0.256	-0.109
250	-0.505	-0.374	-0.460	-0.518	-0.446	-0.478	-0.230	-0.081
260	-0.063	-0.122	-0.096	-0.050	-0.041	-0.059	-0.051	-0.021
270	0.270	0.282	0.220	0.262	0.234	0.191	0.102	0.047
280	0.417	0.386	0.351	0.353	0.312	0.252	0.171	0.103
290	0.439	0.432	0.374	0.391	0.324	0.277	0.201	0.155
300	0.453	0.447	0.385	0.378	0.289	0.256	0.196	0.153
310	0.445	0.462	0.355	0.331	0.246	0.215	0.158	0.130
320	0.402	0.414	0.321	0.248	0.188	0.151	0.104	0.072
330	0.218	0.276	0.167	0.133	0.094	0.064	0.042	-0.011
340	-0.259	-0.258	-0.142	-0.025	-0.035	-0.032	-0.055	-0.086
350	-0.801	-0.892	-0.536	-0.369	-0.223	-0.126	-0.137	-0.156

a. Radial eccentricities are based on the filtered measurements taken at the outside of the cylinder shell. Eccentricities at corrosion patches (shaded cells with bold face font) have been corrected for the corroded shell thickness.

Table 95: Out-of-circularity of specimen L510-No35 based on mechanical displacement gauge measurements

Angle (degrees)	Radial Eccentricity[a] (mm) at Indicated Axial Location (mm)							
	Frame 1	**Frame 2**	**Frame 3**	**Frame 4**	**Frame 5**	**Frame 6**	**Frame 7**	**Frame 8**
	80	130	180	230	280	330	380	430
0	-	-	-0.825	-0.807	-0.667	-0.799	-	-
10	-	-	-0.595	-0.604	-0.561	-0.666	-	-
20	-	-	-0.268	-0.073	-0.347	-0.231	-	-
30	-	-	0.269	0.290	0.221	0.170	-	-
40	-	-	0.411	0.450	0.392	0.347	-	-
50	-	-	0.458	0.540	0.479	0.443	-	-
60	-	-	0.468	0.569	0.527	0.468	-	-
70	-	-	0.452	0.542	0.561	0.437	-	-
80	-	-	0.380	0.444	0.559	0.341	-	-
90	-	-	0.249	0.161	0.305	0.184	-	-
100	-	-	-0.095	-0.485	-0.427	-0.050	-	-
110	-	-	-0.695	-0.741	-0.741	-0.425	-	-
120	-	-	-0.824	-0.859	-0.661	-0.771	-	-
130	-	-	-0.548	-0.680	-0.635	-0.786	-	-
140	-	-	-0.236	-0.073	-0.426	-0.275	-	-
150	-	-	0.177	0.256	0.187	0.177	-	-
160	-	-	0.301	0.403	0.380	0.349	-	-
170	-	-	0.364	0.462	0.456	0.438	-	-
180	-	-	0.377	0.471	0.492	0.438	-	-
190	-	-	0.369	0.432	0.490	0.386	-	-
200	-	-	0.306	0.335	0.465	0.273	-	-
210	-	-	0.199	0.127	0.224	0.097	-	-
220	-	-	-0.101	-0.355	-0.581	-0.158	-	-
230	-	-	-0.590	-0.637	-0.845	-0.504	-	-
240	-	-	-0.705	-0.842	-0.590	-0.746	-	-
250	-	-	-0.544	-0.651	-0.421	-0.599	-	-
260	-	-	-0.200	0.010	-0.166	-0.111	-	-
270	-	-	0.279	0.368	0.290	0.278	-	-
280	-	-	0.410	0.486	0.398	0.382	-	-
290	-	-	0.451	0.515	0.444	0.424	-	-
300	-	-	0.436	0.495	0.469	0.407	-	-
310	-	-	0.371	0.430	0.480	0.360	-	-
320	-	-	0.255	0.292	0.479	0.259	-	-
330	-	-	0.081	0.025	0.215	0.128	-	-
340	-	-	-0.184	-0.530	-0.562	-0.125	-	-
350	-	-	-0.654	-0.770	-0.885	-0.540	-	-

a. Radial eccentricity is taken as the raw gauge reading less the n=0 and n=1 Fourier components at that axial location.

Table 96: Measured shell thicknesses for specimen L510-No35 – global measurements

Angle (degrees)	Shell Thickness[a] (mm) at Indicated Axial Location (mm)						
	Bay 1	**Bay 2**	**Bay 3**	**Bay 4**	**Bay 5**	**Bay 6**	**Bay 7**
	105	155	205	255	305	355	405
0	2.927	3.038	3.071	**2.468**	3.058	2.996	3.012
10	2.896	3.015	3.050	3.053	3.021	2.994	3.025
20	2.893	2.999	3.035	3.040	2.999	3.000	3.036
30	2.897	2.994	3.028	3.012	2.995	3.018	3.050
40	2.945	3.007	3.030	2.994	3.005	3.032	3.064
50	2.984	3.028	3.044	3.003	3.021	3.041	3.060
60	3.033	3.056	3.050	3.013	3.037	3.038	3.045
70	3.075	3.084	3.056	3.032	3.050	3.031	3.024
80	3.115	3.109	3.062	3.046	3.035	3.022	3.005
90	3.157	3.136	3.077	3.064	3.049	3.007	2.972
100	3.185	3.161	3.103	3.068	3.036	2.987	2.932
110	3.219	3.171	3.114	3.056	3.028	2.970	2.904
120	3.231	3.159	3.110	3.046	3.012	2.943	2.893
130	3.202	3.149	3.094	3.019	3.005	2.924	2.885
140	3.173	3.126	3.065	2.997	2.962	2.932	2.901
150	3.109	3.093	3.039	2.983	2.962	2.940	2.909
160	3.040	3.054	3.016	2.973	2.964	2.945	2.947
170	2.979	2.991	3.003	2.968	2.968	2.958	2.973
180	2.926	2.982	2.988	2.966	2.976	2.964	3.017
190	2.893	2.959	2.959	2.964	2.971	2.981	3.052
200	2.880	2.938	2.962	2.961	2.975	2.995	3.081
210	2.878	2.929	2.947	2.937	2.970	2.995	3.093
220	2.880	2.926	2.926	2.921	2.951	3.016	3.107
230	2.890	2.921	2.899	2.903	2.924	3.021	3.102
240	2.924	2.914	2.875	2.890	2.934	3.034	3.104
250	2.951	2.929	2.898	2.884	2.939	3.031	3.086
260	2.977	2.925	2.896	2.887	2.954	3.026	3.066
270	2.994	2.936	2.908	2.906	2.950	3.007	3.051
280	3.014	2.958	2.922	2.928	3.002	3.030	3.037
290	3.026	2.980	2.958	2.950	3.023	3.002	3.008
300	3.049	3.005	2.993	3.019	3.051	3.047	2.979
310	3.055	3.024	3.020	3.058	3.069	3.055	2.953
320	3.047	3.039	3.038	3.082	3.077	3.045	2.938
330	3.028	3.031	3.059	3.089	3.109	3.037	2.954
340	2.995	3.069	3.103	3.098	3.103	2.997	2.904
350	2.952	3.015	3.090	3.089	3.089	2.998	2.990

a. Shell thickness determined by ultrasonic thickness gauge measurements of the shell. Corroded locations are indicated by shaded cells with bold faced font.

Table 97: Measured shell thicknesses for specimen L510-No35 – corrosion patch measurements

Angle (degrees)	**Shell Thickness[a] (mm) at Indicated Axial Location (mm)**		
	236	255	274
-9	2.502	2.494	2.477
0	2.469	2.463	2.465
9	2.472	2.444	2.437

a. Shell thickness determined by ultrasonic thickness gauge measurements of the shell.

B.12 L510-No36

Table 98: Out-of-circularity of specimen L510-No36 based on laser displacement gauge measurements – Part 1

Angle (degrees)	Radial Eccentricity[a] (mm) at Indicated Axial Location (mm)							
	Frame 1	**Bay 1**	**Frame 2**	**Bay 2**	**Frame 3**	**Bay 3**	**Frame 4**	**Bay 4**
	80	105	130	155	180	205	230	255
0	0.226	0.299	0.351	0.429	0.462	0.520	0.538	**0.558**
10	0.217	0.275	0.335	0.402	0.442	0.501	0.525	0.610
20	0.162	0.199	0.259	0.312	0.348	0.395	0.413	0.364
30	0.068	0.085	0.149	0.171	0.207	0.180	0.178	0.163
40	-0.036	-0.030	0.005	-0.047	-0.078	-0.209	-0.238	-0.205
50	-0.135	-0.210	-0.265	-0.392	-0.512	-0.611	-0.608	-0.589
60	-0.201	-0.404	-0.591	-0.652	-0.700	-0.618	-0.557	-0.664
70	-0.183	-0.292	-0.389	-0.487	-0.465	-0.450	-0.418	-0.411
80	-0.117	-0.082	-0.019	-0.065	-0.021	-0.084	-0.095	-0.096
90	-0.047	0.027	0.085	0.143	0.195	0.162	0.164	0.129
100	0.026	0.090	0.147	0.204	0.235	0.243	0.240	0.232
110	0.067	0.128	0.172	0.215	0.254	0.289	0.305	0.308
120	0.094	0.150	0.178	0.233	0.252	0.322	0.332	0.347
130	0.088	0.121	0.153	0.221	0.247	0.317	0.325	0.347
140	0.065	0.088	0.126	0.206	0.235	0.280	0.270	0.283
150	0.013	0.048	0.072	0.138	0.147	0.104	0.052	0.116
160	-0.037	-0.036	-0.039	-0.146	-0.254	-0.352	-0.406	-0.281
170	-0.083	-0.214	-0.382	-0.511	-0.644	-0.631	-0.639	-0.685
180	-0.096	-0.286	-0.534	-0.610	-0.708	-0.642	-0.648	-0.838
190	-0.061	-0.123	-0.175	-0.290	-0.312	-0.398	-0.448	-0.452
200	-0.002	0.044	0.087	0.076	0.093	0.027	0.002	0.015
210	0.053	0.117	0.170	0.232	0.262	0.250	0.255	0.281
220	0.104	0.153	0.226	0.286	0.345	0.362	0.390	0.409
230	0.127	0.174	0.248	0.313	0.396	0.420	0.486	0.498
240	0.124	0.166	0.251	0.315	0.394	0.457	0.524	0.522
250	0.088	0.142	0.233	0.304	0.377	0.438	0.507	0.502
260	0.033	0.090	0.184	0.264	0.310	0.375	0.417	0.394
270	-0.029	0.022	0.108	0.174	0.216	0.192	0.213	0.206
280	-0.104	-0.055	0.013	-0.082	-0.159	-0.247	-0.294	-0.185
290	-0.181	-0.228	-0.286	-0.537	-0.682	-0.715	-0.784	-0.724
300	-0.221	-0.459	-0.779	-0.828	-0.883	-0.833	-0.856	-1.038
310	-0.200	-0.404	-0.665	-0.657	-0.673	-0.765	-0.794	-0.869
320	-0.111	-0.127	-0.140	-0.202	-0.215	-0.313	-0.373	-0.306
330	0.003	0.074	0.136	0.149	0.153	0.162	0.170	0.170
340	0.103	0.186	0.253	0.316	0.318	0.385	0.370	0.394
350	0.176	0.270	0.326	0.403	0.417	0.487	0.482	0.494

a. Radial eccentricities are based on the filtered measurements taken at the outside of the cylinder shell. Eccentricities at corrosion patches (shaded cells with bold face font) have been corrected for the corroded shell thickness.

Table 99: Out-of-circularity of specimen L510-No36 based on laser displacement gauge measurements – Part 2

Angle (degrees)	Radial Eccentricity[a] (mm) at Indicated Axial Location (mm)							
	Bay 4	**Frame 5**	**Bay 5**	**Frame 6**	**Bay 6**	**Frame 7**	**Bay 7**	**Frame 8**
	255	280	305	330	355	380	405	430
0	**0.558**	0.548	0.509	0.451	0.424	0.316	0.265	0.189
10	0.610	0.510	0.457	0.410	0.363	0.285	0.224	0.190
20	0.364	0.390	0.355	0.324	0.314	0.246	0.164	0.154
30	0.163	0.196	0.183	0.214	0.215	0.183	0.063	0.065
40	-0.205	-0.145	-0.098	-0.048	0.027	0.036	-0.023	-0.018
50	-0.589	-0.615	-0.516	-0.485	-0.506	-0.299	-0.170	-0.091
60	-0.664	-0.724	-0.690	-0.664	-0.739	-0.533	-0.264	-0.127
70	-0.411	-0.401	-0.477	-0.433	-0.398	-0.355	-0.222	-0.120
80	-0.096	-0.038	-0.085	-0.068	-0.061	-0.053	-0.098	-0.073
90	0.129	0.145	0.142	0.145	0.141	0.104	0.011	-0.007
100	0.232	0.236	0.226	0.212	0.207	0.161	0.097	0.050
110	0.308	0.316	0.295	0.276	0.266	0.205	0.150	0.096
120	0.347	0.355	0.356	0.318	0.313	0.236	0.211	0.117
130	0.347	0.359	0.368	0.360	0.327	0.241	0.183	0.095
140	0.283	0.306	0.342	0.344	0.331	0.209	0.127	0.037
150	0.116	0.152	0.178	0.238	0.232	0.139	0.015	-0.047
160	-0.281	-0.302	-0.297	-0.321	-0.238	-0.182	-0.154	-0.126
170	-0.685	-0.844	-0.826	-0.955	-0.957	-0.666	-0.338	-0.182
180	-0.838	-0.920	-0.879	-0.935	-0.856	-0.693	-0.366	-0.183
190	-0.452	-0.443	-0.457	-0.410	-0.325	-0.290	-0.226	-0.131
200	0.015	0.069	0.053	0.119	0.108	0.078	-0.013	-0.036
210	0.281	0.307	0.311	0.348	0.307	0.236	0.126	0.072
220	0.409	0.442	0.426	0.431	0.377	0.312	0.209	0.156
230	0.498	0.518	0.472	0.479	0.411	0.352	0.247	0.213
240	0.522	0.540	0.486	0.479	0.425	0.367	0.271	0.221
250	0.502	0.506	0.472	0.469	0.412	0.357	0.240	0.198
260	0.394	0.406	0.411	0.418	0.390	0.315	0.184	0.122
270	0.206	0.238	0.259	0.324	0.309	0.235	0.091	0.010
280	-0.185	-0.128	-0.110	-0.063	0.000	0.017	-0.073	-0.104
290	-0.724	-0.762	-0.733	-0.812	-0.679	-0.545	-0.308	-0.208
300	-1.038	-1.132	-1.087	-1.174	-1.163	-0.942	-0.464	-0.252
310	-0.869	-0.889	-0.852	-0.852	-0.863	-0.715	-0.408	-0.247
320	-0.306	-0.282	-0.290	-0.236	-0.224	-0.195	-0.177	-0.170
330	0.170	0.187	0.189	0.234	0.246	0.202	0.023	-0.058
340	0.394	0.388	0.406	0.401	0.414	0.303	0.163	0.058
350	0.494	0.513	0.499	0.461	0.450	0.332	0.238	0.138

a. Radial eccentricities are based on the filtered measurements taken at the outside of the cylinder shell. Eccentricities at corrosion patches (shaded cells with bold face font) have been corrected for the corroded shell thickness.

Table 100: Out-of-circularity of specimen L510-No36 based on mechanical displacement gauge measurements

Angle (degrees)	Radial Eccentricity[a] (mm) at Indicated Axial Location (mm)							
	Frame 1	**Frame 2**	**Frame 3**	**Frame 4**	**Frame 5**	**Frame 6**	**Frame 7**	**Frame 8**
	80	130	180	230	280	330	380	430
0	-	-	0.435	0.519	0.539	0.462	-	-
10	-	-	0.423	0.502	0.493	0.408	-	-
20	-	-	0.345	0.401	0.349	0.326	-	-
30	-	-	0.215	0.198	0.178	0.226	-	-
40	-	-	-0.062	-0.223	-0.156	0.003	-	-
50	-	-	-0.481	-0.598	-0.621	-0.441	-	-
60	-	-	-0.712	-0.626	-0.779	-0.691	-	-
70	-	-	-0.561	-0.489	-0.475	-0.564	-	-
80	-	-	-0.103	-0.160	-0.090	-0.208	-	-
90	-	-	0.154	0.113	0.106	0.049	-	-
100	-	-	0.214	0.217	0.215	0.196	-	-
110	-	-	0.239	0.274	0.299	0.266	-	-
120	-	-	0.251	0.317	0.355	0.325	-	-
130	-	-	0.254	0.335	0.375	0.365	-	-
140	-	-	0.249	0.306	0.350	0.382	-	-
150	-	-	0.226	0.228	0.244	0.345	-	-
160	-	-	-0.023	-0.204	-0.063	0.035	-	-
170	-	-	-0.466	-0.549	-0.627	-0.682	-	-
180	-	-	-0.729	-0.635	-0.984	-1.021	-	-
190	-	-	-0.497	-0.576	-0.662	-0.702	-	-
200	-	-	-0.011	-0.146	-0.045	-0.078	-	-
210	-	-	0.223	0.211	0.267	0.289	-	-
220	-	-	0.316	0.359	0.425	0.424	-	-
230	-	-	0.368	0.468	0.521	0.484	-	-
240	-	-	0.411	0.520	0.551	0.506	-	-
250	-	-	0.391	0.526	0.513	0.494	-	-
260	-	-	0.300	0.432	0.407	0.440	-	-
270	-	-	0.214	0.210	0.222	0.321	-	-
280	-	-	-0.211	-0.382	-0.217	-0.106	-	-
290	-	-	-0.765	-0.854	-0.911	-0.925	-	-
300	-	-	-0.896	-0.890	-1.211	-1.197	-	-
310	-	-	-0.573	-0.765	-0.717	-0.763	-	-
320	-	-	-0.078	-0.175	-0.062	-0.112	-	-
330	-	-	0.197	0.251	0.264	0.287	-	-
340	-	-	0.335	0.397	0.430	0.410	-	-
350	-	-	0.405	0.486	0.518	0.447	-	-

a. Radial eccentricity is taken as the raw gauge reading less the n=0 and n=1 Fourier components at that axial location.

Table 101: Measured shell thicknesses for specimen L510-No36 – global measurements

Angle (degrees)	Shell Thickness[a] (mm) at Indicated Axial Location (mm)						
	Bay 1	**Bay 2**	**Bay 3**	**Bay 4**	**Bay 5**	**Bay 6**	**Bay 7**
	105	155	205	255	305	355	405
0	2.963	2.967	2.942	**2.301**	2.894	2.956	2.984
10	2.984	2.966	2.940	2.928	2.928	2.981	2.988
20	3.009	2.986	2.958	2.950	2.961	3.016	3.018
30	3.043	3.012	2.985	2.982	3.021	3.073	3.075
40	3.078	3.038	3.002	3.000	3.071	3.100	3.051
50	3.091	3.043	3.010	3.029	3.101	3.117	3.088
60	3.089	3.046	3.017	3.069	3.144	3.144	3.110
70	3.067	3.039	3.035	3.110	3.162	3.141	3.109
80	3.041	3.026	3.049	3.135	3.169	3.136	3.100
90	3.015	3.029	3.076	3.154	3.167	3.112	3.087
100	2.985	3.021	3.073	3.148	3.128	3.056	3.046
110	2.982	3.043	3.113	3.165	3.114	3.034	3.029
120	2.966	3.001	3.101	3.121	3.068	2.988	2.998
130	3.004	3.085	3.136	3.129	3.063	2.992	2.989
140	3.028	3.105	3.126	3.084	3.043	2.975	2.974
150	3.069	3.121	3.126	3.066	3.024	2.969	2.969
160	3.094	3.127	3.106	3.046	3.020	2.984	2.973
170	3.086	3.121	3.086	3.031	3.016	2.998	2.989
180	3.121	3.124	3.063	3.018	3.010	3.012	2.996
190	3.117	3.114	3.049	3.021	3.014	3.026	3.037
200	3.114	3.105	3.044	3.031	3.026	3.043	3.058
210	3.112	3.090	3.066	3.029	3.002	3.034	3.059
220	3.103	3.084	3.067	3.063	3.061	3.017	3.063
230	3.094	3.076	3.074	3.082	3.105	3.081	3.090
240	3.084	3.075	3.077	3.111	3.115	3.094	3.084
250	3.073	3.061	3.073	3.105	3.116	3.085	3.072
260	3.062	3.054	3.069	3.090	3.098	3.062	3.058
270	3.047	3.040	3.042	3.066	3.053	3.031	3.022
280	3.029	3.022	3.018	3.017	2.999	2.978	2.975
290	3.003	2.993	2.963	2.953	2.928	2.913	2.934
300	2.978	2.967	2.928	2.902	2.875	2.872	2.916
310	2.947	2.930	2.907	2.872	2.829	2.820	2.900
320	2.930	2.929	2.896	2.858	2.811	2.823	2.897
330	2.932	2.937	2.894	2.845	2.809	2.828	2.925
340	2.933	2.938	2.893	2.861	2.820	2.861	2.928
350	2.943	2.938	2.920	2.890	2.855	2.916	2.935

a. Shell thickness determined by ultrasonic thickness gauge measurements of the shell. Corroded locations are indicated by shaded cells with bold faced font.

Table 102: Measured shell thicknesses for specimen L510-No36 – corrosion patch measurements

Angle (degrees)	**Shell Thickness[a] (mm) at Indicated Axial Location (mm)**		
	236	255	274
-9	2.278	2.286	2.344
0	2.283	2.295	2.346
9	2.292	2.320	2.368

a. Shell thickness determined by ultrasonic thickness gauge measurements of the shell.

Annex C Out-of-circularity and shell thickness plots

C.1 L510-No13

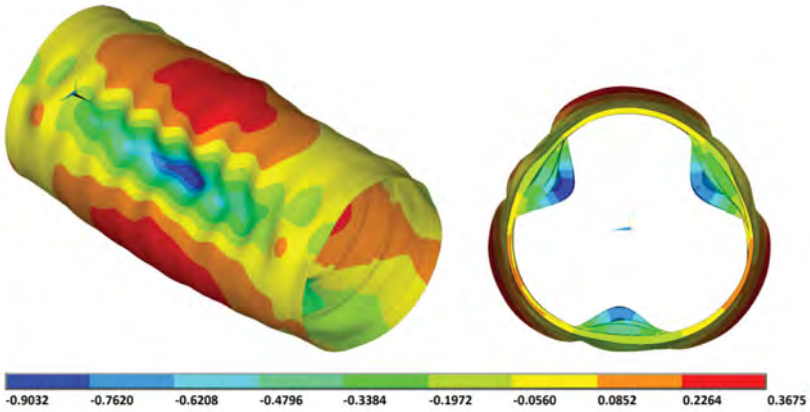

Figure 117: Graphical representation of out-of-circularity of specimen L510-No13. The colour contour maps describe the radial eccentricity (mm) based on a double Fourier analysis of the measurements of the outer shell taken by the laser displacement gauges. OOC is also indicated by the deformed shape, whereby the imperfections are magnified by a factor of 50.

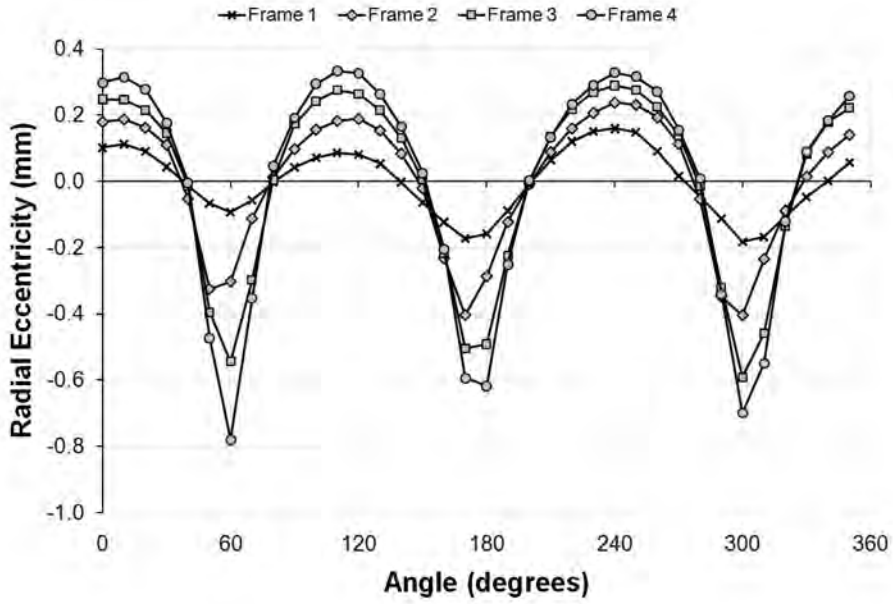

Figure 118: Showing the circumferential out-of-circularity mode of specimen L510-No13 based on measurements at the outside of the shell surface. The filtered measurements taken about the circumference using a laser displacement gauge are shown for axial locations nearby the indicated ring-stiffeners.

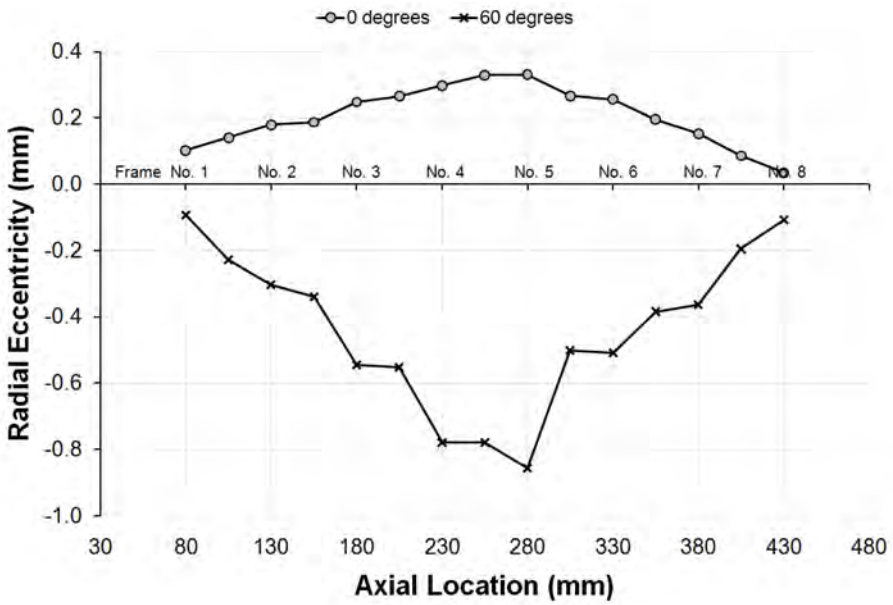

Figure 119: Showing the axial out-of-circularity mode of specimen L510-No13 based on measurements at the outside of the shell surface. The filtered measurements taken over the cylinder length using a laser displacement gauge are shown for circumferential locations associated with the maximum inward and outward radial eccentricities.

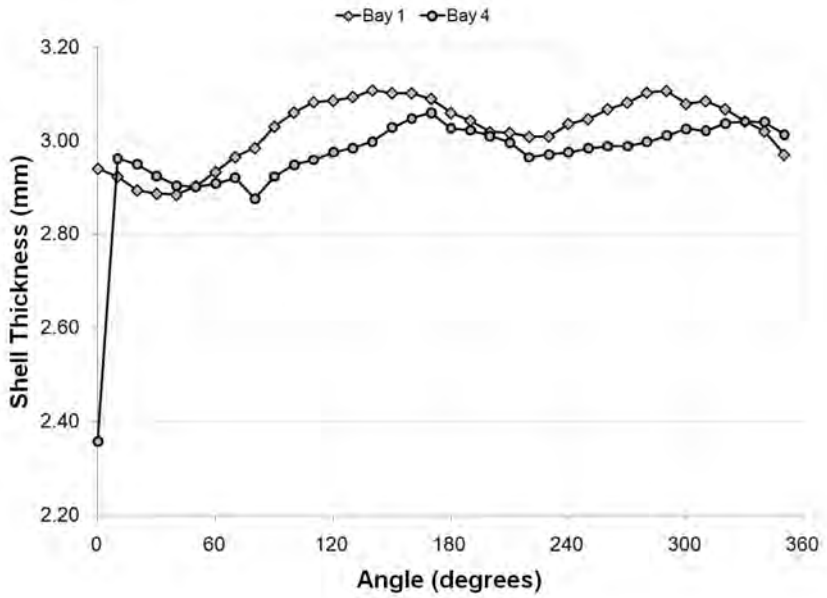

Figure 120: Showing the circumferential distribution of shell thickness at representative axial locations for specimen L510-No13, based on ultrasonic thickness gauge readings.

C.2 L510-No14

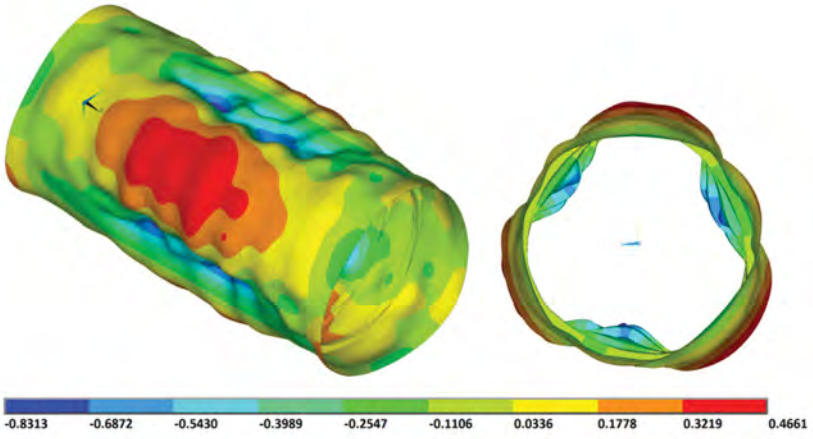

Figure 121: Graphical representation of out-of-circularity of specimen L510-No14. The colour contour maps describe the radial eccentricity (mm) based on a double Fourier analysis of the measurements of the outer shell taken by the laser displacement gauges. OOC is also indicated by the deformed shape, whereby the imperfections are magnified by a factor of 50.

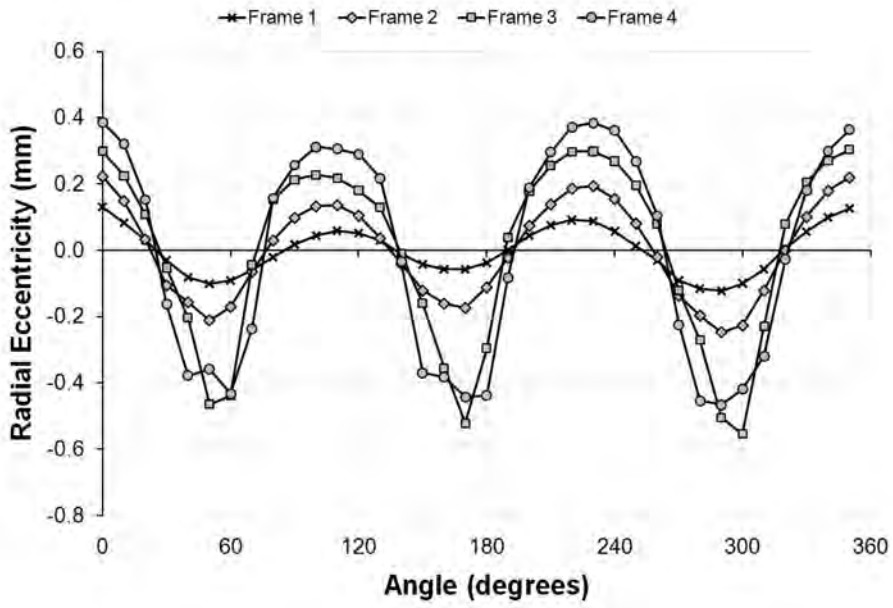

Figure 122: Showing the circumferential out-of-circularity mode of specimen L510-No14 based on measurements at the outside of the shell surface. The filtered measurements taken about the circumference using a laser displacement gauge are shown for axial locations nearby the indicated ring-stiffeners.

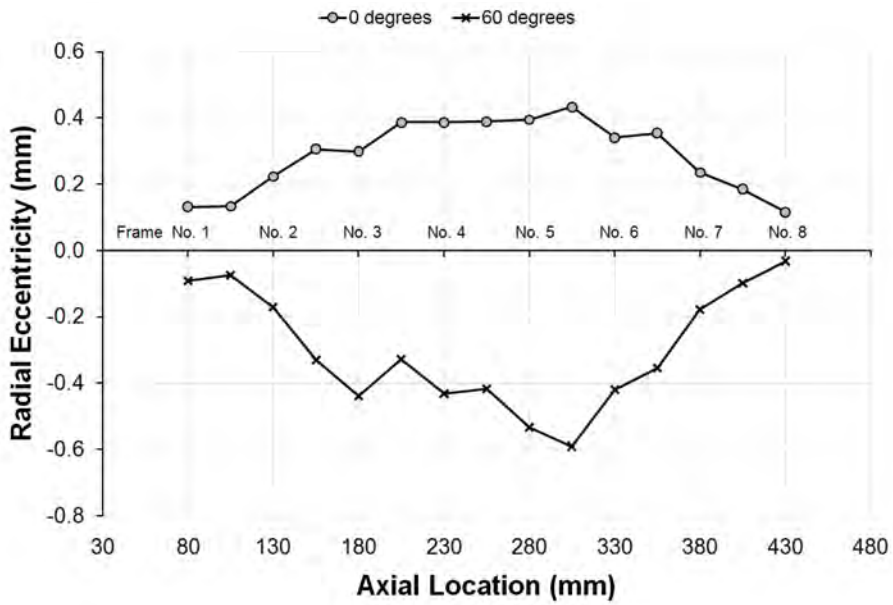

Figure 123: Showing the axial out-of-circularity mode of specimen L510-No14 based on measurements at the outside of the shell surface. The filtered measurements taken over the cylinder length using a laser displacement gauge are shown for circumferential locations associated with the maximum inward and outward radial eccentricities.

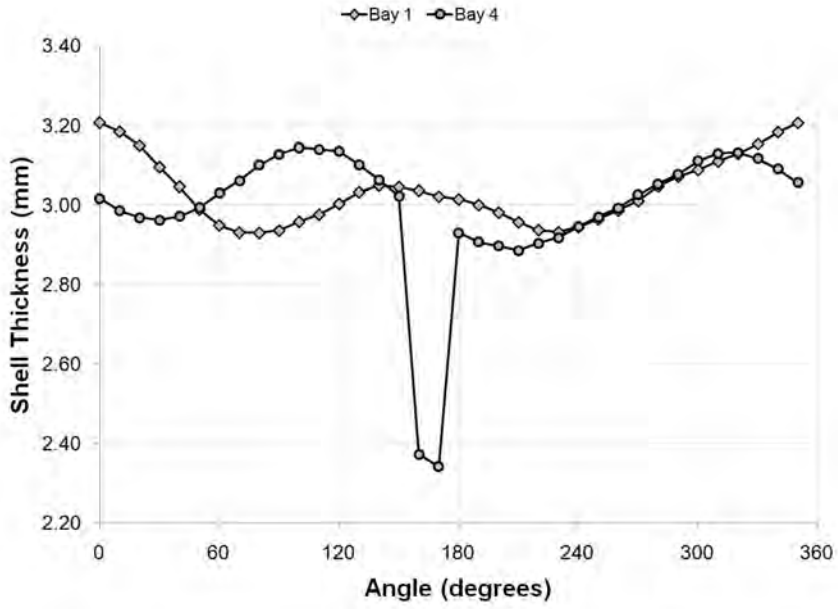

Figure 124: Showing the circumferential distribution of shell thickness at representative axial locations for specimen L510-No14, based on ultrasonic thickness gauge readings.

C.3 L510-No17

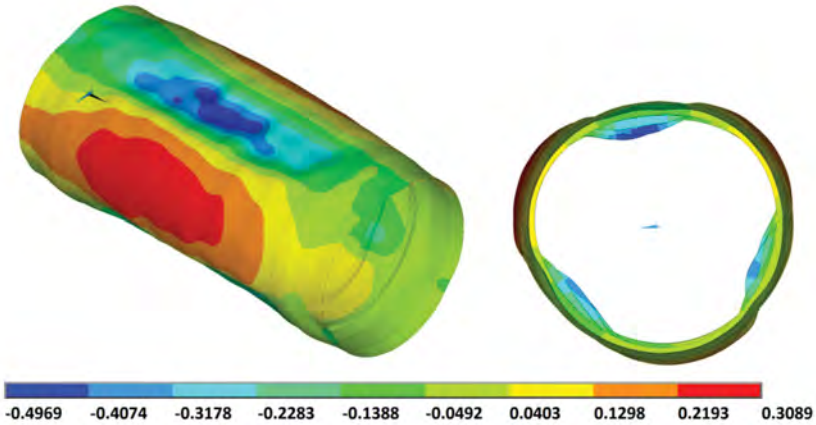

Figure 125: Graphical representation of out-of-circularity of specimen L510-No17. The colour contour maps describe the radial eccentricity (mm) based on a double Fourier analysis of the measurements of the outer shell taken by the CMM. OOC is also indicated by the deformed shape, whereby the imperfections are magnified by a factor of 50.

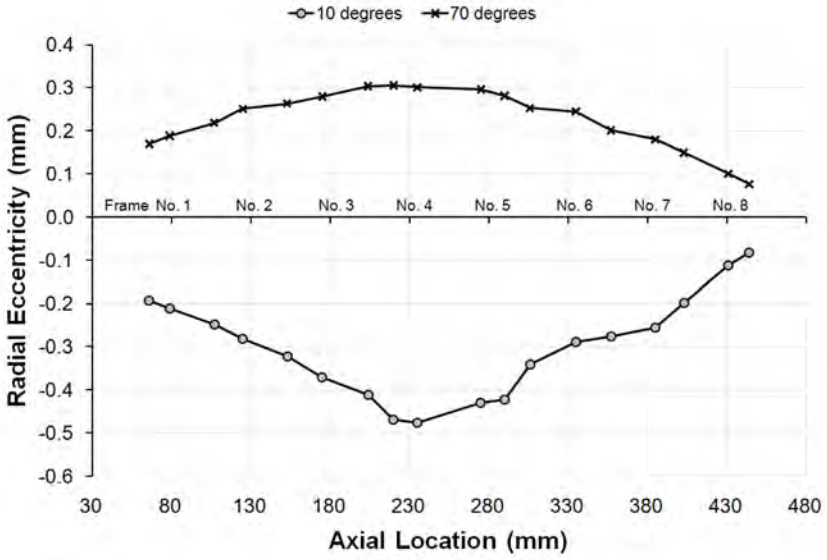

Figure 126: Showing the axial out-of-circularity mode of specimen L510-No17 based on measurements at the outside of the shell surface. All measurements taken over the cylinder length using a CMM are shown for circumferential locations associated with the maximum inward and outward radial eccentricities (10° and 70°, respectively).

C.4 L510-No18

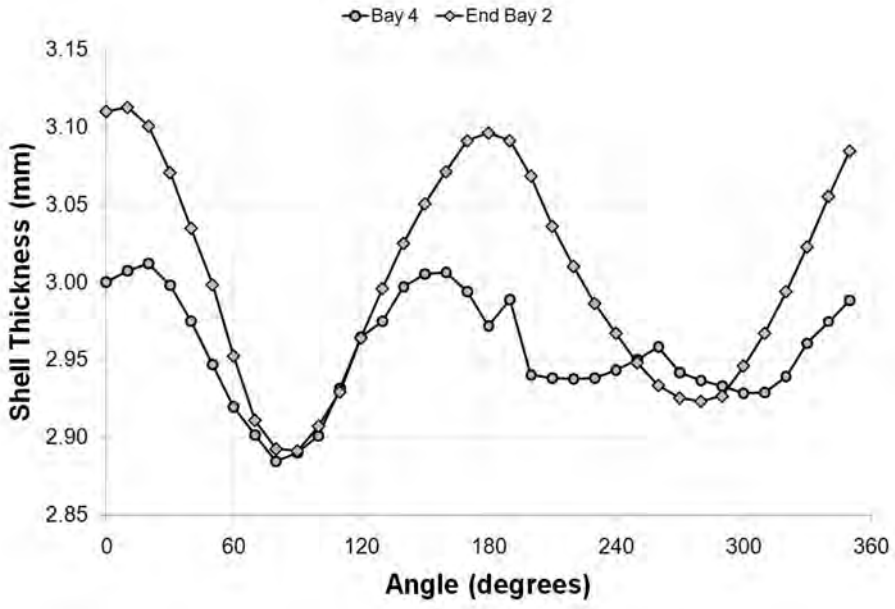

Figure 127: Showing the circumferential distribution of shell thickness at representative axial locations for specimen L510-No18, based on CMM measurements of the inner and outer shell radii.

C.5 L510-No19

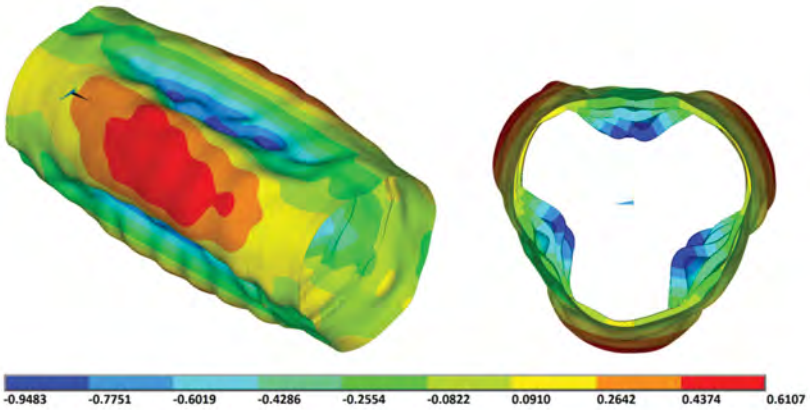

Figure 128: Graphical representation of out-of-circularity of specimen L510-No19. The colour contour maps describe the radial eccentricity (mm) based on a double Fourier analysis of the measurements of the outer shell taken by the laser displacement gauges. OOC is also indicated by the deformed shape, whereby the imperfections are magnified by a factor of 50.

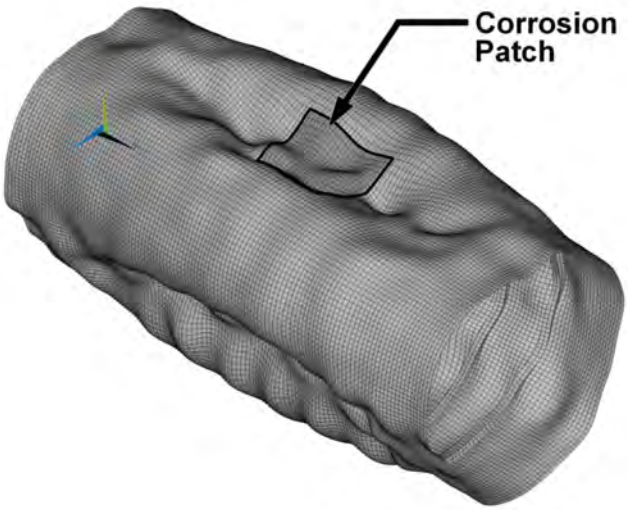

Figure 129: Graphical representation of out-of-circularity of specimen L510-No19, showing the location of the in-phase corrosion patch with respect to the out-of-circularity shape. OOC is indicated by the deformed shape, whereby the imperfections are magnified by a factor of 50.

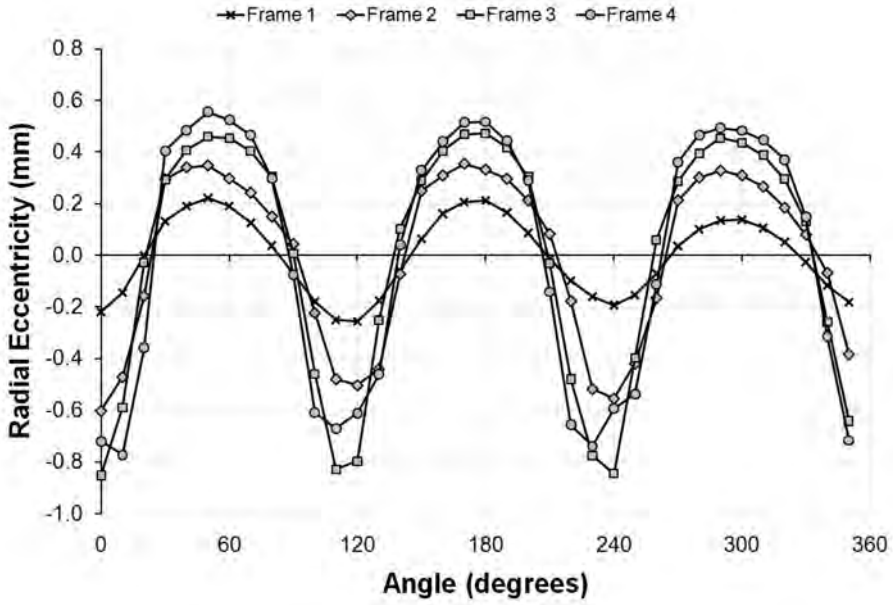

Figure 130: Showing the circumferential out-of-circularity mode of specimen L510-No19 based on measurements at the outside of the shell surface. The filtered measurements taken about the circumference using a laser displacement gauge are shown for axial locations nearby the indicated ring-stiffeners.

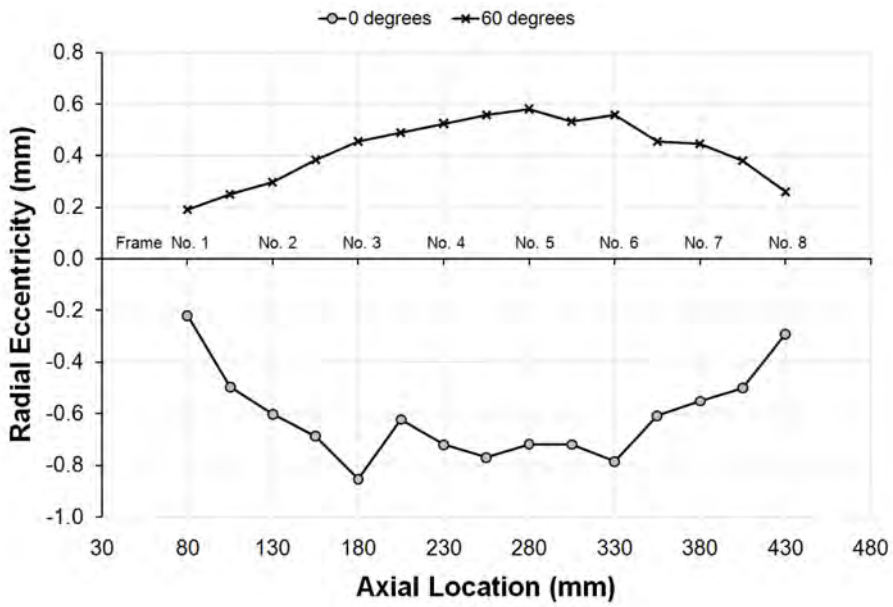

Figure 131: Showing the axial out-of-circularity mode of specimen L510-No19 based on measurements at the outside of the shell surface. The filtered measurements taken over the cylinder length using a laser displacement gauge are shown for circumferential locations associated with the maximum inward and outward radial eccentricities.

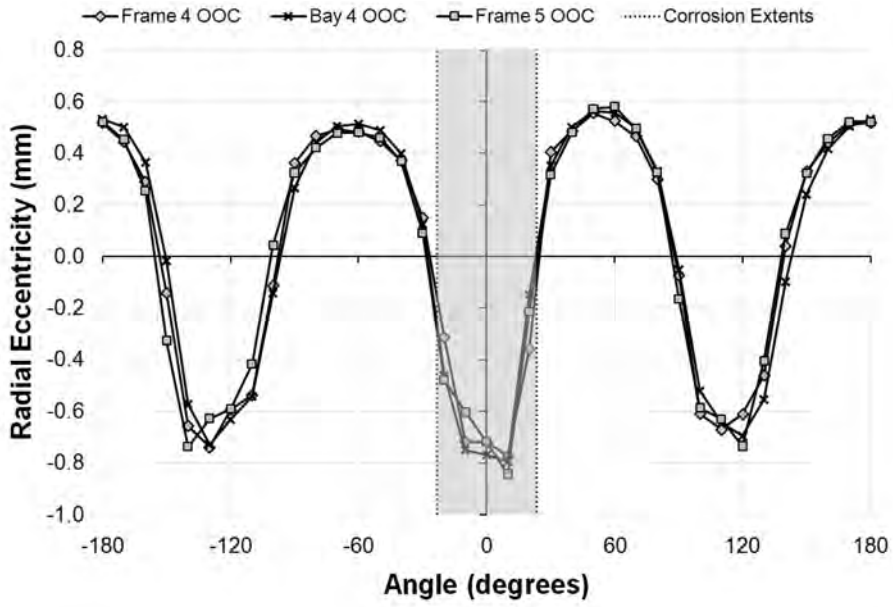

Figure 132: Showing the circumferential OOC mode of specimen L510-No19 based on filtered laser displacement gauge measurements at the outside of the shell surface at the central bay and the adjacent frames. The circumferential extents of the large, in-phase corrosion patch are indicated by the dashed lines and shaded area.

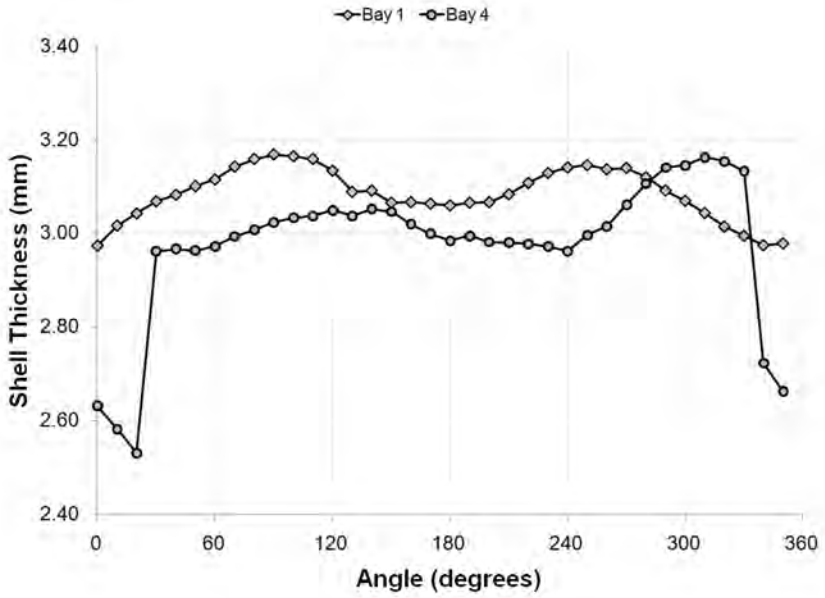

Figure 133: Showing the circumferential distribution of shell thickness at representative axial locations for specimen L510-No19, based on ultrasonic thickness gauge readings.

C.6 L510-No20

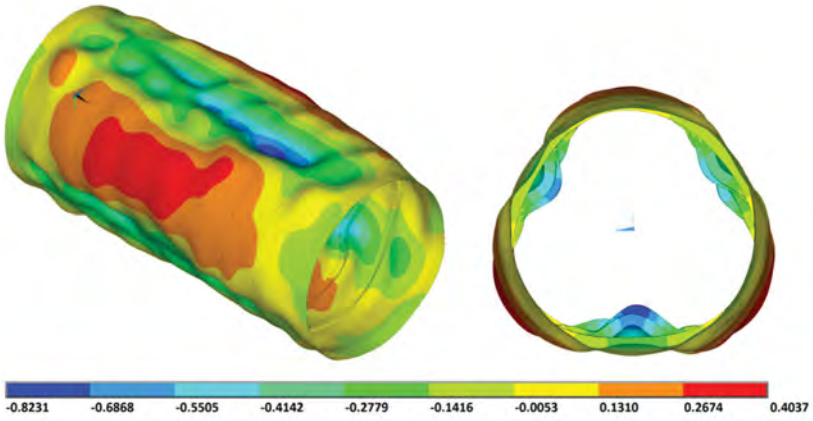

Figure 134: Graphical representation of out-of-circularity of specimen L510-No20. The colour contour maps describe the radial eccentricity (mm) based on a double Fourier analysis of the measurements of the outer shell taken by the laser displacement gauges. OOC is also indicated by the deformed shape, whereby the imperfections are magnified by a factor of 50.

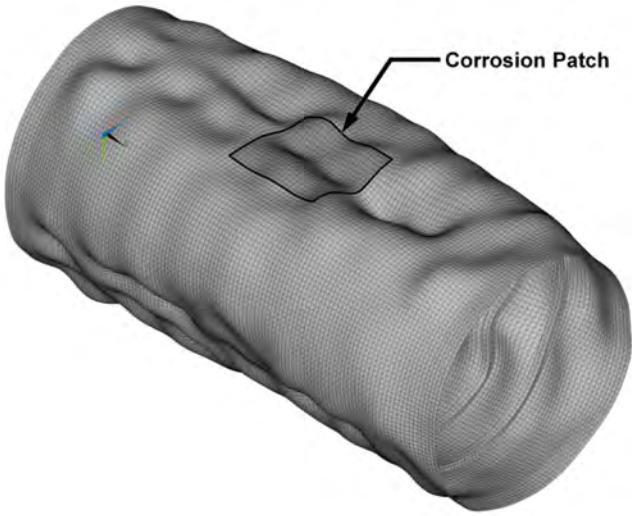

Figure 135: Graphical representation of out-of-circularity of specimen L510-No20, showing the location of the in-phase corrosion patch with respect to the out-of-circularity shape. OOC is indicated by the deformed shape, whereby the imperfections are magnified by a factor of 50.

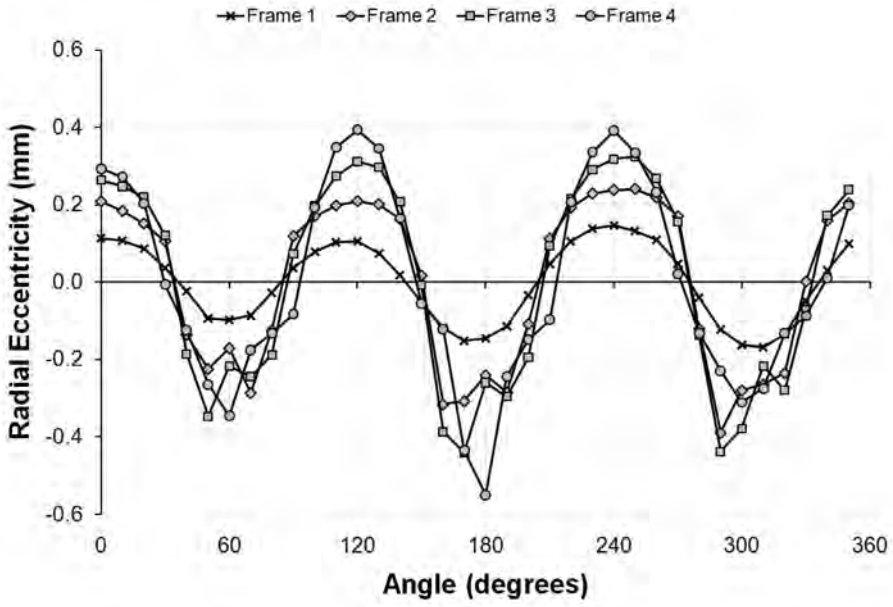

Figure 136: Showing the circumferential out-of-circularity mode of specimen L510-No20 based on measurements at the outside of the shell surface. The filtered measurements taken about the circumference using a laser displacement gauge are shown for axial locations nearby the indicated ring-stiffeners.

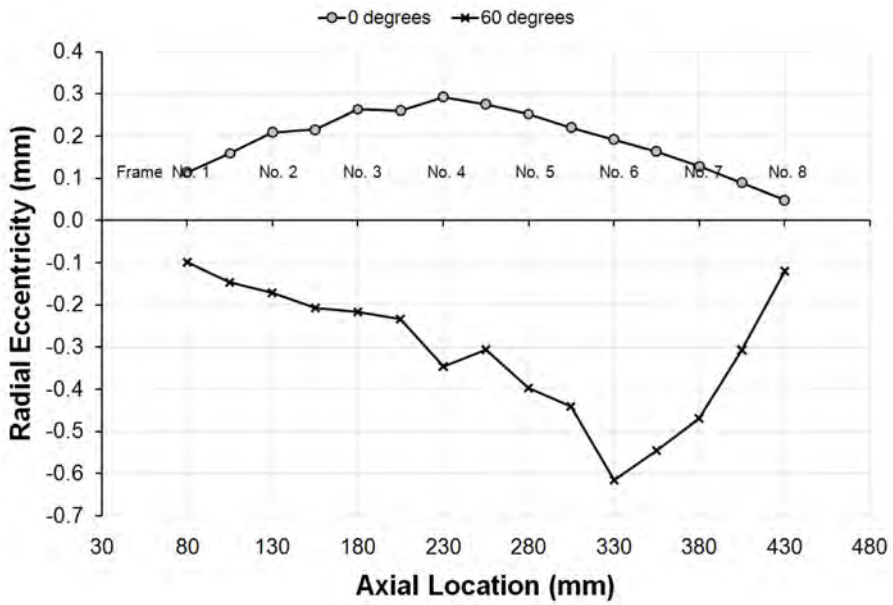

Figure 137: Showing the axial out-of-circularity mode of specimen L510-No20 based on measurements at the outside of the shell surface. The filtered measurements taken over the cylinder length using a laser displacement gauge are shown for circumferential locations associated with the maximum inward and outward radial eccentricities.

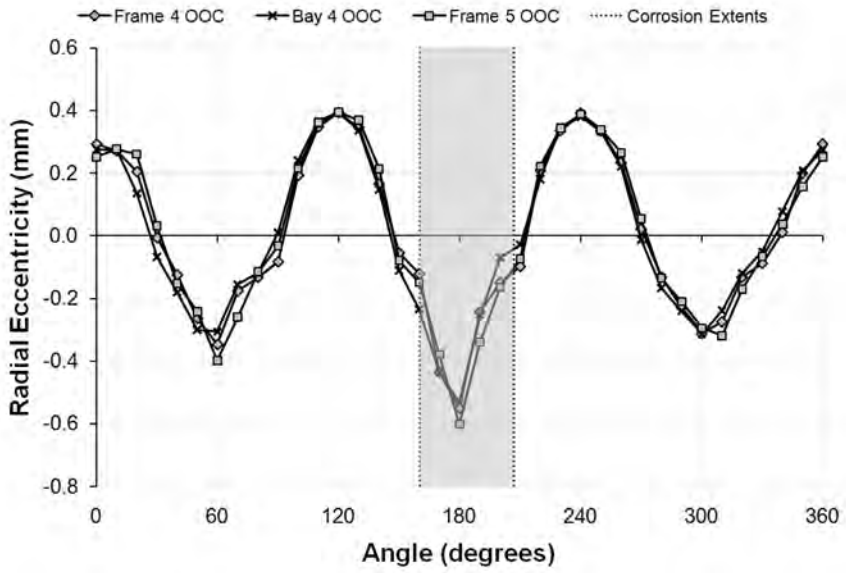

Figure 138: Showing the circumferential OOC mode of specimen L510-No20 based on filtered laser displacement gauge measurements at the outside of the shell surface at the central bay and the adjacent frames. The circumferential extents of the large, in-phase corrosion patch are indicated by the dashed lines and shaded area.

C.7 L510-No25

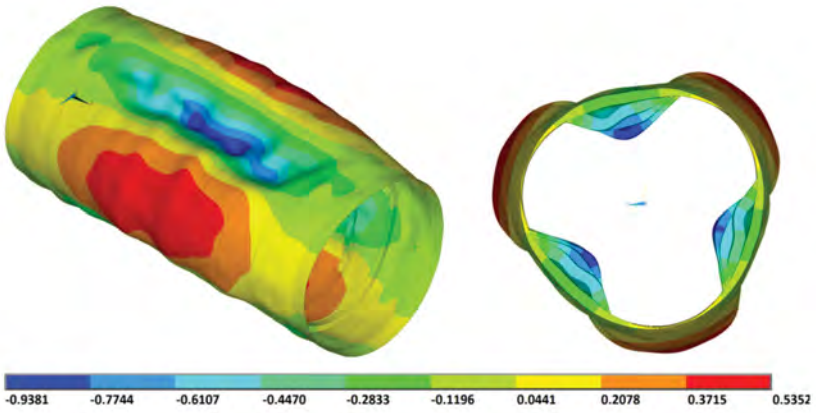

Figure 139: Graphical representation of out-of-circularity of specimen L510-No25. The colour contour maps describe the radial eccentricity (mm) based on a double Fourier analysis of the measurements of the outer shell taken by the CMM. OOC is also indicated by the deformed shape, whereby the imperfections are magnified by a factor of 50.

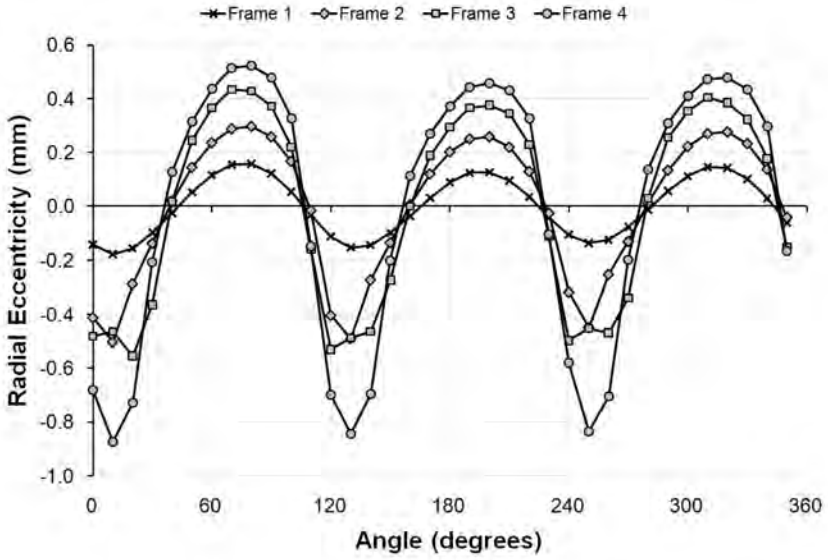

Figure 140: Showing the circumferential out-of-circularity mode of specimen L510-No25 based on measurements at the outside of the shell surface. All measurements taken about the circumference using a CMM are shown for axial locations nearby the indicated ring-stiffeners.

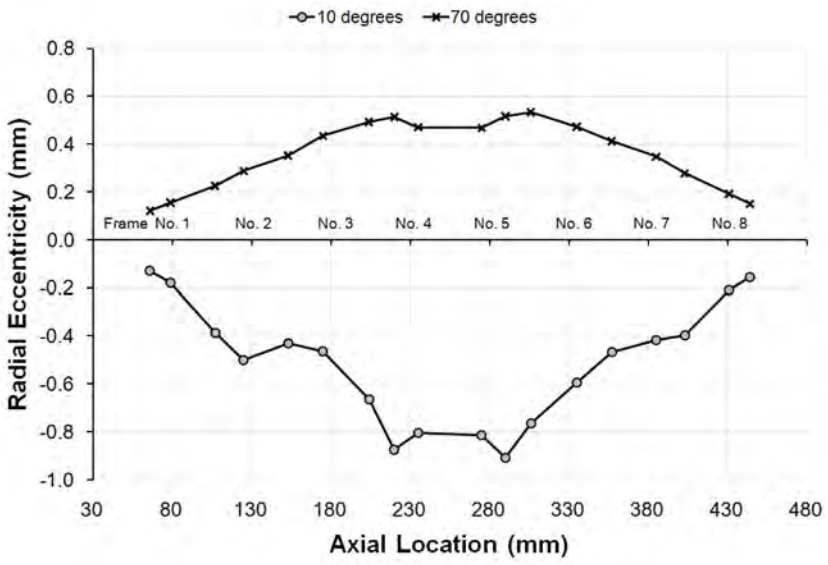

Figure 141: Showing the axial out-of-circularity mode of specimen L510-No25 based on measurements at the outside of the shell surface. All measurements taken over the cylinder length using a CMM are shown for circumferential locations associated with the maximum inward and outward radial eccentricities.

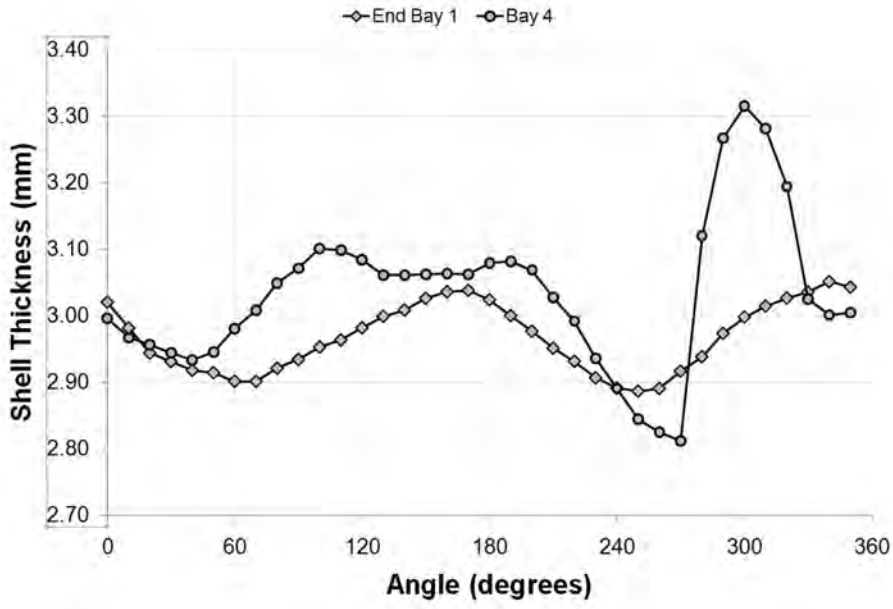

Figure 142: Showing the circumferential distribution of shell thickness at representative axial locations for specimen L510-No25, based on CMM measurements of the inner and outer shell radii.

C.8 L510-No26

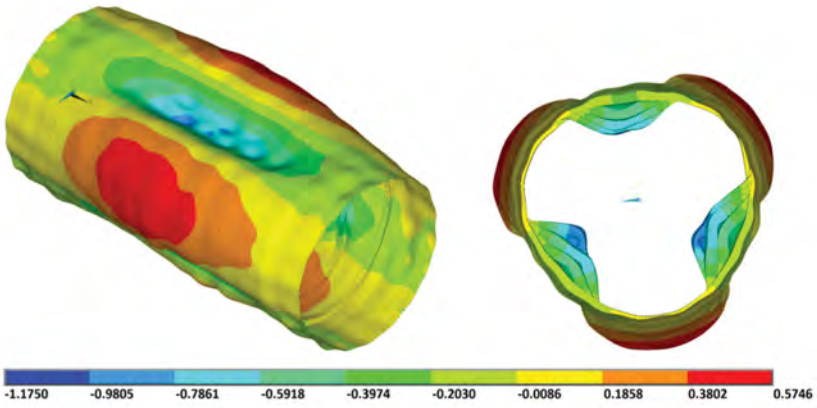

Figure 143: Graphical representation of out-of-circularity of specimen L510-No26. The colour contour maps describe the radial eccentricity (mm) based on a double Fourier analysis of the measurements of the outer shell taken by the CMM. OOC is also indicated by the deformed shape, whereby the imperfections are magnified by a factor of 50.

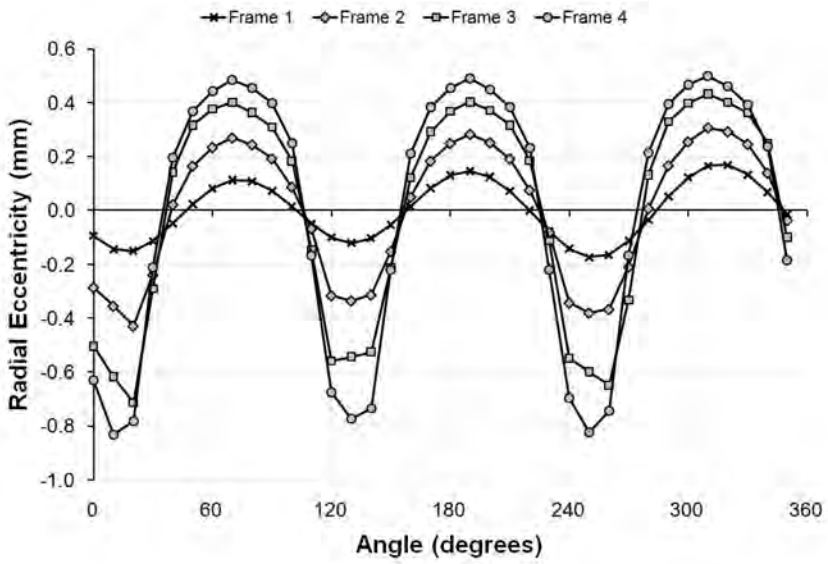

Figure 144: Showing the circumferential out-of-circularity mode of specimen L510-No26 based on measurements at the outside of the shell surface. All measurements taken about the circumference using a CMM are shown for axial locations nearby the indicated ring-stiffeners.

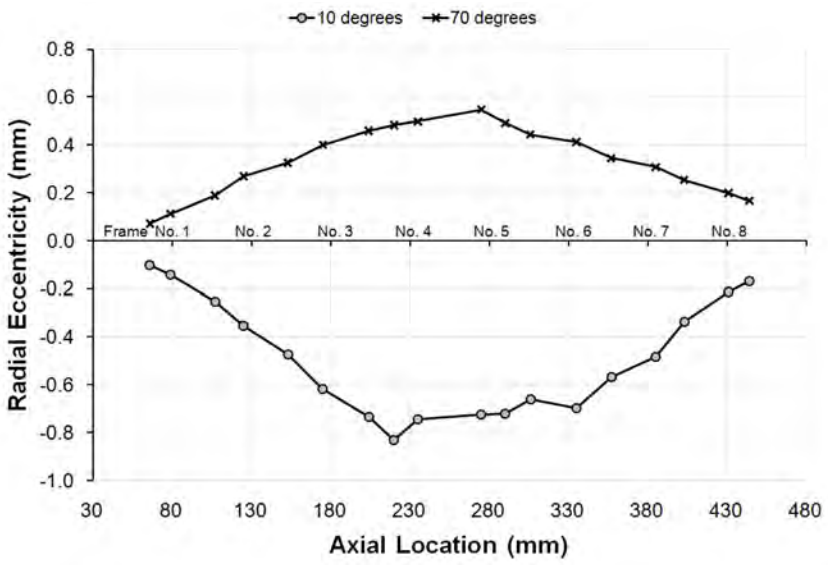

Figure 145: Showing the axial out-of-circularity mode of specimen L510-No26 based on measurements at the outside of the shell surface. All measurements taken over the cylinder length using a CMM are shown for circumferential locations associated with the maximum inward and outward radial eccentricities.

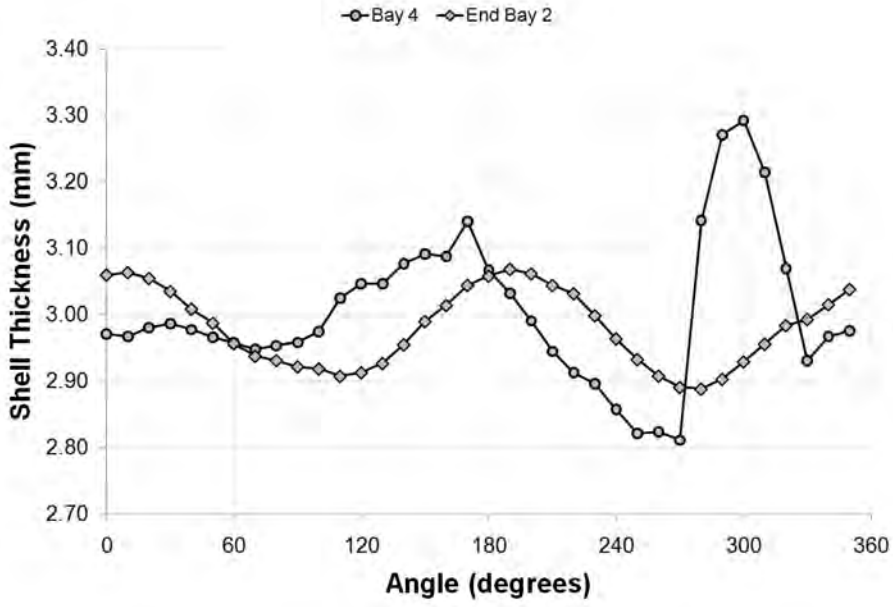

Figure 146: Showing the circumferential distribution of shell thickness at representative axial locations for specimen L510-No26, based on CMM measurements of the inner and outer shell radii.

C.9 L510-No33

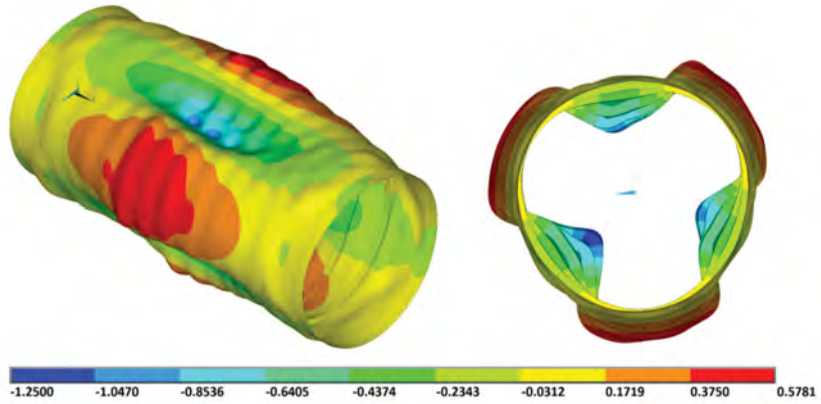

Figure 147: Graphical representation of out-of-circularity of specimen L510-No33. The colour contour maps describe the radial eccentricity (mm) based on a double Fourier analysis of the measurements of the outer shell taken by the CMM. OOC is also indicated by the deformed shape, whereby the imperfections are magnified by a factor of 50.

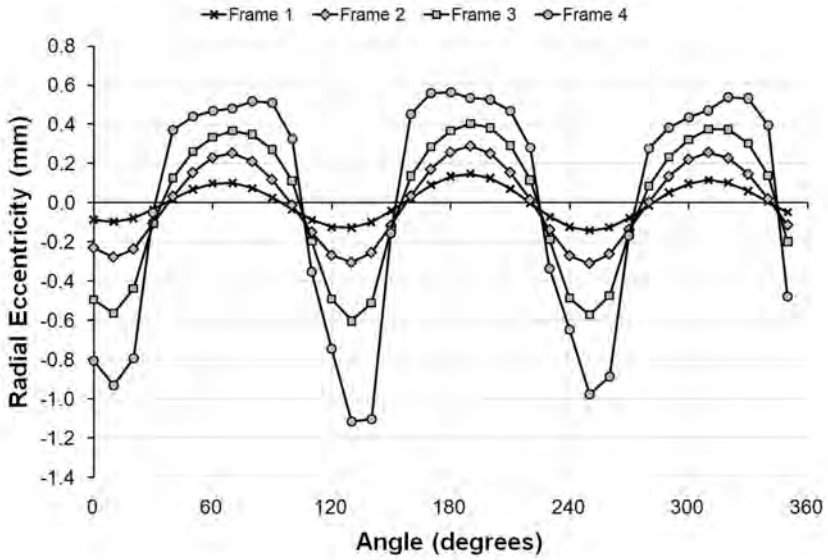

Figure 148: Showing the circumferential out-of-circularity mode of specimen L510-No33 based on measurements at the outside of the shell surface. All measurements taken about the circumference using a CMM are shown for axial locations nearby the indicated ring-stiffeners.

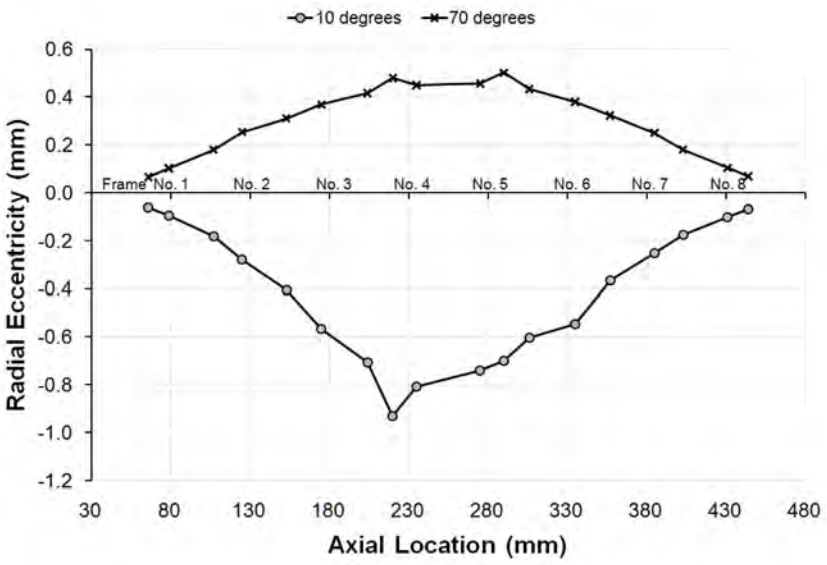

Figure 149: Showing the axial out-of-circularity mode of specimen L510-No33 based on measurements at the outside of the shell surface. All measurements taken over the cylinder length using a CMM are shown for circumferential locations associated with the maximum inward and outward radial eccentricities.

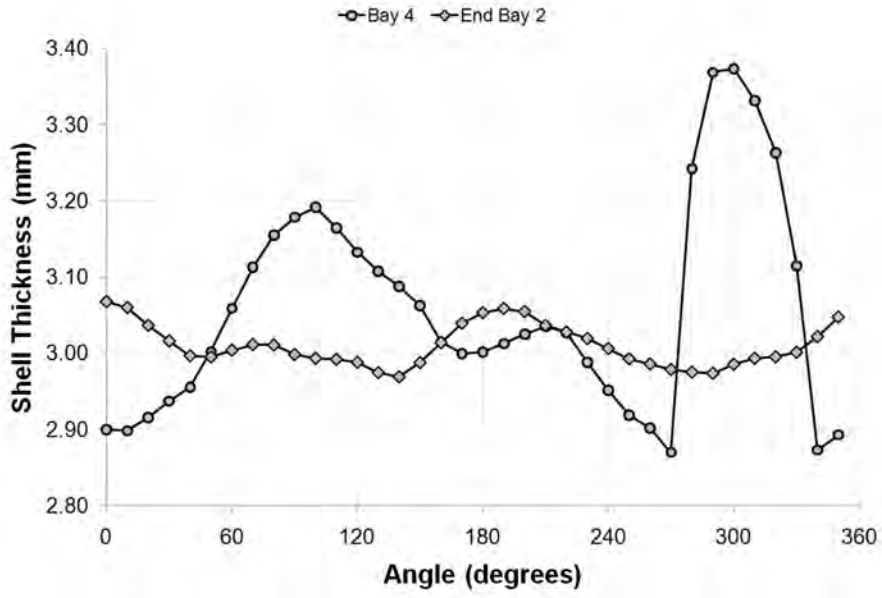

Figure 150: Showing the circumferential distribution of shell thickness at representative axial locations for specimen L510-No33, based on CMM measurements of the inner and outer shell radii.

C.10 L510-No34

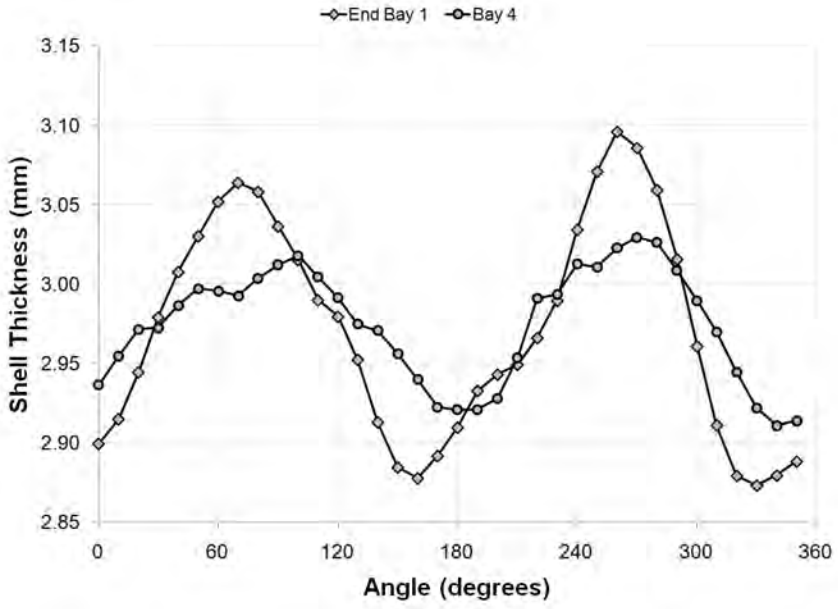

Figure 151: Showing the circumferential distribution of shell thickness at representative axial locations for specimen L510-No34, based on CMM measurements of the inner and outer shell radii.

C.11 L510-No35

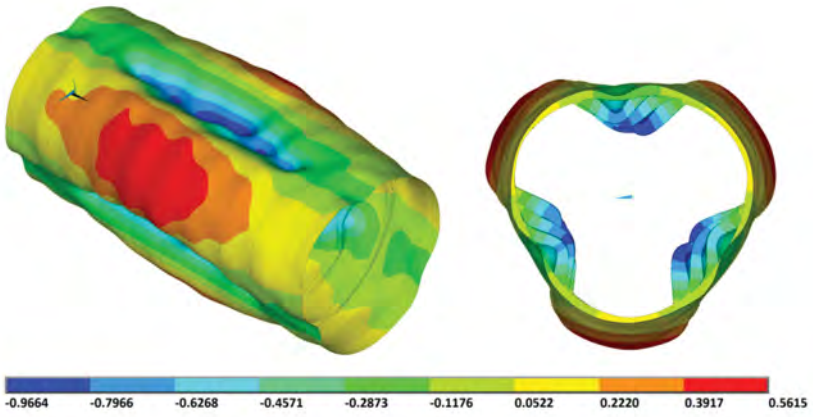

Figure 152: Graphical representation of out-of-circularity of specimen L510-No35. The colour contour maps describe the radial eccentricity (mm) based on a double Fourier analysis of the measurements of the outer shell taken by the laser displacement gauges. OOC is also indicated by the deformed shape, whereby the imperfections are magnified by a factor of 50.

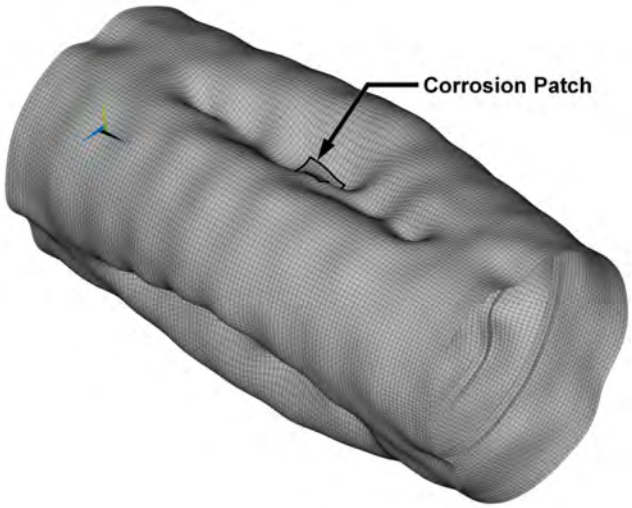

Figure 153: Graphical representation of out-of-circularity of specimen L510-No35, showing the location of the in-phase corrosion patch with respect to the out-of-circularity shape. OOC is indicated by the deformed shape, whereby the imperfections are magnified by a factor of 50.

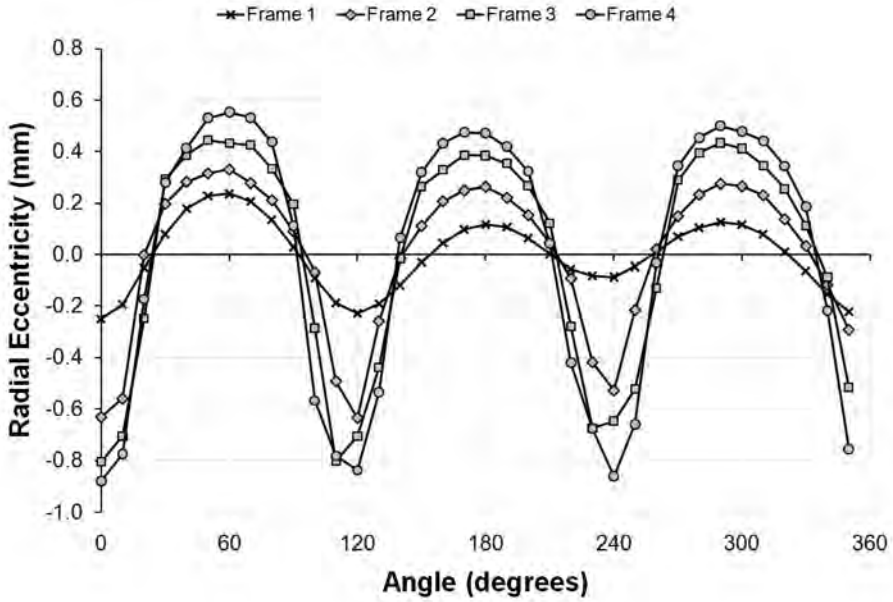

Figure 154: Showing the circumferential out-of-circularity mode of specimen L510-No35 based on measurements at the outside of the shell surface. The filtered measurements taken about the circumference using a laser displacement gauge are shown for axial locations nearby the indicated ring-stiffeners.

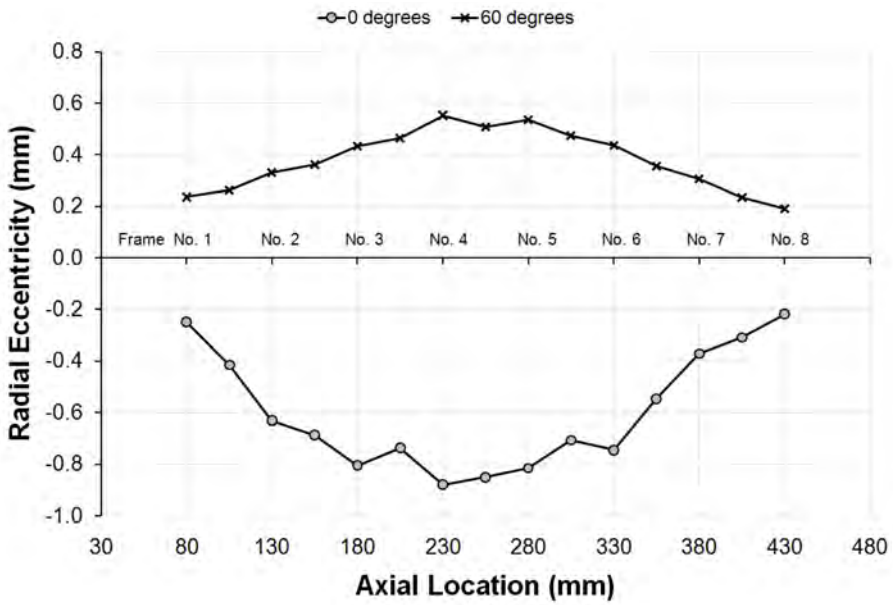

Figure 155: Showing the axial out-of-circularity mode of specimen L510-No35 based on measurements at the outside of the shell surface. The filtered measurements taken over the cylinder length using a laser displacement gauge are shown for circumferential locations associated with the maximum inward and outward radial eccentricities.

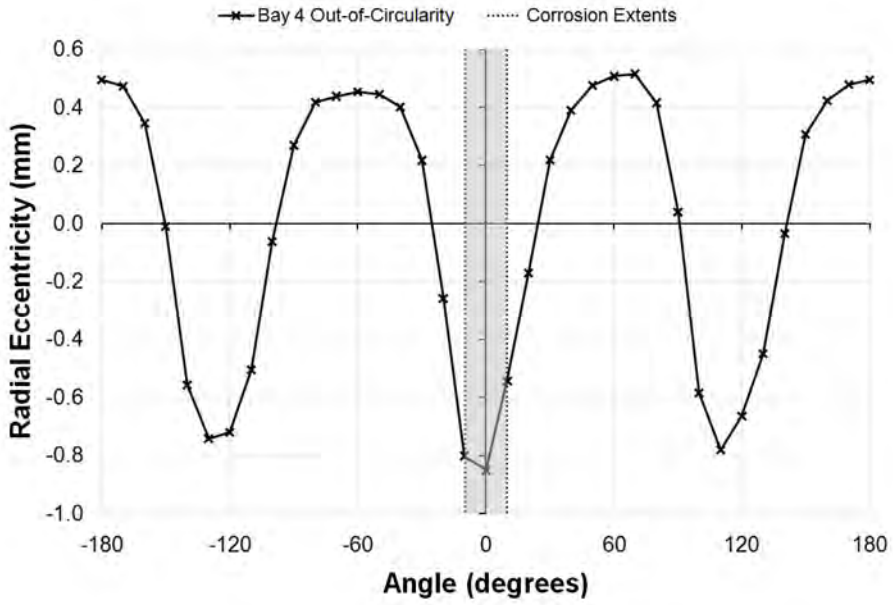

Figure 156: Showing the circumferential OOC mode of specimen L510-No35 based on filtered laser displacement gauge measurements at the outside of the shell surface at the central bay. The circumferential extents of the small, in-phase corrosion patch are indicated by the dashed lines and shaded area.

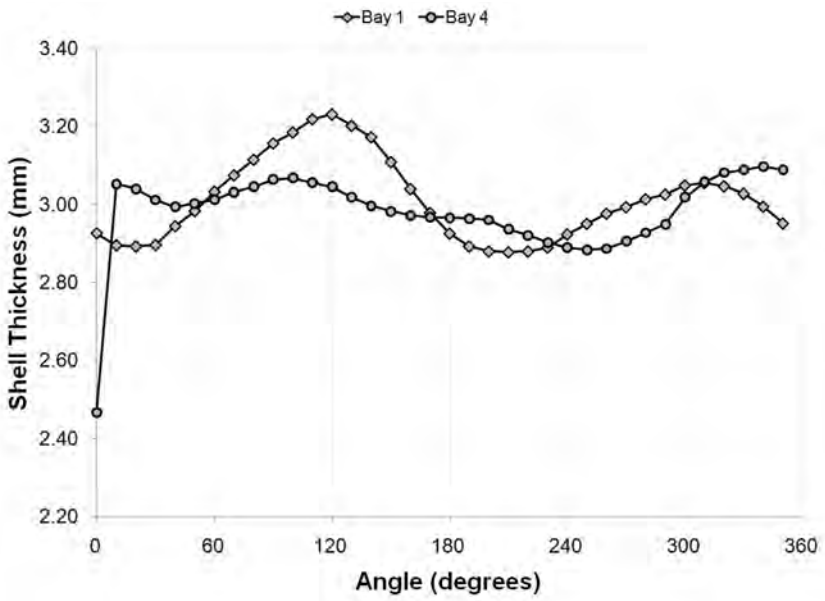

Figure 157: Showing the circumferential distribution of shell thickness at representative axial locations for specimen L510-No35, based on ultrasonic thickness gauge readings.

C.12 L510-No36

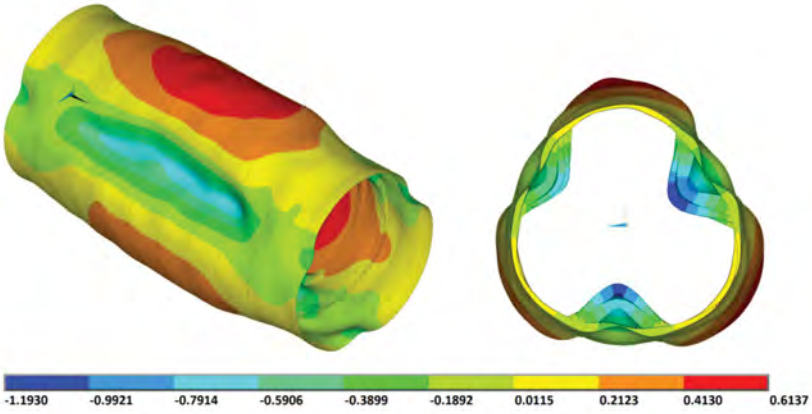

Figure 158: Graphical representation of out-of-circularity of specimen L510-No36. The colour contour maps describe the radial eccentricity (mm) based on a double Fourier analysis of the measurements of the outer shell taken by the laser displacement gauges. OOC is also indicated by the deformed shape, whereby the imperfections are magnified by a factor of 50.

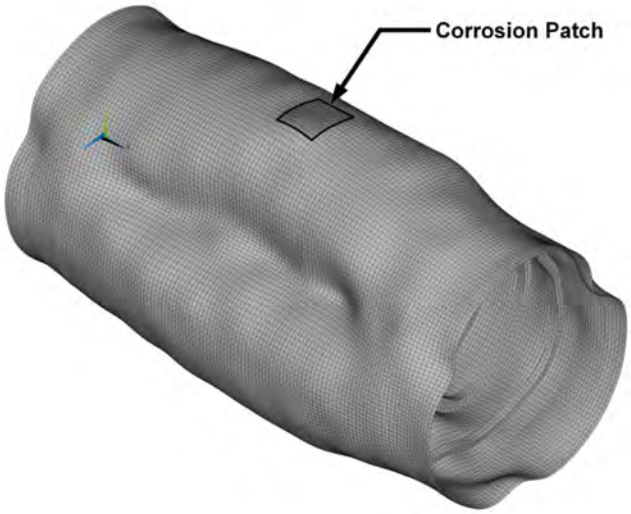

Figure 159: Graphical representation of out-of-circularity of specimen L510-No36, showing the location of the out-of-phase corrosion patch with respect to the OOC shape. OOC is indicated by the deformed shape, whereby the imperfections are magnified by a factor of 50.

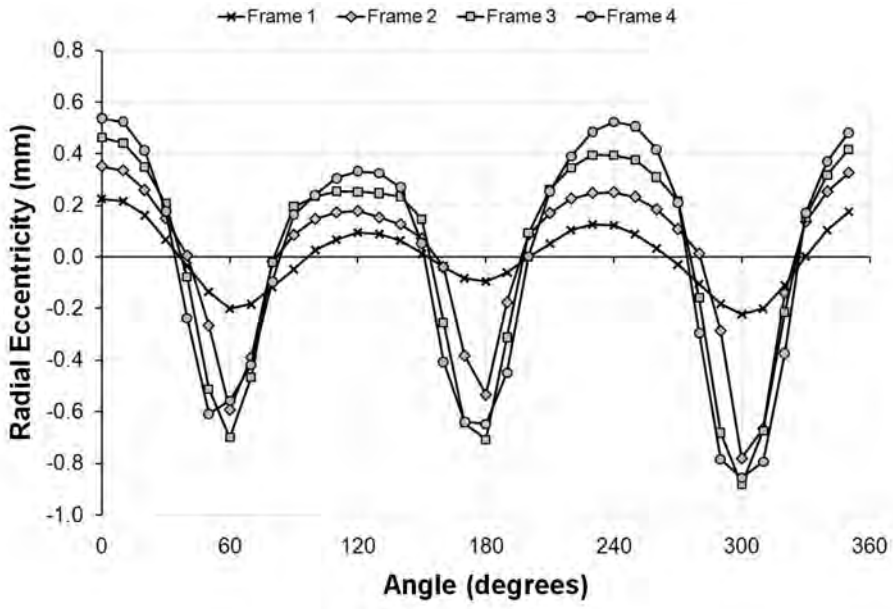

Figure 160: Showing the circumferential out-of-circularity mode of specimen L510-No36 based on measurements at the outside of the shell surface. The filtered measurements taken about the circumference using a laser displacement gauge are shown for axial locations nearby the indicated ring-stiffeners.

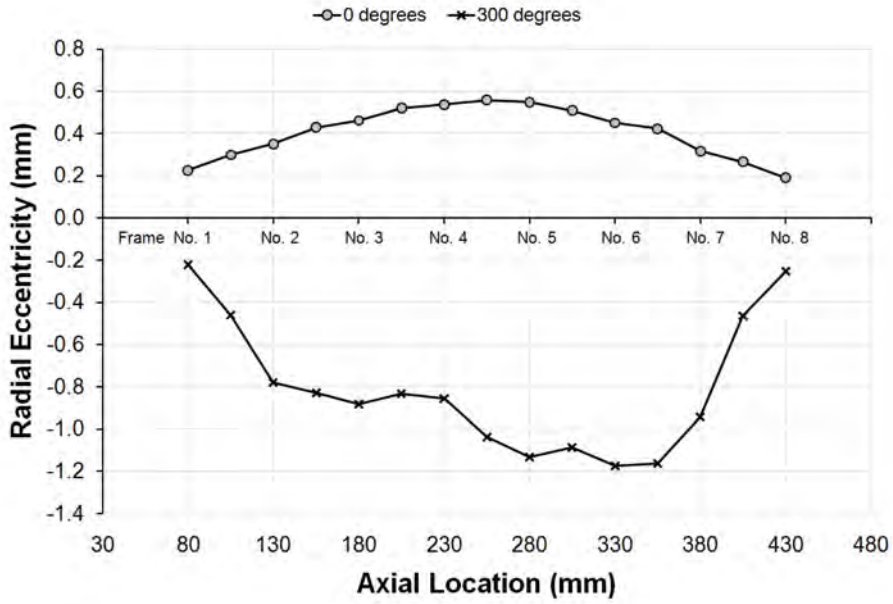

Figure 161: Showing the axial out-of-circularity mode of specimen L510-No36 based on measurements at the outside of the shell surface. The filtered measurements taken over the cylinder length using a laser displacement gauge are shown for circumferential locations associated with the maximum inward and outward radial eccentricities.

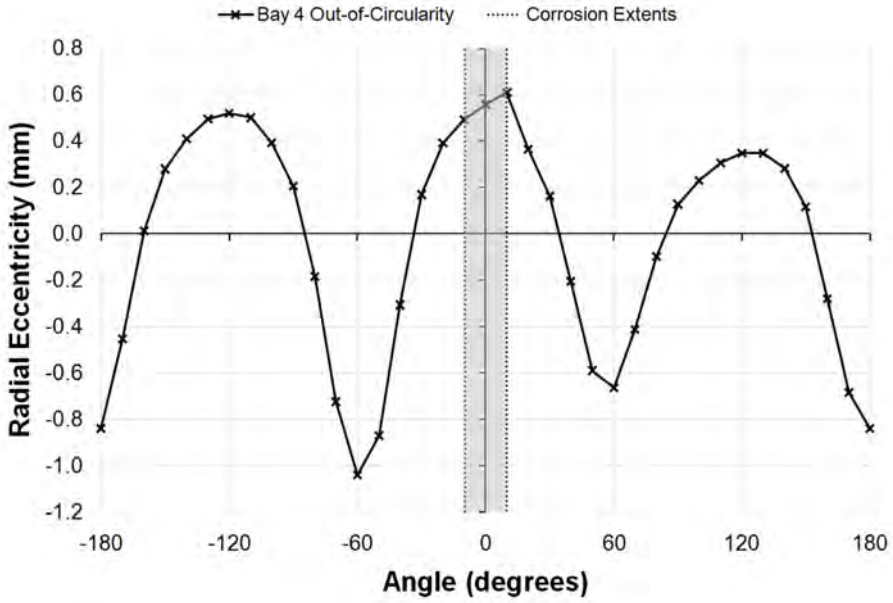

Figure 162: Showing the circumferential OOC mode of specimen L510-No36 based on filtered laser displacement gauge measurements at the outside of the shell surface at the central bay. The circumferential extents of the small, out-of-phase corrosion patch are indicated by the dashed lines and shaded area.

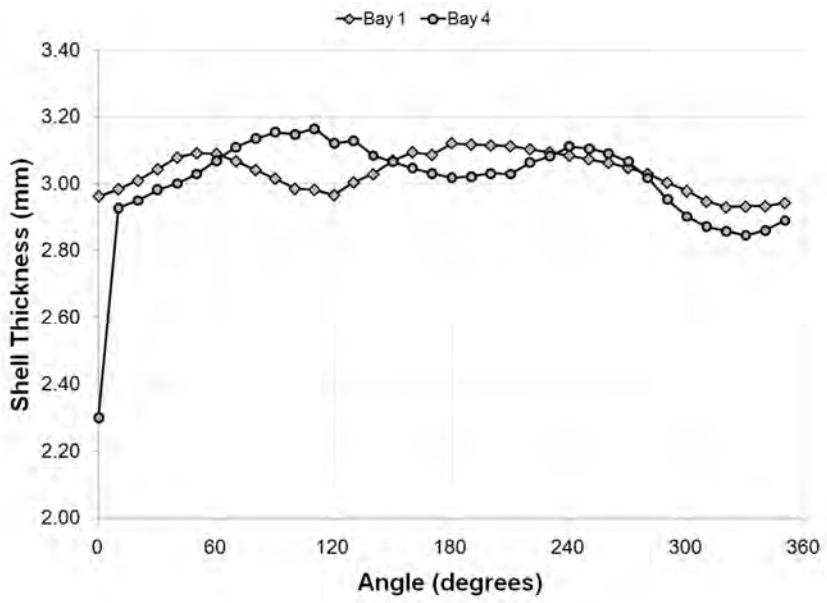

Figure 163: Showing the circumferential distribution of shell thickness at representative axial locations for specimen L510-No36, based on ultrasonic thickness gauge readings.

Annex D Measured material properties

Table 103: Measured engineering material properties in the circumferential direction, reporting the properties determined from each of three coupons machined from each cylinder model after collapse testing.

Specimen Name	Coupon No.	Young's Modulus (GPa)	Yield Strength, 0.2% Offset (MPa)	Tensile Strength (MPa)	Elongation at Break
L510-No13	10	59.4	330.3	350.6	10.8%
L510-No13	11	54.0	330.7	348.8	13.3%
L510-No13	12	53.3	321.5	342.6	13.6%
L510-No14	43	53.0	343.5	351.5	7.4%
L510-No14	44	57.3	329.5	349.6	15.1%
L510-No14	45	55.3	329.7	348.7	10.4%
L510-No17	34	54.8	305.2	328.7	15.8%
L510-No17	35	64.2	306.6	326.4	7.2%
L510-No17	36	55.5	306.2	328.1	15.4%
L510-No18	37	58.1	302.8	327.1	12.1%
L510-No18	38	55.2	311.8	332.1	12.3%
L510-No18	39	58.4	300.8	324.9	10.7%
L510-No19	31	57.9	332.0	352.5	10.8%
L510-No19	32	57.9	329.4	350.5	12.3%
L510-No19	33	58.1	325.4	345.7	8.6%
L510-No20	40	54.9	327.8	346.3	9.9%
L510-No20	41	56.5	326.0	347.2	14.7%
L510-No20	42	57.7	321.5	345.2	17.6%
L510-No25	55	56.0	307.3	330.3	12.2%
L510-No25	56	58.0	303.3	329.3	15.2%
L510-No25	57	56.4	305.6	328.7	8.5%
L510-No26	1	58.9	309.3	331.7	9.9%
L510-No26	2	59.8	308.8	333.6	12.2%
L510-No26	3	57.9	310.7	332.3	12.9%
L510-No33	58	56.9	302.6	325.9	14.7%
L510-No33	59	57.4	301.9	324.6	13.6%
L510-No33	60	58.5	298.3	323.8	13.9%
L510-No34	13	56.0	299.1	324.1	7.9%
L510-No34	14	54.6	301.8	325.1	11.1%
L510-No34	15	54.6	302.1	325.8	13.0%
L510-No35	16	55.5	332.5	352.9	16.1%
L510-No35	17	57.5	331.9	353.0	11.6%
L510-No35	18	56.7	330.6	351.2	13.9%
L510-No36	25	57.3	326.7	344.0	11.7%
L510-No36	26	58.0	332.0	347.5	9.1%
L510-No36	27	60.6	333.8	350.5	9.9%

a. Material properties are based on load cell and extensometer data acquired during testing at a sampling rate of 10Hz.

Table 104: Measured engineering stress-strain curves for coupons machined from specimen L510-No13 in the circumferential direction.

Coupon No. 10		Coupon No. 11		Coupon No. 12	
Engineering Strain (-)	**Engineering Stress (MPa)**	**Engineering Strain (-)**	**Engineering Stress (MPa)**	**Engineering Strain (-)**	**Engineering Stress (MPa)**
0.000119	3.86	0.000032	6.85	-0.000030	7.02
0.000452	29.51	0.000798	47.48	0.000500	38.78
0.001214	79.76	0.001833	102.13	0.001451	88.43
0.002265	142.10	0.002962	163.60	0.002592	148.19
0.003398	208.38	0.004146	228.24	0.003811	212.24
0.004665	276.54	0.005405	292.15	0.004988	273.14
0.006511	325.48	0.007498	326.95	0.006964	317.94
0.009434	333.87	0.010478	332.13	0.010087	325.58
0.012554	335.84	0.013848	333.73	0.013471	327.33
0.015660	336.84	0.017361	335.05	0.017051	328.47
0.018914	338.16	0.020945	335.96	0.020648	329.51
0.022469	339.10	0.024624	336.77	0.024218	330.35
0.025901	339.85	0.028260	337.44	0.027498	331.64
0.029432	340.70	0.031667	338.25	0.031189	332.05
0.032912	341.81	0.035056	338.97	0.034744	332.94
0.036345	342.36	0.038658	339.98	0.038247	333.51
0.039646	342.91	0.042154	340.59	0.041770	334.62
0.042962	343.57	0.045623	341.16	0.045184	335.27
0.046369	344.40	0.048975	341.81	0.048641	336.19
0.049430	344.95	0.057879	346.16	0.056510	340.02
0.058984	348.85	0.069350	347.71	0.068078	341.56
0.069634	349.42	0.080640	348.47	0.079530	342.08
0.079758	348.84	0.091731	347.70	0.091386	341.87
0.088753	344.64	0.102084	344.15	0.102624	339.96
0.097180	336.70	0.111692	337.53	0.113394	334.40
0.105405	325.10	0.121456	327.24	0.123934	325.42
		0.131093	311.94	0.136204	305.27

a. Engineering stress-strain curves are derived from load cell and extensometer data, and calliper measurements of coupon diameter. Load cell and extensometer data was acquired at a rate of 10Hz during coupon testing. The data reported here has been reduced to an equivalent sampling rate of 0.1Hz by discarding 99 data points out of 100.

Table 105: Measured engineering stress-strain curves for coupons machined from specimen L510-No14 in the circumferential direction.

Coupon No. 43		Coupon No. 44		Coupon No. 45	
Engineering Strain (-)	**Engineering Stress (MPa)**	**Engineering Strain (-)**	**Engineering Stress (MPa)**	**Engineering Strain (-)**	**Engineering Stress (MPa)**
0.000010	1.49	-0.000018	4.17	0.000043	0.68
0.000410	28.43	0.000594	28.71	0.000030	0.76
0.001420	82.01	0.001426	76.89	0.000034	0.80
0.002666	147.00	0.002526	138.42	0.000034	0.62
0.004030	216.28	0.003705	206.05	-0.000035	0.81
0.005435	284.33	0.004990	273.59	0.000394	26.45
0.007212	338.92	0.006838	325.06	0.001290	74.25
0.010518	343.25	0.010296	334.37	0.002414	134.87
0.013946	343.49	0.013967	336.41	0.003651	198.03
0.017469	343.73	0.017731	337.57	0.004886	261.45
0.020795	344.12	0.021630	338.50	0.006578	317.55
0.024014	344.74	0.025515	339.08	0.009615	333.52
0.027218	345.26	0.029194	340.10	0.012881	335.56
0.030361	345.33	0.032758	340.95	0.016410	337.30
0.033431	346.27	0.036340	341.85	0.019971	338.21
0.036414	346.74	0.039682	342.55	0.023542	339.35
0.039578	347.23	0.043177	343.17	0.027102	340.15
0.042588	347.34	0.046667	344.00	0.030887	340.98
0.045628	347.62	0.050154	345.45	0.034537	341.75
0.048645	347.92	0.061810	347.47	0.038072	342.26
0.054721	348.91	0.074082	348.54	0.041602	343.01
0.062854	347.75	0.086935	348.31	0.045062	343.50
0.068609	344.06	0.100790	345.77	0.048525	344.15
0.072008	336.38	0.115762	339.26	0.056159	347.18
0.074094	325.01	0.131765	328.75	0.067153	347.57
		0.148314	312.84	0.077514	345.43
				0.087110	338.78
				0.096561	328.50

a. Engineering stress-strain curves are derived from load cell and extensometer data, and calliper measurements of coupon diameter. Load cell and extensometer data was acquired at a rate of 10Hz during coupon testing. The data reported here has been reduced to an equivalent sampling rate of 0.1Hz by discarding 99 data points out of 100.

Table 106: Measured engineering stress-strain curves for coupons machined from specimen L510-No17 in the circumferential direction.

Coupon No. 34		Coupon No. 35		Coupon No. 36	
Engineering Strain (-)	**Engineering Stress (MPa)**	**Engineering Strain (-)**	**Engineering Stress (MPa)**	**Engineering Strain (-)**	**Engineering Stress (MPa)**
-0.000038	3.78	0.000018	1.13	0.000016	3.15
0.000289	20.44	0.000449	35.79	0.000530	34.33
0.001094	68.52	0.001189	86.75	0.001411	82.54
0.002166	126.08	0.002234	148.55	0.002503	143.63
0.003382	190.53	0.003395	215.61	0.003715	209.30
0.004618	255.67	0.004656	280.73	0.005019	274.40
0.006526	302.97	0.006275	305.52	0.007368	305.32
0.009778	308.27	0.008518	307.96	0.010823	308.03
0.013317	309.69	0.011077	309.49	0.014178	309.43
0.016911	310.77	0.014162	310.89	0.017714	310.63
0.020426	311.81	0.017411	312.36	0.021094	311.71
0.023807	313.07	0.020803	313.46	0.024356	312.68
0.027151	314.27	0.024174	314.64	0.027704	314.17
0.030420	315.48	0.027425	316.00	0.030991	315.19
0.033722	316.85	0.030556	316.93	0.034283	316.61
0.036994	318.20	0.033486	317.78	0.037358	317.53
0.040313	319.28	0.036490	319.32	0.040606	318.69
0.043594	319.76	0.039530	320.32	0.043833	319.69
0.046780	321.43	0.042449	321.05	0.047144	320.69
0.050410	325.55	0.045331	321.90	0.051671	324.92
0.061834	326.65	0.048144	322.38	0.062794	326.61
0.073287	328.04	0.052719	324.33	0.074594	327.56
0.085165	328.68	0.061046	325.17	0.087023	327.38
0.097590	327.36	0.067305	323.66	0.100832	324.19
0.110543	323.19	0.070537	318.83	0.116045	316.59
0.124199	315.22	0.071970	310.03	0.132030	305.58
0.138596	303.79	0.072433	298.03	0.148863	289.98
0.153871	287.75	0.072394	281.22		

a. Engineering stress-strain curves are derived from load cell and extensometer data, and calliper measurements of coupon diameter. Load cell and extensometer data was acquired at a rate of 10Hz during coupon testing. The data reported here has been reduced to an equivalent sampling rate of 0.1Hz by discarding 99 data points out of 100.

Table 107: Measured engineering stress-strain curves for coupons machined from specimen L510-No18 in the circumferential direction.

Coupon No. 37		Coupon No. 38		Coupon No. 39	
Engineering Strain (-)	**Engineering Stress (MPa)**	**Engineering Strain (-)**	**Engineering Stress (MPa)**	**Engineering Strain (-)**	**Engineering Stress (MPa)**
0.000506	38.37	0.000005	5.79	-0.000027	11.10
0.001522	94.73	0.000883	49.58	0.000867	57.92
0.002710	160.85	0.001889	105.58	0.001913	118.70
0.003967	229.50	0.003035	168.43	0.003026	184.22
0.005546	289.66	0.004280	233.23	0.004225	250.36
0.008326	304.82	0.005836	289.34	0.005937	297.29
0.011434	307.03	0.008000	313.63	0.008742	304.04
0.014644	308.84	0.010730	318.51	0.011945	305.79
0.018037	310.28	0.014054	320.41	0.015274	307.09
0.021414	311.66	0.017446	320.90	0.018846	308.40
0.024840	312.82	0.020834	322.06	0.022371	309.53
0.028226	314.07	0.024314	323.08	0.025822	310.64
0.031536	315.35	0.027727	324.01	0.029094	312.21
0.034821	316.32	0.031094	324.60	0.032402	313.50
0.037991	317.67	0.034246	325.43	0.035698	314.70
0.041222	318.40	0.037648	326.53	0.038897	315.74
0.044341	319.50	0.041033	326.99	0.042129	316.98
0.047546	320.17	0.044248	327.61	0.045370	317.93
0.052554	324.88	0.047652	327.73	0.048572	318.18
0.063326	326.31	0.053555	330.80	0.055683	321.09
0.074029	326.84	0.065388	330.83	0.066469	322.82
0.084283	325.61	0.077604	327.47	0.076835	323.63
0.093714	320.53	0.090531	319.62	0.086324	323.20
0.102938	311.65	0.103841	308.29	0.093738	319.96
0.112003	299.17	0.117620	292.79	0.098945	312.58
0.120498	280.20			0.102971	301.99
				0.106042	286.85

a. Engineering stress-strain curves are derived from load cell and extensometer data, and calliper measurements of coupon diameter. Load cell and extensometer data was acquired at a rate of 10Hz during coupon testing. The data reported here has been reduced to an equivalent sampling rate of 0.1Hz by discarding 99 data points out of 100.

Table 108: Measured engineering stress-strain curves for coupons machined from specimen L510-No19 in the circumferential direction.

Coupon No. 31		Coupon No. 32		Coupon No. 33	
Engineering Strain (-)	**Engineering Stress (MPa)**	**Engineering Strain (-)**	**Engineering Stress (MPa)**	**Engineering Strain (-)**	**Engineering Stress (MPa)**
-0.000022	2.67	0.000020	3.86	0.000013	1.07
0.000256	27.36	0.000263	22.88	0.000170	14.17
0.001019	72.49	0.000870	61.66	0.000761	51.45
0.002053	129.59	0.001882	116.76	0.001750	105.80
0.003235	193.74	0.003018	178.04	0.002873	167.81
0.004486	260.24	0.004199	243.23	0.004074	230.74
0.006030	318.01	0.005647	305.14	0.005355	293.23
0.008714	334.70	0.008214	331.13	0.007487	324.70
0.011709	337.25	0.011623	334.92	0.010105	329.02
0.014811	338.38	0.015096	336.07	0.012794	331.01
0.018018	339.80	0.018689	337.31	0.015703	331.76
0.021179	340.54	0.022231	338.44	0.018827	332.79
0.024656	341.61	0.025793	339.07	0.021962	333.41
0.028069	342.34	0.029349	340.24	0.025377	334.85
0.031512	343.19	0.032981	340.97	0.028754	335.59
0.034991	343.81	0.036475	341.67	0.032045	336.61
0.038394	344.54	0.039997	342.48	0.035242	337.37
0.041660	345.31	0.043378	343.27	0.038590	338.41
0.044902	346.11	0.046687	344.04	0.041837	338.90
0.048179	346.87	0.050050	345.79	0.044967	339.76
0.054610	350.66	0.061347	349.18	0.048089	340.24
0.065230	351.91	0.072638	350.37	0.053726	343.50
0.075295	352.30	0.083634	349.83	0.063705	344.80
0.084356	351.03	0.093810	346.97	0.072848	345.07
0.091779	345.91	0.103319	340.00	0.080039	343.97
0.098575	337.07	0.112854	328.90	0.083755	339.63
0.104911	323.94	0.122364	311.03	0.085305	331.38
				0.085794	319.85
				0.085622	299.95

a. Engineering stress-strain curves are derived from load cell and extensometer data, and calliper measurements of coupon diameter. Load cell and extensometer data was acquired at a rate of 10Hz during coupon testing. The data reported here has been reduced to an equivalent sampling rate of 0.1Hz by discarding 99 data points out of 100.

Table 109: Measured engineering stress-strain curves for coupons machined from specimen L510-No20 in the circumferential direction.

Coupon No. 40		Coupon No. 41		Coupon No. 42	
Engineering Strain (-)	**Engineering Stress (MPa)**	**Engineering Strain (-)**	**Engineering Stress (MPa)**	**Engineering Strain (-)**	**Engineering Stress (MPa)**
-0.000007	1.81	0.000014	10.16	-0.000028	10.34
0.000281	12.74	0.000969	55.52	0.000818	59.59
0.000928	45.20	0.002030	114.95	0.001788	115.56
0.001865	96.33	0.003118	177.77	0.002903	179.30
0.002952	156.24	0.004344	244.63	0.004053	244.90
0.004140	219.73	0.005818	303.50	0.005507	302.21
0.005440	286.34	0.008178	327.64	0.008099	324.73
0.007382	325.05	0.011100	332.30	0.011415	329.15
0.010074	331.46	0.014266	333.94	0.014830	330.60
0.012813	333.16	0.017738	334.87	0.018399	332.04
0.015687	334.17	0.021382	335.82	0.022026	332.75
0.018711	335.35	0.024926	336.63	0.025507	332.96
0.021850	336.08	0.028547	337.51	0.028836	334.34
0.025222	336.97	0.032061	338.32	0.032342	335.19
0.028450	337.42	0.035396	339.07	0.035706	335.87
0.031766	338.52	0.038762	339.31	0.039134	337.05
0.035002	338.57	0.042122	340.17	0.042578	337.87
0.038276	339.59	0.045486	341.00	0.045994	338.46
0.041481	340.47	0.048894	341.74	0.049415	339.31
0.044721	341.46	0.057757	345.50	0.059102	341.56
0.047899	341.46	0.069166	346.65	0.070777	343.04
0.053106	345.21	0.081032	347.00	0.082468	343.97
0.063062	345.88	0.092804	346.13	0.095129	343.73
0.072246	345.88	0.104626	343.85	0.108118	342.80
0.079988	343.52	0.115871	337.29	0.122214	340.06
0.086425	337.80	0.127587	327.44	0.137309	333.84
0.091814	328.80	0.139302	314.72	0.153514	325.01
0.096649	316.60			0.169935	312.92

a. Engineering stress-strain curves are derived from load cell and extensometer data, and calliper measurements of coupon diameter. Load cell and extensometer data was acquired at a rate of 10Hz during coupon testing. The data reported here has been reduced to an equivalent sampling rate of 0.1Hz by discarding 99 data points out of 100.

Table 110: Measured engineering stress-strain curves for coupons machined from specimen L510-No25 in the circumferential direction.

Coupon No. 55		Coupon No. 56		Coupon No. 57	
Engineering Strain (-)	**Engineering Stress (MPa)**	**Engineering Strain (-)**	**Engineering Stress (MPa)**	**Engineering Strain (-)**	**Engineering Stress (MPa)**
0.000059	1.15	0.000005	4.37	-0.000034	1.53
0.000640	21.73	0.000757	52.01	0.000533	33.12
0.001332	45.25	0.001751	109.10	0.001427	82.62
0.002278	94.84	0.002870	171.35	0.002548	145.44
0.003371	157.60	0.004090	239.37	0.003697	208.26
0.004638	226.07	0.005810	295.59	0.004986	274.19
0.006130	289.59	0.008706	306.24	0.006927	305.39
0.008794	307.84	0.012038	308.23	0.009380	308.57
0.011957	309.68	0.015514	309.60	0.012306	310.37
0.015400	310.91	0.018870	310.21	0.015406	311.78
0.019095	312.14	0.022272	311.69	0.018866	313.06
0.022563	313.35	0.025549	313.27	0.022293	313.72
0.026026	314.63	0.028890	314.86	0.025365	315.34
0.029419	316.03	0.032197	316.09	0.028670	316.71
0.032707	317.03	0.035394	317.02	0.031867	317.70
0.035866	318.30	0.038702	318.40	0.034988	318.82
0.039137	319.67	0.041862	319.56	0.038131	319.98
0.042448	320.43	0.045028	320.54	0.041203	320.99
0.045555	321.44	0.048286	321.60	0.044262	322.08
0.048840	322.25	0.055327	325.24	0.047074	323.00
0.057151	326.96	0.066640	327.07	0.050273	326.73
0.068343	328.69	0.078198	328.14	0.060139	327.37
0.080061	329.71	0.090379	328.67	0.069223	328.07
0.091546	329.43	0.102580	328.21	0.076468	326.52
0.102897	327.93	0.108013	325.65	0.080667	321.17
0.087122	323.34	0.118410	319.87	0.083303	311.38
0.097619	314.42	0.133313	309.79	0.084825	297.70
0.108150	302.54	0.148362	296.22		
0.115401	286.97				

a. Engineering stress-strain curves are derived from load cell and extensometer data, and calliper measurements of coupon diameter. Load cell and extensometer data was acquired at a rate of 10Hz during coupon testing. The data reported here has been reduced to an equivalent sampling rate of 0.1Hz by discarding 99 data points out of 100.

Table 111: Measured engineering stress-strain curves for coupons machined from specimen L510-No26 in the circumferential direction.

Coupon No. 1		Coupon No. 2		Coupon No. 3	
Engineering Strain (-)	**Engineering Stress (MPa)**	**Engineering Strain (-)**	**Engineering Stress (MPa)**	**Engineering Strain (-)**	**Engineering Stress (MPa)**
-0.000008	7.28	0.000024	8.03	-0.000014	5.99
0.000622	44.71	0.000445	38.77	0.000514	36.98
0.001495	96.08	0.001136	80.40	0.001310	85.05
0.002459	152.37	0.002030	134.97	0.002308	144.92
0.003467	212.33	0.003050	195.03	0.003390	206.19
0.004656	276.28	0.004138	256.40	0.004636	270.84
0.006631	308.55	0.006010	304.17	0.006614	308.72
0.009306	311.94	0.009120	311.45	0.009669	312.64
0.012304	313.88	0.012246	312.78	0.013010	314.11
0.015619	315.64	0.015395	314.27	0.016356	315.32
0.019133	317.14	0.018692	315.63	0.019731	316.39
0.022543	318.31	0.022008	316.42	0.023042	317.64
0.025892	319.66	0.025219	317.95	0.026463	318.96
0.029247	320.82	0.028517	319.11	0.029786	320.13
0.032482	321.97	0.031730	320.59	0.033118	321.27
0.035658	323.24	0.034937	321.89	0.036394	322.49
0.038718	324.50	0.038078	323.02	0.039570	323.42
0.041856	325.50	0.041219	323.90	0.042760	324.65
0.044882	326.27	0.044370	325.19	0.045846	325.48
0.047935	327.27	0.047446	326.15	0.049130	326.33
0.053267	329.73	0.051878	330.13	0.057814	330.39
0.063158	330.92	0.062596	331.49	0.068726	331.81
0.072221	330.41	0.073220	332.82	0.079696	331.96
0.079818	326.80	0.083703	333.44	0.090083	329.30
0.086144	319.10	0.094035	333.25	0.100229	322.56
0.091862	307.72	0.103746	332.19	0.110412	311.90
0.097203	290.73	0.111388	329.19	0.120931	297.52
		0.116291	320.71		
		0.119790	308.17		

a. Engineering stress-strain curves are derived from load cell and extensometer data, and calliper measurements of coupon diameter. Load cell and extensometer data was acquired at a rate of 10Hz during coupon testing. The data reported here has been reduced to an equivalent sampling rate of 0.1Hz by discarding 99 data points out of 100.

Table 112: Measured engineering stress-strain curves for coupons machined from specimen L510-No33 in the circumferential direction.

Coupon No. 58		Coupon No. 59		Coupon No. 60	
Engineering Strain (-)	**Engineering Stress (MPa)**	**Engineering Strain (-)**	**Engineering Stress (MPa)**	**Engineering Strain (-)**	**Engineering Stress (MPa)**
0.000029	7.72	-0.000026	5.28	-0.000002	17.19
0.000664	46.60	0.000768	50.99	0.000887	71.12
0.001616	97.98	0.001734	108.15	0.001921	131.43
0.002704	160.20	0.002876	171.44	0.003110	197.10
0.003886	226.94	0.004049	235.96	0.004418	263.62
0.005303	286.45	0.005532	292.14	0.006527	297.40
0.007651	303.48	0.008042	304.19	0.009618	302.21
0.010868	305.80	0.011002	305.90	0.013006	304.06
0.014195	306.61	0.014202	307.09	0.016447	305.35
0.017698	308.09	0.017558	307.87	0.020124	306.87
0.021361	309.07	0.020888	309.28	0.023742	308.29
0.024802	310.30	0.024178	310.43	0.027272	309.53
0.028203	311.67	0.027456	311.16	0.030678	310.64
0.031566	312.94	0.030758	312.79	0.033990	312.19
0.034903	313.94	0.034004	313.93	0.037368	313.45
0.038086	315.14	0.037196	314.93	0.040443	314.50
0.041400	316.51	0.040426	316.02	0.043738	315.17
0.044777	317.11	0.043632	317.14	0.047118	316.01
0.047954	318.21	0.046742	317.59	0.051416	321.13
0.054082	322.36	0.049880	318.44	0.062599	322.22
0.065590	324.37	0.060464	321.73	0.073715	323.63
0.077320	325.25	0.071469	323.06	0.085017	323.34
0.089205	325.59	0.082315	323.05	0.095702	321.74
0.100951	324.21	0.092989	321.34	0.106114	316.25
0.112222	320.21	0.103107	316.81	0.116059	307.67
0.122966	312.26	0.113149	308.03	0.126693	295.40
0.133833	300.48	0.123173	296.02	0.137598	276.97
0.144438	284.71	0.133645	279.29		

a. Engineering stress-strain curves are derived from load cell and extensometer data, and calliper measurements of coupon diameter. Load cell and extensometer data was acquired at a rate of 10Hz during coupon testing. The data reported here has been reduced to an equivalent sampling rate of 0.1Hz by discarding 99 data points out of 100.

Table 113: Measured engineering stress-strain curves for coupons machined from specimen L510-No34 in the circumferential direction.

Coupon No. 13		Coupon No. 14		Coupon No. 15	
Engineering Strain (-)	**Engineering Stress (MPa)**	**Engineering Strain (-)**	**Engineering Stress (MPa)**	**Engineering Strain (-)**	**Engineering Stress (MPa)**
-0.000026	5.89	0.000042	7.86	-0.000018	6.67
0.000458	35.10	0.000535	36.43	0.000475	33.25
0.001161	81.29	0.001357	84.49	0.001281	79.02
0.002261	141.25	0.002458	142.96	0.002339	135.31
0.003460	206.18	0.003690	206.80	0.003487	196.29
0.004810	270.21	0.004998	271.20	0.004730	261.08
0.007034	300.28	0.007101	299.73	0.006554	299.52
0.009668	305.40	0.010162	303.22	0.009400	303.69
0.012493	307.90	0.013637	305.19	0.012593	305.56
0.015680	309.63	0.017357	306.61	0.016076	306.63
0.018976	310.78	0.020976	307.65	0.019369	307.44
0.022431	312.25	0.024478	308.91	0.022733	308.78
0.025945	313.23	0.027954	310.18	0.026118	310.18
0.029286	314.10	0.031069	311.41	0.029470	311.21
0.032510	315.85	0.034222	312.20	0.032734	312.31
0.035856	316.57	0.037383	313.73	0.035967	313.68
0.039054	317.90	0.040584	314.69	0.039218	314.90
0.042177	318.56	0.043754	315.78	0.042333	315.94
0.045226	319.75	0.047006	316.69	0.045450	316.76
0.048299	320.38	0.050693	322.18	0.048621	317.60
0.053653	321.41	0.061726	322.91	0.056410	321.00
0.062676	322.10	0.072742	323.08	0.067365	322.54
0.069559	320.71	0.083022	319.99	0.078301	323.00
0.073783	315.25	0.093291	311.99	0.088891	321.43
0.076246	305.97	0.103363	299.78	0.098936	315.86
0.077847	293.64			0.109200	305.89
0.078544	276.36			0.119653	292.72

a. Engineering stress-strain curves are derived from load cell and extensometer data, and calliper measurements of coupon diameter. Load cell and extensometer data was acquired at a rate of 10Hz during coupon testing. The data reported here has been reduced to an equivalent sampling rate of 0.1Hz by discarding 99 data points out of 100.

Table 114: Measured engineering stress-strain curves for coupons machined from specimen L510-No35 in the circumferential direction.

Coupon No. 16		Coupon No. 17		Coupon No. 18	
Engineering Strain (-)	**Engineering Stress (MPa)**	**Engineering Strain (-)**	**Engineering Stress (MPa)**	**Engineering Strain (-)**	**Engineering Stress (MPa)**
-0.000023	4.43	-0.000058	6.75	-0.000037	10.06
0.000555	35.56	0.000405	33.17	0.000608	52.10
0.001435	86.63	0.001215	82.20	0.001559	106.11
0.002514	145.78	0.002256	141.67	0.002650	168.61
0.003752	212.84	0.003443	206.97	0.003862	234.87
0.005008	279.54	0.004662	274.18	0.005174	300.45
0.006774	327.07	0.006440	326.38	0.007494	331.35
0.009878	335.14	0.009372	335.94	0.010729	335.56
0.013302	337.08	0.012420	337.86	0.014147	336.76
0.016990	338.15	0.015635	338.53	0.017477	338.13
0.020631	338.98	0.018974	339.79	0.021177	339.06
0.024254	339.66	0.022542	340.82	0.024882	339.81
0.027886	340.56	0.026097	341.88	0.028509	340.87
0.031357	341.38	0.029746	342.57	0.032118	341.70
0.034918	342.44	0.033290	343.26	0.035689	342.47
0.038378	343.03	0.036715	344.37	0.039094	343.10
0.041899	344.06	0.040072	345.09	0.042309	344.29
0.045211	344.39	0.043250	345.79	0.045741	344.69
0.048439	345.06	0.046636	346.29	0.049088	345.44
0.056331	348.50	0.050067	348.00	0.058510	348.84
0.068179	350.17	0.060920	350.96	0.070034	350.24
0.080128	351.14	0.071688	352.12	0.081729	350.47
0.092594	350.66	0.082262	352.21	0.093298	349.19
0.105693	348.76	0.091765	350.78	0.105331	343.95
0.119932	342.67	0.100086	346.08	0.117421	335.30
0.134878	332.88	0.107218	337.83	0.130168	323.22
0.150591	319.26	0.114079	324.75		

a. Engineering stress-strain curves are derived from load cell and extensometer data, and calliper measurements of coupon diameter. Load cell and extensometer data was acquired at a rate of 10Hz during coupon testing. The data reported here has been reduced to an equivalent sampling rate of 0.1Hz by discarding 99 data points out of 100.

Table 115: Measured engineering stress-strain curves for coupons machined from specimen L510-No36 in the circumferential direction.

Coupon No. 25		Coupon No. 26		Coupon No. 27	
Engineering Strain (-)	**Engineering Stress (MPa)**	**Engineering Strain (-)**	**Engineering Stress (MPa)**	**Engineering Strain (-)**	**Engineering Stress (MPa)**
-0.000018	2.16	-0.000012	4.49	0.000022	1.56
0.000392	25.07	0.000526	33.59	0.000430	20.80
0.001328	77.27	0.001414	82.24	0.001250	61.28
0.002400	139.20	0.002447	142.27	0.002149	117.99
0.003606	207.50	0.003568	207.19	0.003223	182.77
0.004906	277.85	0.004794	274.31	0.004343	247.08
0.006782	322.87	0.006511	324.80	0.005642	307.15
0.009810	329.80	0.009151	334.18	0.008148	334.96
0.012932	331.35	0.011766	335.86	0.011202	338.67
0.016053	332.39	0.014605	336.93	0.014340	339.86
0.019484	333.28	0.017763	337.68	0.017629	340.65
0.022838	334.04	0.021019	338.29	0.020945	341.28
0.026246	334.88	0.024238	338.91	0.024383	341.87
0.029710	335.73	0.027547	339.72	0.027562	342.60
0.033314	336.46	0.030970	340.40	0.031027	343.25
0.036690	337.30	0.034376	341.17	0.034451	344.00
0.040016	337.99	0.037706	341.87	0.037910	344.67
0.043318	338.70	0.040971	342.53	0.041344	345.23
0.046560	339.36	0.044237	343.07	0.044663	345.83
0.049902	339.96	0.047292	343.56	0.047890	346.36
0.061070	343.22	0.050476	345.35	0.052341	350.11
0.071666	343.79	0.061738	347.14	0.064953	350.13
0.081796	343.29	0.071124	347.33	0.074940	350.38
0.091378	339.82	0.078684	345.62	0.084259	349.96
0.100894	332.35	0.083833	339.64	0.091340	347.14
0.110453	321.31	0.087366	330.29	0.095352	340.31
		0.089902	316.00	0.097710	329.41
				0.098990	314.97

a. Engineering stress-strain curves are derived from load cell and extensometer data, and calliper measurements of coupon diameter. Load cell and extensometer data was acquired at a rate of 10Hz during coupon testing. The data reported here has been reduced to an equivalent sampling rate of 0.1Hz by discarding 99 data points out of 100.

This page intentionally left blank.

Annex E Strain gauge locations

E.1 L510-No13

Table 116: Location of uni-axial strain gauges on the ring-stiffeners of specimen L510-No13

Strain Gauge ID	Strain Gauge Location			
	Description	Axial (mm)	Radial (mm)	Circumferential (°)
L510-No13-13	Flange, Fr 4	230.0	110.0	0.0
L510-No13-14	Flange, Fr 4	230.0	110.0	30.0
L510-No13-15	Flange, Fr 4	230.0	110.0	60.0
L510-No13-16	Flange, Fr 4	230.0	110.0	90.0
L510-No13-17	Flange, Fr 4	230.0	110.0	120.0
L510-No13-18	Flange, Fr 4	230.0	110.0	150.0
L510-No13-19	Flange, Fr 4	230.0	110.0	180.0
L510-No13-20	Flange, Fr 4	230.0	110.0	210.0
L510-No13-21	Flange, Fr 4	230.0	110.0	240.0
L510-No13-22	Flange, Fr 4	230.0	110.0	270.0
L510-No13-23	Flange, Fr 4	230.0	110.0	300.0
L510-No13-24	Flange, Fr 4	230.0	110.0	330.0
L510-No13-01	Flange, Fr 5	280.0	110.0	0.0
L510-No13-02	Flange, Fr 5	280.0	110.0	30.0
L510-No13-03	Flange, Fr 5	280.0	110.0	60.0
L510-No13-04	Flange, Fr 5	280.0	110.0	90.0
L510-No13-05	Flange, Fr 5	280.0	110.0	120.0
L510-No13-06	Flange, Fr 5	280.0	110.0	150.0
L510-No13-07	Flange, Fr 5	280.0	110.0	180.0
L510-No13-08	Flange, Fr 5	280.0	110.0	210.0
L510-No13-09	Flange, Fr 5	280.0	110.0	240.0
L510-No13-10	Flange, Fr 5	280.0	110.0	270.0
L510-No13-11	Flange, Fr 5	280.0	110.0	300.0
L510-No13-12	Flange, Fr 5	280.0	110.0	330.0

Table 117: Location of bi-axial strain gauges on the shell of specimen L510-No13

Strain Gauge ID	Strain Gauge Location			
	Description	**Axial (mm)**	**Radial (mm)**	**Circumferential (°)**
L510-No13-42	Outside Shell, Fr 4	230.0	123.0	0.0
L510-No13-26	Outside Shell, Mid-Bay 4	255.0	123.0	0.0
L510-No13-27	Outside Shell, Mid-Bay 4	255.0	123.0	7.5
L510-No13-28	Outside Shell, Mid-Bay 4	255.0	123.0	15.0
L510-No13-29	Outside Shell, Mid-Bay 4	255.0	123.0	30.0
L510-No13-30	Outside Shell, Mid-Bay 4	255.0	123.0	60.0
L510-No13-31	Outside Shell, Mid-Bay 4	255.0	123.0	90.0
L510-No13-32	Outside Shell, Mid-Bay 4	255.0	123.0	120.0
L510-No13-33	Outside Shell, Mid-Bay 4	255.0	123.0	150.0
L510-No13-34	Outside Shell, Mid-Bay 4	255.0	123.0	180.0
L510-No13-35	Outside Shell, Mid-Bay 4	255.0	123.0	210.0
L510-No13-36	Outside Shell, Mid-Bay 4	255.0	123.0	240.0
L510-No13-37	Outside Shell, Mid-Bay 4	255.0	123.0	270.0
L510-No13-38	Outside Shell, Mid-Bay 4	255.0	123.0	300.0
L510-No13-39	Outside Shell, Mid-Bay 4	255.0	123.0	330.0
L510-No13-40	Outside Shell, Mid-Bay 4	255.0	123.0	345.0
L510-No13-41	Outside Shell, Mid-Bay 4	255.0	123.0	352.5
L510-No13-25	Outside Shell, Fr 5	280.0	123.0	0.0
L510-No13-43	Inside Shell, Mid-Bay 4	255.0	120.0	0.0
L510-No13-44	Inside Shell, Mid-Bay 4	255.0	120.0	9.8
L510-No13-45	Inside Shell, Mid-Bay 4	255.0	120.0	15.0
L510-No13-46	Inside Shell, Mid-Bay 4	255.0	120.0	345.0
L510-No13-47	Inside Shell, Mid-Bay 4	255.0	120.0	350.2

E.2 L510-No14

Table 118: Location of uni-axial strain gauges on the ring-stiffeners of specimen L510-No14

Strain Gauge ID	Strain Gauge Location			
	Description	Axial (mm)	Radial (mm)	Circumferential (°)
L510-No14-20	Flange, Fr 4	230.0	110.0	15.0
L510-No14-21	Flange, Fr 4	230.0	110.0	45.0
L510-No14-22	Flange, Fr 4	230.0	110.0	75.0
L510-No14-23	Flange, Fr 4	230.0	110.0	105.0
L510-No14-24	Flange, Fr 4	230.0	110.0	135.0
L510-No14-13	Flange, Fr 4	230.0	110.0	165.0
L510-No14-14	Flange, Fr 4	230.0	110.0	195.0
L510-No14-15	Flange, Fr 4	230.0	110.0	225.0
L510-No14-16	Flange, Fr 4	230.0	110.0	255.0
L510-No14-17	Flange, Fr 4	230.0	110.0	285.0
L510-No14-18	Flange, Fr 4	230.0	110.0	315.0
L510-No14-19	Flange, Fr 4	230.0	110.0	345.0
L510-No14-08	Flange, Fr 5	280.0	110.0	15.0
L510-No14-09	Flange, Fr 5	280.0	110.0	45.0
L510-No14-10	Flange, Fr 5	280.0	110.0	75.0
L510-No14-11	Flange, Fr 5	280.0	110.0	105.0
L510-No14-12	Flange, Fr 5	280.0	110.0	135.0
L510-No14-01	Flange, Fr 5	280.0	110.0	165.0
L510-No14-02	Flange, Fr 5	280.0	110.0	195.0
L510-No14-03	Flange, Fr 5	280.0	110.0	225.0
L510-No14-04	Flange, Fr 5	280.0	110.0	255.0
L510-No14-05	Flange, Fr 5	280.0	110.0	285.0
L510-No14-06	Flange, Fr 5	280.0	110.0	315.0
L510-No14-07	Flange, Fr 5	280.0	110.0	345.0

Table 119: Location of bi-axial strain gauges on the shell of specimen L510-No14

Strain Gauge ID	Strain Gauge Location			
	Description	**Axial (mm)**	**Radial (mm)**	**Circumferential (°)**
L510-No14-42	Outside Shell, Fr 4	230.0	123.0	165.0
L510-No14-35	Outside Shell, Mid-Bay 4	255.0	123.0	15.0
L510-No14-36	Outside Shell, Mid-Bay 4	255.0	123.0	45.0
L510-No14-37	Outside Shell, Mid-Bay 4	255.0	123.0	75.0
L510-No14-38	Outside Shell, Mid-Bay 4	255.0	123.0	105.0
L510-No14-39	Outside Shell, Mid-Bay 4	255.0	123.0	135.0
L510-No14-40	Outside Shell, Mid-Bay 4	255.0	123.0	150.0
L510-No14-41	Outside Shell, Mid-Bay 4	255.0	123.0	157.5
L510-No14-26	Outside Shell, Mid-Bay 4	255.0	123.0	165.0
L510-No14-27	Outside Shell, Mid-Bay 4	255.0	123.0	172.5
L510-No14-28	Outside Shell, Mid-Bay 4	255.0	123.0	180.0
L510-No14-29	Outside Shell, Mid-Bay 4	255.0	123.0	195.0
L510-No14-30	Outside Shell, Mid-Bay 4	255.0	123.0	225.0
L510-No14-31	Outside Shell, Mid-Bay 4	255.0	123.0	255.0
L510-No14-32	Outside Shell, Mid-Bay 4	255.0	123.0	285.0
L510-No14-33	Outside Shell, Mid-Bay 4	255.0	123.0	315.0
L510-No14-34	Outside Shell, Mid-Bay 4	255.0	123.0	345.0
L510-No14-25	Outside Shell, Fr 5	280.0	123.0	165.0
L510-No14-46	Inside Shell, Mid-Bay 4	255.0	120.0	150.0
L510-No14-47	Inside Shell, Mid-Bay 4	255.0	120.0	155.2
L510-No14-43	Inside Shell, Mid-Bay 4	255.0	120.0	165.0
L510-No14-44	Inside Shell, Mid-Bay 4	255.0	120.0	174.8
L510-No14-45	Inside Shell, Mid-Bay 4	255.0	120.0	180.0

E.3 L510-No17

Table 120: Location of uni-axial strain gauges on the ring-stiffeners of specimen L510-No17

Strain Gauge ID	Strain Gauge Location			
	Description	Axial (mm)	Radial (mm)	Circumferential (°)
L510-No17-13	Flange, Fr 4	230.0	110.0	20.0
L510-No17-24	Flange, Fr 4	230.0	110.0	50.0
L510-No17-23	Flange, Fr 4	230.0	110.0	80.0
L510-No17-22	Flange, Fr 4	230.0	110.0	110.0
L510-No17-21	Flange, Fr 4	230.0	110.0	140.0
L510-No17-20	Flange, Fr 4	230.0	110.0	170.0
L510-No17-19	Flange, Fr 4	230.0	110.0	200.0
L510-No17-18	Flange, Fr 4	230.0	110.0	230.0
L510-No17-17	Flange, Fr 4	230.0	110.0	260.0
L510-No17-16	Flange, Fr 4	230.0	110.0	290.0
L510-No17-15	Flange, Fr 4	230.0	110.0	320.0
L510-No17-14	Flange, Fr 4	230.0	110.0	350.0
L510-No17-01	Flange, Fr 5	280.0	110.0	20.0
L510-No17-12	Flange, Fr 5	280.0	110.0	50.0
L510-No17-11	Flange, Fr 5	280.0	110.0	80.0
L510-No17-10	Flange, Fr 5	280.0	110.0	110.0
L510-No17-09	Flange, Fr 5	280.0	110.0	140.0
L510-No17-08	Flange, Fr 5	280.0	110.0	170.0
L510-No17-07	Flange, Fr 5	280.0	110.0	200.0
L510-No17-06	Flange, Fr 5	280.0	110.0	230.0
L510-No17-05	Flange, Fr 5	280.0	110.0	260.0
L510-No17-04	Flange, Fr 5	280.0	110.0	290.0
L510-No17-03	Flange, Fr 5	280.0	110.0	320.0
L510-No17-02	Flange, Fr 5	280.0	110.0	350.0

Table 121: Location of bi-axial strain gauges on the shell of specimen L510-No17

Strain Gauge ID	Strain Gauge Location			
	Description	**Axial (mm)**	**Radial (mm)**	**Circumferential (°)**
L510-No17-25	Outside Shell, Mid-Bay 4	255.0	123.0	20.0
L510-No17-36	Outside Shell, Mid-Bay 4	255.0	123.0	50.0
L510-No17-35	Outside Shell, Mid-Bay 4	255.0	123.0	80.0
L510-No17-34	Outside Shell, Mid-Bay 4	255.0	123.0	110.0
L510-No17-33	Outside Shell, Mid-Bay 4	255.0	123.0	140.0
L510-No17-32	Outside Shell, Mid-Bay 4	255.0	123.0	170.0
L510-No17-31	Outside Shell, Mid-Bay 4	255.0	123.0	200.0
L510-No17-30	Outside Shell, Mid-Bay 4	255.0	123.0	230.0
L510-No17-29	Outside Shell, Mid-Bay 4	255.0	123.0	260.0
L510-No17-28	Outside Shell, Mid-Bay 4	255.0	123.0	290.0
L510-No17-27	Outside Shell, Mid-Bay 4	255.0	123.0	320.0
L510-No17-26	Outside Shell, Mid-Bay 4	255.0	123.0	350.0
L510-No17-48	Outside Shell, Mid-Bay 1	105.0	123.0	140.0
L510-No17-47	Outside Shell, Fr 2	130.0	123.0	140.0
L510-No17-46	Outside Shell, Mid-Bay 2	155.0	123.0	140.0
L510-No17-45	Outside Shell, Fr 3	180.0	123.0	140.0
L510-No17-44	Outside Shell, Mid-Bay 3	205.0	123.0	140.0
L510-No17-43	Outside Shell, Fr 4	230.0	123.0	140.0
L510-No17-42	Outside Shell, Fr 5	280.0	123.0	140.0
L510-No17-41	Outside Shell, Mid-Bay 5	305.0	123.0	140.0
L510-No17-40	Outside Shell, Fr 6	330.0	123.0	140.0
L510-No17-39	Outside Shell, Mid-Bay 6	355.0	123.0	140.0
L510-No17-38	Outside Shell, Fr 7	380.0	123.0	140.0
L510-No17-37	Outside Shell, Mid-Bay 7	405.0	123.0	140.0

E.4 L510-No18

Table 122: Location of uni-axial strain gauges on the ring-stiffeners of specimen L510-No18

Strain Gauge ID	Strain Gauge Location			
	Description	Axial (mm)	Radial (mm)	Circumferential (°)
L510-No18-13	Flange, Fr 4	230.0	110.0	4.6
L510-No18-24	Flange, Fr 4	230.0	110.0	34.6
L510-No18-23	Flange, Fr 4	230.0	110.0	64.6
L510-No18-22	Flange, Fr 4	230.0	110.0	94.6
L510-No18-21	Flange, Fr 4	230.0	110.0	124.6
L510-No18-20	Flange, Fr 4	230.0	110.0	154.6
L510-No18-19	Flange, Fr 4	230.0	110.0	184.6
L510-No18-18	Flange, Fr 4	230.0	110.0	214.6
L510-No18-17	Flange, Fr 4	230.0	110.0	244.6
L510-No18-16	Flange, Fr 4	230.0	110.0	274.6
L510-No18-15	Flange, Fr 4	230.0	110.0	304.6
L510-No18-14	Flange, Fr 4	230.0	110.0	334.6
L510-No18-01	Flange, Fr 5	280.0	110.0	4.6
L510-No18-12	Flange, Fr 5	280.0	110.0	34.6
L510-No18-11	Flange, Fr 5	280.0	110.0	64.6
L510-No18-10	Flange, Fr 5	280.0	110.0	94.6
L510-No18-09	Flange, Fr 5	280.0	110.0	124.6
L510-No18-08	Flange, Fr 5	280.0	110.0	154.6
L510-No18-07	Flange, Fr 5	280.0	110.0	184.6
L510-No18-06	Flange, Fr 5	280.0	110.0	214.6
L510-No18-05	Flange, Fr 5	280.0	110.0	244.6
L510-No18-04	Flange, Fr 5	280.0	110.0	274.6
L510-No18-03	Flange, Fr 5	280.0	110.0	304.6
L510-No18-02	Flange, Fr 5	280.0	110.0	334.6

Table 123: Location of bi-axial strain gauges on the shell of specimen L510-No18

Strain Gauge ID	Strain Gauge Location			
	Description	**Axial (mm)**	**Radial (mm)**	**Circumferential (°)**
L510-No18-25	Outside Shell, Mid-Bay 4	255.0	123.0	4.6
L510-No18-36	Outside Shell, Mid-Bay 4	255.0	123.0	34.6
L510-No18-35	Outside Shell, Mid-Bay 4	255.0	123.0	64.6
L510-No18-34	Outside Shell, Mid-Bay 4	255.0	123.0	94.6
L510-No18-33	Outside Shell, Mid-Bay 4	255.0	123.0	124.6
L510-No18-32	Outside Shell, Mid-Bay 4	255.0	123.0	154.6
L510-No18-31	Outside Shell, Mid-Bay 4	255.0	123.0	184.6
L510-No18-30	Outside Shell, Mid-Bay 4	255.0	123.0	214.6
L510-No18-29	Outside Shell, Mid-Bay 4	255.0	123.0	244.6
L510-No18-28	Outside Shell, Mid-Bay 4	255.0	123.0	274.6
L510-No18-27	Outside Shell, Mid-Bay 4	255.0	123.0	304.6
L510-No18-26	Outside Shell, Mid-Bay 4	255.0	123.0	334.6
L510-No18-48	Outside Shell, Mid-Bay 1	105.0	123.0	124.6
L510-No18-47	Outside Shell, Fr 2	130.0	123.0	124.6
L510-No18-46	Outside Shell, Mid-Bay 2	155.0	123.0	124.6
L510-No18-45	Outside Shell, Fr 3	180.0	123.0	124.6
L510-No18-44	Outside Shell, Mid-Bay 3	205.0	123.0	124.6
L510-No18-43	Outside Shell, Fr 4	230.0	123.0	124.6
L510-No18-42	Outside Shell, Fr 5	280.0	123.0	124.6
L510-No18-41	Outside Shell, Mid-Bay 5	305.0	123.0	124.6
L510-No18-40	Outside Shell, Fr 6	330.0	123.0	124.6
L510-No18-39	Outside Shell, Mid-Bay 6	355.0	123.0	124.6
L510-No18-38	Outside Shell, Fr 7	380.0	123.0	124.6
L510-No18-37	Outside Shell, Mid-Bay 7	405.0	123.0	124.6

E.5 L510-No19

Table 124: Location of uni-axial strain gauges on the ring-stiffeners of specimen L510-No19

Strain Gauge ID	Strain Gauge Location			
	Description	Axial (mm)	Radial (mm)	Circumferential (°)
L510-No19-15	Flange, Fr 4	230.0	110.0	0.0
L510-No19-16	Flange, Fr 4	230.0	110.0	15.0
L510-No19-17	Flange, Fr 4	230.0	110.0	30.0
L510-No19-18	Flange, Fr 4	230.0	110.0	60.0
L510-No19-19	Flange, Fr 4	230.0	110.0	90.0
L510-No19-20	Flange, Fr 4	230.0	110.0	120.0
L510-No19-21	Flange, Fr 4	230.0	110.0	150.0
L510-No19-22	Flange, Fr 4	230.0	110.0	180.0
L510-No19-23	Flange, Fr 4	230.0	110.0	210.0
L510-No19-24	Flange, Fr 4	230.0	110.0	240.0
L510-No19-25	Flange, Fr 4	230.0	110.0	270.0
L510-No19-26	Flange, Fr 4	230.0	110.0	300.0
L510-No19-27	Flange, Fr 4	230.0	110.0	330.0
L510-No19-28	Flange, Fr 4	230.0	110.0	345.0
L510-No19-01	Flange, Fr 5	280.0	110.0	0.0
L510-No19-02	Flange, Fr 5	280.0	110.0	15.0
L510-No19-03	Flange, Fr 5	280.0	110.0	30.0
L510-No19-04	Flange, Fr 5	280.0	110.0	60.0
L510-No19-05	Flange, Fr 5	280.0	110.0	90.0
L510-No19-06	Flange, Fr 5	280.0	110.0	120.0
L510-No19-07	Flange, Fr 5	280.0	110.0	150.0
L510-No19-08	Flange, Fr 5	280.0	110.0	180.0
L510-No19-09	Flange, Fr 5	280.0	110.0	210.0
L510-No19-10	Flange, Fr 5	280.0	110.0	240.0
L510-No19-11	Flange, Fr 5	280.0	110.0	270.0
L510-No19-12	Flange, Fr 5	280.0	110.0	300.0
L510-No19-13	Flange, Fr 5	280.0	110.0	330.0
L510-No19-14	Flange, Fr 5	280.0	110.0	345.0

Table 125: Location of bi-axial strain gauges on the shell of specimen L510-No19

Strain Gauge ID	Strain Gauge Location			
	Description	**Axial (mm)**	**Radial (mm)**	**Circumferential (°)**
L510-No19-37	Outside Shell, Fr 4	230.0	123.0	0.0
L510-No19-38	Outside Shell, Fr 4	230.0	123.0	15.0
L510-No19-39	Outside Shell, Fr 4	230.0	123.0	345.0
L510-No19-32	Outside Shell, Mid-Bay 4	255.0	123.0	0.0
L510-No19-33	Outside Shell, Mid-Bay 4	255.0	123.0	15.0
L510-No19-34	Outside Shell, Mid-Bay 4	255.0	123.0	30.0
L510-No19-35	Outside Shell, Mid-Bay 4	255.0	123.0	330.0
L510-No19-36	Outside Shell, Mid-Bay 4	255.0	123.0	345.0
L510-No19-29	Outside Shell, Fr 5	280.0	123.0	0.0
L510-No19-30	Outside Shell, Fr 5	280.0	123.0	15.0
L510-No19-31	Outside Shell, Fr 5	280.0	123.0	345.0
L510-No19-40	Inside Shell, Mid-Bay 4	255.0	120.0	0.0
L510-No19-41	Inside Shell, Mid-Bay 4	255.0	120.0	15.0
L510-No19-42	Inside Shell, Mid-Bay 4	255.0	120.0	23.3
L510-No19-43	Inside Shell, Mid-Bay 4	255.0	120.0	30.0
L510-No19-44	Inside Shell, Mid-Bay 4	255.0	120.0	330.0
L510-No19-45	Inside Shell, Mid-Bay 4	255.0	120.0	336.7
L510-No19-46	Inside Shell, Mid-Bay 4	255.0	120.0	345.0

E.6 L510-No20

Table 126: Location of uni-axial strain gauges on the ring-stiffeners of specimen L510-No20

Strain Gauge ID	Strain Gauge Location			
	Description	Axial (mm)	Radial (mm)	Circumferential (°)
L510-No20-22	Flange, Fr 4	230.0	110.0	3.5
L510-No20-23	Flange, Fr 4	230.0	110.0	33.5
L510-No20-24	Flange, Fr 4	230.0	110.0	63.5
L510-No20-25	Flange, Fr 4	230.0	110.0	93.5
L510-No20-26	Flange, Fr 4	230.0	110.0	123.5
L510-No20-27	Flange, Fr 4	230.0	110.0	153.5
L510-No20-28	Flange, Fr 4	230.0	110.0	168.5
L510-No20-15	Flange, Fr 4	230.0	110.0	183.5
L510-No20-16	Flange, Fr 4	230.0	110.0	198.5
L510-No20-17	Flange, Fr 4	230.0	110.0	213.5
L510-No20-18	Flange, Fr 4	230.0	110.0	243.5
L510-No20-19	Flange, Fr 4	230.0	110.0	273.5
L510-No20-20	Flange, Fr 4	230.0	110.0	303.5
L510-No20-21	Flange, Fr 4	230.0	110.0	333.5
L510-No20-08	Flange, Fr 5	280.0	110.0	3.5
L510-No20-09	Flange, Fr 5	280.0	110.0	33.5
L510-No20-10	Flange, Fr 5	280.0	110.0	63.5
L510-No20-11	Flange, Fr 5	280.0	110.0	93.5
L510-No20-12	Flange, Fr 5	280.0	110.0	123.5
L510-No20-13	Flange, Fr 5	280.0	110.0	153.5
L510-No20-14	Flange, Fr 5	280.0	110.0	168.5
L510-No20-01	Flange, Fr 5	280.0	110.0	183.5
L510-No20-02	Flange, Fr 5	280.0	110.0	198.5
L510-No20-03	Flange, Fr 5	280.0	110.0	213.5
L510-No20-04	Flange, Fr 5	280.0	110.0	243.5
L510-No20-05	Flange, Fr 5	280.0	110.0	273.5
L510-No20-06	Flange, Fr 5	280.0	110.0	303.5
L510-No20-07	Flange, Fr 5	280.0	110.0	333.5

Table 127: Location of bi-axial strain gauges on the shell of specimen L510-No20

Strain Gauge ID	Strain Gauge Location			
	Description	**Axial (mm)**	**Radial (mm)**	**Circumferential (°)**
L510-No20-39	Outside Shell, Fr 4	230.0	123.0	168.5
L510-No20-37	Outside Shell, Fr 4	230.0	123.0	183.5
L510-No20-38	Outside Shell, Fr 4	230.0	123.0	198.5
L510-No20-35	Outside Shell, Mid-Bay 4	255.0	123.0	153.5
L510-No20-36	Outside Shell, Mid-Bay 4	255.0	123.0	168.5
L510-No20-32	Outside Shell, Mid-Bay 4	255.0	123.0	183.5
L510-No20-33	Outside Shell, Mid-Bay 4	255.0	123.0	198.5
L510-No20-34	Outside Shell, Mid-Bay 4	255.0	123.0	213.5
L510-No20-31	Outside Shell, Fr 5	280.0	123.0	168.5
L510-No20-29	Outside Shell, Fr 5	280.0	123.0	183.5
L510-No20-30	Outside Shell, Fr 5	280.0	123.0	198.5
L510-No20-44	Inside Shell, Mid-Bay 4	255.0	120.0	153.5
L510-No20-45	Inside Shell, Mid-Bay 4	255.0	120.0	160.2
L510-No20-46	Inside Shell, Mid-Bay 4	255.0	120.0	168.5
L510-No20-40	Inside Shell, Mid-Bay 4	255.0	120.0	183.5
L510-No20-41	Inside Shell, Mid-Bay 4	255.0	120.0	198.5
L510-No20-42	Inside Shell, Mid-Bay 4	255.0	120.0	206.8
L510-No20-43	Inside Shell, Mid-Bay 4	255.0	120.0	213.5

E.7 L510-No25

Table 128: Location of uni-axial strain gauges on the ring-stiffeners of specimen L510-No25

Strain Gauge ID	Strain Gauge Location			
	Description	Axial (mm)	Radial (mm)	Circumferential (°)
L510-No25-13	Flange, Fr 4	230.0	110.0	20.0
L510-No25-24	Flange, Fr 4	230.0	110.0	50.0
L510-No25-23	Flange, Fr 4	230.0	110.0	80.0
L510-No25-22	Flange, Fr 4	230.0	110.0	110.0
L510-No25-21	Flange, Fr 4	230.0	110.0	140.0
L510-No25-20	Flange, Fr 4	230.0	110.0	170.0
L510-No25-19	Flange, Fr 4	230.0	110.0	200.0
L510-No25-18	Flange, Fr 4	230.0	110.0	230.0
L510-No25-17	Flange, Fr 4	230.0	110.0	260.0
L510-No25-16	Flange, Fr 4	230.0	110.0	290.0
L510-No25-15	Flange, Fr 4	230.0	110.0	320.0
L510-No25-14	Flange, Fr 4	230.0	110.0	350.0
L510-No25-01	Flange, Fr 5	280.0	110.0	20.0
L510-No25-12	Flange, Fr 5	280.0	110.0	50.0
L510-No25-11	Flange, Fr 5	280.0	110.0	80.0
L510-No25-10	Flange, Fr 5	280.0	110.0	110.0
L510-No25-09	Flange, Fr 5	280.0	110.0	140.0
L510-No25-08	Flange, Fr 5	280.0	110.0	170.0
L510-No25-07	Flange, Fr 5	280.0	110.0	200.0
L510-No25-06	Flange, Fr 5	280.0	110.0	230.0
L510-No25-05	Flange, Fr 5	280.0	110.0	260.0
L510-No25-04	Flange, Fr 5	280.0	110.0	290.0
L510-No25-03	Flange, Fr 5	280.0	110.0	320.0
L510-No25-02	Flange, Fr 5	280.0	110.0	350.0

Table 129: Location of bi-axial strain gauges on the shell of specimen L510-No25

Strain Gauge ID	Strain Gauge Location			
	Description	**Axial (mm)**	**Radial (mm)**	**Circumferential (°)**
L510-No25-25	Outside Shell, Mid-Bay 4	255.0	123.0	20.0
L510-No25-36	Outside Shell, Mid-Bay 4	255.0	123.0	50.0
L510-No25-35	Outside Shell, Mid-Bay 4	255.0	123.0	80.0
L510-No25-34	Outside Shell, Mid-Bay 4	255.0	123.0	110.0
L510-No25-33	Outside Shell, Mid-Bay 4	255.0	123.0	140.0
L510-No25-32	Outside Shell, Mid-Bay 4	255.0	123.0	170.0
L510-No25-31	Outside Shell, Mid-Bay 4	255.0	123.0	200.0
L510-No25-30	Outside Shell, Mid-Bay 4	255.0	123.0	230.0
L510-No25-29	Outside Shell, Mid-Bay 4	255.0	123.0	260.0
L510-No25-28	Outside Shell, Mid-Bay 4	255.0	123.0	290.0
L510-No25-27	Outside Shell, Mid-Bay 4	255.0	123.0	320.0
L510-No25-26	Outside Shell, Mid-Bay 4	255.0	123.0	350.0
L510-No25-48	Outside Shell, Mid-Bay 1	105.0	123.0	260.0
L510-No25-47	Outside Shell, Fr 2	130.0	123.0	260.0
L510-No25-46	Outside Shell, Mid-Bay 2	155.0	123.0	260.0
L510-No25-45	Outside Shell, Fr 3	180.0	123.0	260.0
L510-No25-44	Outside Shell, Mid-Bay 3	205.0	123.0	260.0
L510-No25-43	Outside Shell, Fr 4	230.0	123.0	260.0
L510-No25-42	Outside Shell, Fr 5	280.0	123.0	260.0
L510-No25-41	Outside Shell, Mid-Bay 5	305.0	123.0	260.0
L510-No25-40	Outside Shell, Fr 6	330.0	123.0	260.0
L510-No25-39	Outside Shell, Mid-Bay 6	355.0	123.0	260.0
L510-No25-38	Outside Shell, Fr 7	380.0	123.0	260.0
L510-No25-37	Outside Shell, Mid-Bay 7	405.0	123.0	260.0

E.8 L510-No26

Table 130: Location of uni-axial strain gauges on the ring-stiffeners of specimen L510-No26

Strain Gauge ID	Strain Gauge Location			
	Description	Axial (mm)	Radial (mm)	Circumferential (°)
L510-No26-13	Flange, Fr 4	230.0	110.0	20.0
L510-No26-24	Flange, Fr 4	230.0	110.0	50.0
L510-No26-23	Flange, Fr 4	230.0	110.0	80.0
L510-No26-22	Flange, Fr 4	230.0	110.0	110.0
L510-No26-21	Flange, Fr 4	230.0	110.0	140.0
L510-No26-20	Flange, Fr 4	230.0	110.0	170.0
L510-No26-19	Flange, Fr 4	230.0	110.0	200.0
L510-No26-18	Flange, Fr 4	230.0	110.0	230.0
L510-No26-17	Flange, Fr 4	230.0	110.0	260.0
L510-No26-16	Flange, Fr 4	230.0	110.0	290.0
L510-No26-15	Flange, Fr 4	230.0	110.0	320.0
L510-No26-14	Flange, Fr 4	230.0	110.0	350.0
L510-No26-01	Flange, Fr 5	280.0	110.0	20.0
L510-No26-12	Flange, Fr 5	280.0	110.0	50.0
L510-No26-11	Flange, Fr 5	280.0	110.0	80.0
L510-No26-10	Flange, Fr 5	280.0	110.0	110.0
L510-No26-09	Flange, Fr 5	280.0	110.0	140.0
L510-No26-08	Flange, Fr 5	280.0	110.0	170.0
L510-No26-07	Flange, Fr 5	280.0	110.0	200.0
L510-No26-06	Flange, Fr 5	280.0	110.0	230.0
L510-No26-05	Flange, Fr 5	280.0	110.0	260.0
L510-No26-04	Flange, Fr 5	280.0	110.0	290.0
L510-No26-03	Flange, Fr 5	280.0	110.0	320.0
L510-No26-02	Flange, Fr 5	280.0	110.0	350.0

Table 131: Location of bi-axial strain gauges on the shell of specimen L510-No26

Strain Gauge ID	Strain Gauge Location			
	Description	**Axial (mm)**	**Radial (mm)**	**Circumferential (°)**
L510-No26-25	Outside Shell, Mid-Bay 4	255.0	123.0	20.0
L510-No26-36	Outside Shell, Mid-Bay 4	255.0	123.0	50.0
L510-No26-35	Outside Shell, Mid-Bay 4	255.0	123.0	80.0
L510-No26-34	Outside Shell, Mid-Bay 4	255.0	123.0	110.0
L510-No26-33	Outside Shell, Mid-Bay 4	255.0	123.0	140.0
L510-No26-32	Outside Shell, Mid-Bay 4	255.0	123.0	170.0
L510-No26-31	Outside Shell, Mid-Bay 4	255.0	123.0	200.0
L510-No26-30	Outside Shell, Mid-Bay 4	255.0	123.0	230.0
L510-No26-29	Outside Shell, Mid-Bay 4	255.0	123.0	260.0
L510-No26-28	Outside Shell, Mid-Bay 4	255.0	123.0	290.0
L510-No26-27	Outside Shell, Mid-Bay 4	255.0	123.0	320.0
L510-No26-26	Outside Shell, Mid-Bay 4	255.0	123.0	350.0
L510-No26-48	Outside Shell, Mid-Bay 1	105.0	123.0	260.0
L510-No26-47	Outside Shell, Fr 2	130.0	123.0	260.0
L510-No26-46	Outside Shell, Mid-Bay 2	155.0	123.0	260.0
L510-No26-45	Outside Shell, Fr 3	180.0	123.0	260.0
L510-No26-44	Outside Shell, Mid-Bay 3	205.0	123.0	260.0
L510-No26-43	Outside Shell, Fr 4	230.0	123.0	260.0
L510-No26-42	Outside Shell, Fr 5	280.0	123.0	260.0
L510-No26-41	Outside Shell, Mid-Bay 5	305.0	123.0	260.0
L510-No26-40	Outside Shell, Fr 6	330.0	123.0	260.0
L510-No26-39	Outside Shell, Mid-Bay 6	355.0	123.0	260.0
L510-No26-38	Outside Shell, Fr 7	380.0	123.0	260.0
L510-No26-37	Outside Shell, Mid-Bay 7	405.0	123.0	260.0

E.9 L510-No33

Table 132: Location of uni-axial strain gauges on the ring-stiffeners of specimen L510-No33

Strain Gauge ID	Strain Gauge Location			
	Description	**Axial (mm)**	**Radial (mm)**	**Circumferential (°)**
L510-No33-13	Flange, Fr 4	230.0	110.0	6.4
L510-No33-24	Flange, Fr 4	230.0	110.0	36.4
L510-No33-23	Flange, Fr 4	230.0	110.0	66.4
L510-No33-22	Flange, Fr 4	230.0	110.0	96.4
L510-No33-21	Flange, Fr 4	230.0	110.0	126.4
L510-No33-20	Flange, Fr 4	230.0	110.0	156.4
L510-No33-19	Flange, Fr 4	230.0	110.0	186.4
L510-No33-18	Flange, Fr 4	230.0	110.0	216.4
L510-No33-17	Flange, Fr 4	230.0	110.0	246.4
L510-No33-16	Flange, Fr 4	230.0	110.0	276.4
L510-No33-15	Flange, Fr 4	230.0	110.0	306.4
L510-No33-14	Flange, Fr 4	230.0	110.0	336.4
L510-No33-01	Flange, Fr 5	280.0	110.0	6.4
L510-No33-12	Flange, Fr 5	280.0	110.0	36.4
L510-No33-11	Flange, Fr 5	280.0	110.0	66.4
L510-No33-10	Flange, Fr 5	280.0	110.0	96.4
L510-No33-09	Flange, Fr 5	280.0	110.0	126.4
L510-No33-08	Flange, Fr 5	280.0	110.0	156.4
L510-No33-07	Flange, Fr 5	280.0	110.0	186.4
L510-No33-06	Flange, Fr 5	280.0	110.0	216.4
L510-No33-05	Flange, Fr 5	280.0	110.0	246.4
L510-No33-04	Flange, Fr 5	280.0	110.0	276.4
L510-No33-03	Flange, Fr 5	280.0	110.0	306.4
L510-No33-02	Flange, Fr 5	280.0	110.0	336.4

Table 133: Location of bi-axial strain gauges on the shell of specimen L510-No33

Strain Gauge ID	Strain Gauge Location			
	Description	**Axial (mm)**	**Radial (mm)**	**Circumferential (°)**
L510-No33-25	Outside Shell, Mid-Bay 4	255.0	123.0	6.4
L510-No33-36	Outside Shell, Mid-Bay 4	255.0	123.0	36.4
L510-No33-35	Outside Shell, Mid-Bay 4	255.0	123.0	66.4
L510-No33-34	Outside Shell, Mid-Bay 4	255.0	123.0	96.4
L510-No33-33	Outside Shell, Mid-Bay 4	255.0	123.0	126.4
L510-No33-32	Outside Shell, Mid-Bay 4	255.0	123.0	156.4
L510-No33-31	Outside Shell, Mid-Bay 4	255.0	123.0	186.4
L510-No33-30	Outside Shell, Mid-Bay 4	255.0	123.0	216.4
L510-No33-29	Outside Shell, Mid-Bay 4	255.0	123.0	246.4
L510-No33-28	Outside Shell, Mid-Bay 4	255.0	123.0	276.4
L510-No33-27	Outside Shell, Mid-Bay 4	255.0	123.0	306.4
L510-No33-26	Outside Shell, Mid-Bay 4	255.0	123.0	336.4
L510-No33-48	Outside Shell, Mid-Bay 1	105.0	123.0	6.4
L510-No33-47	Outside Shell, Fr 2	130.0	123.0	6.4
L510-No33-46	Outside Shell, Mid-Bay 2	155.0	123.0	6.4
L510-No33-45	Outside Shell, Fr 3	180.0	123.0	6.4
L510-No33-44	Outside Shell, Mid-Bay 3	205.0	123.0	6.4
L510-No33-43	Outside Shell, Fr 4	230.0	123.0	6.4
L510-No33-42	Outside Shell, Fr 5	280.0	123.0	6.4
L510-No33-41	Outside Shell, Mid-Bay 5	305.0	123.0	6.4
L510-No33-40	Outside Shell, Fr 6	330.0	123.0	6.4
L510-No33-39	Outside Shell, Mid-Bay 6	355.0	123.0	6.4
L510-No33-38	Outside Shell, Fr 7	380.0	123.0	6.4
L510-No33-37	Outside Shell, Mid-Bay 7	405.0	123.0	6.4

E.10 L510-No34

Table 134: Location of uni-axial strain gauges on the ring-stiffeners of specimen L510-No34

Strain Gauge ID	Strain Gauge Location			
	Description	Axial (mm)	Radial (mm)	Circumferential (°)
L510-No34-13	Flange, Fr 3	180.0	110.0	20.4
L510-No34-24	Flange, Fr 3	180.0	110.0	50.4
L510-No34-23	Flange, Fr 3	180.0	110.0	80.4
L510-No34-22	Flange, Fr 3	180.0	110.0	110.4
L510-No34-21	Flange, Fr 3	180.0	110.0	140.4
L510-No34-20	Flange, Fr 3	180.0	110.0	170.4
L510-No34-19	Flange, Fr 3	180.0	110.0	200.4
L510-No34-18	Flange, Fr 3	180.0	110.0	230.4
L510-No34-17	Flange, Fr 3	180.0	110.0	260.4
L510-No34-16	Flange, Fr 3	180.0	110.0	290.4
L510-No34-15	Flange, Fr 3	180.0	110.0	320.4
L510-No34-14	Flange, Fr 3	180.0	110.0	350.4
L510-No34-01	Flange, Fr 6	330.0	110.0	20.4
L510-No34-12	Flange, Fr 6	330.0	110.0	50.4
L510-No34-11	Flange, Fr 6	330.0	110.0	80.4
L510-No34-10	Flange, Fr 6	330.0	110.0	110.4
L510-No34-09	Flange, Fr 6	330.0	110.0	140.4
L510-No34-08	Flange, Fr 6	330.0	110.0	170.4
L510-No34-07	Flange, Fr 6	330.0	110.0	200.4
L510-No34-06	Flange, Fr 6	330.0	110.0	230.4
L510-No34-05	Flange, Fr 6	330.0	110.0	260.4
L510-No34-04	Flange, Fr 6	330.0	110.0	290.4
L510-No34-03	Flange, Fr 6	330.0	110.0	320.4
L510-No34-02	Flange, Fr 6	330.0	110.0	350.4

Table 135: Location of bi-axial strain gauges on the shell of specimen L510-No34

Strain Gauge ID	Strain Gauge Location			
	Description	**Axial (mm)**	**Radial (mm)**	**Circumferential (°)**
L510-No34-25	Outside Shell, Mid-Bay 2	155.0	123.0	20.4
L510-No34-36	Outside Shell, Mid-Bay 2	155.0	123.0	50.4
L510-No34-35	Outside Shell, Mid-Bay 2	155.0	123.0	80.4
L510-No34-34	Outside Shell, Mid-Bay 2	155.0	123.0	110.4
L510-No34-33	Outside Shell, Mid-Bay 2	155.0	123.0	140.4
L510-No34-32	Outside Shell, Mid-Bay 2	155.0	123.0	170.4
L510-No34-31	Outside Shell, Mid-Bay 2	155.0	123.0	200.4
L510-No34-30	Outside Shell, Mid-Bay 2	155.0	123.0	230.4
L510-No34-29	Outside Shell, Mid-Bay 2	155.0	123.0	260.4
L510-No34-28	Outside Shell, Mid-Bay 2	155.0	123.0	290.4
L510-No34-27	Outside Shell, Mid-Bay 2	155.0	123.0	320.4
L510-No34-26	Outside Shell, Mid-Bay 2	155.0	123.0	350.4
L510-No34-48	Outside Shell, Mid-Bay 1	105.0	123.0	320.4
L510-No34-47	Outside Shell, Fr 2	130.0	123.0	320.4
L510-No34-46	Outside Shell, Mid-Bay 2	155.0	123.0	320.4
L510-No34-45	Outside Shell, Fr 3	180.0	123.0	320.4
L510-No34-44	Outside Shell, Mid-Bay 3	205.0	123.0	320.4
L510-No34-43	Outside Shell, Fr 4	230.0	123.0	320.4
L510-No34-42	Outside Shell, Mid-Bay 4	255.0	123.0	320.4
L510-No34-41	Outside Shell, Fr 5	280.0	123.0	320.4
L510-No34-40	Outside Shell, Mid-Bay 5	305.0	123.0	320.4
L510-No34-39	Outside Shell, Fr 6	330.0	123.0	320.4
L510-No34-38	Outside Shell, Fr 7	380.0	123.0	320.4
L510-No34-37	Outside Shell, Mid-Bay 7	405.0	123.0	320.4

E.11 L510-No35

Table 136: Location of uni-axial strain gauges on the ring-stiffeners of specimen L510-No35

Strain Gauge ID	Strain Gauge Location			
	Description	Axial (mm)	Radial (mm)	Circumferential (°)
L510-No35-13	Flange, Fr 4	230.0	110.0	0.0
L510-No35-14	Flange, Fr 4	230.0	110.0	30.0
L510-No35-15	Flange, Fr 4	230.0	110.0	60.0
L510-No35-16	Flange, Fr 4	230.0	110.0	90.0
L510-No35-17	Flange, Fr 4	230.0	110.0	120.0
L510-No35-18	Flange, Fr 4	230.0	110.0	150.0
L510-No35-19	Flange, Fr 4	230.0	110.0	180.0
L510-No35-20	Flange, Fr 4	230.0	110.0	210.0
L510-No35-21	Flange, Fr 4	230.0	110.0	240.0
L510-No35-22	Flange, Fr 4	230.0	110.0	270.0
L510-No35-23	Flange, Fr 4	230.0	110.0	300.0
L510-No35-24	Flange, Fr 4	230.0	110.0	330.0
L510-No35-01	Flange, Fr 5	280.0	110.0	0.0
L510-No35-02	Flange, Fr 5	280.0	110.0	30.0
L510-No35-03	Flange, Fr 5	280.0	110.0	60.0
L510-No35-04	Flange, Fr 5	280.0	110.0	90.0
L510-No35-05	Flange, Fr 5	280.0	110.0	120.0
L510-No35-06	Flange, Fr 5	280.0	110.0	150.0
L510-No35-07	Flange, Fr 5	280.0	110.0	180.0
L510-No35-08	Flange, Fr 5	280.0	110.0	210.0
L510-No35-09	Flange, Fr 5	280.0	110.0	240.0
L510-No35-10	Flange, Fr 5	280.0	110.0	270.0
L510-No35-11	Flange, Fr 5	280.0	110.0	300.0
L510-No35-12	Flange, Fr 5	280.0	110.0	330.0

Table 137: Location of bi-axial strain gauges on the shell of specimen L510-No35

Strain Gauge ID	Strain Gauge Location			
	Description	**Axial (mm)**	**Radial (mm)**	**Circumferential (°)**
L510-No35-42	Outside Shell, Fr 4	230.0	123.0	0.0
L510-No35-26	Outside Shell, Mid-Bay 4	255.0	123.0	0.0
L510-No35-27	Outside Shell, Mid-Bay 4	255.0	123.0	7.5
L510-No35-28	Outside Shell, Mid-Bay 4	255.0	123.0	15.0
L510-No35-29	Outside Shell, Mid-Bay 4	255.0	123.0	30.0
L510-No35-30	Outside Shell, Mid-Bay 4	255.0	123.0	60.0
L510-No35-31	Outside Shell, Mid-Bay 4	255.0	123.0	90.0
L510-No35-32	Outside Shell, Mid-Bay 4	255.0	123.0	120.0
L510-No35-33	Outside Shell, Mid-Bay 4	255.0	123.0	150.0
L510-No35-34	Outside Shell, Mid-Bay 4	255.0	123.0	180.0
L510-No35-35	Outside Shell, Mid-Bay 4	255.0	123.0	210.0
L510-No35-36	Outside Shell, Mid-Bay 4	255.0	123.0	240.0
L510-No35-37	Outside Shell, Mid-Bay 4	255.0	123.0	270.0
L510-No35-38	Outside Shell, Mid-Bay 4	255.0	123.0	300.0
L510-No35-39	Outside Shell, Mid-Bay 4	255.0	123.0	330.0
L510-No35-40	Outside Shell, Mid-Bay 4	255.0	123.0	345.0
L510-No35-41	Outside Shell, Mid-Bay 4	255.0	123.0	352.5
L510-No35-25	Outside Shell, Fr 5	280.0	123.0	0.0
L510-No35-43	Inside Shell, Mid-Bay 4	255.0	120.0	0.0
L510-No35-44	Inside Shell, Mid-Bay 4	255.0	120.0	9.8
L510-No35-45	Inside Shell, Mid-Bay 4	255.0	120.0	15.0
L510-No35-46	Inside Shell, Mid-Bay 4	255.0	120.0	345.0
L510-No35-47	Inside Shell, Mid-Bay 4	255.0	120.0	350.2

E.12 L510-No36

Table 138: Location of uni-axial strain gauges on the ring-stiffeners of specimen L510-No36

Strain Gauge ID	Strain Gauge Location			
	Description	Axial (mm)	Radial (mm)	Circumferential (°)
L510-No36-13	Flange, Fr 4	230.0	110.0	0.0
L510-No36-14	Flange, Fr 4	230.0	110.0	30.0
L510-No36-15	Flange, Fr 4	230.0	110.0	60.0
L510-No36-16	Flange, Fr 4	230.0	110.0	90.0
L510-No36-17	Flange, Fr 4	230.0	110.0	120.0
L510-No36-18	Flange, Fr 4	230.0	110.0	150.0
L510-No36-19	Flange, Fr 4	230.0	110.0	180.0
L510-No36-20	Flange, Fr 4	230.0	110.0	210.0
L510-No36-21	Flange, Fr 4	230.0	110.0	240.0
L510-No36-22	Flange, Fr 4	230.0	110.0	270.0
L510-No36-23	Flange, Fr 4	230.0	110.0	300.0
L510-No36-24	Flange, Fr 4	230.0	110.0	330.0
L510-No36-01	Flange, Fr 5	280.0	110.0	0.0
L510-No36-02	Flange, Fr 5	280.0	110.0	30.0
L510-No36-03	Flange, Fr 5	280.0	110.0	60.0
L510-No36-04	Flange, Fr 5	280.0	110.0	90.0
L510-No36-05	Flange, Fr 5	280.0	110.0	120.0
L510-No36-06	Flange, Fr 5	280.0	110.0	150.0
L510-No36-07	Flange, Fr 5	280.0	110.0	180.0
L510-No36-08	Flange, Fr 5	280.0	110.0	210.0
L510-No36-09	Flange, Fr 5	280.0	110.0	240.0
L510-No36-10	Flange, Fr 5	280.0	110.0	270.0
L510-No36-11	Flange, Fr 5	280.0	110.0	300.0
L510-No36-12	Flange, Fr 5	280.0	110.0	330.0

Table 139: Location of bi-axial strain gauges on the shell of specimen L510-No36

Strain Gauge ID	Strain Gauge Location			
	Description	**Axial (mm)**	**Radial (mm)**	**Circumferential (°)**
L510-No36-42	Outside Shell, Fr 4	230.0	123.0	0.0
L510-No36-26	Outside Shell, Mid-Bay 4	255.0	123.0	0.0
L510-No36-27	Outside Shell, Mid-Bay 4	255.0	123.0	7.5
L510-No36-28	Outside Shell, Mid-Bay 4	255.0	123.0	15.0
L510-No36-29	Outside Shell, Mid-Bay 4	255.0	123.0	30.0
L510-No36-30	Outside Shell, Mid-Bay 4	255.0	123.0	60.0
L510-No36-31	Outside Shell, Mid-Bay 4	255.0	123.0	90.0
L510-No36-32	Outside Shell, Mid-Bay 4	255.0	123.0	120.0
L510-No36-33	Outside Shell, Mid-Bay 4	255.0	123.0	150.0
L510-No36-34	Outside Shell, Mid-Bay 4	255.0	123.0	180.0
L510-No36-35	Outside Shell, Mid-Bay 4	255.0	123.0	210.0
L510-No36-36	Outside Shell, Mid-Bay 4	255.0	123.0	240.0
L510-No36-37	Outside Shell, Mid-Bay 4	255.0	123.0	270.0
L510-No36-38	Outside Shell, Mid-Bay 4	255.0	123.0	300.0
L510-No36-39	Outside Shell, Mid-Bay 4	255.0	123.0	330.0
L510-No36-40	Outside Shell, Mid-Bay 4	255.0	123.0	345.0
L510-No36-41	Outside Shell, Mid-Bay 4	255.0	123.0	352.5
L510-No36-25	Outside Shell, Fr 5	280.0	123.0	0.0
L510-No36-43	Inside Shell, Mid-Bay 4	255.0	120.0	0.0
L510-No36-44	Inside Shell, Mid-Bay 4	255.0	120.0	9.8
L510-No36-45	Inside Shell, Mid-Bay 4	255.0	120.0	15.0
L510-No36-46	Inside Shell, Mid-Bay 4	255.0	120.0	345.0
L510-No36-47	Inside Shell, Mid-Bay 4	255.0	120.0	350.2

Annex F Pressure loading histories

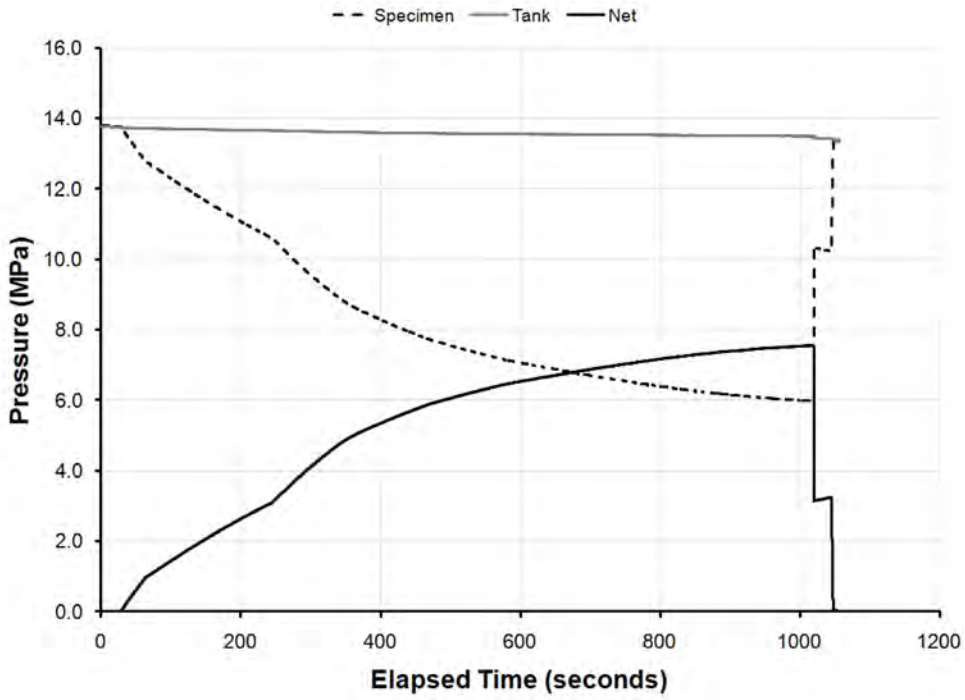

Figure 164: Tank, specimen and net pressures measured during volume-control collapse testing of specimen L510-No13 plotted against the time (showing data reduced to 20 Hz).

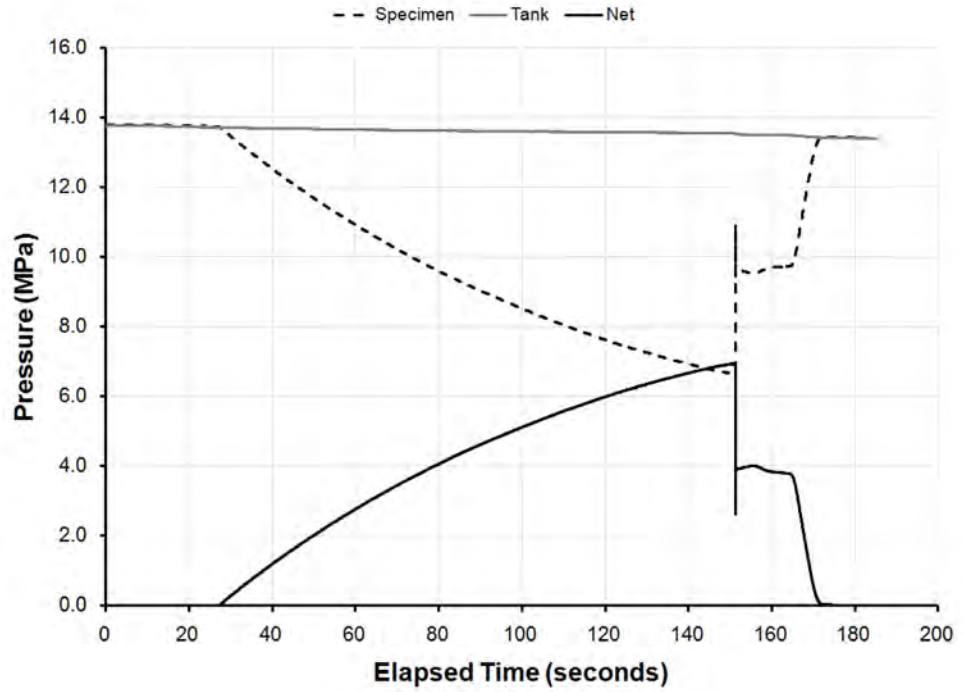

Figure 165: Tank, specimen and net pressures measured during volume-control collapse testing of specimen L510-No14 plotted against the time (showing data reduced to 20 Hz).

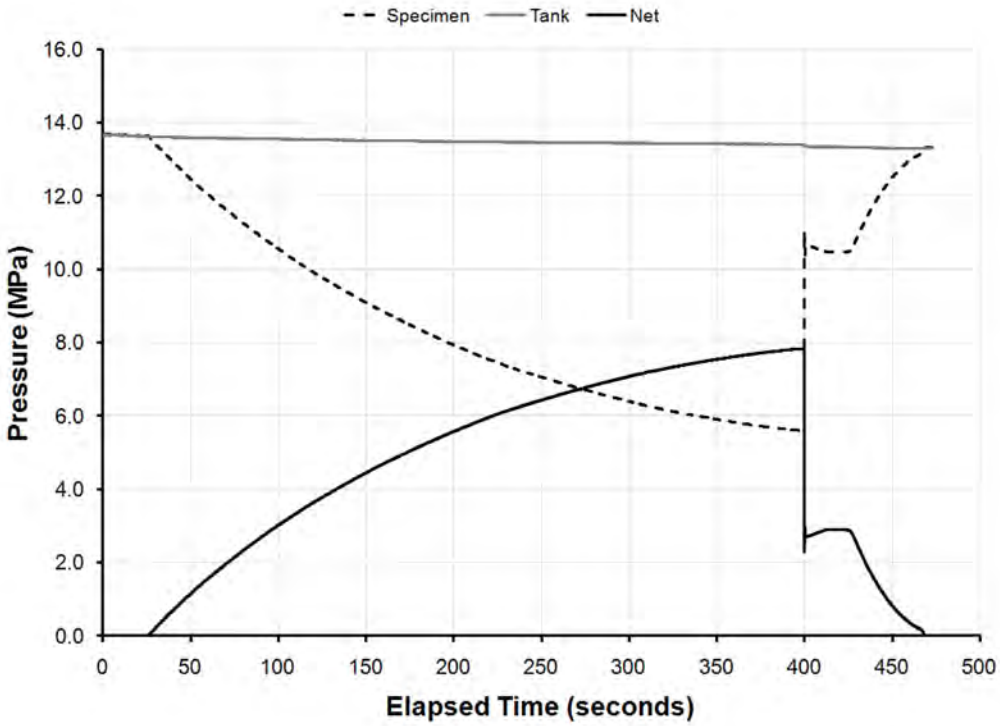

Figure 166: Tank, specimen and net pressures measured during volume-control collapse testing of specimen L510-No17 plotted against the time (showing data reduced to 20 Hz).

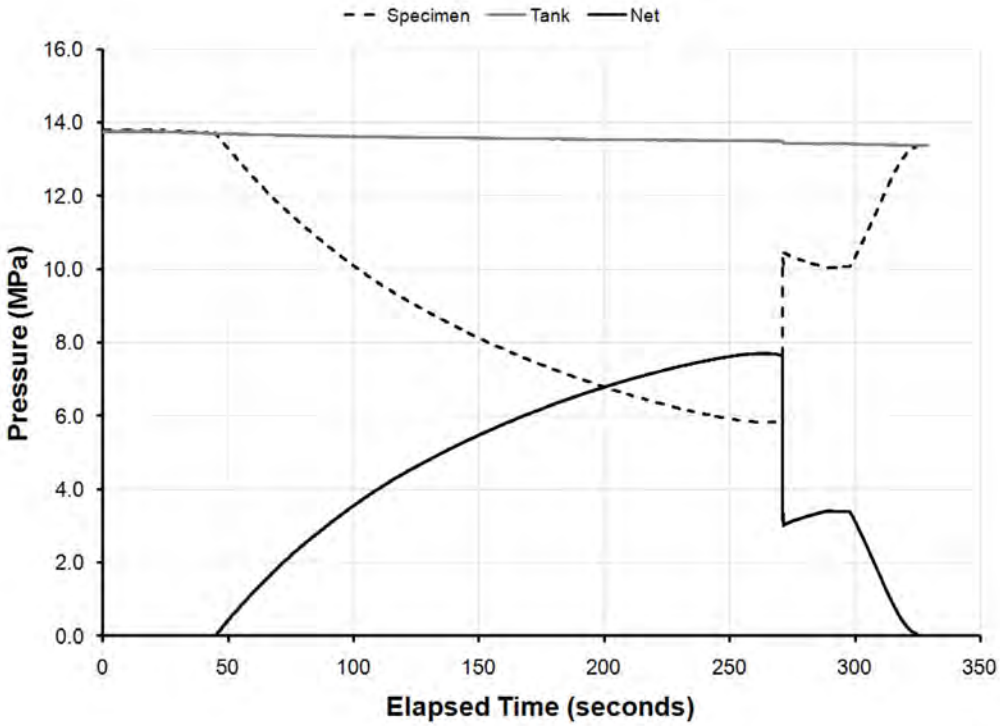

Figure 167: Tank, specimen and net pressures measured during volume-control collapse testing of specimen L510-No18 plotted against the time (showing data reduced to 20 Hz).

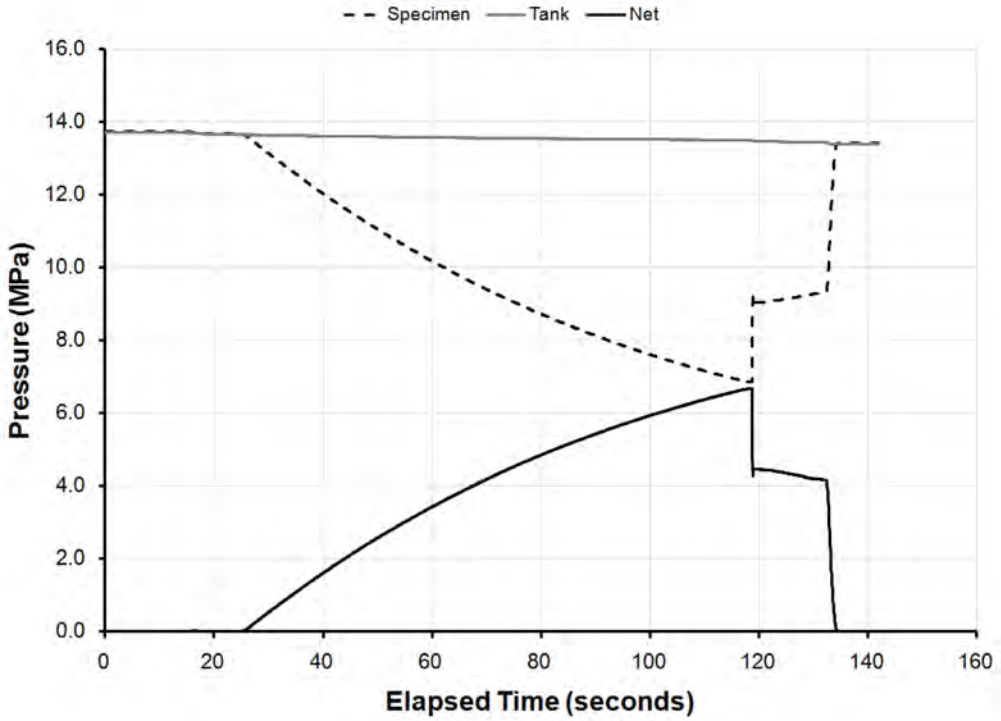

Figure 168: Tank, specimen and net pressures measured during volume-control collapse testing of specimen L510-No19 plotted against the time (showing data reduced to 20 Hz).

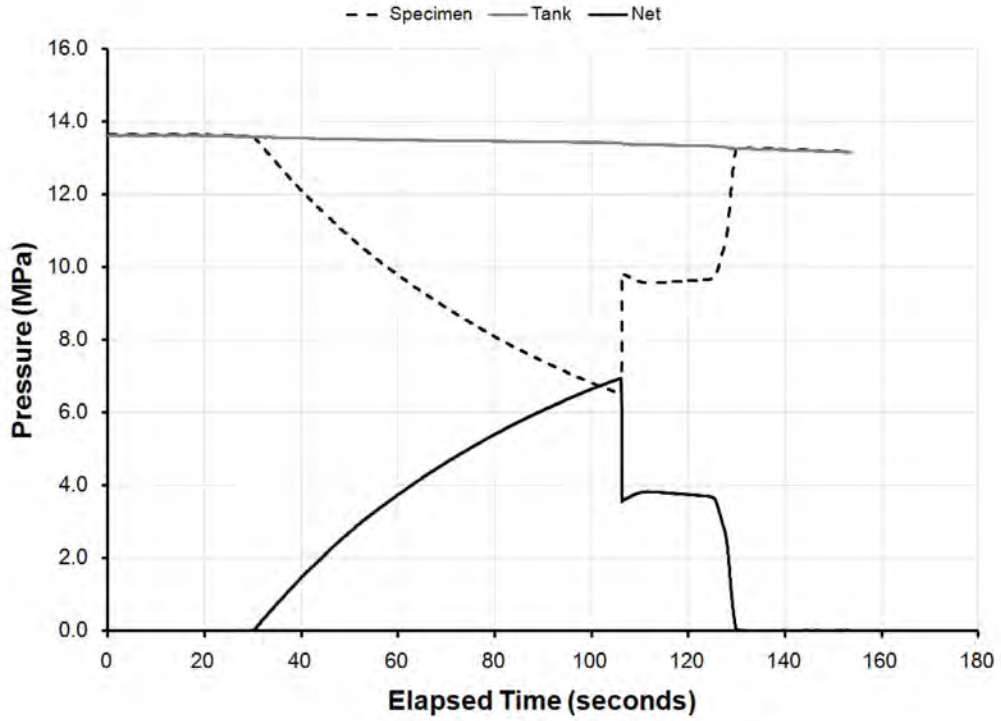

Figure 169: Tank, specimen and net pressures measured during volume-control collapse testing of specimen L510-No20 plotted against the time (showing data reduced to 20 Hz).

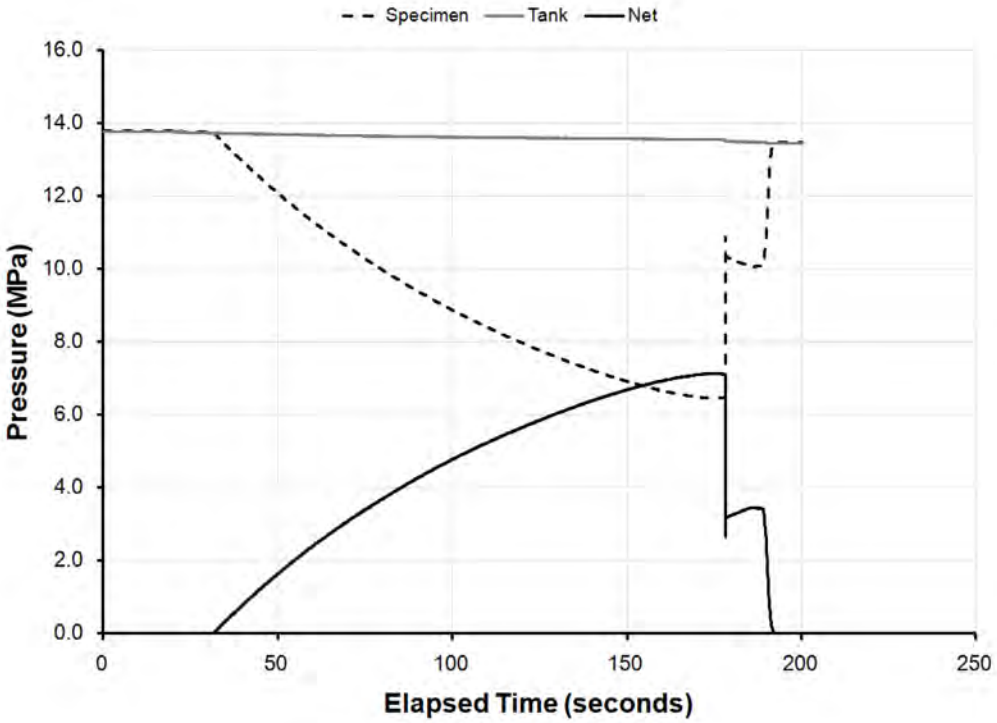

Figure 170: Tank, specimen and net pressures measured during volume-control collapse testing of specimen L510-No25 plotted against the time (showing data reduced to 20 Hz).

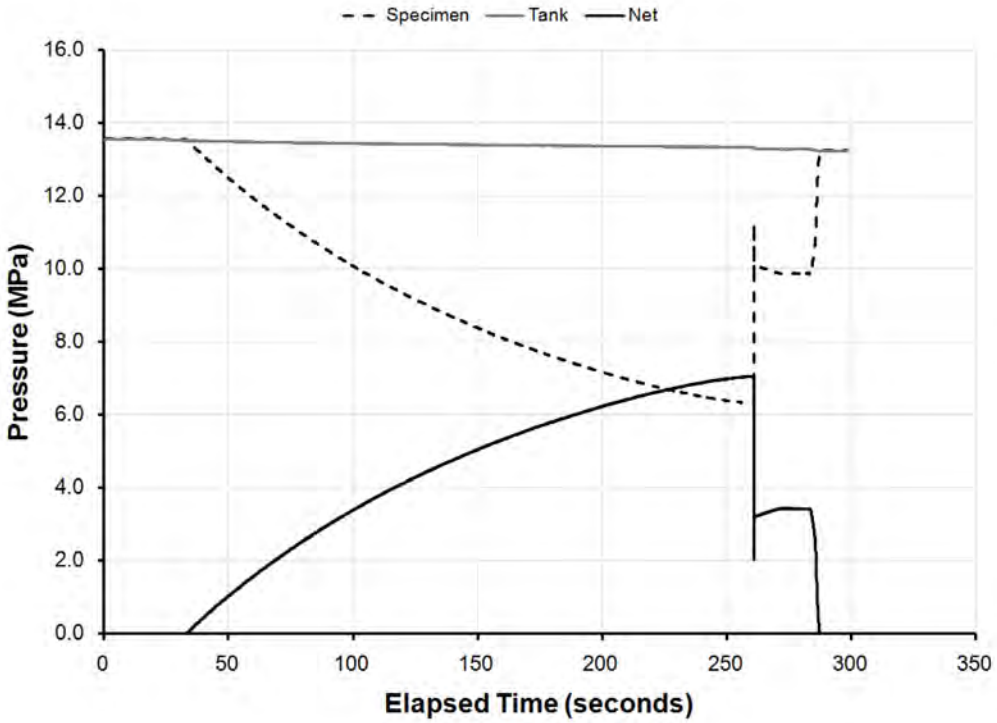

Figure 171: Tank, specimen and net pressures measured during volume-control collapse testing of specimen L510-No26 plotted against the time (showing data reduced to 20 Hz).

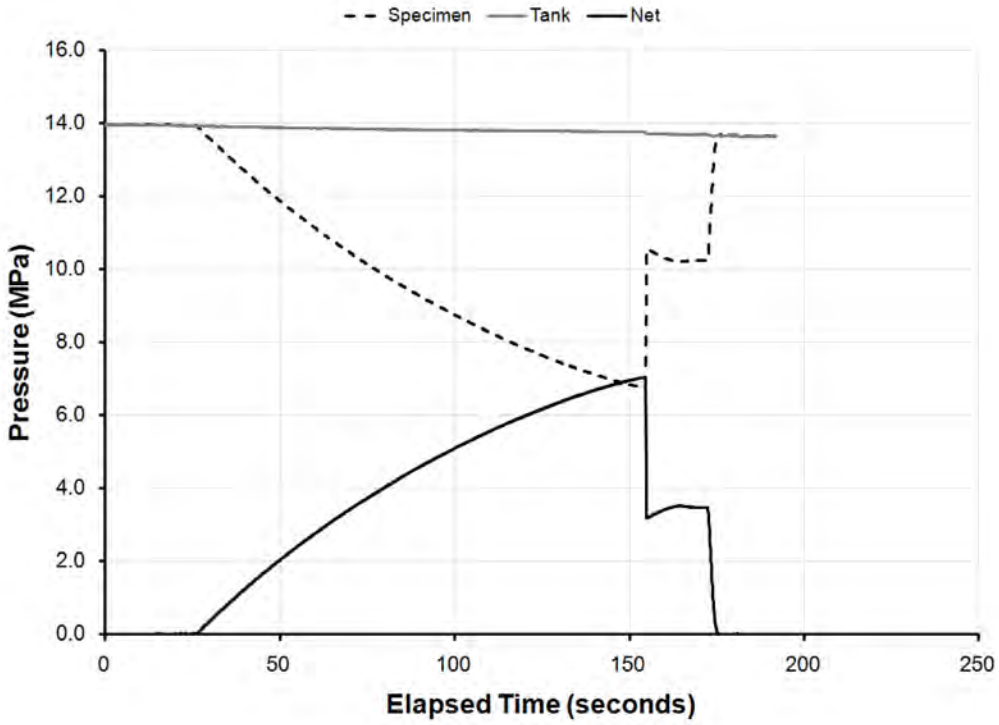

Figure 172: Tank, specimen and net pressures measured during volume-control collapse testing of specimen L510-No33 plotted against the time (showing data reduced to 20 Hz).

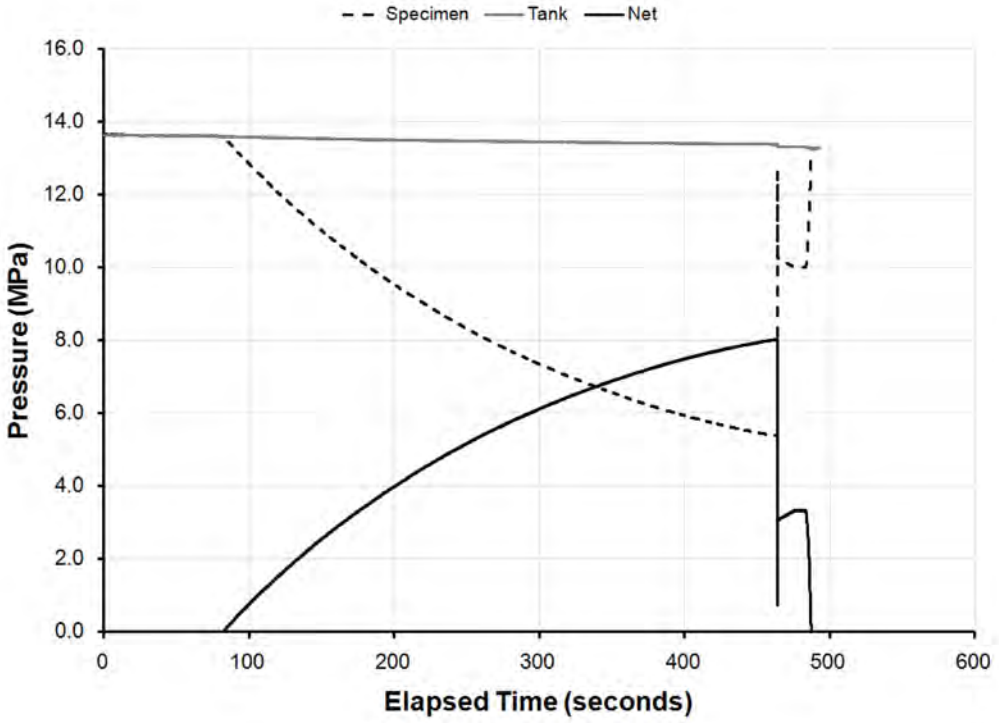

Figure 173: Tank, specimen and net pressures measured during volume-control collapse testing of specimen L510-No34 plotted against the time (showing data reduced to 20 Hz).

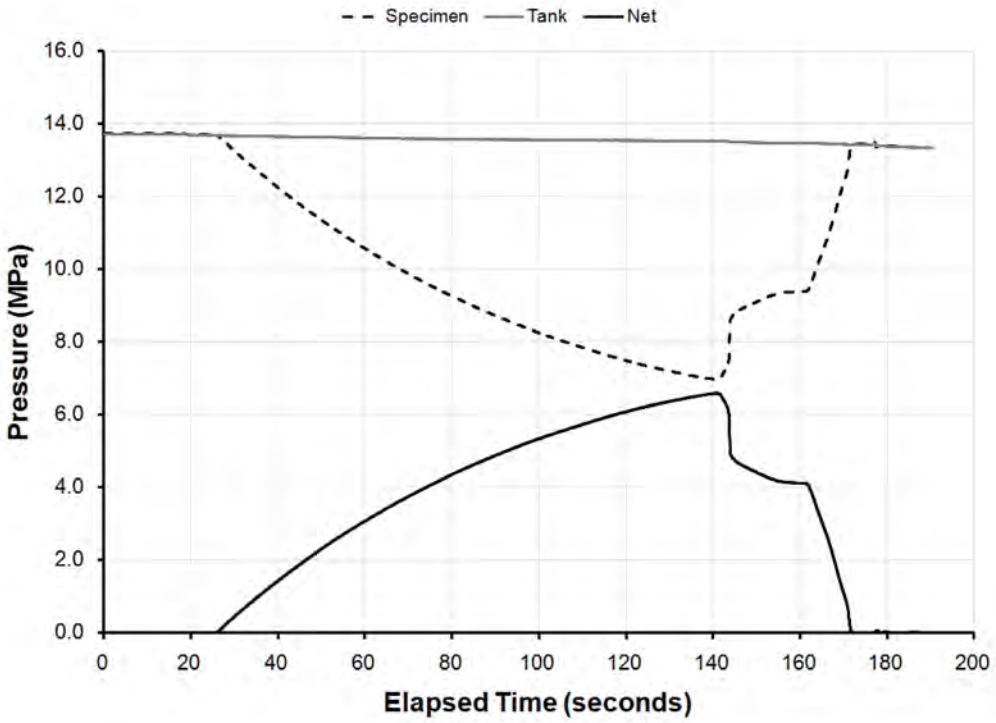

Figure 174: Tank, specimen and net pressures measured during volume-control collapse testing of specimen L510-No35 plotted against the time (showing data reduced to 20 Hz).

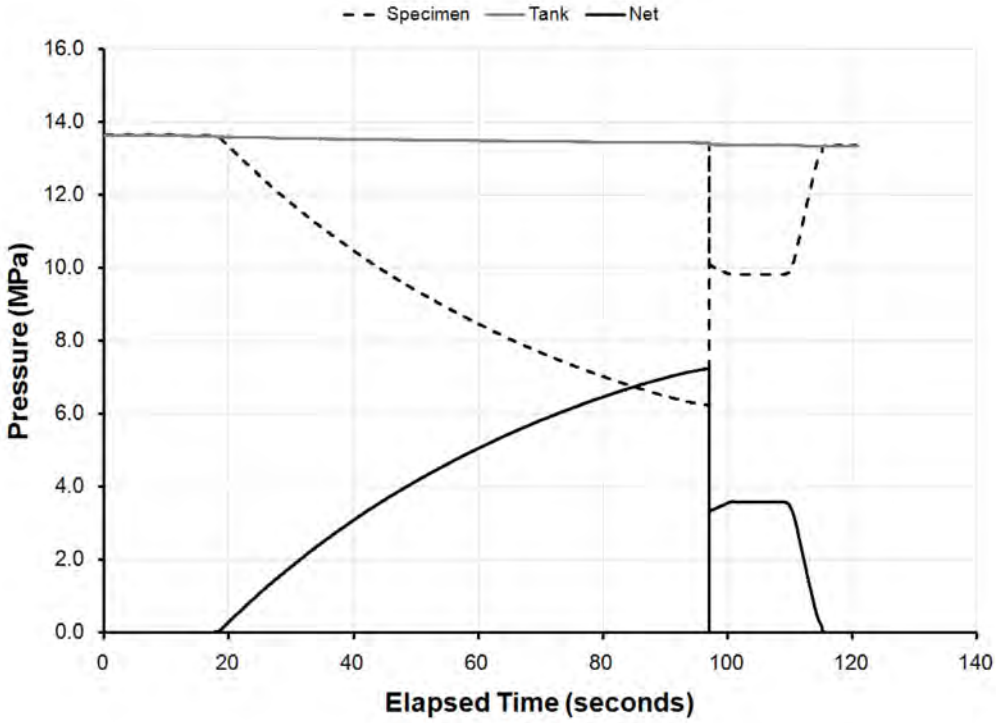

Figure 175: Tank, specimen and net pressures measured during volume-control collapse testing of specimen L510-No36 plotted against the time (showing data reduced to 20 Hz).

Annex G Summary of yield pressures

G.1 L510-No13

Table 140: Summary of yield pressures based on strain gauge measurements taken on the shell of specimen L510-No13 during collapse testing.

Location	**Angle (degrees)**	**Yield Pressure[a,b] (MPa)**
Bay No. 4, Inside Shell at Mid-bay	0	DID NOT YIELD
	9.8	7.476
	15	DID NOT YIELD
	345	DID NOT YIELD
	350.2	DID NOT YIELD
Outside At Stiffener No. 4	0	DID NOT YIELD
Bay No. 4, Outside Shell at Mid-bay	0	6.971
	7.5	6.988
	15	DID NOT YIELD
	30	1.642 *
	60	6.558
	90	1.642 *
	120	DID NOT YIELD
	150	DID NOT YIELD
	180	7.33
	210	DID NOT YIELD
	240	DID NOT YIELD
	270	DID NOT YIELD
	300	7.117
	330	DID NOT YIELD
	345	DID NOT YIELD
	352.5	6.983
Outside At Stiffener No. 5	0	DID NOT YIELD

a. The yield pressure is defined as the external pressure at which the reference stress derived from the strain gauge data first reaches the measured circumferential yield stress of the material. For gauges on the shell, the reference stress is the von Mises stress calculated assuming a plane stress state and neglecting in-plane shear stresses. Yield pressures are based on a 100Hz sampling rate for pressure and strain, and are accurate to within ±0.09 MPa. Residual stresses due to applying out-of-circularity are neglected.

b. An asterisk (*) indicates that yielding occurred after the peak pressure had been reached.

Table 141: Summary of yield pressures based on strain gauge measurements taken on the ring-stiffener flanges of specimen L510-No13 during collapse testing.

Location	**Angle (degrees)**	**Yield Pressure[a,b] (MPa)**
Flange of Stiffener No. 4	0	DID NOT YIELD
	30	7.494 *
	60	7.494 *
	90	7.494 *
	120	DID NOT YIELD
	150	DID NOT YIELD
	180	DID NOT YIELD
	210	DID NOT YIELD
	240	DID NOT YIELD
	270	DID NOT YIELD
	300	DID NOT YIELD
	330	DID NOT YIELD
Flange of Stiffener No. 5	0	DID NOT YIELD
	30	7.494 *
	60	7.494 *
	90	7.494 *
	120	DID NOT YIELD
	150	DID NOT YIELD
	180	DID NOT YIELD
	210	DID NOT YIELD
	240	DID NOT YIELD
	270	DID NOT YIELD
	300	DID NOT YIELD
	330	DID NOT YIELD

a. The yield pressure is defined as the external pressure at which the reference stress derived from the strain gauge data first reaches the measured circumferential yield stress of the material. For gauges on ring-stiffener flanges, axial stresses are considered to be negligible so that the reference stress is equivalent to the uniaxial circumferential stress. Yield pressures are based on a 100Hz sampling rate for pressure and strain, and are accurate to within ±0.09 MPa. Residual stresses due to applying out-of-circularity are neglected.

b. An asterisk (*) indicates that yielding occurred after the peak pressure had been reached.

G.2 L510-No14

Table 142: Summary of yield pressures based on strain gauge measurements taken on the shell of specimen L510-No14 during collapse testing.

Location	**Angle (degrees)**	**Yield Pressure[a,b] (MPa)**
Bay No. 4, Inside Shell at Mid-bay	150	6.903 *
	155.2	6.886
	165	5.953
	174.8	6.912
	180	6.920 *
Outside At Stiffener No. 4	165	6.854 *
Bay No. 4, Outside Shell at Mid-bay	15	DID NOT YIELD
	45	DID NOT YIELD
	75	DID NOT YIELD
	105	DID NOT YIELD
	135	2.691 *
	150	6.923
	157.5	5.434
	165	6.926 *
	172.5	6.064
	180	6.910 *
	195	6.854 *
	225	DID NOT YIELD
	255	DID NOT YIELD
	285	DID NOT YIELD
	315	DID NOT YIELD
	345	DID NOT YIELD
Outside At Stiffener No. 5	165	6.854 *

a. The yield pressure is defined as the external pressure at which the reference stress derived from the strain gauge data first reaches the measured circumferential yield stress of the material. For gauges on the shell, the reference stress is the von Mises stress calculated assuming a plane stress state and neglecting in-plane shear stresses. Yield pressures are based on a 100Hz sampling rate for pressure and strain, and are accurate to within ±0.09 MPa. Residual stresses due to applying out-of-circularity are neglected.

b. An asterisk (*) indicates that yielding occurred after the peak pressure had been reached.

Table 143: Summary of yield pressures based on strain gauge measurements taken on the ring-stiffener flanges of specimen L510-No14 during collapse testing.

Location	**Angle (degrees)**	**Yield Pressure[a,b] (MPa)**
Flange of Stiffener No. 4	15	DID NOT YIELD
	45	DID NOT YIELD
	75	DID NOT YIELD
	105	DID NOT YIELD
	135	6.854 *
	165	6.854 *
	195	6.854 *
	225	DID NOT YIELD
	255	DID NOT YIELD
	285	DID NOT YIELD
	315	DID NOT YIELD
	345	DID NOT YIELD
Flange of Stiffener No. 5	15	DID NOT YIELD
	45	DID NOT YIELD
	75	DID NOT YIELD
	105	DID NOT YIELD
	135	6.854 *
	165	6.854 *
	195	6.854 *
	225	DID NOT YIELD
	255	DID NOT YIELD
	285	DID NOT YIELD
	315	DID NOT YIELD
	345	DID NOT YIELD

a. The yield pressure is defined as the external pressure at which the reference stress derived from the strain gauge data first reaches the measured circumferential yield stress of the material. For gauges on ring-stiffener flanges, axial stresses are considered to be negligible so that the reference stress is equivalent to the uniaxial circumferential stress. Yield pressures are based on a 100Hz sampling rate for pressure and strain, and are accurate to within ±0.09 MPa. Residual stresses due to applying out-of-circularity are neglected.

b. An asterisk (*) indicates that yielding occurred after the peak pressure had been reached.

G.3 L510-No17

Table 144: Summary of yield pressures based on strain gauge measurements taken on the shell of specimen L510-No17 during collapse testing.

Location	**Angle (degrees)**	**Yield Pressure[a,b] (MPa)**
Bay No. 4, Outside Shell at Mid-bay	20	7.351
	50	0.420 *
	80	DID NOT YIELD
	110	DID NOT YIELD
	140	7.806
	170	DID NOT YIELD
	200	DID NOT YIELD
	230	DID NOT YIELD
	260	7.52
	290	DID NOT YIELD
	320	DID NOT YIELD
	350	5.888 *
Bay No. 1, Outside Shell at Mid-bay	140	DID NOT YIELD
Outside At Stiffener No. 2	140	DID NOT YIELD
Bay No. 2, Outside Shell at Mid-bay	140	DID NOT YIELD
Outside At Stiffener No. 3	140	DID NOT YIELD
Bay No. 3, Outside Shell at Mid-bay	140	7.833
Outside At Stiffener No. 4	140	DID NOT YIELD
Outside At Stiffener No. 5	140	DID NOT YIELD
Bay No. 5, Outside Shell at Mid-bay	140	7.811
Outside At Stiffener No. 6	140	DID NOT YIELD
Bay No. 6, Outside Shell at Mid-bay	140	7.771
Outside At Stiffener No. 7	140	DID NOT YIELD
Bay No. 7, Outside Shell at Mid-bay	140	DID NOT YIELD

a. The yield pressure is defined as the external pressure at which the reference stress derived from the strain gauge data first reaches the measured circumferential yield stress of the material. For gauges on the shell, the reference stress is the von Mises stress calculated assuming a plane stress state and neglecting in-plane shear stresses. Yield pressures are based on a 100Hz sampling rate for pressure and strain, and are accurate to within ±0.09 MPa. Residual stresses due to applying out-of-circularity are neglected.

b. An asterisk (*) indicates that yielding occurred after the peak pressure had been reached.

Table 145: Summary of yield pressures based on strain gauge measurements taken on the ring-stiffener flanges of specimen L510-No17 during collapse testing.

Location	**Angle (degrees)**	**Yield Pressure[a,b] (MPa)**
Flange of Stiffener No. 4	20	7.809 *
	50	7.718
	80	DID NOT YIELD
	110	DID NOT YIELD
	140	DID NOT YIELD
	170	DID NOT YIELD
	200	7.83
	230	DID NOT YIELD
	260	DID NOT YIELD
	290	DID NOT YIELD
	320	7.818
	350	5.888 *
Flange of Stiffener No. 5	20	5.888 *
	50	5.888 *
	80	7.832 *
	110	DID NOT YIELD
	140	DID NOT YIELD
	170	DID NOT YIELD
	200	7.827
	230	DID NOT YIELD
	260	DID NOT YIELD
	290	DID NOT YIELD
	320	DID NOT YIELD
	350	7.809 *

a. The yield pressure is defined as the external pressure at which the reference stress derived from the strain gauge data first reaches the measured circumferential yield stress of the material. For gauges on ring-stiffener flanges, axial stresses are considered to be negligible so that the reference stress is equivalent to the uniaxial circumferential stress. Yield pressures are based on a 100Hz sampling rate for pressure and strain, and are accurate to within ±0.09 MPa. Residual stresses due to applying out-of-circularity are neglected.

b. An asterisk (*) indicates that yielding occurred after the peak pressure had been reached.

G.4 L510-No18

Table 146: Summary of yield pressures based on strain gauge measurements taken on the shell of specimen L510-No18 during collapse testing.

Location	**Angle (degrees)**	**Yield Pressure[a,b] (MPa)**
Bay No. 4, Outside Shell at Mid-bay	4.6	DID NOT YIELD
	34.6	DID NOT YIELD
	64.6	DID NOT YIELD
	94.6	DID NOT YIELD
	124.6	7.699 *
	154.6	DID NOT YIELD
	184.6	DID NOT YIELD
	214.6	-0.585 *
	244.6	7.606 *
	274.6	6.546 *
	304.6	DID NOT YIELD
	334.6	DID NOT YIELD
Bay No. 1, Outside Shell at Mid-bay	124.6	DID NOT YIELD
Outside At Stiffener No. 2	124.6	DID NOT YIELD
Bay No. 2, Outside Shell at Mid-bay	124.6	DID NOT YIELD
Outside At Stiffener No. 3	124.6	DID NOT YIELD
Bay No. 3, Outside Shell at Mid-bay	124.6	DID NOT YIELD
Outside At Stiffener No. 4	124.6	DID NOT YIELD
Outside At Stiffener No. 5	124.6	DID NOT YIELD
Bay No. 5, Outside Shell at Mid-bay	124.6	DID NOT YIELD
Outside At Stiffener No. 6	124.6	DID NOT YIELD
Bay No. 6, Outside Shell at Mid-bay	124.6	7.573
Outside At Stiffener No. 7	124.6	DID NOT YIELD
Bay No. 7, Outside Shell at Mid-bay	124.6	DID NOT YIELD

a. The yield pressure is defined as the external pressure at which the reference stress derived from the strain gauge data first reaches the measured circumferential yield stress of the material. For gauges on the shell, the reference stress is the von Mises stress calculated assuming a plane stress state and neglecting in-plane shear stresses. Yield pressures are based on a 100Hz sampling rate for pressure and strain, and are accurate to within ±0.09 MPa. Residual stresses due to applying out-of-circularity are neglected.

b. An asterisk (*) indicates that yielding occurred after the peak pressure had been reached.

Table 147: Summary of yield pressures based on strain gauge measurements taken on the ring-stiffener flanges of specimen L510-No18 during collapse testing.

Location	**Angle (degrees)**	**Yield Pressure[a,b] (MPa)**
Flange of Stiffener No. 4	4.6	DID NOT YIELD
	34.6	DID NOT YIELD
	64.6	DID NOT YIELD
	94.6	DID NOT YIELD
	124.6	DID NOT YIELD
	154.6	DID NOT YIELD
	184.6	7.503
	214.6	6.546 *
	244.6	6.546 *
	274.6	6.546 *
	304.6	7.511
	334.6	DID NOT YIELD
Flange of Stiffener No. 5	4.6	DID NOT YIELD
	34.6	DID NOT YIELD
	64.6	DID NOT YIELD
	94.6	DID NOT YIELD
	124.6	DID NOT YIELD
	154.6	DID NOT YIELD
	184.6	7.505
	214.6	6.546 *
	244.6	6.546 *
	274.6	6.546 *
	304.6	7.523
	334.6	DID NOT YIELD

a. The yield pressure is defined as the external pressure at which the reference stress derived from the strain gauge data first reaches the measured circumferential yield stress of the material. For gauges on ring-stiffener flanges, axial stresses are considered to be negligible so that the reference stress is equivalent to the uniaxial circumferential stress. Yield pressures are based on a 100Hz sampling rate for pressure and strain, and are accurate to within ±0.09 MPa. Residual stresses due to applying out-of-circularity are neglected.

b. An asterisk (*) indicates that yielding occurred after the peak pressure had been reached.

G.5 L510-No19

Table 148: Summary of yield pressures based on strain gauge measurements taken on the shell of specimen L510-No19 during collapse testing.

Location	**Angle (degrees)**	**Yield Pressure[a,b] (MPa)**
Bay No. 4, Inside Shell at Mid-bay	0	6.623 *
	15	6.623 *
	23.3	6.659
	30	4.383 *
	330	4.764 *
	336.7	DID NOT YIELD
	345	DID NOT YIELD
Outside Shell at Stiffener No. 4	0	6.623 *
	15	6.623 *
	345	DID NOT YIELD
Bay No. 4, Outside Shell at Mid-bay	0	6.671 *
	15	6.614
	30	4.764 *
	330	4.257 *
	345	6.623 *
Outside Shell at Stiffener No. 5	0	6.623 *
	15	6.623 *
	345	4.415 *

a. The yield pressure is defined as the external pressure at which the reference stress derived from the strain gauge data first reaches the measured circumferential yield stress of the material. For gauges on the shell, the reference stress is the von Mises stress calculated assuming a plane stress state and neglecting in-plane shear stresses. Yield pressures are based on a 100Hz sampling rate for pressure and strain, and are accurate to within ±0.09 MPa. Residual stresses due to applying out-of-circularity are neglected.

b. An asterisk (*) indicates that yielding occurred after the peak pressure had been reached.

Table 149: Summary of yield pressures based on strain gauge measurements taken on the ring-stiffener flanges of specimen L510-No19 during collapse testing.

Location	**Angle (degrees)**	**Yield Pressure[a,b] (MPa)**
Flange of Stiffener No. 4	0	6.623 *
	15	6.623 *
	30	6.623 *
	60	6.665 *
	90	DID NOT YIELD
	120	DID NOT YIELD
	150	DID NOT YIELD
	180	DID NOT YIELD
	210	DID NOT YIELD
	240	DID NOT YIELD
	270	DID NOT YIELD
	300	6.669 *
	330	6.623 *
	345	DID NOT YIELD
Flange of Stiffener No. 5	0	6.623 *
	15	6.623 *
	30	6.623 *
	60	DID NOT YIELD
	90	DID NOT YIELD
	120	DID NOT YIELD
	150	DID NOT YIELD
	180	DID NOT YIELD
	210	DID NOT YIELD
	240	DID NOT YIELD
	270	DID NOT YIELD
	300	DID NOT YIELD
	330	6.623 *
	345	4.291 *

a. The yield pressure is defined as the external pressure at which the reference stress derived from the strain gauge data first reaches the measured circumferential yield stress of the material. For gauges on ring-stiffener flanges, axial stresses are considered to be negligible so that the reference stress is equivalent to the uniaxial circumferential stress. Yield pressures are based on a 100Hz sampling rate for pressure and strain, and are accurate to within ±0.09 MPa. Residual stresses due to applying out-of-circularity are neglected.

b. An asterisk (*) indicates that yielding occurred after the peak pressure had been reached.

G.6 L510-No20

Table 150: Summary of yield pressures based on strain gauge measurements taken on the shell of specimen L510-No20 during collapse testing.

Location	**Angle (degrees)**	**Yield Pressure[a,b] (MPa)**
Bay No. 4, Inside Shell at Mid-bay	153.5	1.171 *
	160.2	DID NOT YIELD
	168.5	6.896
	183.5	6.922 *
	198.5	6.918
	206.8	DID NOT YIELD
	213.5	1.171 *
Outside Shell at Stiffener No. 4	168.5	1.171 *
	183.5	6.930 *
	198.5	6.856 *
Bay No. 4, Outside Shell at Mid-bay	153.5	6.856 *
	168.5	1.171 *
	183.5	6.214
	198.5	DID NOT YIELD
	213.5	1.171 *
Outside Shell at Stiffener No. 5	168.5	1.171 *
	183.5	6.930 *
	198.5	6.856 *

a. The yield pressure is defined as the external pressure at which the reference stress derived from the strain gauge data first reaches the measured circumferential yield stress of the material. For gauges on the shell, the reference stress is the von Mises stress calculated assuming a plane stress state and neglecting in-plane shear stresses. Yield pressures are based on a 100Hz sampling rate for pressure and strain, and are accurate to within ±0.09 MPa. Residual stresses due to applying out-of-circularity are neglected.

b. An asterisk (*) indicates that yielding occurred after the peak pressure had been reached.

Table 151: Summary of yield pressures based on strain gauge measurements taken on the ring-stiffener flanges of specimen L510-No20 during collapse testing.

Location	**Angle (degrees)**	**Yield Pressure[a,b] (MPa)**
Flange of Stiffener No. 4	3.5	DID NOT YIELD
	33.5	DID NOT YIELD
	63.5	DID NOT YIELD
	93.5	DID NOT YIELD
	123.5	DID NOT YIELD
	153.5	6.856 *
	168.5	DID NOT YIELD
	183.5	6.856 *
	198.5	DID NOT YIELD
	213.5	6.856 *
	243.5	DID NOT YIELD
	273.5	DID NOT YIELD
	303.5	DID NOT YIELD
	333.5	DID NOT YIELD
Flange of Stiffener No. 5	3.5	DID NOT YIELD
	33.5	DID NOT YIELD
	63.5	DID NOT YIELD
	93.5	DID NOT YIELD
	123.5	6.931 *
	153.5	6.856 *
	168.5	3.633 *
	183.5	6.856 *
	198.5	DID NOT YIELD
	213.5	6.856 *
	243.5	DID NOT YIELD
	273.5	DID NOT YIELD
	303.5	DID NOT YIELD
	333.5	DID NOT YIELD

a. The yield pressure is defined as the external pressure at which the reference stress derived from the strain gauge data first reaches the measured circumferential yield stress of the material. For gauges on ring-stiffener flanges, axial stresses are considered to be negligible so that the reference stress is equivalent to the uniaxial circumferential stress. Yield pressures are based on a 100Hz sampling rate for pressure and strain, and are accurate to within ±0.09 MPa. Residual stresses due to applying out-of-circularity are neglected.

b. An asterisk (*) indicates that yielding occurred after the peak pressure had been reached.

G.7 L510-No25

Table 152: Summary of yield pressures based on strain gauge measurements taken on the shell of specimen L510-No25 during collapse testing.

Location	**Angle (degrees)**	**Yield Pressure[a,b] (MPa)**
Bay No. 4, Outside Shell at Mid-bay	20	6.762
	50	1.588 *
	80	DID NOT YIELD
	110	DID NOT YIELD
	140	7.052
	170	DID NOT YIELD
	200	DID NOT YIELD
	230	DID NOT YIELD
	260	6.878
	290	DID NOT YIELD
	320	DID NOT YIELD
	350	5.274 *
Bay No. 1, Outside Shell at Mid-bay	260	DID NOT YIELD
Outside At Stiffener No. 2	260	DID NOT YIELD
Bay No. 2, Outside Shell at Mid-bay	260	7.119 *
Outside At Stiffener No. 3	260	DID NOT YIELD
Bay No. 3, Outside Shell at Mid-bay	260	DID NOT YIELD
Outside At Stiffener No. 4	260	DID NOT YIELD
Outside At Stiffener No. 5	260	DID NOT YIELD
Bay No. 5, Outside Shell at Mid-bay	260	6.987
Outside At Stiffener No. 6	260	DID NOT YIELD
Bay No. 6, Outside Shell at Mid-bay	260	DID NOT YIELD
Outside At Stiffener No. 7	260	DID NOT YIELD
Bay No. 7, Outside Shell at Mid-bay	260	DID NOT YIELD

a. The yield pressure is defined as the external pressure at which the reference stress derived from the strain gauge data first reaches the measured circumferential yield stress of the material. For gauges on the shell, the reference stress is the von Mises stress calculated assuming a plane stress state and neglecting in-plane shear stresses. Yield pressures are based on a 100Hz sampling rate for pressure and strain, and are accurate to within ±0.09 MPa. Residual stresses due to applying out-of-circularity are neglected.

b. An asterisk (*) indicates that yielding occurred after the peak pressure had been reached.

Table 153: Summary of yield pressures based on strain gauge measurements taken on the ring-stiffener flanges of specimen L510-No25 during collapse testing.

Location	**Angle (degrees)**	**Yield Pressure[a,b] (MPa)**
Flange of Stiffener No. 4	20	7.071 *
	50	7.071 *
	80	6.569
	110	DID NOT YIELD
	140	DID NOT YIELD
	170	DID NOT YIELD
	200	6.836
	230	DID NOT YIELD
	260	DID NOT YIELD
	290	DID NOT YIELD
	320	6.826
	350	5.274 *
Flange of Stiffener No. 5	20	7.071 *
	50	7.071 *
	80	6.864
	110	DID NOT YIELD
	140	DID NOT YIELD
	170	DID NOT YIELD
	200	6.87
	230	DID NOT YIELD
	260	DID NOT YIELD
	290	DID NOT YIELD
	320	7.071 *
	350	5.274 *

a. The yield pressure is defined as the external pressure at which the reference stress derived from the strain gauge data first reaches the measured circumferential yield stress of the material. For gauges on ring-stiffener flanges, axial stresses are considered to be negligible so that the reference stress is equivalent to the uniaxial circumferential stress. Yield pressures are based on a 100Hz sampling rate for pressure and strain, and are accurate to within ±0.09 MPa. Residual stresses due to applying out-of-circularity are neglected.

b. An asterisk (*) indicates that yielding occurred after the peak pressure had been reached.

G.8 L510-No26

Table 154: Summary of yield pressures based on strain gauge measurements taken on the shell of specimen L510-No26 during collapse testing.

Location	**Angle (degrees)**	**Yield Pressure[a,b] (MPa)**
Bay No. 4, Outside Shell at Mid-bay	20	6.779
	50	DID NOT YIELD
	80	DID NOT YIELD
	110	6.948 *
	140	6.948 *
	170	DID NOT YIELD
	200	DID NOT YIELD
	230	DID NOT YIELD
	260	6.772
	290	DID NOT YIELD
	320	DID NOT YIELD
	350	DID NOT YIELD
Bay No. 1, Outside Shell at Mid-bay	260	DID NOT YIELD
Outside At Stiffener No. 2	260	DID NOT YIELD
Bay No. 2, Outside Shell at Mid-bay	260	DID NOT YIELD
Outside At Stiffener No. 3	260	DID NOT YIELD
Bay No. 3, Outside Shell at Mid-bay	260	6.546
Outside At Stiffener No. 4	260	DID NOT YIELD
Outside At Stiffener No. 5	260	DID NOT YIELD
Bay No. 5, Outside Shell at Mid-bay	260	6.899
Outside At Stiffener No. 6	260	DID NOT YIELD
Bay No. 6, Outside Shell at Mid-bay	260	DID NOT YIELD
Outside At Stiffener No. 7	260	DID NOT YIELD
Bay No. 7, Outside Shell at Mid-bay	260	DID NOT YIELD

a. The yield pressure is defined as the external pressure at which the reference stress derived from the strain gauge data first reaches the measured circumferential yield stress of the material. For gauges on the shell, the reference stress is the von Mises stress calculated assuming a plane stress state and neglecting in-plane shear stresses. Yield pressures are based on a 100Hz sampling rate for pressure and strain, and are accurate to within ±0.09 MPa. Residual stresses due to applying out-of-circularity are neglected.

b. An asterisk (*) indicates that yielding occurred after the peak pressure had been reached.

Table 155: Summary of yield pressures based on strain gauge measurements taken on the ring-stiffener flanges of specimen L510-No26 during collapse testing.

Location	**Angle (degrees)**	**Yield Pressure[a,b] (MPa)**
Flange of Stiffener No. 4	20	DID NOT YIELD
	50	DID NOT YIELD
	80	6.598
	110	DID NOT YIELD
	140	2.038 *
	170	7.017 *
	200	6.791
	230	DID NOT YIELD
	260	DID NOT YIELD
	290	6.788
	320	6.957
	350	DID NOT YIELD
Flange of Stiffener No. 5	20	DID NOT YIELD
	50	DID NOT YIELD
	80	6.311
	110	6.948 *
	140	DID NOT YIELD
	170	7.014 *
	200	6.598
	230	DID NOT YIELD
	260	DID NOT YIELD
	290	DID NOT YIELD
	320	6.799
	350	DID NOT YIELD

a. The yield pressure is defined as the external pressure at which the reference stress derived from the strain gauge data first reaches the measured circumferential yield stress of the material. For gauges on ring-stiffener flanges, axial stresses are considered to be negligible so that the reference stress is equivalent to the uniaxial circumferential stress. Yield pressures are based on a 100Hz sampling rate for pressure and strain, and are accurate to within ±0.09 MPa. Residual stresses due to applying out-of-circularity are neglected.

b. An asterisk (*) indicates that yielding occurred after the peak pressure had been reached.

G.9 L510-No33

Table 156: Summary of yield pressures based on strain gauge measurements taken on the shell of specimen L510-No33 during collapse testing.

Location	**Angle (degrees)**	**Yield Pressure[a,b] (MPa)**
Bay No. 4, Outside Shell at Mid-bay	6.4	DID NOT YIELD
	36.4	DID NOT YIELD
	66.4	DID NOT YIELD
	96.4	0.198 *
	126.4	1.898 *
	156.4	6.281 *
	186.4	DID NOT YIELD
	216.4	DID NOT YIELD
	246.4	DID NOT YIELD
	276.4	DID NOT YIELD
	306.4	DID NOT YIELD
	336.4	DID NOT YIELD
Bay No. 1, Outside Shell at Mid-bay	6.4	DID NOT YIELD
Outside At Stiffener No. 2	6.4	DID NOT YIELD
Bay No. 2, Outside Shell at Mid-bay	6.4	DID NOT YIELD
Outside At Stiffener No. 3	6.4	DID NOT YIELD
Bay No. 3, Outside Shell at Mid-bay	6.4	DID NOT YIELD
Outside At Stiffener No. 4	6.4	DID NOT YIELD
Outside At Stiffener No. 5	6.4	DID NOT YIELD
Bay No. 5, Outside Shell at Mid-bay	6.4	DID NOT YIELD
Outside At Stiffener No. 6	6.4	DID NOT YIELD
Bay No. 6, Outside Shell at Mid-bay	6.4	DID NOT YIELD
Outside At Stiffener No. 7	6.4	DID NOT YIELD
Bay No. 7, Outside Shell at Mid-bay	6.4	DID NOT YIELD

a. The yield pressure is defined as the external pressure at which the reference stress derived from the strain gauge data first reaches the measured circumferential yield stress of the material. For gauges on the shell, the reference stress is the von Mises stress calculated assuming a plane stress state and neglecting in-plane shear stresses. Yield pressures are based on a 100Hz sampling rate for pressure and strain, and are accurate to within ±0.09 MPa. Residual stresses due to applying out-of-circularity are neglected.

b. An asterisk (*) indicates that yielding occurred after the peak pressure had been reached.

Table 157: Summary of yield pressures based on strain gauge measurements taken on the ring-stiffener flanges of specimen L510-No33 during collapse testing.

Location	**Angle (degrees)**	**Yield Pressure[a,b] (MPa)**
Flange of Stiffener No. 4	6.4	DID NOT YIELD
	36.4	DID NOT YIELD
	66.4	6.982
	96.4	7.015 *
	126.4	6.281 *
	156.4	6.281 *
	186.4	6.845
	216.4	DID NOT YIELD
	246.4	DID NOT YIELD
	276.4	DID NOT YIELD
	306.4	6.936
	336.4	DID NOT YIELD
Flange of Stiffener No. 5	6.4	DID NOT YIELD
	36.4	DID NOT YIELD
	66.4	6.804
	96.4	6.281 *
	126.4	DID NOT YIELD
	156.4	6.281 *
	186.4	6.692
	216.4	DID NOT YIELD
	246.4	DID NOT YIELD
	276.4	DID NOT YIELD
	306.4	6.725
	336.4	DID NOT YIELD

a. The yield pressure is defined as the external pressure at which the reference stress derived from the strain gauge data first reaches the measured circumferential yield stress of the material. For gauges on ring-stiffener flanges, axial stresses are considered to be negligible so that the reference stress is equivalent to the uniaxial circumferential stress. Yield pressures are based on a 100Hz sampling rate for pressure and strain, and are accurate to within ±0.09 MPa. Residual stresses due to applying out-of-circularity are neglected.

b. An asterisk (*) indicates that yielding occurred after the peak pressure had been reached.

G.10 L510-No34

Table 158: Summary of yield pressures based on strain gauge measurements taken on the shell of specimen L510-No34 during collapse testing.

Location	**Angle (degrees)**	**Yield Pressure[a,b] (MPa)**
Bay No. 2, Outside Shell at Mid-bay	20.4	7.521
	50.4	DID NOT YIELD
	80.4	DID NOT YIELD
	110.4	DID NOT YIELD
	140.4	7.902
	170.4	DID NOT YIELD
	200.4	DID NOT YIELD
	230.4	8.013
	260.4	DID NOT YIELD
	290.4	DID NOT YIELD
	320.4	DID NOT YIELD
	350.4	DID NOT YIELD
Bay No. 1, Outside Shell at Mid-bay	320.4	DID NOT YIELD
Outside At Stiffener No. 2	320.4	DID NOT YIELD
Outside At Stiffener No. 3	320.4	DID NOT YIELD
Bay No. 3, Outside Shell at Mid-bay	320.4	DID NOT YIELD
Outside At Stiffener No. 4	320.4	DID NOT YIELD
Bay No. 4 Outside Shell at Mid-bay	320.4	DID NOT YIELD
Outside At Stiffener No. 5	320.4	DID NOT YIELD
Bay No. 5, Outside Shell at Mid-bay	320.4	7.917
Outside At Stiffener No. 6	320.4	DID NOT YIELD
Bay No. 6, Outside Shell at Mid-bay	320.4	7.857
Outside At Stiffener No. 7	320.4	DID NOT YIELD
Bay No. 7, Outside Shell at Mid-bay	320.4	DID NOT YIELD

a. The yield pressure is defined as the external pressure at which the reference stress derived from the strain gauge data first reaches the measured circumferential yield stress of the material. For gauges on the shell, the reference stress is the von Mises stress calculated assuming a plane stress state and neglecting in-plane shear stresses. Yield pressures are based on a 100Hz sampling rate for pressure and strain, and are accurate to within ±0.09 MPa. Residual stresses due to applying out-of-circularity are neglected.

b. An asterisk (*) indicates that yielding occurred after the peak pressure had been reached.

Table 159: Summary of yield pressures based on strain gauge measurements taken on the ring-stiffener flanges of specimen L510-No34 during collapse testing.

Location	**Angle (degrees)**	**Yield Pressure[a,b] (MPa)**
Flange of Stiffener No. 3	20.4	DID NOT YIELD
	50.4	DID NOT YIELD
	80.4	DID NOT YIELD
	110.4	DID NOT YIELD
	140.4	DID NOT YIELD
	170.4	DID NOT YIELD
	200.4	DID NOT YIELD
	230.4	DID NOT YIELD
	260.4	DID NOT YIELD
	290.4	DID NOT YIELD
	320.4	DID NOT YIELD
	350.4	DID NOT YIELD
Flange of Stiffener No. 6	20.4	7.980 *
	50.4	DID NOT YIELD
	80.4	2.146 *
	110.4	7.980 *
	140.4	DID NOT YIELD
	170.4	DID NOT YIELD
	200.4	DID NOT YIELD
	230.4	DID NOT YIELD
	260.4	DID NOT YIELD
	290.4	DID NOT YIELD
	320.4	DID NOT YIELD
	350.4	DID NOT YIELD

a. The yield pressure is defined as the external pressure at which the reference stress derived from the strain gauge data first reaches the measured circumferential yield stress of the material. For gauges on ring-stiffener flanges, axial stresses are considered to be negligible so that the reference stress is equivalent to the uniaxial circumferential stress. Yield pressures are based on a 100Hz sampling rate for pressure and strain, and are accurate to within ±0.09 MPa. Residual stresses due to applying out-of-circularity are neglected.

b. An asterisk (*) indicates that yielding occurred after the peak pressure had been reached.

G.11 L510-No35

Table 160: Summary of yield pressures based on strain gauge measurements taken on the shell of specimen L510-No35 during collapse testing.

Location	**Angle (degrees)**	**Yield Pressure[a,b] (MPa)**
Bay No. 4, Inside Shell at Mid-bay	0	6.133
	9.8	6.571 *
	15	6.534 *
	345	6.551
	350.2	6.518
Outside At Stiffener No. 4	0	6.542 *
Bay No. 4, Outside Shell at Mid-bay	0	6.344
	7.5	5.793
	15	6.238 *
	30	4.870 *
	60	DID NOT YIELD
	90	DID NOT YIELD
	120	DID NOT YIELD
	150	DID NOT YIELD
	180	DID NOT YIELD
	210	DID NOT YIELD
	240	DID NOT YIELD
	270	DID NOT YIELD
	300	DID NOT YIELD
	330	5.595 *
	345	6.567
	352.5	5.184
Outside At Stiffener No. 5	0	6.564 *

a. The yield pressure is defined as the external pressure at which the reference stress derived from the strain gauge data first reaches the measured circumferential yield stress of the material. For gauges on the shell, the reference stress is the von Mises stress calculated assuming a plane stress state and neglecting in-plane shear stresses. Yield pressures are based on a 100Hz sampling rate for pressure and strain, and are accurate to within ±0.09 MPa. Residual stresses due to applying out-of-circularity are neglected.

b. An asterisk (*) indicates that yielding occurred after the peak pressure had been reached.

Table 161: Summary of yield pressures based on strain gauge measurements taken on the ring-stiffener flanges of specimen L510-No35 during collapse testing.

Location	**Angle (degrees)**	**Yield Pressure[a,b] (MPa)**
Flange of Stiffener No. 4	0	6.222 *
	30	6.475 *
	60	DID NOT YIELD
	90	DID NOT YIELD
	120	DID NOT YIELD
	150	DID NOT YIELD
	180	DID NOT YIELD
	210	DID NOT YIELD
	240	DID NOT YIELD
	270	DID NOT YIELD
	300	DID NOT YIELD
	330	6.265 *
Flange of Stiffener No. 5	0	6.321 *
	30	6.531 *
	60	DID NOT YIELD
	90	DID NOT YIELD
	120	DID NOT YIELD
	150	DID NOT YIELD
	180	DID NOT YIELD
	210	DID NOT YIELD
	240	DID NOT YIELD
	270	DID NOT YIELD
	300	6.540 *
	330	6.079 *

a. The yield pressure is defined as the external pressure at which the reference stress derived from the strain gauge data first reaches the measured circumferential yield stress of the material. For gauges on ring-stiffener flanges, axial stresses are considered to be negligible so that the reference stress is equivalent to the uniaxial circumferential stress. Yield pressures are based on a 100Hz sampling rate for pressure and strain, and are accurate to within ±0.09 MPa. Residual stresses due to applying out-of-circularity are neglected.

b. An asterisk (*) indicates that yielding occurred after the peak pressure had been reached.

G.12 L510-No36

Table 162: Summary of yield pressures based on strain gauge measurements taken on the shell of specimen L510-No36 during collapse testing.

Location	**Angle (degrees)**	**Yield Pressure[a,b] (MPa)**
Bay No. 4, Inside Shell at Mid-bay	0	DID NOT YIELD
	9.8	DID NOT YIELD
	15	DID NOT YIELD
	345	DID NOT YIELD
	350.2	DID NOT YIELD
Outside At Stiffener No. 4	0	DID NOT YIELD
Bay No. 4, Outside Shell at Mid-bay	0	DID NOT YIELD
	7.5	6.927
	15	DID NOT YIELD
	30	DID NOT YIELD
	60	DID NOT YIELD
	90	DID NOT YIELD
	120	DID NOT YIELD
	150	DID NOT YIELD
	180	7.169
	210	DID NOT YIELD
	240	DID NOT YIELD
	270	DID NOT YIELD
	300	6.848
	330	DID NOT YIELD
	345	DID NOT YIELD
	352.5	DID NOT YIELD
Outside At Stiffener No. 5	0	DID NOT YIELD

a. The yield pressure is defined as the external pressure at which the reference stress derived from the strain gauge data first reaches the measured circumferential yield stress of the material. For gauges on the shell, the reference stress is the von Mises stress calculated assuming a plane stress state and neglecting in-plane shear stresses. Yield pressures are based on a 100Hz sampling rate for pressure and strain, and are accurate to within ±0.09 MPa. Residual stresses due to applying out-of-circularity are neglected.

b. An asterisk (*) indicates that yielding occurred after the peak pressure had been reached.

Table 163: Summary of yield pressures based on strain gauge measurements taken on the ring-stiffener flanges of specimen L510-No36 during collapse testing.

Location	**Angle (degrees)**	**Yield Pressure[a,b] (MPa)**
Flange of Stiffener No. 4	0	DID NOT YIELD
	30	DID NOT YIELD
	60	DID NOT YIELD
	90	DID NOT YIELD
	120	6.92
	150	DID NOT YIELD
	180	DID NOT YIELD
	210	DID NOT YIELD
	240	6.893
	270	6.963 *
	300	6.963 *
	330	6.963 *
Flange of Stiffener No. 5	0	6.963 *
	30	DID NOT YIELD
	60	DID NOT YIELD
	90	DID NOT YIELD
	120	6.974
	150	DID NOT YIELD
	180	DID NOT YIELD
	210	DID NOT YIELD
	240	6.899
	270	DID NOT YIELD
	300	6.963 *
	330	DID NOT YIELD

a. The yield pressure is defined as the external pressure at which the reference stress derived from the strain gauge data first reaches the measured circumferential yield stress of the material. For gauges on ring-stiffener flanges, axial stresses are considered to be negligible so that the reference stress is equivalent to the uniaxial circumferential stress. Yield pressures are based on a 100Hz sampling rate for pressure and strain, and are accurate to within ±0.09 MPa. Residual stresses due to applying out-of-circularity are neglected.

b. An asterisk (*) indicates that yielding occurred after the peak pressure had been reached.

Annex H Pressure-strain plots

H.1 L510-No13

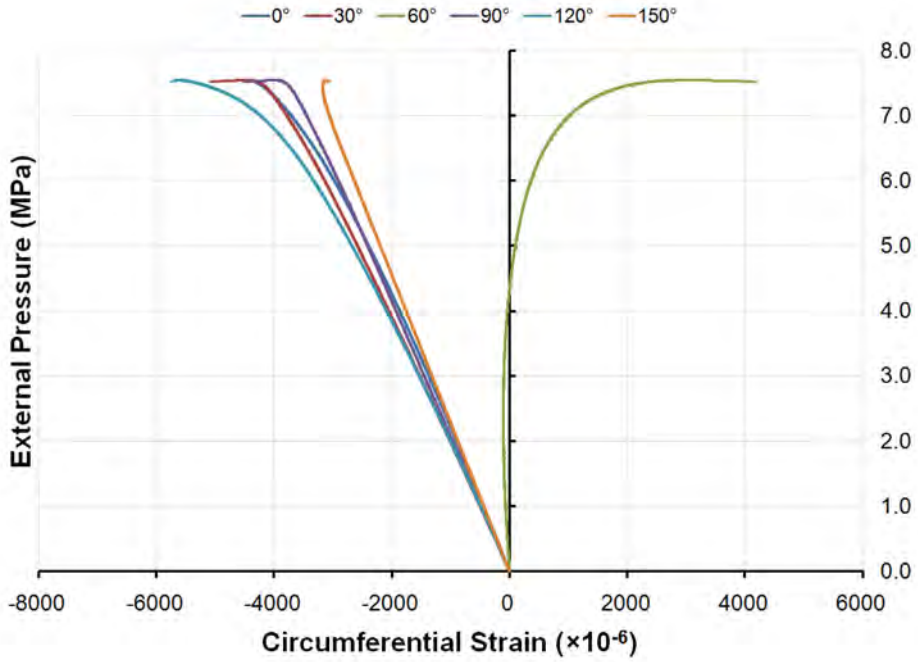

Figure 176: Pressure-strain curves showing circumferential strains at the flange of Frame 4 of specimen L510-No13 (0°-150°)

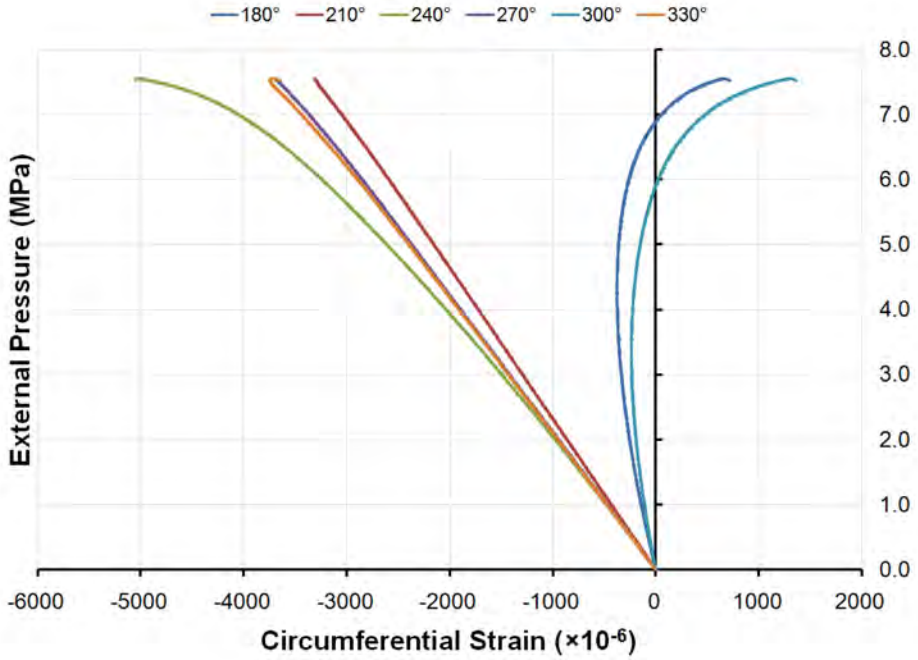

Figure 177: Pressure-strain curves showing circumferential strains at the flange of Frame 4 of specimen L510-No13 (180°-330°)

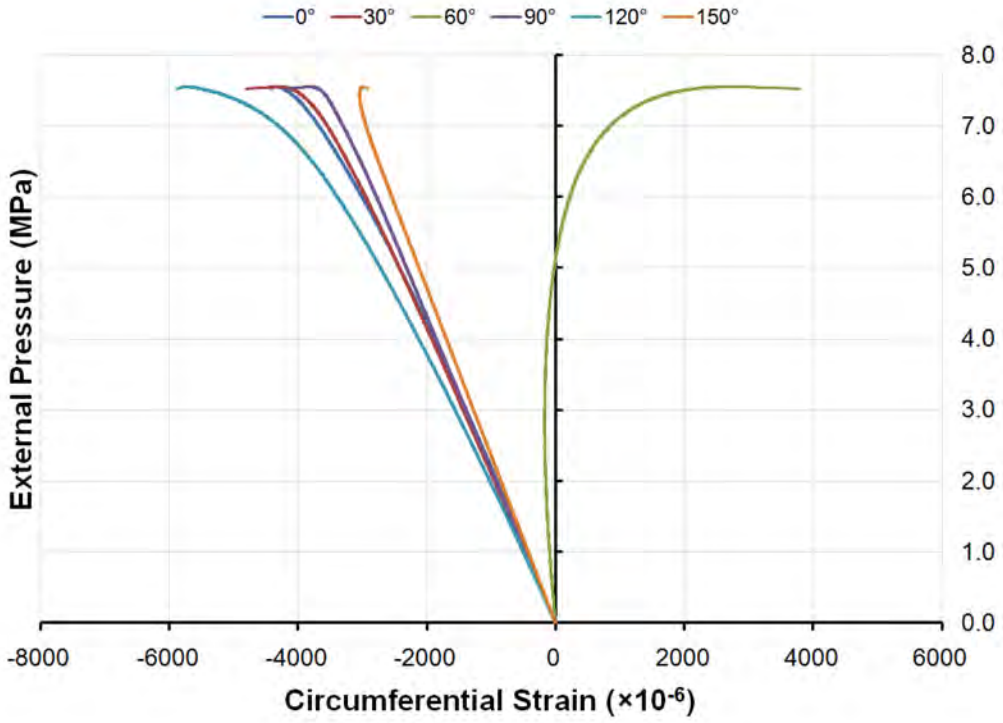

Figure 178: Pressure-strain curves showing circumferential strains at the flange of Frame 5 of specimen L510-No13 (0°-150°)

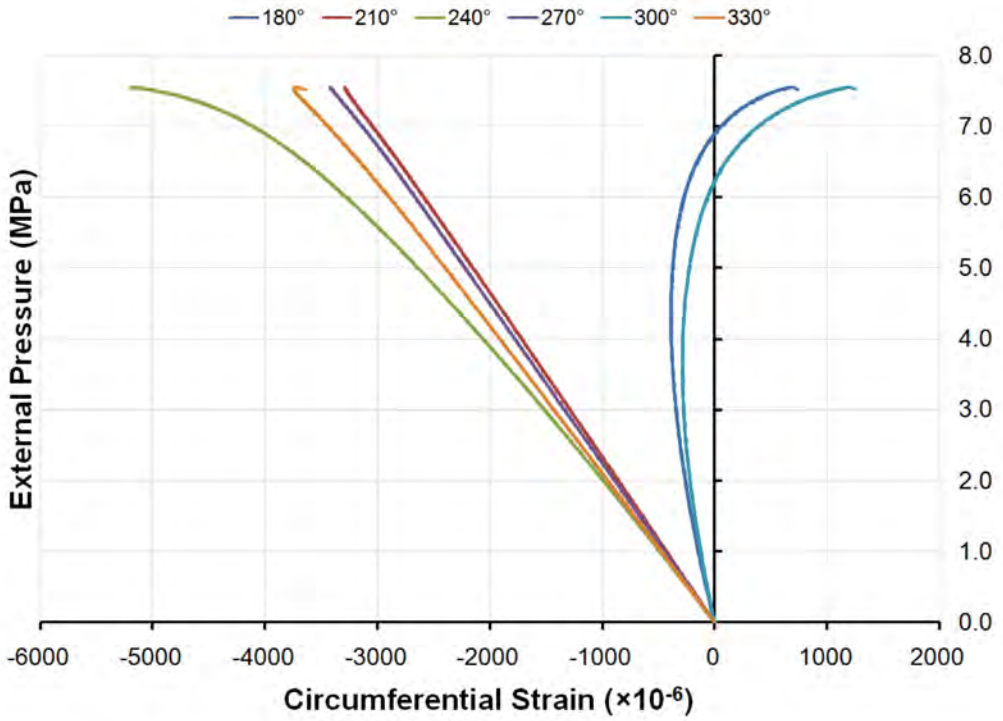

Figure 179: Pressure-strain curves showing circumferential strains at the flange of Frame 5 of specimen L510-No13 (180°-330°)

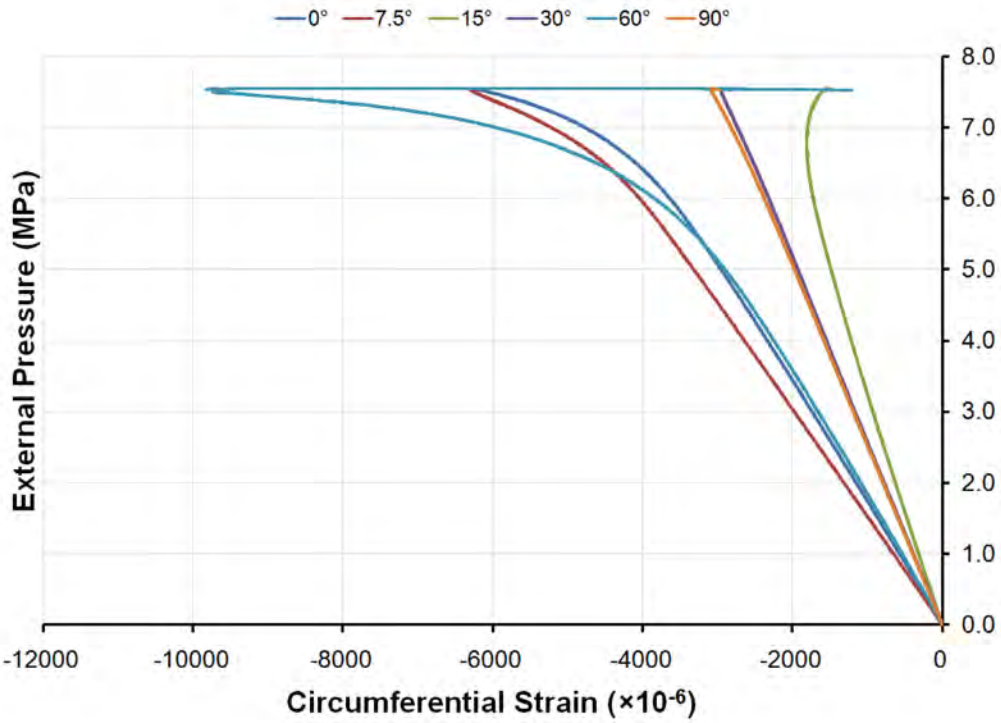

Figure 180: Pressure-strain curves showing circumferential shell strains mid-way between frames outside Bay 4 of specimen L510-No13 (0°-90°)

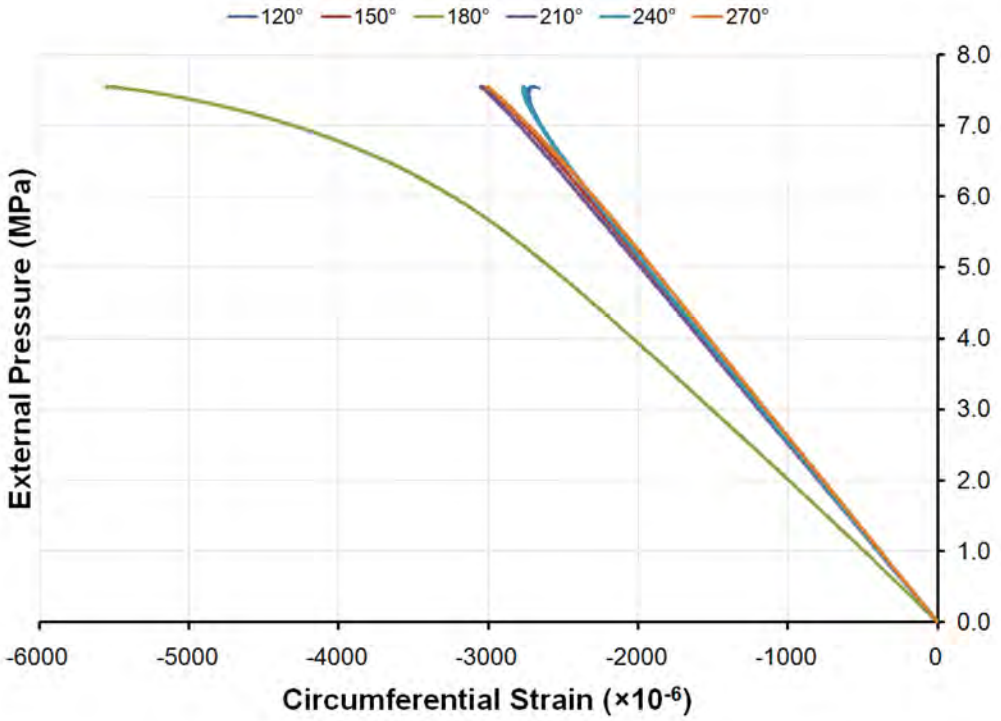

Figure 181: Pressure-strain curves showing circumferential shell strains mid-way between frames outside Bay 4 of specimen L510-No13 (120°-270°)

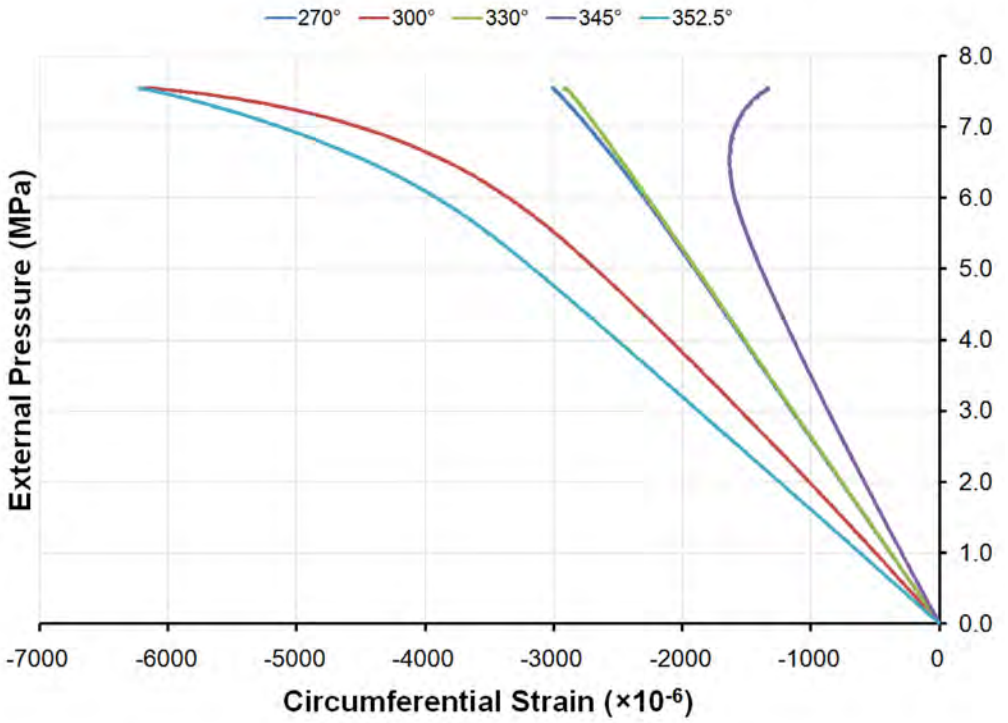

Figure 182: Pressure-strain curves showing circumferential shell strains mid-way between frames outside Bay 4 of specimen L510-No13 (270°-352.5°)

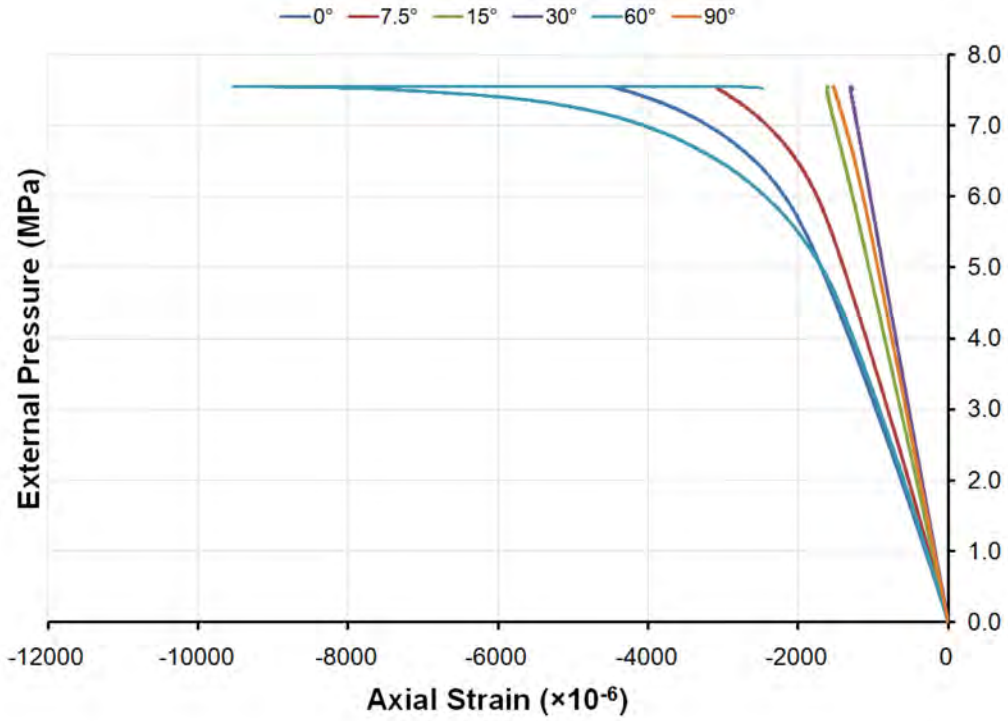

Figure 183: Pressure-strain curves showing axial shell strains mid-way between frames outside Bay 4 of specimen L510-No13 (0°-90°)

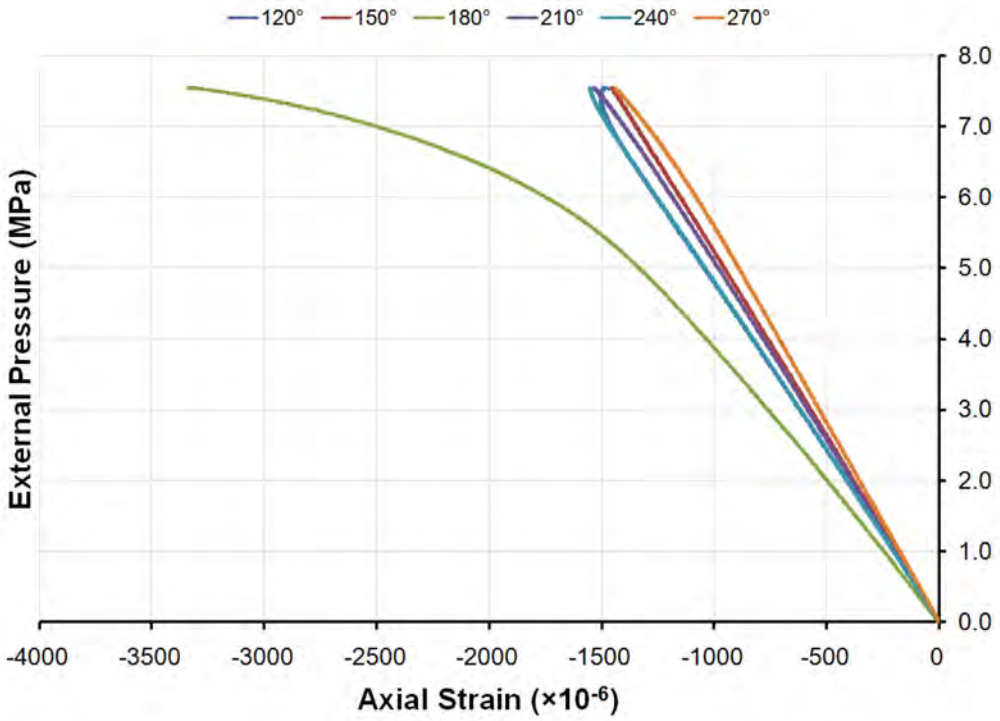

Figure 184: Pressure-strain curves showing axial shell strains mid-way between frames outside Bay 4 of specimen L510-No13 (120°-270°)

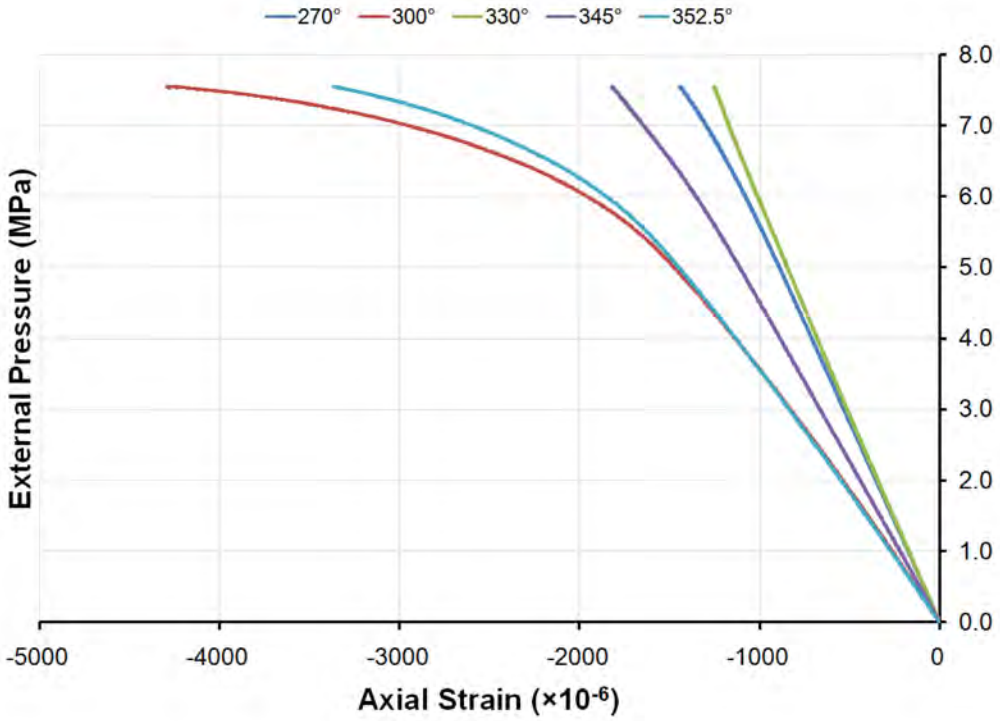

Figure 185: Pressure-strain curves showing axial shell strains mid-way between frames outside Bay 4 of specimen L510-No13 (270°-352.5°)

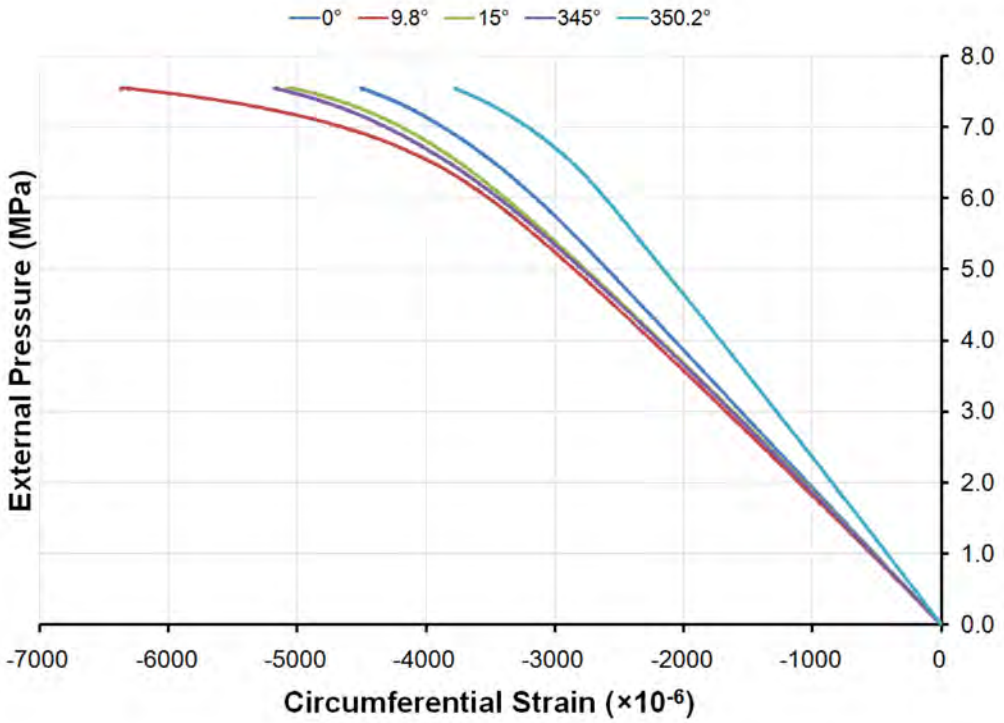

Figure 186: Pressure-strain curves showing circumferential shell strains mid-way between frames inside Bay 4 of specimen L510-No13

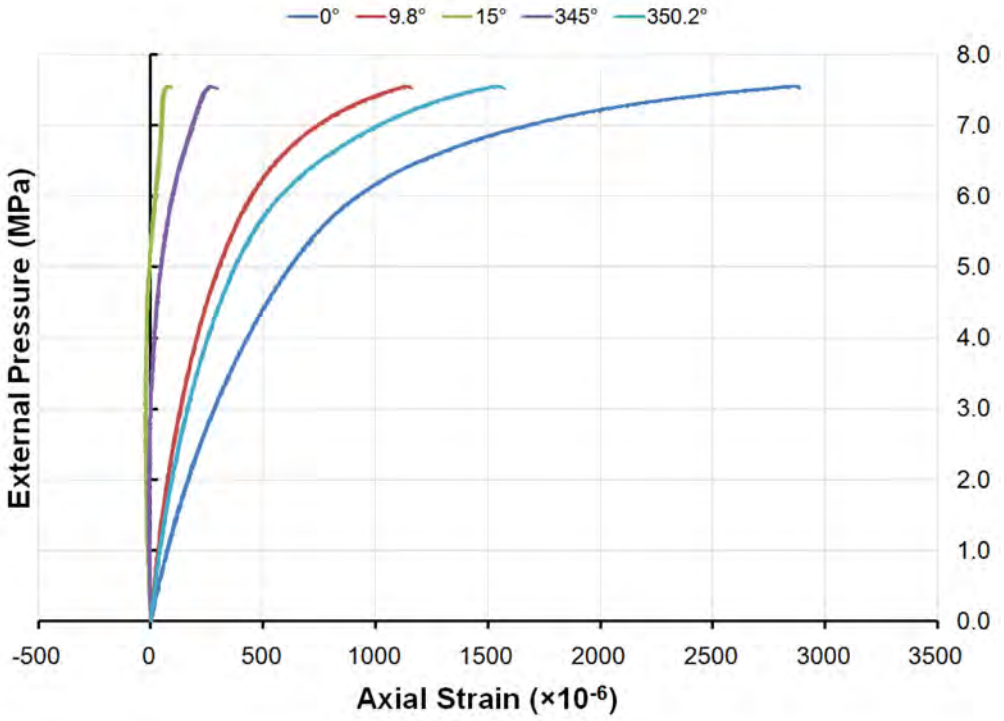

Figure 187: Pressure-strain curves showing axial shell strains mid-way between frames inside Bay 4 of specimen L510-No13

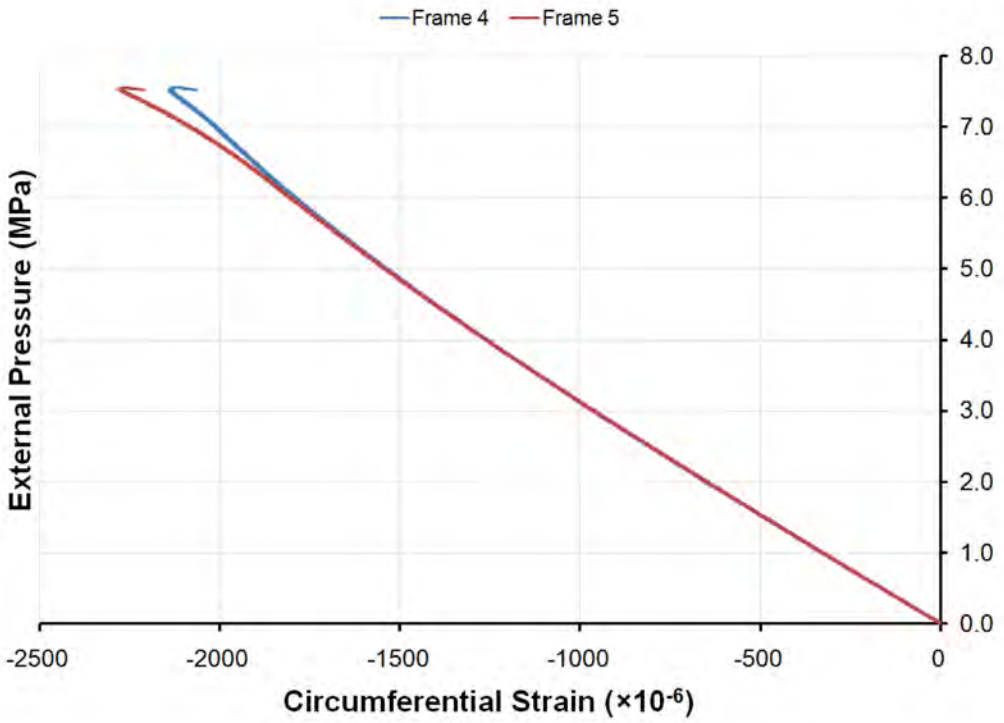

Figure 188: Pressure-strain curves showing circumferential shell strains outside Frames 4 and 5 of specimen L510-No13 at 0°

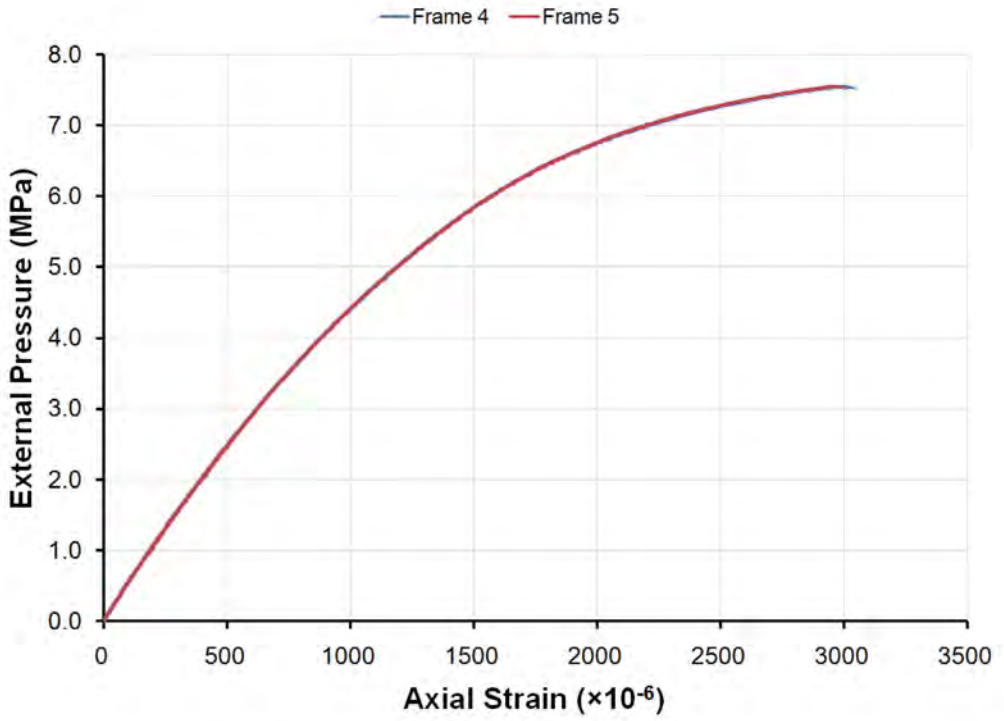

Figure 189: Pressure-strain curves showing axial shell strains outside Frames 4 and 5 of specimen L510-No13 at 0°

H.2 L510-No14

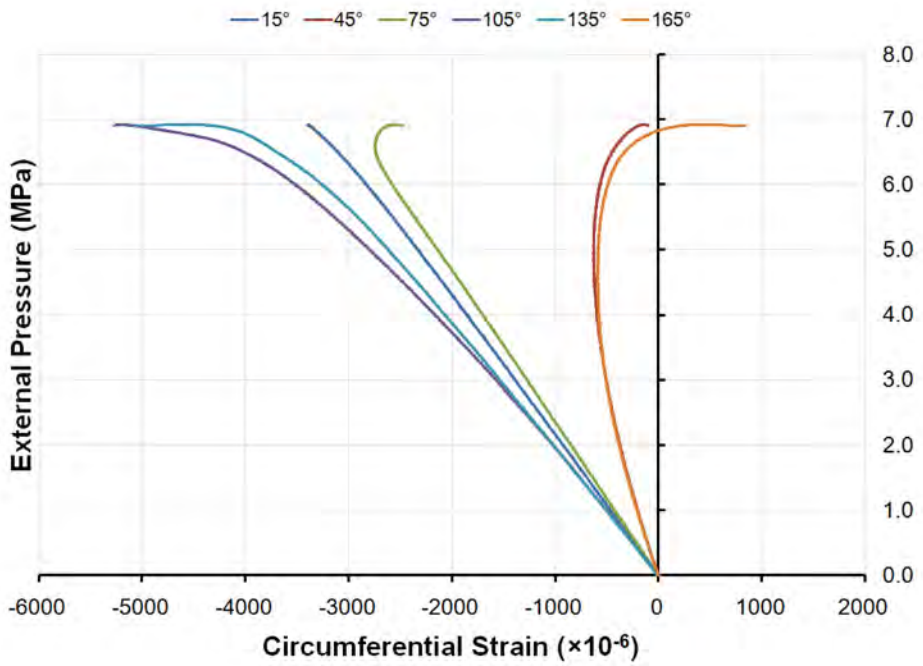

Figure 190: Pressure-strain curves showing circumferential strains at the flange of Frame 4 of specimen L510-No14 (15°-165°)

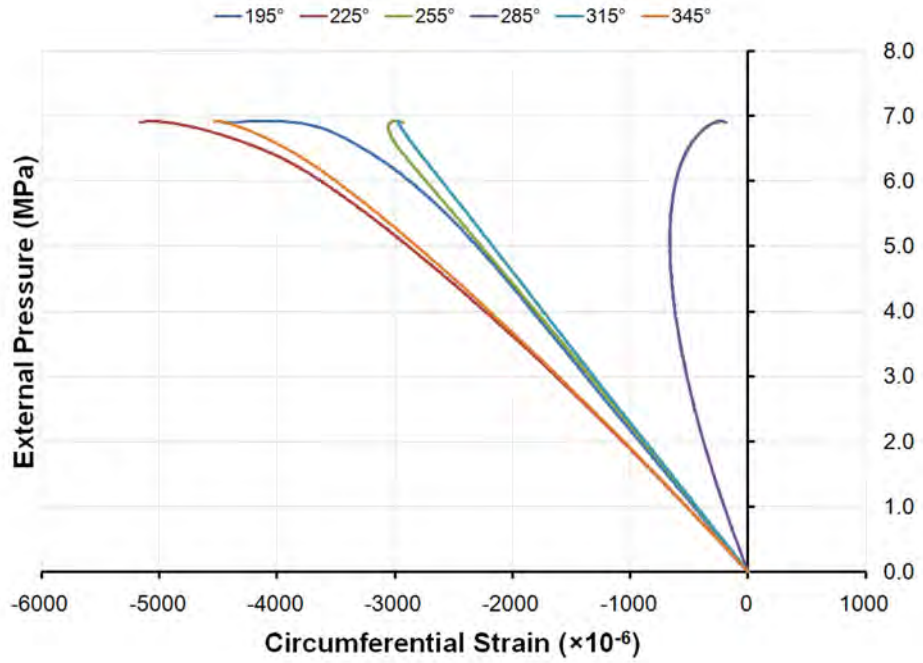

Figure 191: Pressure-strain curves showing circumferential strains at the flange of Frame 4 of specimen L510-No14 (195°-345°)

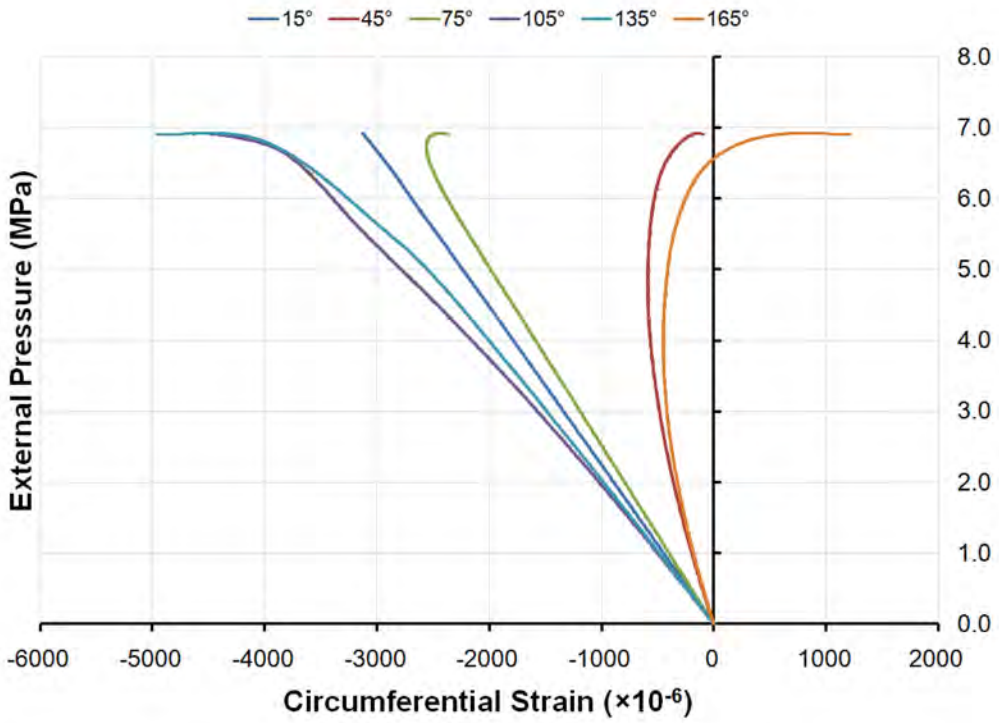

Figure 192: Pressure-strain curves showing circumferential strains at the flange of Frame 5 of specimen L510-No14 (15°-165°)

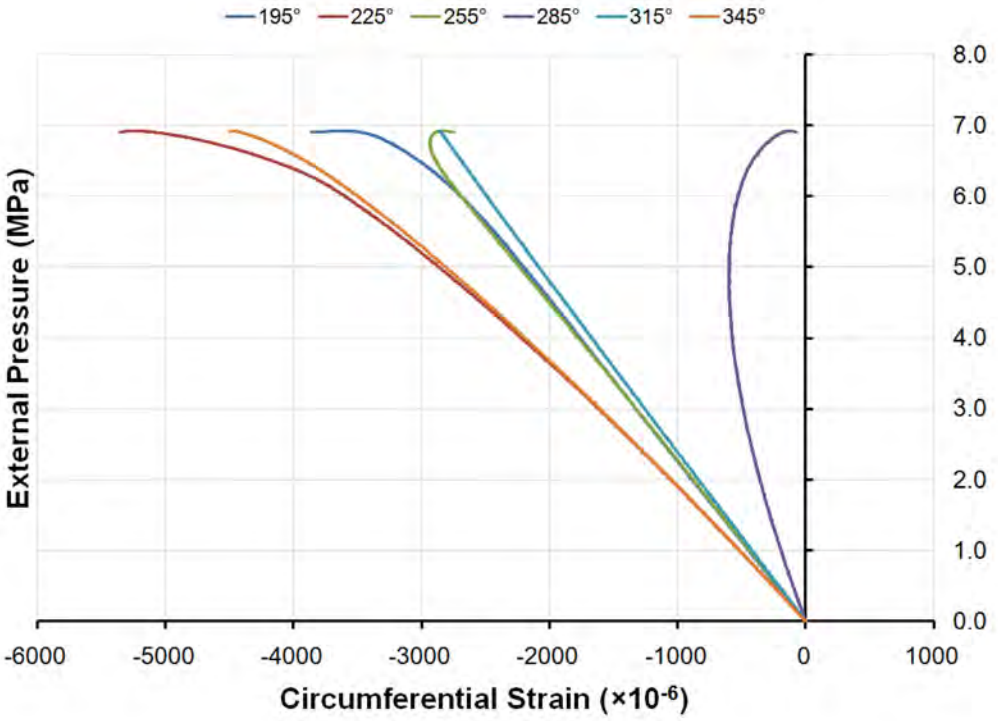

Figure 193: Pressure-strain curves showing circumferential strains at the flange of Frame 5 of specimen L510-No14 (195°-345°)

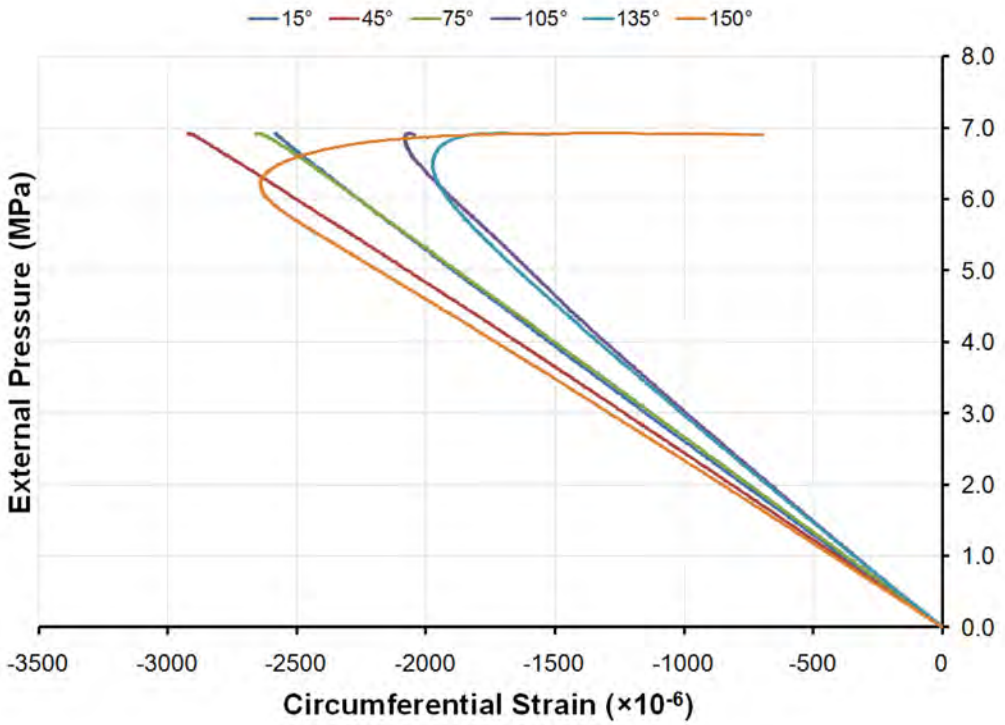

Figure 194: Pressure-strain curves showing circumferential shell strains mid-way between frames outside Bay 4 of specimen L510-No14 (15°-150°)

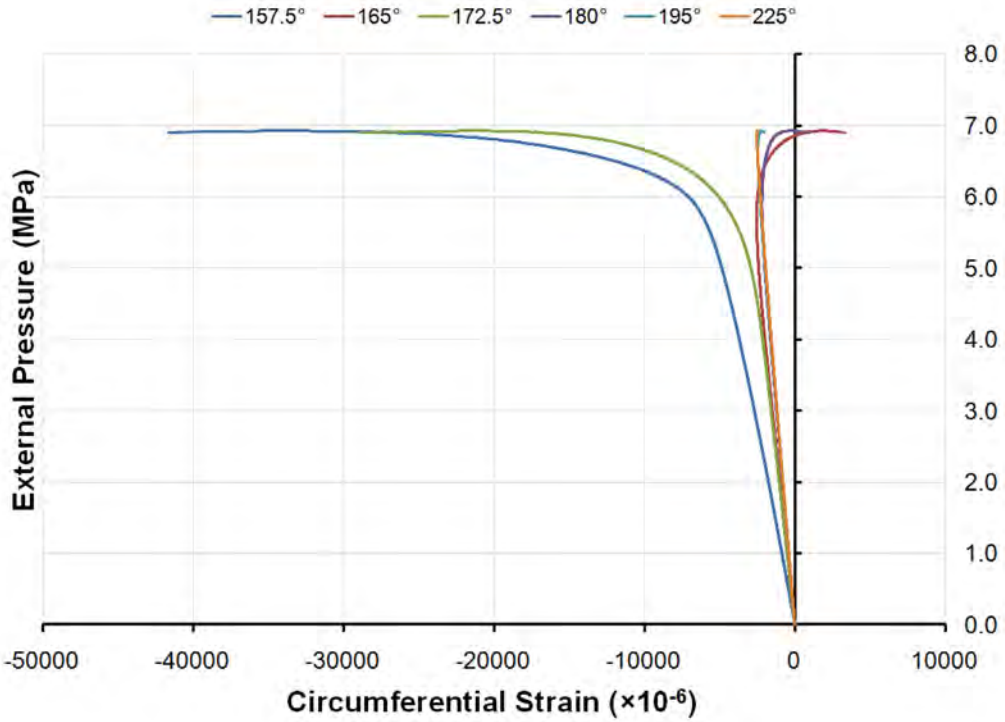

Figure 195: Pressure-strain curves showing circumferential shell strains mid-way between frames outside Bay 4 of specimen L510-No14 (157.5°-225°)

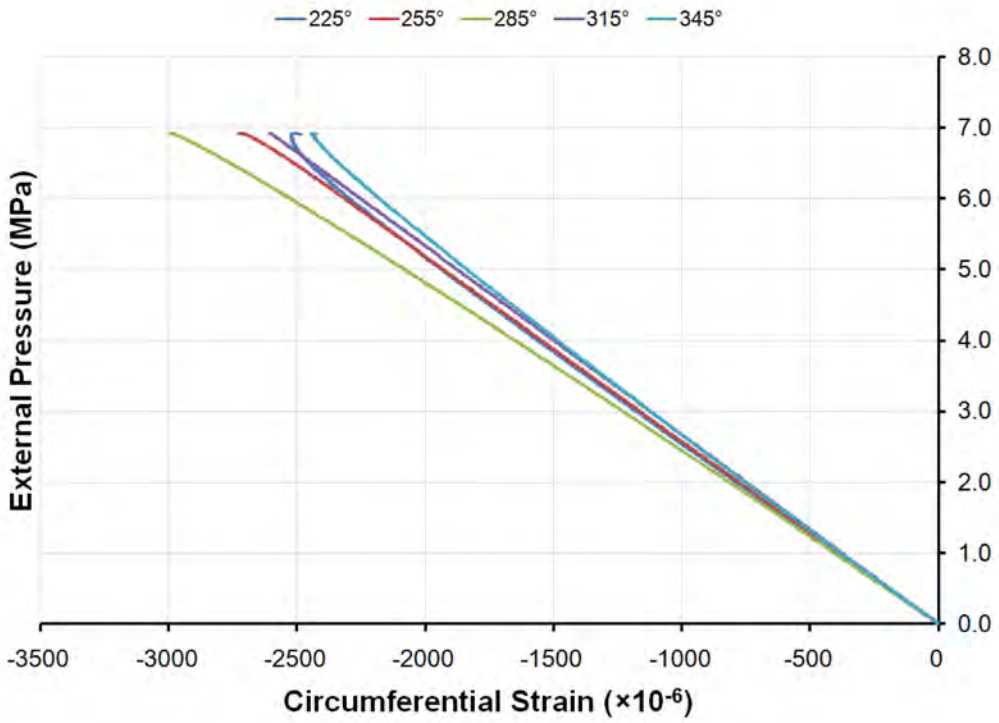

Figure 196: Pressure-strain curves showing circumferential shell strains mid-way between frames outside Bay 4 of specimen L510-No14 (225°-345°)

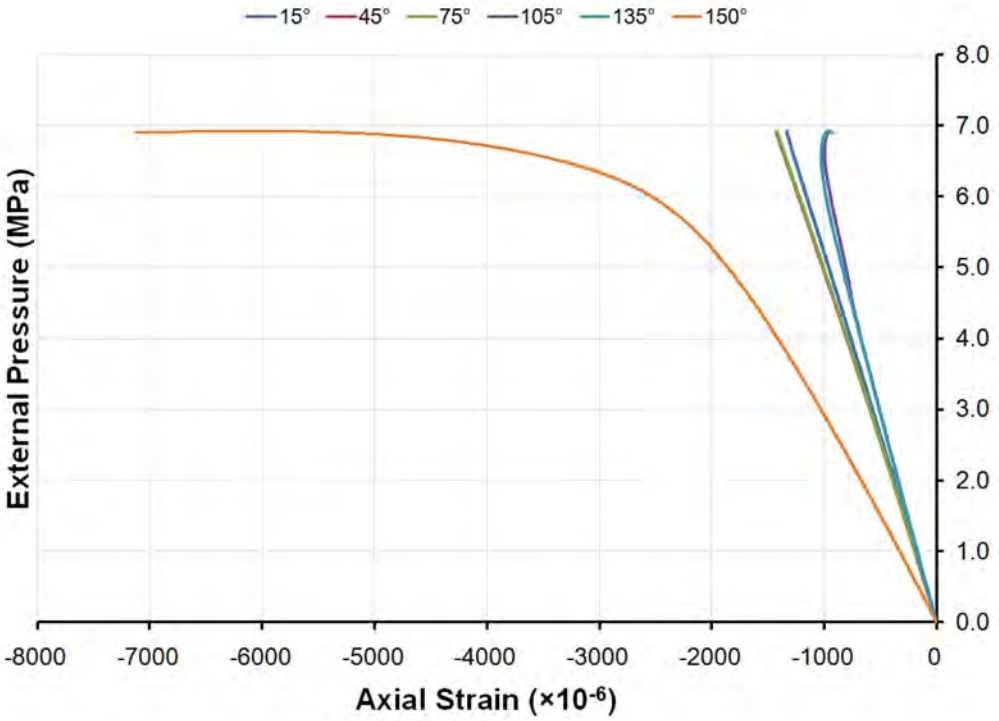

Figure 197: Pressure-strain curves showing axial shell strains mid-way between frames outside Bay 4 of specimen L510-No14 (15°-150°)

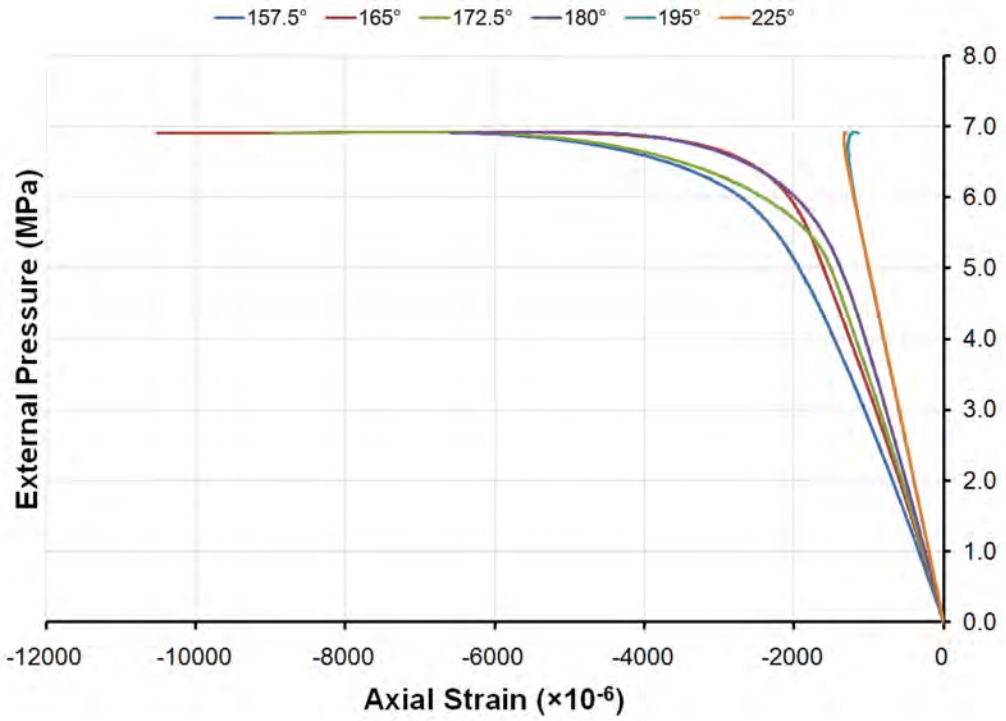

Figure 198: Pressure-strain curves showing axial shell strains mid-way between frames outside Bay 4 of specimen L510-No14 (157.5°-225°)

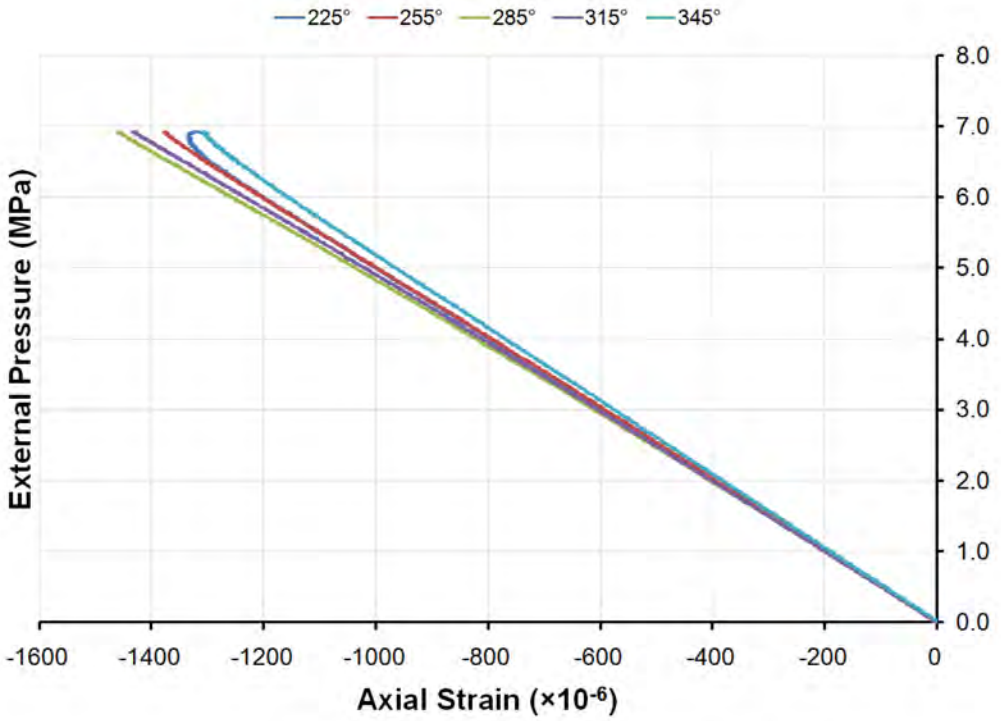

Figure 199: Pressure-strain curves showing axial shell strains mid-way between frames outside Bay 4 of specimen L510-No14 (225°-345°)

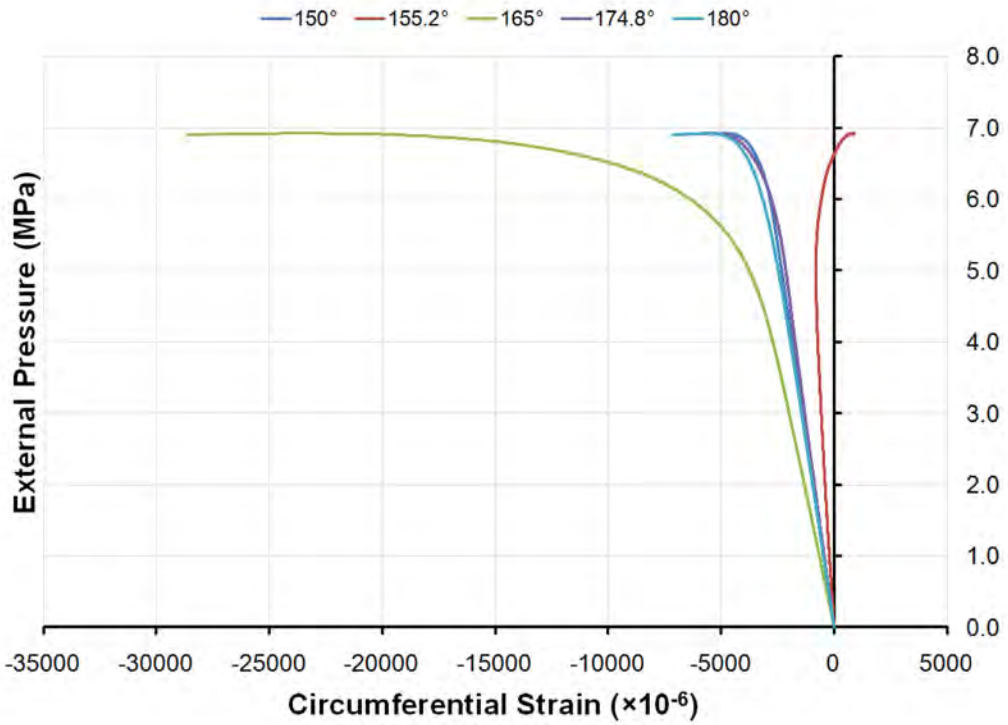

Figure 200: Pressure-strain curves showing circumferential shell strains mid-way between frames inside Bay 4 of specimen L510-No14

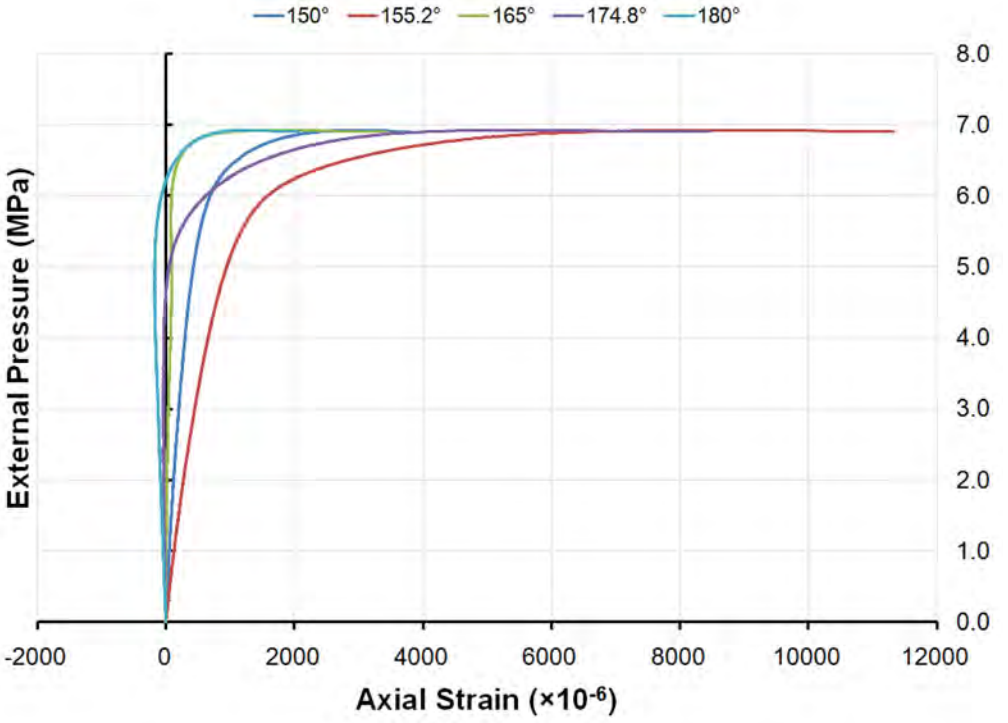

Figure 201: Pressure-strain curves showing axial shell strains mid-way between frames inside Bay 4 of specimen L510-No14

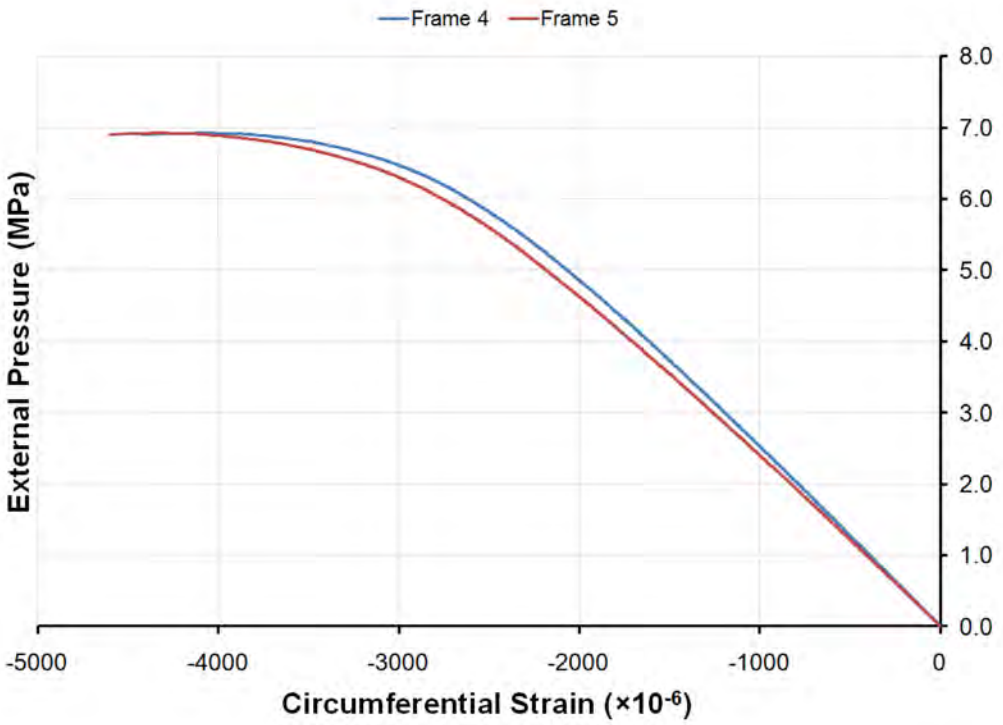

Figure 202: Pressure-strain curves showing circumferential shell strains outside Frames 4 and 5 of specimen L510-No14 at 165°

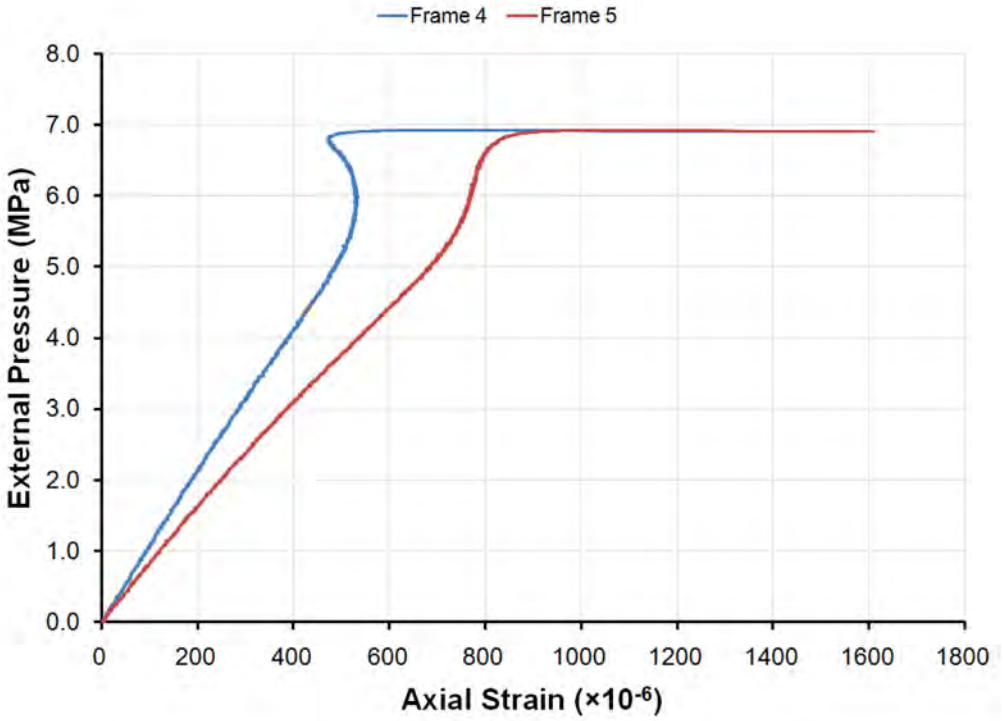

Figure 203: Pressure-strain curves showing axial shell strains outside Frames 4 and 5 of specimen L510-No14 at 165°

H.3 L510-No17

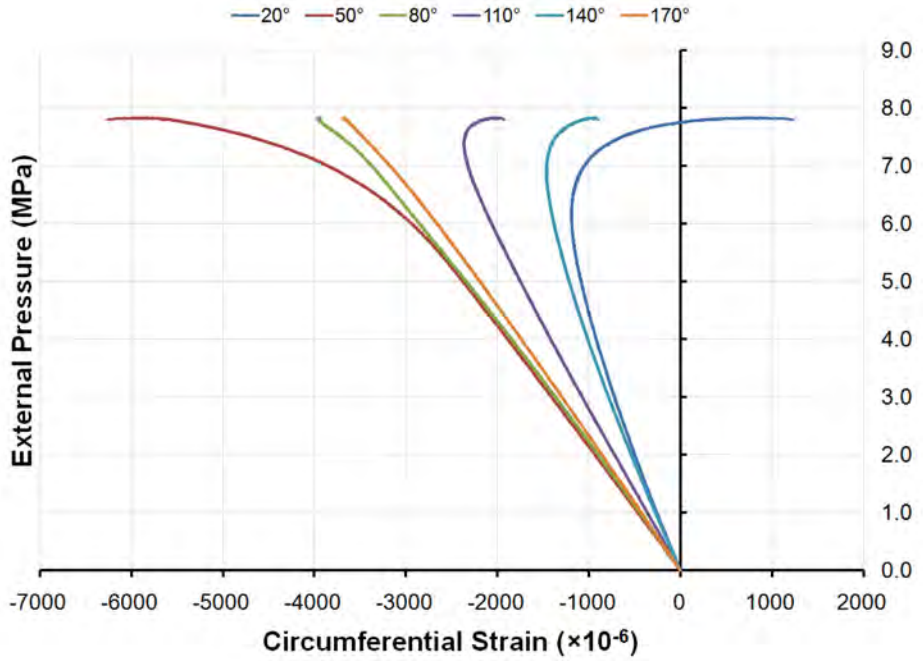

Figure 204: Pressure-strain curves showing circumferential strains at the flange of Frame 4 of specimen L510-No17 (20°-170°)

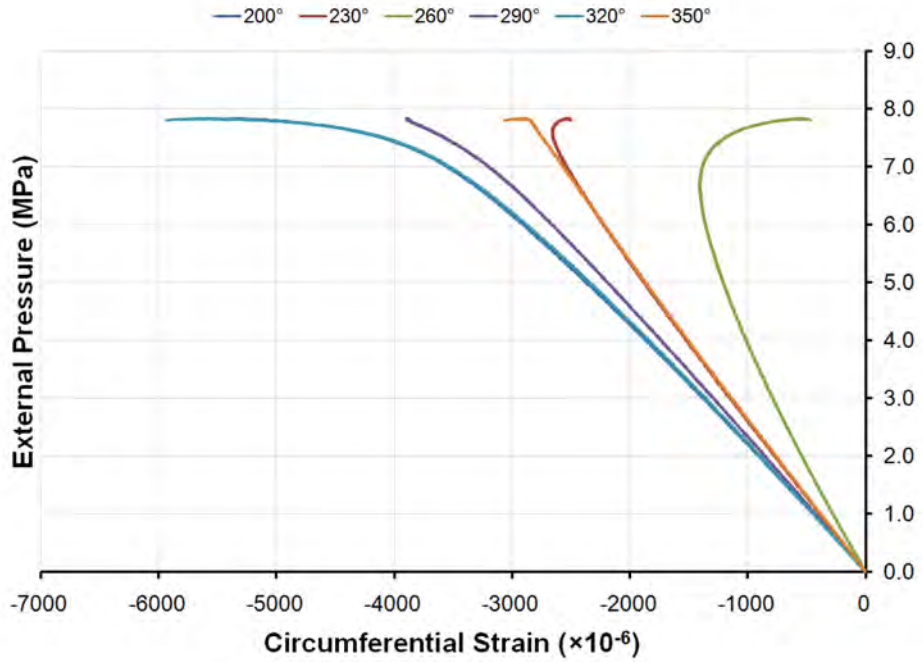

Figure 205: Pressure-strain curves showing circumferential strains at the flange of Frame 4 of specimen L510-No17 (200°-350°)

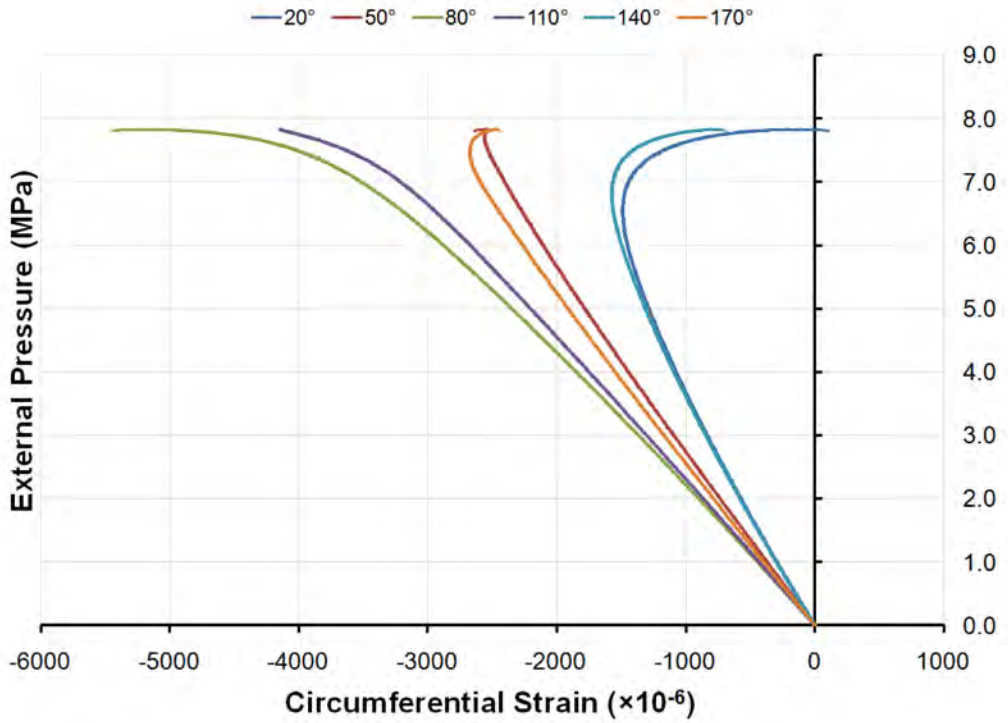

Figure 206: Pressure-strain curves showing circumferential strains at the flange of Frame 5 of specimen L510-No17 (20°-170°)

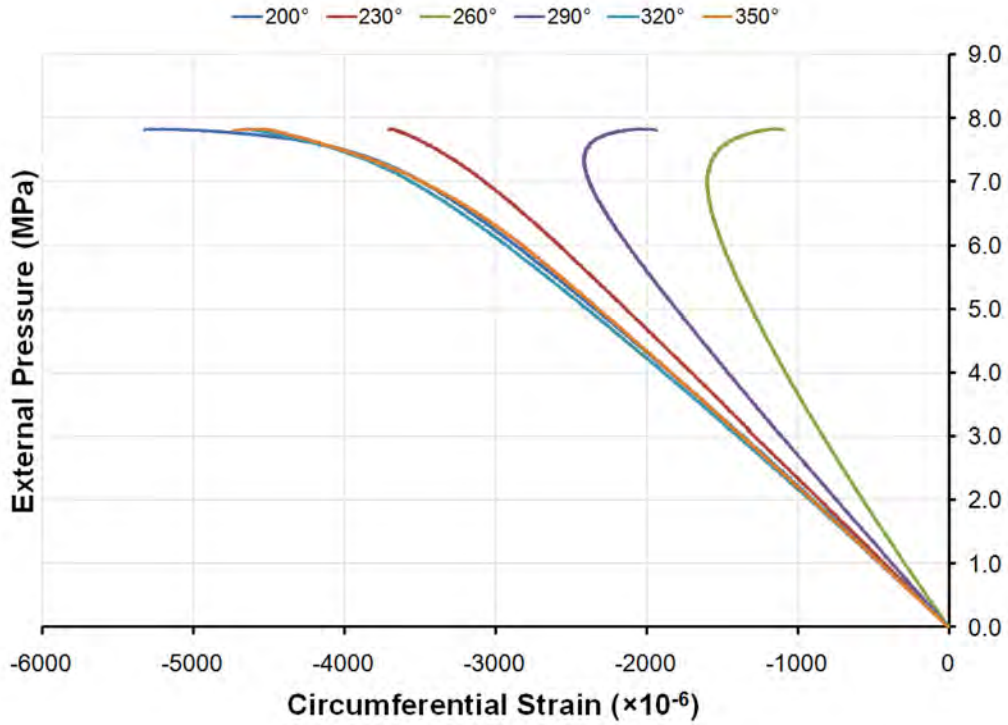

Figure 207: Pressure-strain curves showing circumferential strains at the flange of Frame 5 of specimen L510-No17 (200°-350°)

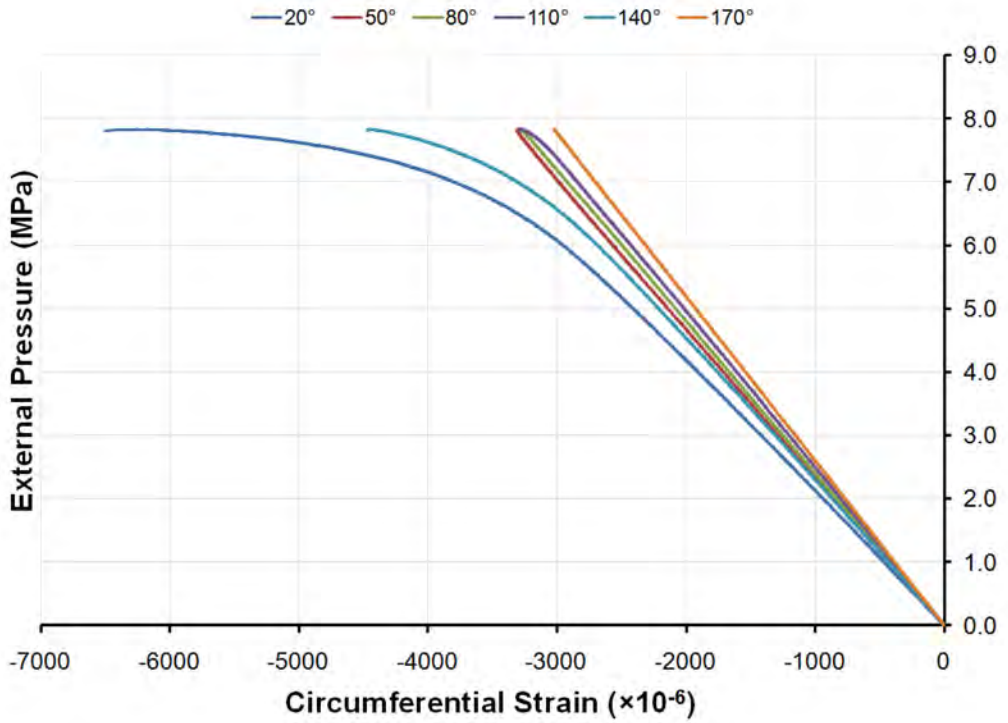

Figure 208: Pressure-strain curves showing circumferential shell strains mid-way between frames outside Bay 4 of specimen L510-No17 (20°-170°)

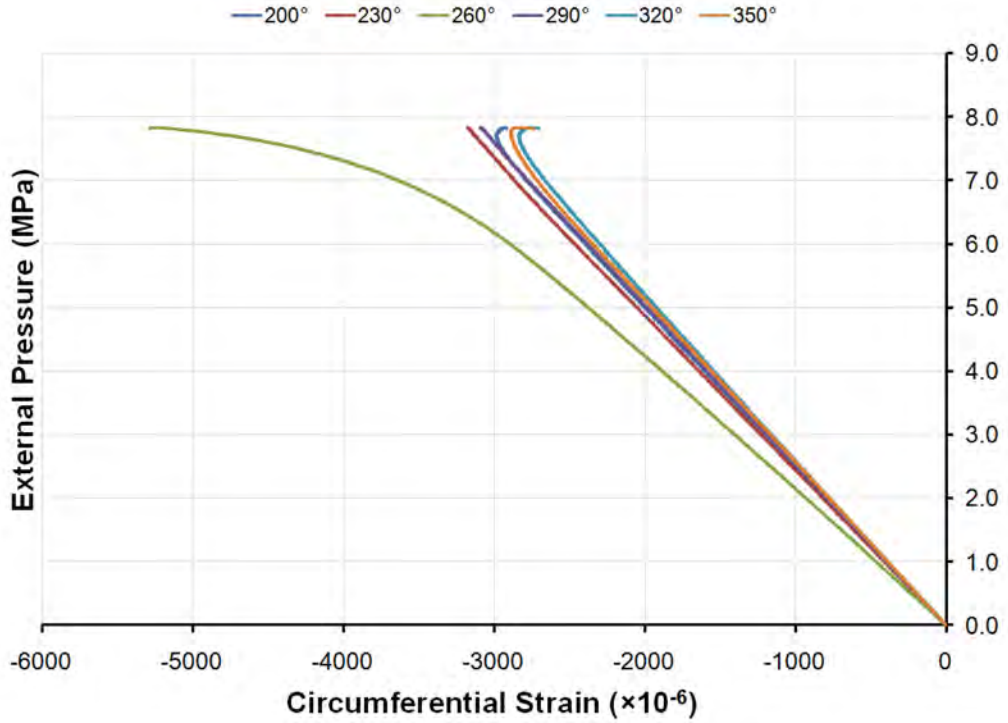

Figure 209: Pressure-strain curves showing circumferential shell strains mid-way between frames outside Bay 4 of specimen L510-No17 (200°-350°)

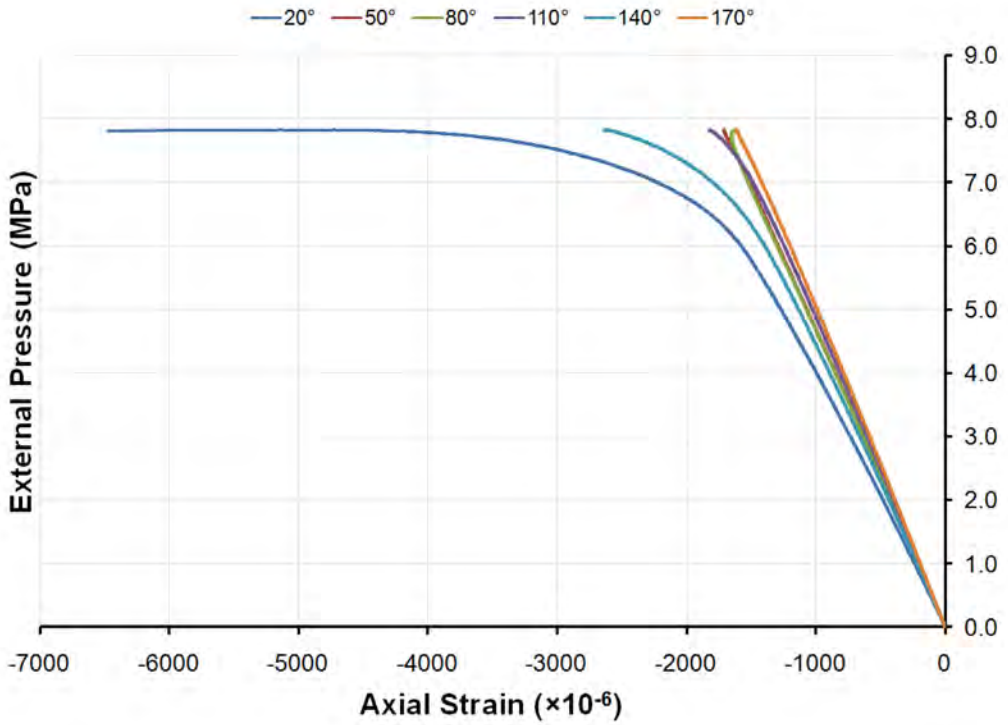

Figure 210: Pressure-strain curves showing axial shell strains mid-way between frames outside Bay 4 of specimen L510-No17 (20°-170°)

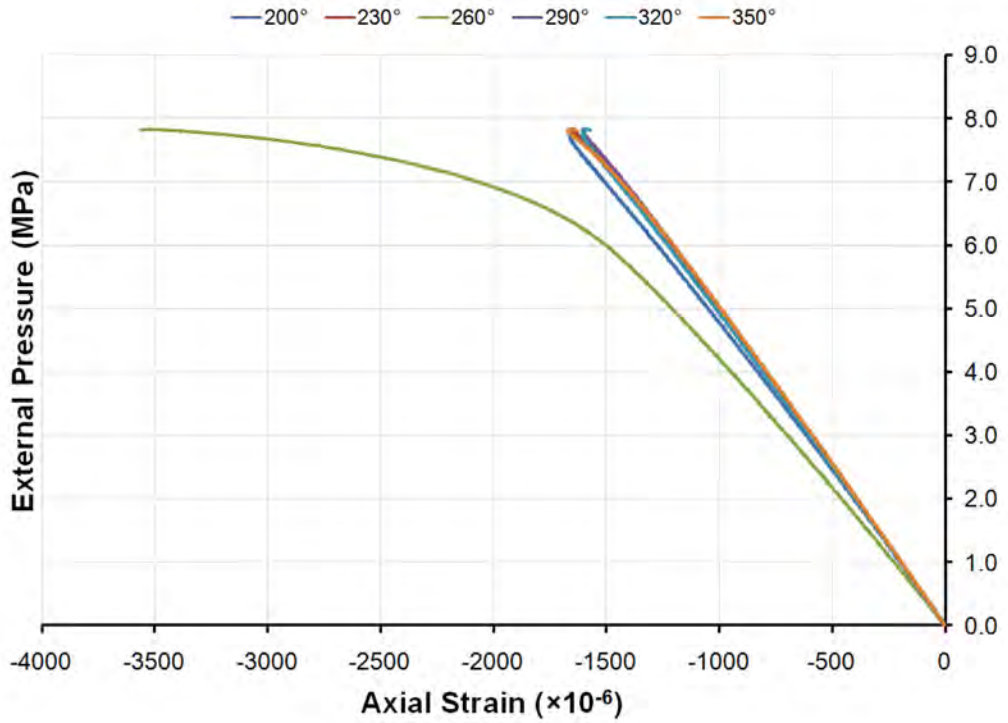

Figure 211: Pressure-strain curves showing axial shell strains mid-way between frames outside Bay 4 of specimen L510-No17 (200°-350°)

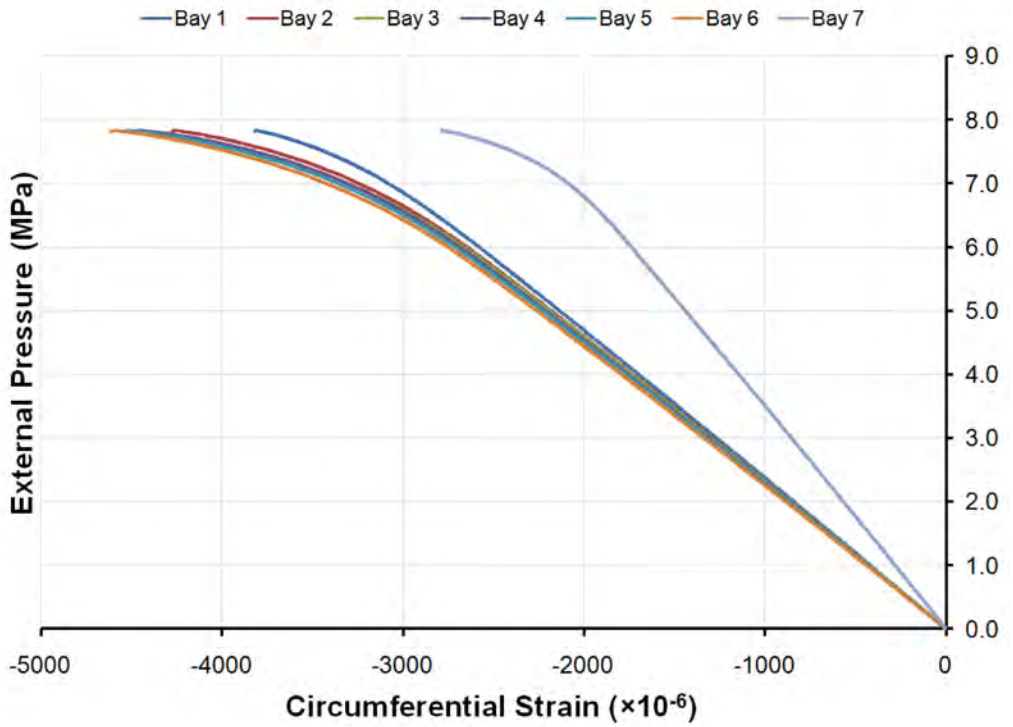

Figure 212: Pressure-strain curves showing circumferential shell strains mid-way between frames outside Bays 1 to 7 of specimen L510-No17 at 140°

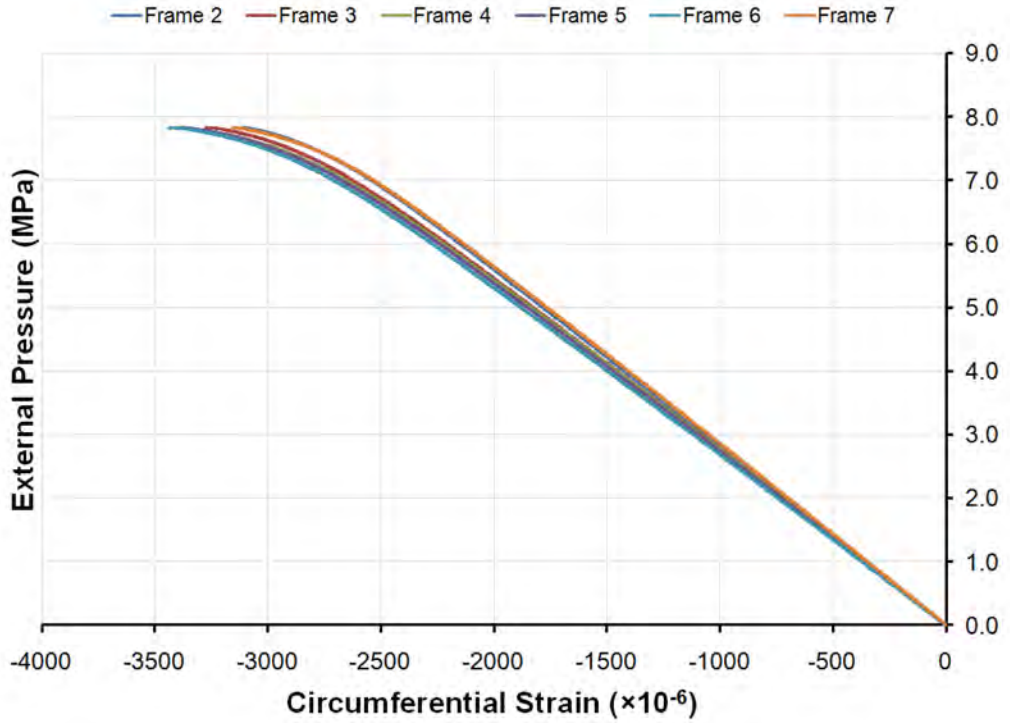

Figure 213: Pressure-strain curves showing circumferential shell strains outside Frames 2 to 7 of specimen L510-No17 at 140°

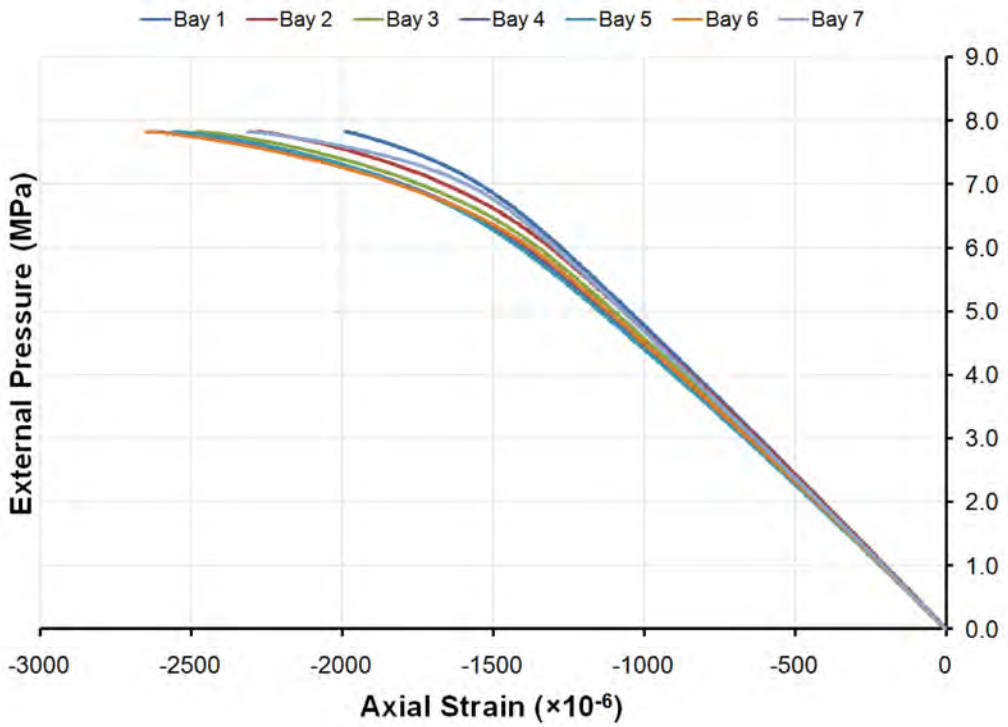

Figure 214: Pressure-strain curves showing axial shell strains mid-way between frames outside Bays 1 to 7 of specimen L510-No17 at 140°

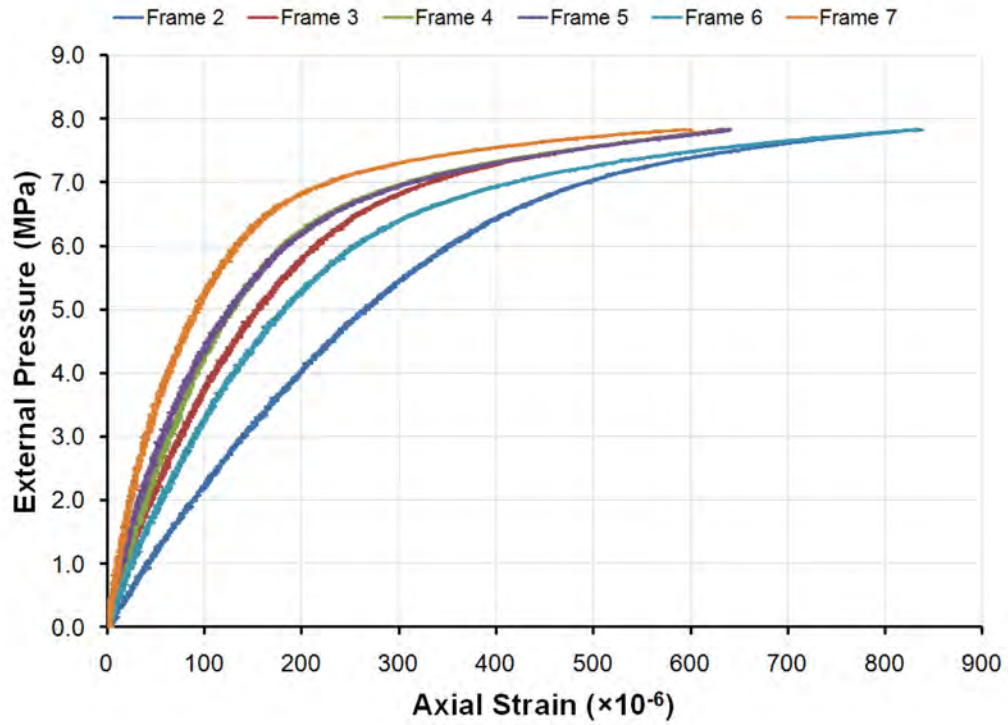

Figure 215: Pressure-strain curves showing axial shell strains outside Frames 2 to 7 of specimen L510-No17 at 140°

H.4 L510-No18

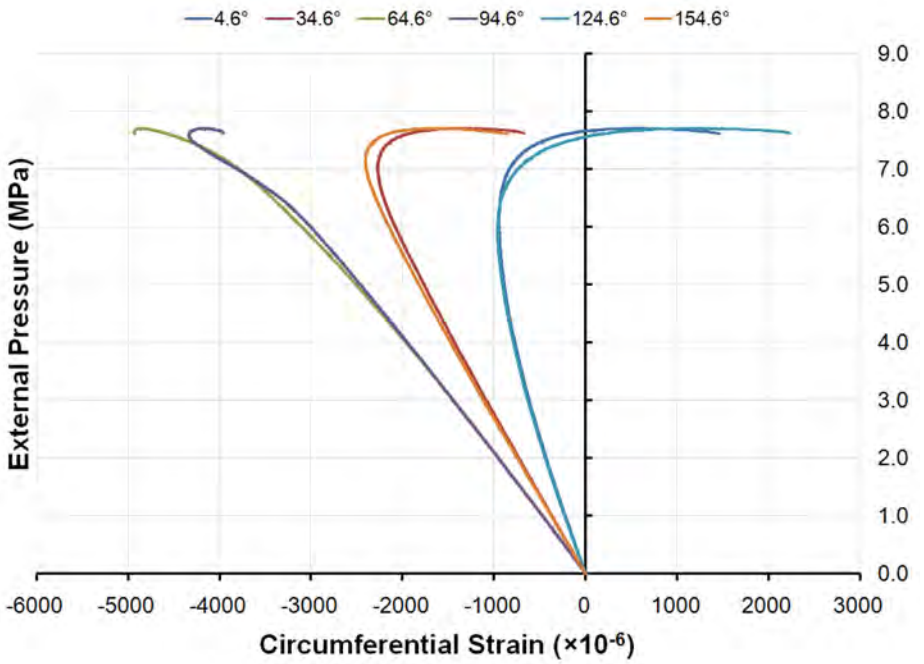

Figure 216: Pressure-strain curves showing circumferential strains at the flange of Frame 4 of specimen L510-No18 (4.6°-154.6°)

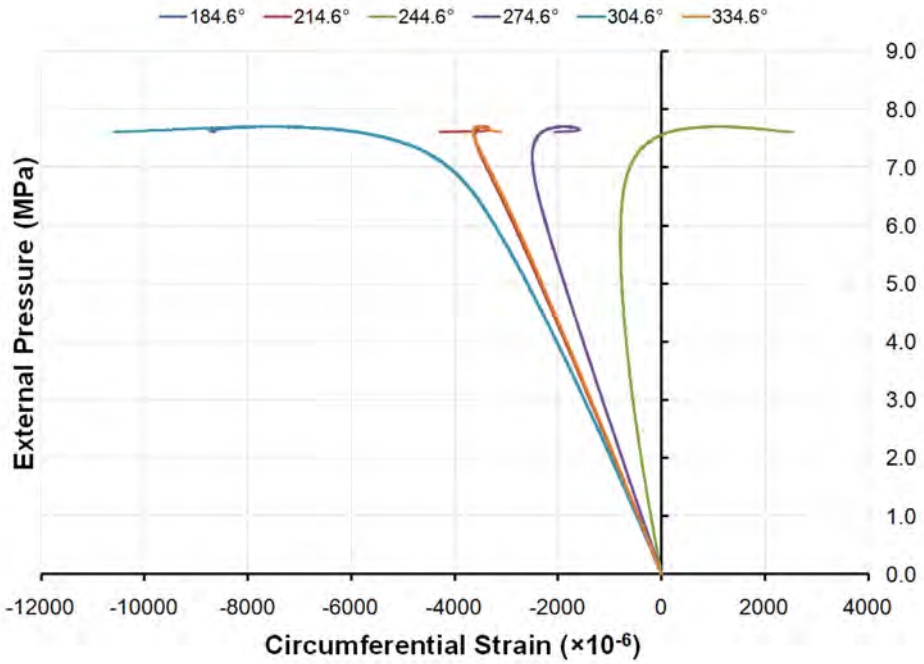

Figure 217: Pressure-strain curves showing circumferential strains at the flange of Frame 4 of specimen L510-No18 (184.6°-334.6°)

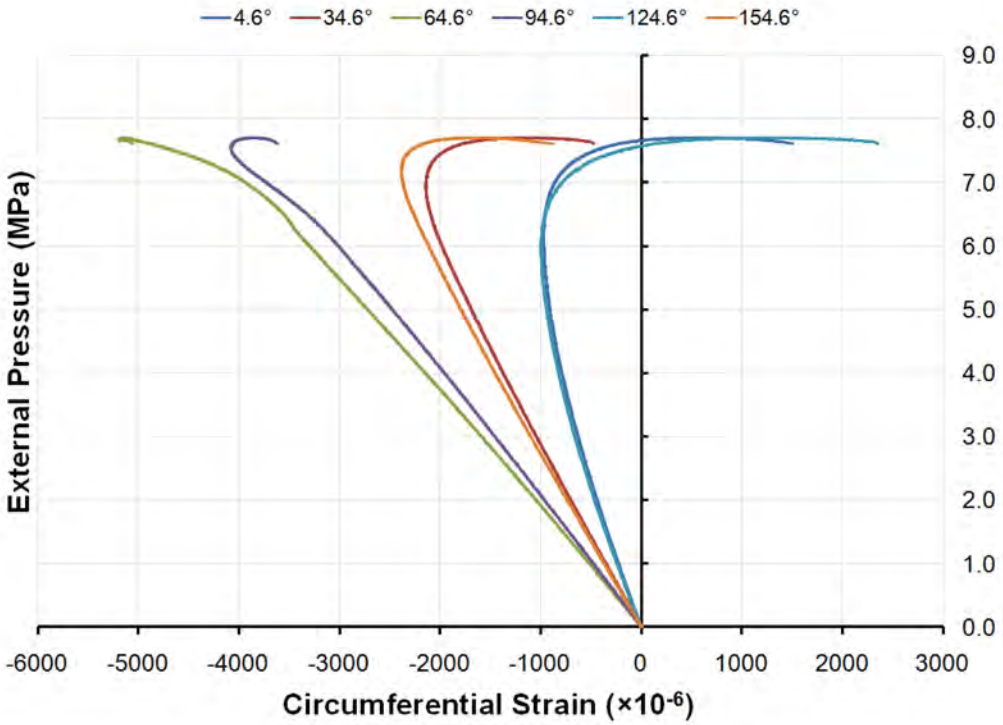

Figure 218: Pressure-strain curves showing circumferential strains at the flange of Frame 5 of specimen L510-No18 (4.6°-154.6°)

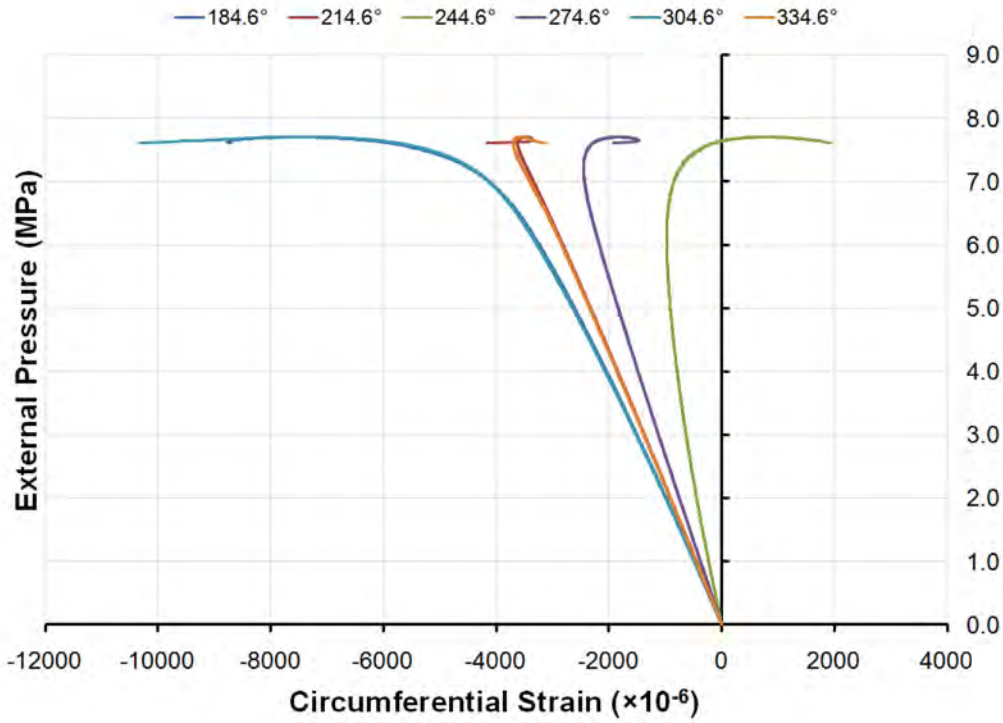

Figure 219: Pressure-strain curves showing circumferential strains at the flange of Frame 5 of specimen L510-No18 (184.6°-334.6°)

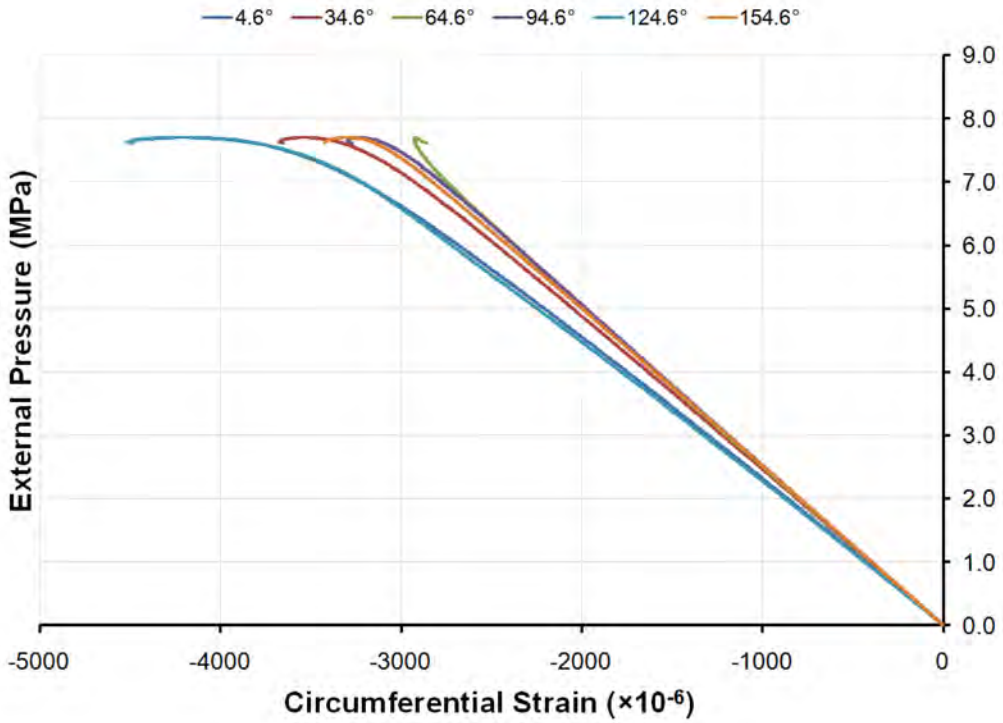

Figure 220: Pressure-strain curves showing circumferential shell strains mid-way between frames outside Bay 4 of specimen L510-No18 (4.6°-154.6°)

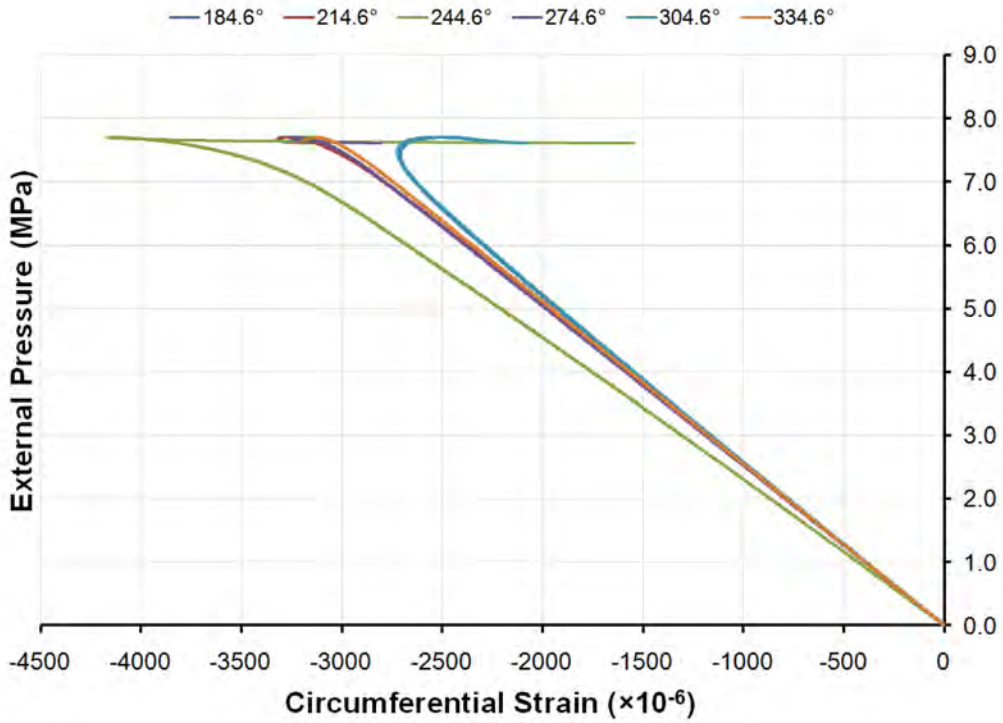

Figure 221: Pressure-strain curves showing circumferential shell strains mid-way between frames outside Bay 4 of specimen L510-No18 (184.6°-334.6°)

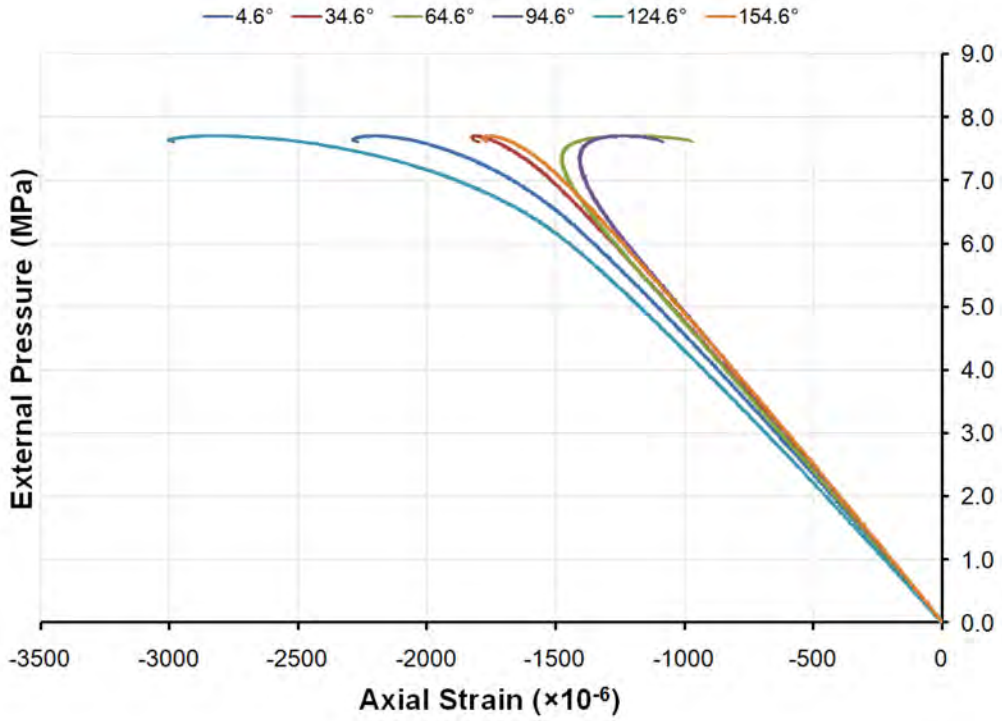

Figure 222: Pressure-strain curves showing axial shell strains mid-way between frames outside Bay 4 of specimen L510-No18 (4.6°-154.6°)

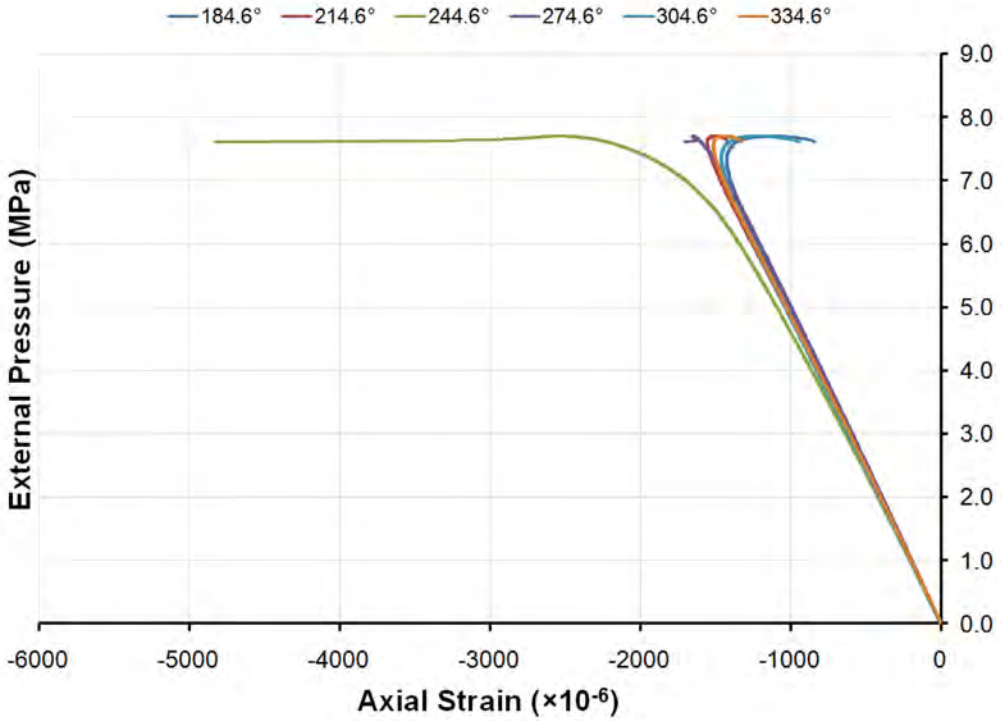

Figure 223: Pressure-strain curves showing axial shell strains mid-way between frames outside Bay 4 of specimen L510-No18 (184.6°-334.6°)

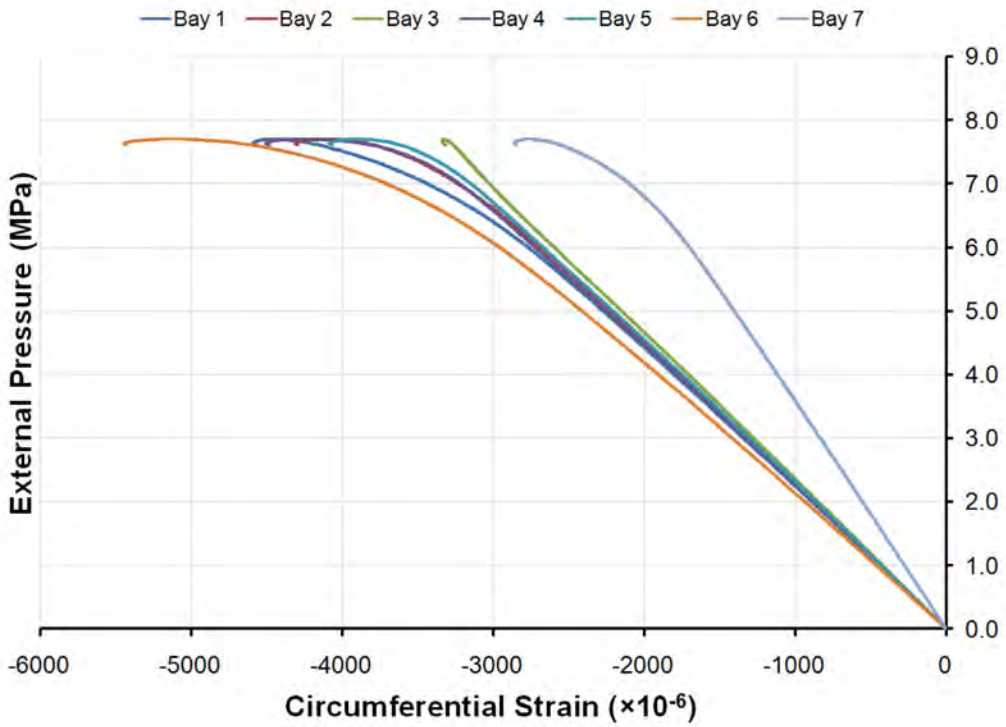

Figure 224: Pressure-strain curves showing circumferential shell strains mid-way between frames outside Bays 1 to 7 of specimen L510-No18 at 124.6°

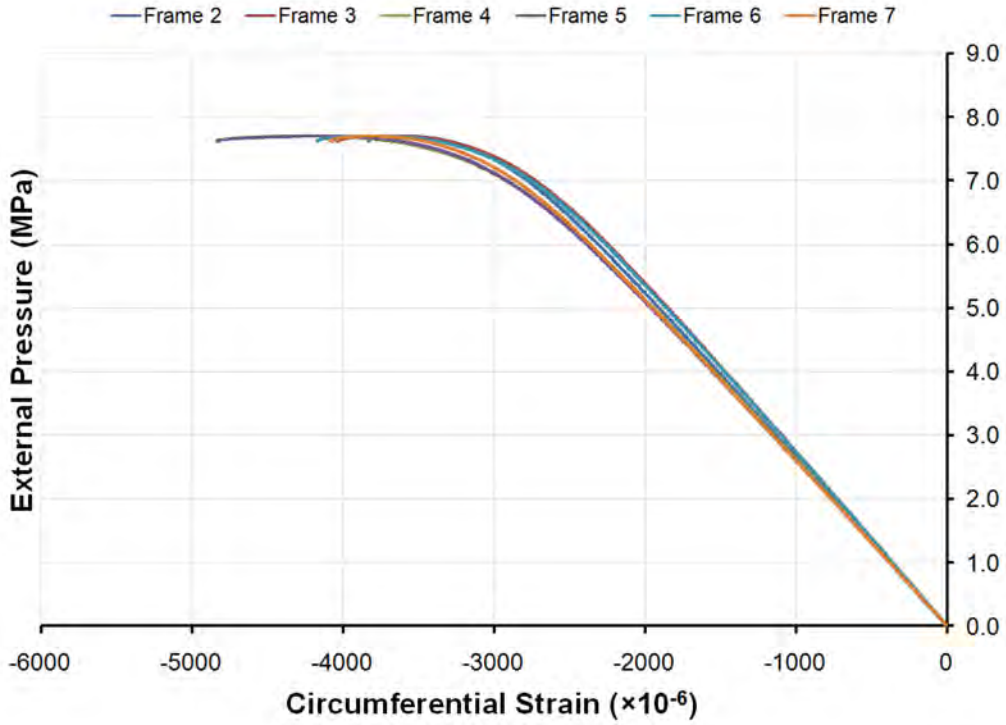

Figure 225: Pressure-strain curves showing circumferential shell strains outside Frames 2 to 7 of specimen L510-No18 at 124.6°

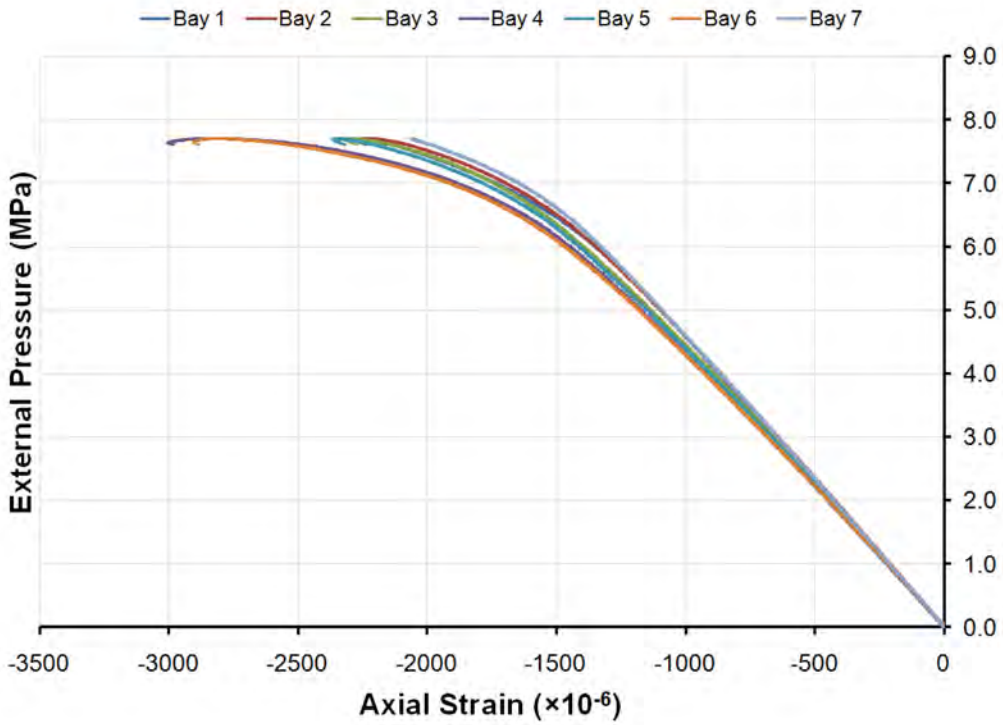

Figure 226: Pressure-strain curves showing axial shell strains mid-way between frames outside Bays 1 to 7 of specimen L510-No18 at 124.6°

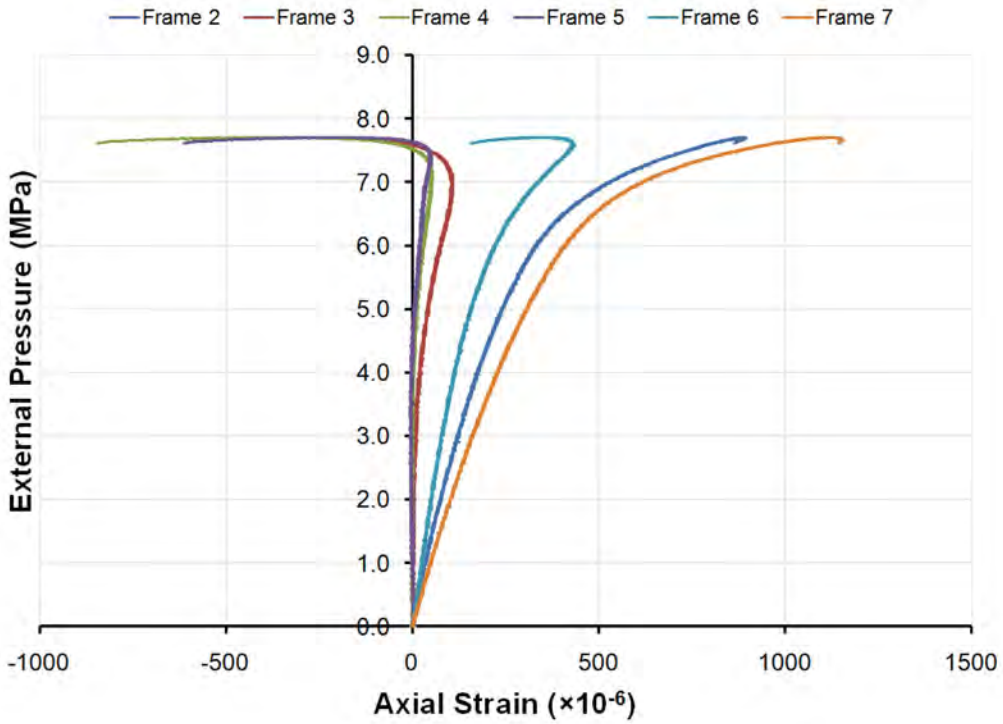

Figure 227: Pressure-strain curves showing axial shell strains outside Frames 2 to 7 of specimen L510-No18 at 124.6°

H.5 L510-No19

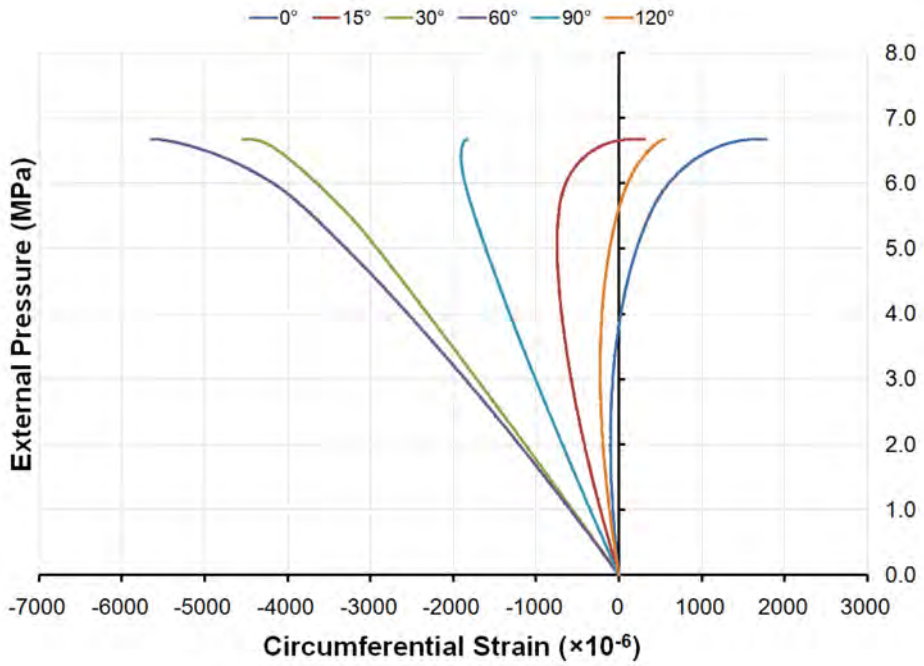

Figure 228: Pressure-strain curves showing circumferential strains at the flange of Frame 4 of specimen L510-No19 (0°-120°)

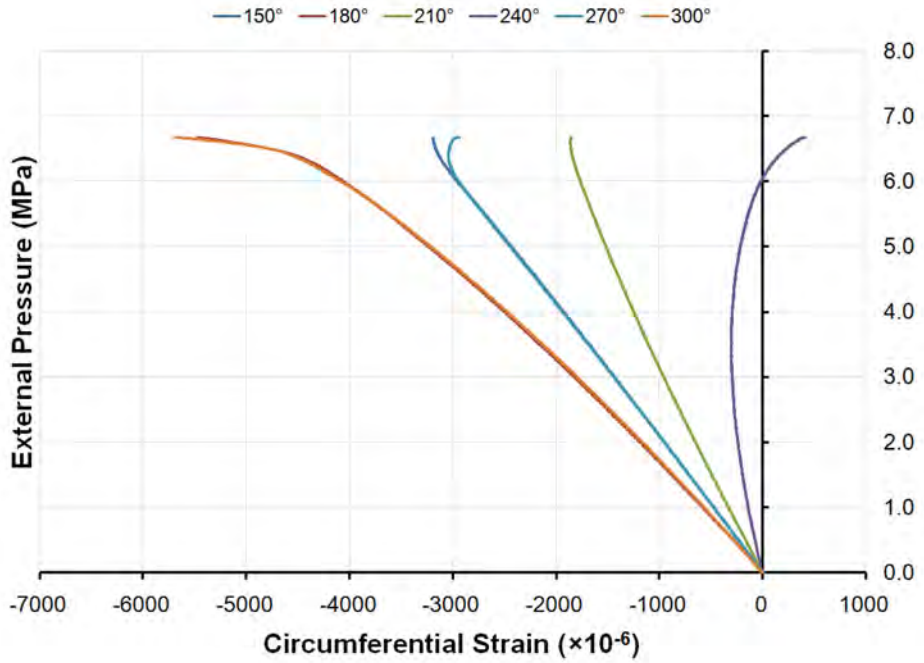

Figure 229: Pressure-strain curves showing circumferential strains at the flange of Frame 4 of specimen L510-No19 (150°-300°)

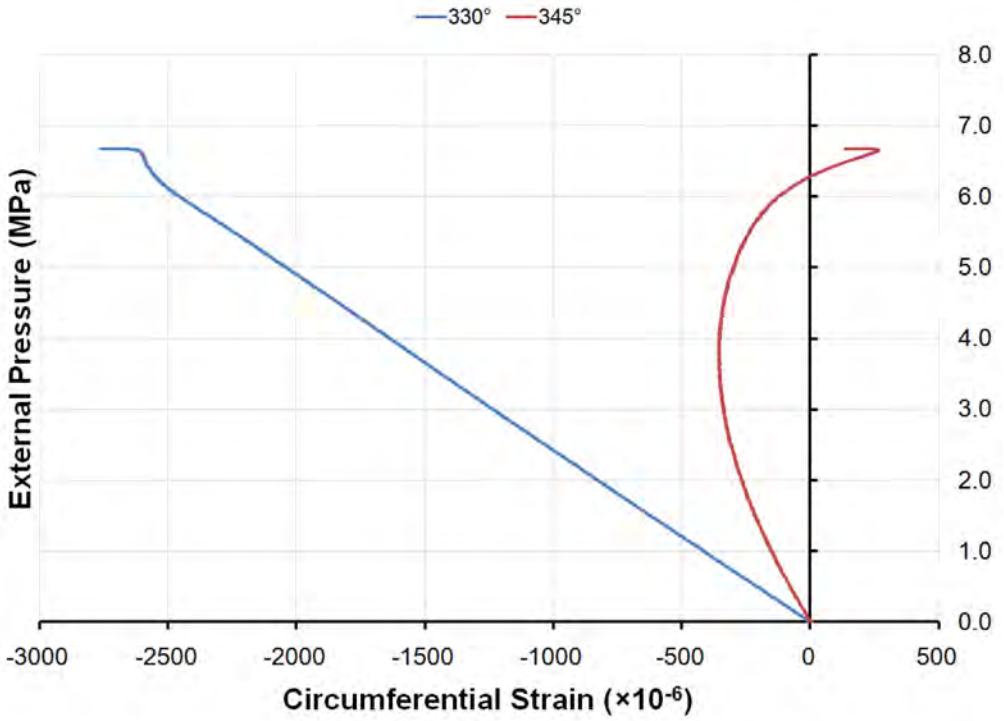

Figure 230: Pressure-strain curves showing circumferential strains at the flange of Frame 4 of specimen L510-No19 (300°-345°)

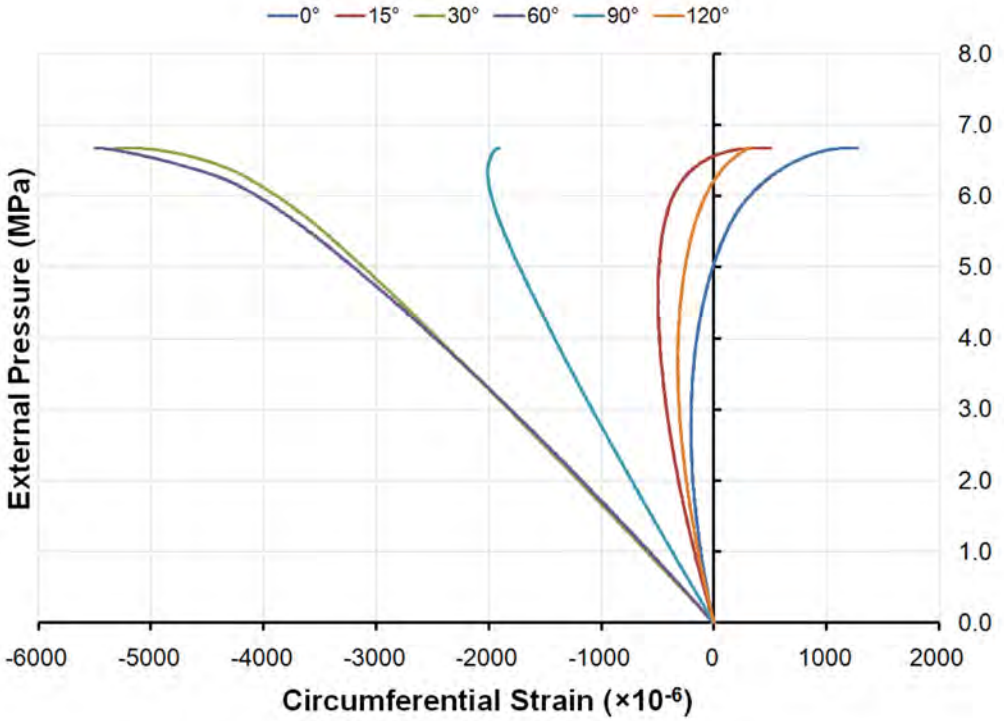

Figure 231: Pressure-strain curves showing circumferential strains at the flange of Frame 5 of specimen L510-No19 (0°-120°)

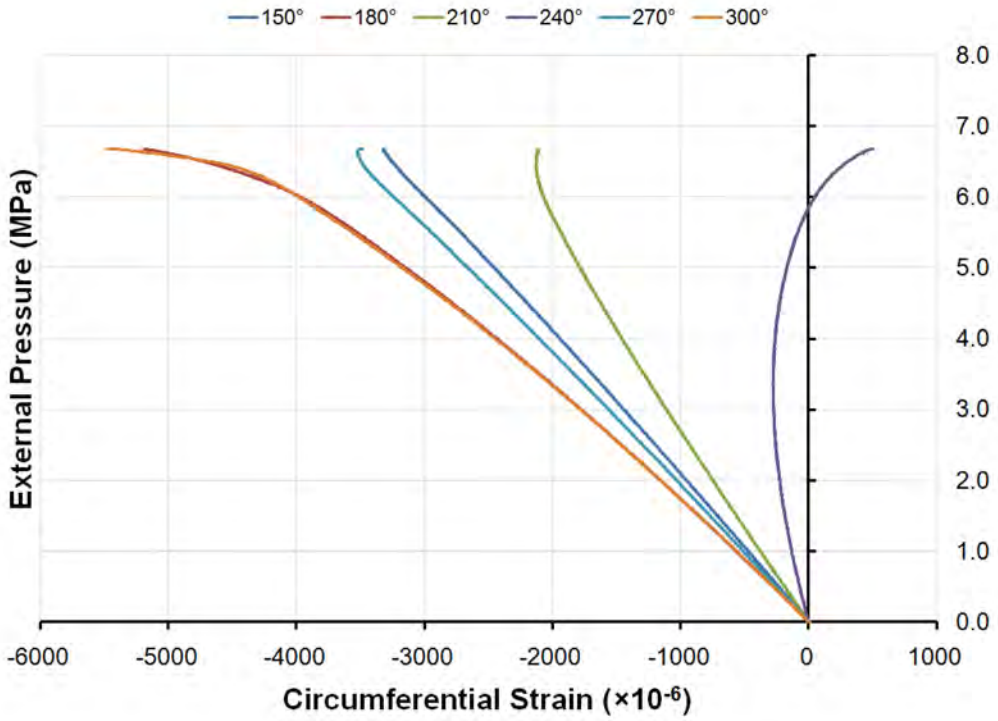

Figure 232: Pressure-strain curves showing circumferential strains at the flange of Frame 5 of specimen L510-No19 (150°-300°)

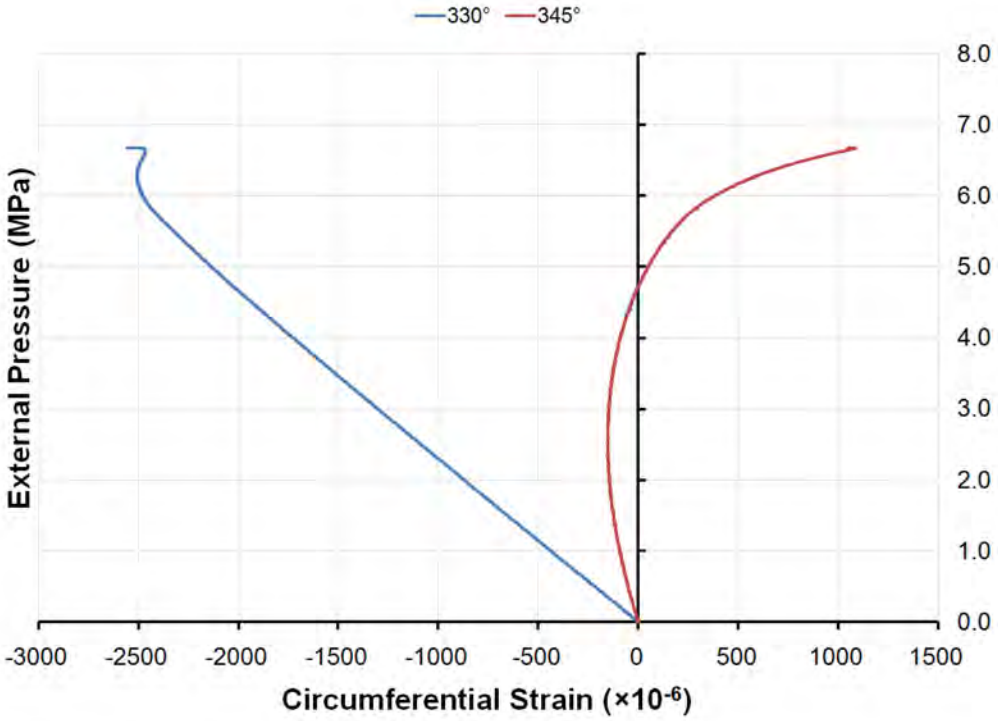

Figure 233: Pressure-strain curves showing circumferential strains at the flange of Frame 5 of specimen L510-No19 (300°-345°)

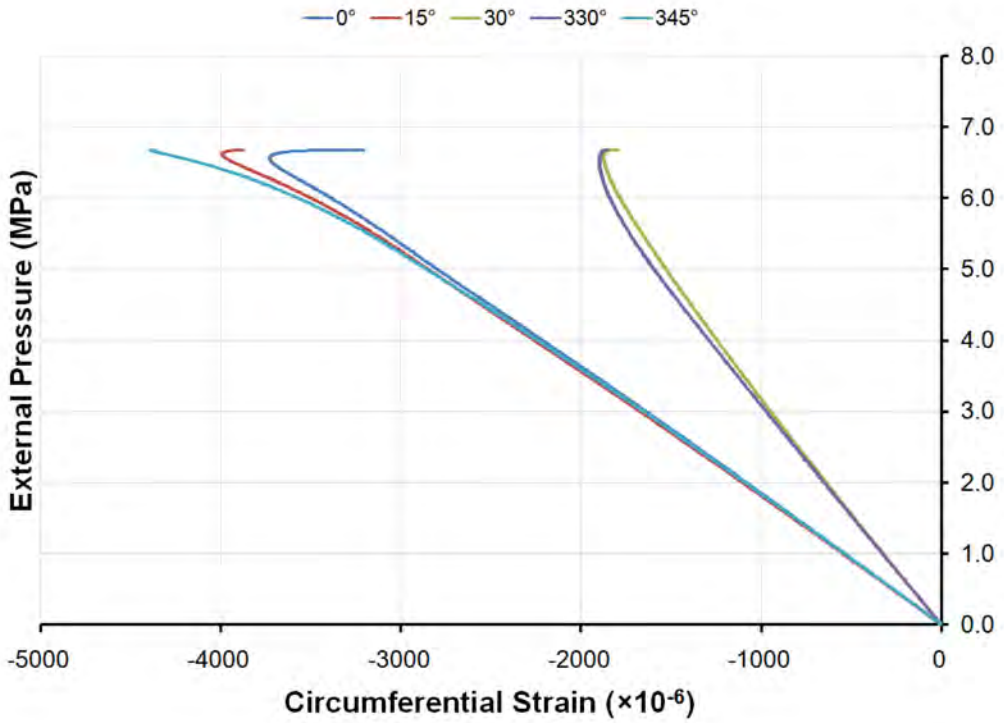

Figure 234: Pressure-strain curves showing circumferential shell strains mid-way between frames outside Bay 4 of specimen L510-No19

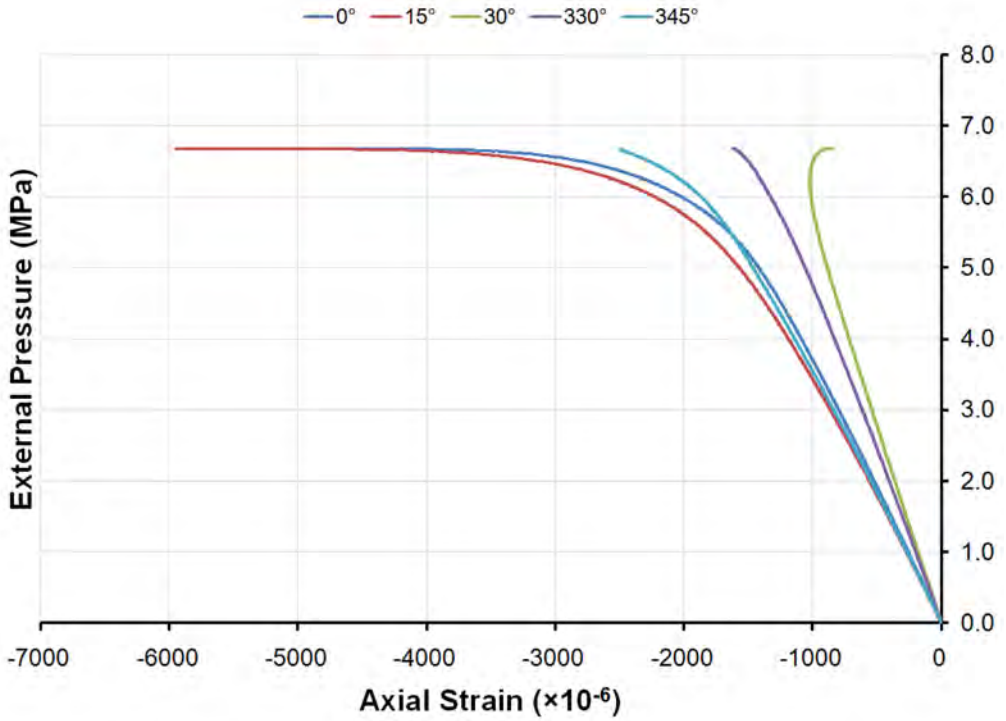

Figure 235: Pressure-strain curves showing axial shell strains mid-way between frames outside Bay 4 of specimen L510-No19

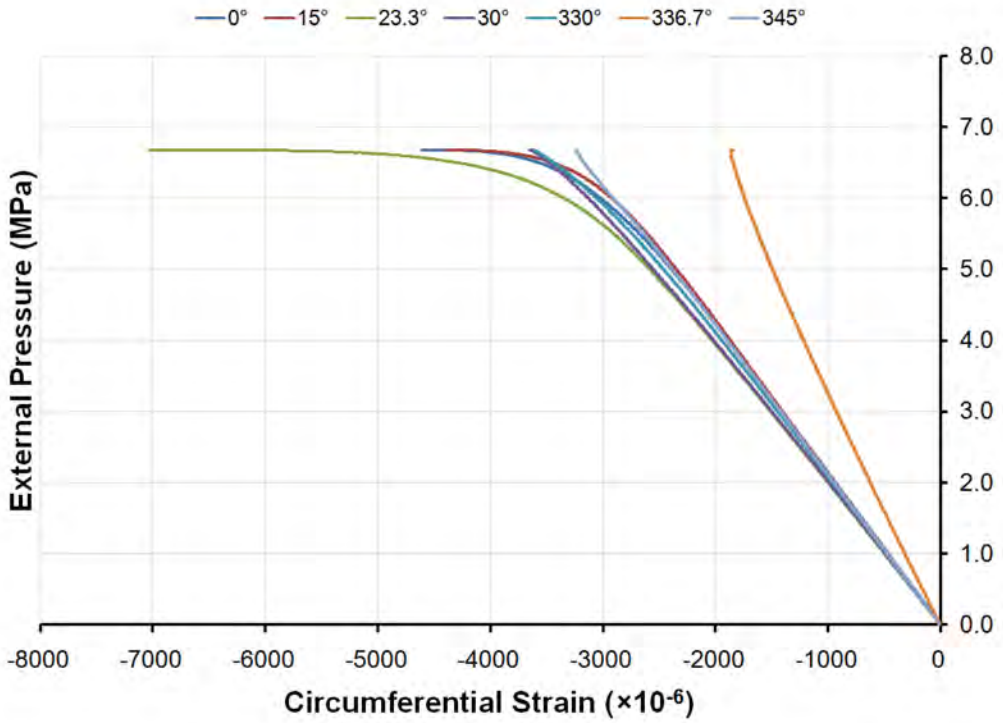

Figure 236: Pressure-strain curves showing circumferential shell strains mid-way between frames inside Bay 4 of specimen L510-No19

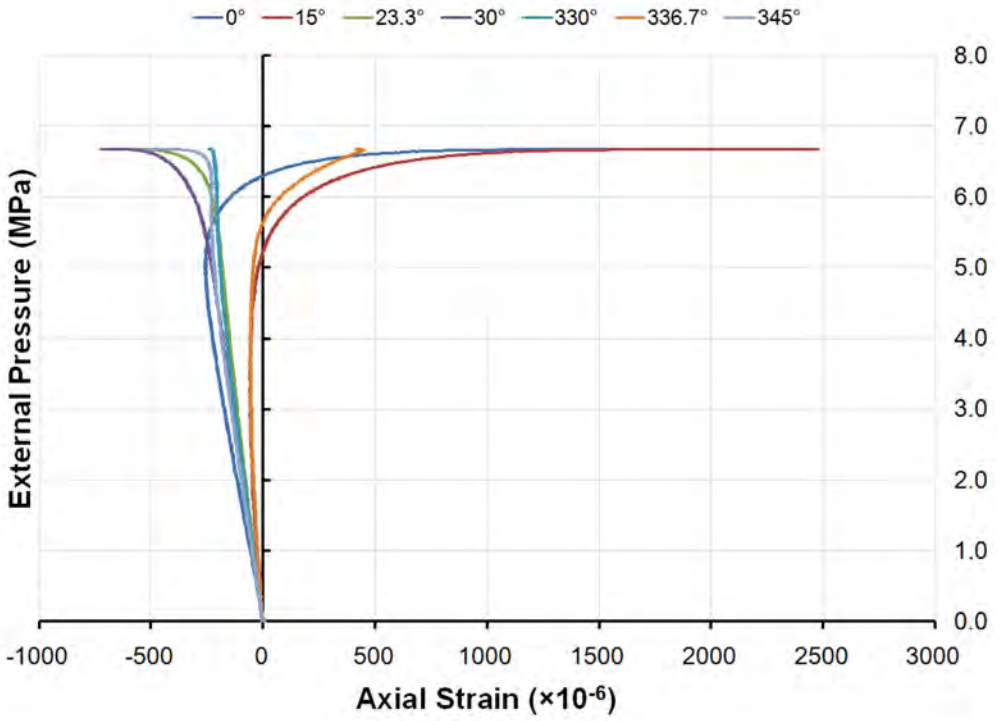

Figure 237: Pressure-strain curves showing axial shell strains mid-way between frames inside Bay 4 of specimen L510-No19

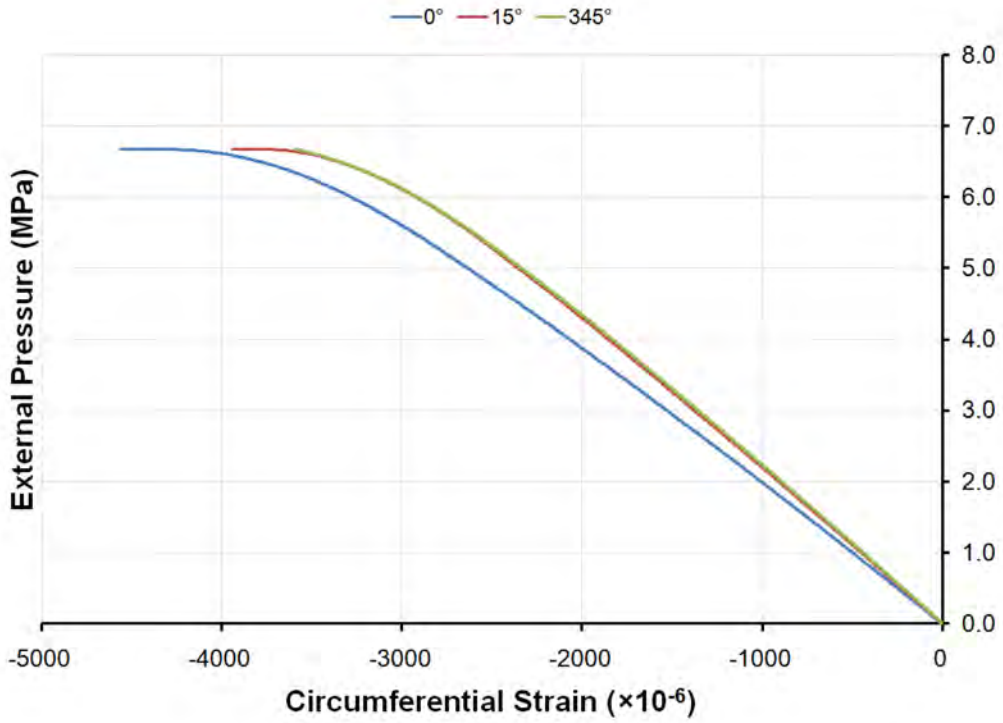

Figure 238: Pressure-strain curves showing circumferential shell strains outside Frame 4 of specimen L510-No19

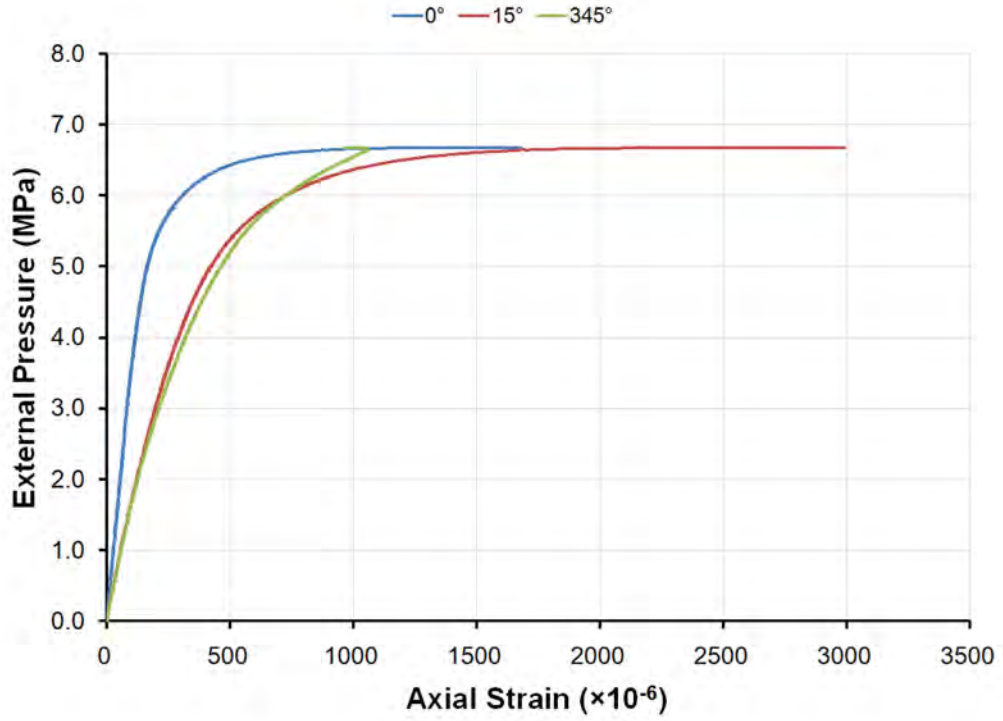

Figure 239: Pressure-strain curves showing axial shell strains outside Frame 4 of specimen L510-No19

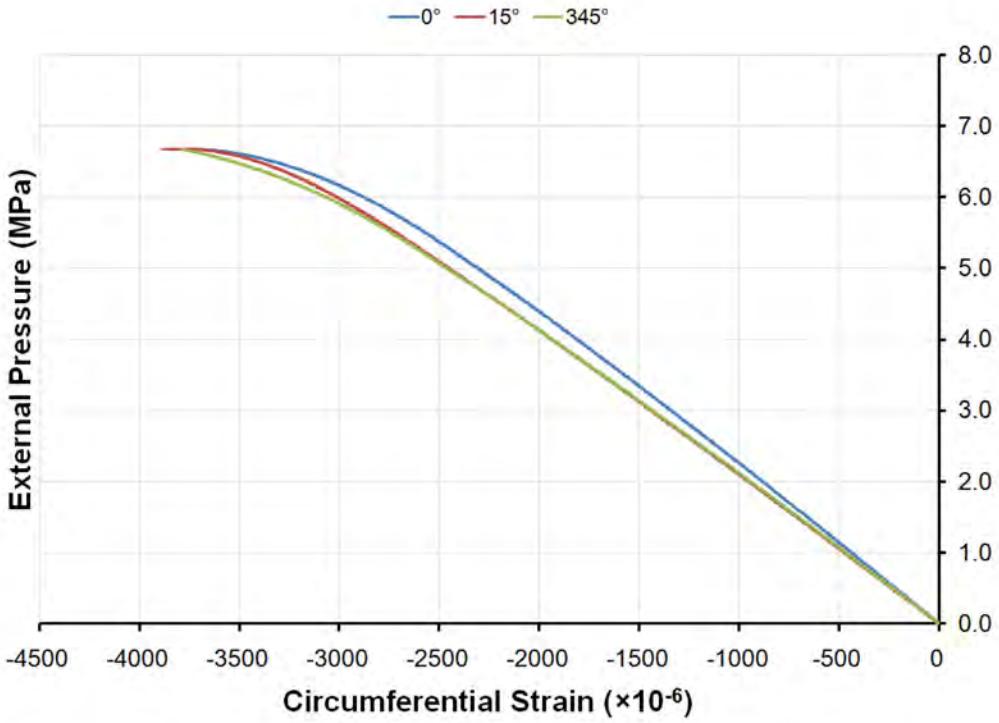

Figure 240: Pressure-strain curves showing circumferential shell strains outside Frame 5 of specimen L510-No19

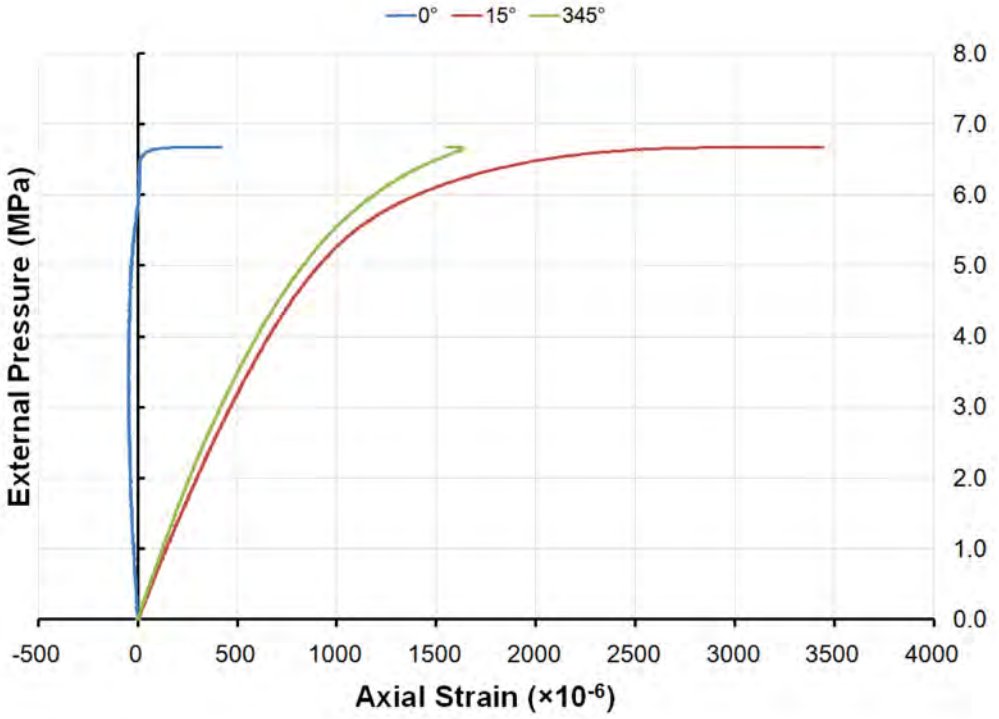

Figure 241: Pressure-strain curves showing axial shell strains outside Frame 5 of specimen L510-No19

H.6 L510-No20

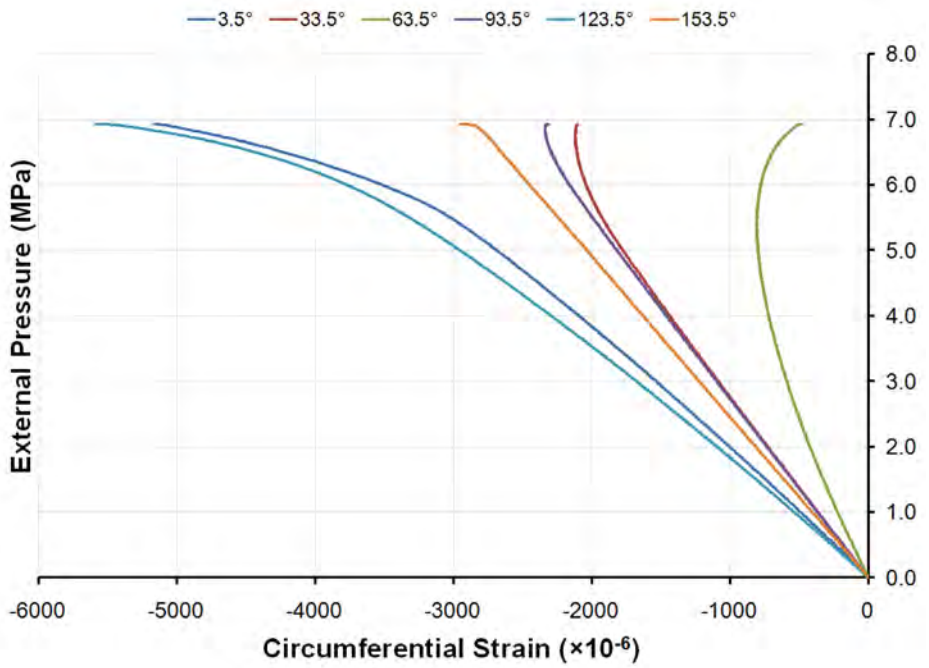

Figure 242: Pressure-strain curves showing circumferential strains at the flange of Frame 4 of specimen L510-No20 (3.5°-153.5°)

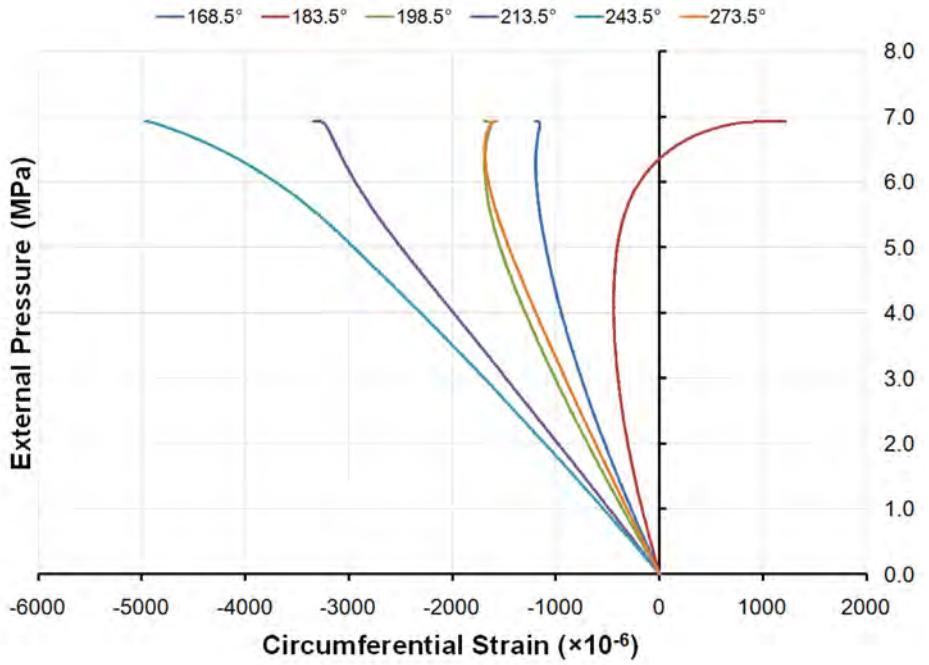

Figure 243: Pressure-strain curves showing circumferential strains at the flange of Frame 4 of specimen L510-No20 (168.5°-273.5°)

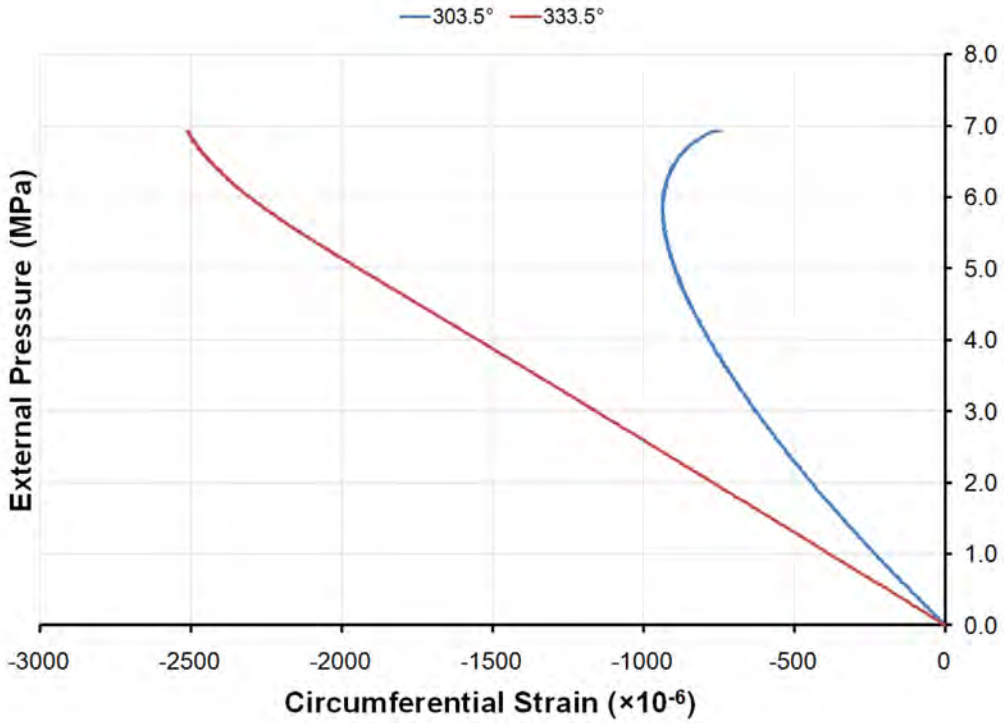

Figure 244: Pressure-strain curves showing circumferential strains at the flange of Frame 4 of specimen L510-No20 (303.5°-333.5°)

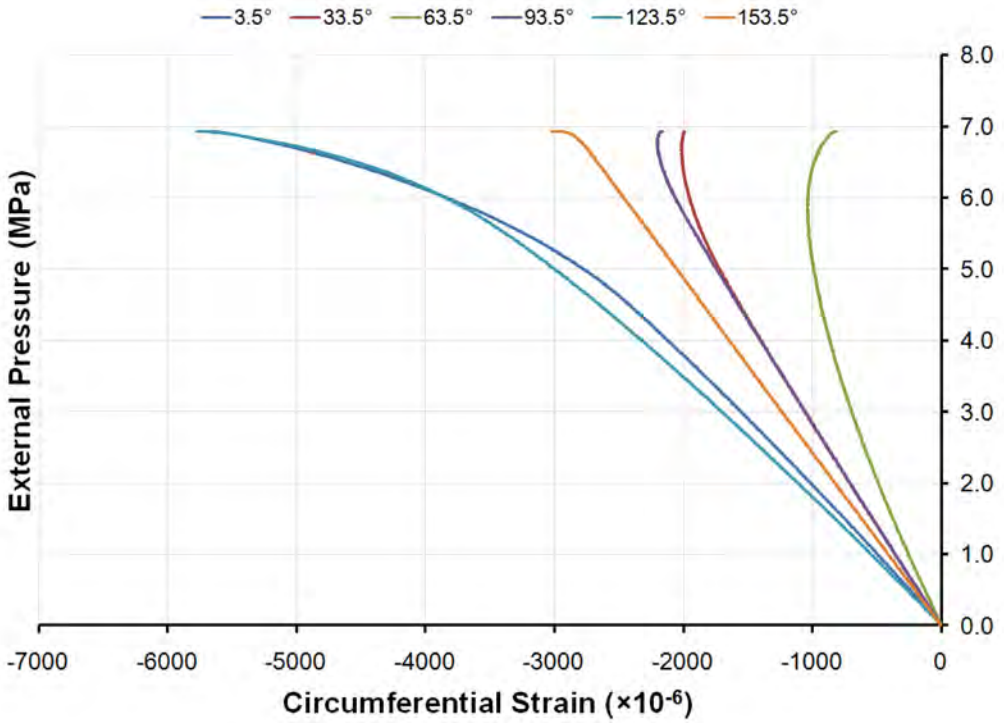

Figure 245: Pressure-strain curves showing circumferential strains at the flange of Frame 5 of specimen L510-No20 (3.5°-153.5°)

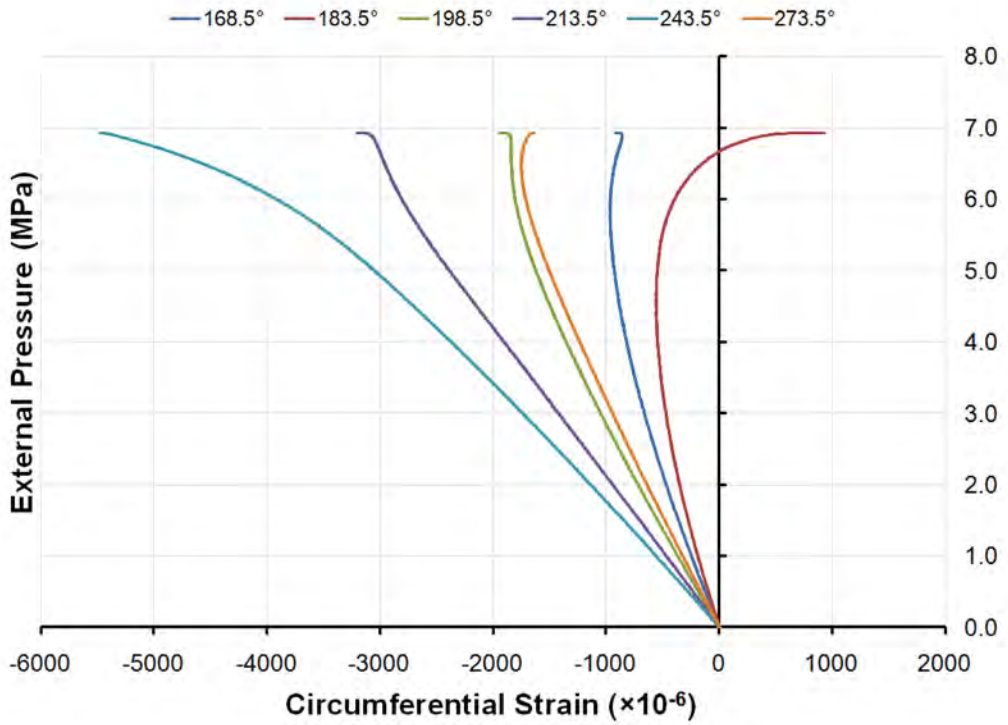

Figure 246: Pressure-strain curves showing circumferential strains at the flange of Frame 5 of specimen L510-No20 (168.5°-273.5°)

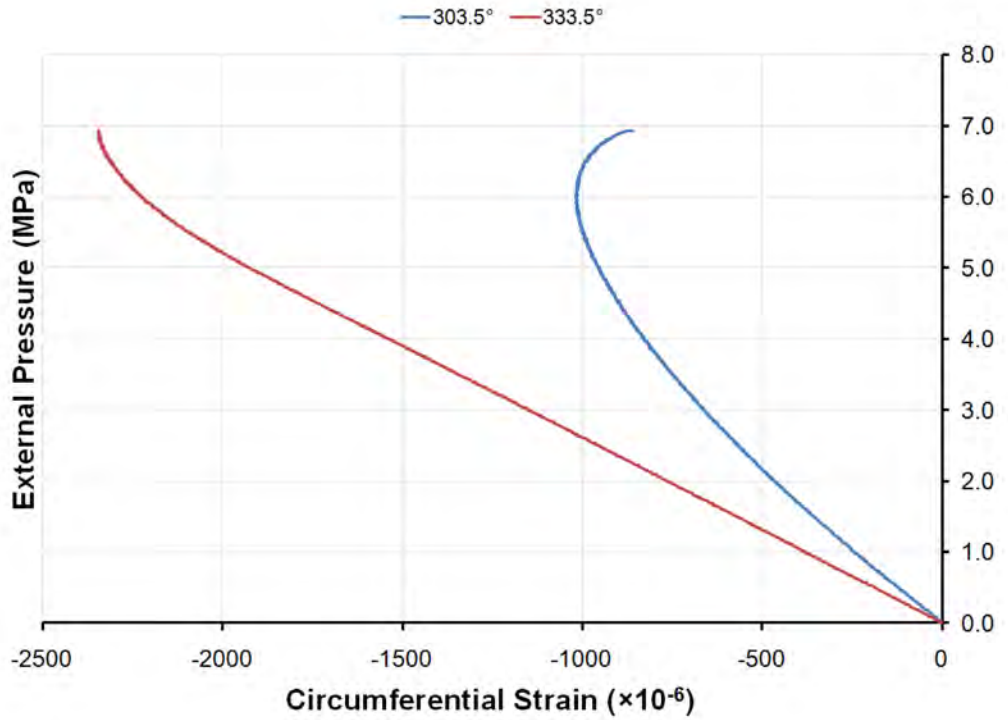

Figure 247: Pressure-strain curves showing circumferential strains at the flange of Frame 5 of specimen L510-No20 (303.5°-333.5°)

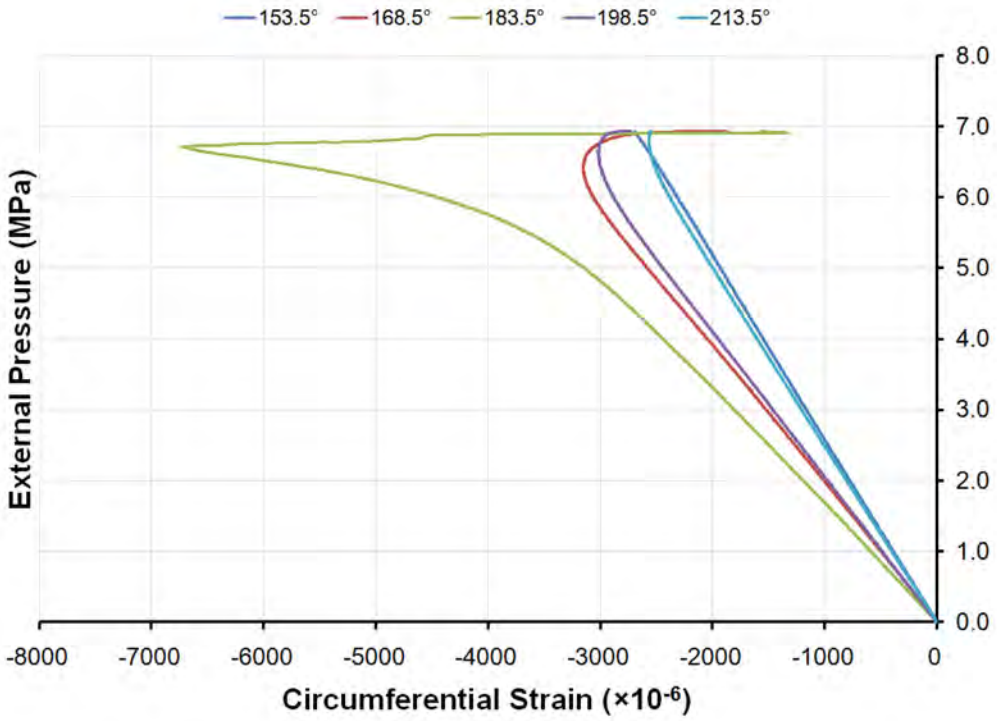

Figure 248: Pressure-strain curves showing circumferential shell strains mid-way between frames outside Bay 4 of specimen L510-No20

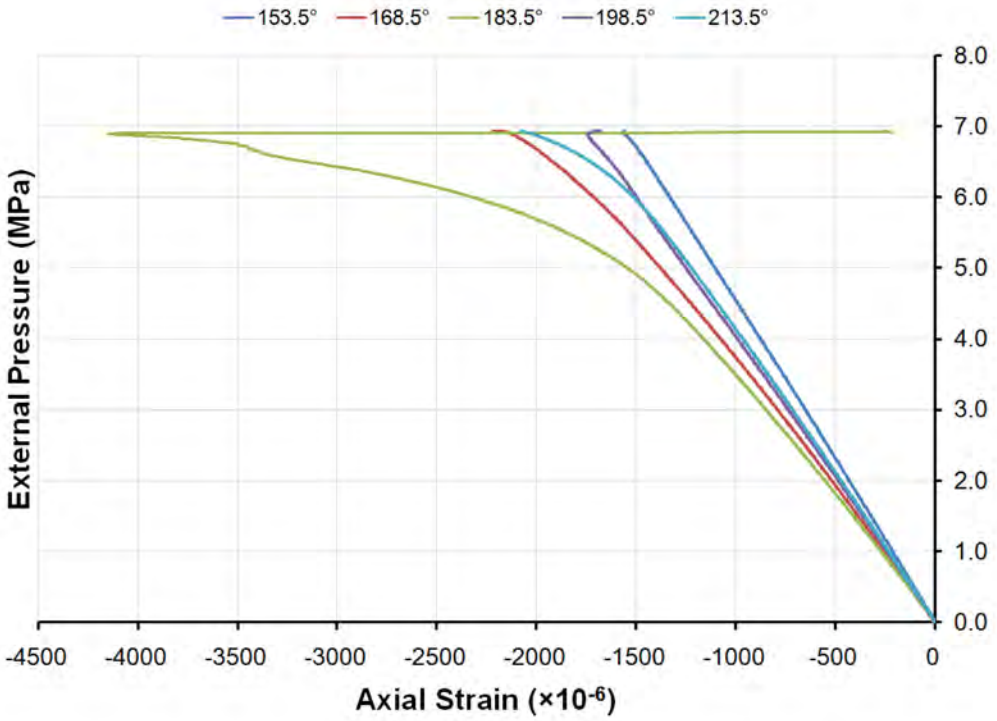

Figure 249: Pressure-strain curves showing axial shell strains mid-way between frames outside Bay 4 of specimen L510-No20

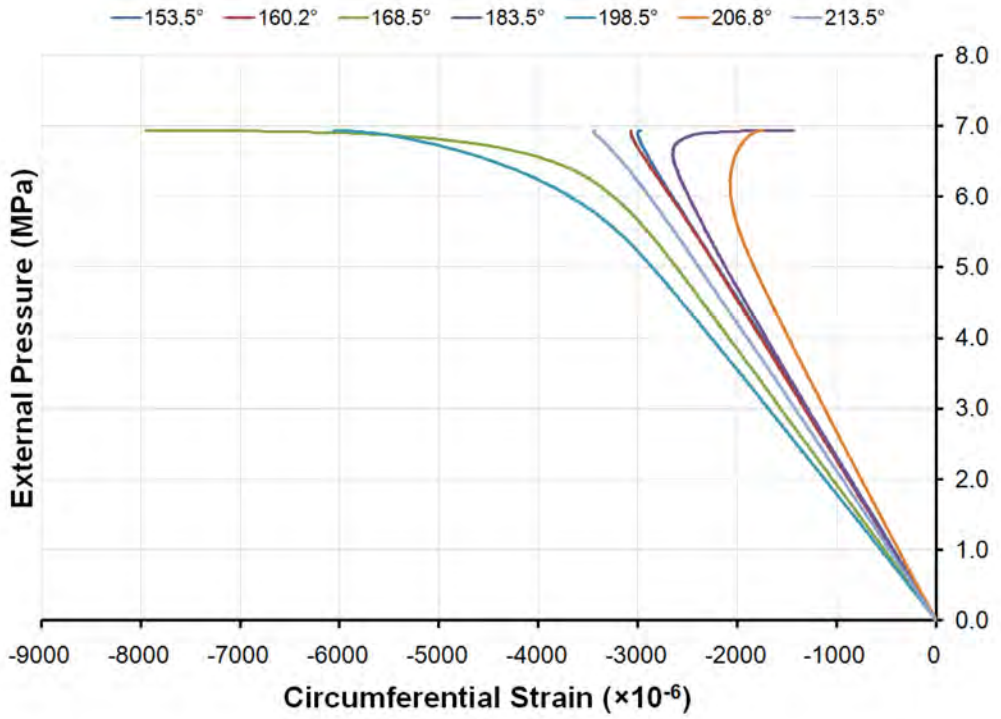

Figure 250: Pressure-strain curves showing circumferential shell strains mid-way between frames inside Bay 4 of specimen L510-No20

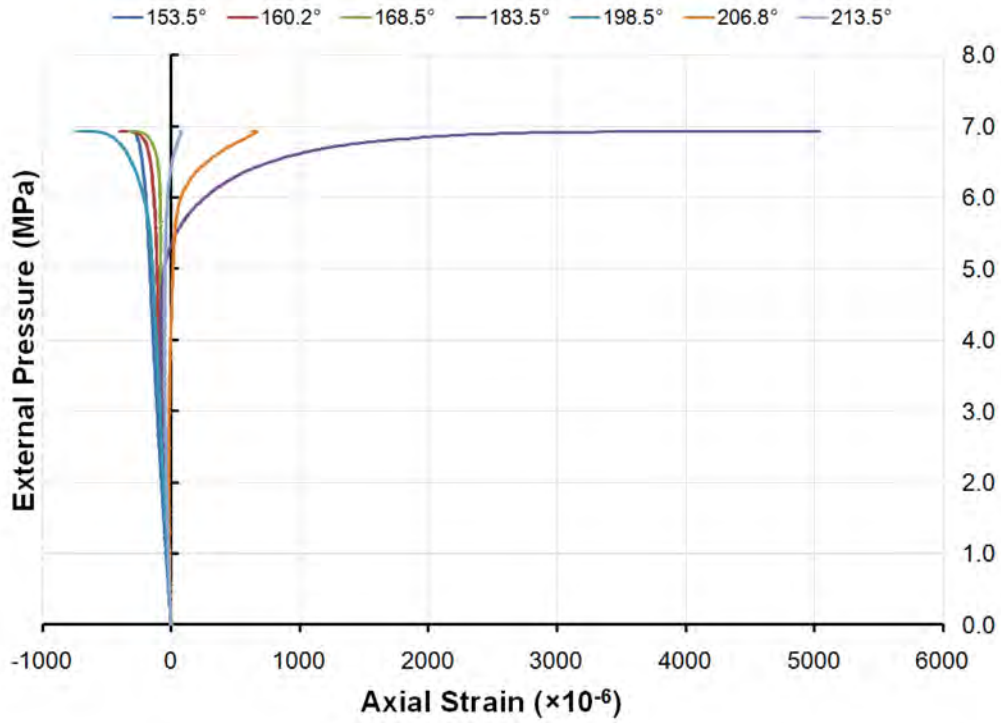

Figure 251: Pressure-strain curves showing axial shell strains mid-way between frames inside Bay 4 of specimen L510-No20

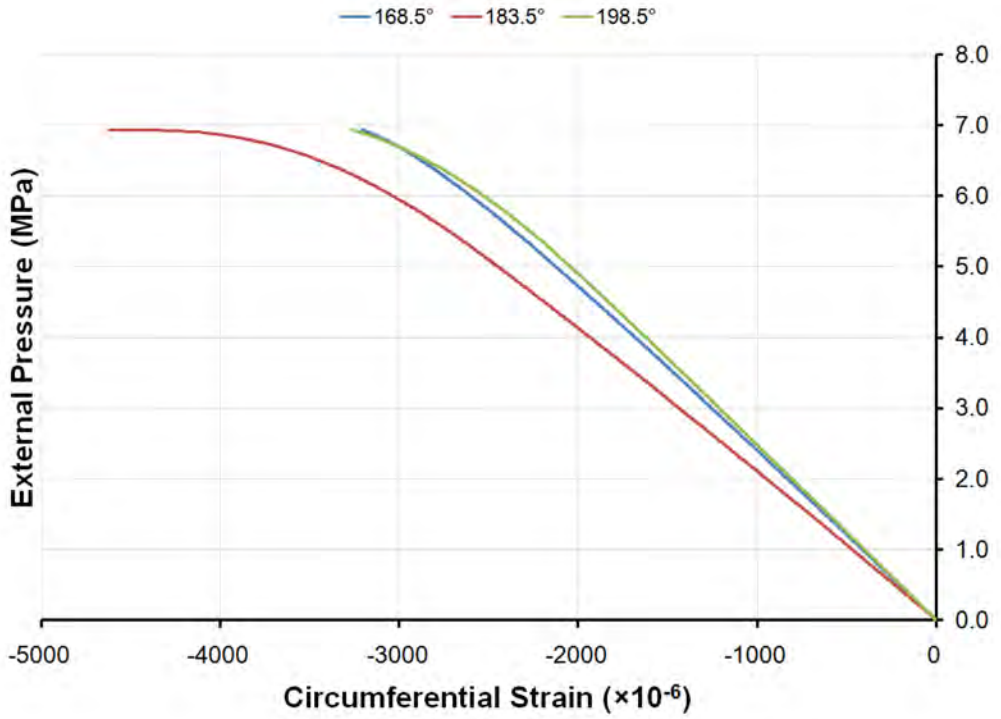

Figure 252: Pressure-strain curves showing circumferential shell strains outside Frame 4 of specimen L510-No20

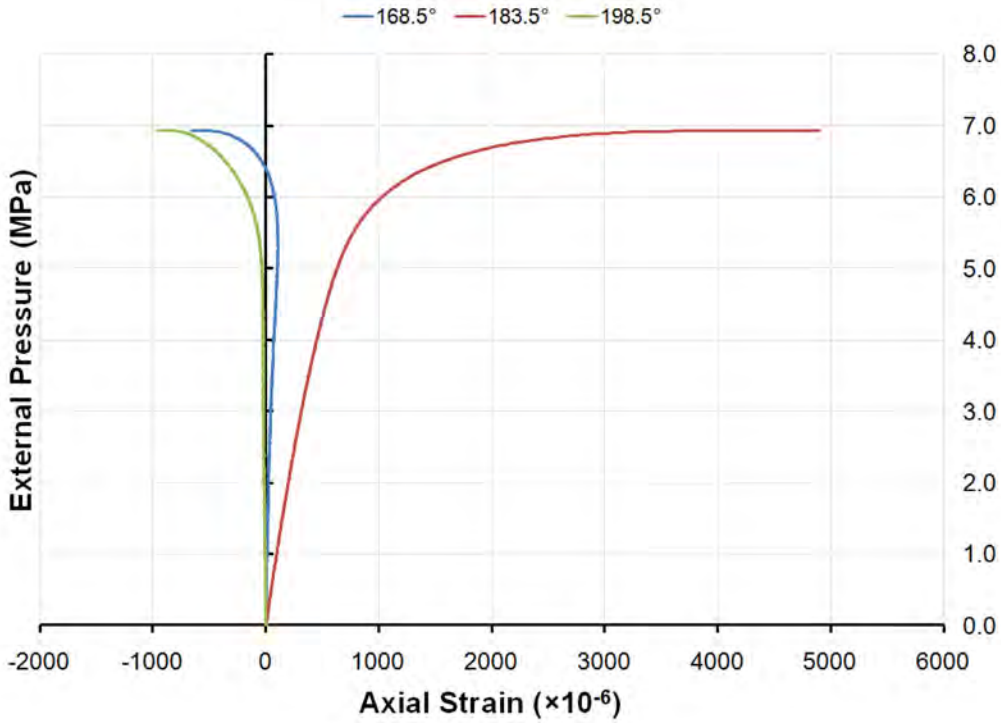

Figure 253: Pressure-strain curves showing axial shell strains outside Frame 4 of specimen L510-No20

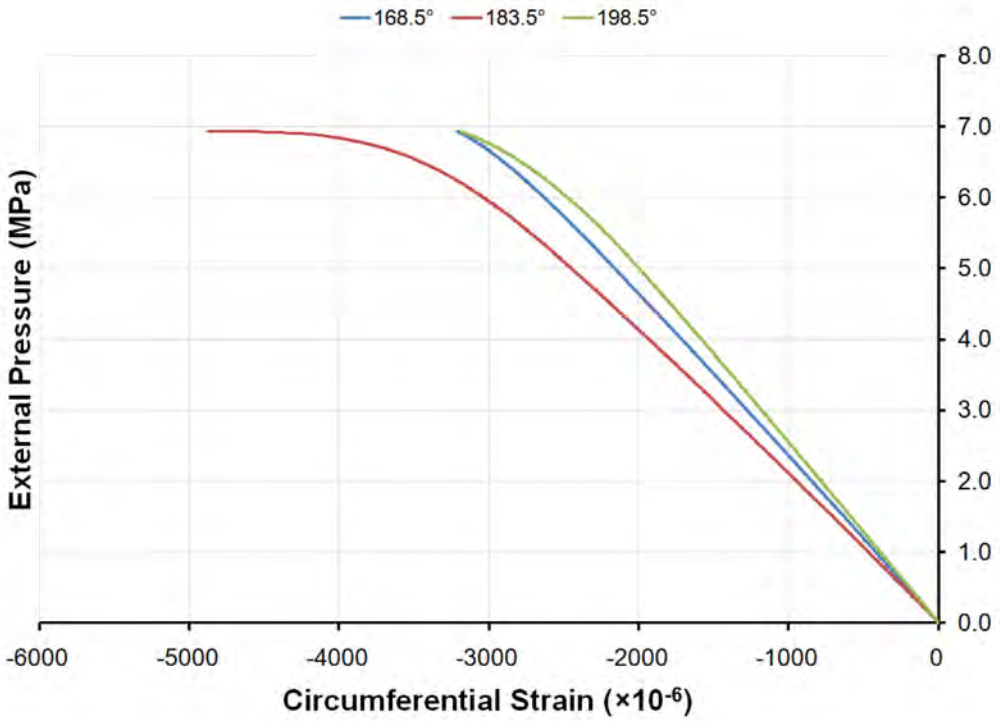

Figure 254: Pressure-strain curves showing circumferential shell strains outside Frame 5 of specimen L510-No20

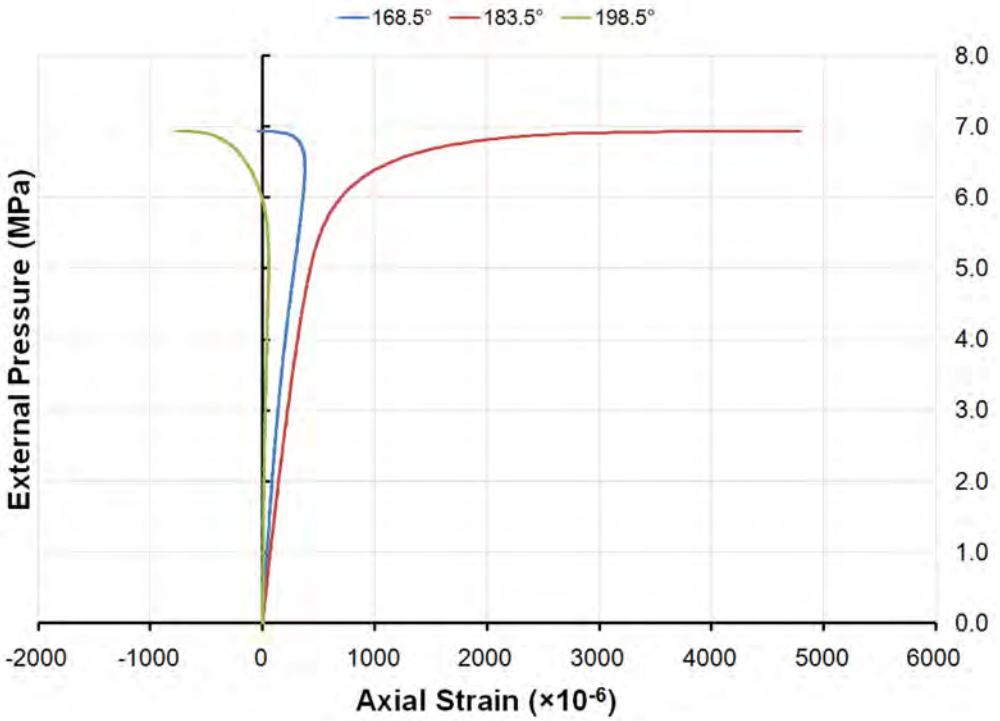

Figure 255: Pressure-strain curves showing axial shell strains outside Frame 5 of specimen L510-No20

H.7 L510-No25

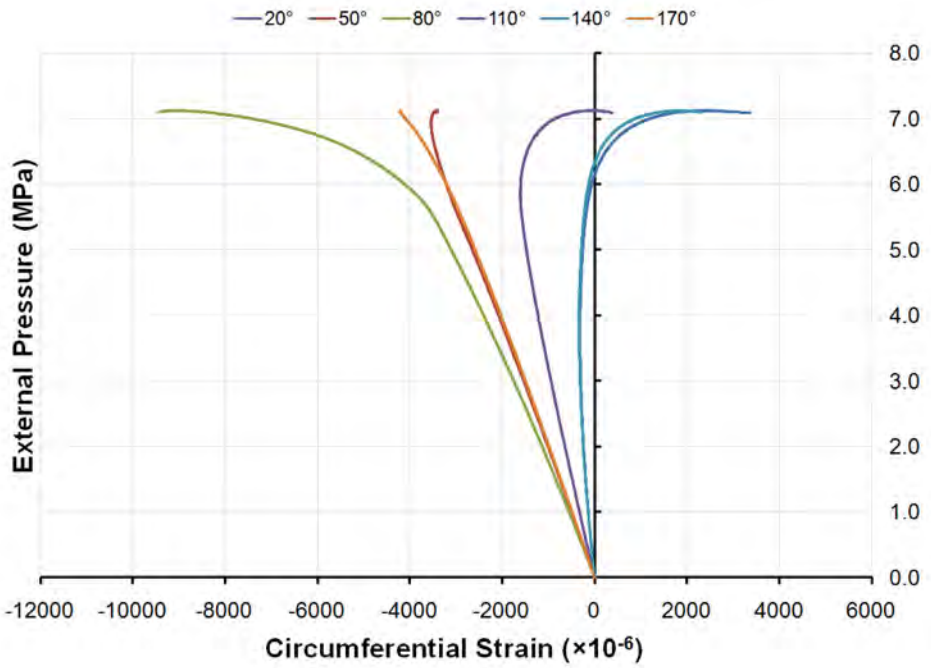

Figure 256: Pressure-strain curves showing circumferential strains at the flange of Frame 4 of specimen L510-No25 (20°-170°)

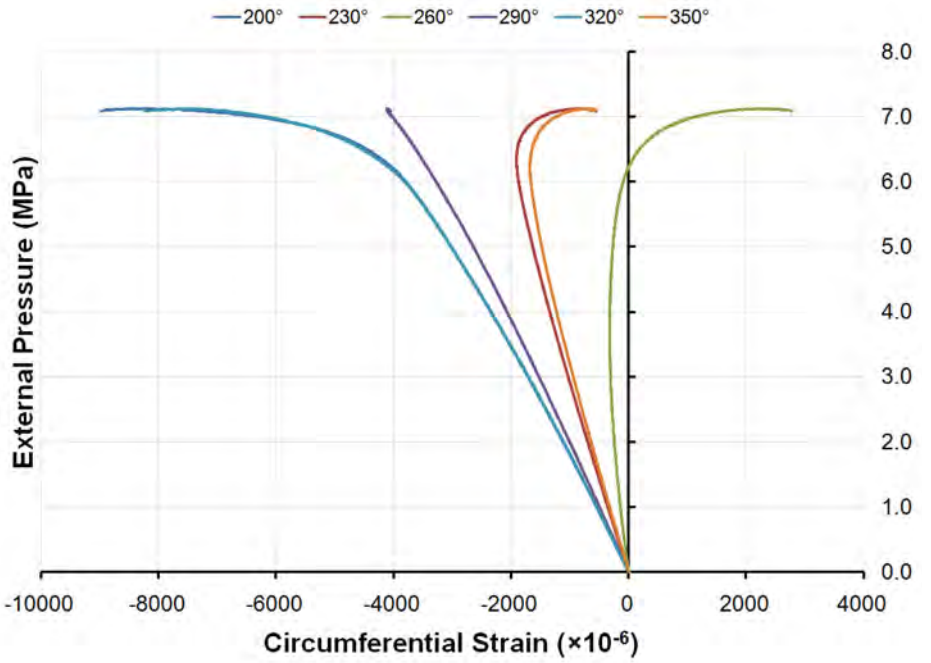

Figure 257: Pressure-strain curves showing circumferential strains at the flange of Frame 4 of specimen L510-No25 (200°-350°)

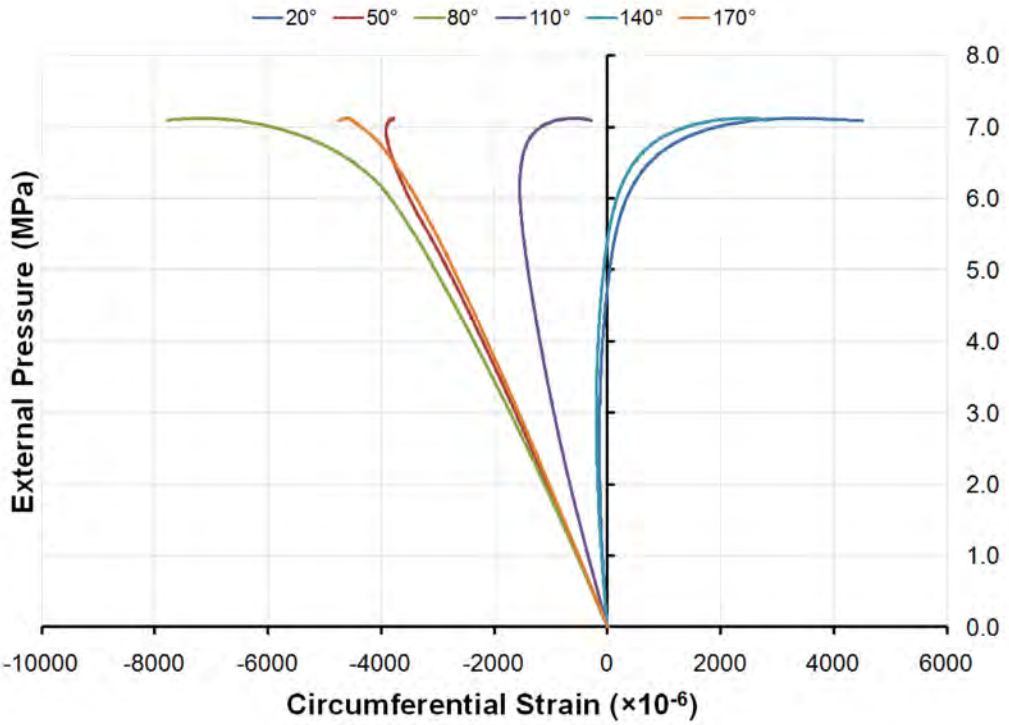

Figure 258: Pressure-strain curves showing circumferential strains at the flange of Frame 5 of specimen L510-No25 (20°-170°)

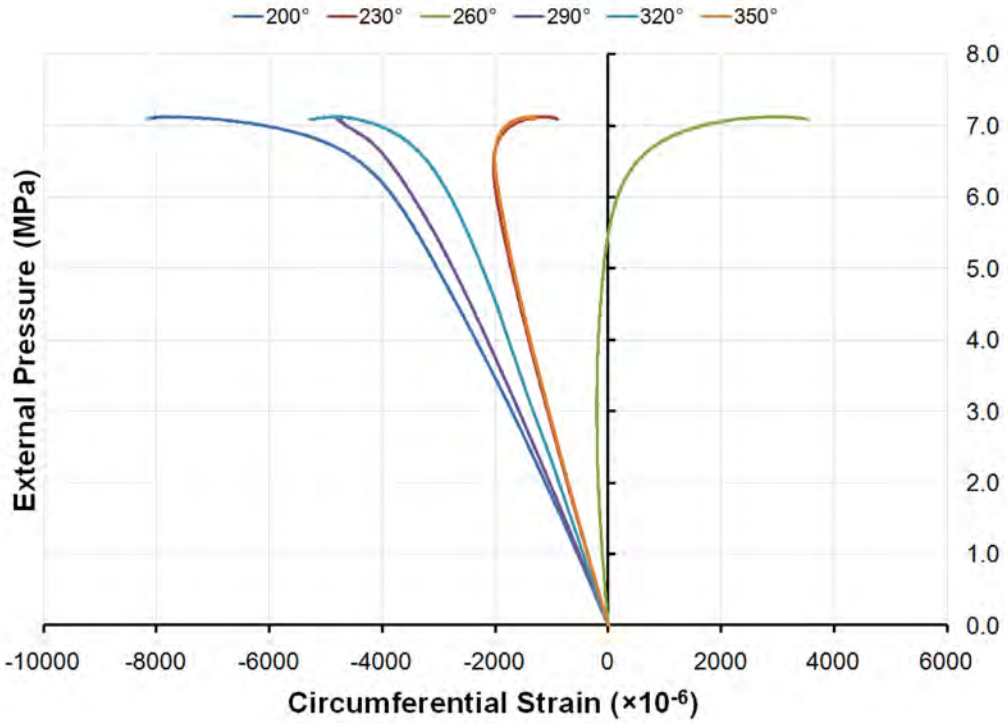

Figure 259: Pressure-strain curves showing circumferential strains at the flange of Frame 5 of specimen L510-No25 (200°-350°)

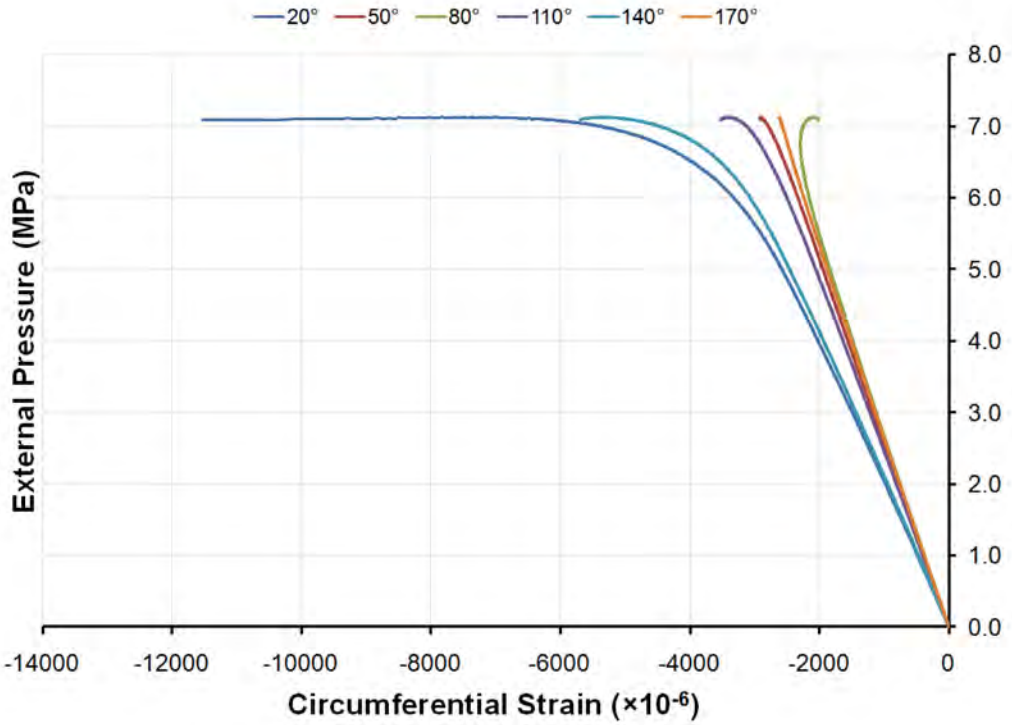

Figure 260: Pressure-strain curves showing circumferential shell strains mid-way between frames outside Bay 4 of specimen L510-No25 (20°-170°)

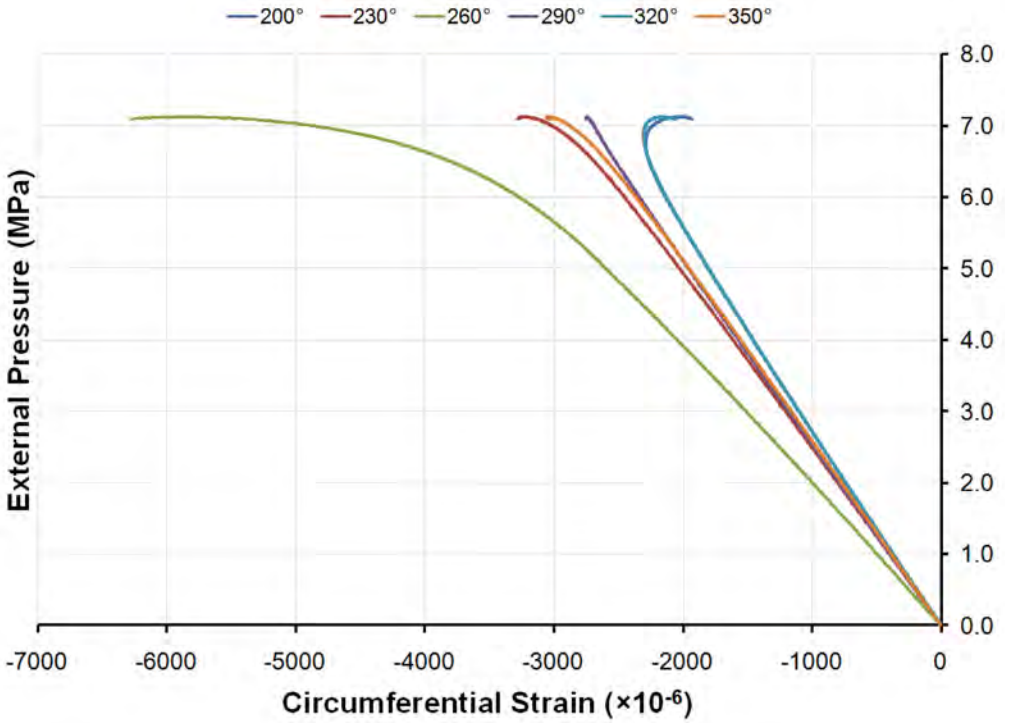

Figure 261: Pressure-strain curves showing circumferential shell strains mid-way between frames outside Bay 4 of specimen L510-No25 (200°-350°)

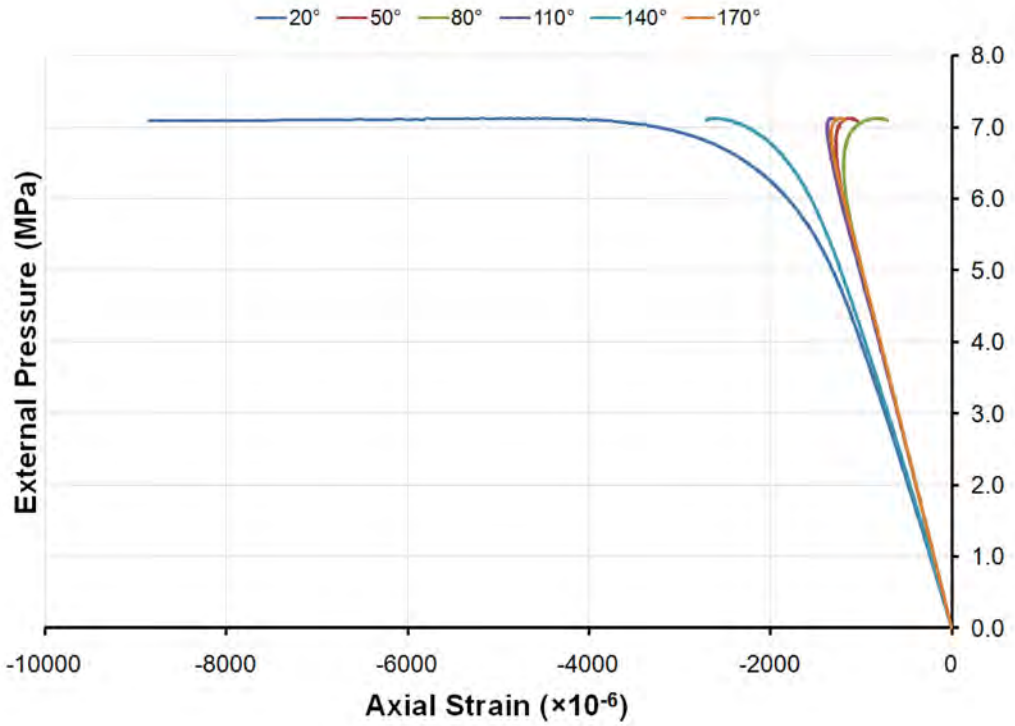

Figure 262: Pressure-strain curves showing axial shell strains mid-way between frames outside Bay 4 of specimen L510-No25 (20°-170°)

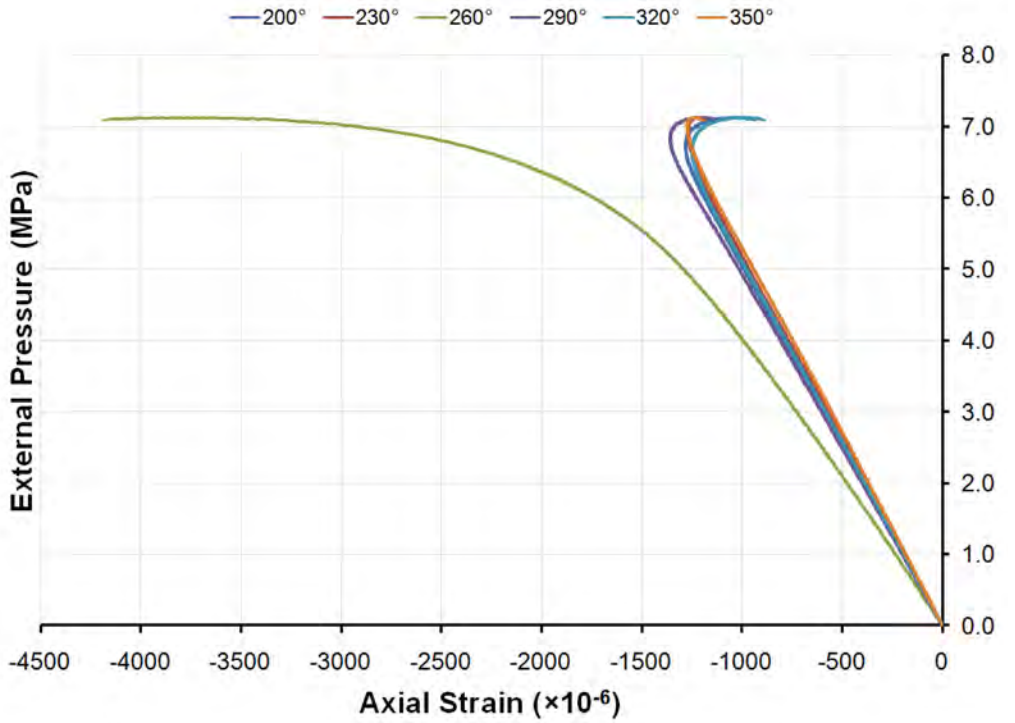

Figure 263: Pressure-strain curves showing axial shell strains mid-way between frames outside Bay 4 of specimen L510-No25 (200°-350°)

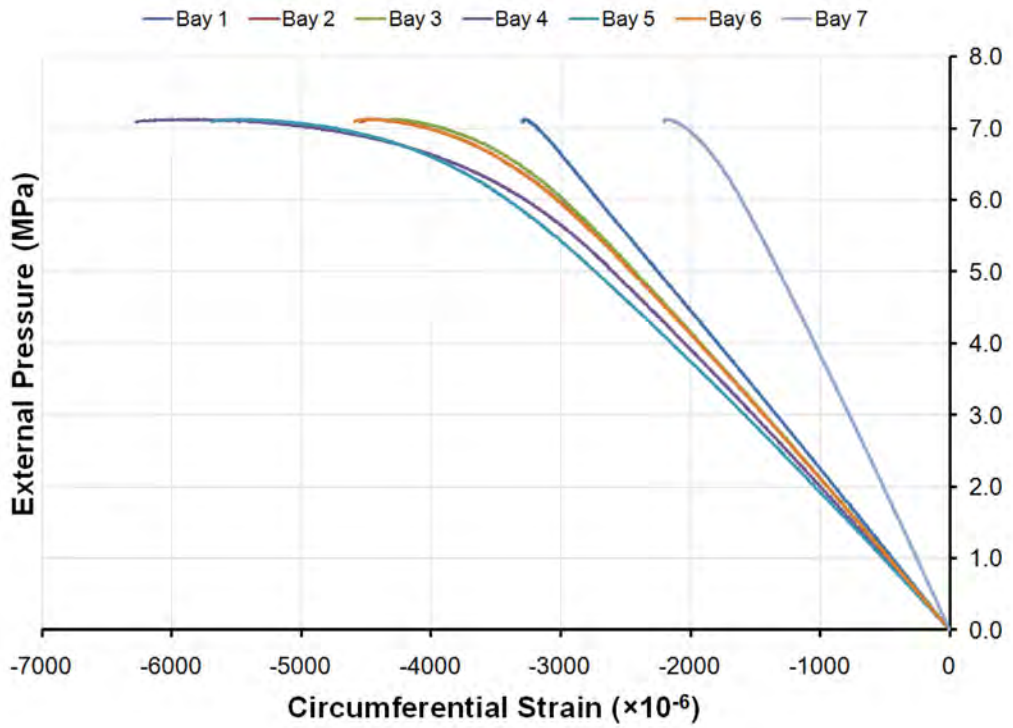

Figure 264: Pressure-strain curves showing circumferential shell strains mid-way between frames outside Bays 1 to 7 of specimen L510-No25 at 260°

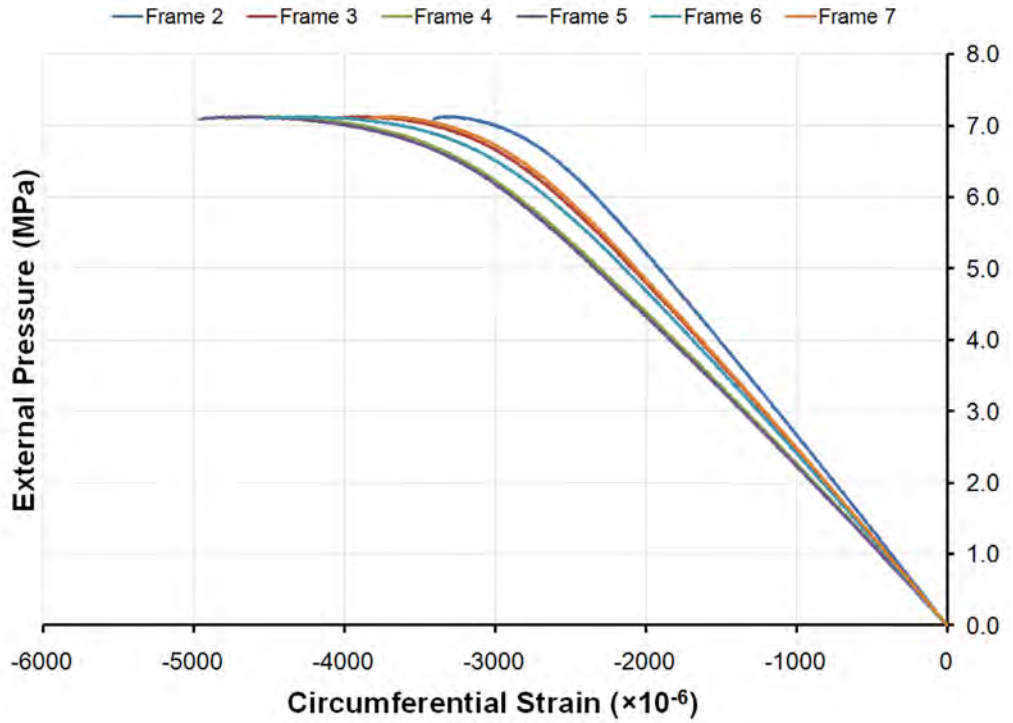

Figure 265: Pressure-strain curves showing circumferential shell strains outside Frames 2 to 7 of specimen L510-No25 at 260°

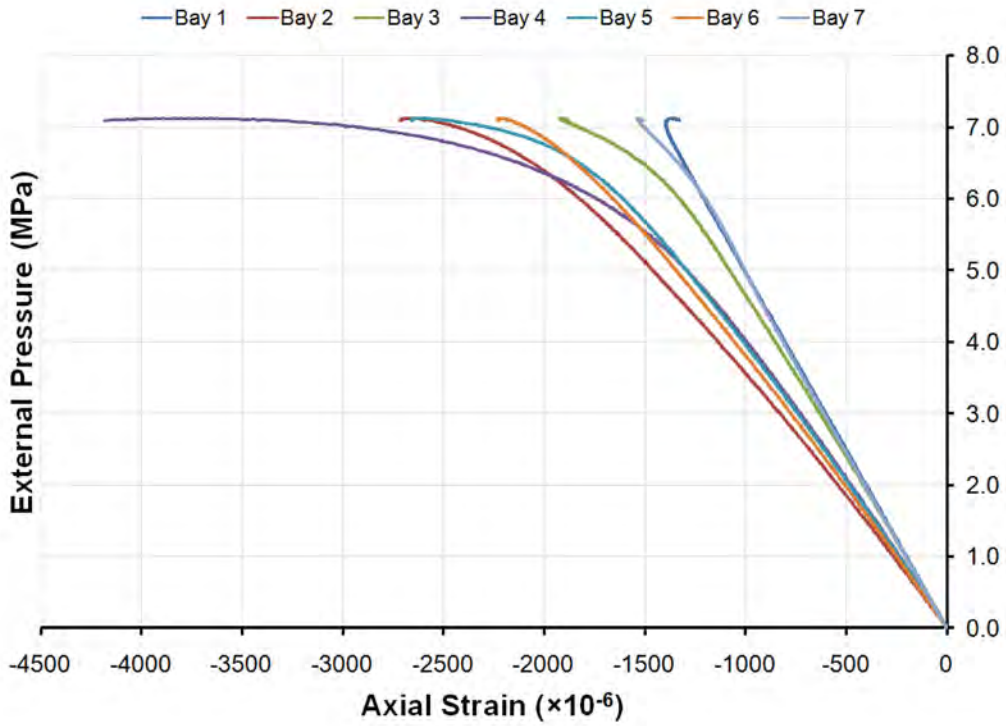

Figure 266: Pressure-strain curves showing axial shell strains mid-way between frames outside Bays 1 to 7 of specimen L510-No25 at 260°

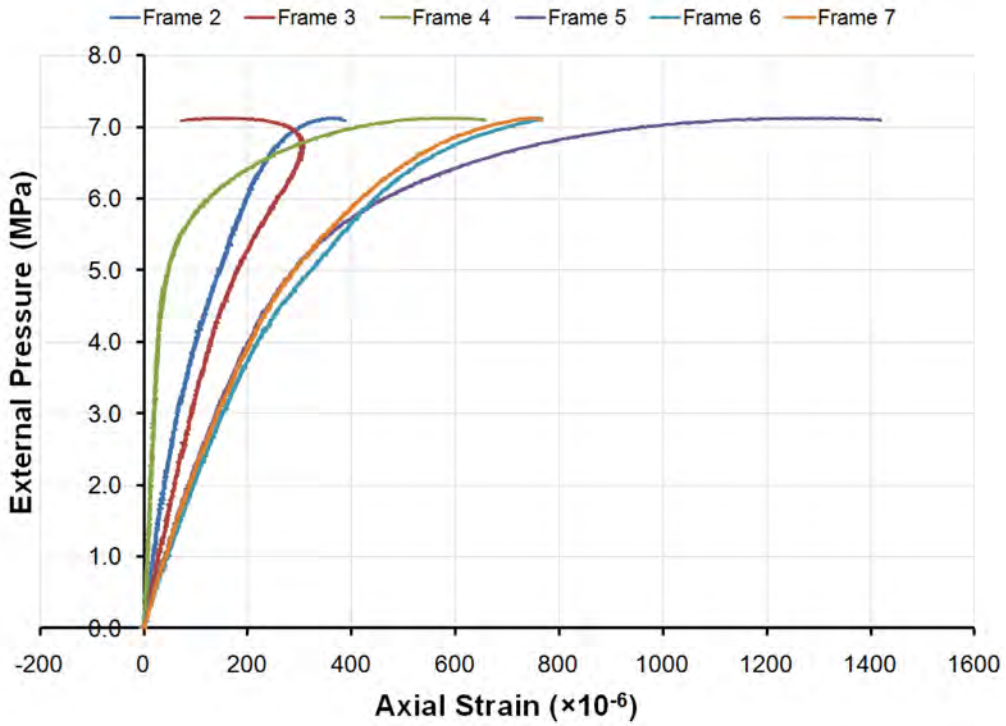

Figure 267: Pressure-strain curves showing axial shell strains outside Frames 2 to 7 of specimen L510-No25 at 260°

H.8 L510-No26

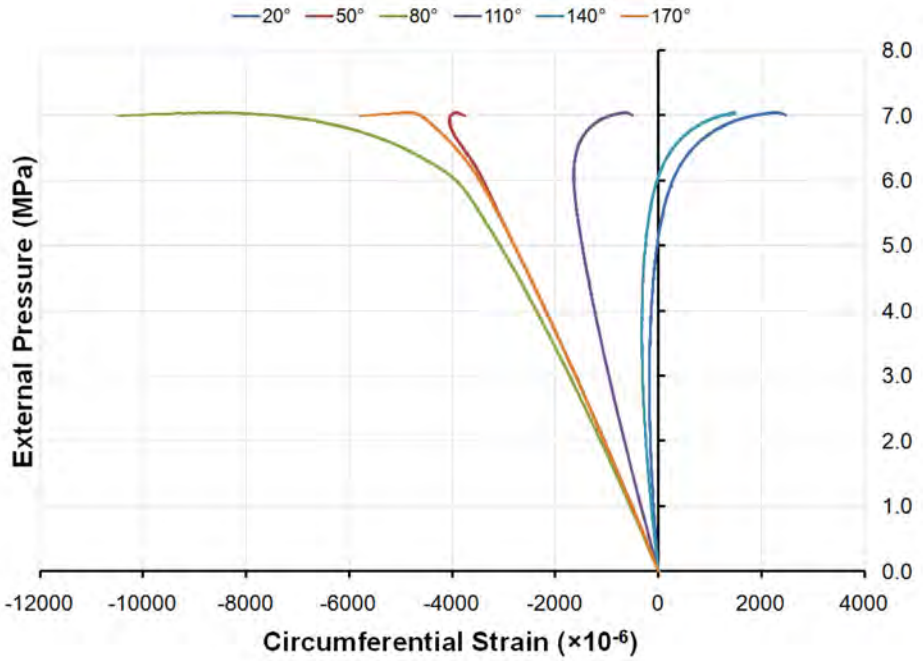

Figure 268: Pressure-strain curves showing circumferential strains at the flange of Frame 4 of specimen L510-No26 (20°-170°)

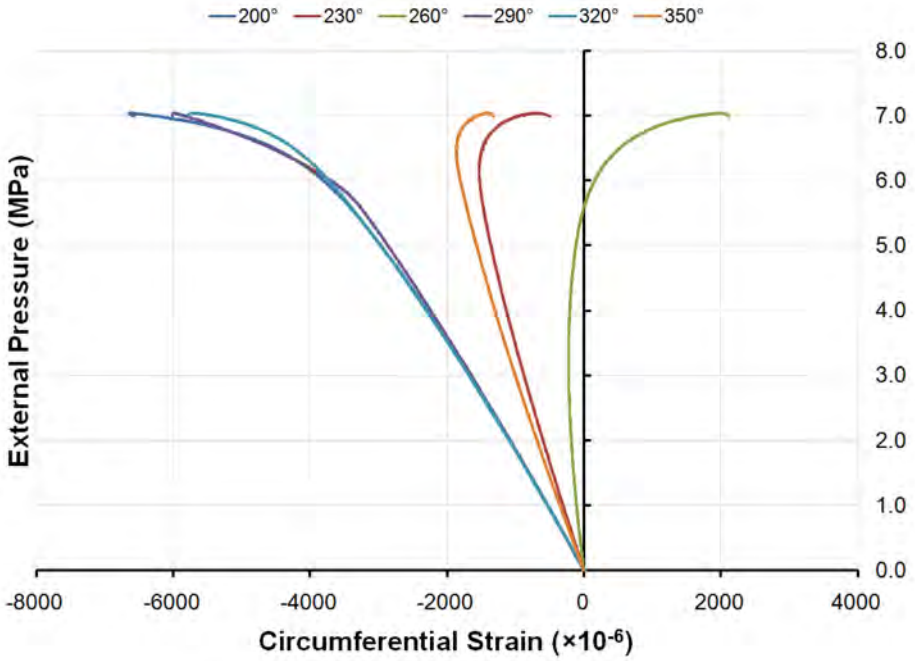

Figure 269: Pressure-strain curves showing circumferential strains at the flange of Frame 4 of specimen L510-No26 (200°-350°)

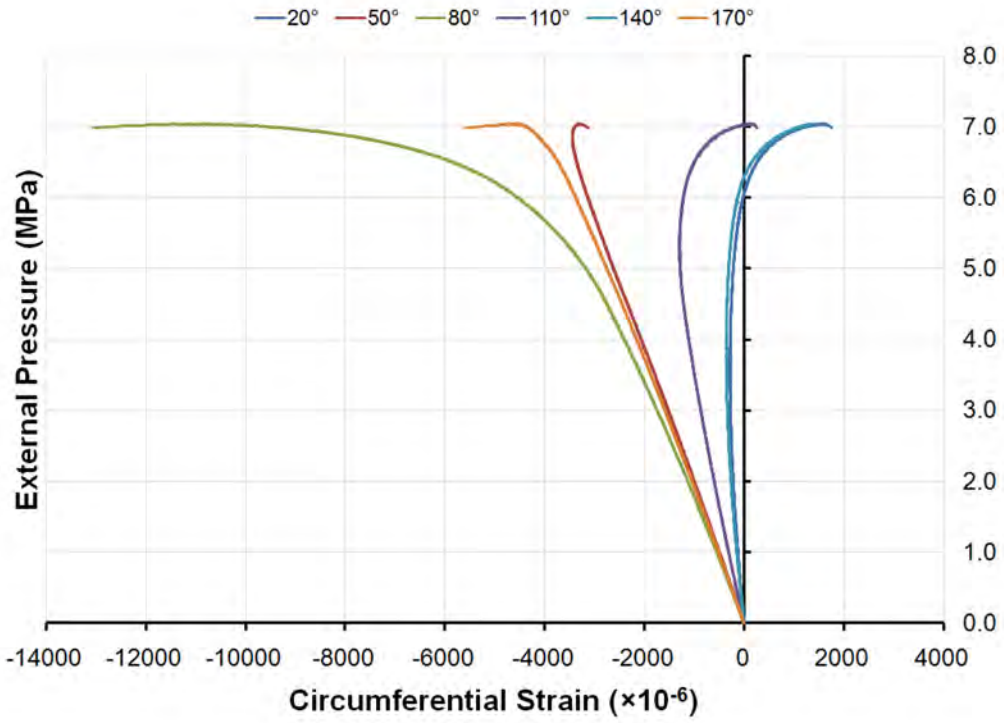

Figure 270: Pressure-strain curves showing circumferential strains at the flange of Frame 5 of specimen L510-No26 (20°-170°)

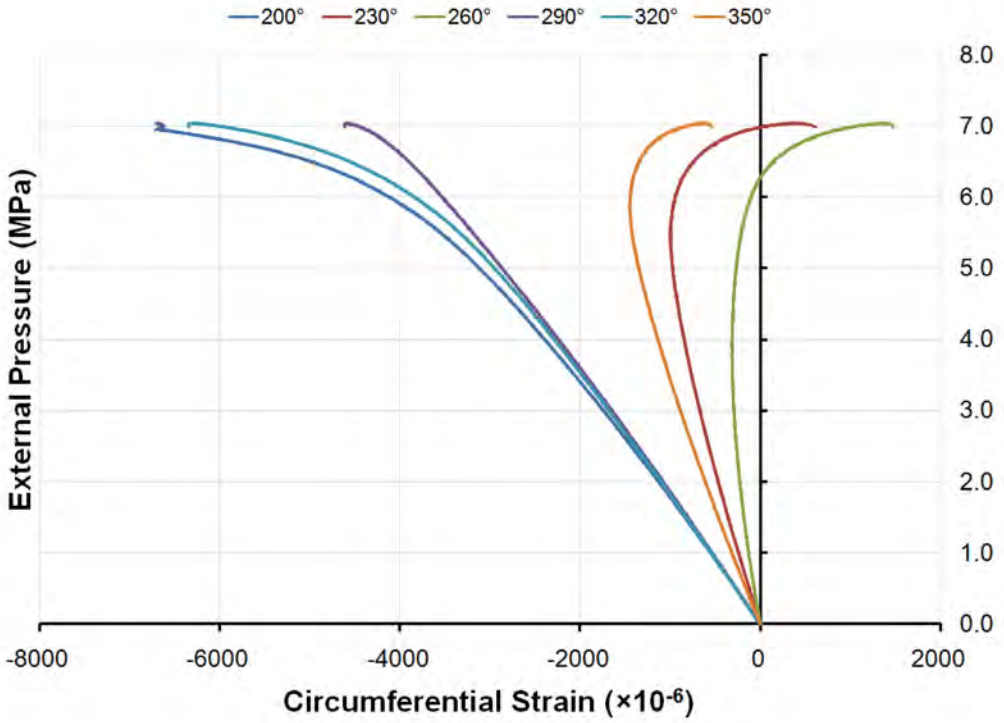

Figure 271: Pressure-strain curves showing circumferential strains at the flange of Frame 5 of specimen L510-No26 (200°-350°)

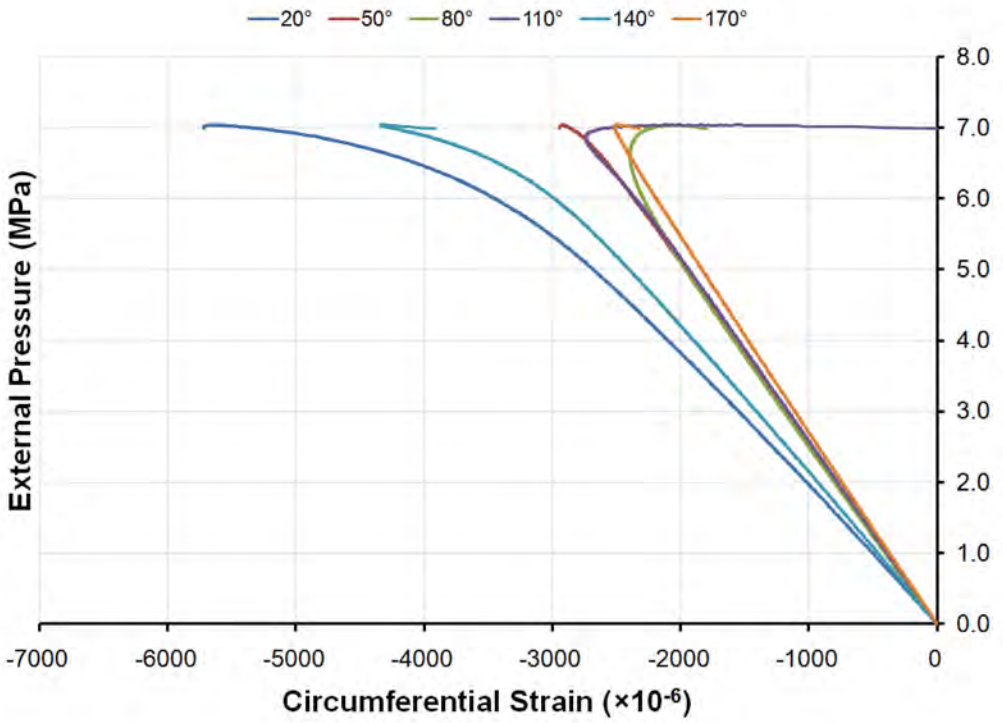

Figure 272: Pressure-strain curves showing circumferential shell strains mid-way between frames outside Bay 4 of specimen L510-No26 (20°-170°)

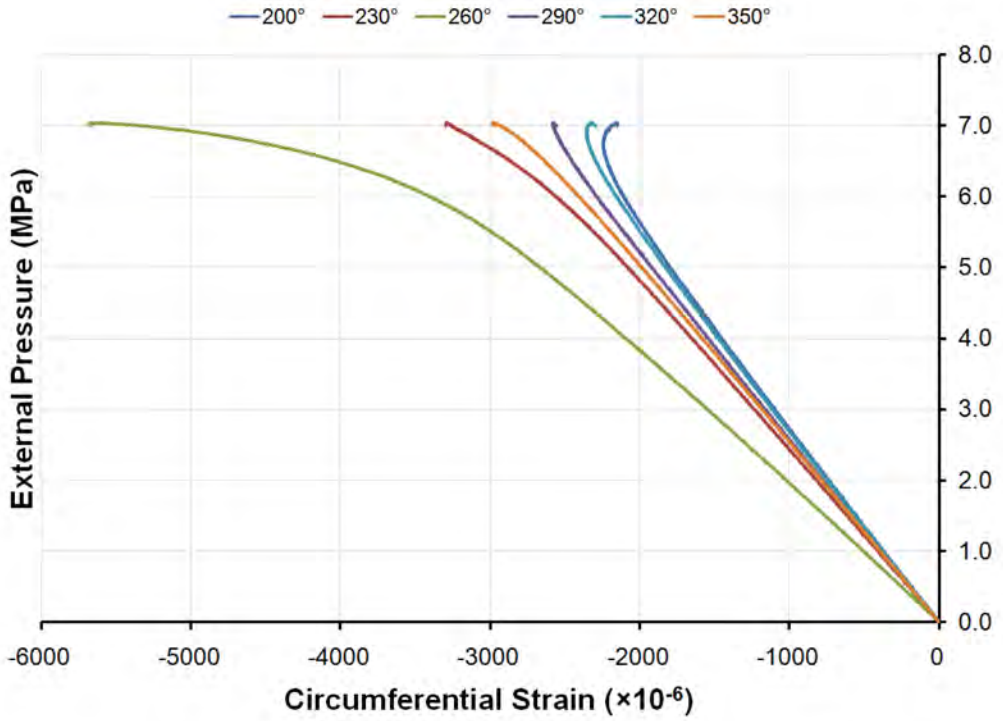

Figure 273: Pressure-strain curves showing circumferential shell strains mid-way between frames outside Bay 4 of specimen L510-No26 (200°-350°)

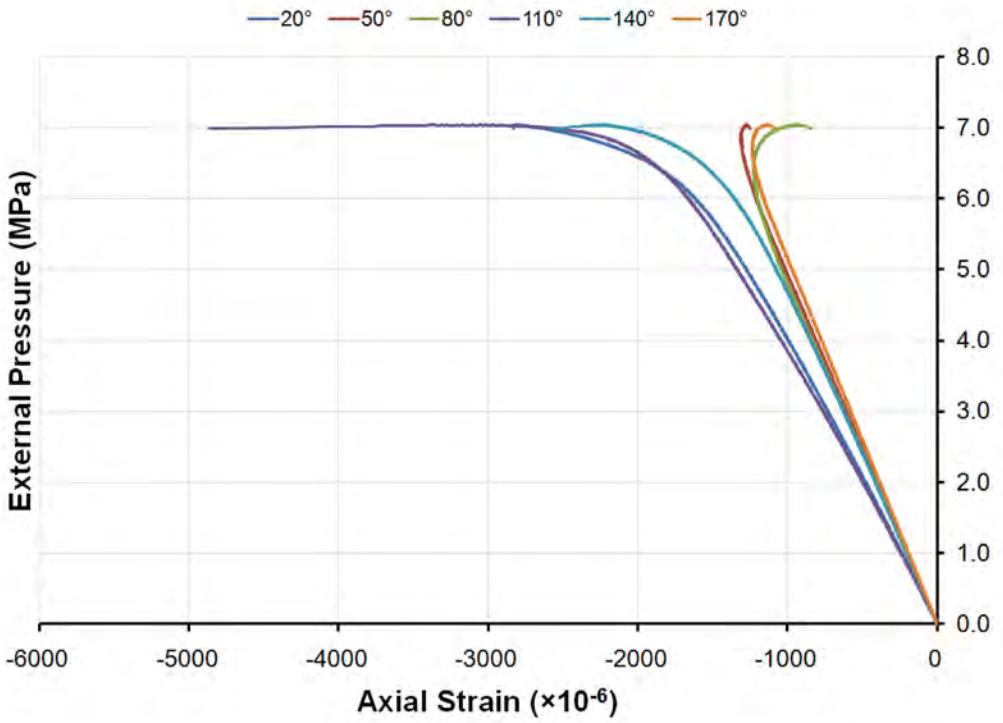

Figure 274: Pressure-strain curves showing axial shell strains mid-way between frames outside Bay 4 of specimen L510-No26 (20°-170°)

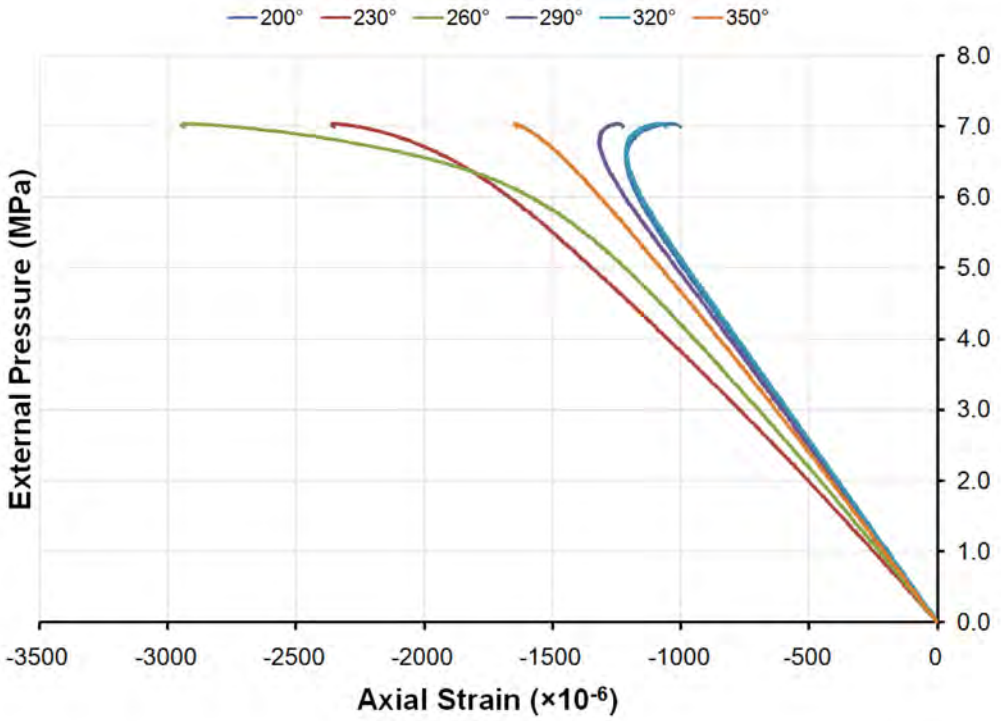

Figure 275: Pressure-strain curves showing axial shell strains mid-way between frames outside Bay 4 of specimen L510-No26 (200°-350°)

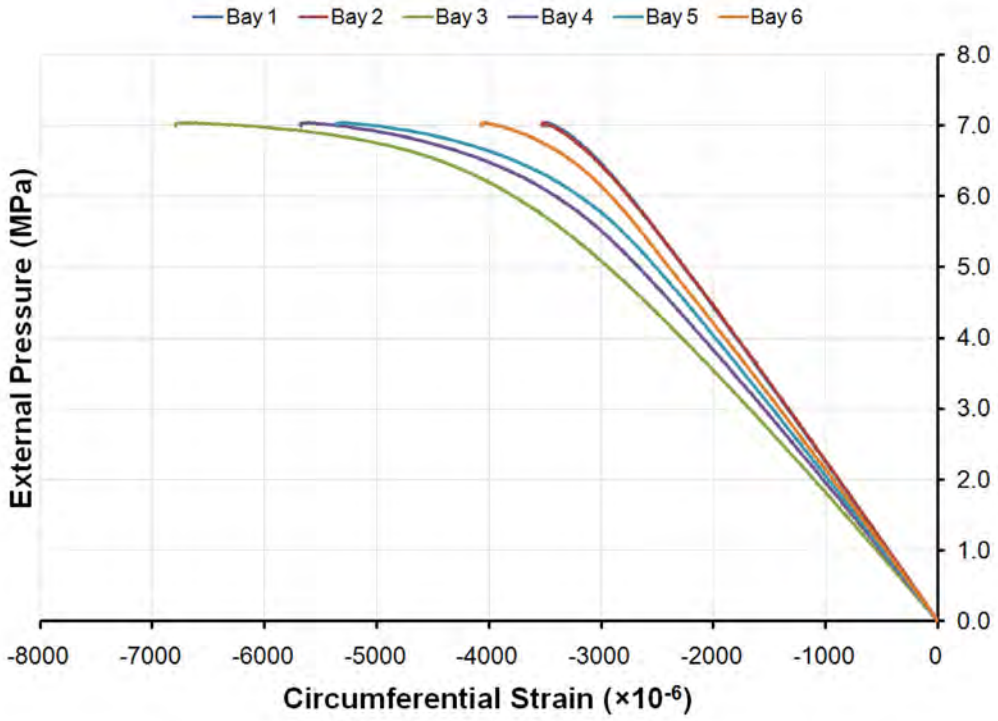

Figure 276: Pressure-strain curves showing circumferential shell strains mid-way between frames outside Bays 1 to 7 of specimen L510-No26 at 260°

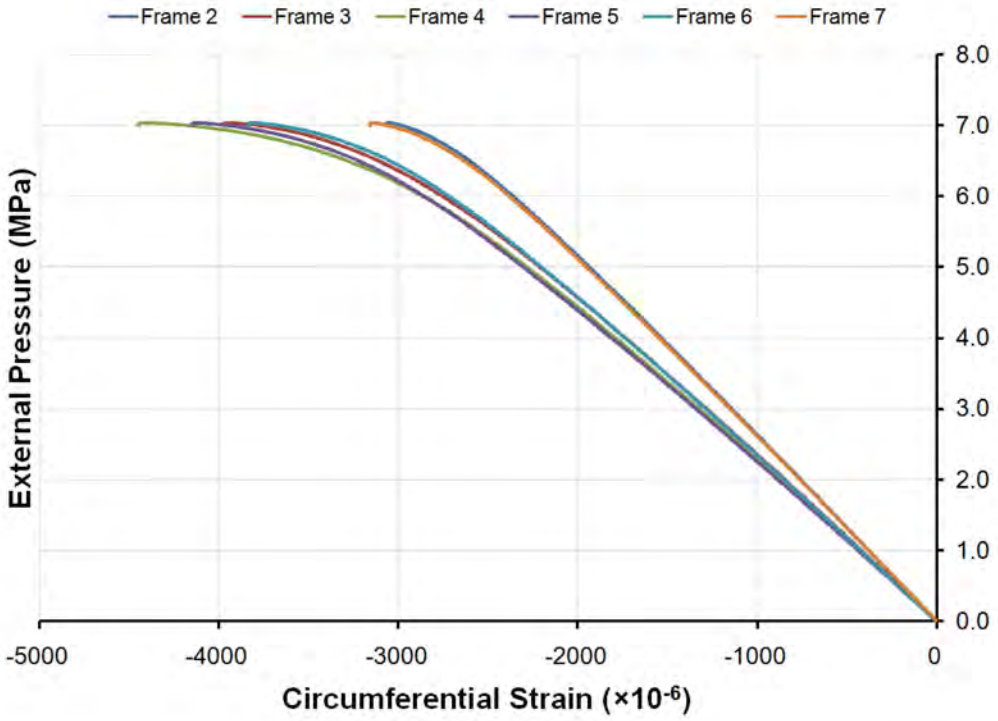

Figure 277: Pressure-strain curves showing circumferential shell strains outside Frames 2 to 7 of specimen L510-No26 at 260°

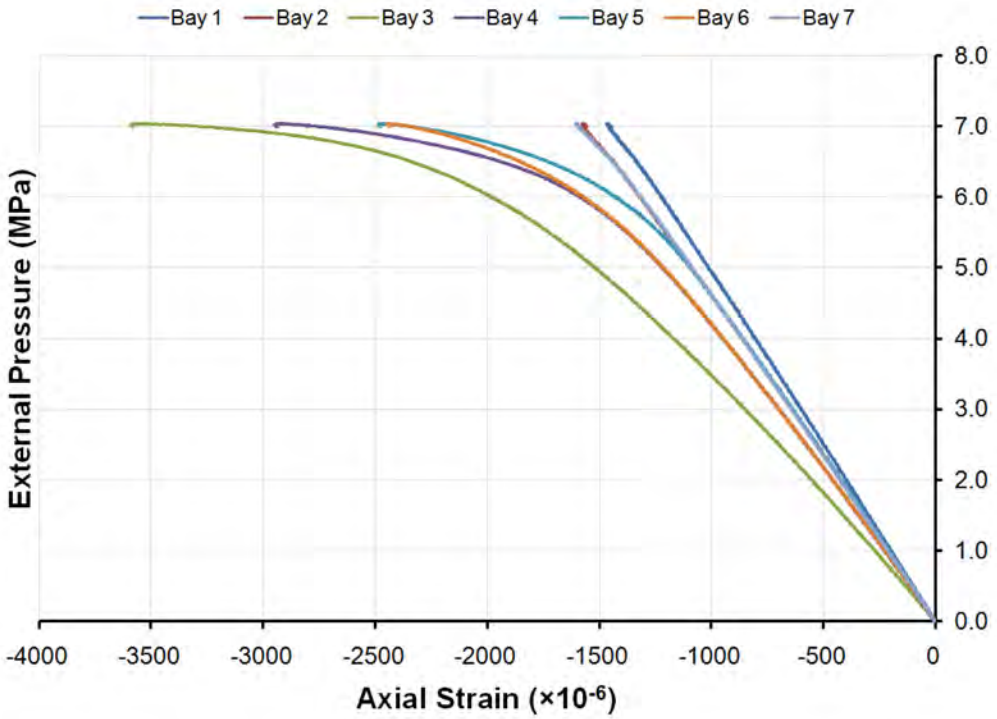

Figure 278: Pressure-strain curves showing axial shell strains mid-way between frames outside Bays 1 to 7 of specimen L510-No26 at 260°

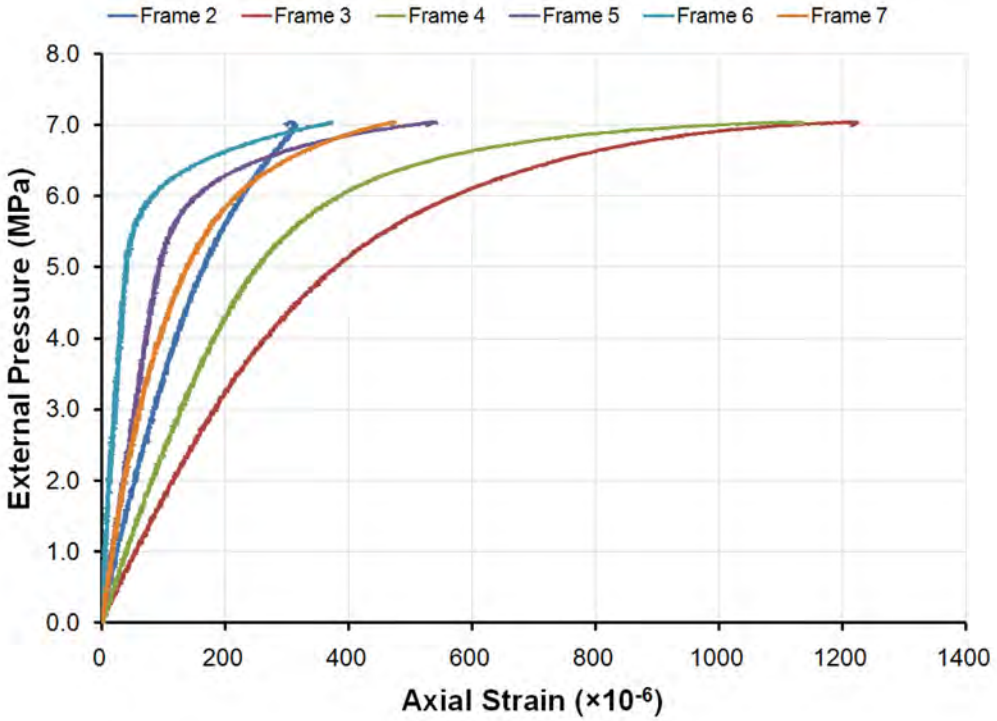

Figure 279: Pressure-strain curves showing axial shell strains outside Frames 2 to 7 of specimen L510-No26 at 260°

H.9 L510-No33

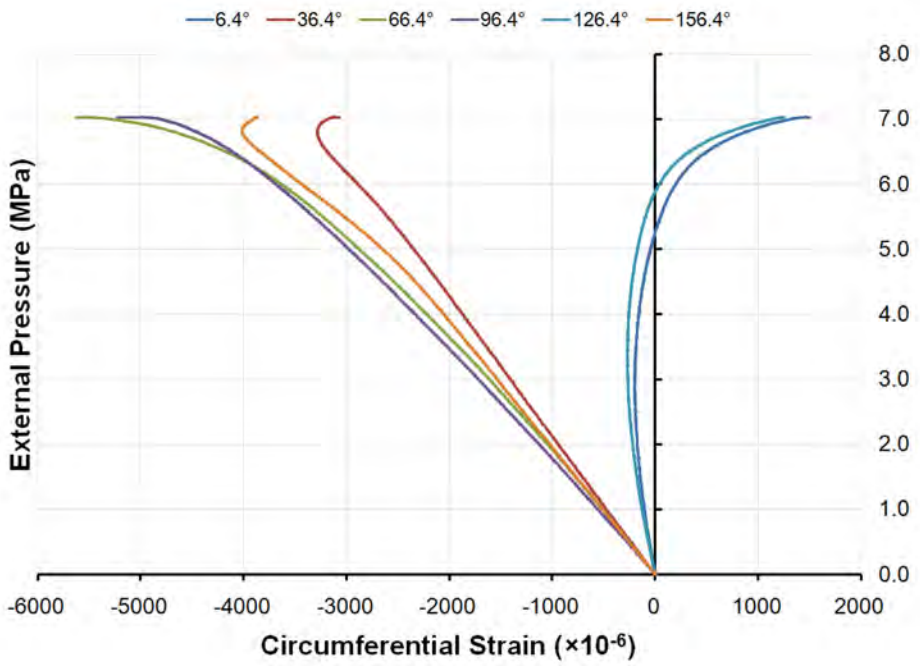

Figure 280: Pressure-strain curves showing circumferential strains at the flange of Frame 4 of specimen L510-No33 (6.4°-156.4°)

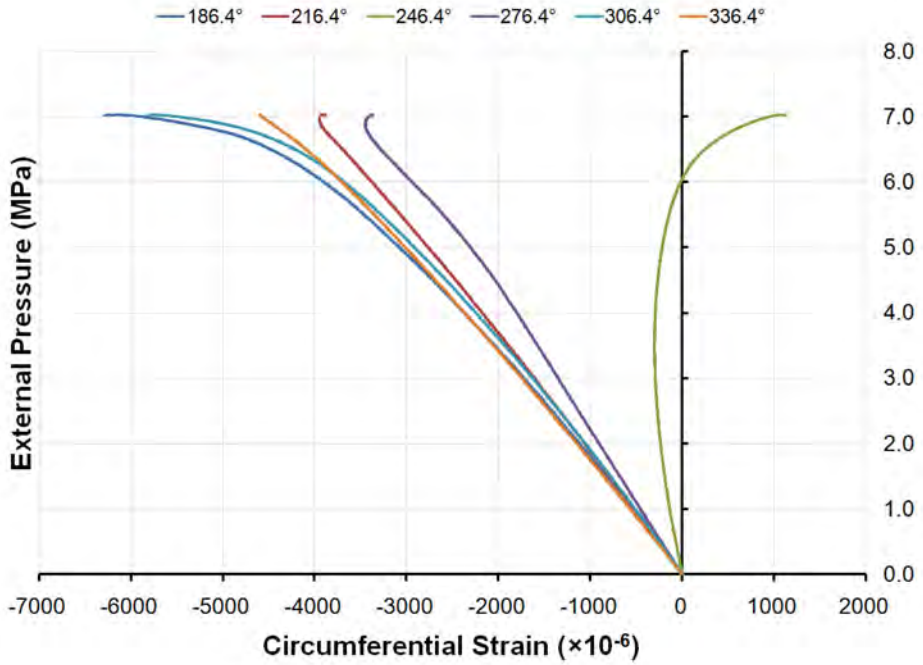

Figure 281: Pressure-strain curves showing circumferential strains at the flange of Frame 4 of specimen L510-No33 (186.4°-336.4°)

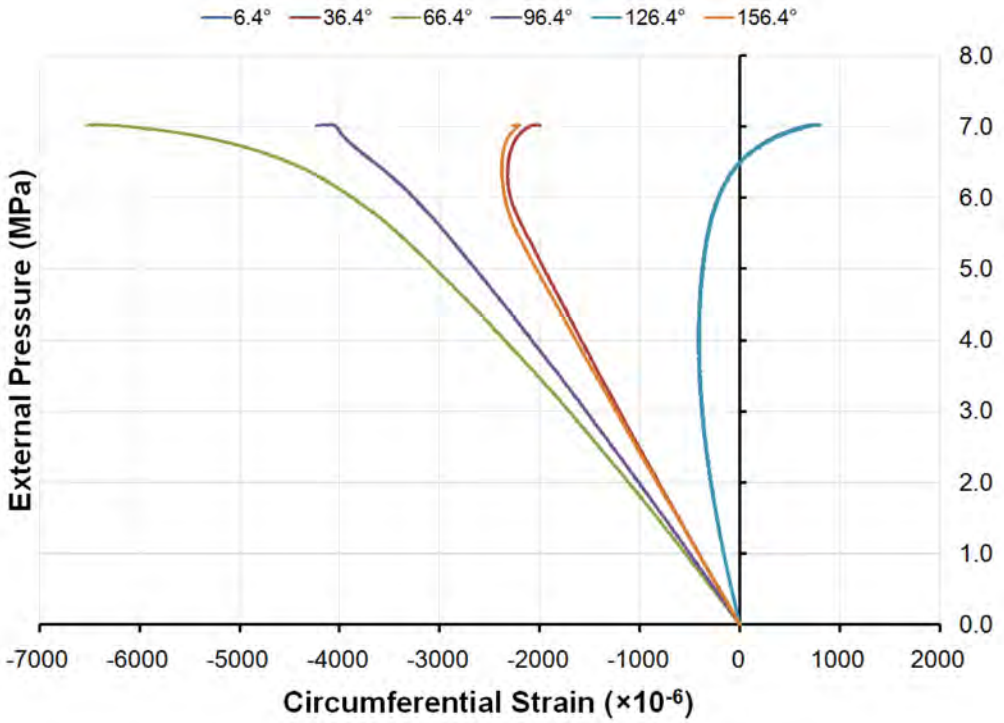

Figure 282: Pressure-strain curves showing circumferential strains at the flange of Frame 5 of specimen L510-No33 (6.4°-156.4°)

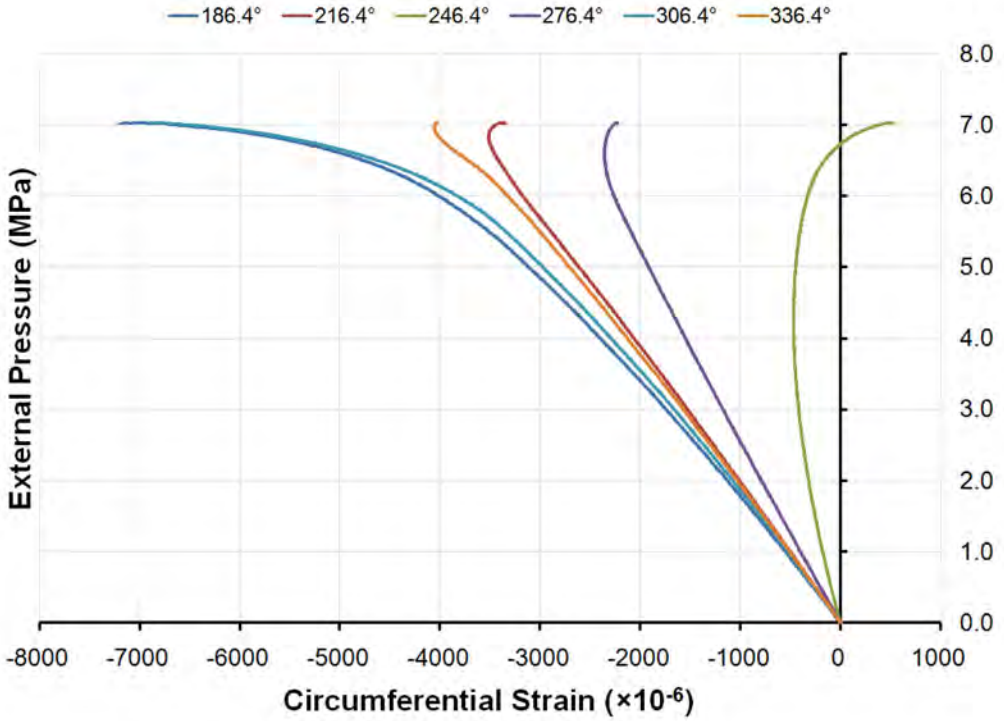

Figure 283: Pressure-strain curves showing circumferential strains at the flange of Frame 5 of specimen L510-No33 (186.4°-336.4°)

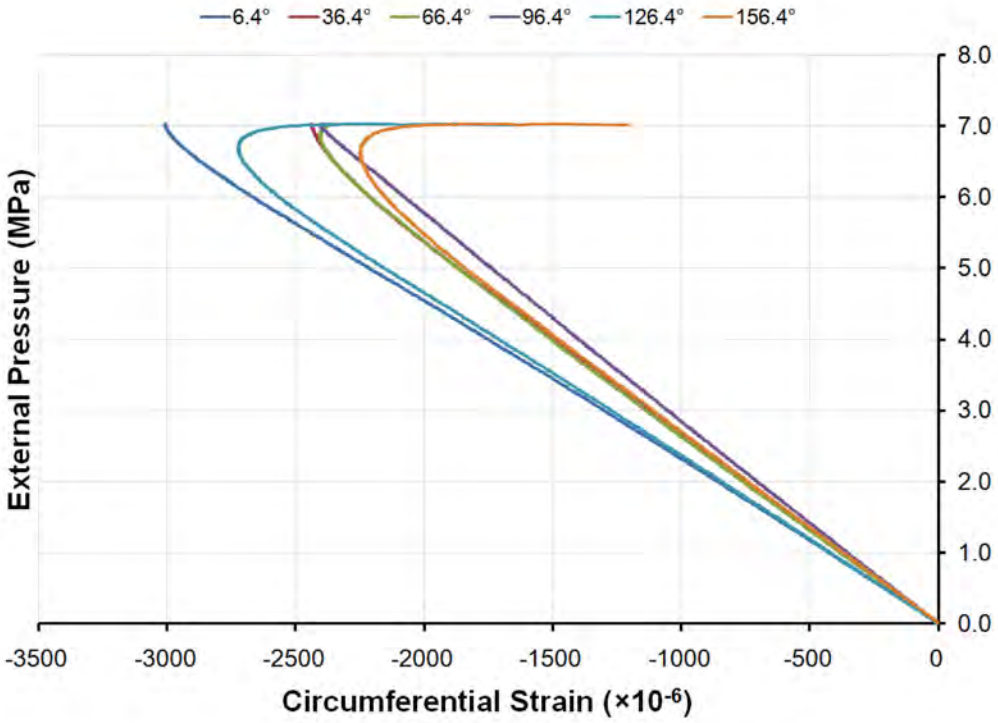

Figure 284: Pressure-strain curves showing circumferential shell strains mid-way between frames outside Bay 4 of specimen L510-No33 (6.4°-156.4°)

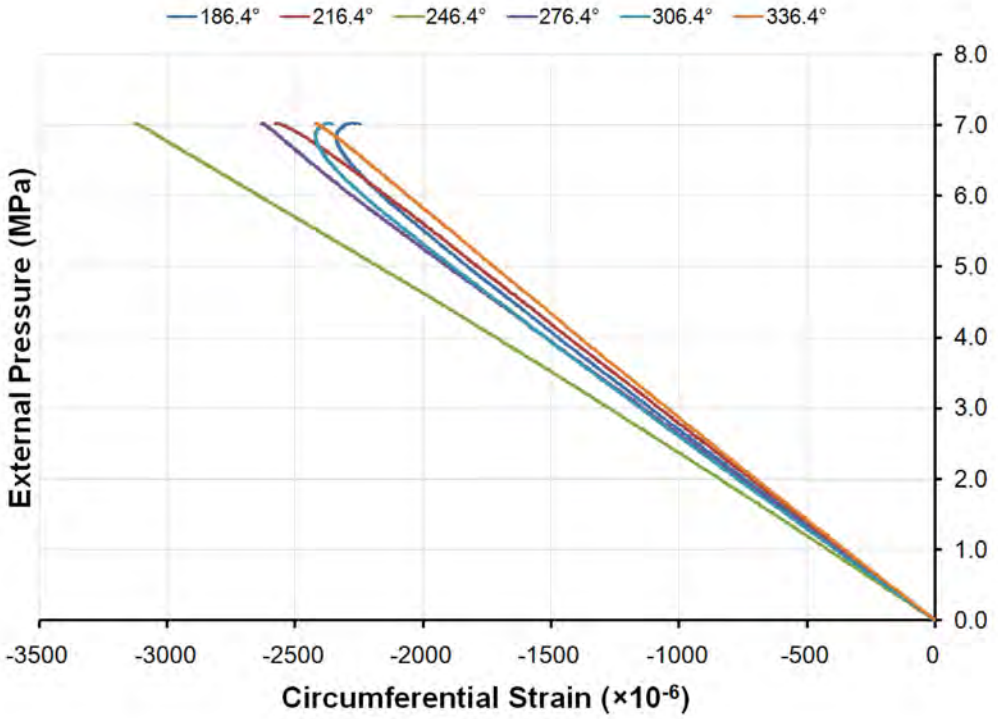

Figure 285: Pressure-strain curves showing circumferential shell strains mid-way between frames outside Bay 4 of specimen L510-No33 (186.4°-336.4°)

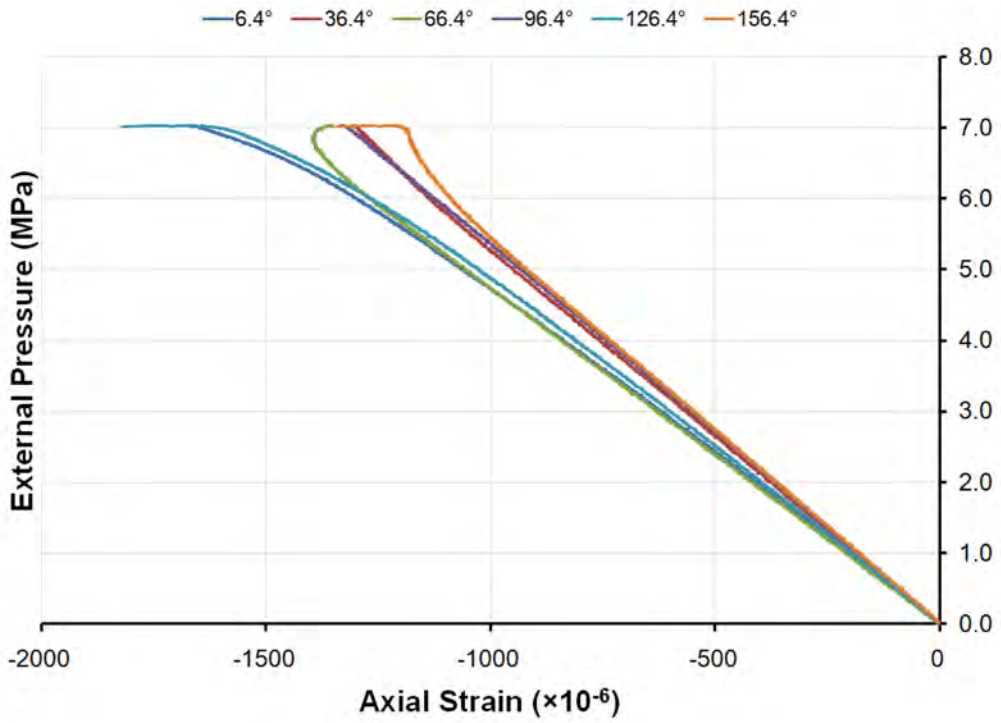

Figure 286: Pressure-strain curves showing axial shell strains mid-way between frames outside Bay 4 of specimen L510-No33 (6.4°-156.4°)

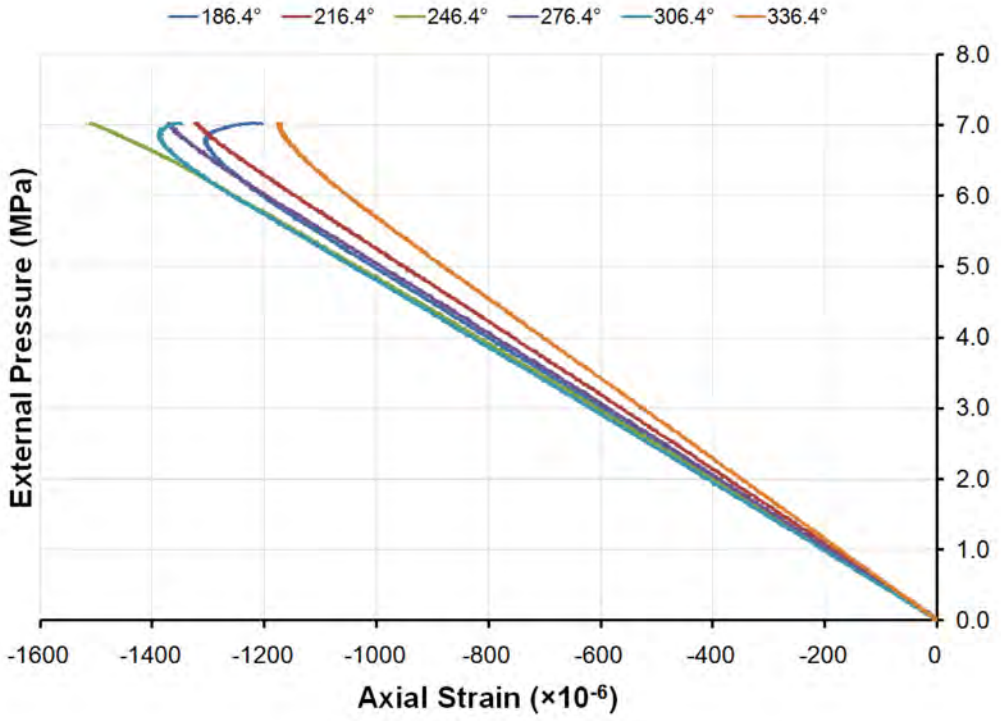

Figure 287: Pressure-strain curves showing axial shell strains mid-way between frames outside Bay 4 of specimen L510-No33 (186.4°-336.4°)

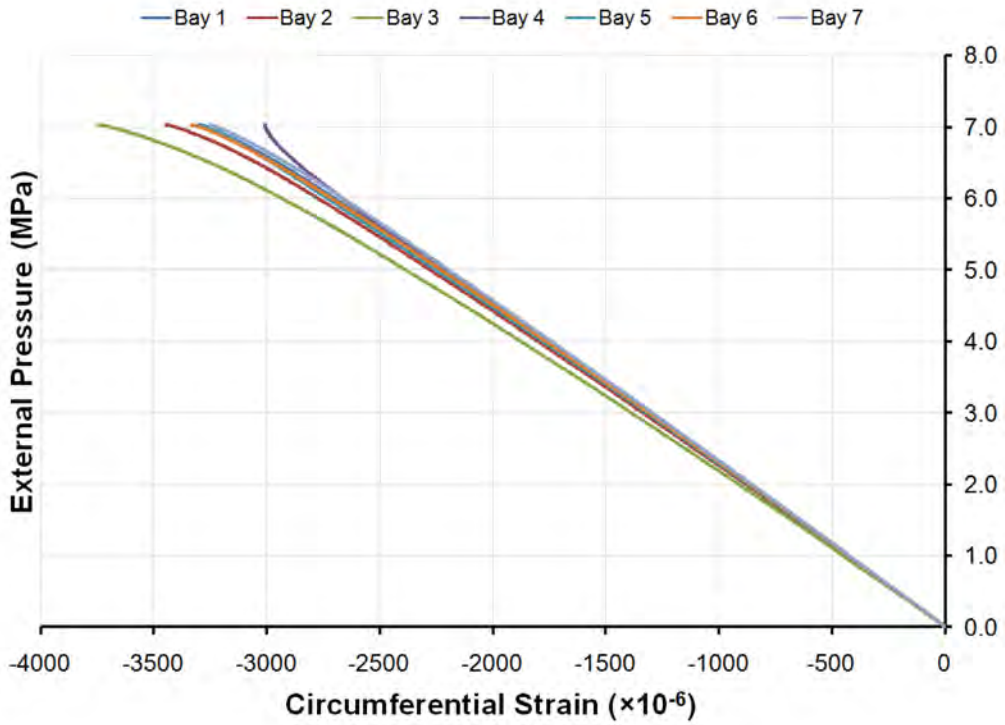

Figure 288: Pressure-strain curves showing circumferential shell strains mid-way between frames outside Bays 1 to 7 of specimen L510-No33 at 6.4°

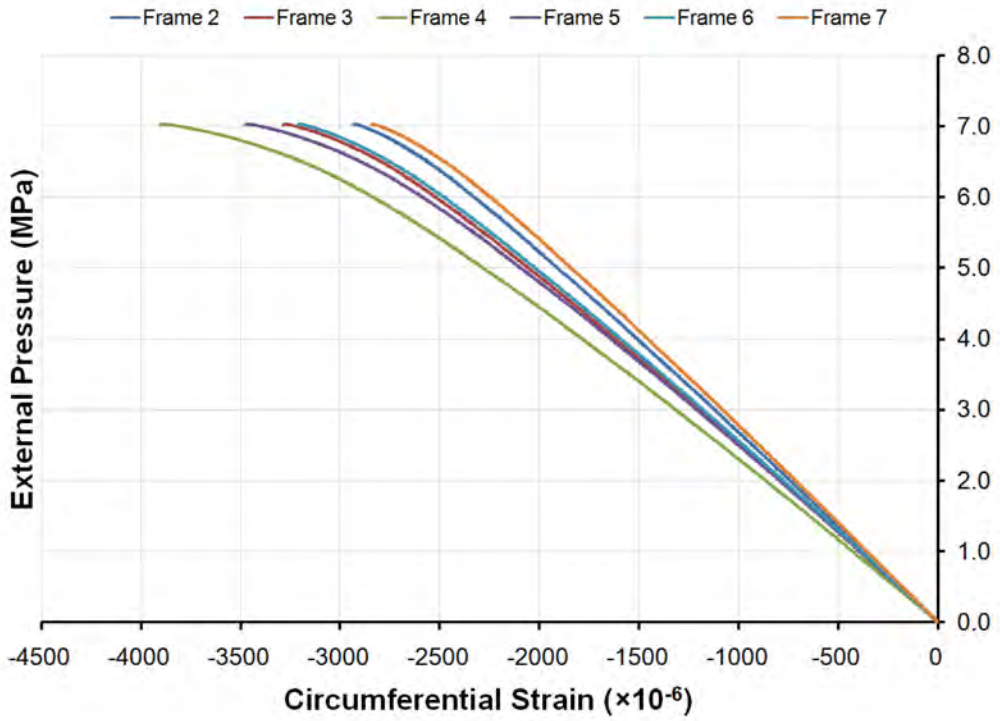

Figure 289: Pressure-strain curves showing circumferential shell strains outside Frames 2 to 7 of specimen L510-No33 at 6.4°

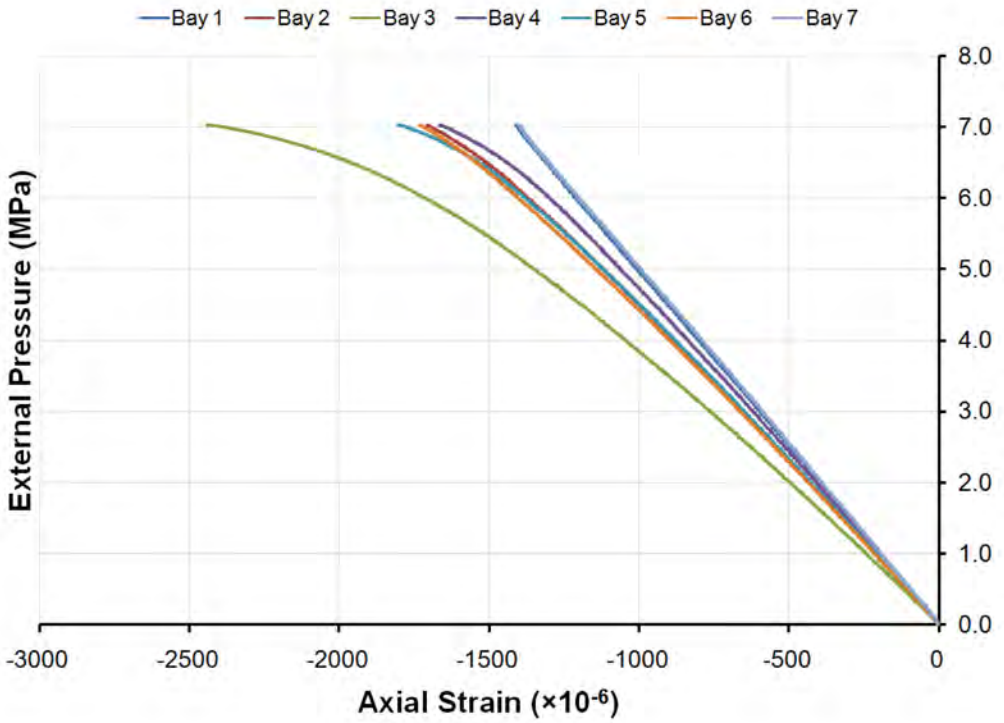

Figure 290: Pressure-strain curves showing axial shell strains mid-way between frames outside Bays 1 to 7 of specimen L510-No33 at 6.4°

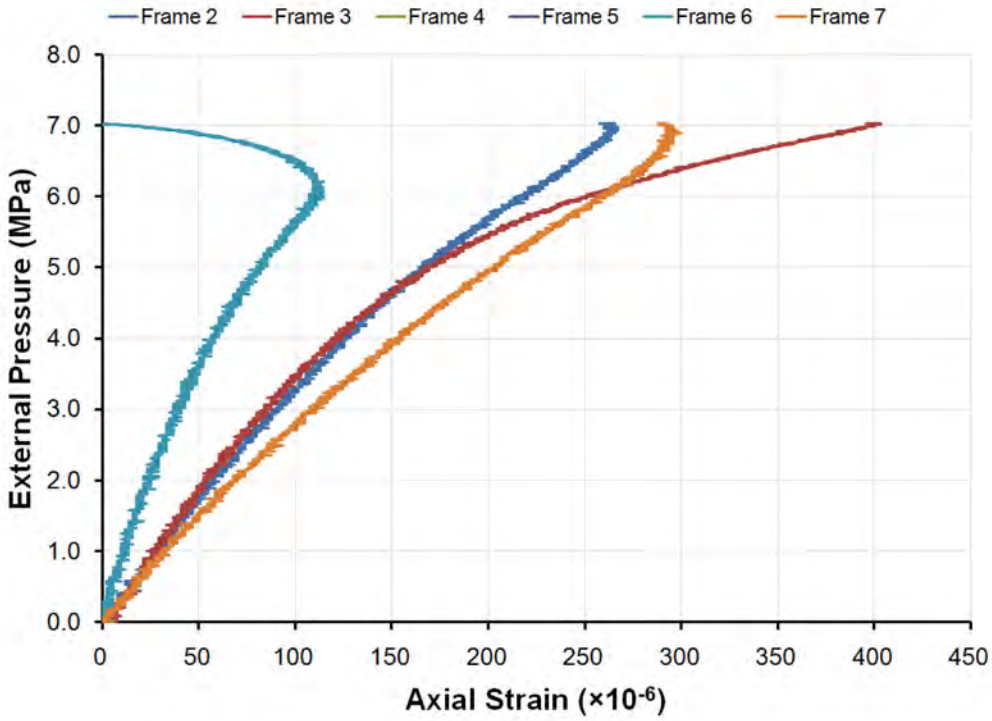

Figure 291: Pressure-strain curves showing axial shell strains outside Frames 2 to 7 of specimen L510-No33 at 6.4°

H.10 L510-No34

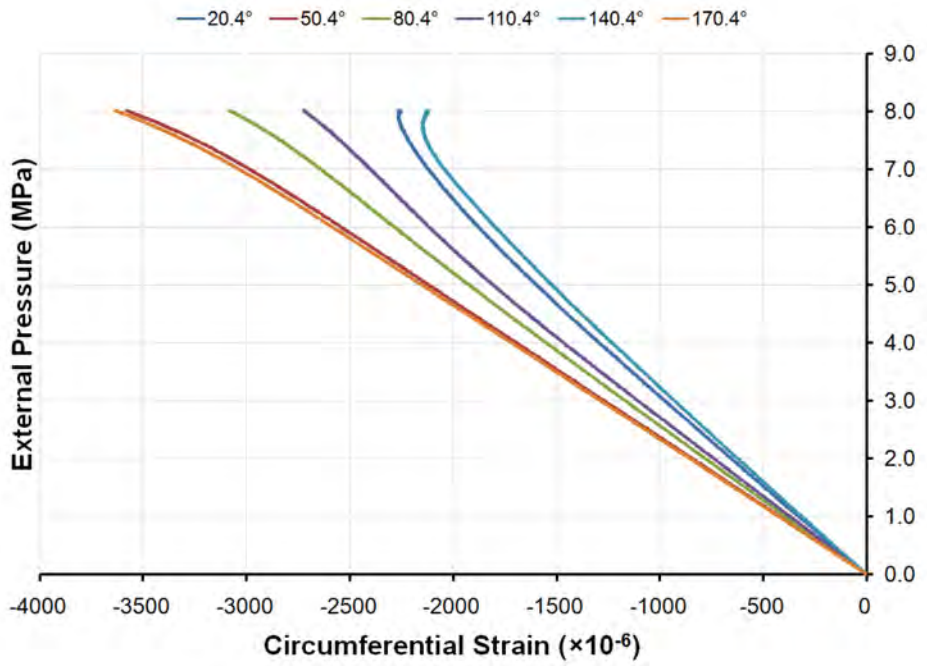

Figure 292: Pressure-strain curves showing circumferential strains at the flange of Frame 3 of specimen L510-No34 (20.4°-170.4°)

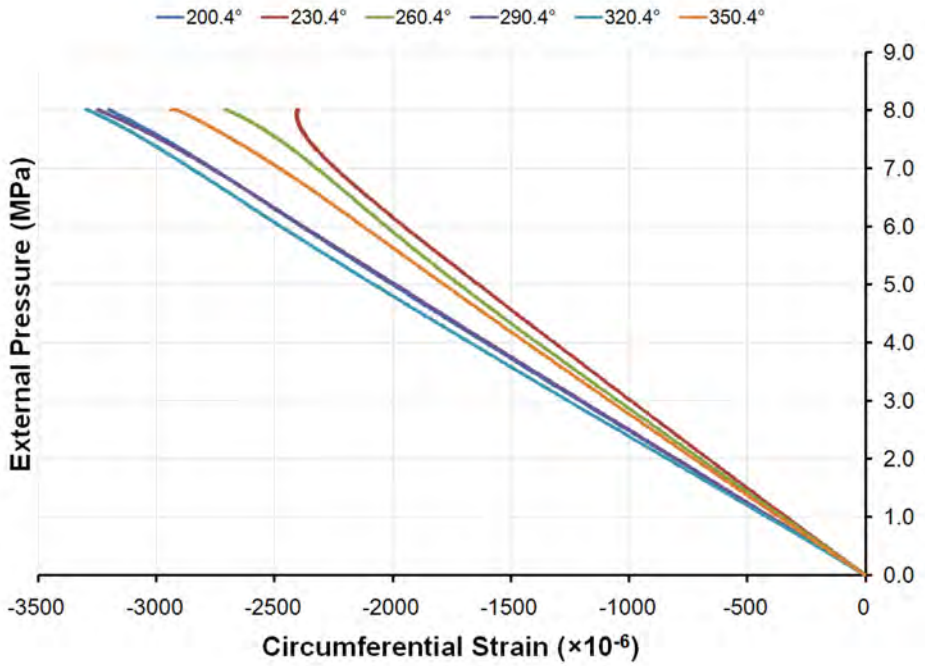

Figure 293: Pressure-strain curves showing circumferential strains at the flange of Frame 3 of specimen L510-No34 (200.4°-350.4°)

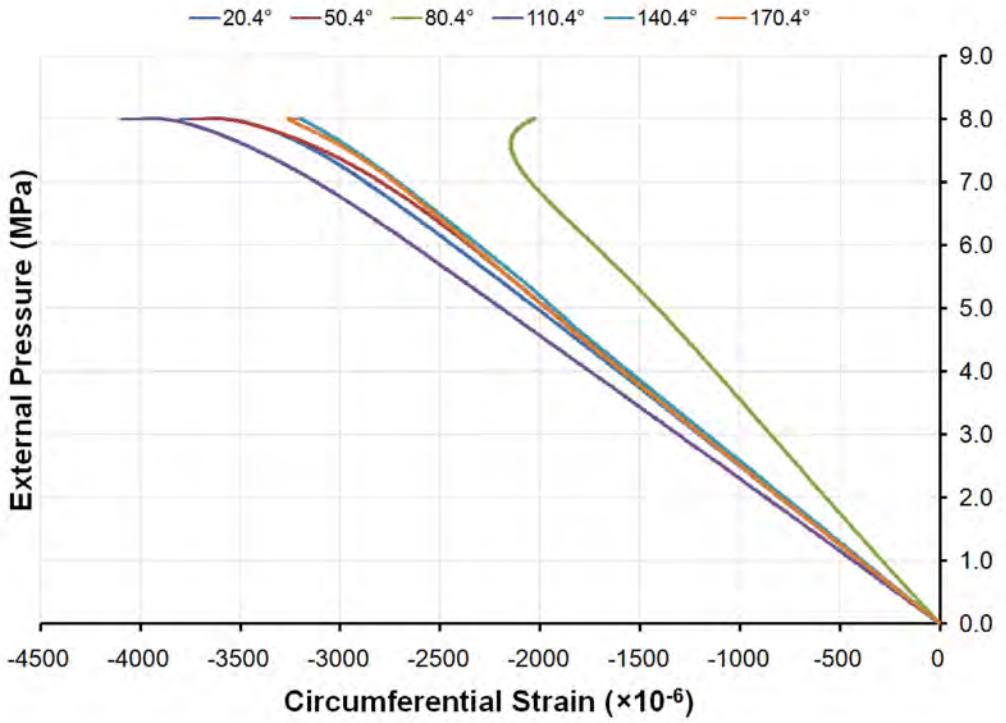

Figure 294: Pressure-strain curves showing circumferential strains at the flange of Frame 6 of specimen L510-No34 (20.4°-170.4°)

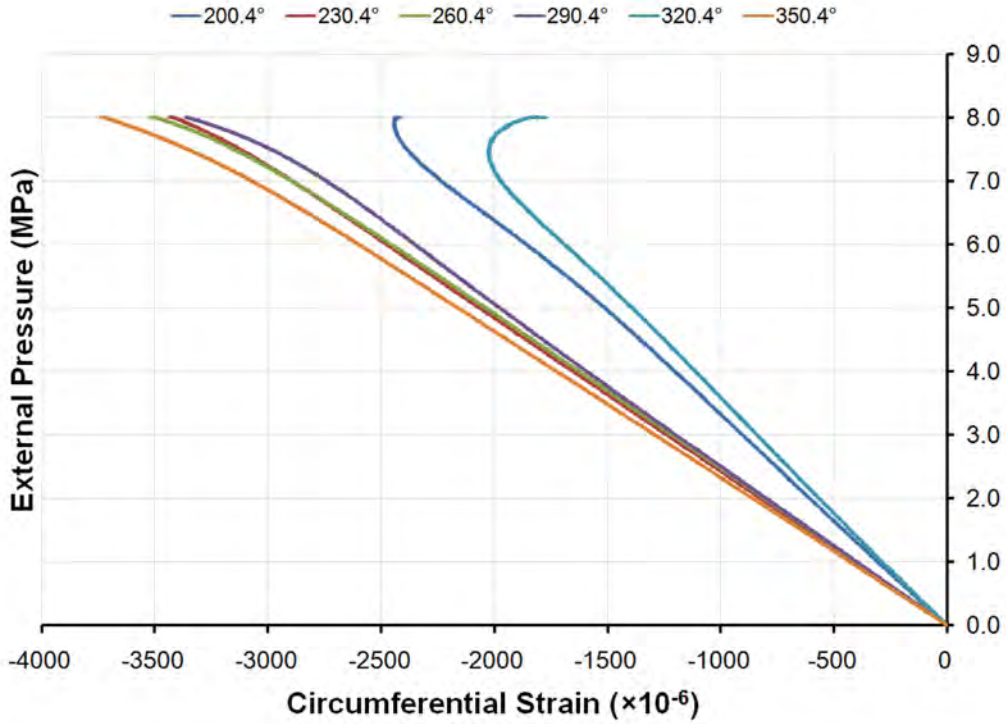

Figure 295: Pressure-strain curves showing circumferential strains at the flange of Frame 6 of specimen L510-No34 (200.4°-350.4°)

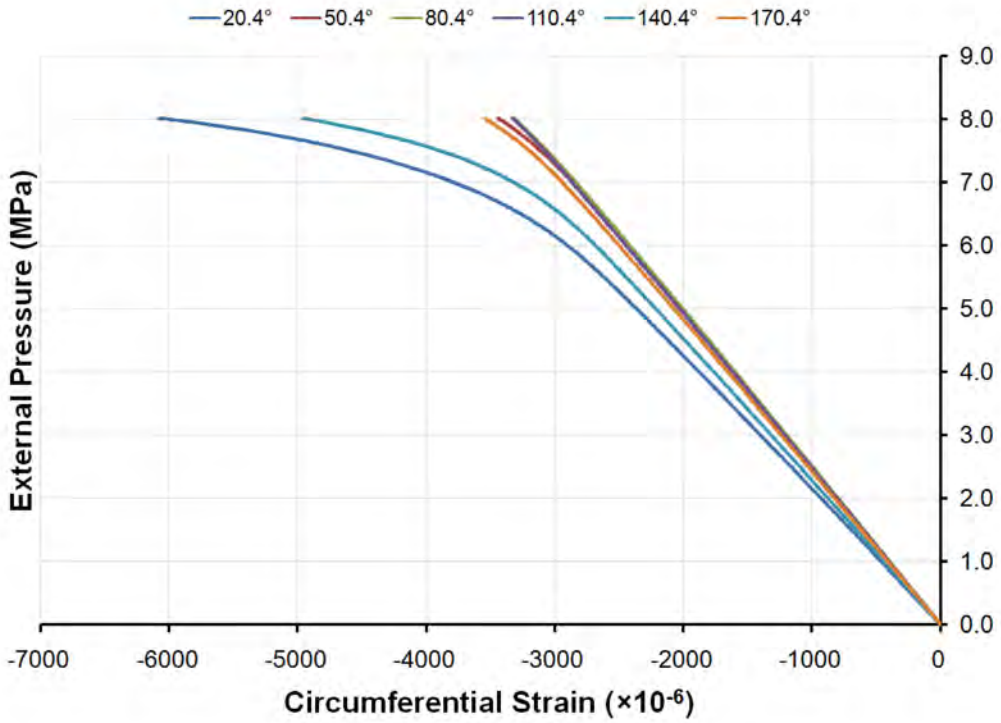

Figure 296: Pressure-strain curves showing circumferential shell strains mid-way between frames outside Bay 2 of specimen L510-No34 (20.4°-170.4°)

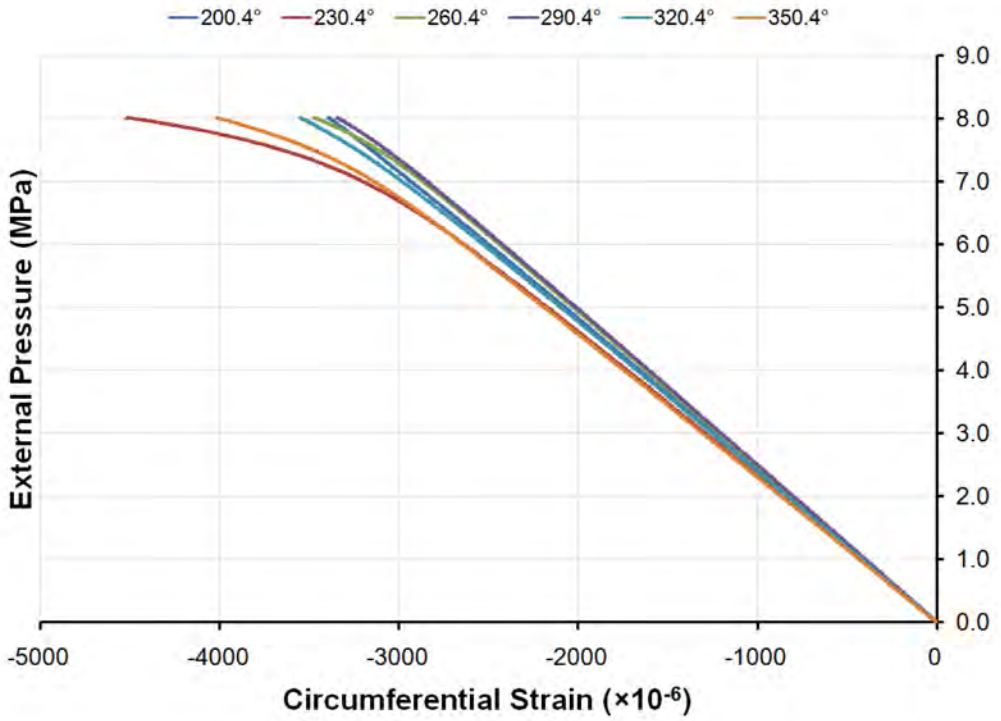

Figure 297: Pressure-strain curves showing circumferential shell strains mid-way between frames outside Bay 2 of specimen L510-No34 (200.4°-350.4°)

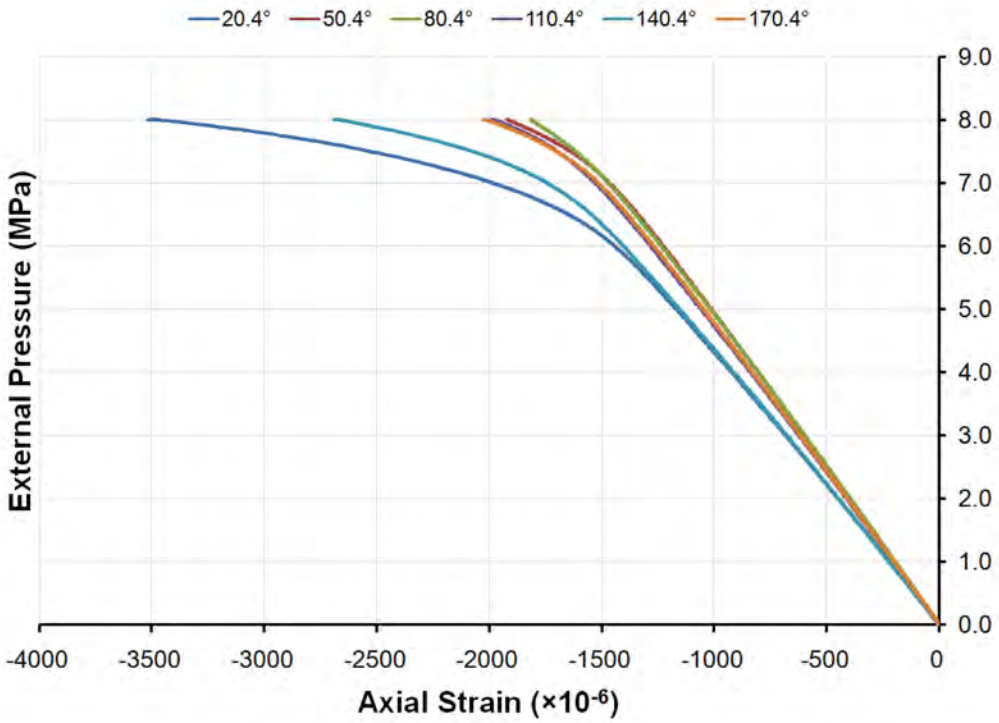

Figure 298: Pressure-strain curves showing axial shell strains mid-way between frames outside Bay 2 of specimen L510-No34 (20.4°-170.4°)

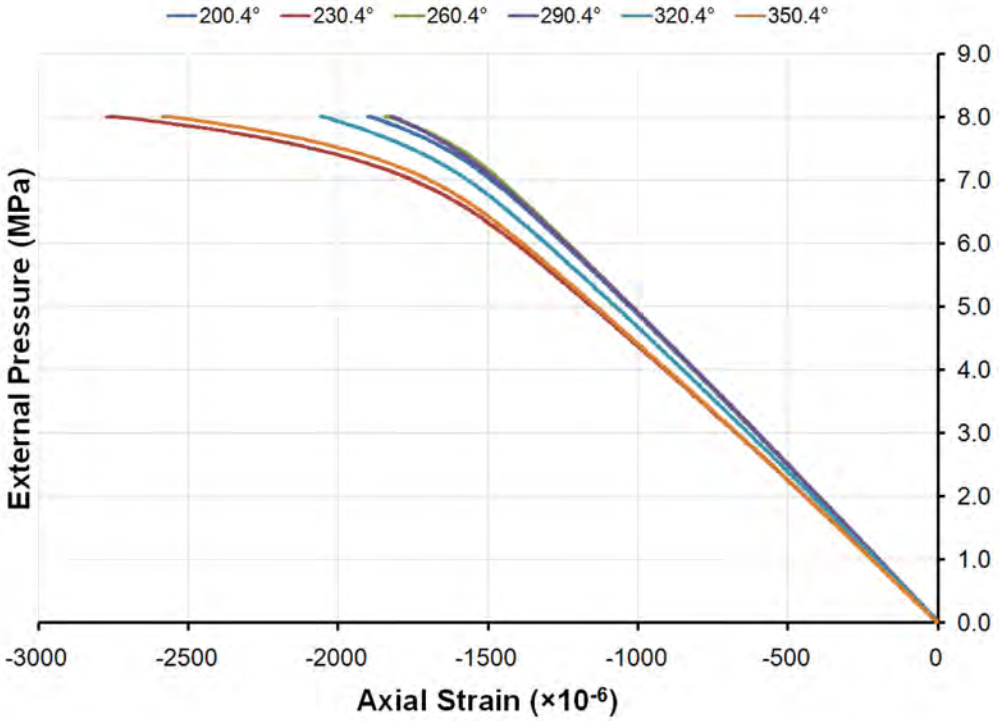

Figure 299: Pressure-strain curves showing axial shell strains mid-way between frames outside Bay 2 of specimen L510-No34 (200.4°-350.4°)

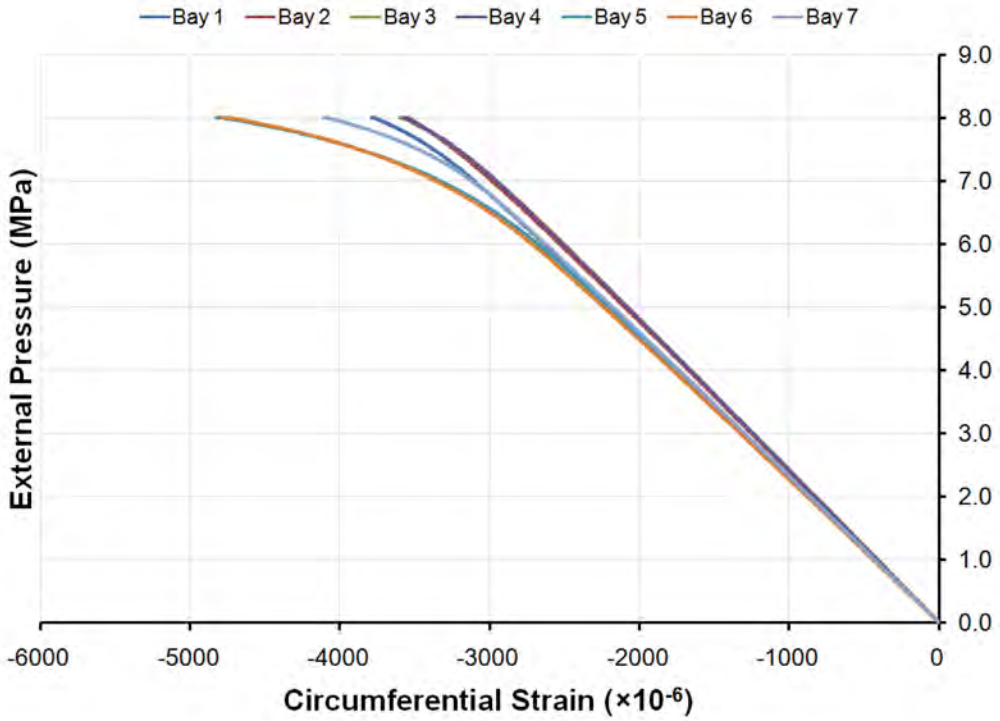

Figure 300: Pressure-strain curves showing circumferential shell strains mid-way between frames outside Bays 1 to 7 of specimen L510-No34 at 320.4°

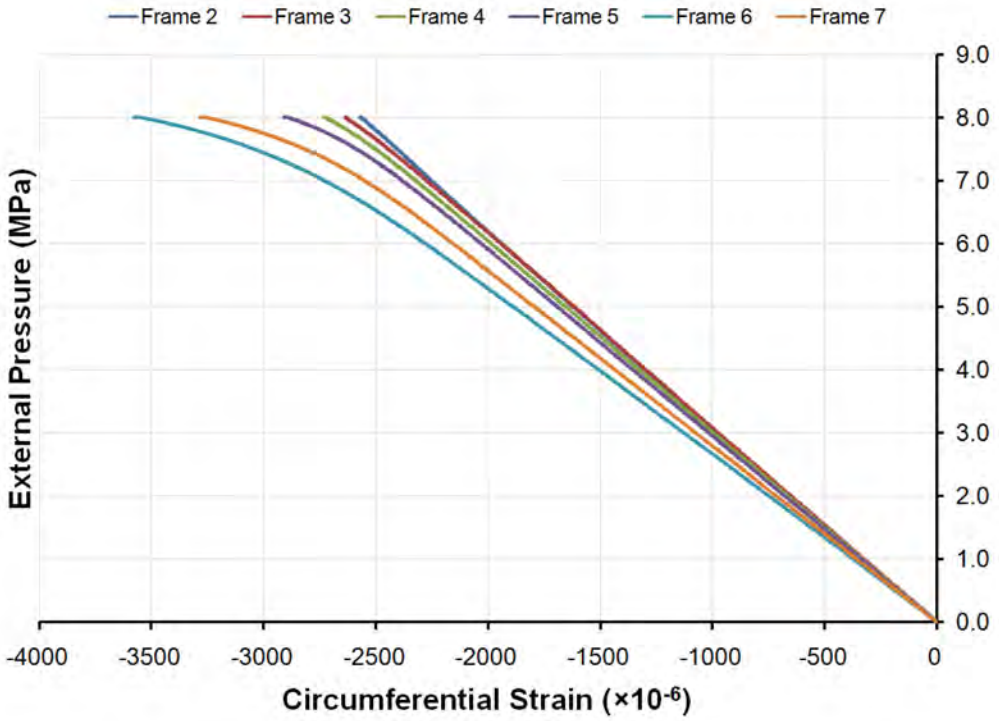

Figure 301: Pressure-strain curves showing circumferential shell strains outside Frames 2 to 7 of specimen L510-No34 at 320.4°

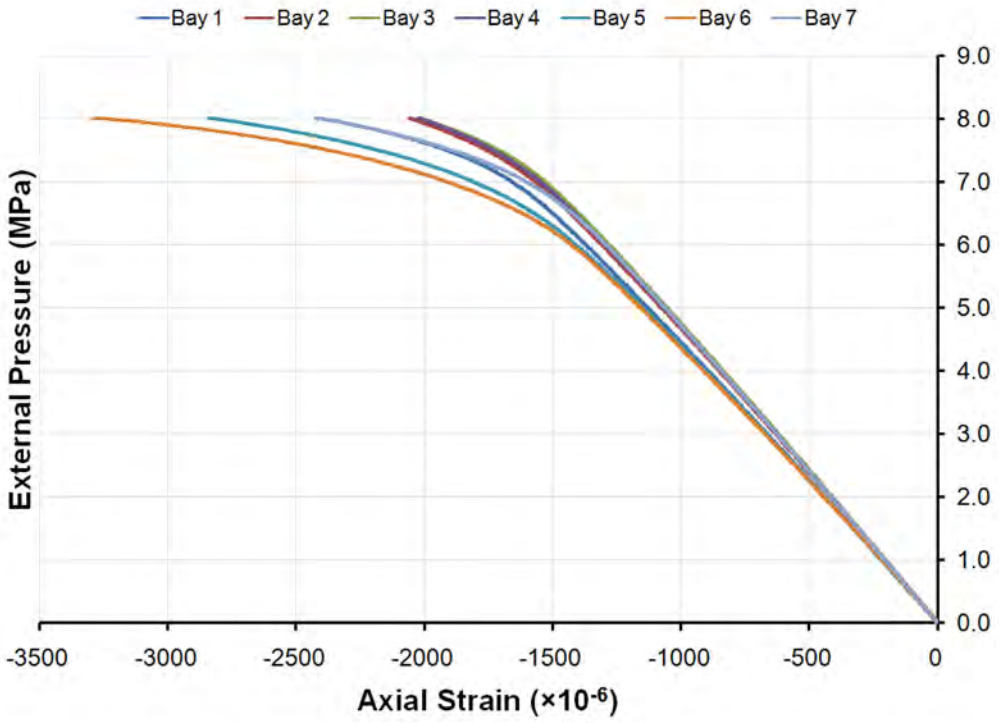

Figure 302: Pressure-strain curves showing axial shell strains mid-way between frames outside Bays 1 to 7 of specimen L510-No34 at 320.4°

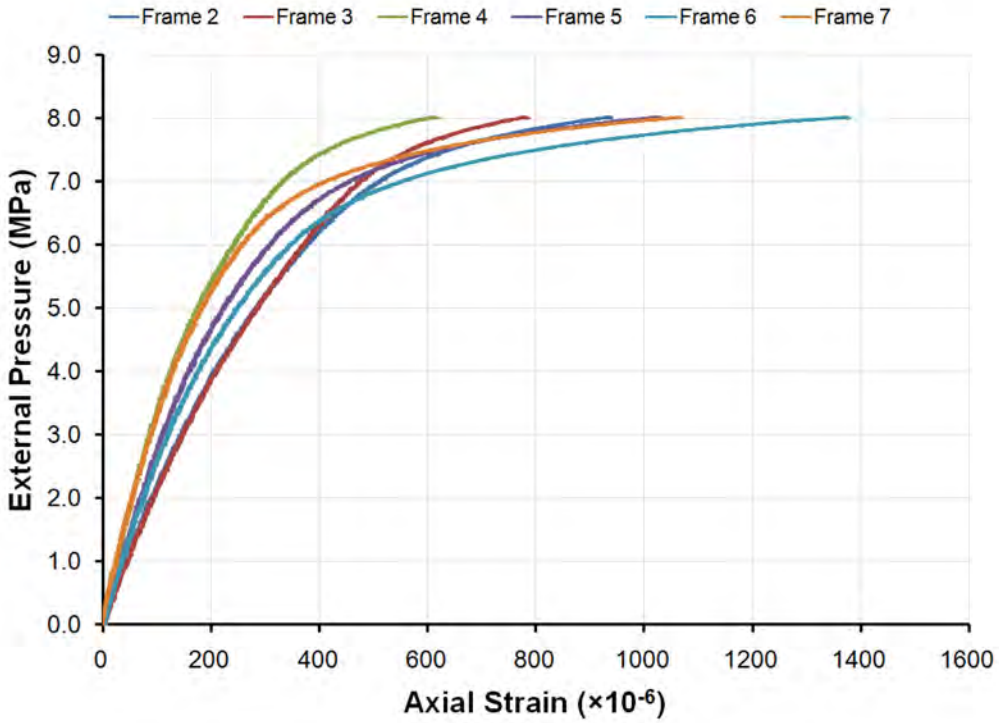

Figure 303: Pressure-strain curves showing axial shell strains outside Frames 2 to 7 of specimen L510-No34 at 320.4°

H.11 L510-No35

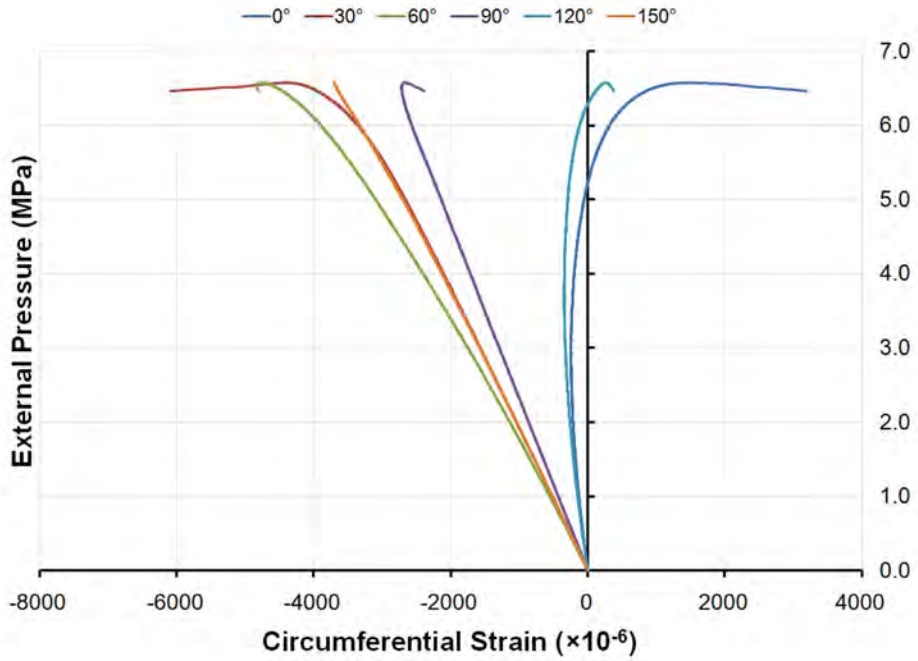

Figure 304: Pressure-strain curves showing circumferential strains at the flange of Frame 4 of specimen L510-No35 (0°-150°)

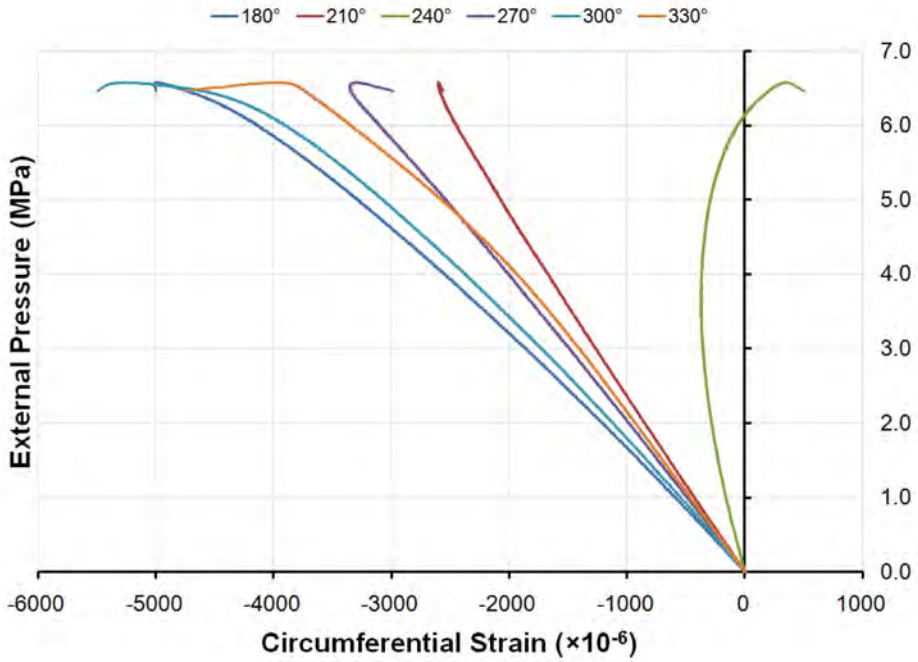

Figure 305: Pressure-strain curves showing circumferential strains at the flange of Frame 4 of specimen L510-No35 (180°-330°)

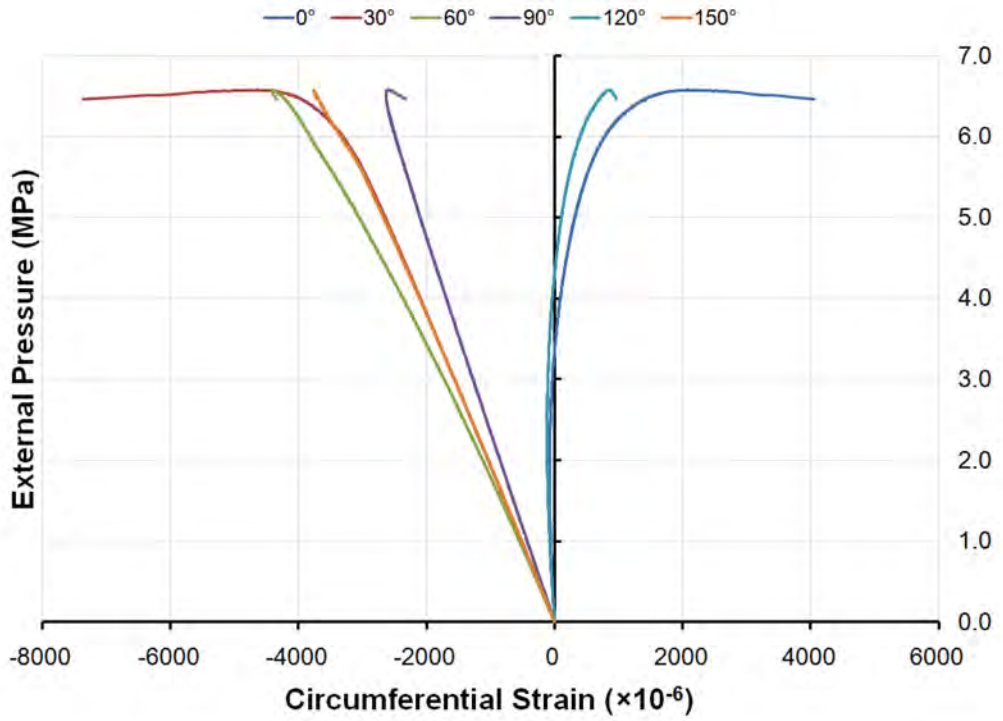

Figure 306: Pressure-strain curves showing circumferential strains at the flange of Frame 5 of specimen L510-No35 (0°-150°)

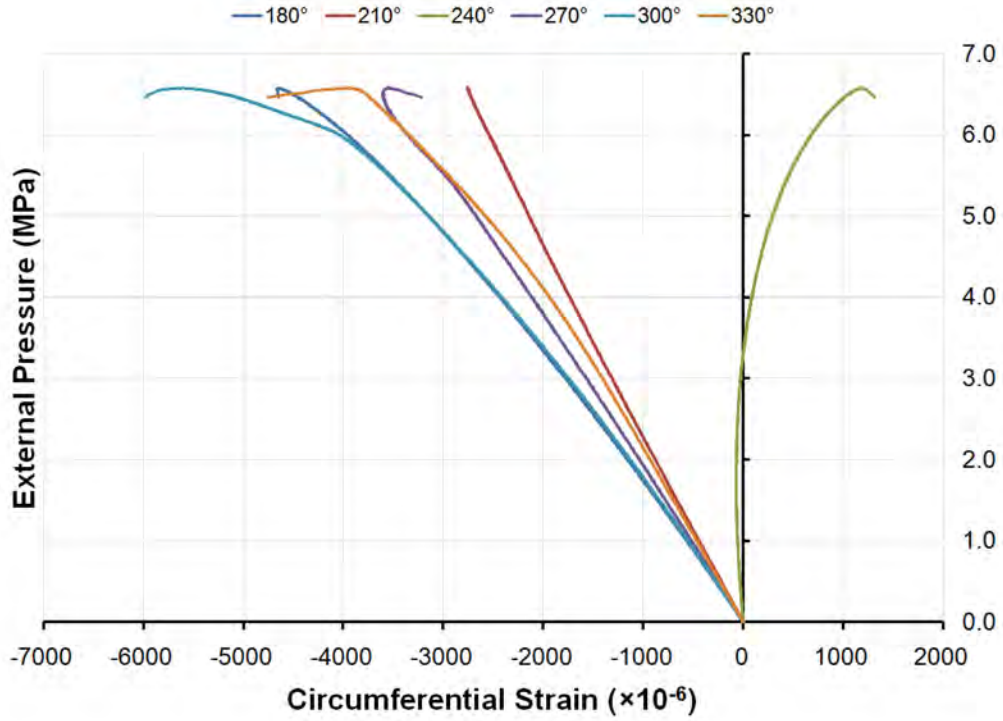

Figure 307: Pressure-strain curves showing circumferential strains at the flange of Frame 5 of specimen L510-No35 (180°-330°)

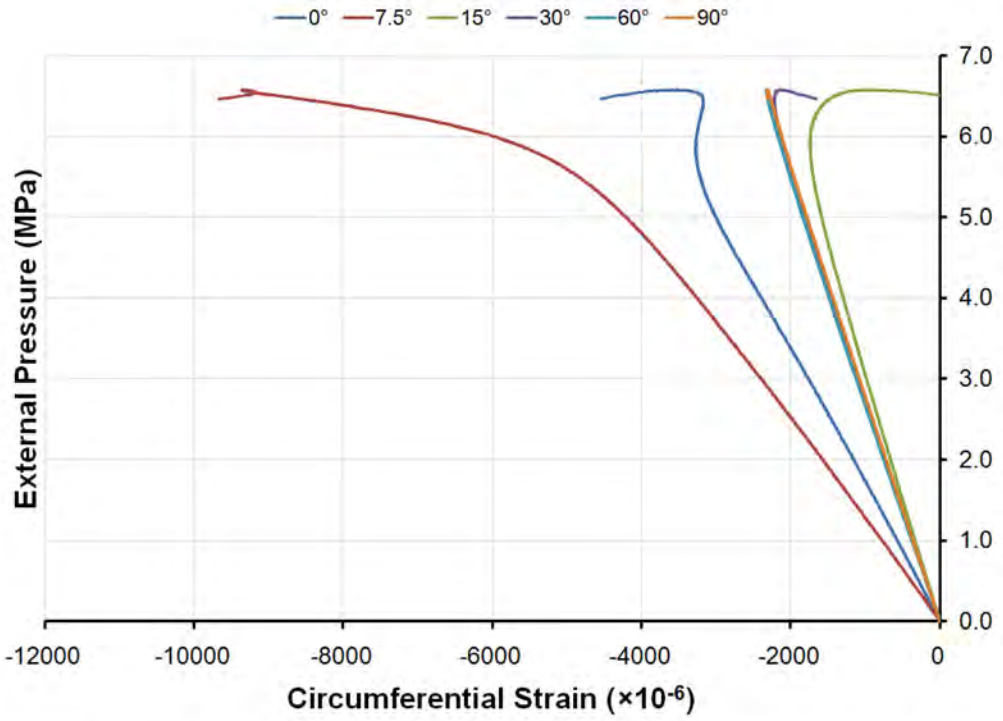

Figure 308: Pressure-strain curves showing circumferential shell strains mid-way between frames outside Bay 4 of specimen L510-No35 (0°-90°)

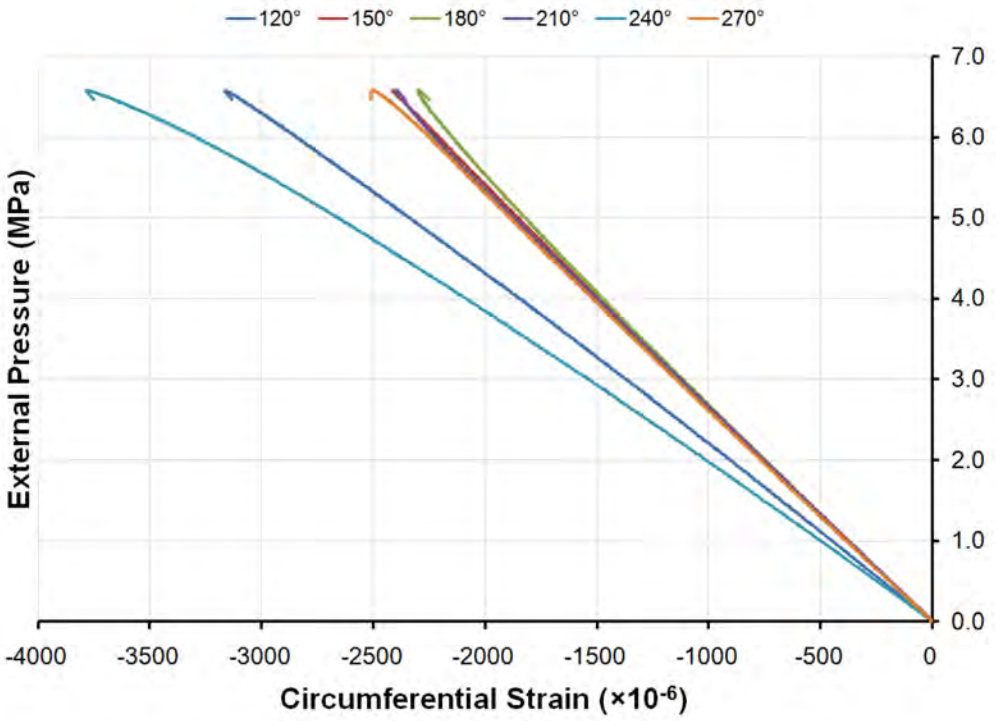

Figure 309: Pressure-strain curves showing circumferential shell strains mid-way between frames outside Bay 4 of specimen L510-No35 (120°-270°)

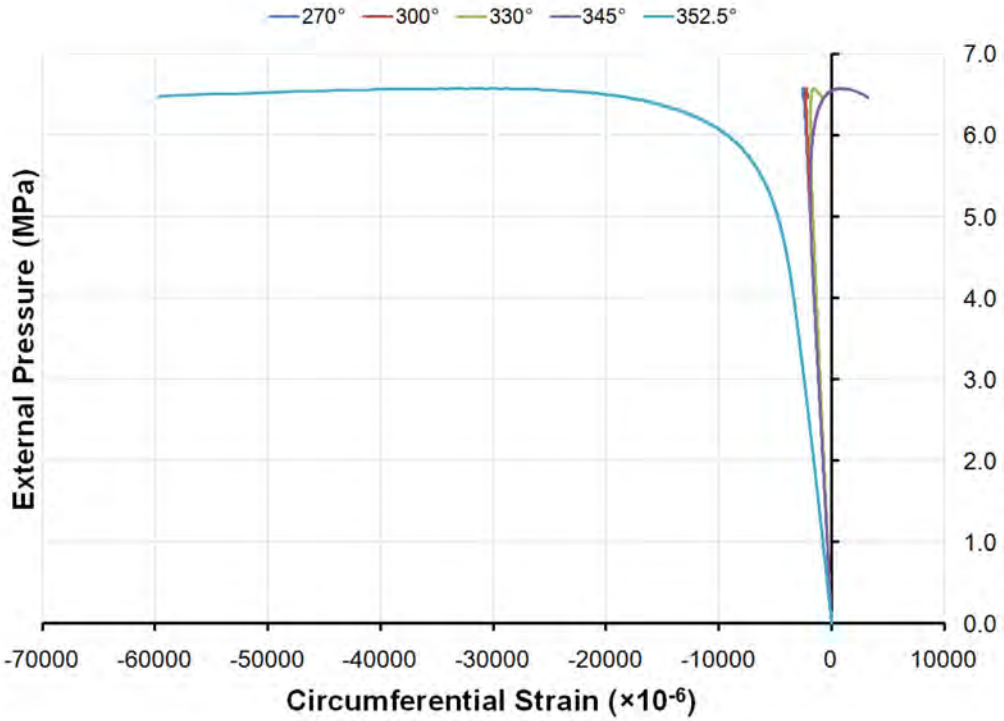

Figure 310: Pressure-strain curves showing circumferential shell strains mid-way between frames outside Bay 4 of specimen L510-No35 (270°-352.5°)

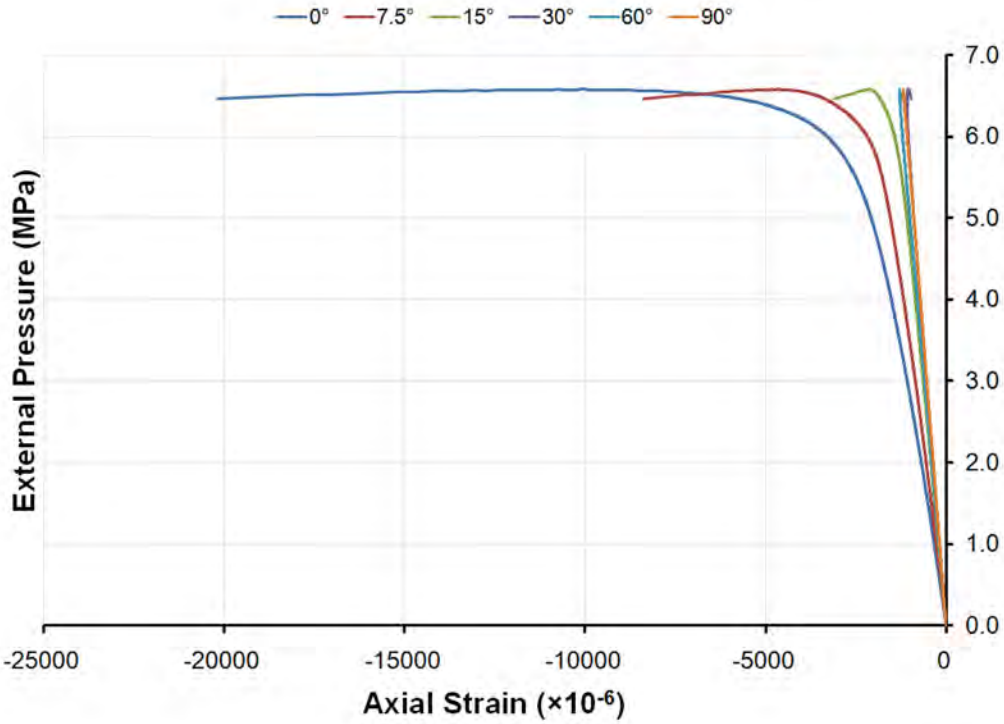

Figure 311: Pressure-strain curves showing axial shell strains mid-way between frames outside Bay 4 of specimen L510-No35 (0°-90°)

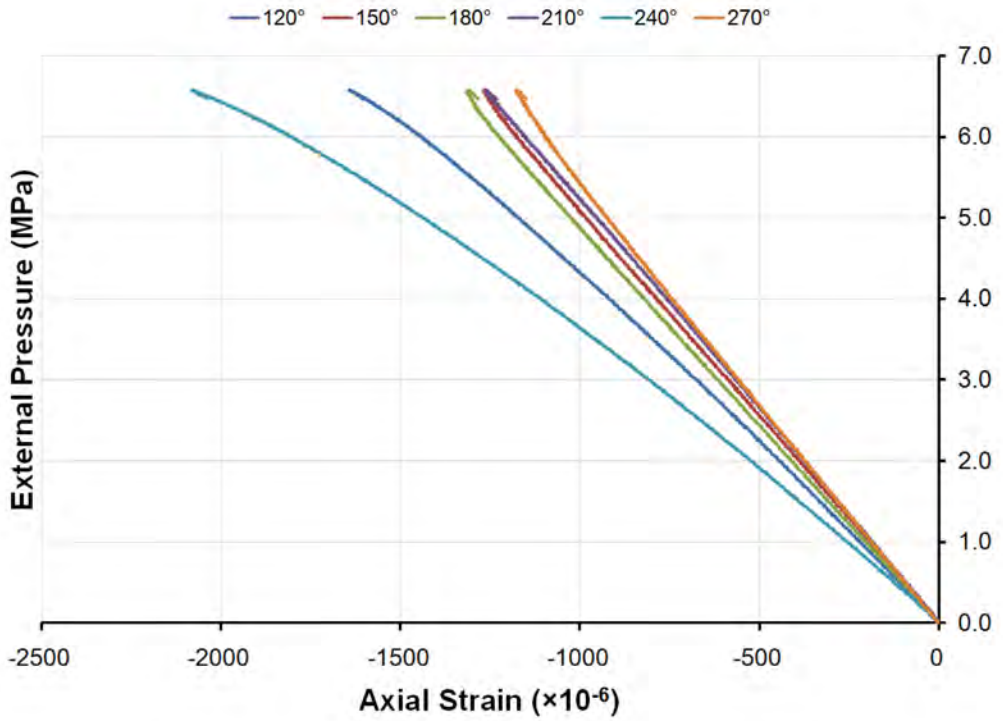

Figure 312: Pressure-strain curves showing axial shell strains mid-way between frames outside Bay 4 of specimen L510-No35 (120°-270°)

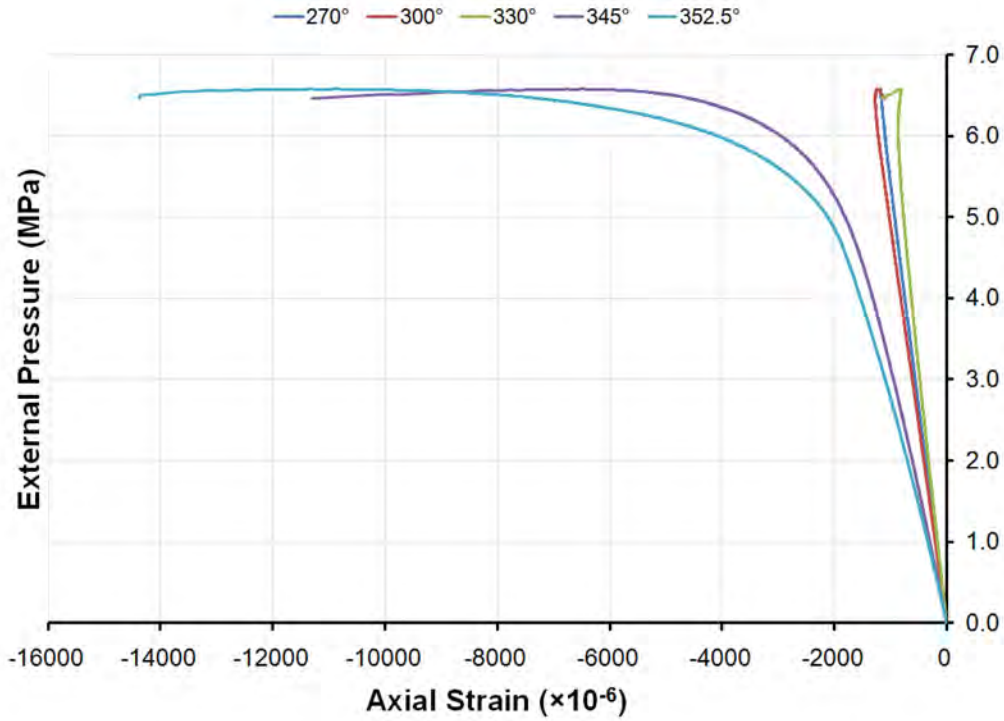

Figure 313: Pressure-strain curves showing axial shell strains mid-way between frames outside Bay 4 of specimen L510-No35 (270°-352.5°)

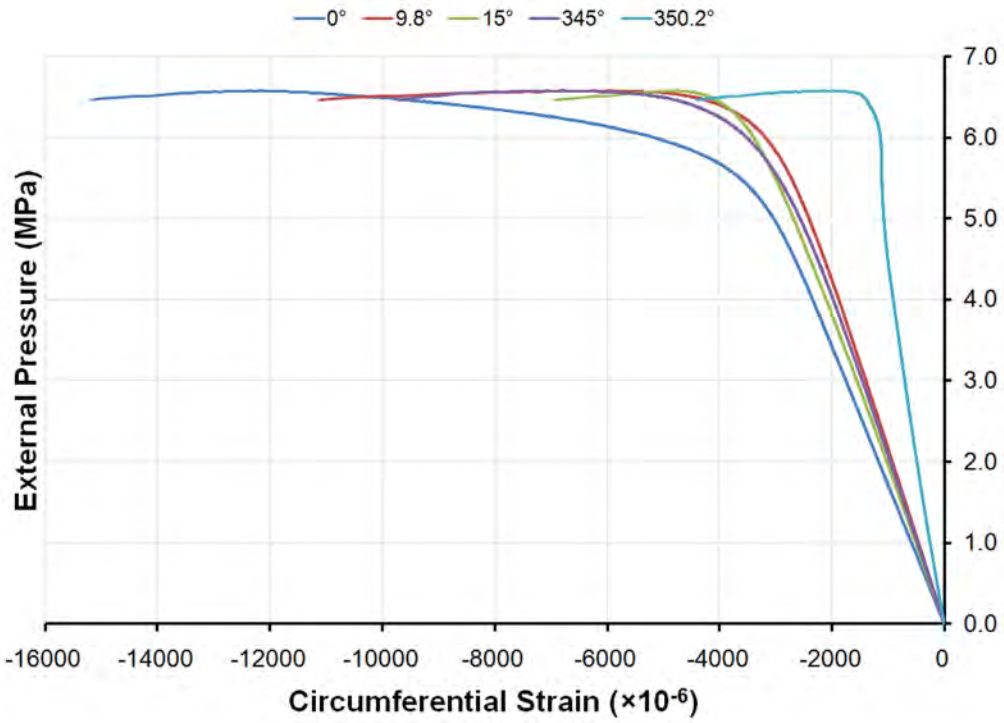

Figure 314: Pressure-strain curves showing circumferential shell strains mid-way between frames inside Bay 4 of specimen L510-No35

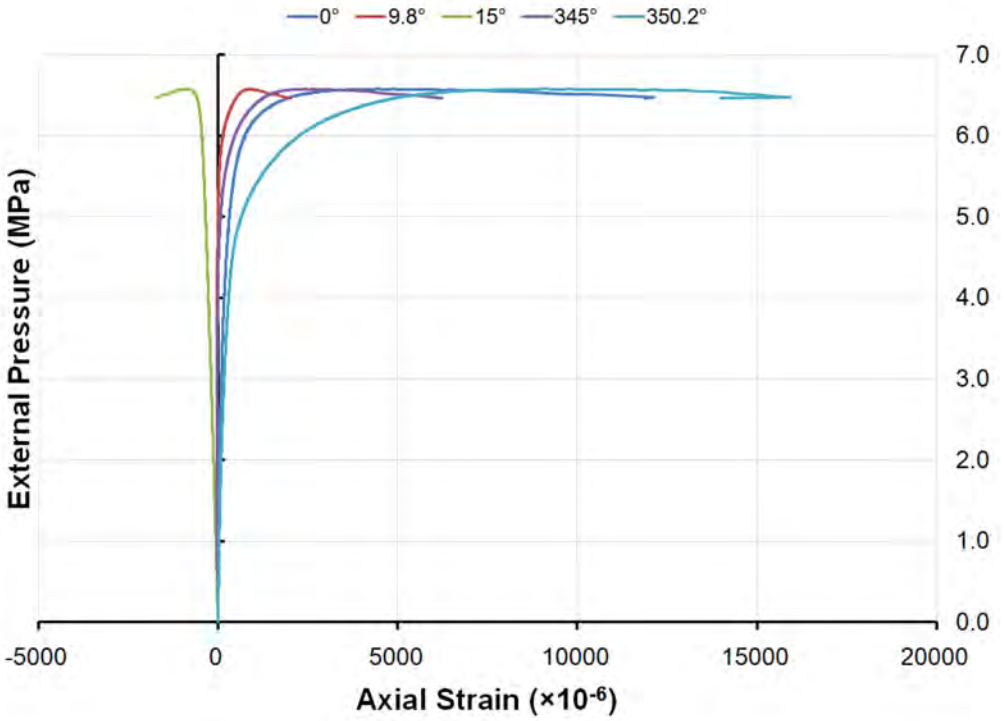

Figure 315: Pressure-strain curves showing axial shell strains mid-way between frames inside Bay 4 of specimen L510-No35

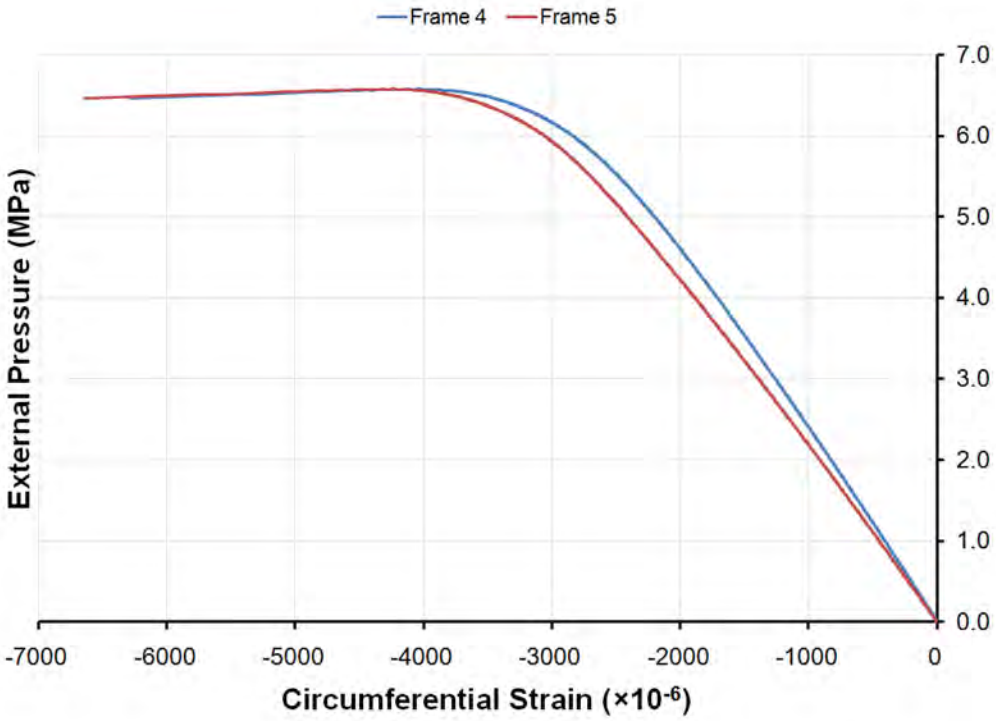

Figure 316: Pressure-strain curves showing circumferential shell strains outside Frames 4 and 5 of specimen L510-No35 at 0°

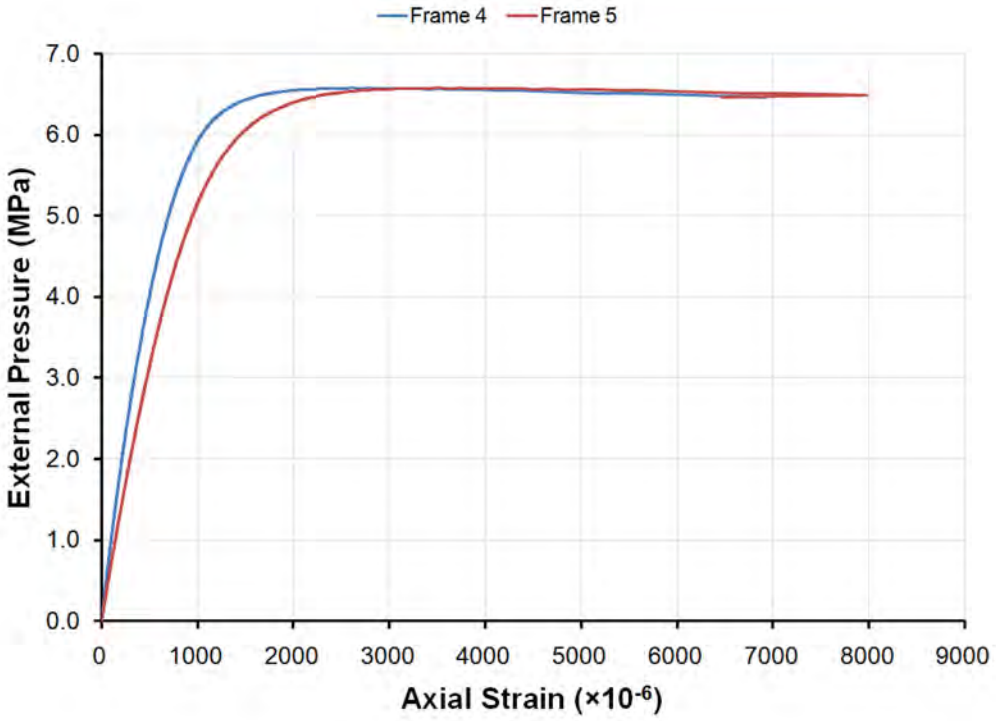

Figure 317: Pressure-strain curves showing axial shell strains outside Frames 4 and 5 of specimen L510-No35 at 0°

H.12 L510-No36

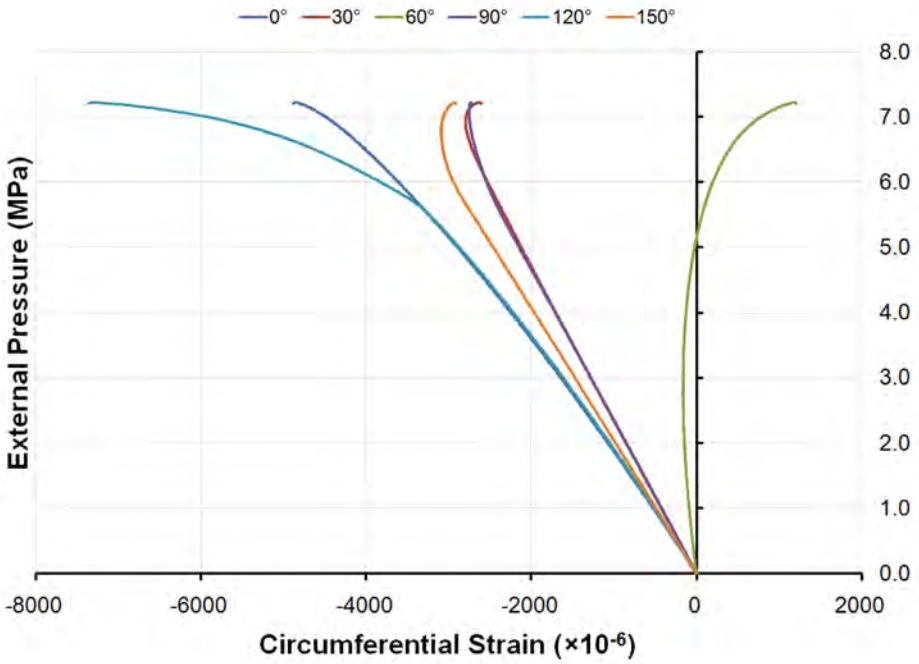

Figure 318: Pressure-strain curves showing circumferential strains at the flange of Frame 4 of specimen L510-No36 (0°-150°)

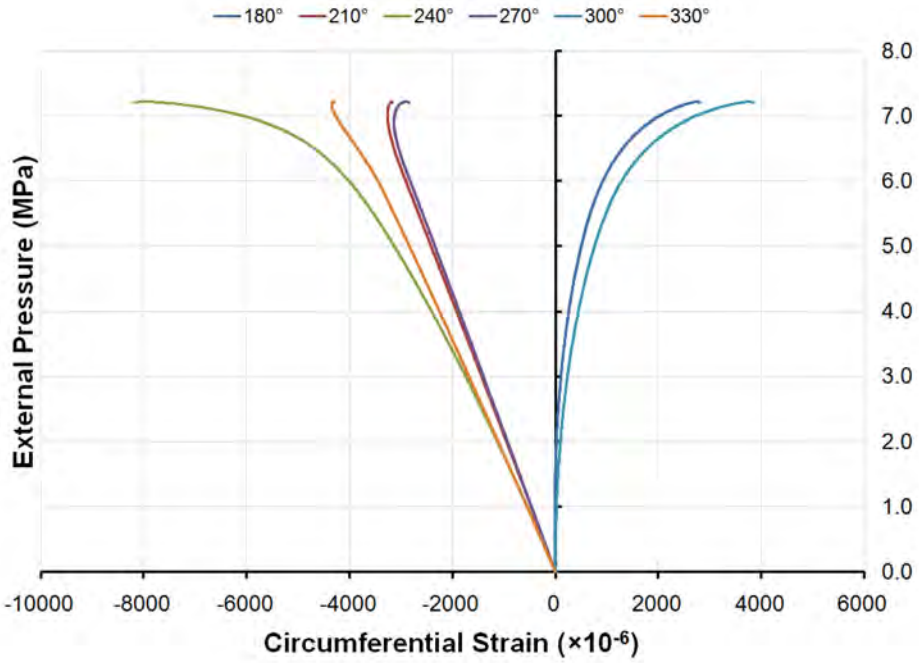

Figure 319: Pressure-strain curves showing circumferential strains at the flange of Frame 4 of specimen L510-No36 (180°-330°)

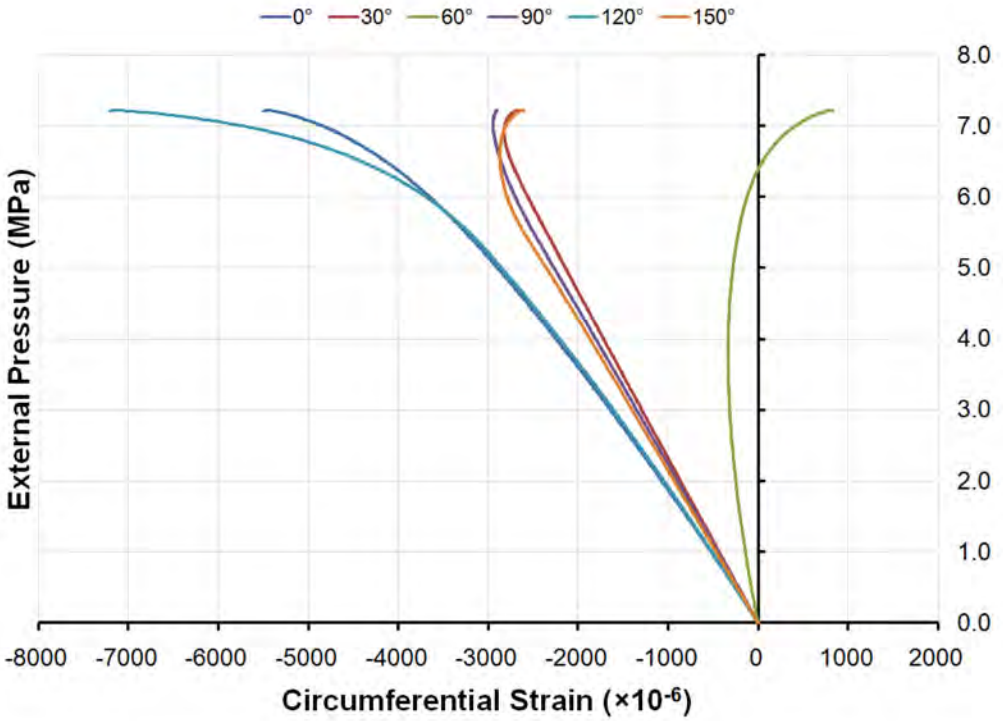

Figure 320: Pressure-strain curves showing circumferential strains at the flange of Frame 5 of specimen L510-No36 (0°-150°)

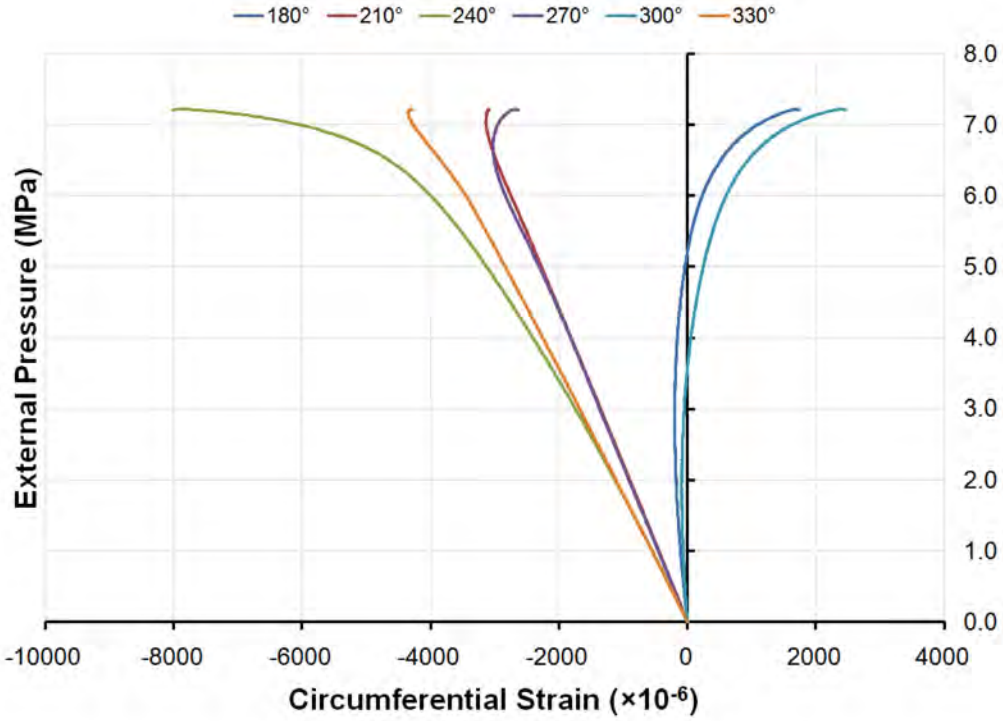

Figure 321: Pressure-strain curves showing circumferential strains at the flange of Frame 5 of specimen L510-No36 (180°-330°)

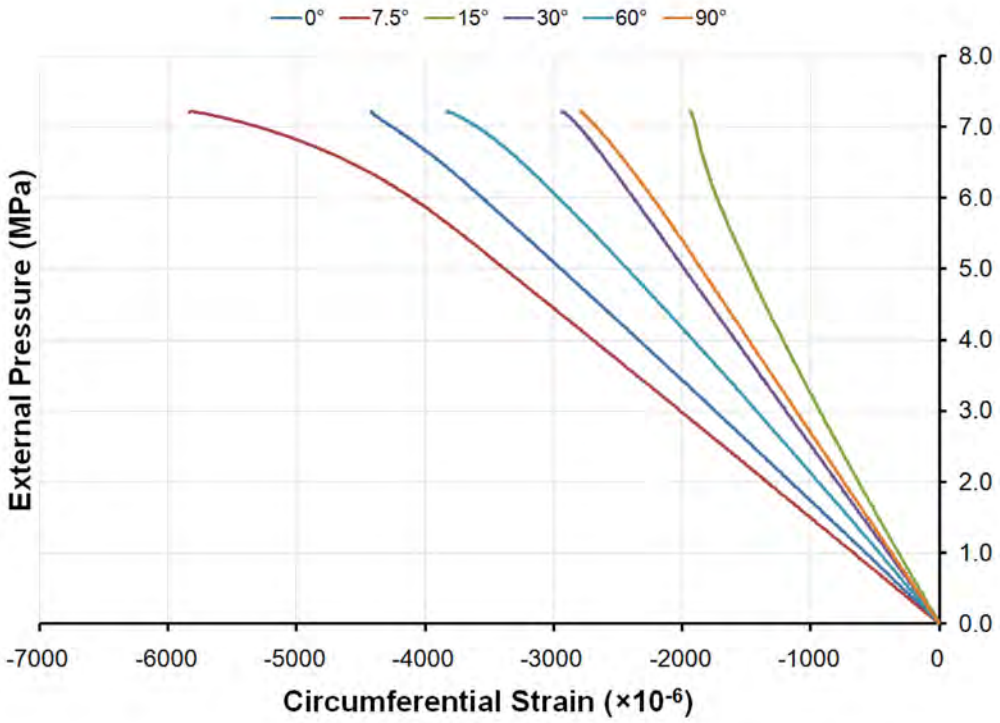

Figure 322: Pressure-strain curves showing circumferential shell strains mid-way between frames outside Bay 4 of specimen L510-No36 (0°-90°)

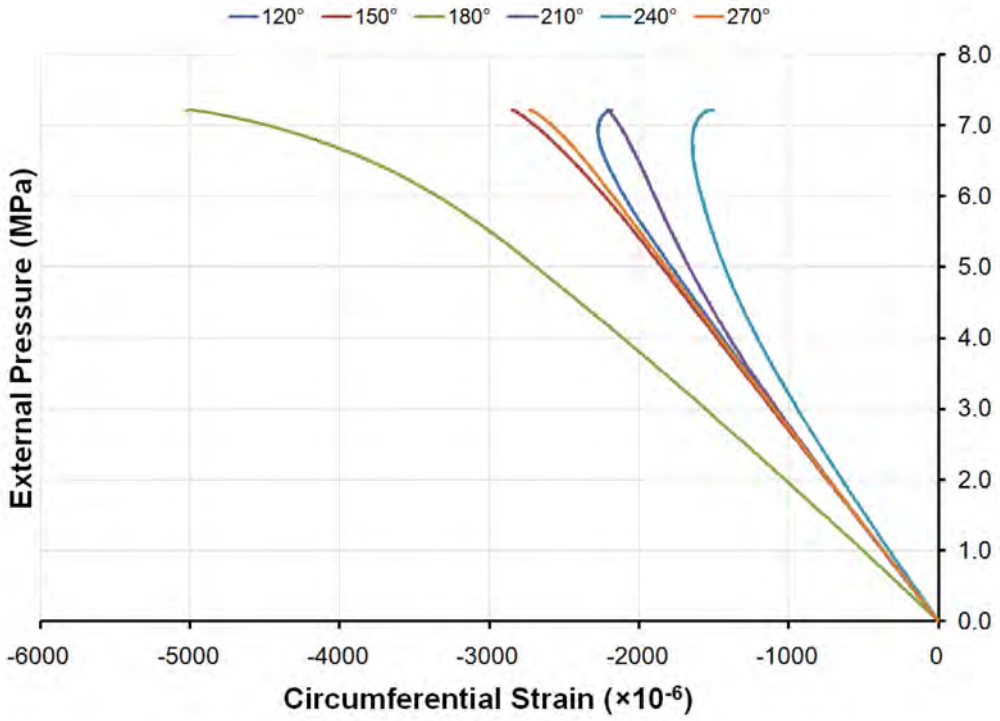

Figure 323: Pressure-strain curves showing circumferential shell strains mid-way between frames outside Bay 4 of specimen L510-No36 (120°-270°)

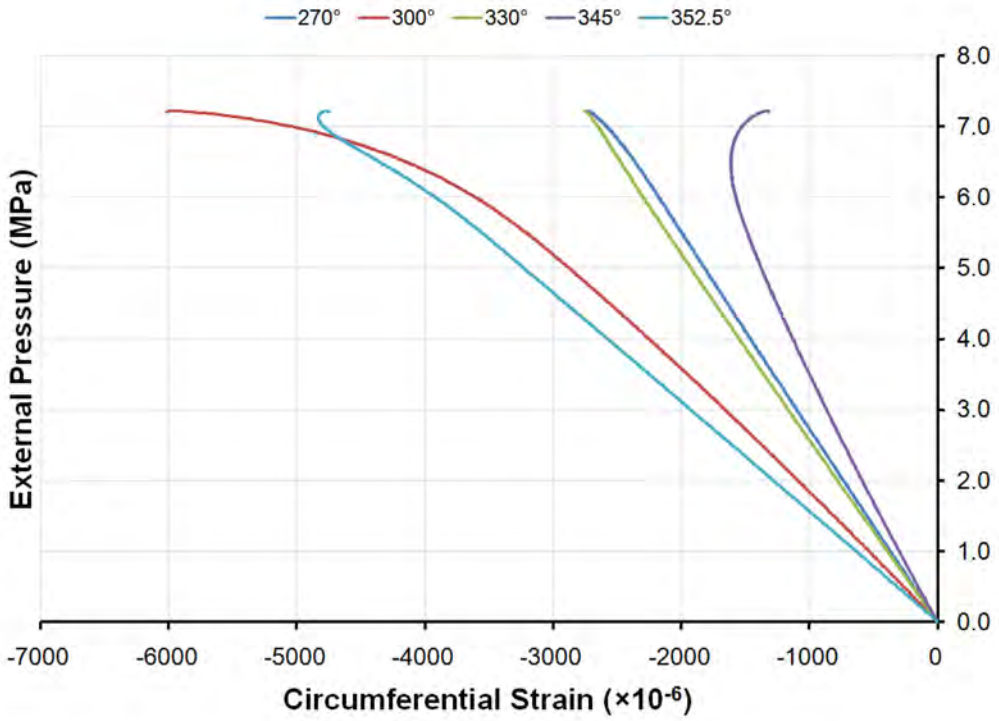

Figure 324: Pressure-strain curves showing circumferential shell strains mid-way between frames outside Bay 4 of specimen L510-No36 (270°-352.5°)

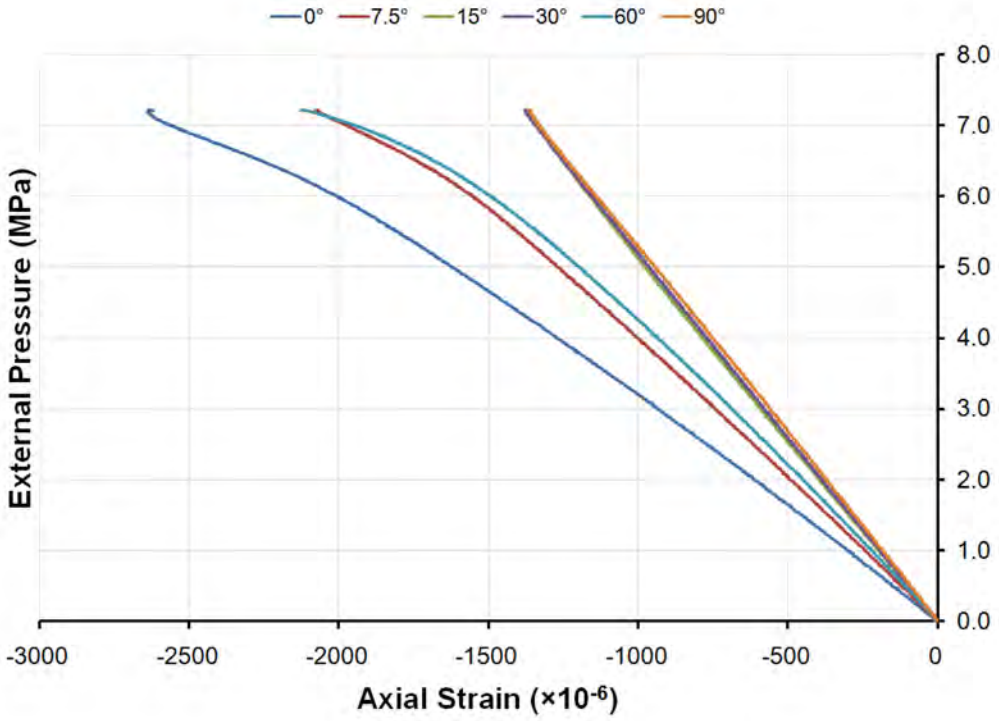

Figure 325: Pressure-strain curves showing axial shell strains mid-way between frames outside Bay 4 of specimen L510-No36 (0°-90°)

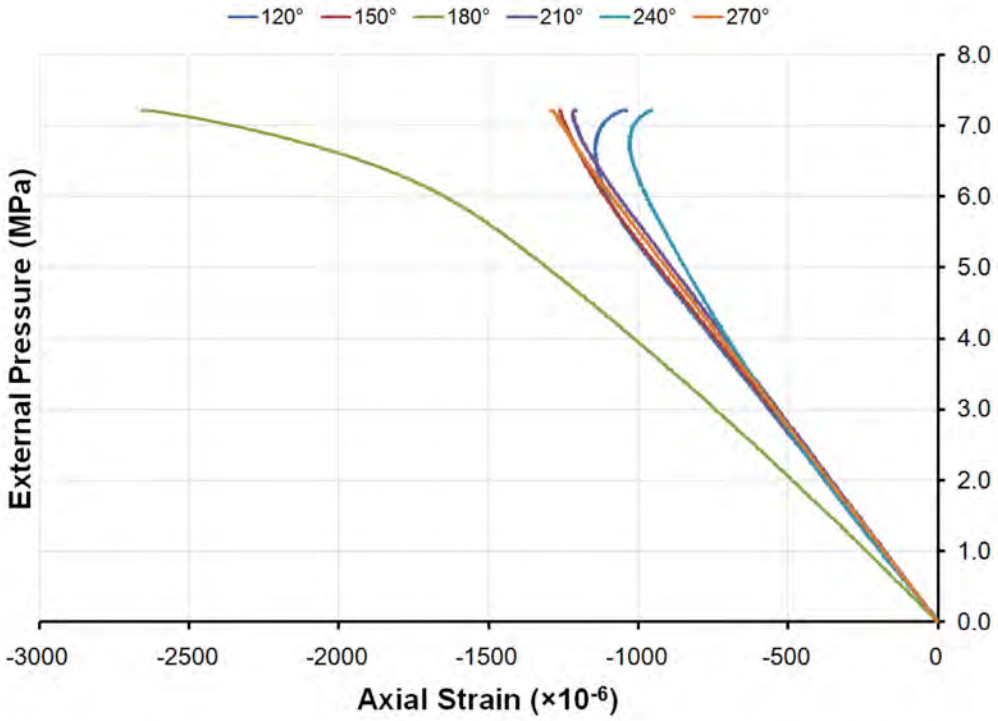

Figure 326: Pressure-strain curves showing axial shell strains mid-way between frames outside Bay 4 of specimen L510-No36 (120°-270°)

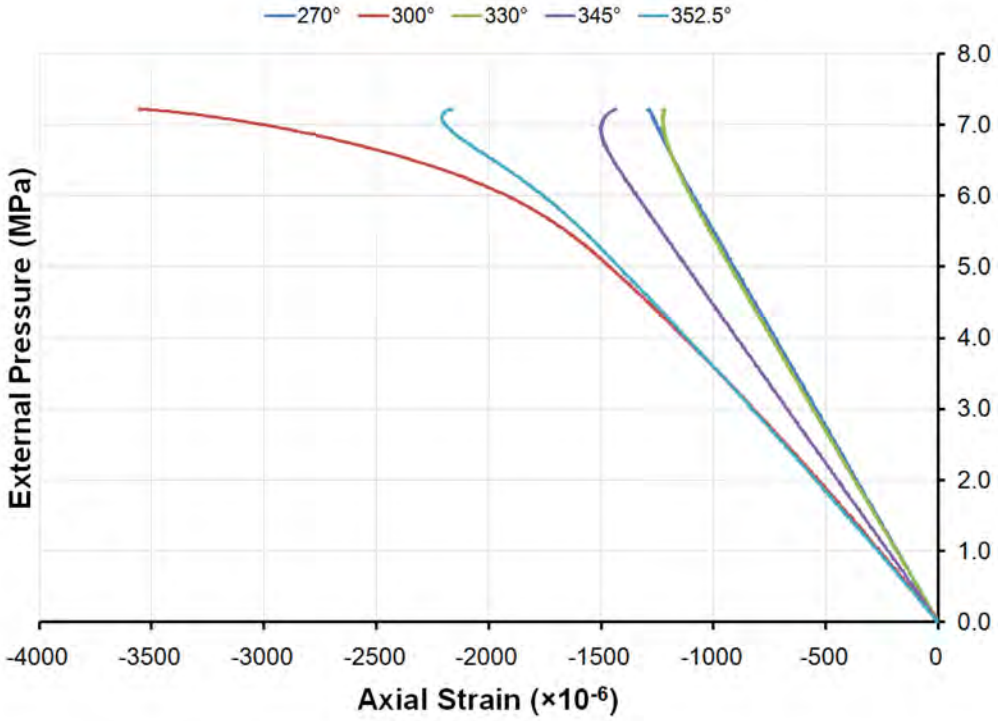

Figure 327: Pressure-strain curves showing axial shell strains mid-way between frames outside Bay 4 of specimen L510-No36 (270°-352.5°)

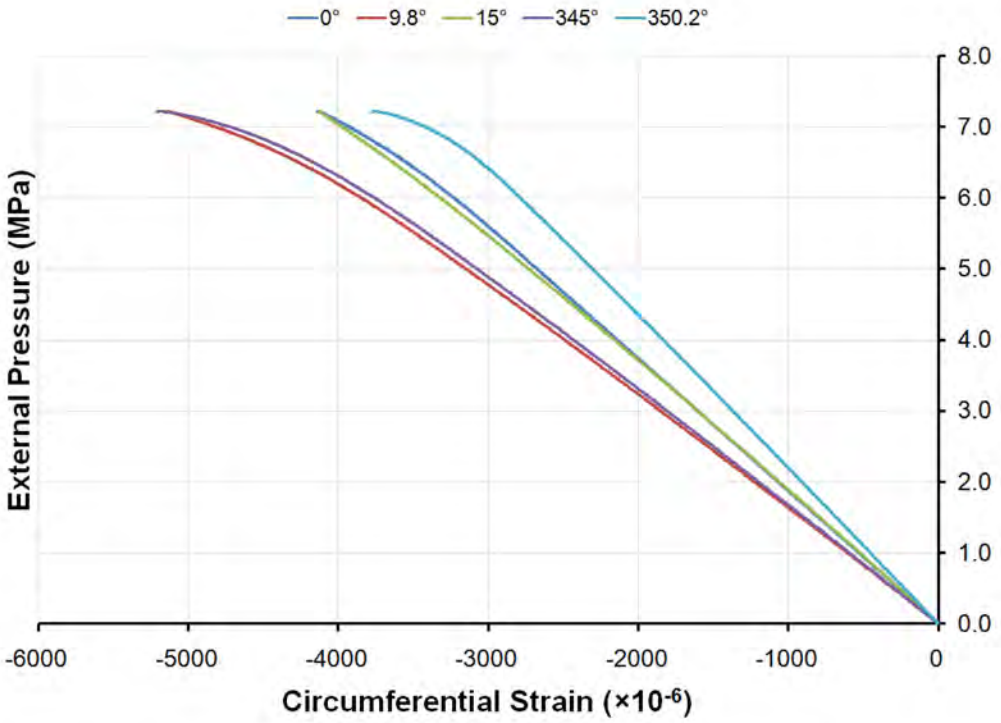

Figure 328: Pressure-strain curves showing circumferential shell strains mid-way between frames inside Bay 4 of specimen L510-No36

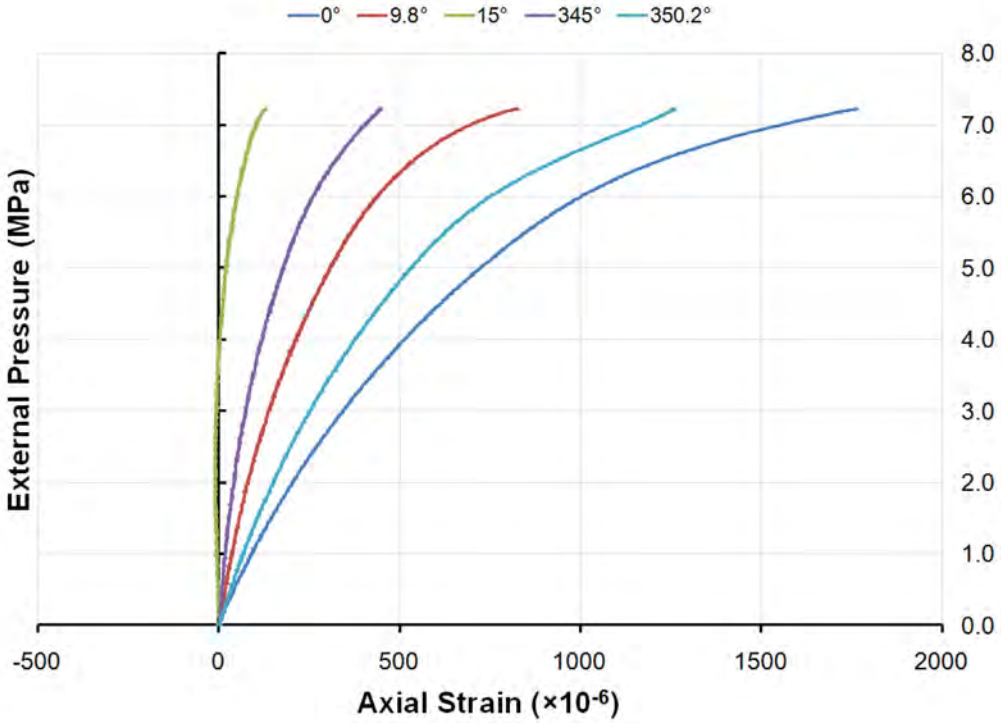

Figure 329: Pressure-strain curves showing axial shell strains mid-way between frames inside Bay 4 of specimen L510-No36

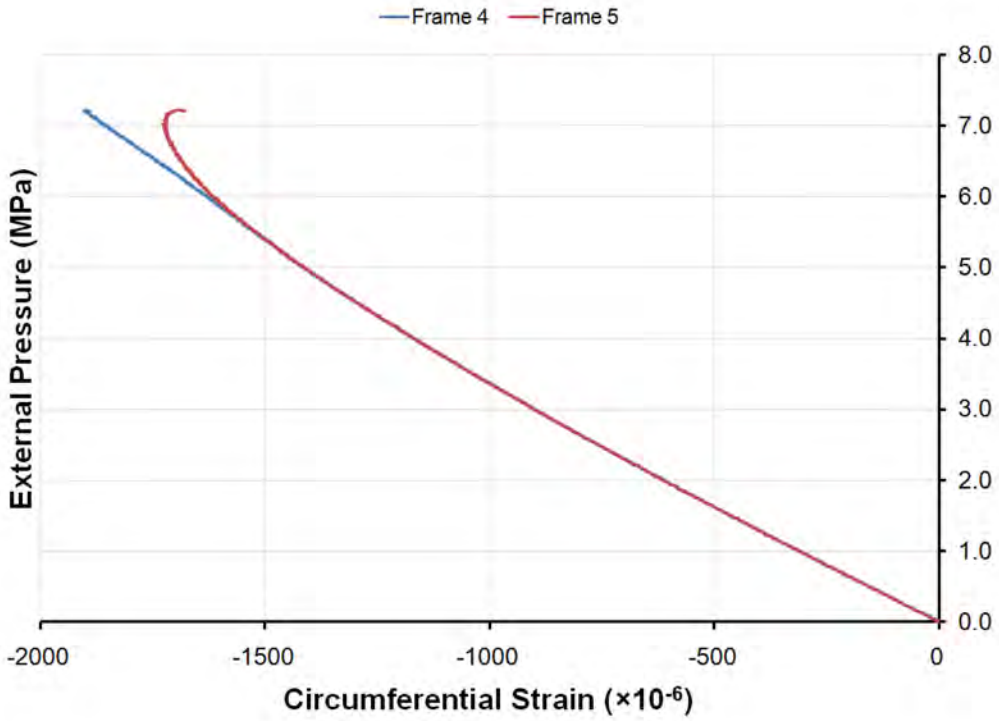

Figure 330: Pressure-strain curves showing circumferential shell strains outside Frames 4 and 5 of specimen L510-No36 at 0°

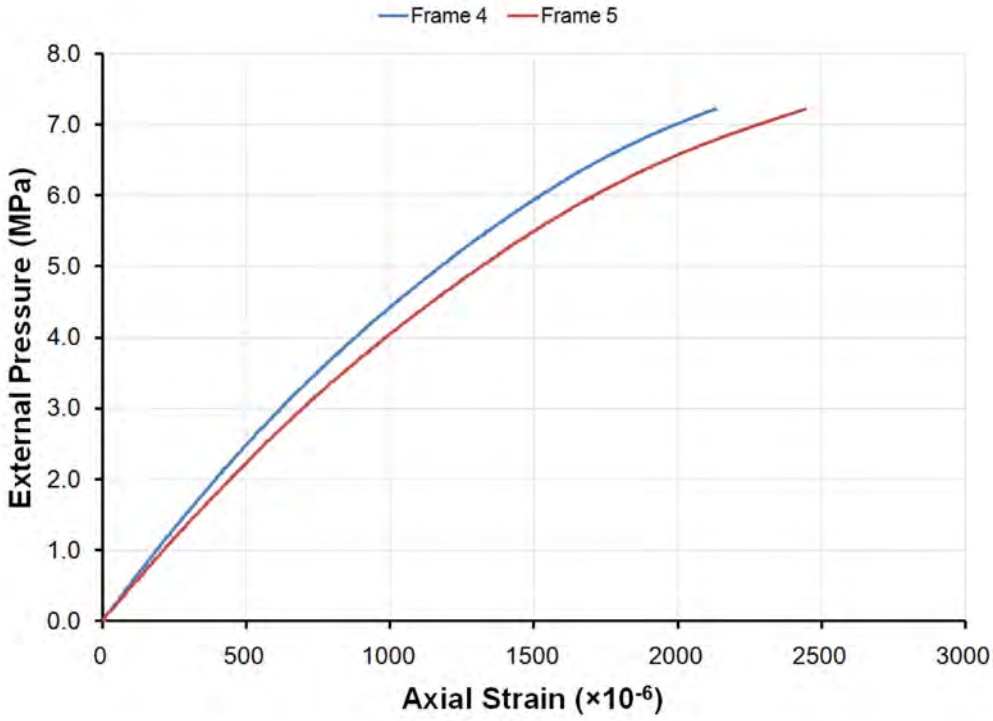

Figure 331: Pressure-strain curves showing axial shell strains outside Frames 4 and 5 of specimen L510-No36 at 0°

Annex I Strain distribution about circumference

I.1 L510-No13

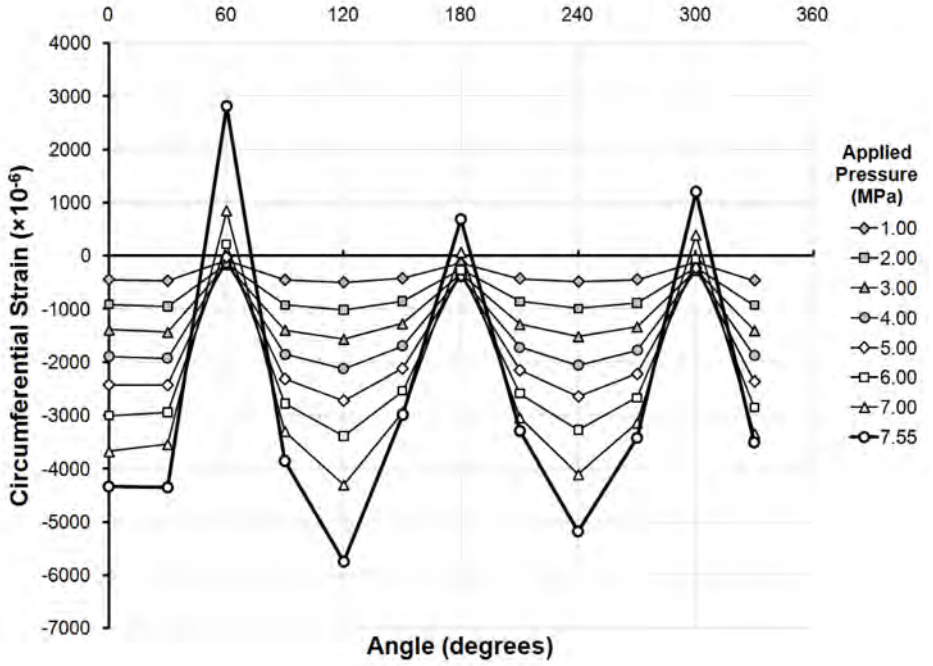

Figure 332: Circumferential strain distribution at the flange of Frame 5 of specimen L510-No13, at pressures up to and including the collapse pressure.

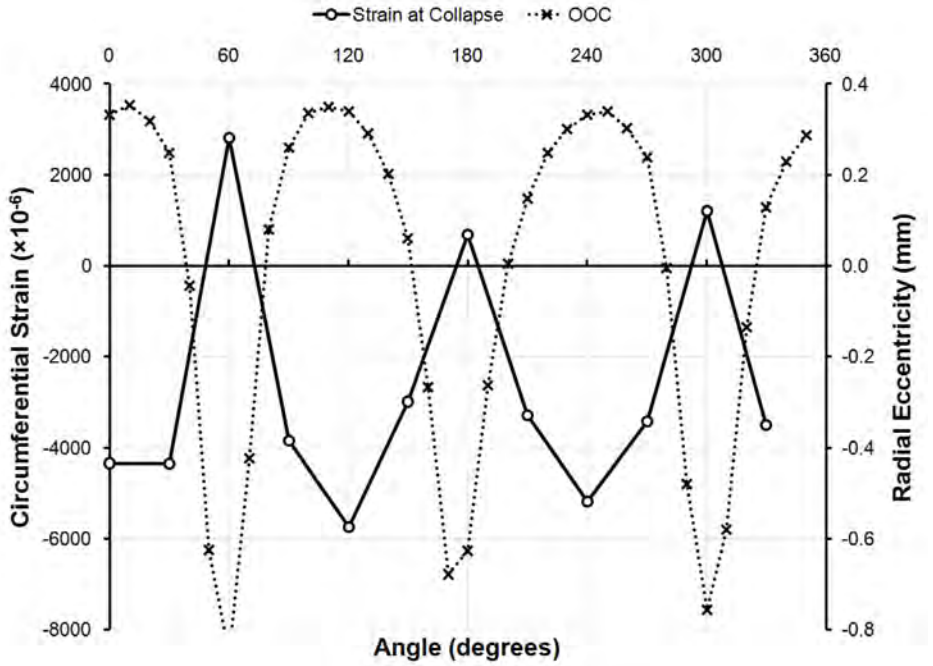

Figure 333: Circumferential strain distribution at the flange of Frame 5 of specimen L510-No13 at the collapse pressure, plotted with the initial out-of-circularity at that location.

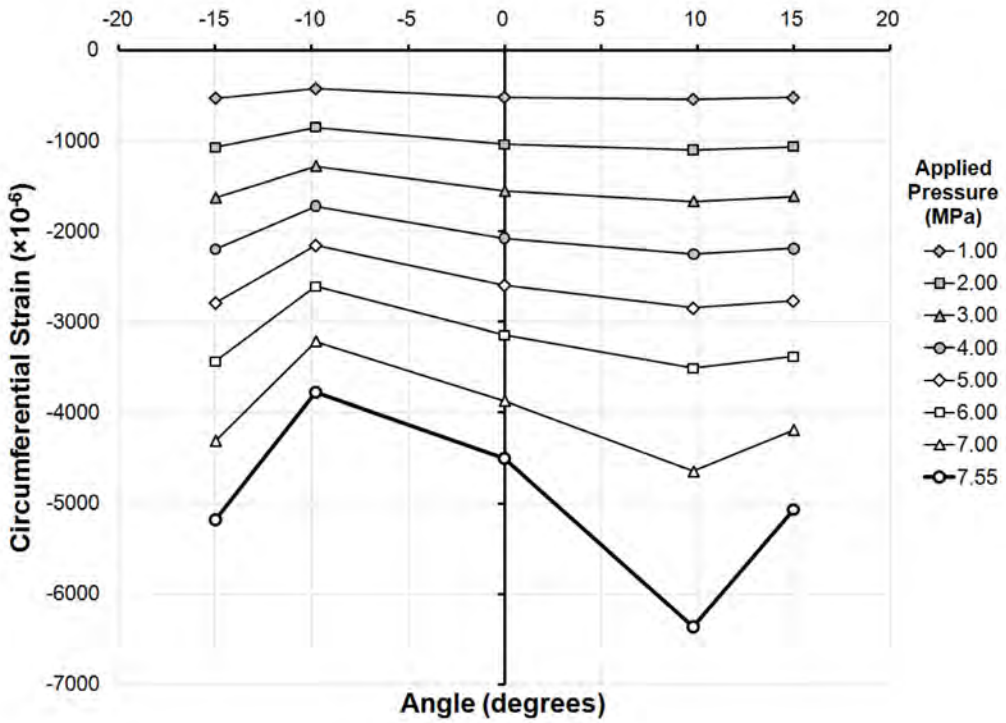

Figure 334: Circumferential strain distribution inside the shell in the centre of Bay 4 of specimen L510-No13, at pressures up to and including the collapse pressure.

I.2 L510-No14

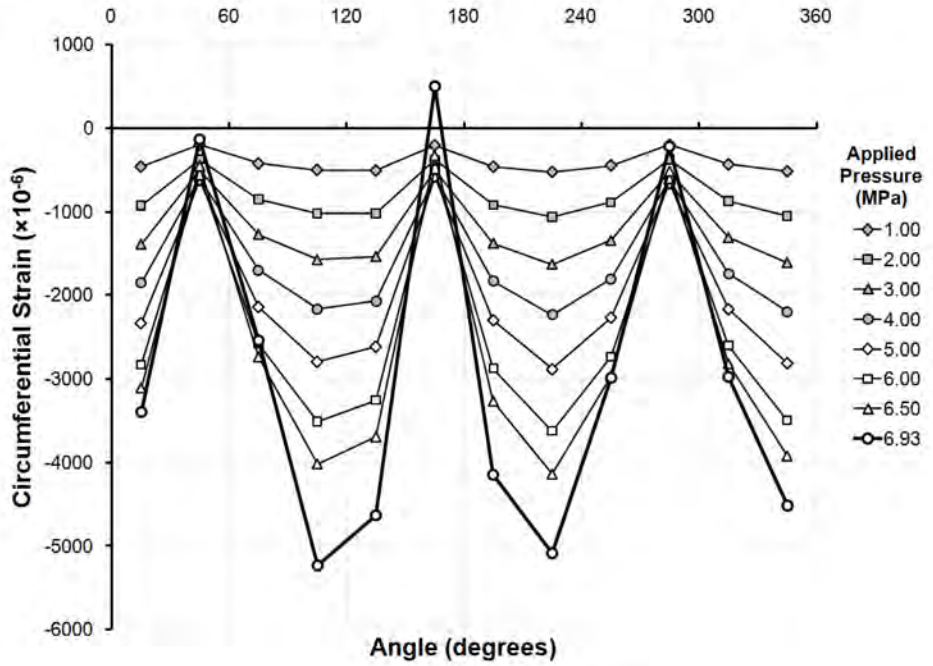

Figure 335: Circumferential strain distribution at the flange of Frame 4 of specimen L510-No14, at pressures up to and including the collapse pressure.

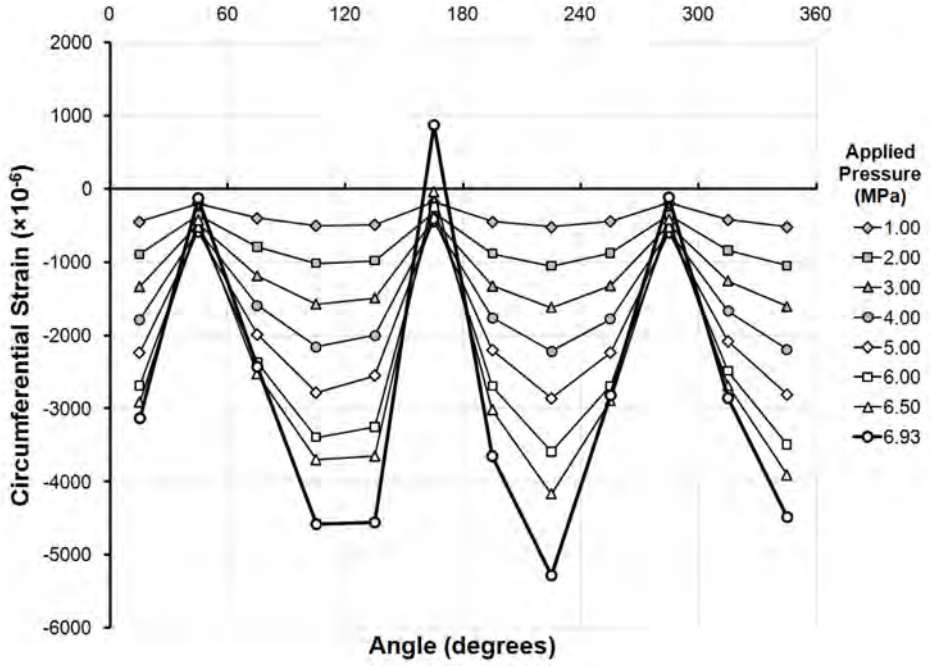

Figure 336: Circumferential strain distribution at the flange of Frame 5 of specimen L510-No14, at pressures up to and including the collapse pressure.

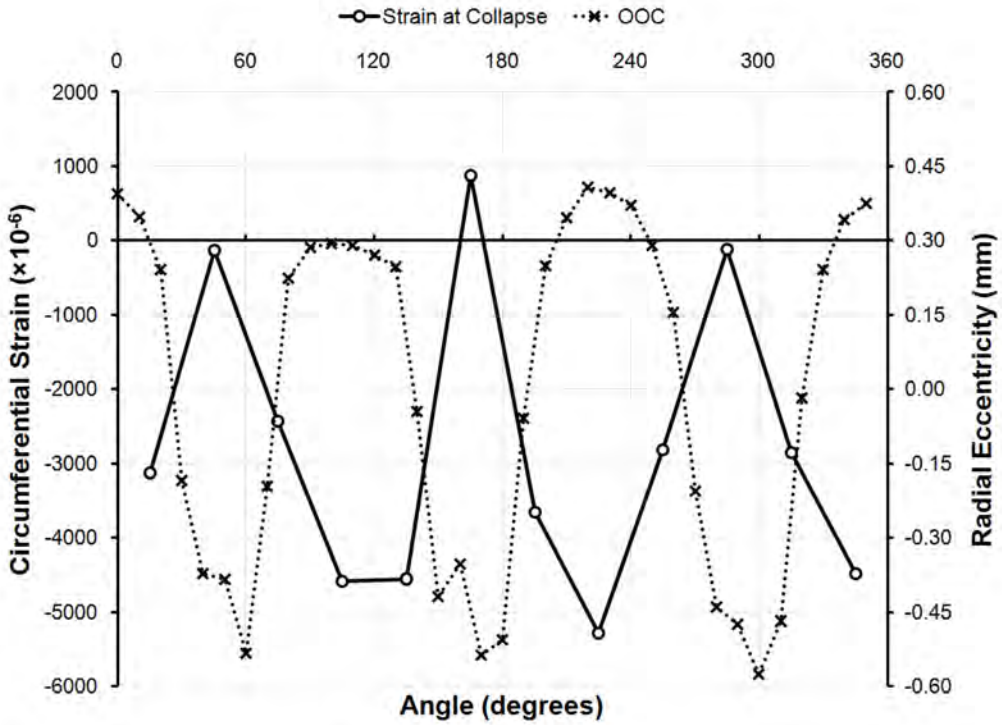

Figure 337: Circumferential strain distribution at the flange of Frame 5 of specimen L510-No14 at the collapse pressure, plotted with the initial out-of-circularity at that location.

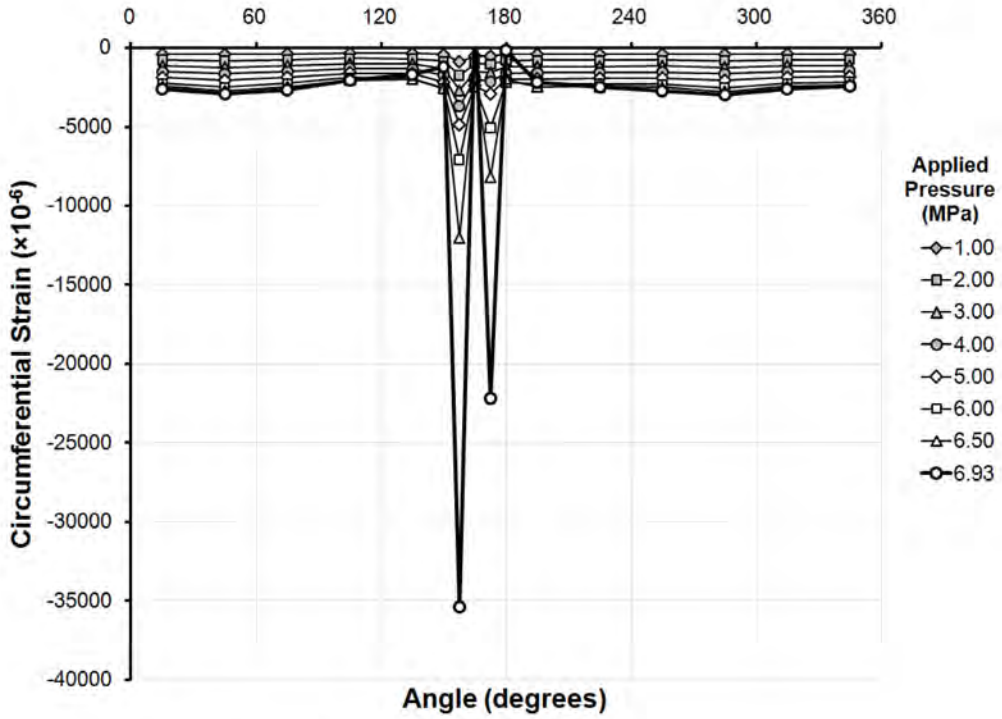

Figure 338: Circumferential strain distribution outside the shell in the centre of Bay 4 of specimen L510-No14, at pressures up to and including the collapse pressure.

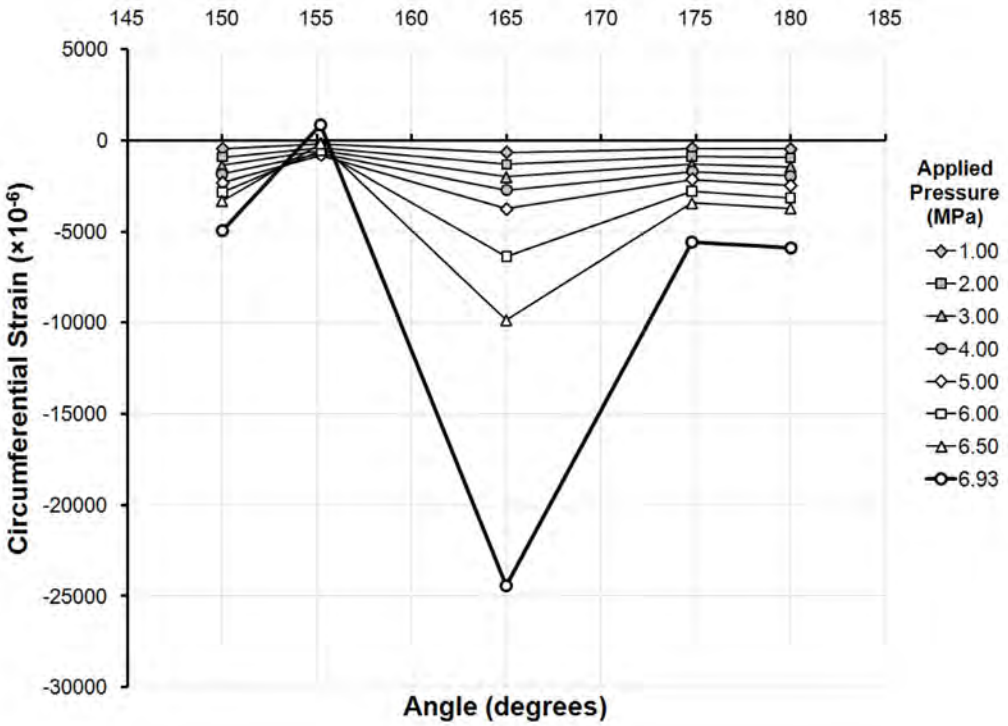

Figure 339: Circumferential strain distribution inside the shell in the centre of Bay 4 of specimen L510-No14, at pressures up to and including the collapse pressure.

I.3 L510-No17

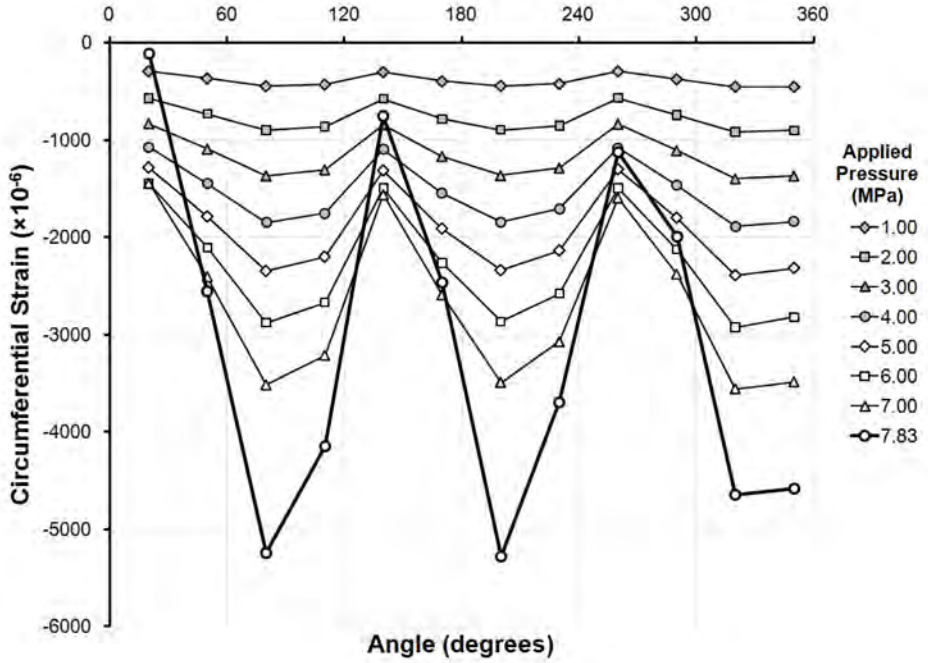

Figure 340: Circumferential strain distribution at the flange of Frame 5 of specimen L510-No17, at pressures up to and including the collapse pressure.

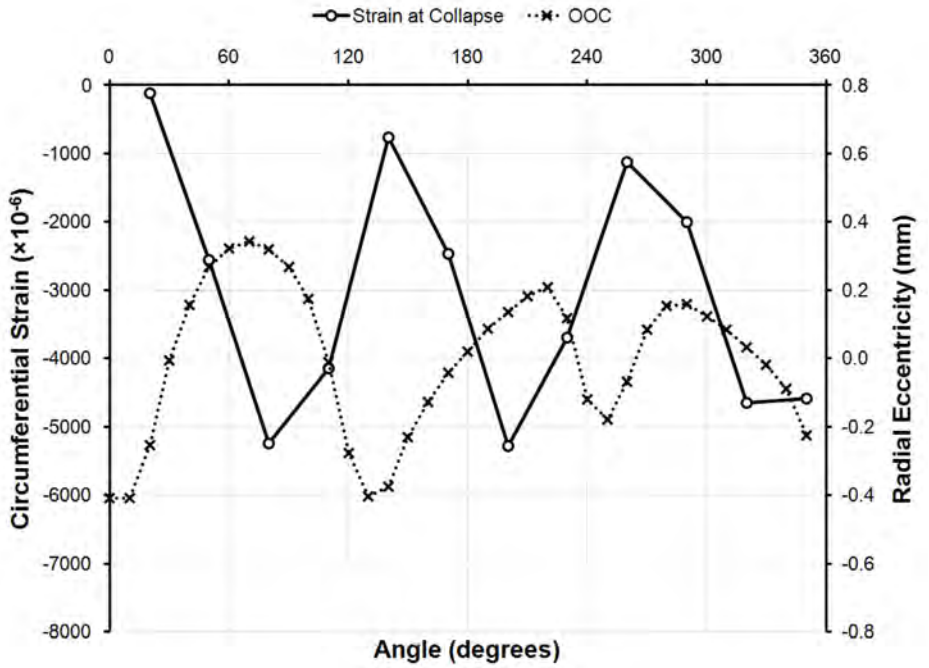

Figure 341: Circumferential strain distribution at the flange of Frame 5 of specimen L510-No17 at the collapse pressure, plotted with the initial out-of-circularity at that location.

I.4 L510-No18

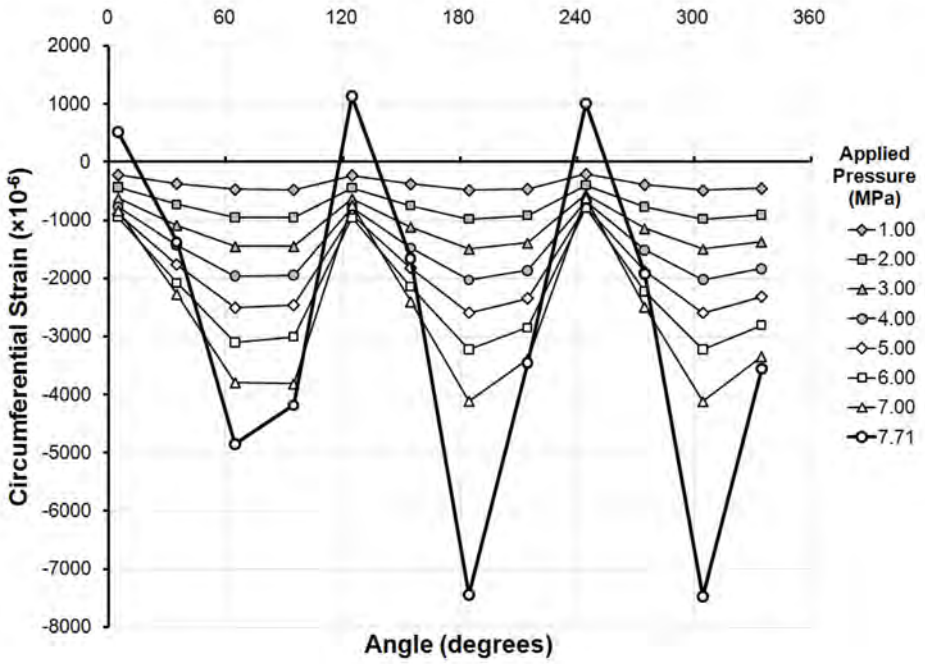

Figure 342: Circumferential strain distribution at the flange of Frame 4 of specimen L510-No18, at pressures up to and including the collapse pressure.

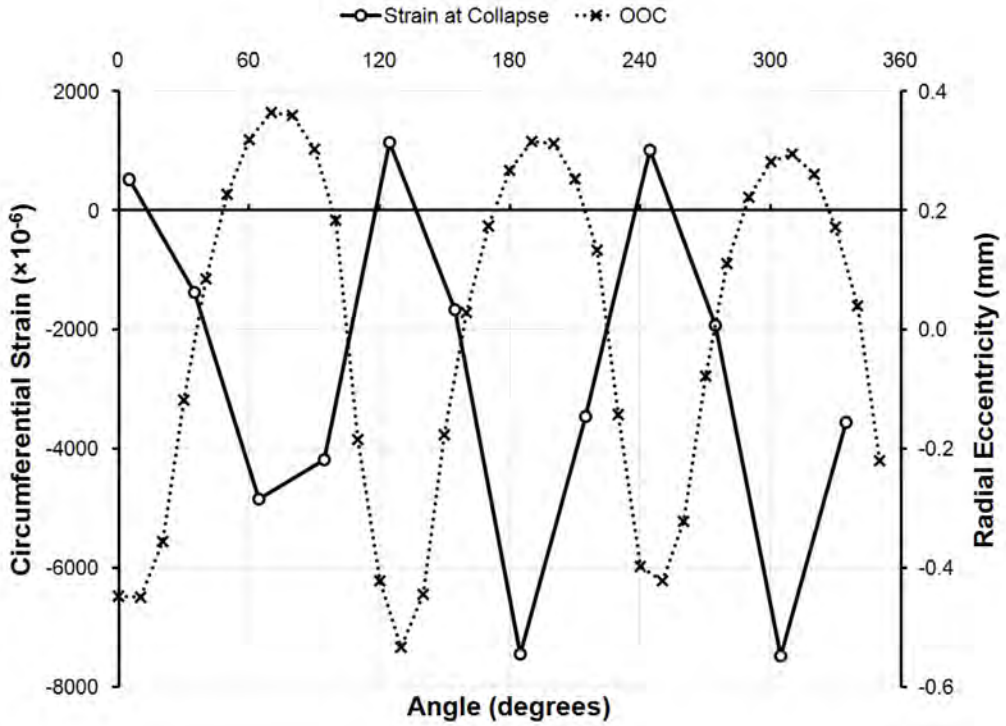

Figure 343: Circumferential strain distribution at the flange of Frame 4 of specimen L510-No18 at the collapse pressure, plotted with the initial out-of-circularity at that location.

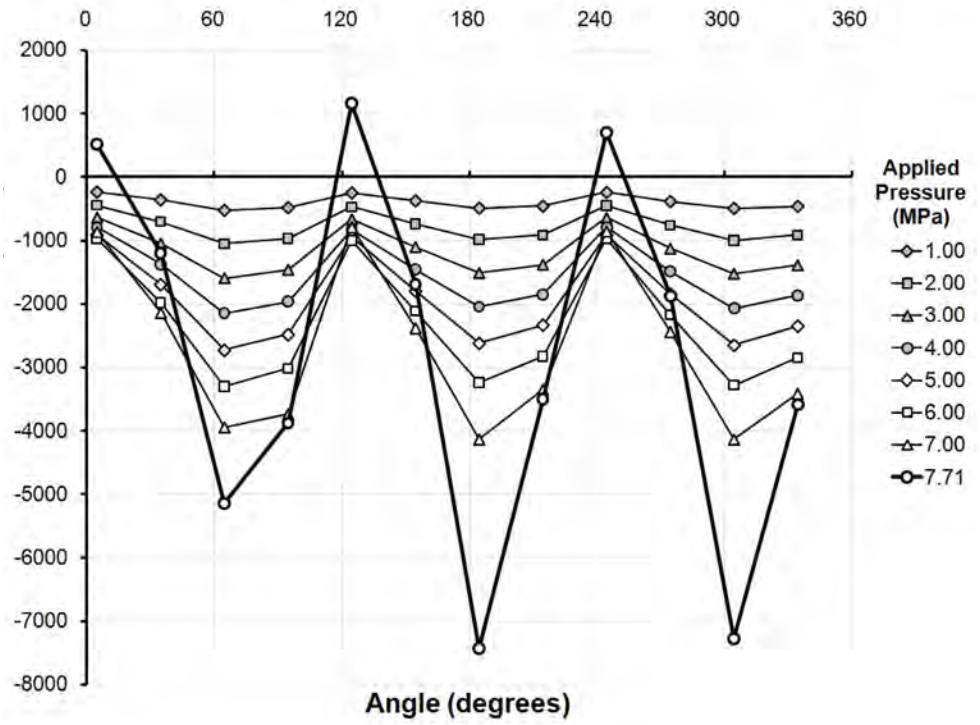

Figure 344: Circumferential strain distribution at the flange of Frame 5 of specimen L510-No18, at pressures up to and including the collapse pressure.

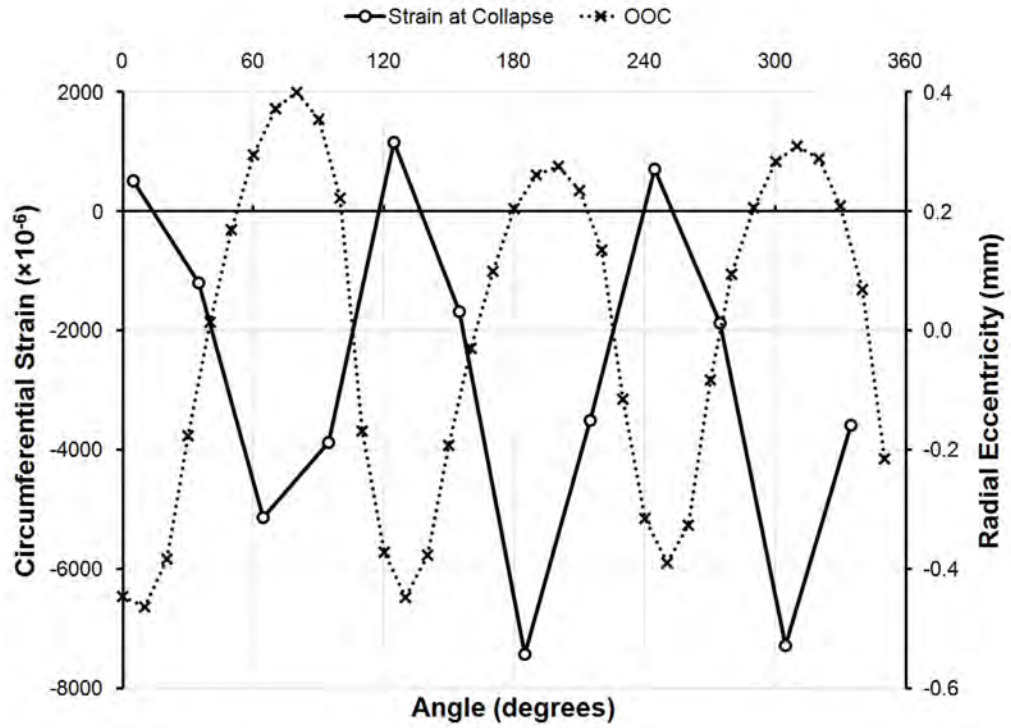

Figure 345: Circumferential strain distribution at the flange of Frame 5 of specimen L510-No18 at the collapse pressure, plotted with the initial out-of-circularity at that location.

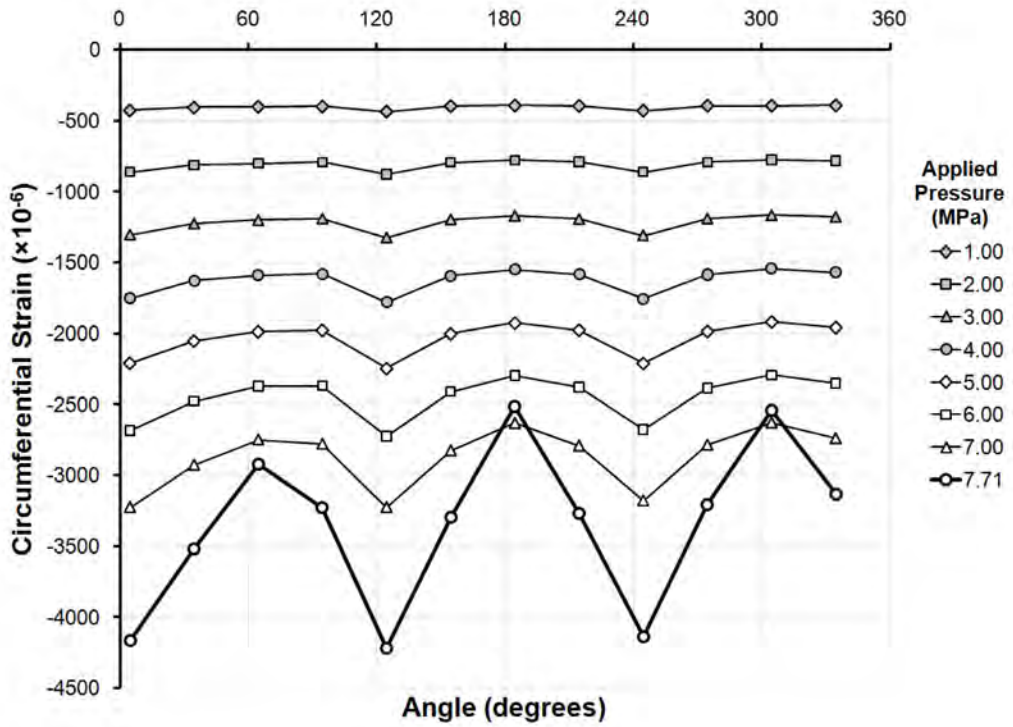

Figure 346: Circumferential strain distribution outside the shell in the centre of Bay 4 of specimen L510-No18, at pressures up to and including the collapse pressure.

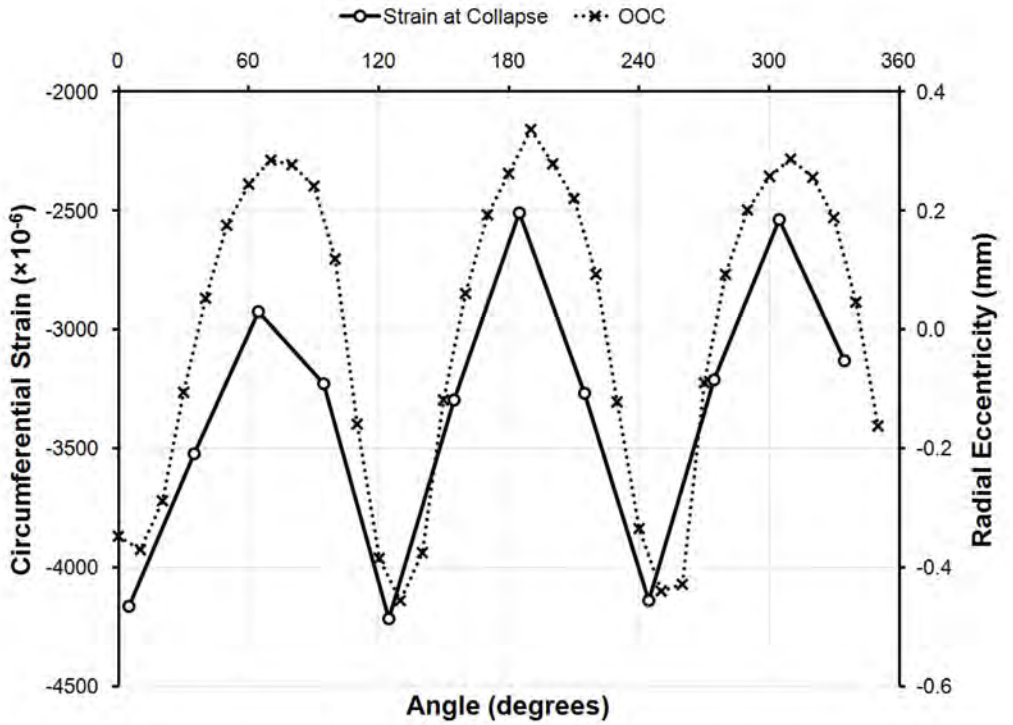

Figure 347: Circumferential strain distribution outside the shell at Bay 4 of specimen L510-No18 at the collapse pressure, plotted with the initial out-of-circularity at that location.

I.5 L510-No19

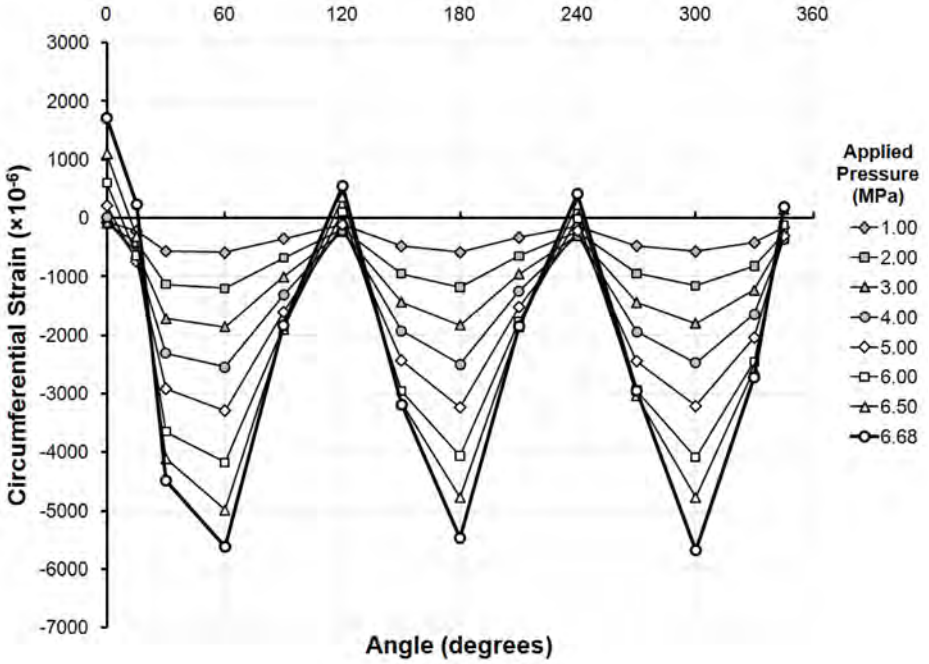

Figure 348: Circumferential strain distribution at the flange of Frame 4 of specimen L510-No19, at pressures up to and including the collapse pressure.

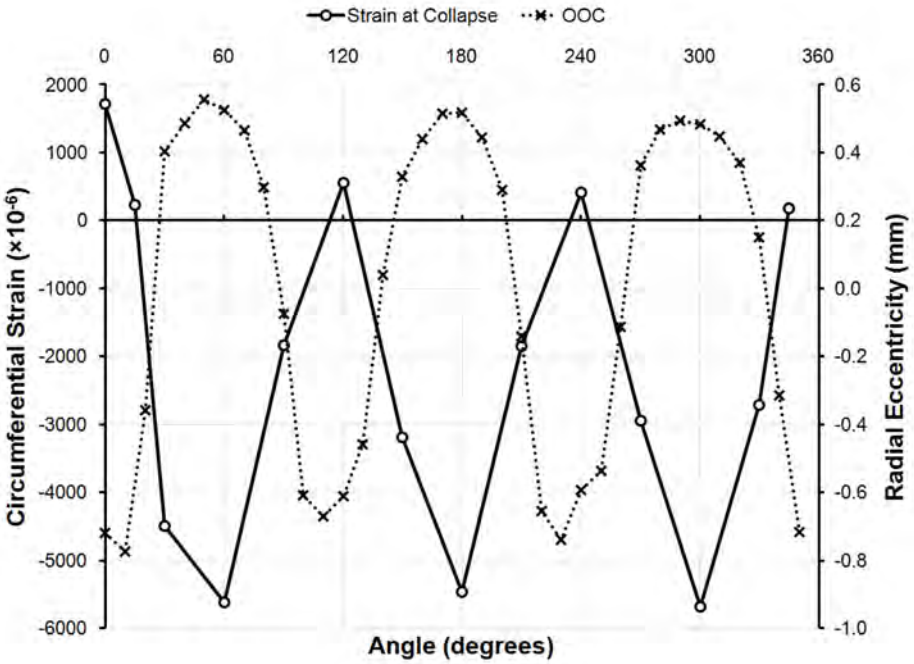

Figure 349: Circumferential strain distribution at the flange of Frame 4 of specimen L510-No19 at the collapse pressure, plotted with the initial out-of-circularity at that location.

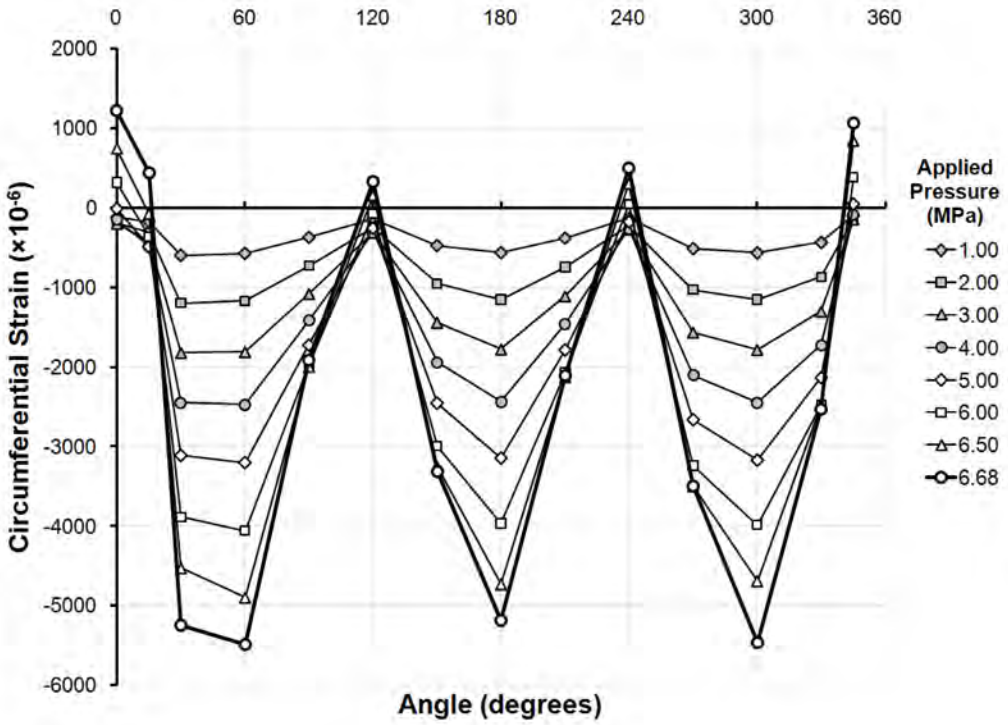

Figure 350: Circumferential strain distribution at the flange of Frame 5 of specimen L510-No19, at pressures up to and including the collapse pressure.

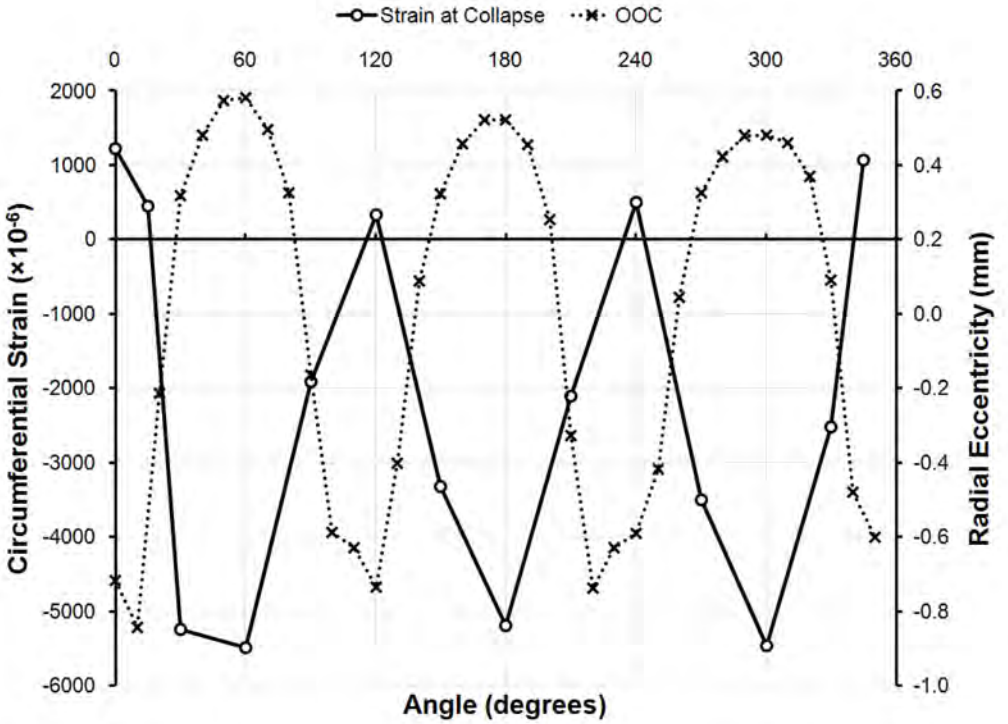

Figure 351: Circumferential strain distribution at the flange of Frame 5 of specimen L510-No19 at the collapse pressure, plotted with the initial out-of-circularity at that location.

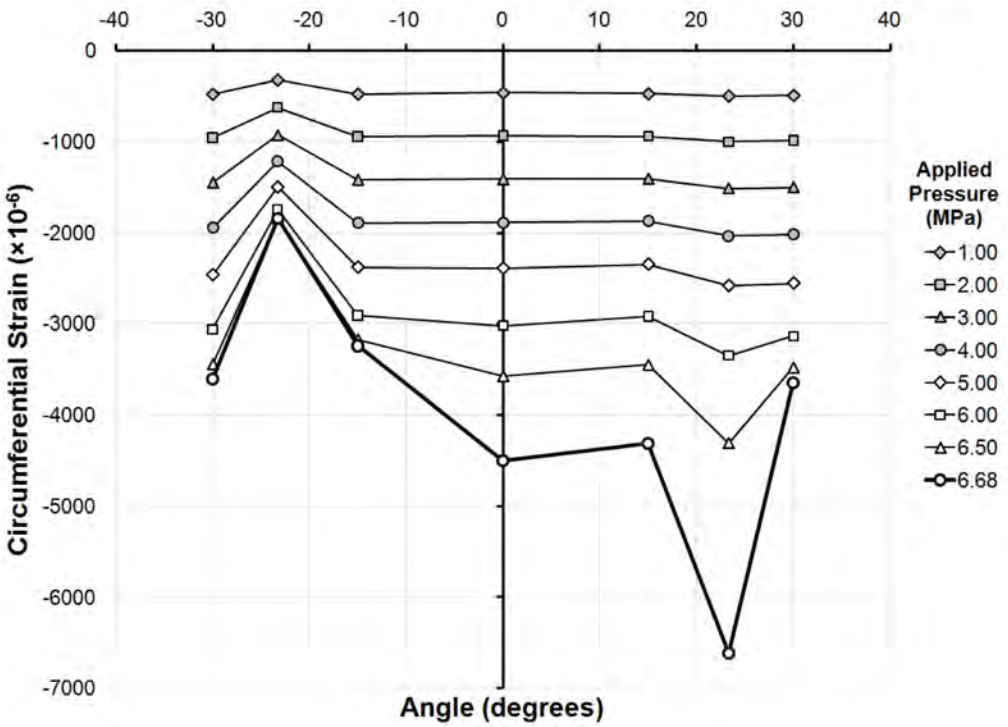

Figure 352: Circumferential strain distribution inside the shell in the centre of Bay 4 of specimen L510-No19, at pressures up to and including the collapse pressure.

I.6 L510-No20

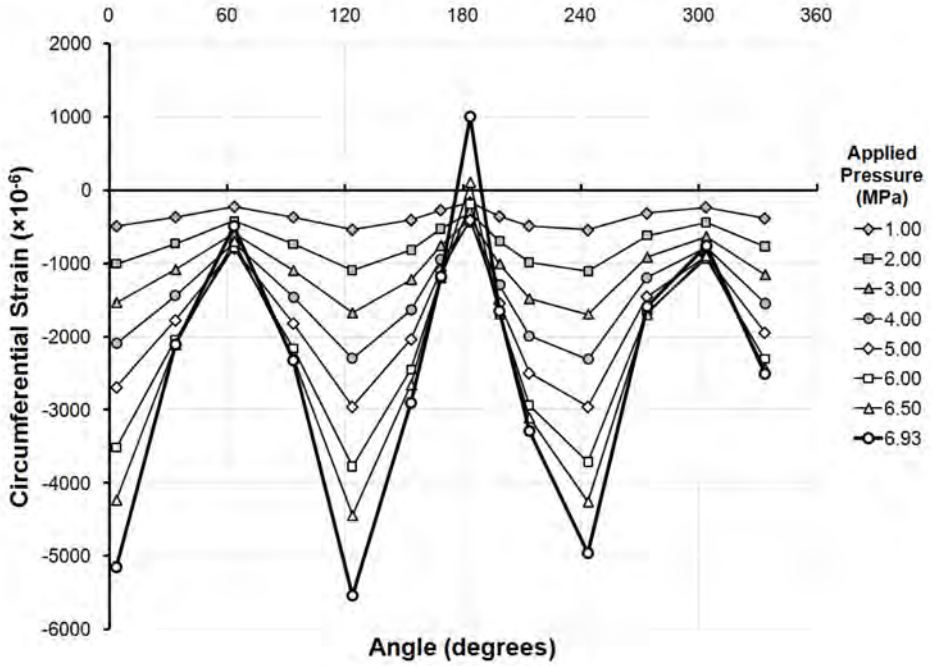

Figure 353: Circumferential strain distribution at the flange of Frame 4 of specimen L510-No20, at pressures up to and including the collapse pressure.

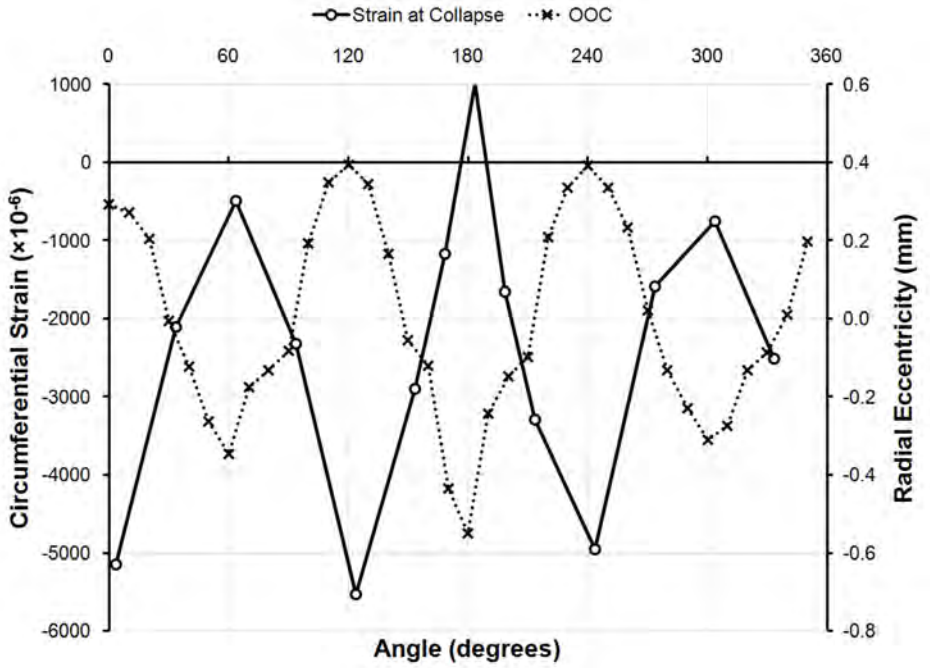

Figure 354: Circumferential strain distribution at the flange of Frame 4 of specimen L510-No20 at the collapse pressure, plotted with the initial out-of-circularity at that location.

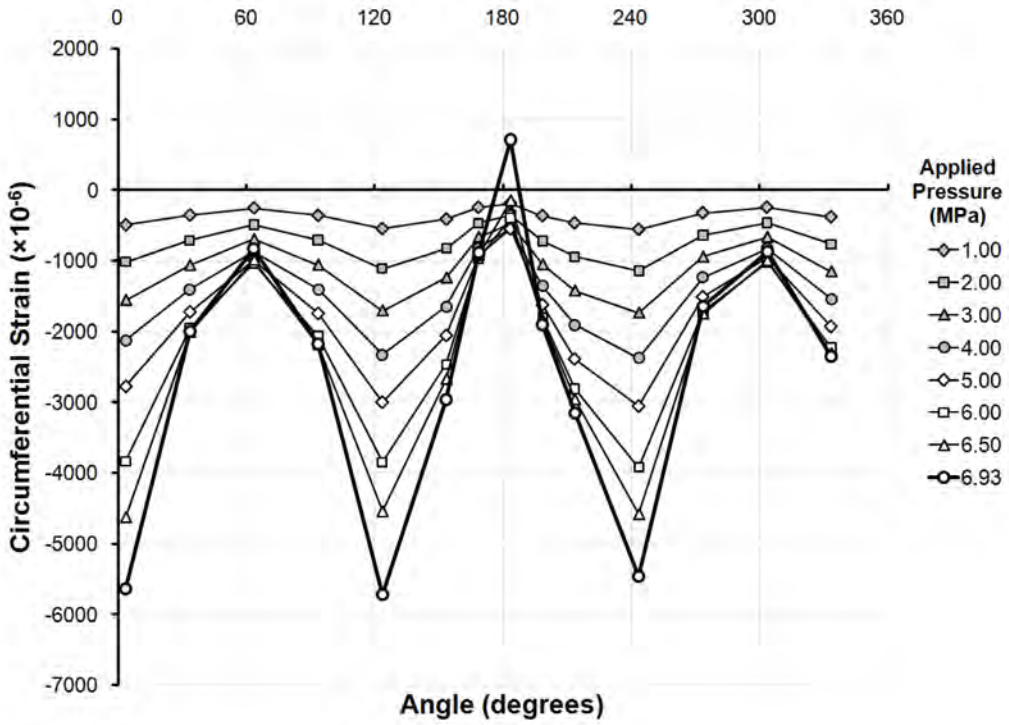

Figure 355: Circumferential strain distribution at the flange of Frame 5 of specimen L510-No20, at pressures up to and including the collapse pressure.

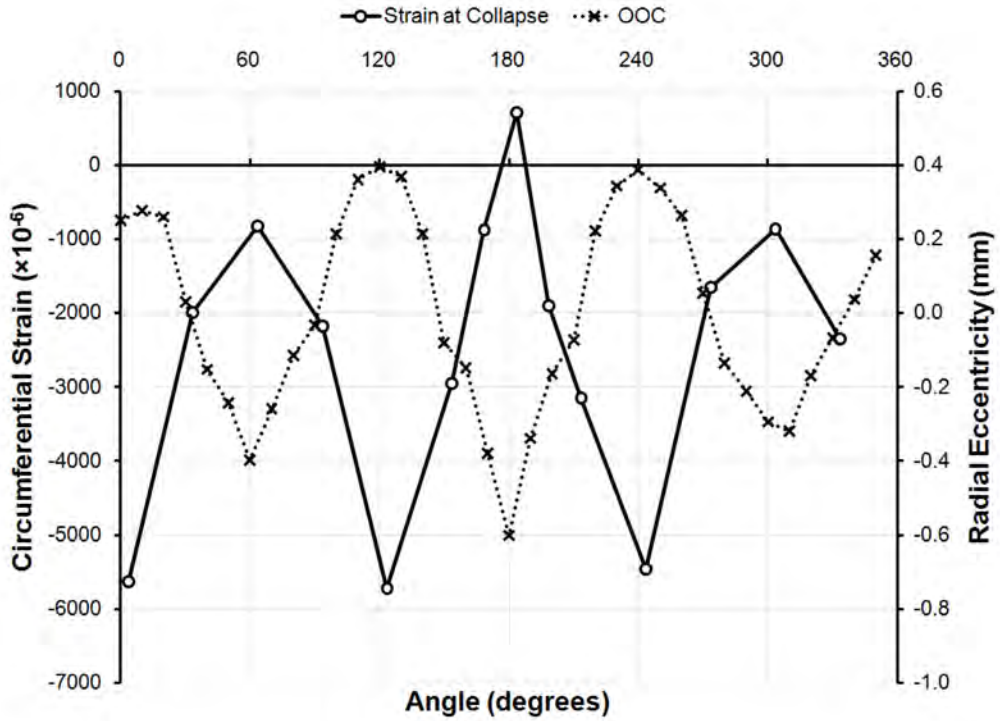

Figure 356: Circumferential strain distribution at the flange of Frame 5 of specimen L510-No20 at the collapse pressure, plotted with the initial out-of-circularity at that location.

I.7 L510-No25

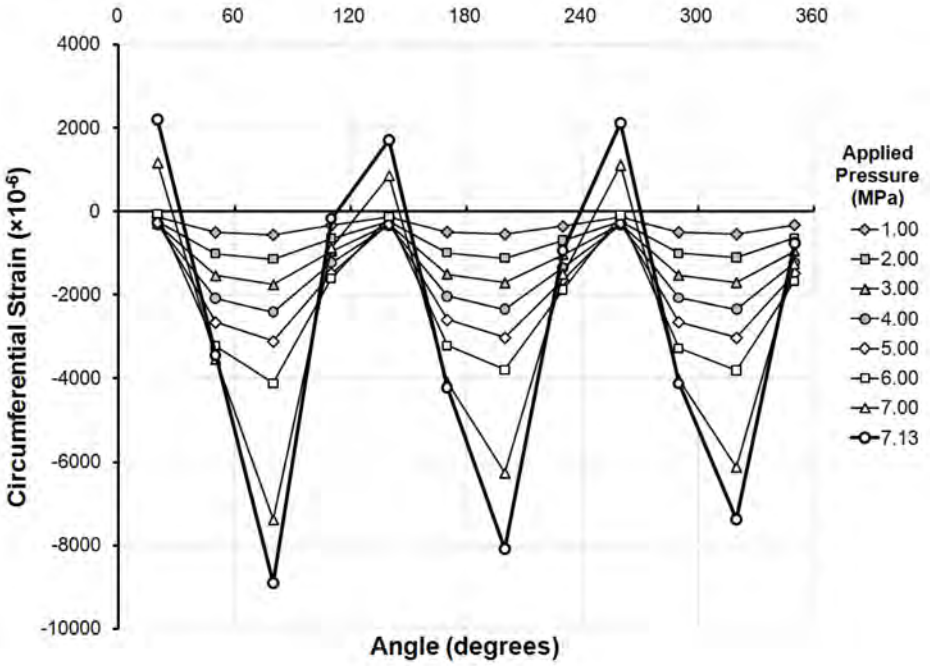

Figure 357: Circumferential strain distribution at the flange of Frame 4 of specimen L510-No25, at pressures up to and including the collapse pressure.

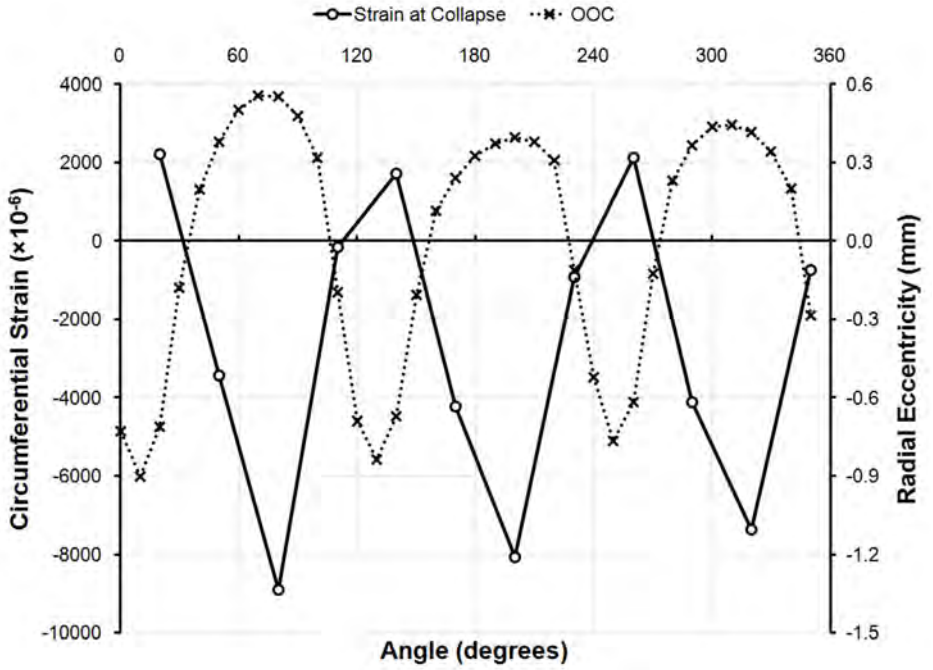

Figure 358: Circumferential strain distribution at the flange of Frame 4 of specimen L510-No25 at the collapse pressure, plotted with the initial out-of-circularity at that location.

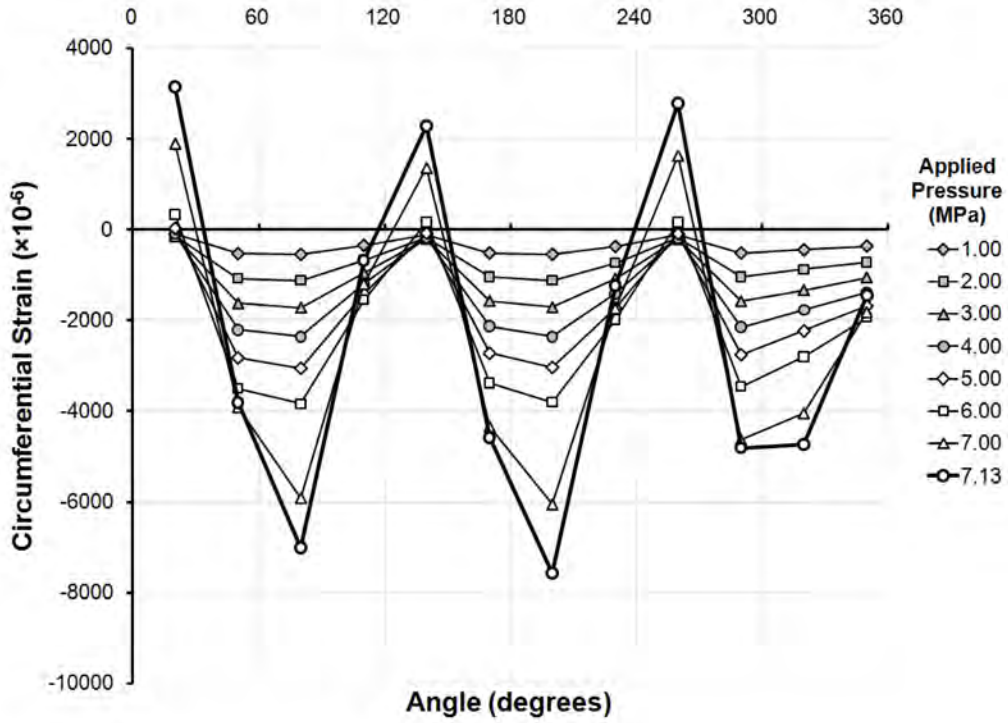

Figure 359: Circumferential strain distribution at the flange of Frame 5 of specimen L510-No25, at pressures up to and including the collapse pressure.

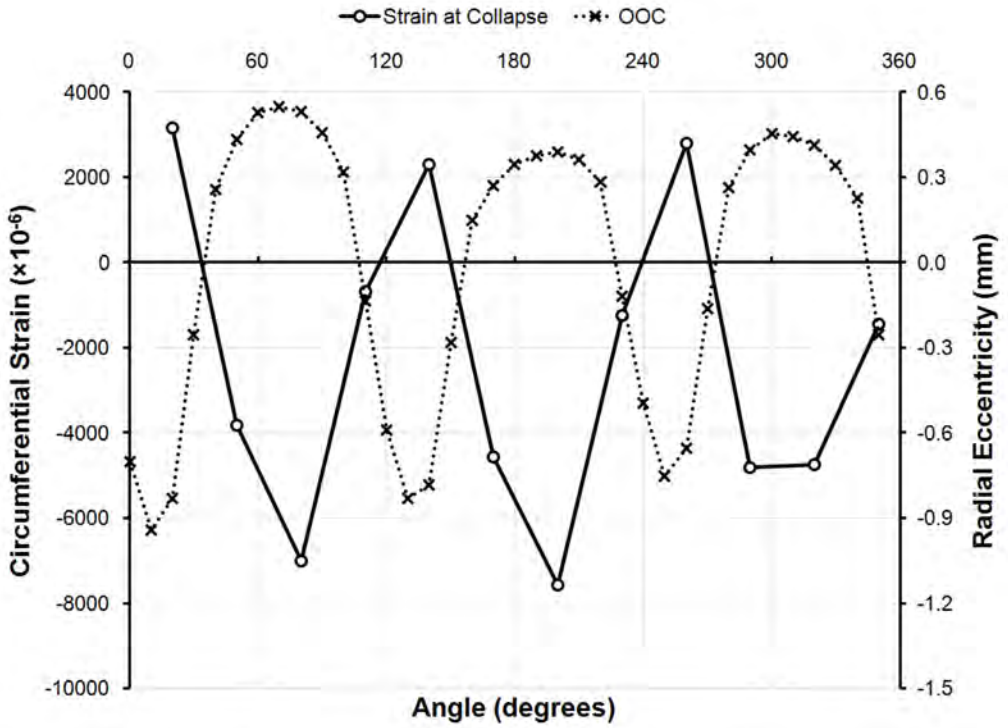

Figure 360: Circumferential strain distribution at the flange of Frame 5 of specimen L510-No25 at the collapse pressure, plotted with the initial out-of-circularity at that location.

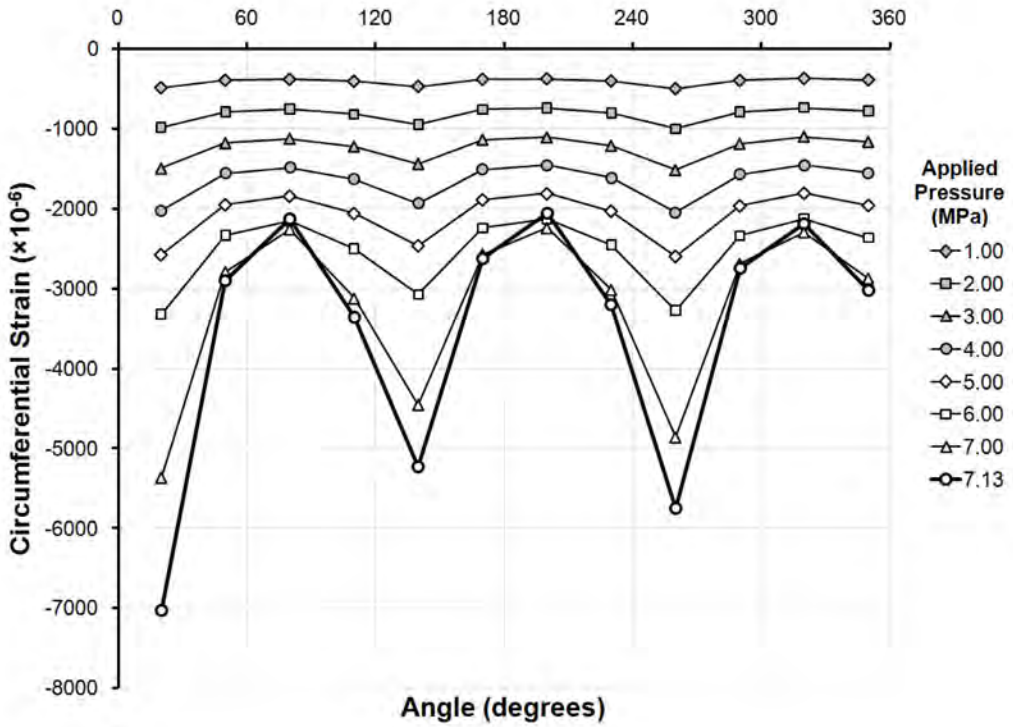

Figure 361: Circumferential strain distribution outside the shell in the centre of Bay 4 of specimen L510-No25, at pressures up to and including the collapse pressure.

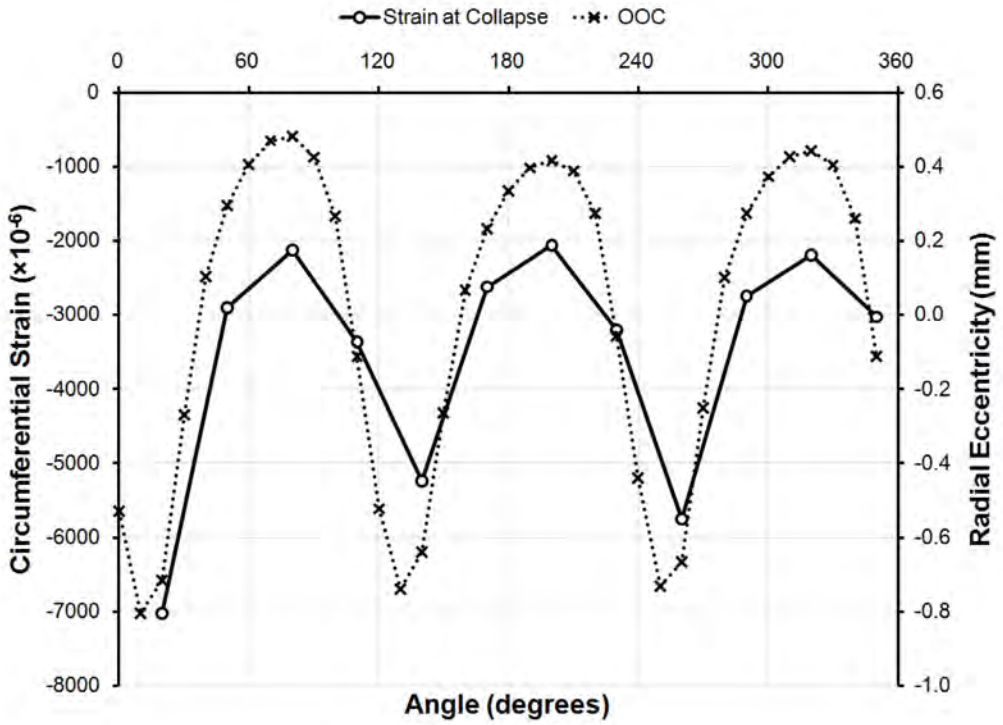

Figure 362: Circumferential strain distribution outside the shell at Bay 4 of specimen L510-No25 at the collapse pressure, plotted with the initial out-of-circularity at that location.

I.8 L510-No26

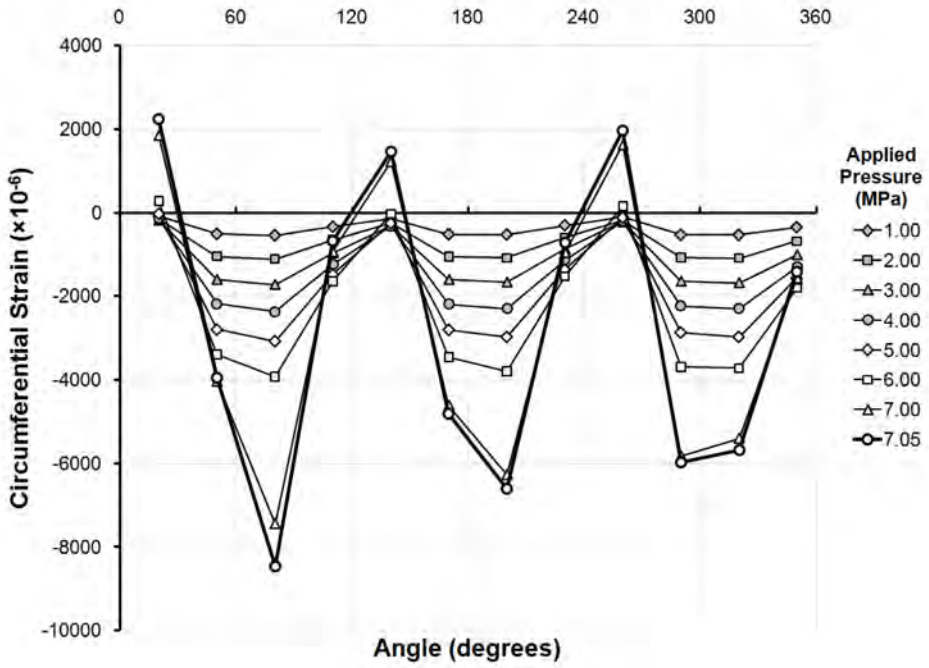

Figure 363: Circumferential strain distribution at the flange of Frame 4 of specimen L510-No26, at pressures up to and including the collapse pressure.

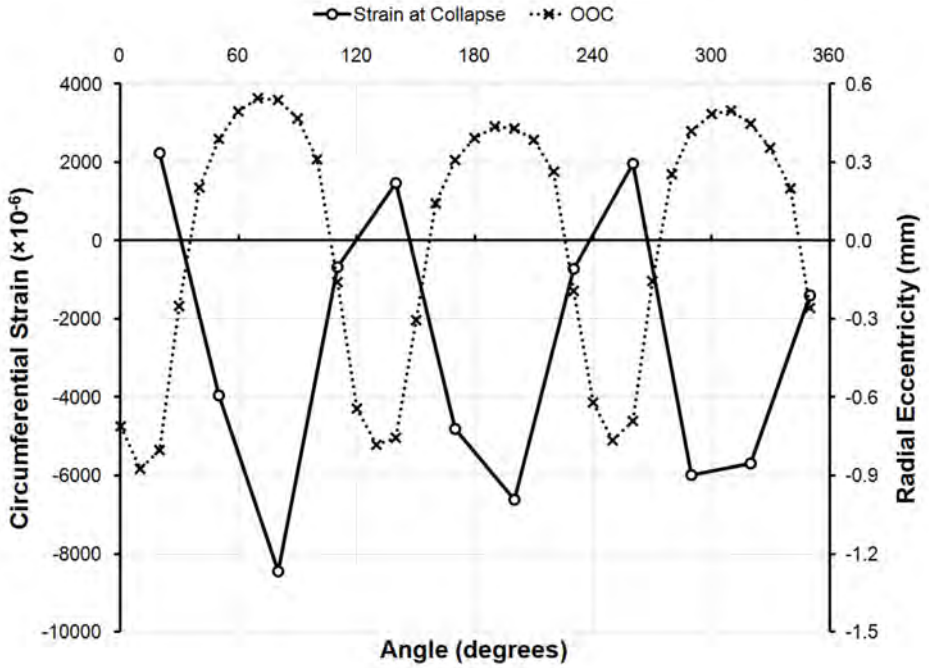

Figure 364: Circumferential strain distribution at the flange of Frame 4 of specimen L510-No26 at the collapse pressure, plotted with the initial out-of-circularity at that location.

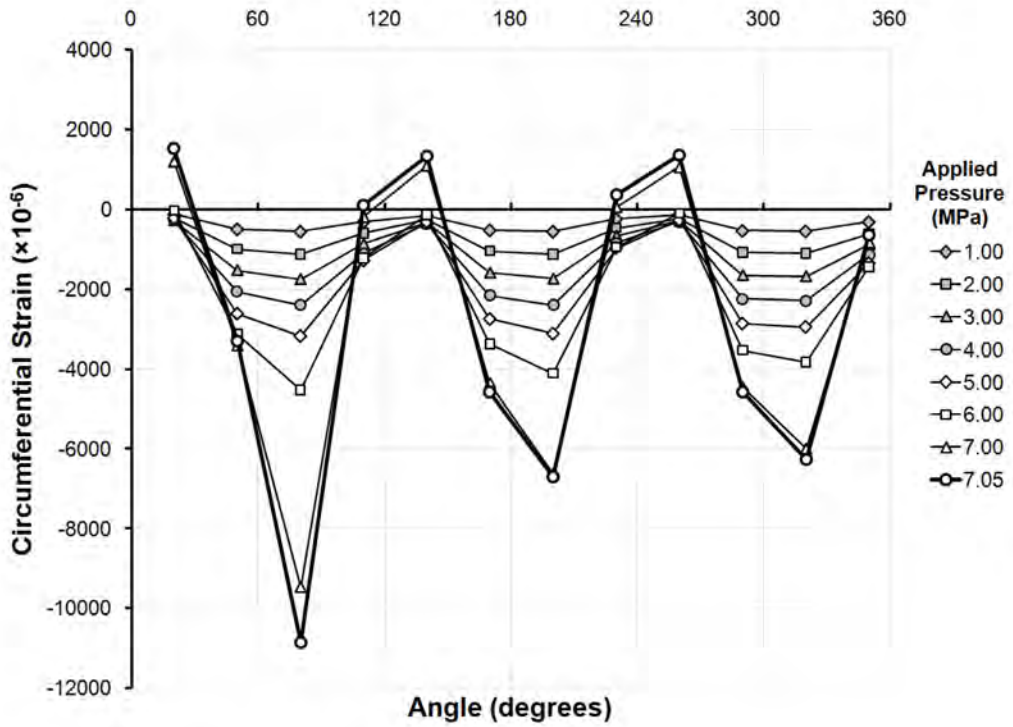

Figure 365: Circumferential strain distribution at the flange of Frame 5 of specimen L510-No26, at pressures up to and including the collapse pressure.

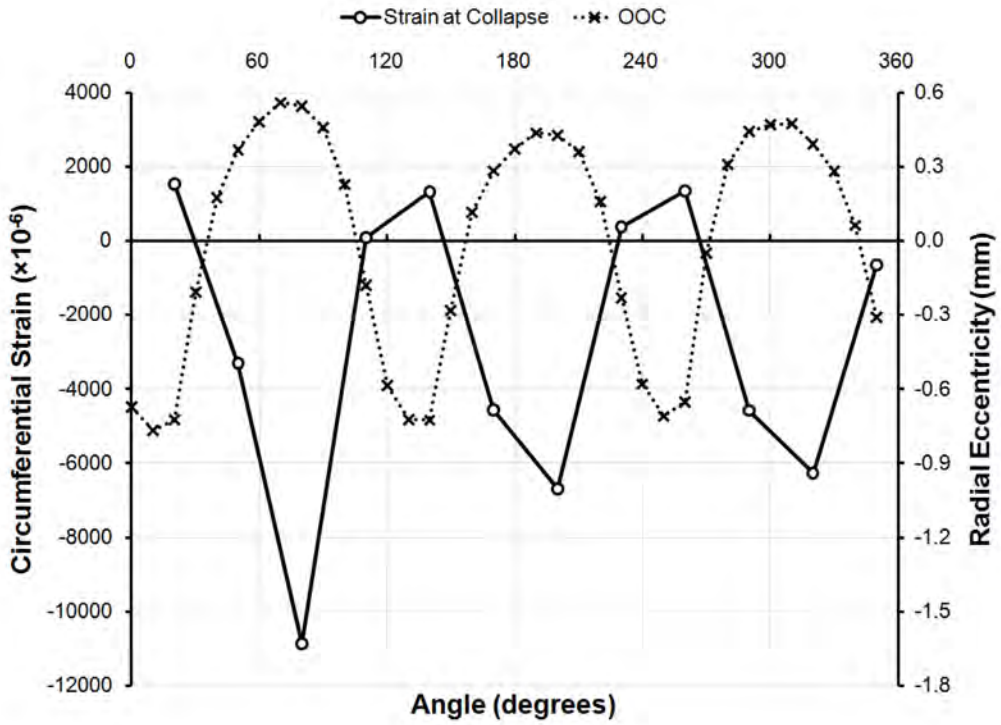

Figure 366: Circumferential strain distribution at the flange of Frame 5 of specimen L510-No26 at the collapse pressure, plotted with the initial out-of-circularity at that location.

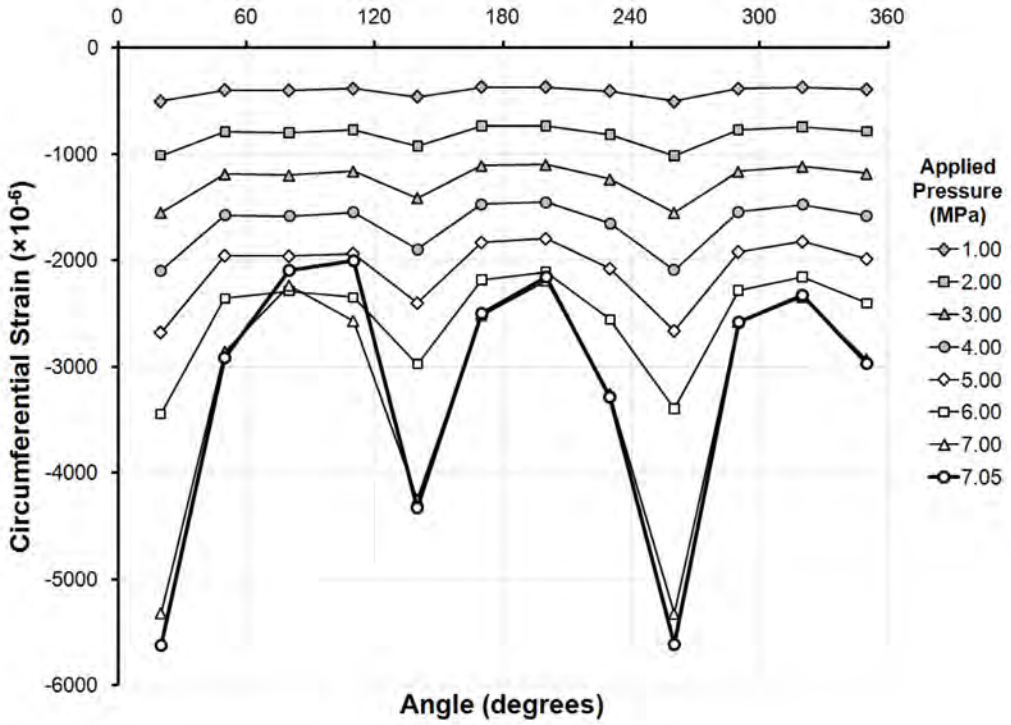

Figure 367: Circumferential strain distribution outside the shell in the centre of Bay 4 of specimen L510-No26, at pressures up to and including the collapse pressure.

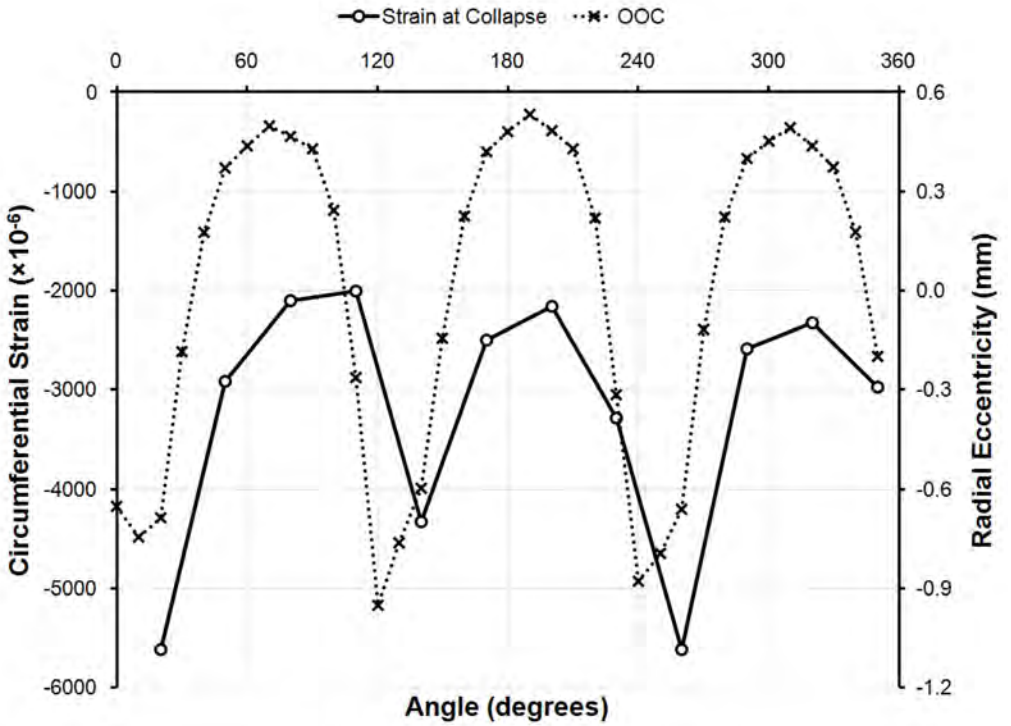

Figure 368: Circumferential strain distribution outside the shell at Bay 4 of specimen L510-No26 at the collapse pressure, plotted with the initial out-of-circularity at that location.

I.9 L510-No33

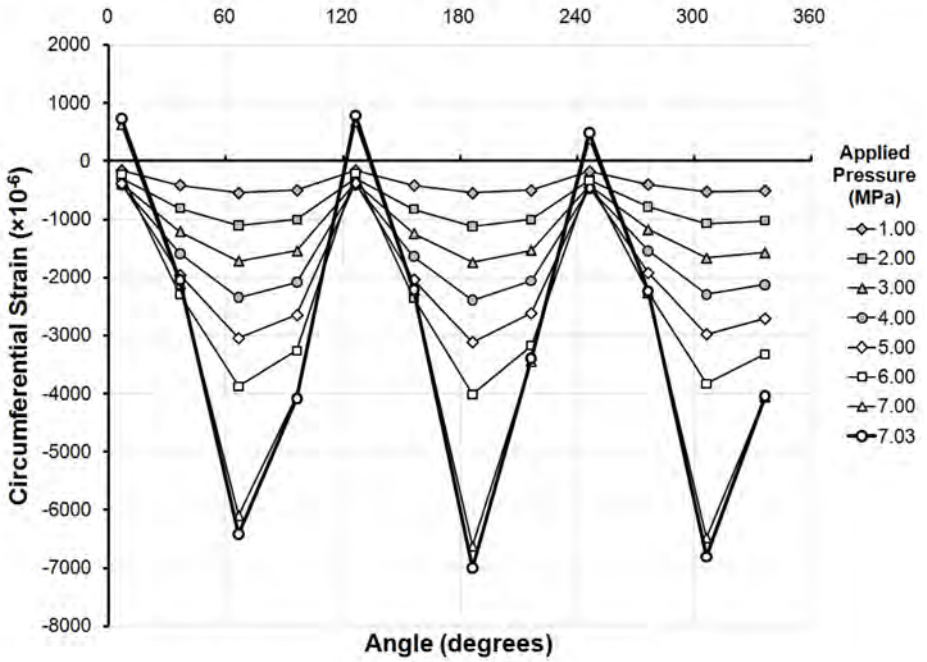

Figure 369: Circumferential strain distribution at the flange of Frame 5 of specimen L510-No33, at pressures up to and including the collapse pressure.

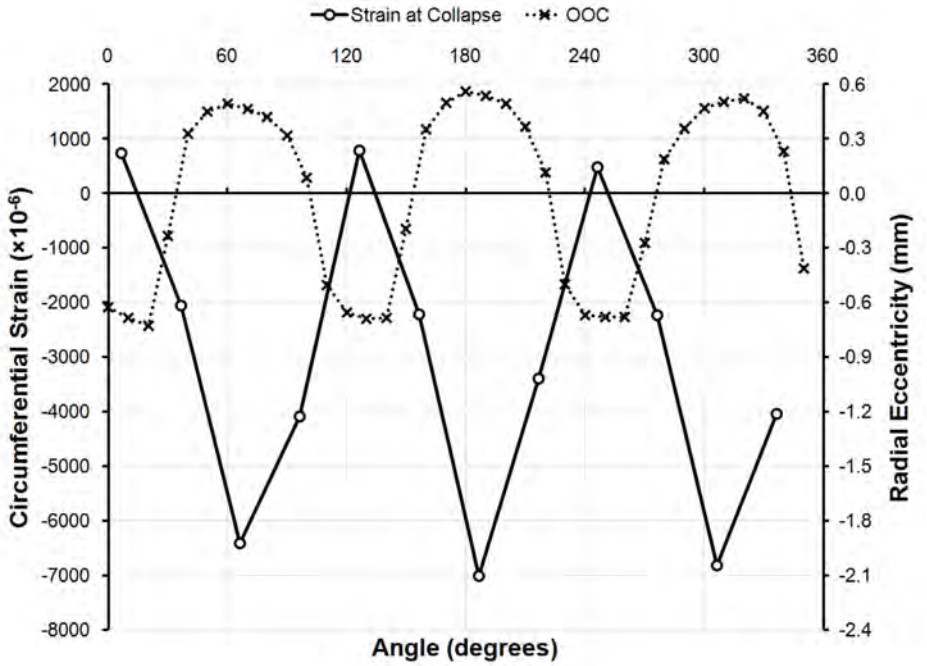

Figure 370: Circumferential strain distribution at the flange of Frame 5 of specimen L510-No33 at the collapse pressure, plotted with the initial out-of-circularity at that location.

I.10 L510-No34

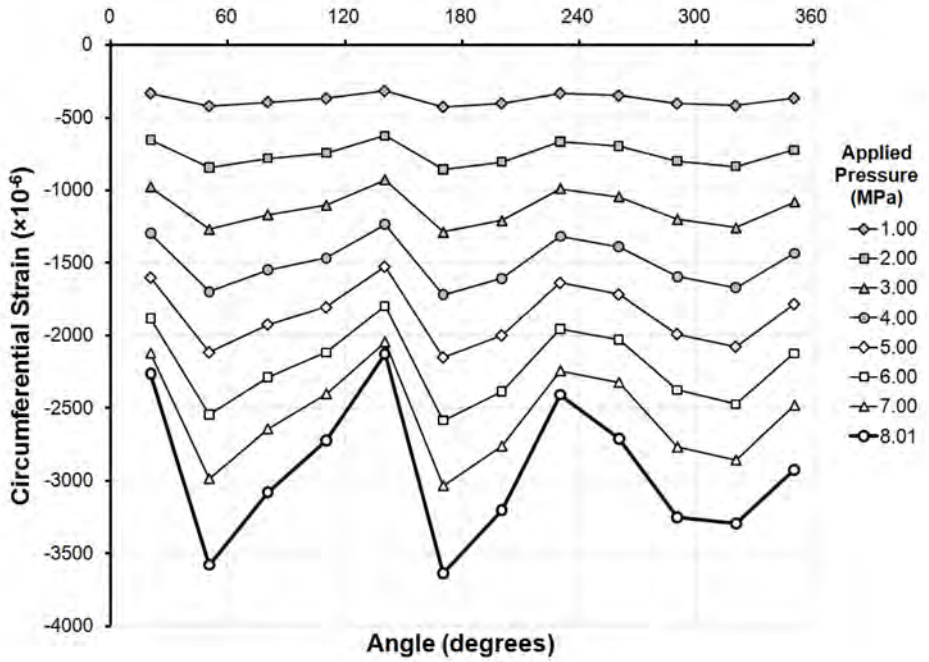

Figure 371: Circumferential strain distribution at the flange of Frame 3 of specimen L510-No34, at pressures up to and including the collapse pressure.

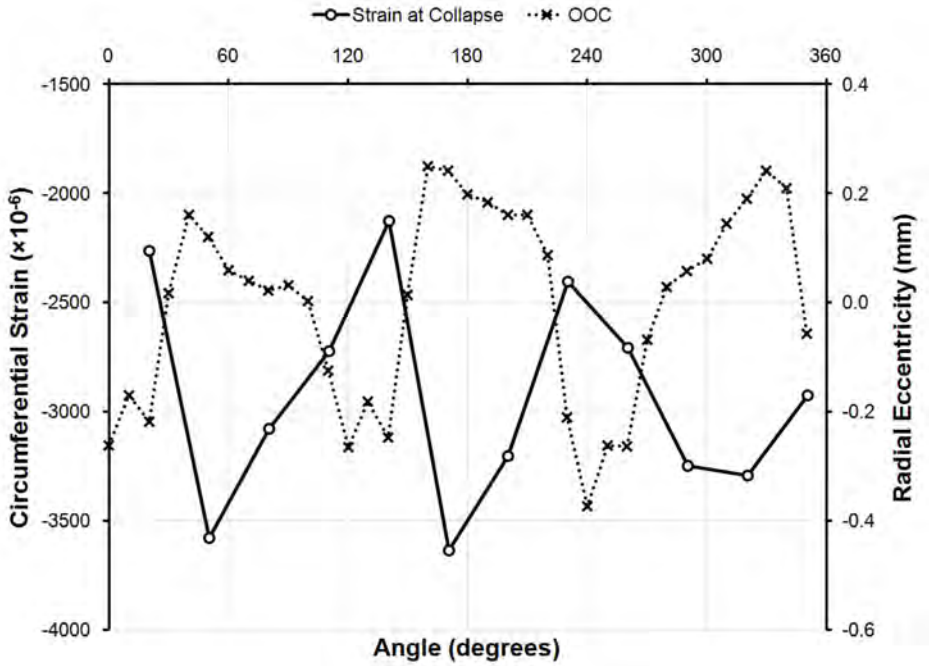

Figure 372: Circumferential strain distribution at the flange of Frame 3 of specimen L510-No34 at the collapse pressure, plotted with the initial out-of-circularity at that location.

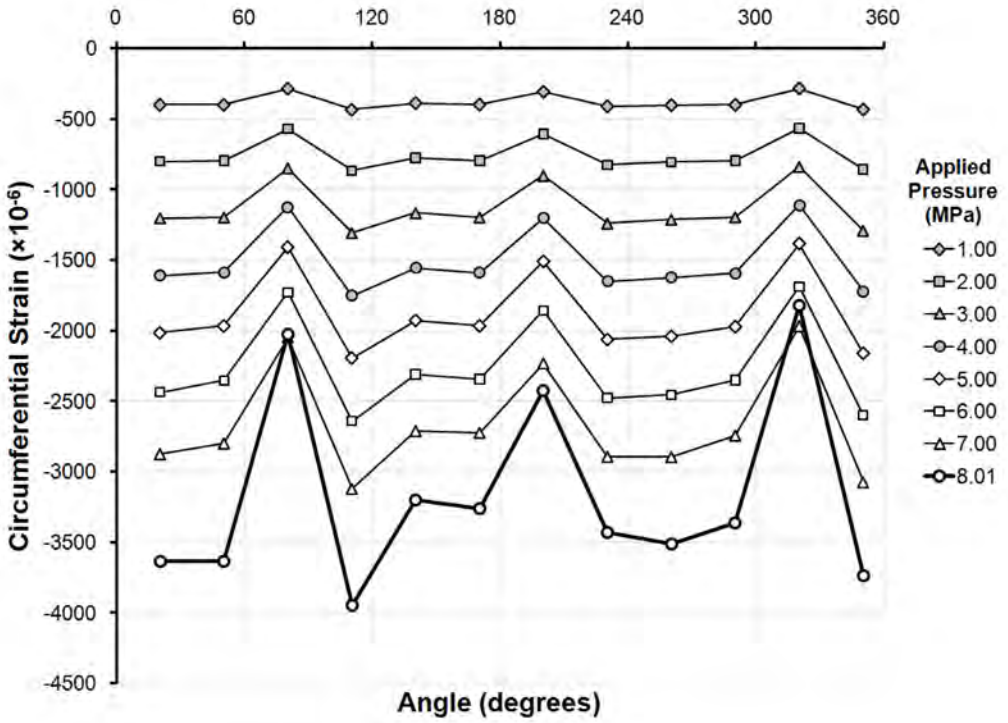

Figure 373: Circumferential strain distribution at the flange of Frame 6 of specimen L510-No34, at pressures up to and including the collapse pressure.

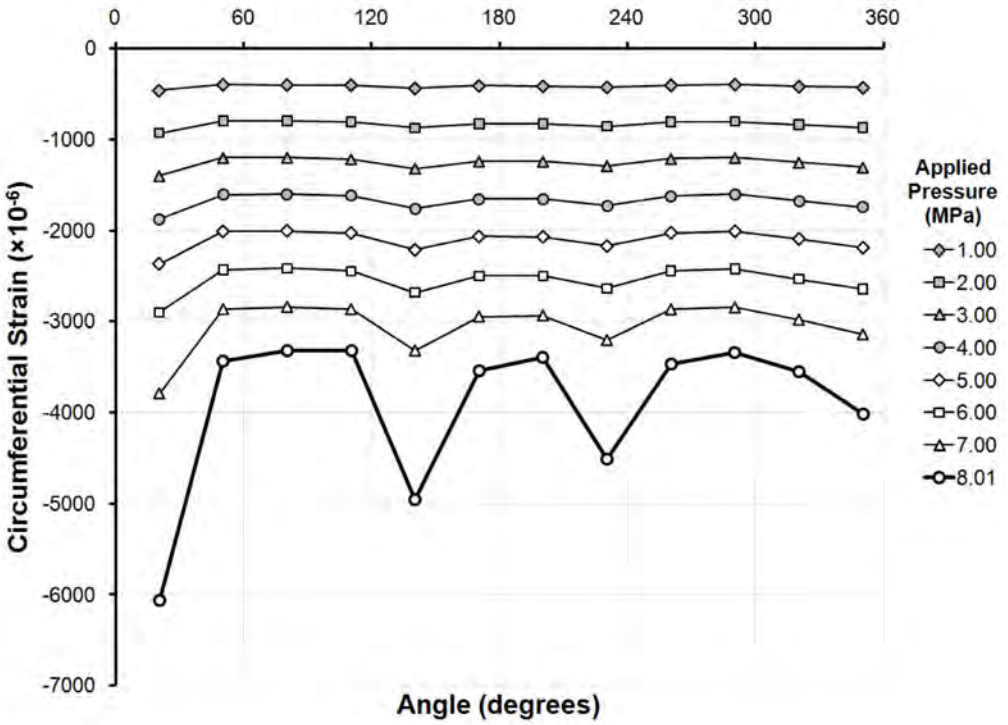

Figure 374: Circumferential strain distribution outside the shell in the centre of Bay 2 of specimen L510-No34, at pressures up to and including the collapse pressure.

I.11 L510-No35

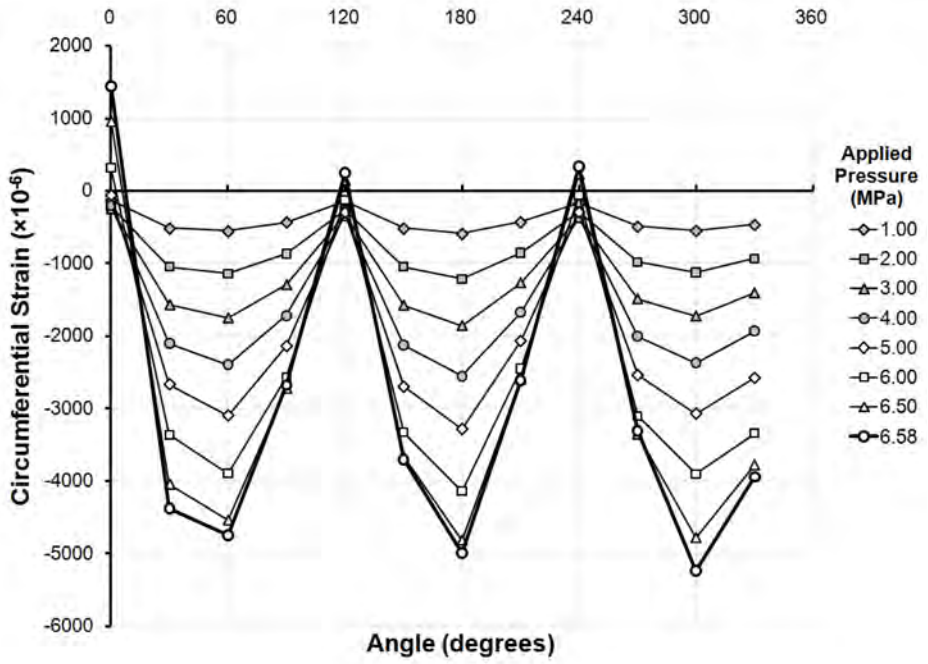

Figure 375: Circumferential strain distribution at the flange of Frame 4 of specimen L510-No35, at pressures up to and including the collapse pressure.

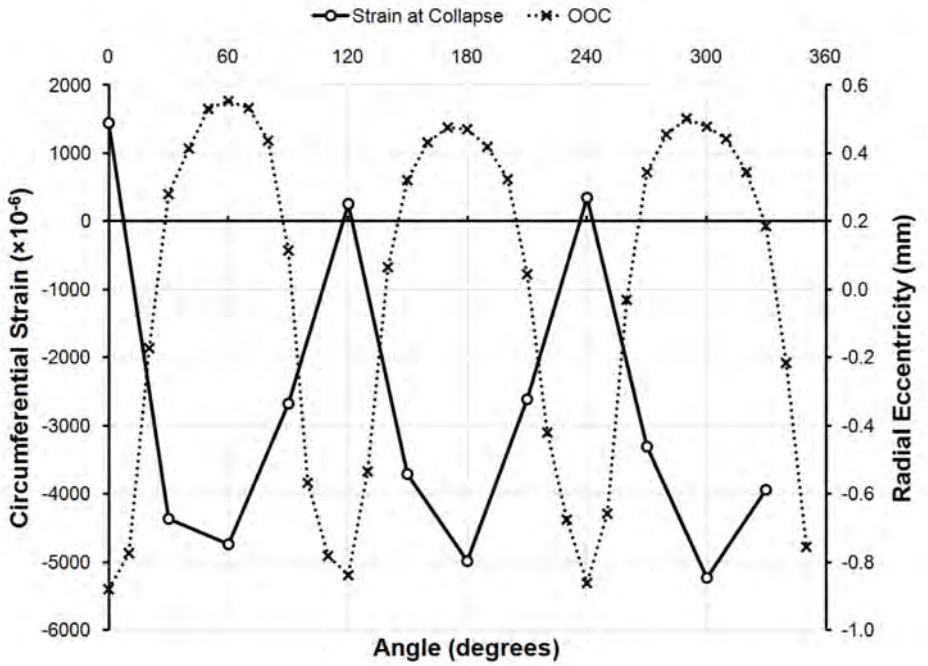

Figure 376: Circumferential strain distribution at the flange of Frame 4 of specimen L510-No35 at the collapse pressure, plotted with the initial out-of-circularity at that location.

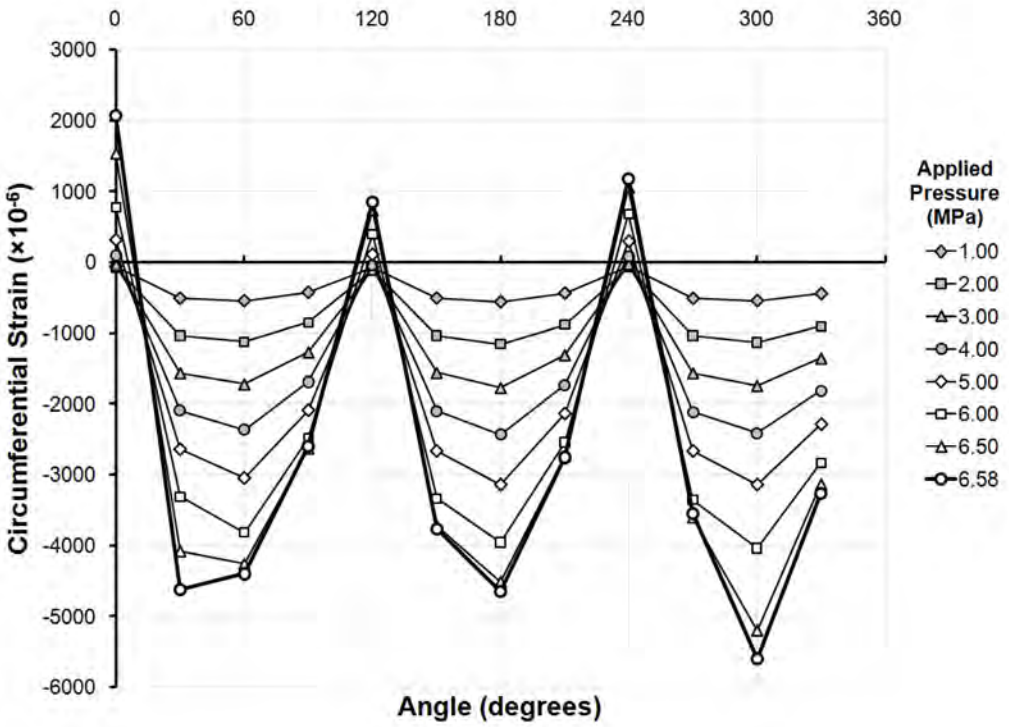

Figure 377: Circumferential strain distribution at the flange of Frame 5 of specimen L510-No35, at pressures up to and including the collapse pressure.

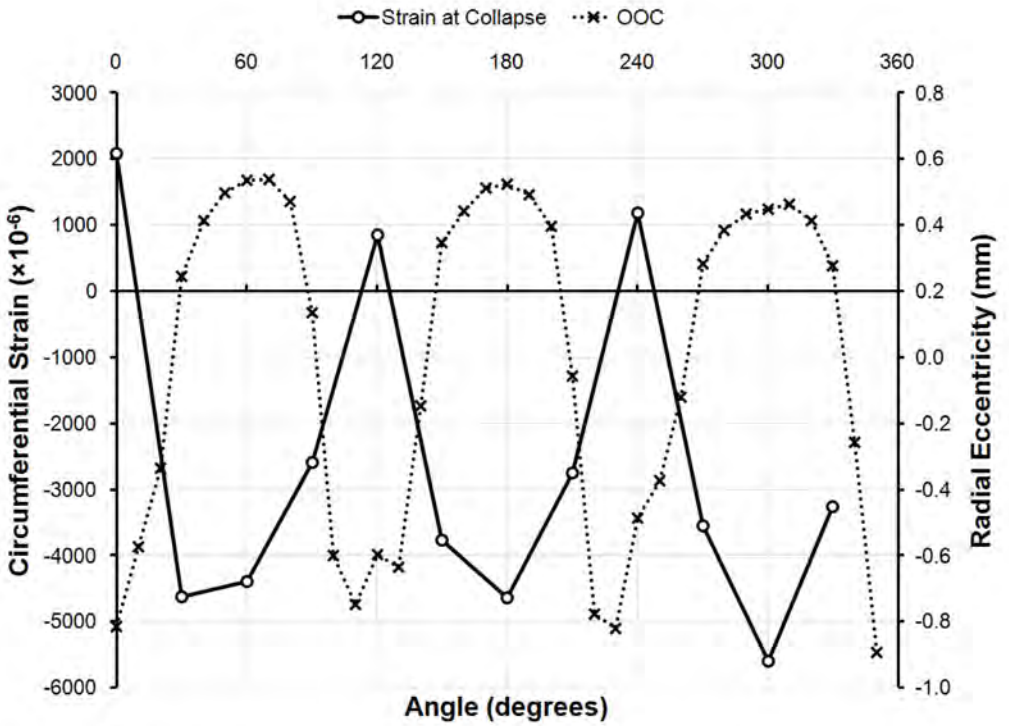

Figure 378: Circumferential strain distribution at the flange of Frame 5 of specimen L510-No35 at the collapse pressure, plotted with the initial out-of-circularity at that location.

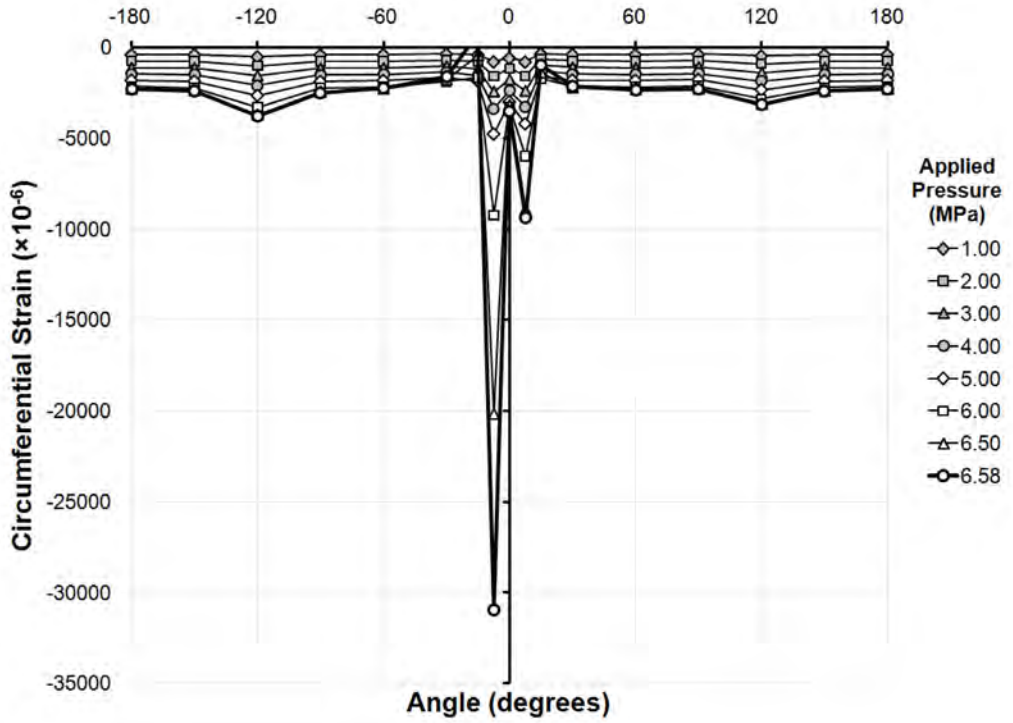

Figure 379: Circumferential strain distribution outside the shell in the centre of Bay 4 of specimen L510-No35, at pressures up to and including the collapse pressure.

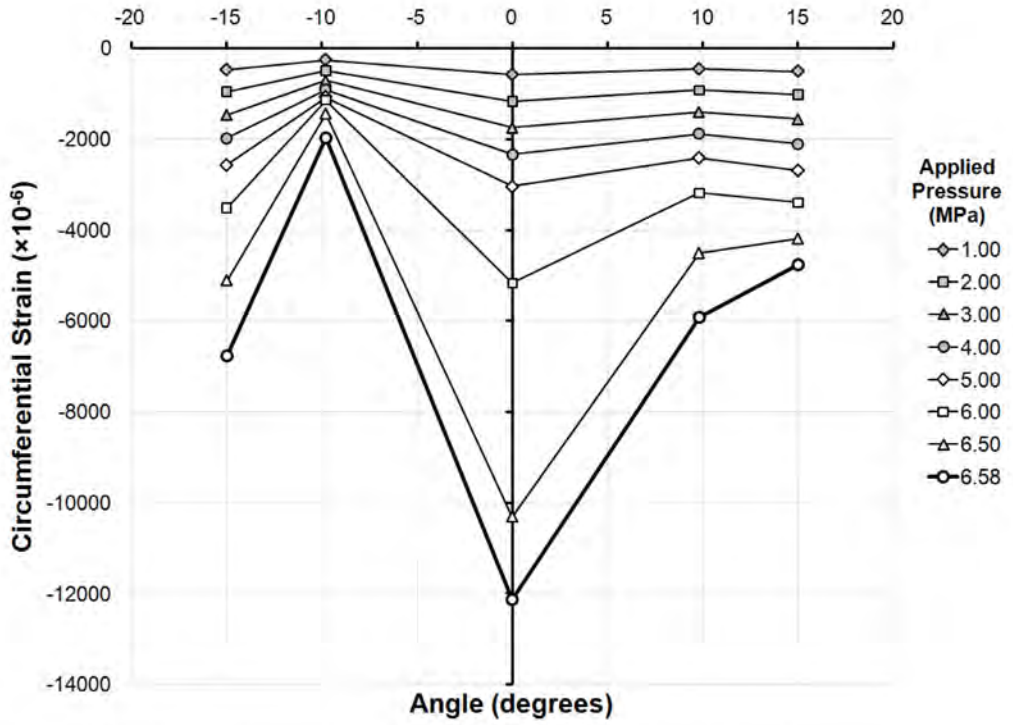

Figure 380: Circumferential strain distribution inside the shell in the centre of Bay 4 of specimen L510-No35, at pressures up to and including the collapse pressure.

I.12 L510-No36

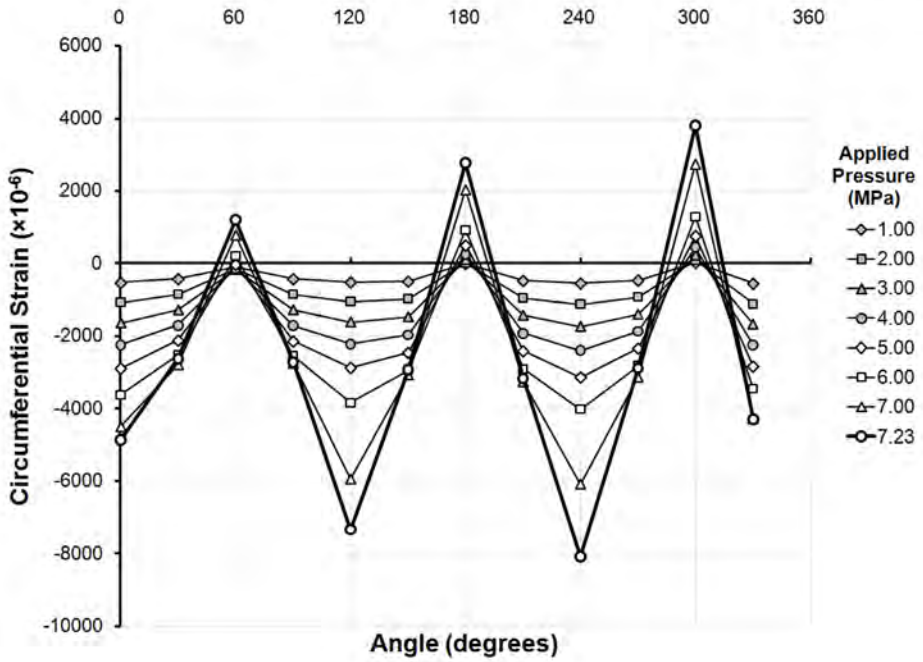

Figure 381: Circumferential strain distribution at the flange of Frame 4 of specimen L510-No36, at pressures up to and including the collapse pressure.

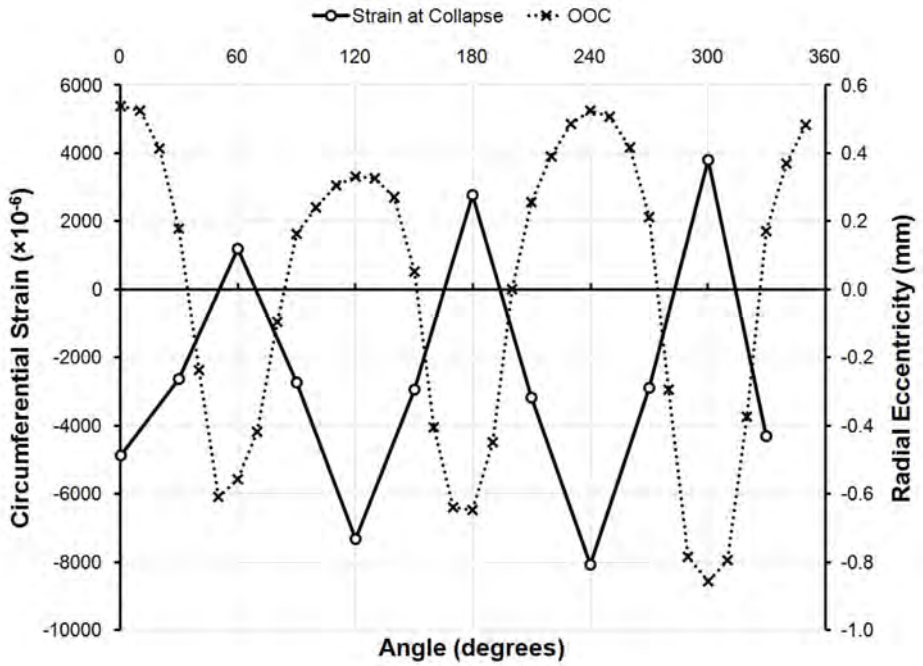

Figure 382: Circumferential strain distribution at the flange of Frame 4 of specimen L510-No36 at the collapse pressure, plotted with the initial out-of-circularity at that location.

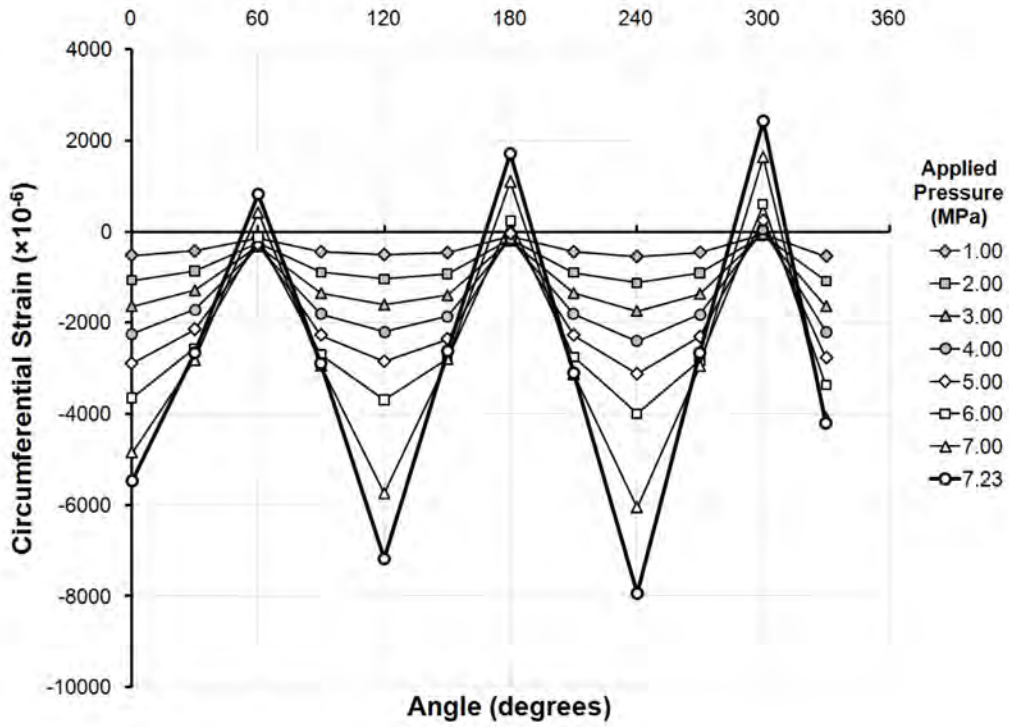

Figure 383: Circumferential strain distribution at the flange of Frame 5 of specimen L510-No36, at pressures up to and including the collapse pressure.

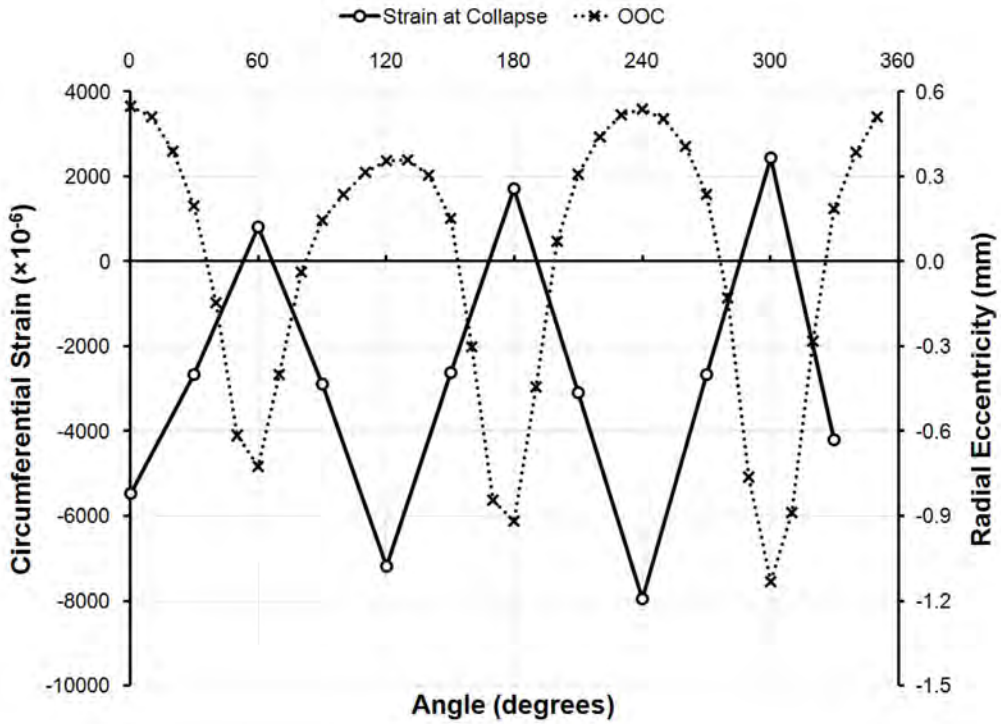

Figure 384: Circumferential strain distribution at the flange of Frame 5 of specimen L510-No36 at the collapse pressure, plotted with the initial out-of-circularity at that location.

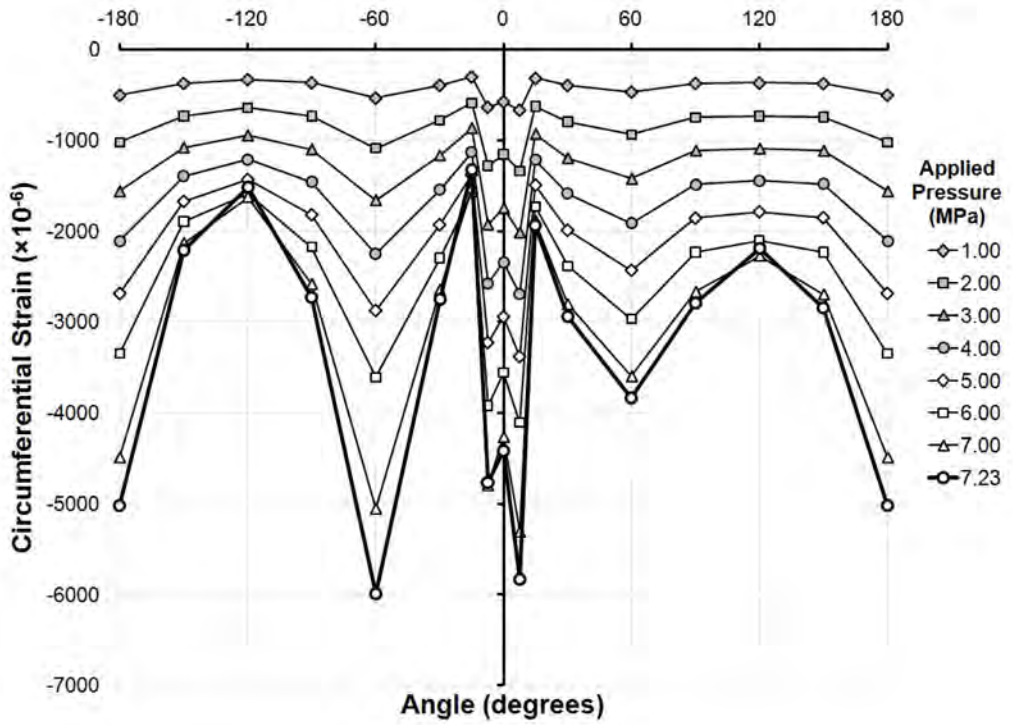

Figure 385: Circumferential strain distribution outside the shell in the centre of Bay 4 of specimen L510-No36, at pressures up to and including the collapse pressure.

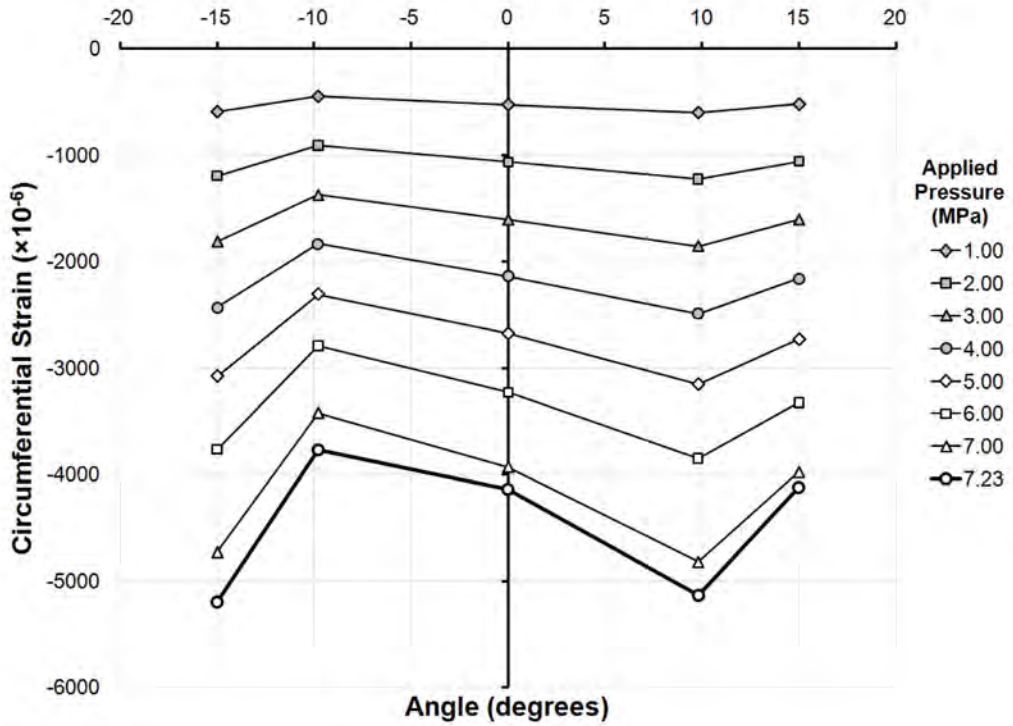

Figure 386: Circumferential strain distribution inside the shell in the centre of Bay 4 of specimen L510-No36, at pressures up to and including the collapse pressure.

This page intentionally left blank.

Annex J Fourier decomposition of strain

J.1 L510-No13

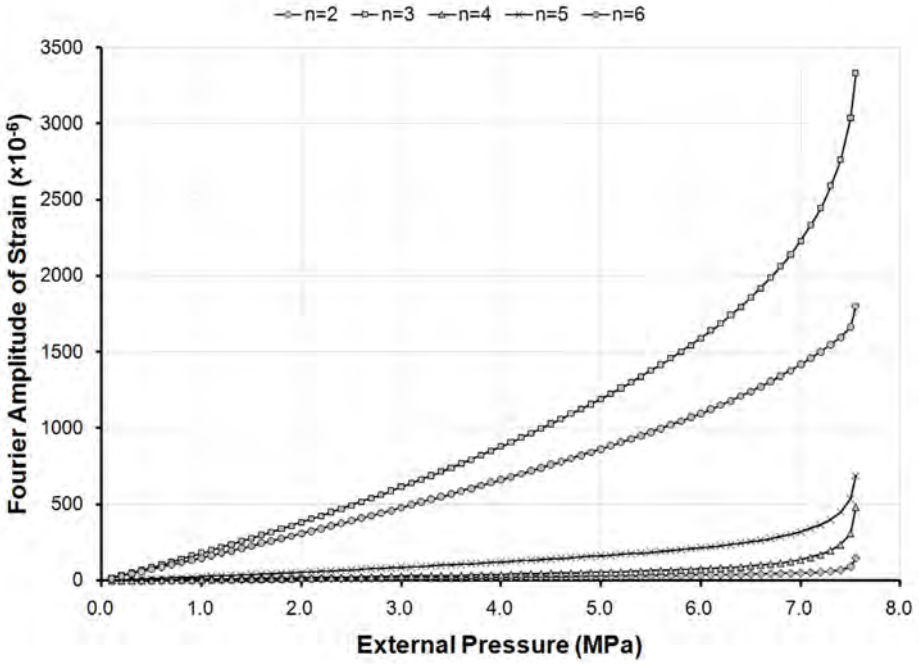

Figure 387: Bending strain amplitudes at the flange of Frame 5 of specimen L510-No13, derived from Fourier decomposition, and plotted against the applied pressure.

J.2 L510-No14

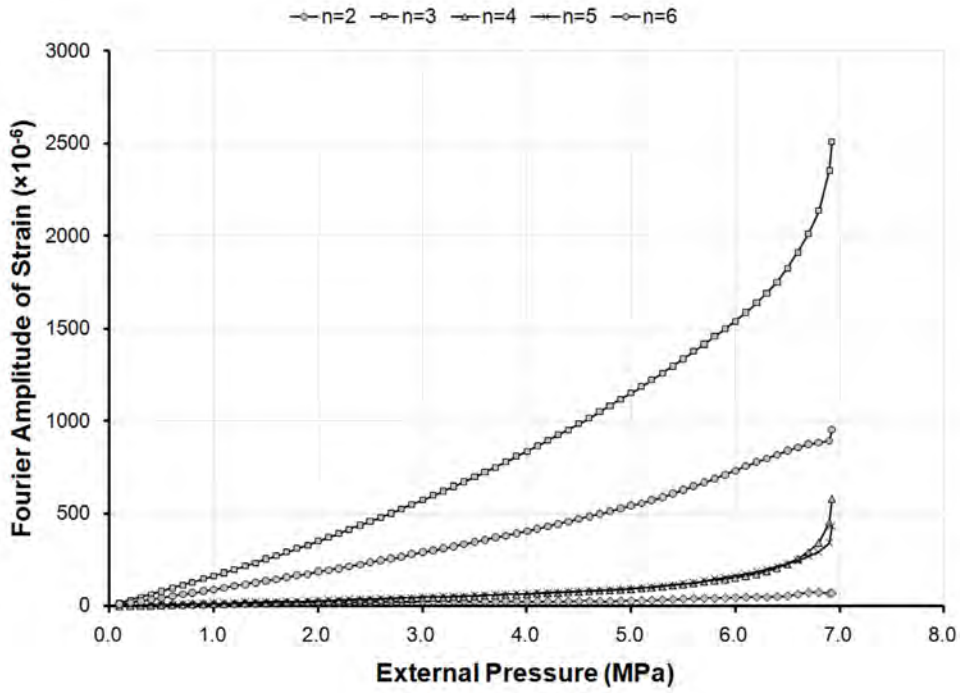

Figure 388: Bending strain amplitudes at the flange of Frame 5 of specimen L510-No14, derived from Fourier decomposition, and plotted against the applied pressure.

J.3 L510-No17

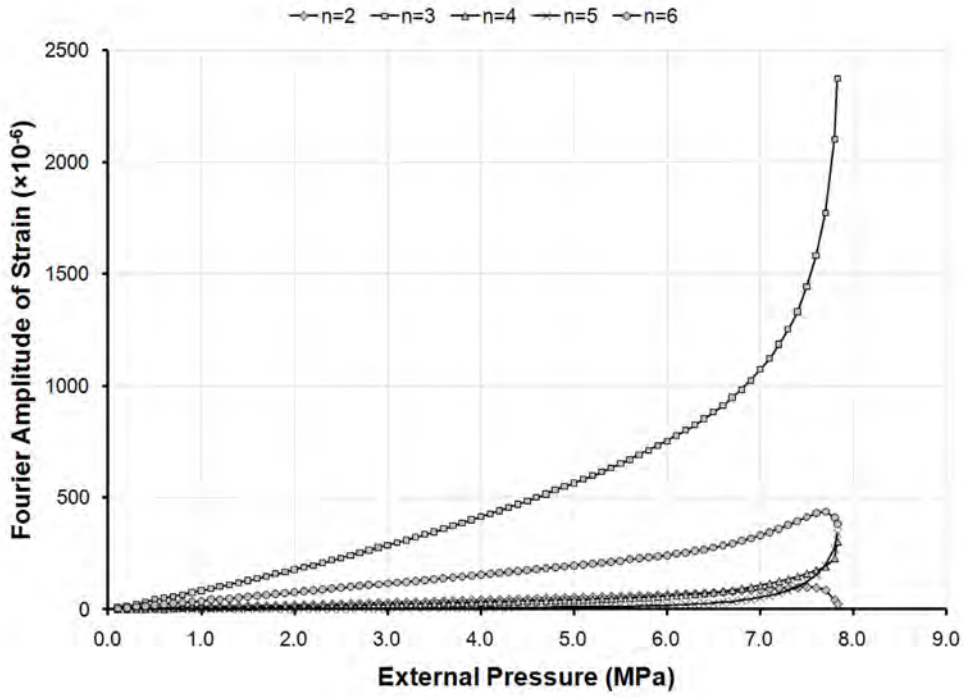

Figure 389: Bending strain amplitudes at the flange of Frame 5 of specimen L510-No17, derived from Fourier decomposition, and plotted against the applied pressure.

J.4 L510-No18

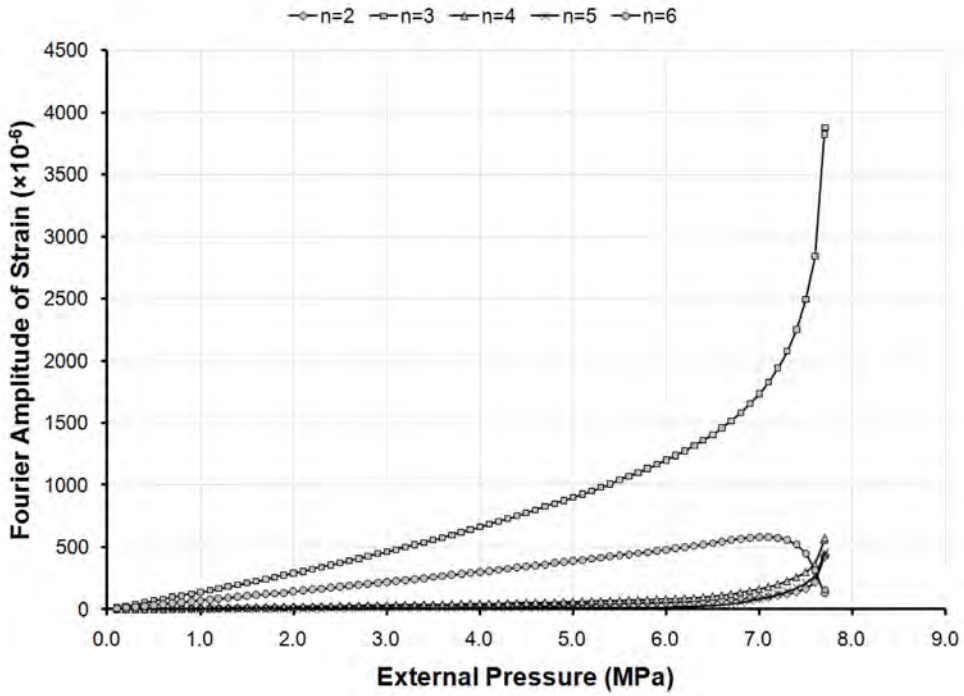

Figure 390: Bending strain amplitudes at the flange of Frame 4 of specimen L510-No18, derived from Fourier decomposition, and plotted against the applied pressure.

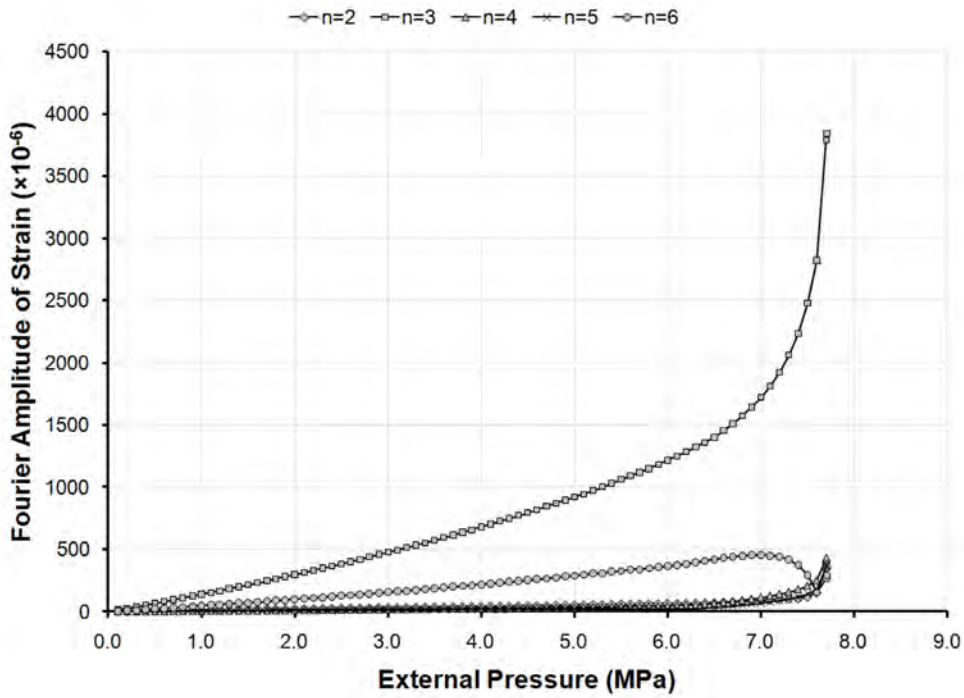

Figure 391: Bending strain amplitudes at the flange of Frame 5 of specimen L510-No18, derived from Fourier decomposition, and plotted against the applied pressure.

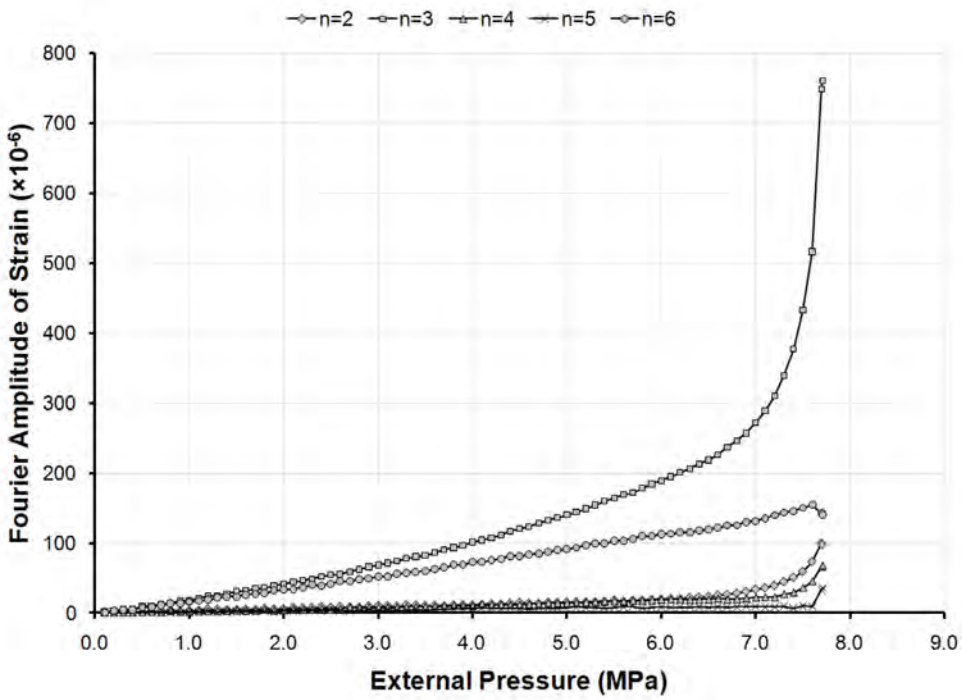

Figure 392: Bending strain amplitudes outside the shell in Bay 4 of specimen L510-No18, derived from Fourier decomposition, and plotted against the applied pressure.

J.5 L510-No25

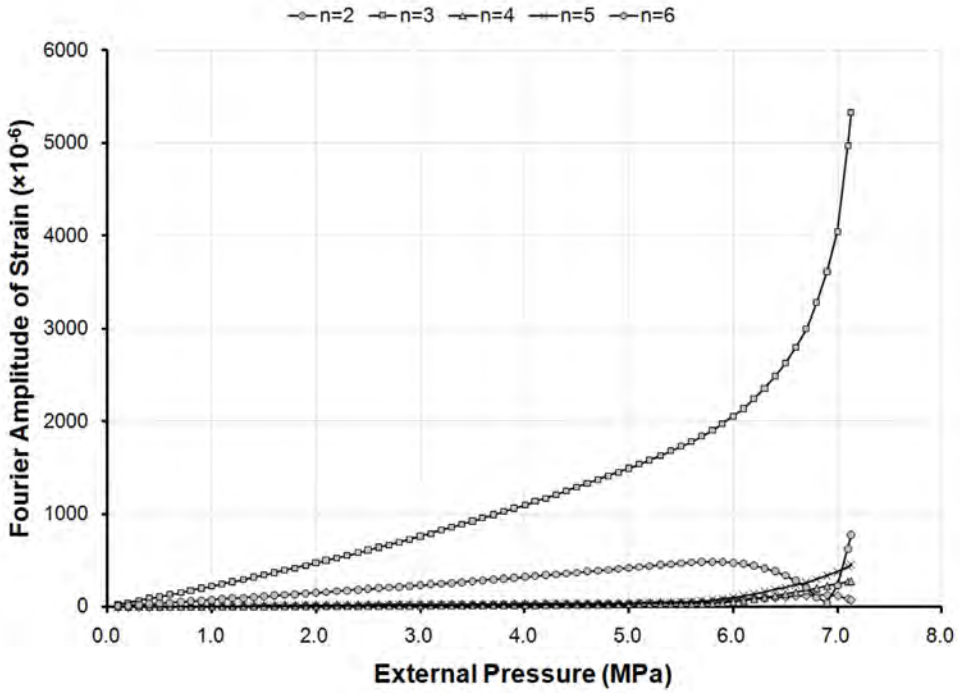

Figure 393: Bending strain amplitudes at the flange of Frame 4 of specimen L510-No25, derived from Fourier decomposition, and plotted against the applied pressure.

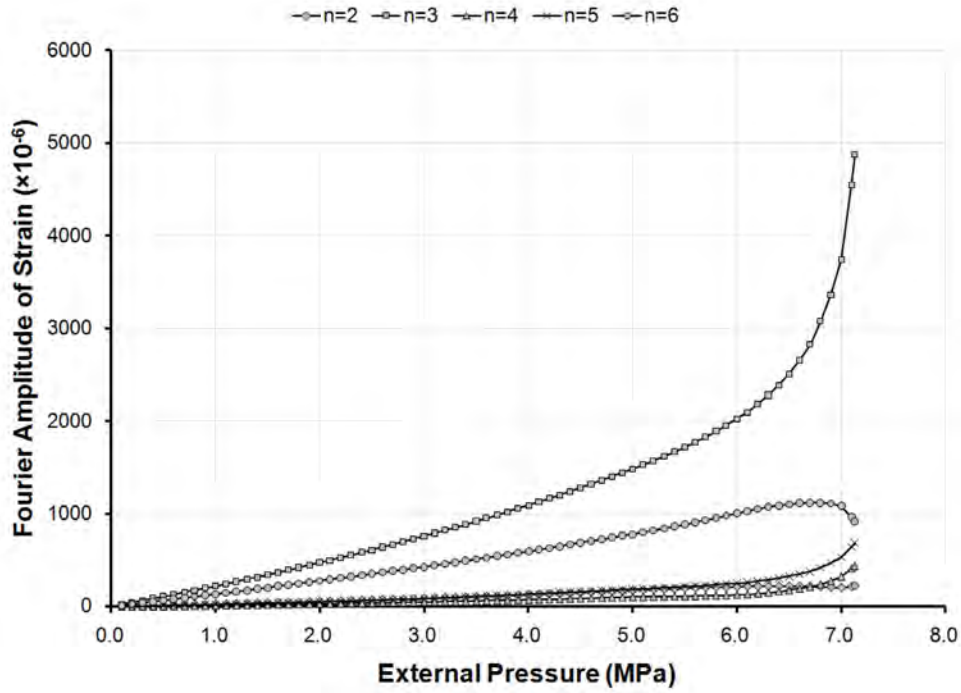

Figure 394: Bending strain amplitudes at the flange of Frame 5 of specimen L510-No25, derived from Fourier decomposition, and plotted against the applied pressure.

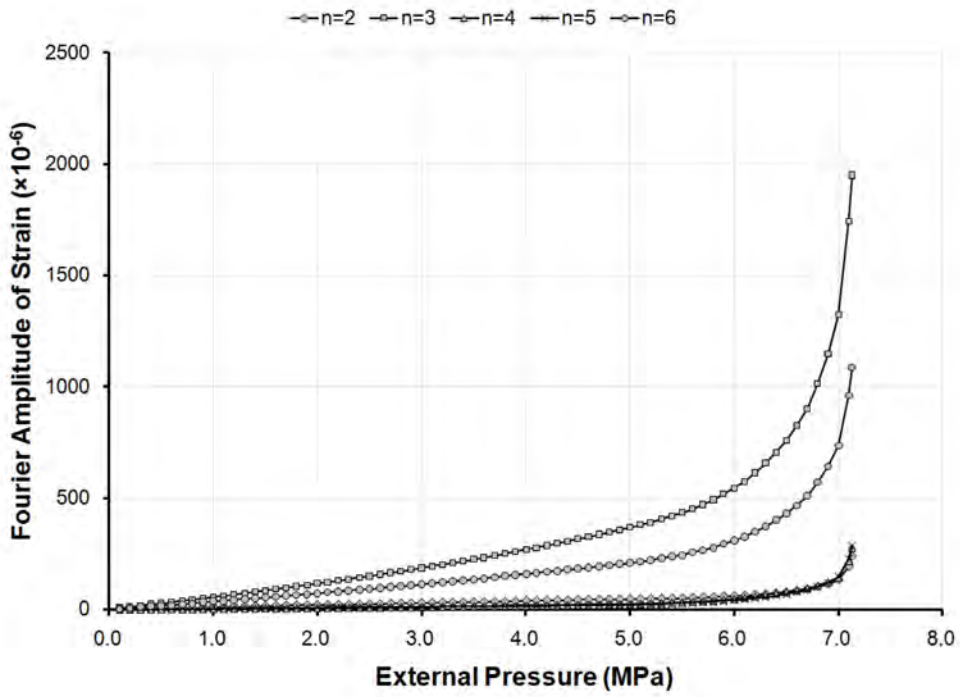

Figure 395: Bending strain amplitudes outside the shell in Bay 4 of specimen L510-No25, derived from Fourier decomposition, and plotted against the applied pressure.

J.6 L510-No26

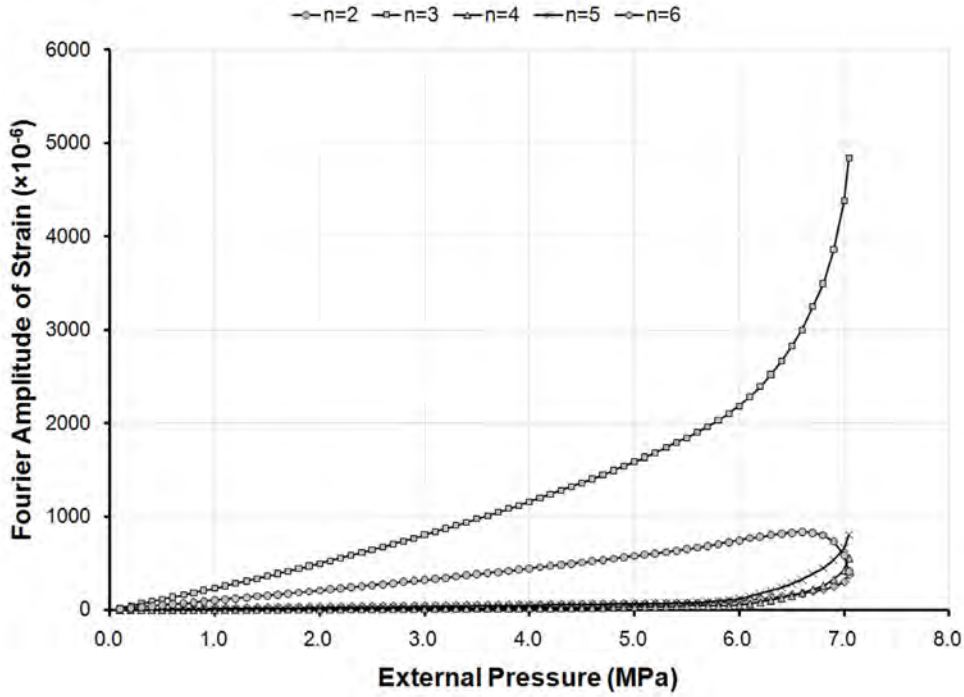

Figure 396: Bending strain amplitudes at the flange of Frame 4 of specimen L510-No26, derived from Fourier decomposition, and plotted against the applied pressure.

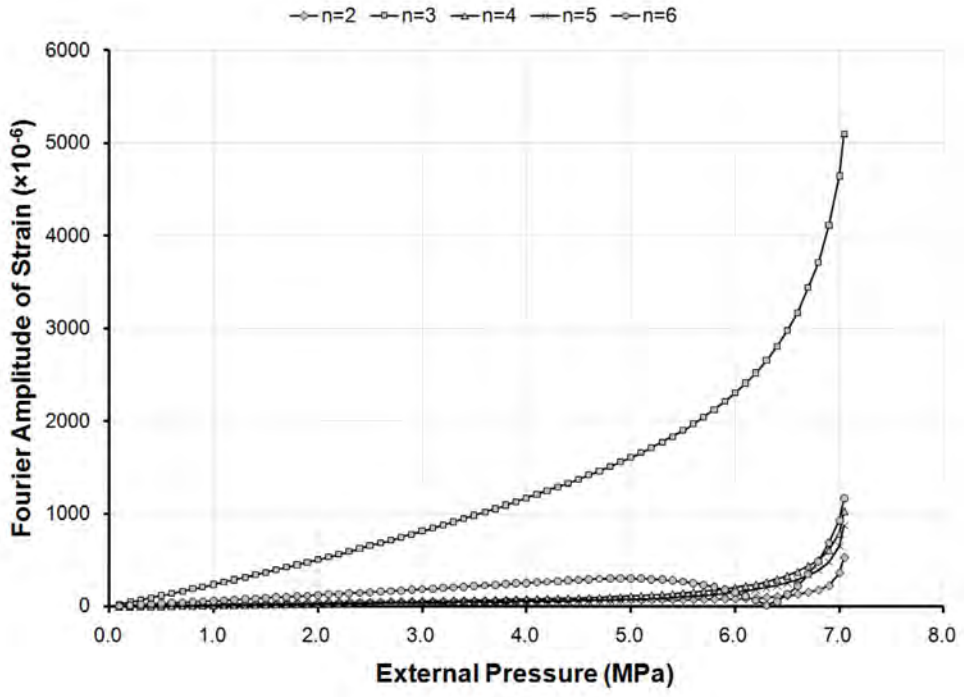

Figure 397: Bending strain amplitudes at the flange of Frame 5 of specimen L510-No26, derived from Fourier decomposition, and plotted against the applied pressure.

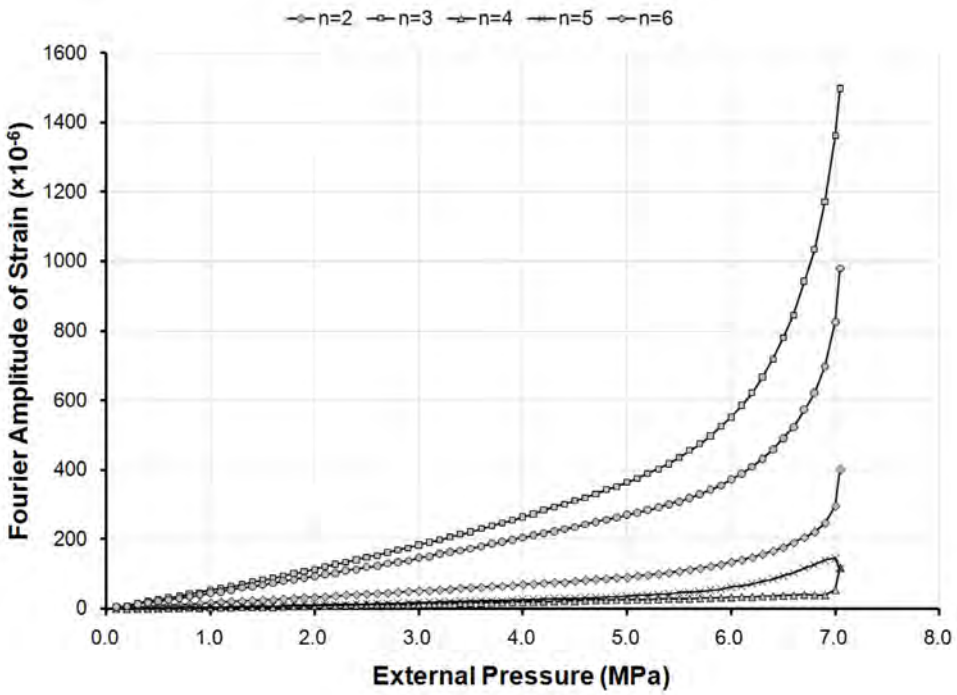

Figure 398: Bending strain amplitudes outside the shell in Bay 4 of specimen L510-No26, derived from Fourier decomposition, and plotted against the applied pressure.

J.7 L510-No33

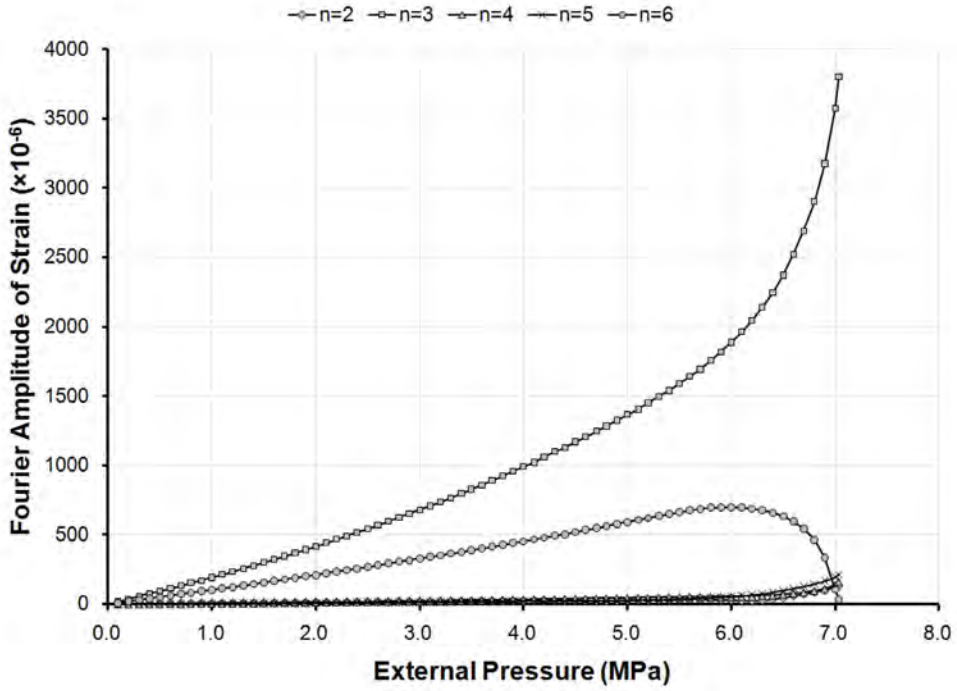

Figure 399: Bending strain amplitudes at the flange of Frame 5 of specimen L510-No33, derived from Fourier decomposition, and plotted against the applied pressure.

J.8 L510-No34

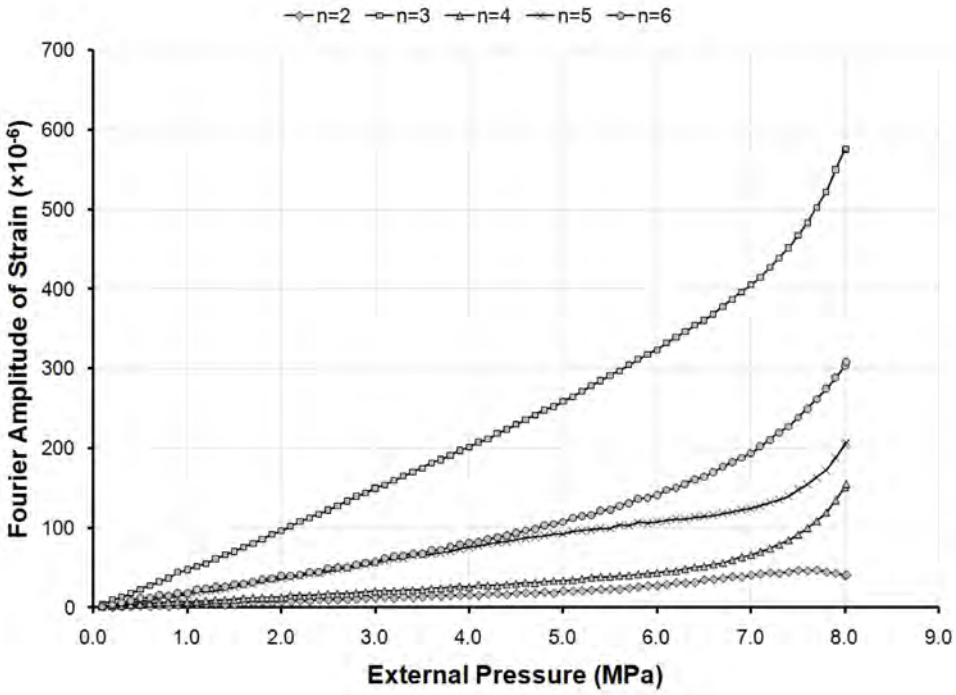

Figure 400: Bending strain amplitudes at the flange of Frame 3 of specimen L510-No34, derived from Fourier decomposition, and plotted against the applied pressure.

J.9 L510-No35

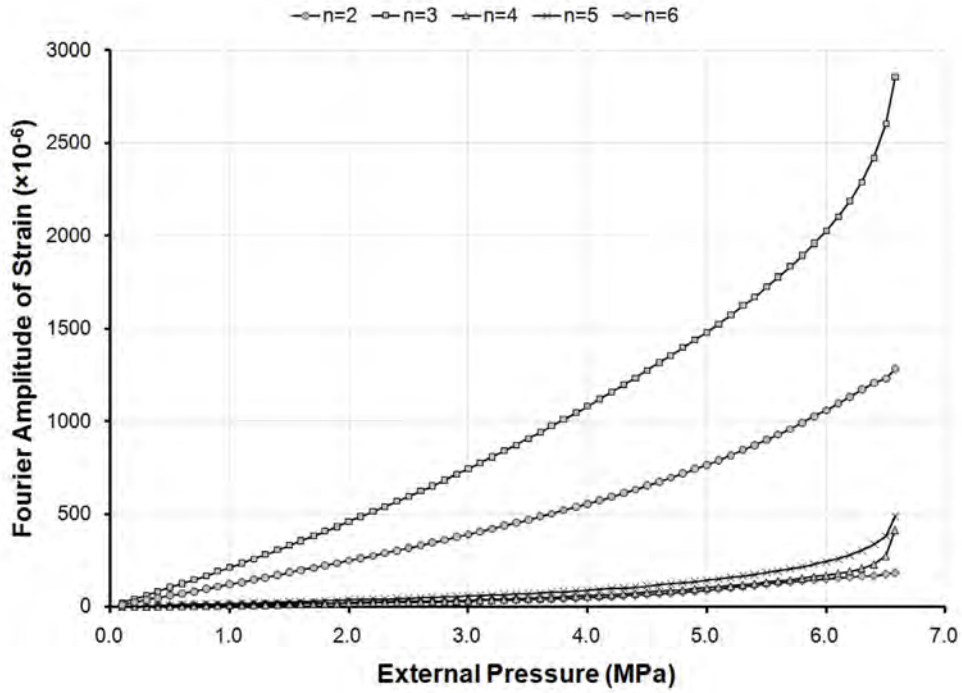

Figure 401: Bending strain amplitudes at the flange of Frame 4 of specimen L510-No35, derived from Fourier decomposition, and plotted against the applied pressure.

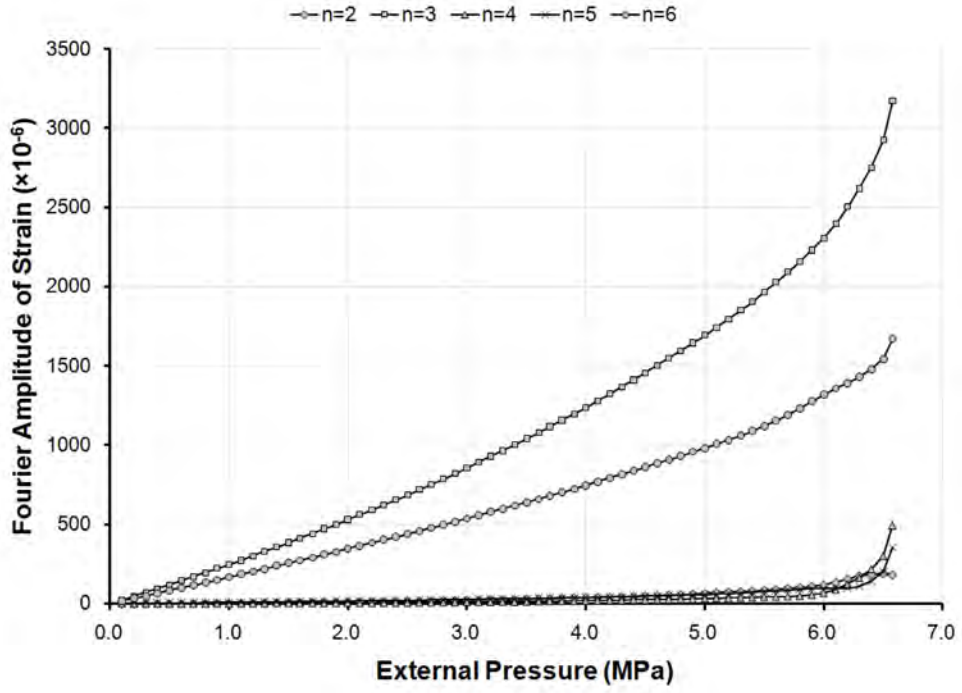

Figure 402: Bending strain amplitudes at the flange of Frame 5 of specimen L510-No35, derived from Fourier decomposition, and plotted against the applied pressure.

J.10 L510-No36

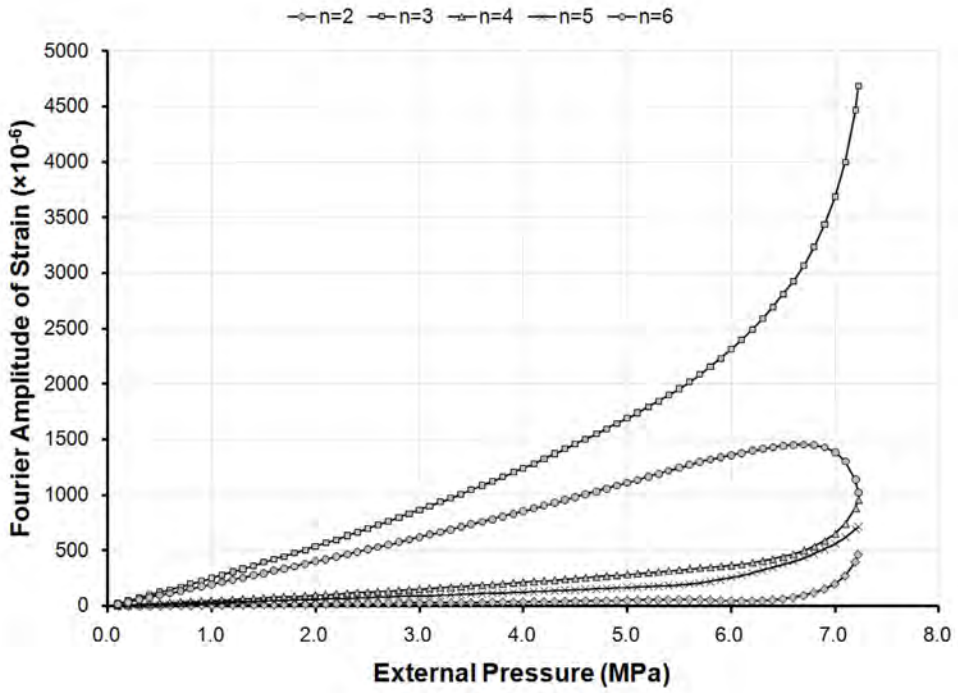

Figure 403: Bending strain amplitudes at the flange of Frame 4 of specimen L510-No36, derived from Fourier decomposition, and plotted against the applied pressure.

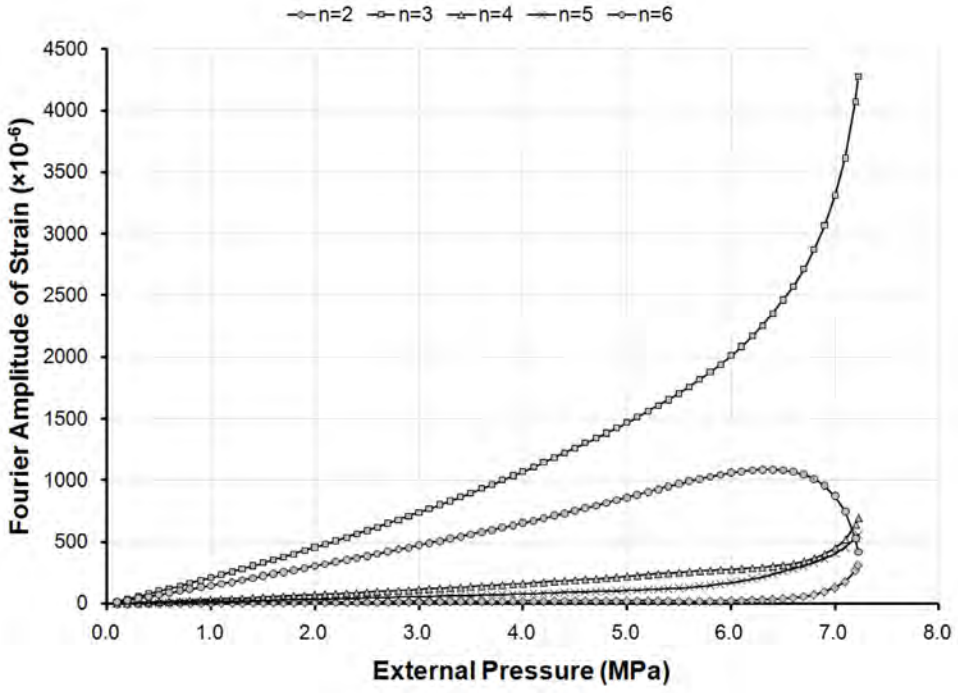

Figure 404: Bending strain amplitudes at the flange of Frame 5 of specimen L510-No36, derived from Fourier decomposition, and plotted against the applied pressure.

This page intentionally left blank.

Annex K Strain distribution over cylinder length

K.1 L510-No17

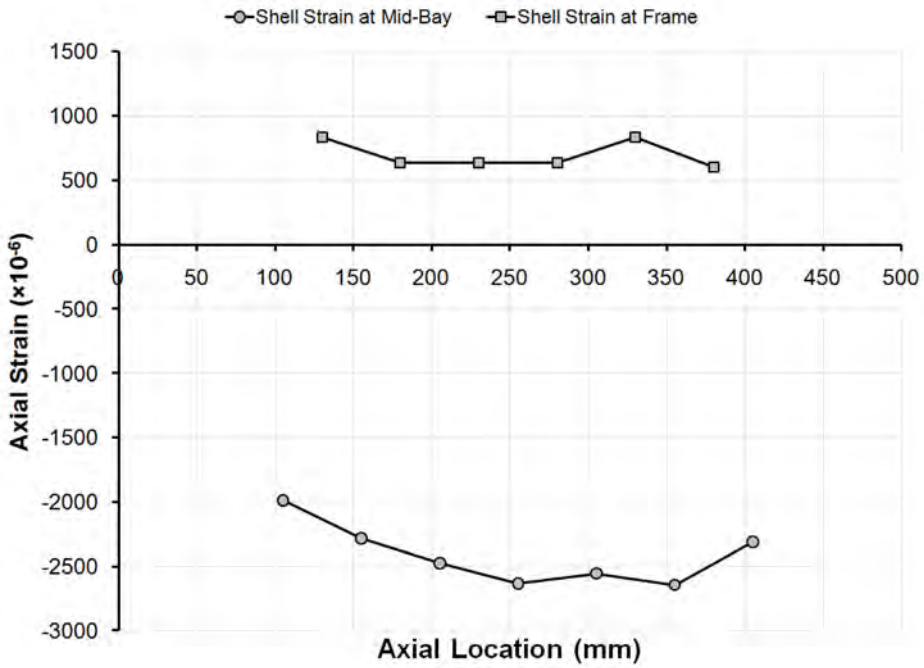

Figure 405: Distribution of axial shell strains over the length of specimen L510-No17 at 140°, based on strain measurements taken at the collapse pressure.

K.2 L510-No18

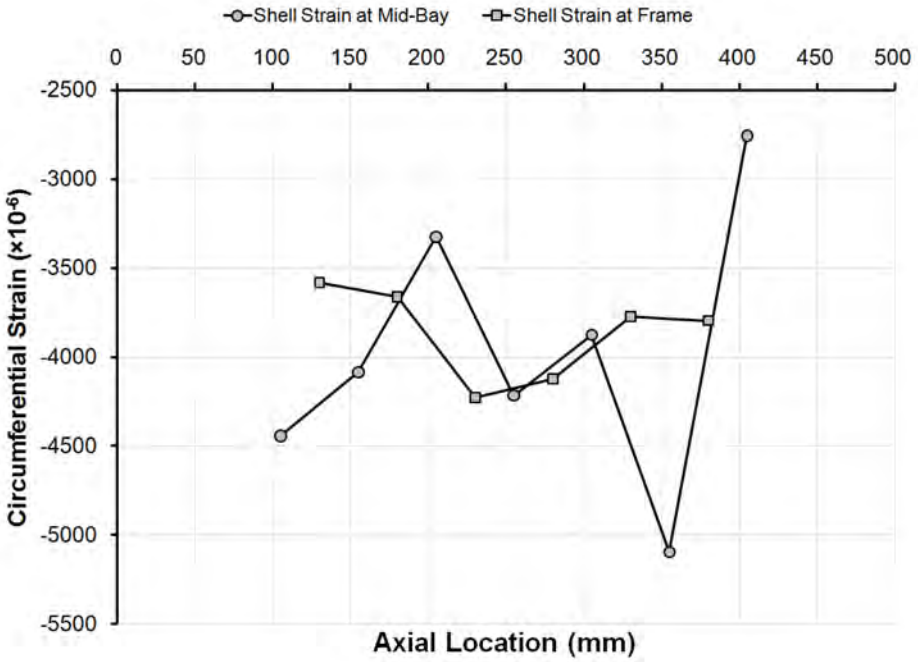

Figure 406: Axial distribution of circumferential strains at 124.6° measured at the collapse pressure for specimen L510-No18.

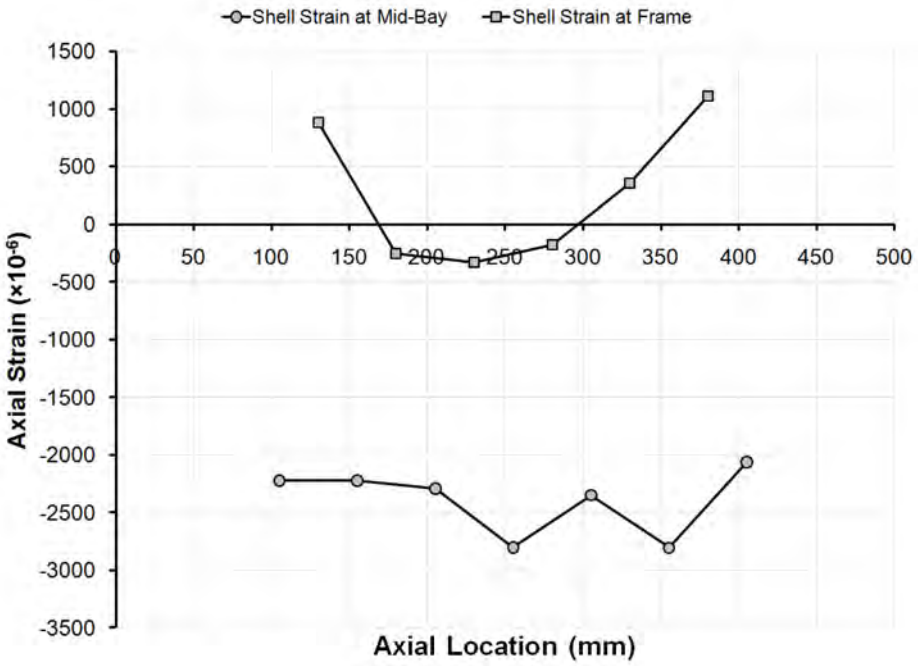

Figure 407: Distribution of axial shell strains over the length of specimen L510-No18 at 124.6°, based on strain measurements taken at the collapse pressure.

K.3 L510-No25

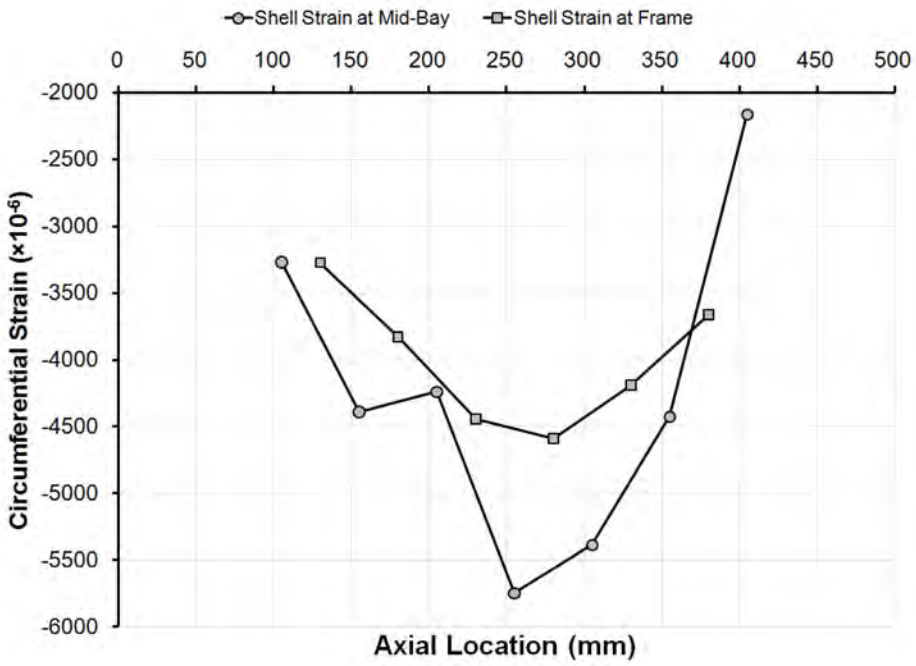

Figure 408: Distribution of circumferential shell strains over the length of specimen L510-No25 at 260°, based on strain measurements taken at the collapse pressure.

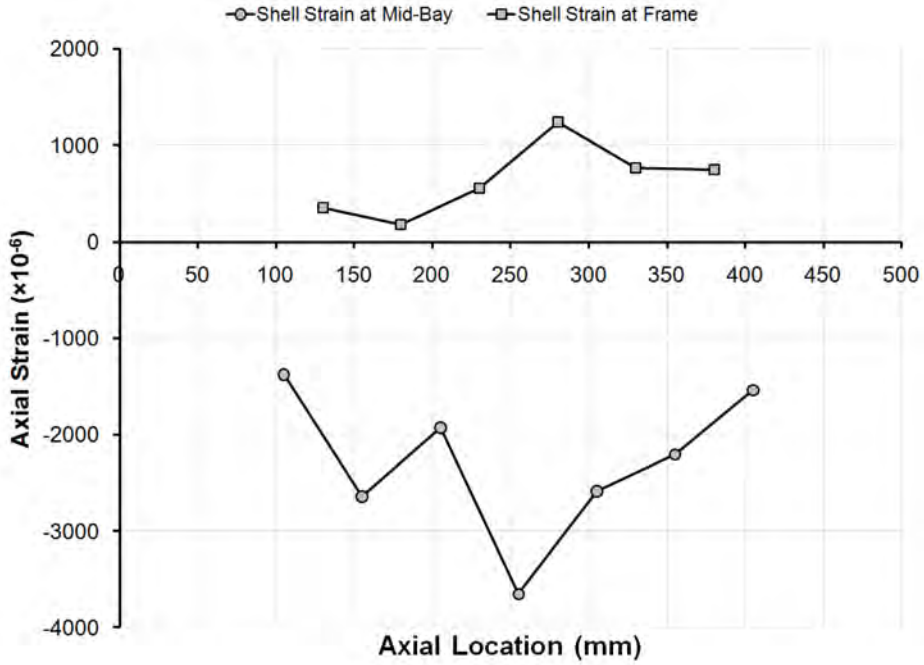

Figure 409: Distribution of axial shell strains over the length of specimen L510-No25 at 260°, based on strain measurements taken at the collapse pressure.

K.4 L510-No26

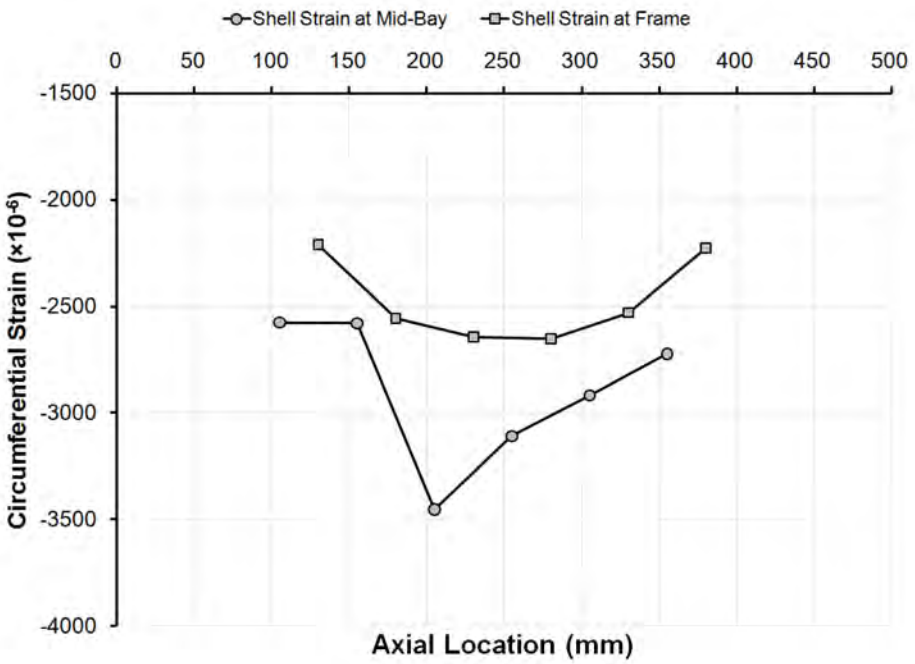

Figure 410: Distribution of circumferential shell strains over the length of specimen L510-No26 at 260°, based on strain measurements taken at the collapse pressure.

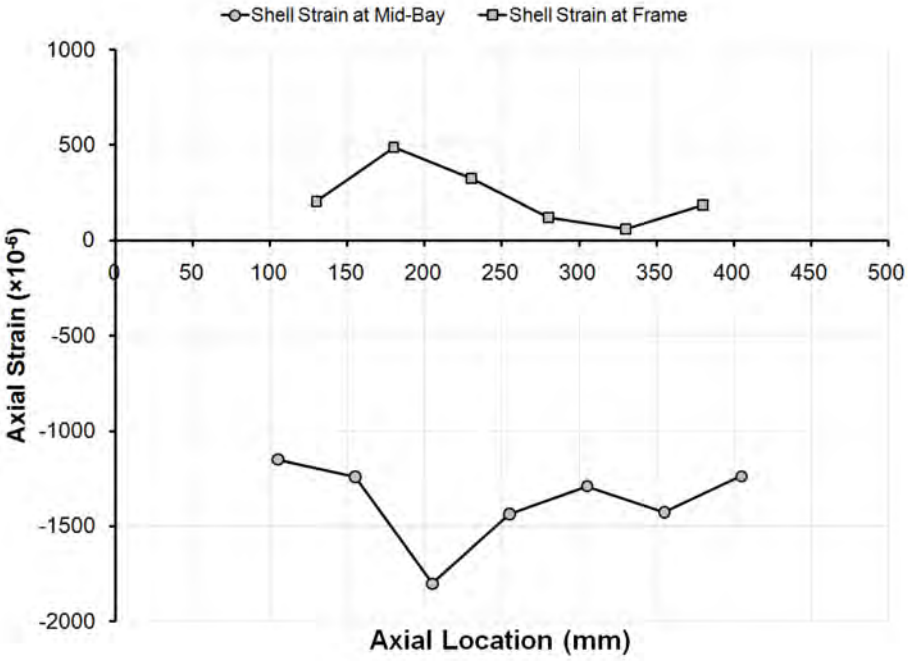

Figure 411: Distribution of axial shell strains over the length of specimen L510-No26 at 260°, based on strain measurements taken at the collapse pressure.

K.5 L510-No33

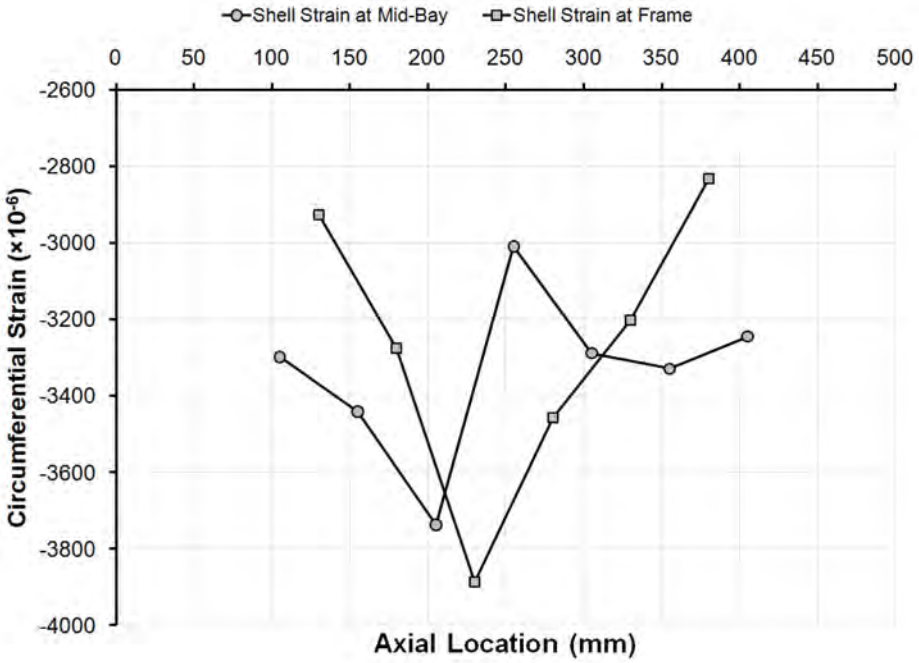

Figure 412: Distribution of circumferential shell strains over the length of specimen L510-No33 at 6.4°, based on strain measurements taken at the collapse pressure.

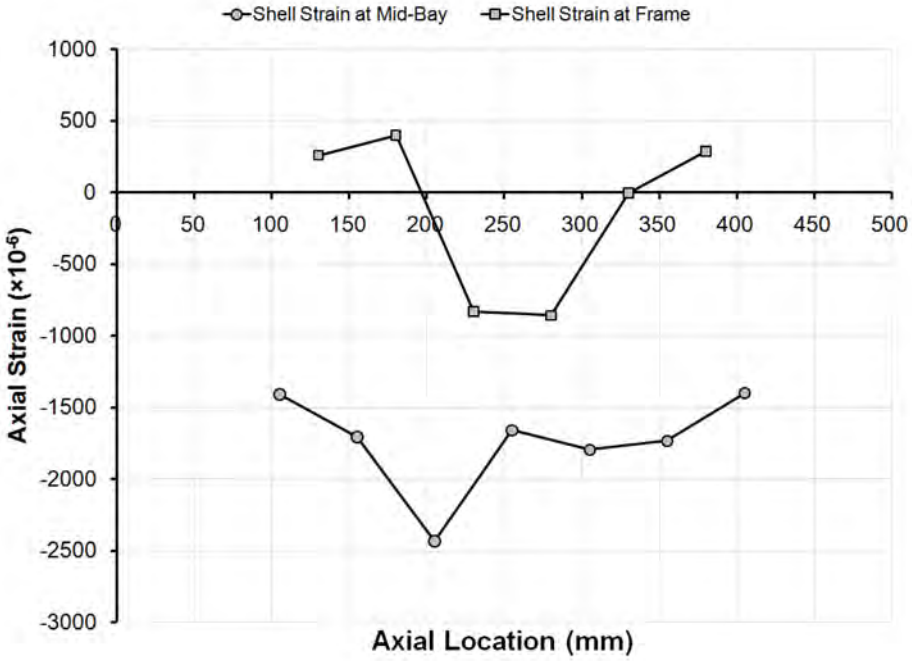

Figure 413: Distribution of axial shell strains over the length of specimen L510-No33 at 6.4°, based on strain measurements taken at the collapse pressure.

K.6 L510-No34

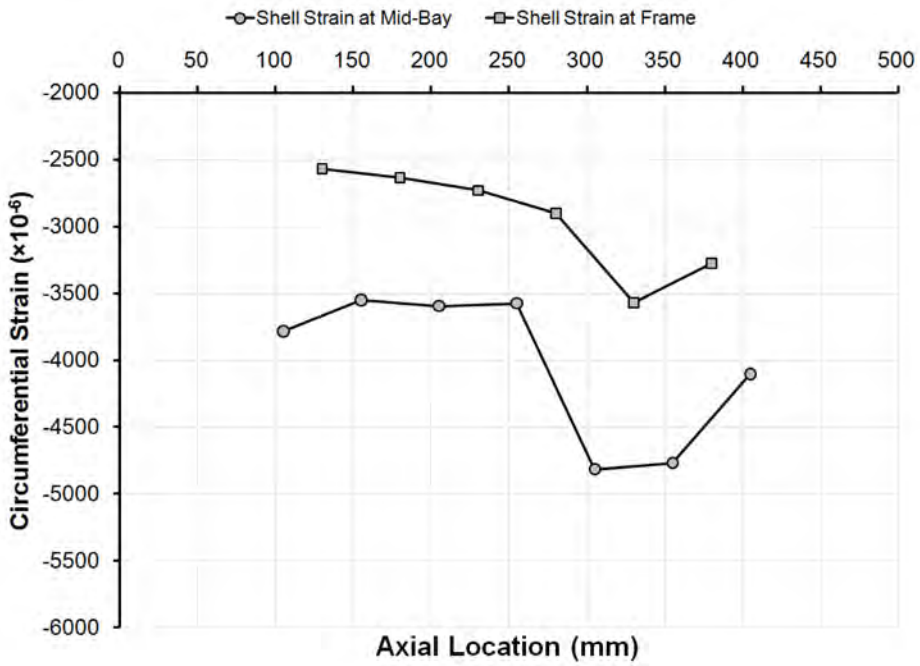

Figure 414: Distribution of circumferential shell strains over the length of specimen L510-No34 at 320.4°, based on strain measurements taken at the collapse pressure.

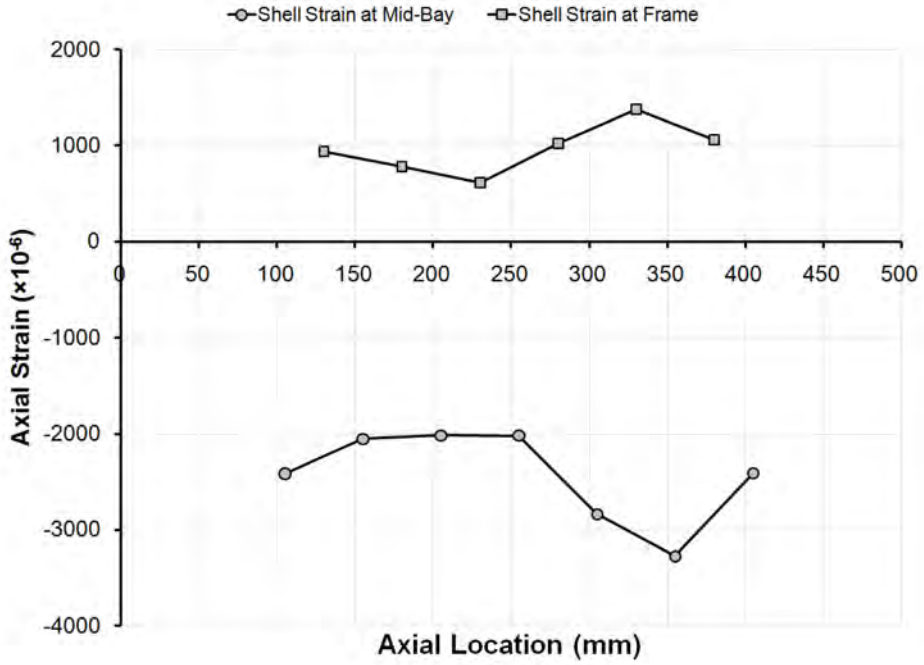

Figure 415: Distribution of axial shell strains over the length of specimen L510-No34 at 320.4°, based on strain measurements taken at the collapse pressure.

Annex L Mesh convergence studies for finite element analyses of test specimens

Table 164: Results of a mesh convergence study for CylMesh/ANSYS finite element models of the intact specimen L510-No17.

Mesh	Number of Elements					Predicted Collapse Pressure (MPa)
	About Circumference	Between Frames	Through Web Depth	Across Flange Breadth	Total	
A	36	2	1	2	1,656	8.346
B	72	5	1	2	5,400	8.329
C	108	7	2	2	11,340	8.303
D	144	9	2	2	18,288	8.271
E	180	12	3	2	29,520	8.244
F	288	19	4	4	74,592	8.238

Table 165: Results of a mesh convergence study for CylMesh/ANSYS finite element models of the corroded specimen L510-No13, with a small corrosion patch.

Mesh	Number of Elements					Predicted Collapse Pressure (MPa)
	About Circumference	Between Frames[a]	Through Web Depth	Across Flange Breadth	Total	
A	36	2/4	1	2	1,728	8.288
B	72	5/6	1	2	5,472	8.225
C	108	7/8	2	2	11,448	8.040
D	144	9/10	2	2	18,432	8.011
E	180	12/12	3	2	29,520	8.005
F	288	19/20	4	4	74,880	7.972

a. Specifying the number of elements between frames for intact/corroded bays.

Table 166: Results of a mesh convergence study for CylMesh/ANSYS finite element models of the corroded specimen L510-No19, with a large corrosion patch.

Mesh	**Number of Elements**					**Predicted Collapse Pressure (MPa)**
	About Circumference	**Between Frames[a]**	**Through Web Depth**	**Across Flange Breadth**	**Total**	
A	35	2/2/2	1	2	1,610	7.544
B	73	5/4/5	1	2	5,329	7.151
C	108	7/8/7	2	2	11,556	6.911
D	143	9/10/9	2	2	18,447	6.903
E	181	12/12/12	3	2	29,684	6.882
F	289	19/18/19	4	4	74,273	6.857

a. Specifying the number of elements between frames for intact/transition/corroded bays.

List of symbols/abbreviations/acronyms/initialisms

ν	Poisson's ratio
σ_y	0.2% yield stress
a	mid-plane shell radius
A_n	Fourier amplitude for mode n
CMM	coordinate-measuring machine
CNC	computer numerical control
COV	coefficient of variation
DDD	deep diving depth of a submarine
DEMO	Electronic and Mechanical Support Division of the Delft University of Technology in the Netherlands
DND	Department of National Defence
DRDC	Defence Research & Development Canada
DRDKIM	Director Research and Development Knowledge and Information Management
E	Young's modulus
e_3	radial eccentricity value for defining out-of-circularity; associated with the maximum n=3 Fourier amplitude for a test specimen
e_{avg}	radial eccentricity value for defining out-of-circularity; taken as the average of the absolute maximum inward and outward eccentricities for a test specimen
e_i	measured radial eccentricity at a given location on a test specimen, for an out-of-circularity measurement method for which the error is being calculated
e_{max}	radial eccentricity value for defining out-of-circularity; associated with the absolute maximum inward or outward eccentricity for a test specimen
e_{nom}	nominal radial eccentricity value for defining out-of-circularity of a test specimen
$e_{ref,i}$	measured eccentricity at a given location for a reference out-of-circularity measurement method
E_t	tangent or strain hardening modulus
FE	finite element
GPa	gigaPascals
h	shell thickness
Hz	Hertz

i	generic summation counter
kN	kiloNewton
m	number of complete out-of-circularity or buckling sine waves over the length of a pressure hull compartment or ring-stiffened cylinder
mm	millimetres
MPa	megaPascals
n	number of complete out-of-circularity or buckling waves about the circumference of a pressure hull or ring-stiffened cylinder
N	total number of out-of-circularity measurement comparisons
NETE	Naval Engineering Test Establishment
OOC	out-of-circularity
P_b	boiler pressure
P_c	collapse pressure
P_c*	normalized collapse pressure; taken as the collapse pressure divided by the boiler pressure
P_{co}	overall collapse pressure, as predicted by the elasto-plastic finite difference method of Kendrick
PSF	partial safety factor
P_y	yield pressure
$P_{y(n)}$	pressure causing the circumferential stress in the frame flange to yield; associated with out-of-circularity mode n
R&D	Research & Development
TNO	The Netherlands Organization for Scientific Research
UT	ultrasonic thickness
X_m	modeling uncertainty factor
$(X_m)_{\min}$	minimum expected modeling uncertainty factor for a future experimental-numerical comparison
$X_{m,n+1}$	modeling uncertainty factor for a future experimental-numerical comparison

Distribution list

Document No.: DRDC Atlantic TM 2010-239

LIST PART 1: Internal Distribution by Centre

4 Author (2 paper copies, 2 CDs)

3 DRDC Atlantic Library (1 paper copy, 2 CDs)

7 TOTAL LIST PART 1

LIST PART 2: External Distribution by DRDKIM

1 Library and Archives Canada Attn: Military Archivist, Government Records Branch

1 DRDKIM

2 NDHQ/DMEPM(SM) 4-2

1 Prof. Fred van Keulen
Department of Precision and Microsystems Engineering
Faculty 3mE
Delft University of Technology
Office 4B-1-32
Mekelweg 2
2628 CD Delft
THE NETHERLANDS

2 Mr. Wim Trouwborst
Centre for Mechanical and Maritime Structures (CMC)
Structures and Safety
Business Unit of TNO Built Environment and Geosciences
P.O. Box 49
2600 AA Delft
THE NETHERLANDS

2 Mr. Adrian van der Made
Military Maritime Technology Section
Department of Platform Technology
Sea Systems Branch
Netherlands Defence Materiel Organisation
Frederikkazerne, Van der Burchlaan 31
P.O. Box 90822
2509 LV The Hague
THE NETHERLANDS

9 TOTAL LIST PART 2

16 TOTAL COPIES REQUIRED

DOCUMENT CONTROL DATA

(Security classification of title, body of abstract and indexing annotation must be entered when the overall document is classified)

1. ORIGINATOR (The name and address of the organization preparing the document. Organizations for whom the document was prepared, e.g. Centre sponsoring a contractor's report, or tasking agency, are entered in section 8.)

Defence R&D Canada – Atlantic
9 Grove Street
P.O. Box 1012
Dartmouth, Nova Scotia B2Y 3Z7

2. SECURITY CLASSIFICATION (Overall security classification of the document including special warning terms if applicable.)

UNCLASSIFIED

3. TITLE (The complete document title as indicated on the title page. Its classification should be indicated by the appropriate abbreviation (S, C or U) in parentheses after the title.)

Experimental investigation of the strength of damaged pressure hulls - Phases 5 & 6: The influence of out-of-circularity on collapse

4. AUTHORS (last name, followed by initials – ranks, titles, etc. not to be used)

MacKay, J.R.

5. DATE OF PUBLICATION (Month and year of publication of document.)	6a. NO. OF PAGES (Total containing information, including Annexes, Appendices, etc.)	6b. NO. OF REFS (Total cited in document.)
March 2011	476	22

7. DESCRIPTIVE NOTES (The category of the document, e.g. technical report, technical note or memorandum. If appropriate, enter the type of report, e.g. interim, progress, summary, annual or final. Give the inclusive dates when a specific reporting period is covered.)

Technical Memorandum

8. SPONSORING ACTIVITY (The name of the department project office or laboratory sponsoring the research and development – include address.)

Defence R&D Canada – Atlantic
9 Grove Street
P.O. Box 1012
Dartmouth, Nova Scotia B2Y 3Z7

9a. PROJECT OR GRANT NO. (If appropriate, the applicable research and development project or grant number under which the document was written. Please specify whether project or grant.)	9b. CONTRACT NO. (If appropriate, the applicable number under which the document was written.)
11ga05, 11gx03	

10a. ORIGINATOR'S DOCUMENT NUMBER (The official document number by which the document is identified by the originating activity. This number must be unique to this document.)	10b. OTHER DOCUMENT NO(s). (Any other numbers which may be assigned this document either by the originator or by the sponsor.)
DRDC Atlantic TM 2010-239	

11. DOCUMENT AVAILABILITY (Any limitations on further dissemination of the document, other than those imposed by security classification.)

Unlimited

12. DOCUMENT ANNOUNCEMENT (Any limitation to the bibliographic announcement of this document. This will normally correspond to the Document Availability (11). However, where further distribution (beyond the audience specified in (11) is possible, a wider announcement audience may be selected.))

Unlimited

13. ABSTRACT (A brief and factual summary of the document. It may also appear elsewhere in the body of the document itself. It is highly desirable that the abstract of classified documents be unclassified. Each paragraph of the abstract shall begin with an indication of the security classification of the information in the paragraph (unless the document itself is unclassified) represented as (S), (C), (R), or (U). It is not necessary to include here abstracts in both official languages unless the text is bilingual.)

Collapse tests were performed on twelve small-scale ring-stiffened cylinders. The test specimens were machined from aluminium tubing, and then mechanically deformed in order to introduce more realistic levels of out-of-circularity (OOC) in the critical collapse mode. Six of the test specimens had additional damage in the form of artificial corrosion thinning, which was introduced by machining away some of the shell plating. Corrosion damage was found to affect the strength of cylinders in different ways, depending on its orientation with respect to the OOC shape. When the corrosion damage was aligned with an inward lobe of the applied OOC shape, the effects of thinning and imperfections were additive and led to significant decreases in collapse pressure. When the hull thinning was collocated with outward OOC lobes, the corrosion damage tended to reduce the overall OOC, and only a small reduction in collapse pressure was noted, primarily due to the high stresses in the thinned shell itself. Finite element models were used to simulate the mechanical procedure used to apply OOC to the cylinders. The predicted residual stress field was in the elastic range of the material, and subsequent collapse analysis indicated that those residual stresses resulted in a 3% reduction in collapse pressure compared to a stress-relieved model. It is not thought that residual stresses have significantly affected the collapse behaviour of the actual test specimens. Finite element models based on the measured shape and material properties of forty specimens tested in the current and previous testing phases were able to predict the experimental collapse pressures with an accuracy of 9.5%, with 95% confidence.

Douze cylindres à petite échelle, renforcés d'anneaux ont été soumis à des essais d'affaissement. Les éprouvettes étaient des tubes d'aluminium usinés puis mécaniquement déformés afin de leur donner un niveau plus réaliste d'ovalisation en mode d'affaissement critique. Des dommages supplémentaires ont été infligés à six des cylindres d'essai, sous forme d'amincissement par corrosion artificielle, réalisée par un usinage d'érosion du bordé extérieur. Les dommages associés à la corrosion ont eu des effets différents sur la résistance des cylindres, selon l'orientation de la corrosion par rapport à l'ovalisation. Lorsque la corrosion suivait la ligne du bossage intérieur de l'ovalisation, les effets de l'amincissement et des imperfections étaient cumulatifs et ont conduit à d'importantes réductions de la pression d'affaissement. Lorsque l'amincissement de la coque était au même endroit que les lignes de bossage extérieures de l'ovalisation, les dommages attribuables à la corrosion avaient tendance à amener une réduction généralisée de l'ovalisation. On n'a remarqué qu'une faible réduction de la pression d'affaissement, due essentiellement au niveau élevé de contraintes sur le bordé aminci. On a utilisé un nombre défini de modèles d'éléments pour simuler la procédure mécanique d'ovalisation des cylindres. Le champ de contrainte résiduelle s'inscrivait dans la zone d'élasticité du matériau et les analyses subséquentes de l'affaissement indiquaient que ces contraintes résiduelles causaient une réduction de 3 % de la pression d'affaissement par rapport au modèle stabilisé (sans contrainte). On ne pense pas que les contraintes résiduelles ont eu une incidence marquée sur le comportement à l'affaissement des éprouvettes. Le nombre défini de modèles d'éléments basés sur la forme mesurée et les propriétés du métal de quarante spécimens soumis à l'essai, à l'étape actuelle et aux étapes précédentes, ont permis de prédire les pressions d'affaissement expérimentales avec une précision de 9,5 % et un degré de confiance de 95 %.

14. KEYWORDS, DESCRIPTORS or IDENTIFIERS (Technically meaningful terms or short phrases that characterize a document and could be helpful in cataloguing the document. They should be selected so that no security classification is required. Identifiers, such as equipment model designation, trade name, military project code name, geographic location may also be included. If possible keywords should be selected from a published thesaurus, e.g. Thesaurus of Engineering and Scientific Terms (TEST) and that thesaurus identified. If it is not possible to select indexing terms which are Unclassified, the classification of each should be indicated as with the title.)

submarine pressure hull; ring-stiffened cylinder; collapse pressure; corrosion; buckling; out-of-circularity

This page intentionally left blank.

Defence R&D Canada

Canada's leader in defence
and National Security
Science and Technology

R & D pour la défense Canada

Chef de file au Canada en matière
de science et de technologie pour
la défense et la sécurité nationale

www.drdc-rddc.gc.ca